NASA/CR–2014-218167

Airborne Forward-Looking Interferometer for the Detection of Terminal-Area Hazards

Leanne West, Gary Gimmestad, and Sarah Lane
Georgia Tech Research Institute, Atlanta, Georgia

Bill L. Smith, Stanislav Kireev, and Taumi S. Daniels
Hampton University, Hampton, Virginia

Larry Cornman and Bob Sharman
STAR Institute, Boulder, Colorado

February 2014

NASA STI Program . . . in Profile

Since its founding, NASA has been dedicated to the advancement of aeronautics and space science. The NASA scientific and technical information (STI) program plays a key part in helping NASA maintain this important role.

The NASA STI program operates under the auspices of the Agency Chief Information Officer. It collects, organizes, provides for archiving, and disseminates NASA's STI. The NASA STI program provides access to the NASA Aeronautics and Space Database and its public interface, the NASA Technical Report Server, thus providing one of the largest collections of aeronautical and space science STI in the world. Results are published in both non-NASA channels and by NASA in the NASA STI Report Series, which includes the following report types:

- TECHNICAL PUBLICATION. Reports of completed research or a major significant phase of research that present the results of NASA Programs and include extensive data or theoretical analysis. Includes compilations of significant scientific and technical data and information deemed to be of continuing reference value. NASA counterpart of peer-reviewed formal professional papers, but having less stringent limitations on manuscript length and extent of graphic presentations.

- TECHNICAL MEMORANDUM. Scientific and technical findings that are preliminary or of specialized interest, e.g., quick release reports, working papers, and bibliographies that contain minimal annotation. Does not contain extensive analysis.

- CONTRACTOR REPORT. Scientific and technical findings by NASA-sponsored contractors and grantees.

- CONFERENCE PUBLICATION. Collected papers from scientific and technical conferences, symposia, seminars, or other meetings sponsored or co-sponsored by NASA.

- SPECIAL PUBLICATION. Scientific, technical, or historical information from NASA programs, projects, and missions, often concerned with subjects having substantial public interest.

- TECHNICAL TRANSLATION. English-language translations of foreign scientific and technical material pertinent to NASA's mission.

Specialized services also include organizing and publishing research results, distributing specialized research announcements and feeds, providing information desk and personal search support, and enabling data exchange services.

For more information about the NASA STI program, see the following:

- Access the NASA STI program home page at *http://www.sti.nasa.gov*

- E-mail your question to help@sti.nasa.gov

- Fax your question to the NASA STI Information Desk at 443-757-5803

- Phone the NASA STI Information Desk at 443-757-5802

- Write to:
  STI Information Desk
  NASA Center for AeroSpace Information
  7115 Standard Drive
  Hanover, MD 21076-1320

NASA/CR–2014-218167

Airborne Forward-Looking Interferometer for the Detection of Terminal-Area Hazards

Leanne West, Gary Gimmestad, and Sarah Lane
Georgia Tech Research Institute, Atlanta, Georgia

Bill L. Smith, Stanislav Kireev, and Taumi S. Daniels
Hampton University, Hampton, Virginia

Larry Cornman and Bob Sharman
STAR Institute, Boulder, Colorado

National Aeronautics and
Space Administration

Langley Research Center
Hampton, Virginia 23681-2199

Prepared for Langley Research Center
under Cooperative Agreement NNX09AR67A

February 2014

Available from:

NASA Center for AeroSpace Information
7115 Standard Drive
Hanover, MD 21076-1320
443-757-5802

Executive Summary

Prior to the three-year project summarized here, radiometric efforts to detect aviation hazards were largely experimental, and they were limited to single-line-of sight broadband instruments. In general, the experiments were not adequately supported by simulation and modeling, and truth data were usually not recorded in the field, so it was not possible to know what the radiometers were looking at. Despite tantalizing results dating back to the late 1970s, radiometric detection of aviation hazards did not live up to its promise, with the exception of volcanic ash detection research, which resulted in commercial instruments. In the Forward Looking Interferometer (FLI) program, we investigated the use of imaging radiometers with high spectral resolution, using both modeling/simulation and field experiments, along with sophisticated data analysis techniques that were originally developed for analysis of data from space-based radiometers and hyperspectral imagers. By these means, we have greatly advanced the state of knowledge in this technical area, and the FLI program developed a greatly improved understanding of the radiometric signal strength of aviation hazards in a wide range of scenarios, in addition to a much better understanding of the real-world functionality requirements for hazard detection instruments.

During the course of the project, we conducted field experiments on three hazards (turbulence, runway conditions, and wake vortices) and analytical studies on several others. The main findings of the project are summarized in the sections below.

Turbulence

Clear air turbulence (CAT) remains an unsolved problem for commercial aviation, with a significant annual cost to the industry. For this reason, we studied turbulence detection extensively, beginning with modeling. The horizontal-viewing spectral radiance calculated from the U.S. Standard Atmosphere is shown in Figure 1, for three flight altitudes, in the 650 – 1650 cm^{-1} region.

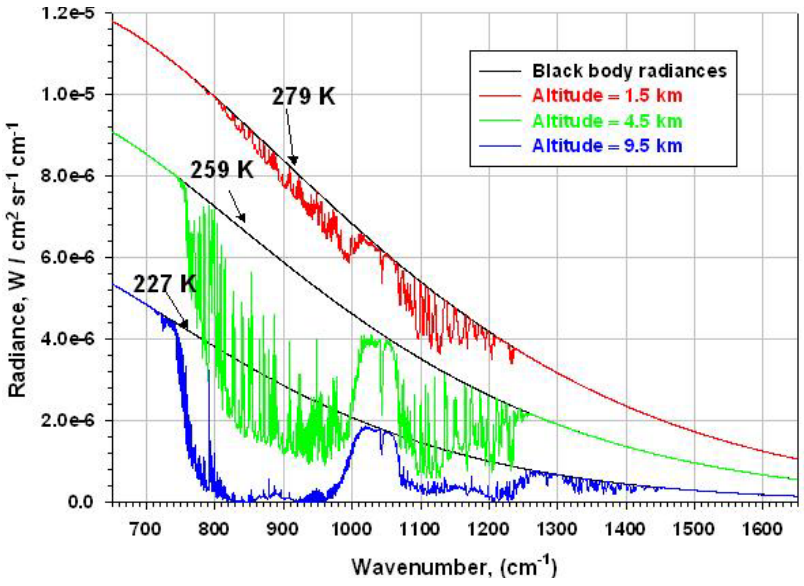

Figure 1. The spectral radiance that would be observed viewing horizontally through the U.S. Standard Atmosphere for aircraft altitudes of 1.5, 4.5, and 9.5 km (reproduced from Figure 70, page 86).

The spectral radiance predictions in Figure 1 were calculated with the standard model known as the Line-by-Line Radiative Transfer Model (LBLRTM). The spectra are primarily caused by three atmospheric gases: carbon dioxide, ozone, and water vapor. The turbulence detection strategy was based on the idea that, when turbulence is present, both the temperature profile and the water vapor concentration will be disturbed. The temperature might be sensed in the CO_2 spectrum, toward the left in Figure 1 whereas water vapor would be sensed with spectral lines toward the right.

The curves in Figure 1 show that the atmosphere is semi-transparent in the 800 – 1200 cm^{-1} region, which offers the hope that a FLI might see radiance from far enough away to provide a useful warning time. This idea was investigated by calculating the relative contributions to the received radiance that came from various ranges. The results are shown in Figure 2.

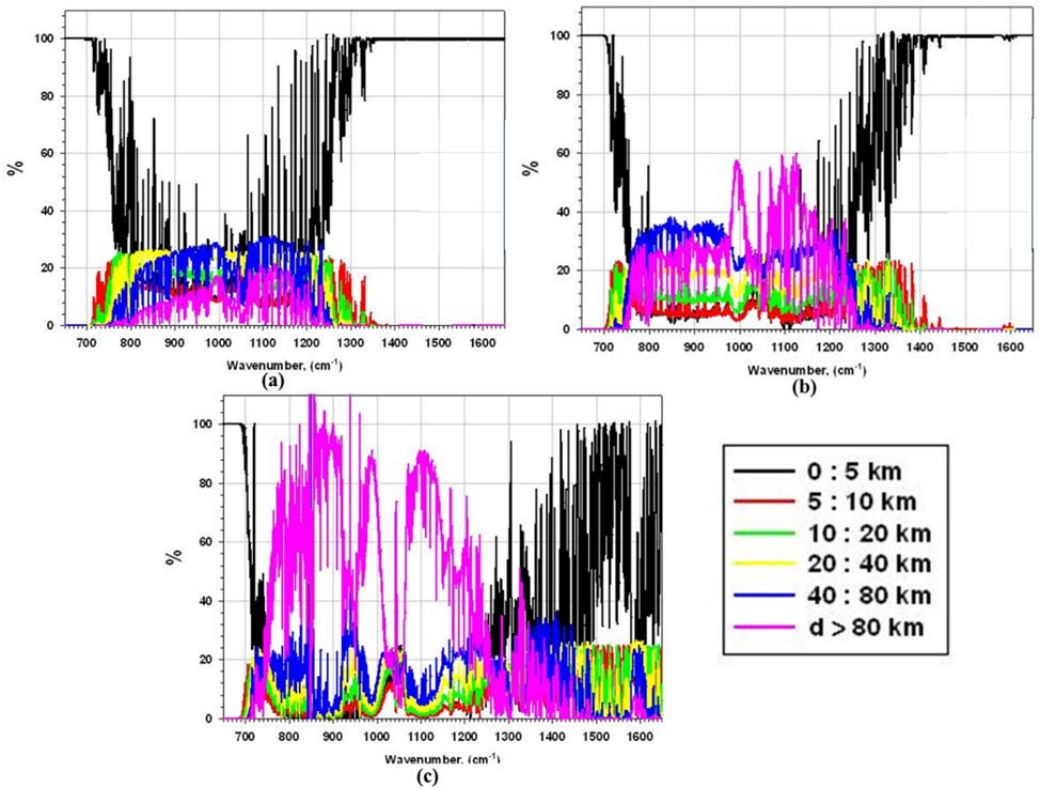

Figure 2. Contributions to the total radiance from various spherical shells along the atmospheric path observed looking forward from an aircraft at three different altitudes: (*a*) 1.5 km (~850 mb), (*b*) 4.5 km (~580 mb), and (*c*) 9.5 km (~280 mb) (reproduced from Figure 71, page 88).

Figure 2 shows that significant fractions of the radiance come from ranges as great as 80 km, and that information from various ranges is contained in different parts of the spectrum, which suggests that there is great value in using a sensor with high spectral resolution.

For cost reasons, all field experiments in the FLI project were ground based, not airborne, so the challenge was to find a scenario that could afford views of a disturbed atmosphere that might resemble CAT at flight altitudes. For this purpose, we decided to house the instruments at the Mountain Research Station (MRS), which is operated by the University of Colorado at an altitude of 9,500 feet near Ward, Colorado, during a wintertime mountain wave event. Because of a particularly severe turbulence event on 6 March 2004, a WRF model of the region was already available, and we developed simulation tools to predict the radiances that an imaging hyperspectral radiometer would have observed at the MRS for various viewing directions. The conclusion was that radiance variations within an image would be observable. Brightness Temperature Differences (BTDs) of several Kelvins were predicted for a realistic FOV and viewing direction, as shown by the typical results in Figure 3 below. The simulations were interpreted as showing that the FLI has the potential to observe the varying atmospheric state (temperature and H_2O) associated with the mountain waves of the 6 March 2004 event.

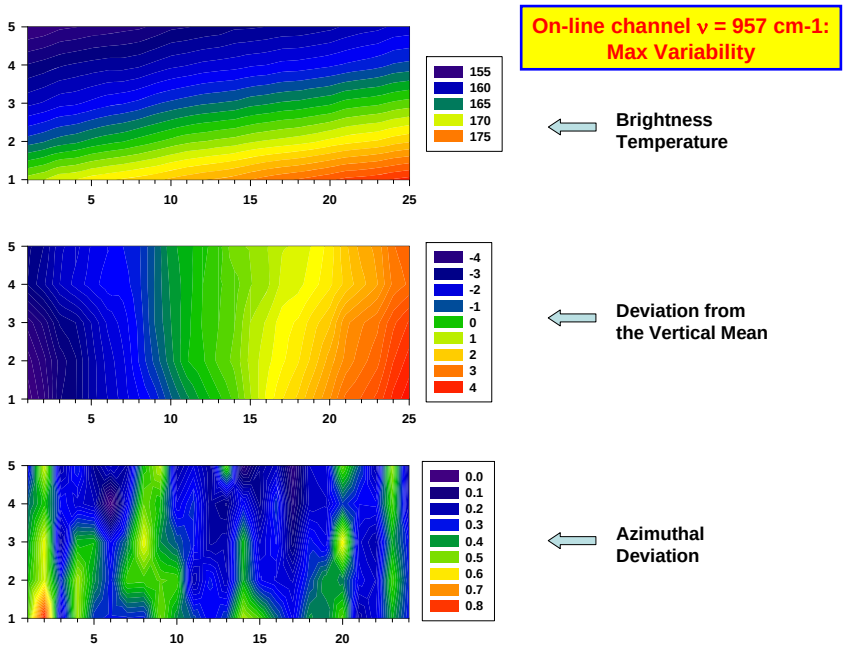

Figure 3. Simulations of radiance values in a scene at 957 cm^{-1}. *(top)* brightness temperature; *(middle)* deviations (in K) when vertical mean values are subtracted out; *(bottom)* deviations (in K) when azimuthal mean values are subtracted out (reproduced from Figure 145, page 128).

GTRI brought two radiometric instruments to the MRS field campaign: a Telops Hyper-Cam and a D&P TurboFT spectro-radiometer. They were on a common mount and boresighted, so that they were always looking at the same part of the sky. The specifications of the Telops LWIR Hyper-Cam are given in Table 1.

Table 1. Telops Hyper-Cam specifications

Parameter	**Specification**
Spectral band	7.7 – 11.5 µm
Number of pixels	320 x 256
Spectral resolution	0.25 – 150 cm^{-1}
IFOV	0.35 mrad
Communication	Ethernet
Data transfer	Cameralink
Detector cooling	Closed cycle

The specifications of the D&P Instruments TurboFT™ Spectral Sensor are given in

Table 2. The D&P is a spectro-radiometer based on a rotary Michelson interferometer, with a scan rate of 95 spectra per second. Its detectors are cooled with liquid nitrogen. Any number of spectra can be averaged together to decrease noise (we typically averaged 4 – 24).

Table 2. D&P TurboFT specifications

Parameter	Specification
Field of View	1.2° with 4-inch telescope (shown)
Detectors	HgCdTe and InSb, LN_2-cooled
Radiometric Calibration	Internal hot/cold blackbody
Spectral Range	2.55 – 16 microns
Spectral Resolution	4, 8, and 16 cm^{-1} (adjustable)
Spectral Accuracy	+/- 2 cm^{-1}
Spectral Radiance Units	W/m^2 – micron – sr
Scan Rate	95 spectra/second
Sampling Frequency	1.2 MHz
IR Signal Filter Bandwidth	512 kHz
A/D Converter	16 bits, +/- 10 V range
FFT Size	1024 – 32,768
Computer	PC compatible, portable
Operating System	Windows XP™
Operating	15 – 35 °C (59 – 95 F)
Sensor Head Size	12" L X 8" W X 8" H
Weight	10 lbs.
Power	120 VAC, 30 W maximum

Knowing that weather is very unpredictable with any type of lead time, the Science and Technology in Atmospheric Research Institute (STAR) team was watching for weather patterns that indicated high winds/turbulence. With only 3 days' notice, the GTRI team went to MRS based on STAR's prediction that high winds were likely. We conducted the field campaign during four days in November 2011. On November 17, lenticular clouds appeared over the mountains as shown in Figure 4. These clouds indicate high winds from the west, which are conducive to mountain waves. It is important to note that mountain waves themselves are a slowly varying standing wave pattern; they are not in themselves turbulent. However, turbulence is often associated with them. The test objectives were to observe the varying atmospheric state associated with the mountain waves using the Telops Hyper-Cam, and to observe the turbulence with the D&P TurboFT. (Previous experience in Boulder, Colorado in 2008 had shown features in time series of spectra recorded quickly that were interpreted as being indicative of turbulence.) Unfortunately, the D&P experienced problems in the field that resulted in unusable data.

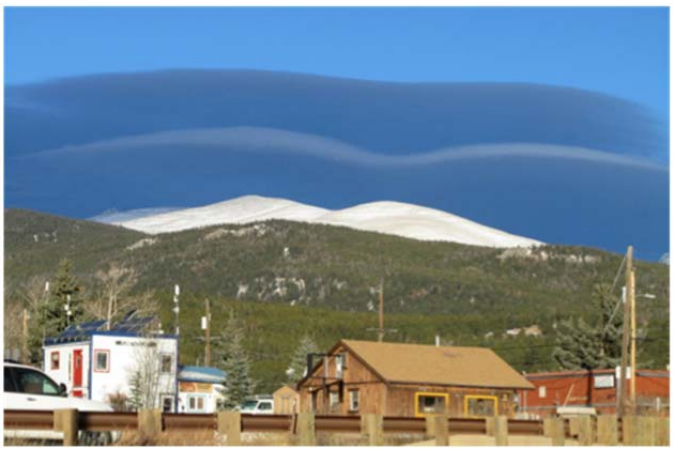

Figure 4. Lenticular clouds over the Rocky Mountains on 17 November 2011. The photo was recorded in Nederland, Colorado, looking toward the west (reproduced from Figure 185, page 154).

Despite an extensive analysis of the Hyper-Cam data, variations in the atmospheric state were not observed in the image data, either for angular variations across the scenes or for temporal variations in long series of images. For this reason post-test, we had a new WRF model developed by the National Center for Atmospheric Research (NCAR) for the conditions on 17 November 2011, and we re-ran our simulations for the viewing directions and spectral resolutions that were actually used. This post analysis showed that the radiance variations were below the noise floor of the instrument, and that fact is reflected in the sensor requirements shown in the table at the end of this summary. Another finding of the field campaign was that the ground-based scenario (even at 9,500 feet elevation where models had showed it would be sufficient) is actually not favorable for observing atmospheric state variations. This limitation, in addition to the winds not being as strong as originally predicted by STAR, are probably key reasons that the FLI program has not yet demonstrated CAT detection.

Several simulation and analysis tools were developed in the course of the turbulence efforts, including the FLI Forward Model (FLI-FM) which is much faster than LBLRTM, and several versions of a cloud clearing algorithm were implemented in Matlab for use in processing the Telops Hyper-Cam data.

Runway Surface Conditions

The concept of the runway condition investigations was that the spectral emissivities of various surfaces are significantly different in the LWIR region, as shown in Figure 5, and so an airborne spectral radiometer may be able to determine the runway surface conditions and thereby enable an estimate of stopping distance. For this reason, we made field measurements with the Telops Hyper-Cam on four different occasions, viewing natural ice and snow, as well as prepared scenes that included wet, dry, and iced surfaces.

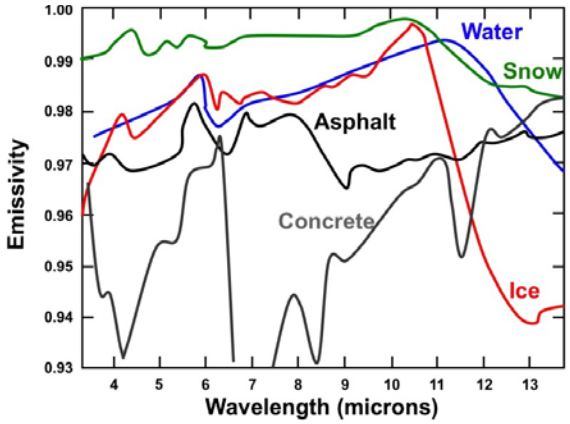

Figure 5. Spectral emissivities of various runway surfaces (reproduced from Figure 314, page 248).

The prepared scenes included a Labsphere InfraGold plate. This plate is roughened, so that it is approximately a Lambertian reflector, and it has an infrared reflectance of 97%. The purpose of the gold plate is to measure the downwelling radiance integrated over the entire sky dome, because that radiance is partially reflected into the direction of the Hyper-Cam by the various surfaces.

We implemented algorithms to retrieve both surface temperature and emissivity maps of the imaged scene, and the results are shown in Figure 6 for 1000, 1100, and 1200 cm^{-1}. The surface types are identified in the temperature map. The results shown in Figure 6 illustrate the power of hyperspectral imaging, but the analysis depended crucially on the radiance from the gold plate. Despite several attempts, were not successful in implementing a reliable algorithm to measure spectral emissivities without the gold plate in the scene.

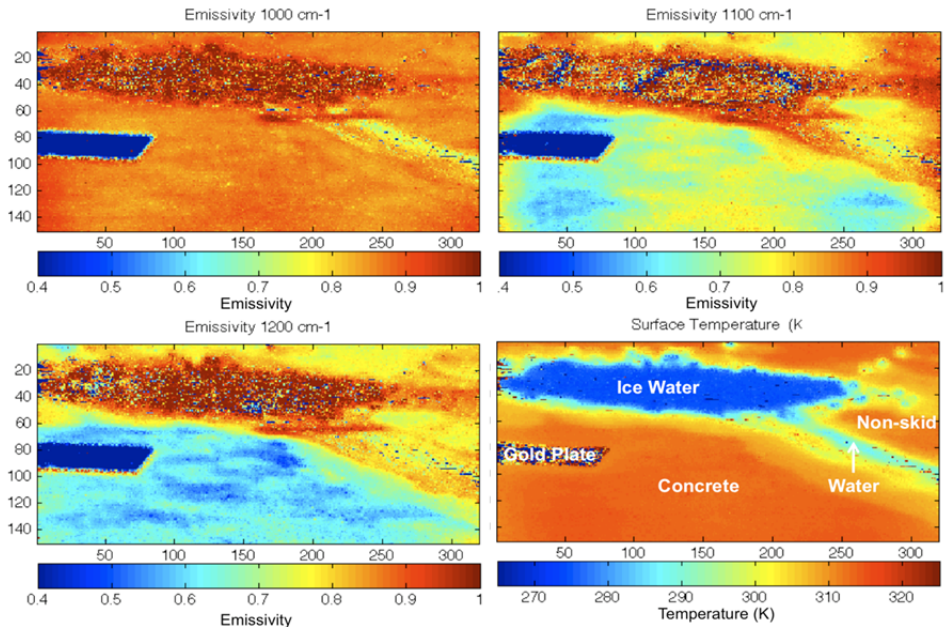

Figure 6. Derived surface emissivity for three wavelengths and the derived surface skin temperature (lower right hand panel). The dark spots are missing data due to the fact that a local emissivity variance minimum was not found in the retrieval process (reproduced from Figure 321, page 258).

Wake Vortices

We first attempted to measure radiometric signatures of wake vortices behind landing aircraft during a previous phase of the FLI program, in Madison, Wisconsin (June 2008), using a Telops MWIR Hyper-Cam and the D&P TurboFT. Analysis of the data did not reveal any detectable radiance signal from wake vortices. However, in Madison the winds were gusting, and they most likely prevented vortices from forming, or quickly moved them out of the field of view. We conducted another series of measurements in Atlanta, Georgia during July through September 2010, using the Telops LWIR Hyper-Cam. Atlanta is an ideal site, being the busiest airport in the world and only 20 minutes away from GTRI. These tests were meant as pre-tests to another larger data collection activity to make sure we knew what settings we needed for the main activity. We obtained permission to set up equipment in an unused lot directly in line with a runway, viewing aircraft landing from the east in calm conditions. We performed the measurements on several occasions.

Despite a very extensive and thorough analysis of the resulting images data, we did not observe radiometric features of wake vortices. We did find exhaust trails immediately after an aircraft passed through the field of view, as shown in Figure 7. In this case, the Matched Filter algorithm was used, and the target spectrum was water vapor, which is a major combustion product. Many other algorithms and target spectra were used in the analysis, including the Adaptive Matched Filter and the Adaptive Cosine/Coherence Estimator. In cases where the vapor trail was observed, the background was modeled in a new way, and was described in an SPIE paper contained in Appendix C of this report.

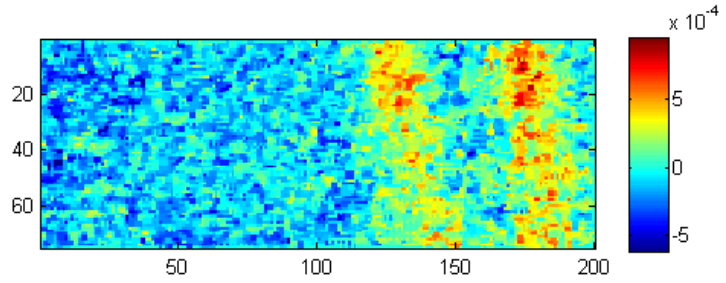

Figure 7. The Matched Filter results on datacube 1452 (reproduced from Figure 52, page 78).

New simulations later showed there is a small, but evident, temperature and moisture structure signature of the wake vortex disturbance, as shown in Figure 8. Wake vortex radiance simulations were then conducted using FLI-FM2 to estimate the magnitude, and spectral location, of the signal.

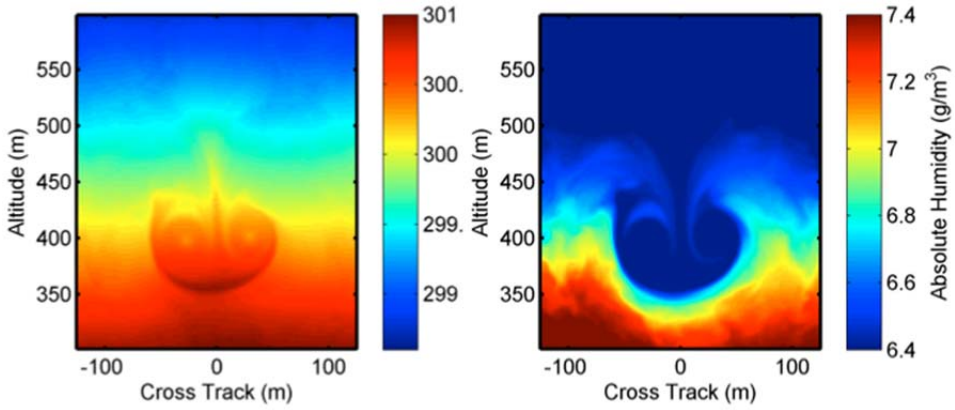

Figure 8. The temperature *(left panel)* and moisture *(*right *panel)* distribution associated with the wake of a Boeing 747 jet aircraft (reproduced from Figure 31, page 63).

Three regions were found where the wake vortex signal is a maximum; these are located at 700 cm^{-1}, 1250 cm^{-1}, and 2000–2200 cm^{-1}, as shown in Figure 9. These regions are all on the edge of, or outside of, the MWIR and LWIR atmospheric windows and hence commercial imagers do not exist for them. Previous simulations had shown that the MWIR and LWIR regions would be of use.

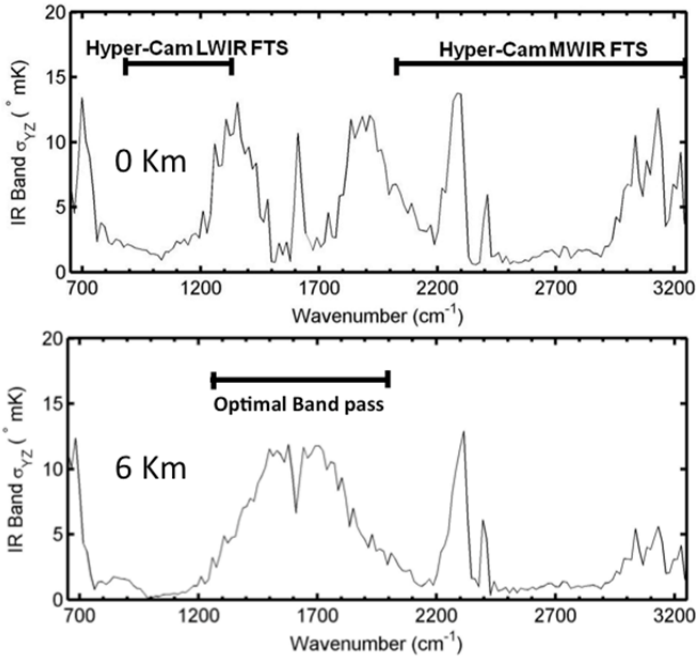

Figure 9. The standard deviation of the radiance spectrum (natural elevation angle dependence removed) as would be observed with a spectral resolution imaging spectrometer operating at a spectral resolution of 16 cm^{-1} at two different aircraft altitudes, 0 km and 6 km (reproduced from Figure 33, page 64).

Other Hazards

Other hazards investigated include volcanic ash, low visibility, and icing in flight. In addition, the distance to the hazard was also assessed.

Volcanic Ash: Detection of volcanic ash has not been investigated by the FLI team since methods of modeling the movement of volcanic ash (PUFF model) and instruments for its detection (Airborne Hazards Detection System, Norwegian Institute for Atmospheric Research) were being commercialized at approximately the same time as this investigation. This report summarizes the literature and patents related to volcanic ash detection.

Low Visibility: Based on the sensitivity studies in the previous Phase 1 FLI project, an imaging FLI spectrometer is expected to provide enhanced vision in the cockpit of an aircraft in low visibility conditions. An algorithm was demonstrated under a restricted set of aircraft altitude and atmospheric conditions. Data of varying visibility due to fog was collected in Atlanta on several occasions. However, after initial preview, it was determined that data collected in thirty-minute intervals on the same day would be better suited for the analysis. The project team was unable to collect this sporadic weather condition during the remainder of the project.

Icing: In-flight icing could not be studied during this program, since no flight tests were conducted. However, previous investigations have shown that the indices of refraction for ice and water differ starting at 11 μm, therefore providing the opportunity for differentiation. That knowledge combined with the knowledge of the temperature of the cloud to diagnose the

existence of supercooled liquid water in clouds could be used to detect water droplets at sub-freezing temperatures that cause airframe icing.

Distance to Hazard: The ability to determine the distance to a hazard relies on the collection of high spectral resolution data (1 cm-1). Because we have shifted to lower spectral resolution data (16 cm-1) to try to detect the signal of the hazards, we have inherently lost the ability to determine the distance to the hazard using the CO2 line structure. However, an additional dedicated detector with two narrowband filters that can look at the amplitudes of the CO2 lines has been proposed as the method of determining the distance to the hazard should the FLI instrument be developed.

Instrument Requirements

We developed a set of instrument requirements for detecting the hazards listed above. These requirements are listed in Table 3. Each hazard is listed with its primary wavelength region of detection, resolution, sensitivity, and any caveats that might exist.

Table 3. Instrument requirements for hazard detection (reproduced from Table 20, page 289).

Hazard	Wavelength Region	Resolution	Sensitivity	Caveat
Wake Vortices	5 – 8 μm	Broadband	1 mK	5 – 8 μm is the opaque region of the atmosphere, and sensors do not exist for this range
Mountain Wave Turbulence	LWIR window region (8 – 12 μm)	16 cm^{-1}	50 mK	Other wavelength regions cannot be excluded because they were not studied during this program
Runway Surface Conditions	LWIR window region (10 – 12 μm for ice/water discrimination)	1 – 4 cm^{-1}		Cannot omit gold plate in calculation of absolute emissivity)
Runway Obscurations (animals)	LWIR or MWIR			Any thermal imager will work (does not require radiometric accuracy).
Low Visibility	LWIR	2.5 cm^{-1}		
Distance to Hazard	CO_2 lines in MWIR, edges of LWIR window	1 cm^{-1}		
Volcanic Ash	6 – 13 μm	Broadband microbolometer with narrowband (0.5 – 1.0 μm) filters	50 mK	This commercialized instrument uses five cameras with narrowband filters at specified bands (including SO_2) [1].
Icing	11 – 17 μm	4 cm^{-1} or less		Differences in slope of the indices of refraction will indicate differences in ice/water. Use this knowledge in conjunction with knowledge of temperature to indicate supercooled liquid.

Table of Contents

Table of Figures

Table of Tables

List of Acronyms, Abbreviations, and Symbols

ACE	Adaptive Cosine/Coherence Estimator
AERI	Atmospheric Emitted Radiance Interferometer
AFIT	Air Force Institute of Technology
AFM	AERI Fast Model
AHDS	Airborne Hazards Detection System
AIAA	American Institute of Aeronautics and Astronautics
AIRIS	Airborne Infrared Imaging Spectroscopy (DRDC-Valcartier)
AMF	Adaptive Matched Filter
ASTER	Advanced Spaceborne Thermal Emission and Reflection Radiometer
ATL	Hartsfield-Jackson International Airport, Atlanta, GA
BOT	Bottom (related to atmospheric layers)
BT	Brightness Temperature
BTD	Brightness Temperature Difference
C1	Site at MRS where meteorological station is located
CAPABLE	Chemistry and Physics Atmospheric Boundary Layer Experiment
CAT	Clear Air Turbulence
CMF	Clutter Matched Filter
CSIRO	Commonwealth Scientific and Industrial Research Organisation
CrIS	Cross-track Infrared Sounder
DEN	Denver International Airport, Denver, CO
DFT	Discrete Fourier Transform
DRDC	Defence Research and Development Canada
D&P	Designs and Prototypes
EDR	Eddy Dissipation Rate
EMI	Electromagnetic Interference
FFM	Fast Forward Model
FFT	Fast Fourier Transform
FLI	Forward Looking Interferometer
FLI-FM	FLI Forward Model
FLI-FM2	FLI Forward Model, version 2

FOR	Field of Regard
FOV	Field of View
FPA	Focal Plane Array
FTS	Fourier Transform Spectrometry/Spectrometer
GOES	Geostationary Operational Environmental Satellite
GTRI	Georgia Tech Research Institute
GUI	Graphical User Interface
HISE	Hyperspectral Imaging and Sounding of the Environment
HU	Hampton University
Hz	Hertz
IASI	Infrared Atmospheric Sounding Interferometer
IR	Infrared
JAIVEx	Joint Airborne IASI Validation Experiment
JPL	Jet Propulsion Laboratory
K	Kelvin
LaRC	Langley Research Center
LBLRTM	Line-by-Line Radiative Transfer Model
LW	Long-wave
LWIR	Long-wave Infrared
MF	Matched Filter
MODIS	Moderate Resolution Imaging Spectroradiometer
MRS	Mountain Research Station
MW	Mid-wave
MWIR	Mid-wave Infrared
NASA	National Aeronautics and Space Administration
NESR	Noise Equivalent Spectral Radiance
NFOV	Narrow Field of View
NPP	National Polar-orbiting Partnership
OD	Optical Depth
OPD	Optical Path Difference
OSA	Optical Society of America
PIREP	Pilot Report
PUFF	Volcanic Ash Tracking Model
R	Radiance

RH	Relative Humidity
RMS	Root Mean Square
RT	Radiative Transfer
SAM	Spectral Angle Mapper
SFO	San Francisco International Airport, San Francisco, CA
SPIE	The International Society for Optics and Photonics
SSEC	Space Science and Engineering Center
STAR	Science and Technology in Atmospheric Research Institute
T	Temperature
TASS	Terminal Area Simulation System
TSAD	Temporal-Spectral Anomaly Detector
TSCD	Temporal-Spectral Covariance Detector
T&E	Temperature and Emissivity
UCAR	University Corporation for Atmospheric Research
UCSB	University of California, Santa Barbara
UTC	Coordinated Universal Time
Q	Water Vapor
WFOV	Wide Field of View
WRF	Weather Research and Forecasting
maxOPD	Maximum Optical Path Difference
netCDF	Network Common Data Form
rad	Radian
sr	Steradian
vmr	Volume Mixing Ratio
α	Azimuth angle
β	Elevation angle
ε	Emissivity
ρ	Normalized Correlation Function (D&P Analysis)
ρ	Reflectivity (Emissivity Analysis)
τ	Transmittance
ν	Wavenumber (cm^{-1})
ω	Frequency
σ	Standard Deviation

Technical Report

This Final Report under Task NNX09AR67A was prepared by personnel at the Georgia Tech Research Institute (GTRI), Hampton University (HU), and the Science and Technology in Atmospheric Research Institute (STAR). Work under this project supports NASA work objectives under the Integrated Intelligent Flight Deck Technologies Research Program, specifically "development of a comprehensive surveillance system design that enables robust detection of external hazards with sufficient time-to-alarm for safe maneuvering to avoid the hazards."

1 Background

The only forward-looking airborne sensor that is currently certified for commercial aviation is the weather radar. As a result, if an external hazard is invisible to both radar and out-the-window human vision, it will go undetected, with potentially disastrous results. Hazards in this category include clear air turbulence (CAT), wake vortices, dry wind shear, volcanic ash, icing conditions, and runway hazards that go undetected due to reduced visibility. In this report, we describe modeling, testing, and analysis of a new sensor concept for detecting such invisible hazards in the terminal area and in flight: an infrared imaging system with high spectral resolution. In addition to its unique capabilities envisioned for specific in-flight hazards, such a sensor can also operate as a conventional infrared imager, which enhances human vision by providing night vision and by improving vision through obscurants such as fog and haze. The sensor's capability to detect runway condition hazards (water, ice, snow, or objects) was also investigated.

Efforts to detect aviation hazards with passive infrared (IR) sensors have a long history. In the late 1970s, Peter Kuhn developed an IR radiometer [4] that was flown and tested on three NASA aircraft, including the Galileo II flying laboratory during the 1979 Clear Air Turbulence Flight Test Program [5]. Kuhn's passive IR system was designed to detect CAT by sensing water vapor variability ahead of the aircraft, (in non-CAT conditions, the water vapor content was assumed to be constant). Several radiometric passbands were investigated, and the 26 – 35 μm (286 – 385 cm^{-1}) region was claimed to be optimal. The radiometer had a single line of sight aimed at an angle of 11 degrees above the horizon. The signal was sampled at one Hz, and its standard deviation was calculated every six seconds as the aircraft flew toward the turbulent region. An increase in the standard deviation of the signal ("IR emission anomalies") was taken as an indication of fluctuations in water vapor concentration ahead of the aircraft. Successful detections of CAT were reported at altitudes above 4.4 km, with a range of up to 60 km and alert times ranging from one minute at 4.4 km altitude increasing to four minutes at 11.3 km. The flight tests resulted in 194 turbulence encounters. The false-alarm rate was less than 8% in non-cloud conditions, and only four percent of the turbulence encounters were not preceded by an alert [6].

In the mid-to-late 1980s, the Commonwealth Scientific and Industrial Research Organisation (CSIRO) Division of Atmospheric Research, located in Melbourne, Australia, developed an airborne passive IR radiometer that employed a two-band technique for detecting volcanic ash.

The researchers published several papers on both theoretical and experimental aspects of volcanic ash detection with their technique [7], [8], [9], [10], [11]. At that time, CSIRO expected the ash cloud detection distance to be 100 - 200 km and planned further research. Several different versions of the CSIRO radiometer were constructed and tested over the next few years, including a pod-mounted sensor that was flown in Tasmania and another version that was flown in Japan inside an aircraft cabin, looking out through an open port.

Beginning in 1990, CSIRO held discussions with a number of airline and aerospace companies in the U.S. in an effort to commercialize the ash sensor. They were advised that a multi-function hazard warning system would receive far greater acceptance in the industry, so CSIRO investigated passive IR detection of other hazards including low-level clear air turbulence, sulfur dioxide (SO_2), and sulfuric acid (H_2SO_4). The multi-function system was named the Airborne Hazard Detection System (AHDS). In March 1991, volcanic ash clouds were detected in ground-based tests in Japan near Mt. Sakurajima. Following these trials, CSIRO obtained patents, including US Patent No. 5,602,543, *Detection System for Use in an Aircraft*.

The AHDS was an imaging radiometer with a 10 x 10 degree field of view. It incorporated five different IR passbands ranging from 6.8 to 11.9 μm for detecting volcanic ash, CAT, sulfur dioxide (SO_2), and sulfuric acid (H_2SO_4). Warning time estimates were between 3 and 6 minutes. In October 1999, CSIRO presented the AHDS to a number of airline and aerospace companies with the hopes of commercializing the technology, but this effort was not successful. The system was eventually commercialized by the Norwegian Institute for Atmospheric Research [1].

In 1986, NASA and the FAA jointly set a timetable for developing and demonstrating a solution to the aviation hazard that was responsible for more than half of the U.S. commercial aviation fatalities of the previous decade: low-level windshear. Several detection technologies were investigated, including radar, Doppler lidar, and infrared radiometry. During the course of this effort, five NASA - FAA windshear conferences were held, with the most recent one in September 1993. During the windshear research effort, passive infrared (IR) detection was studied extensively by H. P. Adamson, who founded the Turbulence Prediction System (TPS) Company to commercialize IR sensors. Most of Adamson's work is described in the proceedings of the NASA - FAA windshear conferences.

In the early 1990s, the first observations of apparent infrared signatures associated with wake vortices were reported by Adamson and Morrison [12]. Under a NASA SBIR Phase 1 contract, Adamson used a scanning multi-band radiometer to make low-resolution images of wake vortices, using a two-band differential signal processing technique to maximize the system's response at a desired range [13]. The vertically-pointing radiometer was positioned so that aircraft would fly over it as they landed on Runway 26L at the Denver Stapleton airport. The scanning technique provided low-resolution images with 2° x 2° pixels arranged in four rows and seven columns (28 pixels total) for an 8° x 14° composite field of view. In each pixel, the difference between the radiometric temperature and the ambient temperature was calculated in degrees Celsius. Images with no aircraft were included to show the noise level, which was +/- 1 $^\circ$C. The time required to acquire one image was 30 to 60 seconds.

Two data sets were collected, during midday on May 12 and May 18, 1993 in calm conditions with temperatures of 24-25 °C and relative humidity 30-33%. Sky conditions were not given. The data sets show the infrared signatures associated with the wakes behind two different types of aircraft, a McDonnell-Douglas DC-10 and a Boeing 727. Because of the low temporal and spatial resolution of the measurements, the data were said to indicate the radiometric temperatures associated with aircraft wakes, but they do not show the structure or motion of vortices.

The radiometric data were acquired from about thirty seconds before the DC-10 flew over the instrument until about ninety seconds after, for both types of aircraft. The vortex signature was normally a cold infrared wake at -2 to -3 °C below ambient, although the DC-10 produced a temperature difference of -7 °C on one occasion. The data indicated that the 727 had a warm wake on one occasion.

In the early 1990's, Kuhn and Sinclair revisited the CAT problem and developed an 'S' layer model to describe the instabilities that lead to clear air turbulence and derived the specifications of a forward looking infrared (FLIR) sensor system capable of detecting the clear air turbulence hazard [6]. Kuhn and Sinclair's specifications are given in Table 4.

Table 4. FLIR Sensor System Specifications

Wavelength	12.8 to 14.3 μm
Field of View	10°
Bandwidth	1.5 μm
Noise Equivalent Radiance	0.169×10^{-6} W/cm^{2}sr
	at a scanning rate of 1 frame/second
Detector	HeCdTe with
	Area = 1×10^{-4} cm^2/pixel
Optics Area	125 mm^2
Optics Transmission	0.32

The 'S' layer model was developed from flight tests conducted by the Air Force during the High Altitude Clear Air Turbulence (HICAT) program. Kuhn and Sinclair claimed that large angle crossings of the horizontal temperature variations that comprise the 'S' Layers are necessary. Flight paths parallel to warm and cool troughs and ridges were said to yield insignificant temperature variations.

More recently, during the AWIN (Aviation Weather INformation) program, GTRI investigators reviewed infrared radiometric techniques for hazard detection and recommended that future work include flight tests with a hyperspectral imager [14].

The prior work on radiometric hazard sensors was reviewed in 2001 by Gimmestad, et al. who recommended that the atmospheric IR signatures of aviation hazards should be studied and documented on flight tests with a forward looking hyperspectral imaging system, and that the tests must include truth data [14]. The recommended flight tests were intended to provide basic data that would enable the development of optimized airborne sensors that would provide both high probability of detection and low false alarm rate.

This long history of investigations into airborne IR radiometric detection of aviation hazards provided examples of apparent detections of both CAT and wind shear, as well as a data set that was interpreted as images of wake vortices. In addition, ground-based radiometric detection of volcanic ash clouds was demonstrated. However, all of the early work was performed with simple instruments that had low spectral, spatial, and radiometric resolution, and many of them employed a single line of site. The detections were generally not supported by truth data, and the atmospheric conditions that the radiometers were responding to were characterized poorly, if at all. Because the atmospheric state was not known, the performance of the radiometers as hazard sensors could not be checked with numerical simulations. These problems led Gimmestad et al. to recommend that flight tests should be conducted with a hyperspectral IR imaging system; that the flights should include truth data; and that the measurement effort should be supported by a parallel simulation effort. The study reported here is an outgrowth of those recommendations aimed specifically at assessing the feasibility of using a hyperspectral IR imaging system for aviation hazard detection.

The Forward Looking Interferometer (FLI) concept is based on high-resolution infrared Fourier transform spectrometry technologies that have been developed for satellite remote sensing. To meet the needs of the commercial fleet, such a sensor should address multiple hazards to warrant the costs of development, certification, installation, training, and maintenance. In the first two phases of the FLI project, the instrument was evaluated for its potential to address multiple hazards during all phases of flight (takeoff, cruise, and landing) including wake vortices, low slant range visibility, dry wind shear, icing, clear air turbulence (CAT), and volcanic ash [15] [16] [17]. In this report, we summarize the results of the entire three-year project.

2 Yearly Summaries

The work discussed in this Final Report was part of a planned three-year project which included these major tasks:

1. Develop improved sensor models and hazard metrics;
2. Validate models and simulations by comparing predicted results to empirical data; and
3. Conduct ground-based field measurements focused on mountain waves and CAT.

Each of these three tasks is summarized by Year in the subsections below. Our technical accomplishments during the entire project are described in detail in the remainder of this report.

2.1 Year 1 Summary

This section of the report gives a brief summary of work completed in Year 1 [18].

Runway Surface Conditions and Obstructions: In the first year several ground-based measurements were conducted. These ground-based measurements included iced and wet asphalt/concrete; runway surroundings such as terrain; and wildlife (with another LWIR imager).

Low Visibility Measurements: Unfortunately in Year 1 reduced visibility conditions, such as fog and smoke, were not present after acquisition of the Telops Hyper-Cam; these measurements were completed in Year 2.

ATL Wake Vortex Measurements: Year 1 included a small-scale ground-based data collection activity at Hartsfield-Jackson (ATL) with the Telops Hyper-Cam as a precursor to the full data collection for the detection of wake vortices that was originally planned for SFO in Year 3. The data collection activities were coordinated with personnel from ATL and Jacoby Development, the company that owns the property on which we were physically located during the data collection activity. Overall, three visits to ATL occurred in Years 1 and 2.

Plan SFO Wake Vortex Measurements: Planning for the larger-scale data collection activity in SFO began; however, during the WakeNet Conference, it was learned that the SFO WindTracer Lidar was temporarily inoperable and that ATL had a WindTracer installed. Financially, operationally, and logistically it made sense to have the data collection activity in ATL. Therefore, the field test was officially moved from SFO to ATL.

Model Validation: Several activities that underlie model validation and updates occurred during Year 1; this, however, is an ongoing process. These activities included wake vortex simulations for comparison with actual data, Line-by-Line Radiative Transfer Model (LBLRTM) calculations, and a Fast Forward Model Development.

Wake Vortex Model Simulations: Hyper-Cam radiance simulations were conducted with wake vortex model data provided by Dr. Fred Proctor. We analyzed data for heavy aircraft typical of what was observed by the Hyper-Cam during measurements conducted at ATL. Also, we used the model simulations to simulate what a FLI would see from an aircraft at 1 km altitude (i.e. on takeoff or landing behind a heavy commercial aircraft). Simulations show small sensitivity to the temperature and water vapor variability produced by a wake vortex.

Hyper-Cam Line-by-Line Radiative Transfer Model (LBLRTM) Calculations: LBLRTM calculations were performed using radiosonde measurements conducted from Peachtree City for comparisons with the sky viewing Hyper-Cam measurements made at GTRI on different occasions. These comparisons were used to evaluate the spectral and radiometric calibration accuracy of the Hyper-Cam measurements.

A Fast Forward Model Development: A Fast Forward Model (FFM) was developed to produce rapid calculations of Hyper-Cam radiances from atmospheric state conditions as well as for use in an inverse radiative transfer model for retrieving atmospheric state parameters from Hyper-Cam measurements. Comparisons with time-consuming Line-by-Line calculations indicate an accuracy of the FFM calculations close to the observational errors of the Hyper-Cam observations.

Instrument Requirements: Development of instrument requirements was an ongoing task and was not specifically addressed in Year 1.

2.2 Year 2 Summary

This section of the report gives a brief summary of work completed in Year 2 [19].

Wake Vortices: Three separate field campaigns for the collection of wake vortex data were conducted at ATL during the summer and fall of 2010 (during Years 1 and 2) in preparation for a full-scale field campaign at either SFO or ATL (later determined to be ATL). The Telops Hyper-Cam was used to collect hyperspectral image data cubes. The main purpose of these tests was to test look angles, data collection parameters, and length of data collection episodes. Additionally it was hoped that wake vortices could readily be seen in the data based on previous modeling and analysis.

Wake vortex data collected with the Telops Hyper-Cam at Hartsfield-Jackson International Airport (ATL) was analyzed by both the GTRI and Hampton University teams. Hyperspectral gas detection algorithms were used in an attempt to detect wake vortices by finding the exhaust gases they entrain. A methodology for the detection of wake vortices by utilizing these gas detection algorithms was presented; while the method does not detect vortices in the data, the directional averaging of sky radiance in the target/background modeling shows what appear to be vapor trails following the aircraft. The results were inconclusive as to whether the exhaust gases were actually being detected or some other disturbance was being seen. However, this method of breaking up the background demonstrates a novel way to detect mixed pixel targets against sky backgrounds; this method yielded results when other similar methods did not. The results warrant more study, since the possible detection of a turbulent effect, though not a vortex, is still relevant to the FLI program. This work was presented at SPIE in August 2011 [20].

Mountain Wave Turbulence: Turbulence associated with mountain waves came to the forefront of the remaining research effort for this program in place of wake vortices. Therefore, while always having been a part of the overall program, the main data collection field campaign was focused on detection of mountain waves. Analysis of previously collected hyperspectral data was re-visited and analyzed, new data for comparison was collected, and a site visit for Year 3's field campaign near Boulder, CO was conducted.

Runway Surface State and Contamination: As a secondary priority, runway surface state and contamination was studied with hyperspectral imaging. Emissivity images, obtained from an aircraft-mounted Forward Looking Interferometer (FLI), are intended to be used to alert the pilot of hazardous landing runway surface conditions and enable the determination of runway friction and associated stopping distance for a particular aircraft. This hazard detection technique is based on the fact that different surfaces have different emissivity spectra in the LWIR spectral region, where the FLI operates. Ground-based measurements taken during Year 2 included: ice; snow; wet/dry asphalt and concrete; and runway surroundings/hazards such as terrain, wildlife, and vehicles. Data was analyzed and a conference paper was presented at the Optical Society of America (OSA) Hyperspectral Imaging and Sounding of the Environment (HISE) conference in July 2011 [21].

Low Visibility: As a secondary priority, reduced visibility conditions (such as fog) were exploited when they occurred to measure hyperspectral images of concrete/asphalt and buildings in these conditions. The main purpose of these measurements was to provide hyperspectral data to investigate a technique that was developed and reported in a previous phase of the FLI project. The technique is aimed at mitigating reduced visibility during landings in obscured conditions.

2.3 Year 3 Summary

This section of the report gives a brief summary of work completed in Year 3 of the current FLI project [22].

Fast FLI Forward Radiative Transfer Model: Updates to the Fast FLI Forward Radiative Transfer Model (FLI-FM) and verification by comparison with Line-by-Line Radiative Transfer Model (LBLRTM) were completed. Much of the modeling and simulation, regardless of the hazard under investigation, was accomplished using the updated FLI-FM2.

Wake Vortices: An overview of infrared FTS for the detection of wake vortices was given during Year 3 in a brief summary from Taumi Daniels' thesis [23]. Wake vortex models developed by Daniels using TASS and LBLRTM were described and are expanded to include FLI-FM2 simulations.

Mountain Wave Turbulence: Mountain wave turbulence was the main hazard under investigation during Year 3. Mountain wave turbulence FLI-FM models and simulations were completed in order to provide guidance for test planning at the Mountain Research Station (MRS). The data collection activity, which was designed in an effort to capture turbulent signals in the atmosphere over the Colorado Rockies, was completed in November 2011. Analysis of MRS data included data correction (including calibration issues, bad pixel replacement, and cloud removal), temporal variability analysis, gas detection analysis, and temporal anomaly analysis.

Runway Surface Conditions and Obstructions: The ability to detect the surface emissivity for various types of runway surface conditions with a FLI is important for the determination of runway friction and aircraft stopping distance. During Year 2, ground-based emissivity measurements were made of ice, snow, and wet/dry asphalt and concrete. The subsequent analysis of these measurements demonstrated a methodology for the detection of hazardous surface conditions; however, the ice and concrete measurements were set up (i.e. artificial man-made conditions, not natural ice). Only one opportunity for measurements of natural ice and snow occurred during Year 2, but it was not fresh (the snow had iced over). During Year 3, the opportunity arose to make the same measurements in a natural environment that was more representative of a hazardous runway condition.

Volcanic Ash: Detection of volcanic ash has not been investigated by the FLI team, as methods of modeling the movement of volcanic ash (PUFF model) and instruments for its detection (Airborne Hazards Detection System, Norwegian Institute for Atmospheric Research) already exist. A summary of the relevant literature and patents was given.

Distance to the Hazard: The ability to determine the distance to a hazard relies on the collection of high spectral resolution data (1 cm^{-1}). Over the last year, we have shifted to lower spectral

resolution data (16 cm^{-1}) to try to detect the signal of the hazards. As such, we have inherently lost the ability to determine the distance to the hazard using the CO_2 line structure. However, an additional dedicated detector with two narrowband filters that can look at the amplitudes of the CO_2 lines has been proposed. Note that these lines appear in the mid-wave infrared (MWIR). Detection has focused on the long-wave infrared (LWIR). Therefore a dedicated detector would be in the MWIR, while the hazard detection detector would be in the LWIR.

3 Fast FLI Forward Radiative Transfer Model

3.1 Atmospheric Profile Retrieval Algorithm

Because of the small unique spectral radiance signals produced by different surface types, as well as those produced by wake vortices, a very accurate specification of natural atmosphere signals is required to validate the radiometric signatures of these surfaces and wake vortex phenomena. A new combined surface and satellite profile retrieval method was developed and tested with the upward-looking ground-based ASSIST (an AERI-like instrument) interferometer and downward-looking MetOp satellite IASI (Infrared Atmospheric Sounding Interferometer) data. The ground-based radiometric measurements are optimal for profiling the lowest levels of the atmosphere, whereas the satellite measurements are optimal for profiling the free atmosphere thermodynamic structure. Figure 10 shows a result obtained at NASA Langley on August 11, 2009. An IASI-only atmospheric retrieval was used as an initial condition for the combined retrieval. The IASI-only retrieval is erroneously cold and dry below the 2-km (i.e. 800 hPa) level due to unaccounted-for cloud attenuation. The small-scale atmospheric boundary layer structure retrieved through the use of the ground-based interferometer data is noteworthy. This atmospheric retrieval technique was developed early in the program so that it could be applied to the surface emissivity and wake vortex measurement experiments.

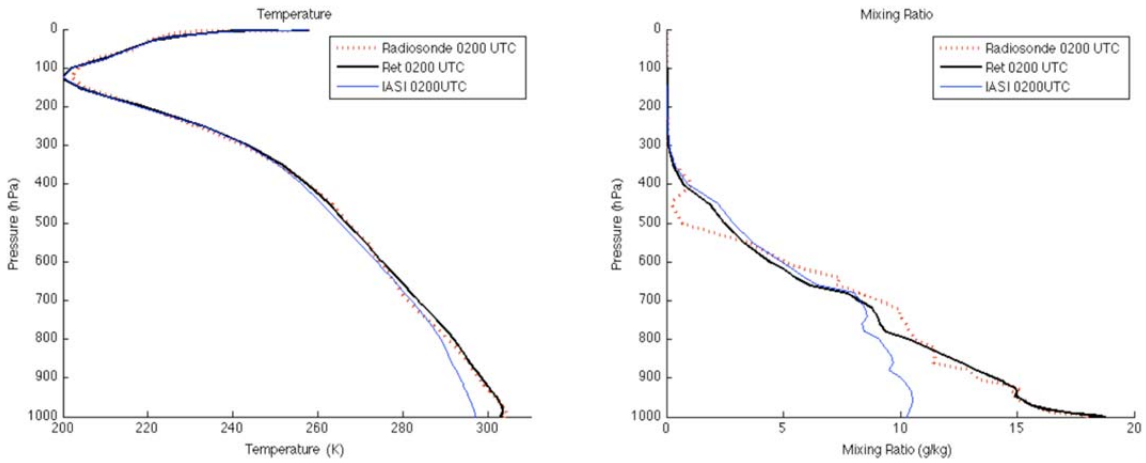

Figure 10: Atmospheric profile retrievals of temperature and moisture using ground-based and satellite interferometer data obtained over NASA LaRC on August 11, 2009. A near simultaneous radiosonde observation is shown to validate the result.

3.2 Cloud Emissivity Modeling

A training set of data for predicting the effective cloud emissivity to be used for simulating the influence of clouds on FLI spectral radiance measurements was prepared. Taking into account the cloud contribution to the observed radiance is important for the specification of runway visibility from FLI measurements and determining aviation weather hazards (e.g. turbulence). Cloud removal algorithms for measured data will be described in Section 5.3.7.

3.2.1 Method

Actual NAST-I radiances, obtained during the JAIVEx validating campaign, were used to obtain estimated spectra of cloud emissivity. Heavy cloud conditions (the day of April 27, 2007) were chosen for this purpose. Two kinds of retrievals, called "clear" and "cloudy," were produced for each input radiance. The "clear" retrieval corresponds to clear-sky conditions (no clouds), and the "cloudy" retrieval is obtained under a simulation of cloudy conditions. The latter one was reached by setting the temperature profile to be isothermal below the cloud altitude; the regression predicting matrix was derived from the training sets of atmospheric states and corresponding calculated radiances. The isothermal atmospheric state is equivalent to the opaque region for IR radiative transfer. Both kinds of retrievals were produced with a dual physical-statistical retrieval algorithm developed at HU. The level where "clear-trained" and "cloudy-trained" retrieved temperature profiles begin to split (looking from the top to the bottom of the atmosphere), provides an estimate of cloud top altitude, cloud fraction, and effective cloud emissivity.

If $R_{CLR}(v)$ and $R_{CLD}(v)$ are radiances, computed for "clear-trained" and "cloudy-trained" retrieved atmospheric states respectively, then effective cloud emissivity $\varepsilon^*_{CLD}(v)$ can be derived from the following relation:

$$R_{OBS}(v) = \varepsilon^*_{CLD}(v) \times R_{CLD}(v) + (1 - \varepsilon^*_{CLD}(v)) \times R_{CLR}(v) \tag{3.2.1}$$

Which results in the effective cloud emissivity, $\varepsilon^*_{CLD}(v)$:

$$\varepsilon^*_{CLD}(v) = \frac{R_{CLR} - R_{OBS}}{R_{CLR} - R_{CLD}} \tag{3.2.2}$$

3.2.2 Channel Selection

The selection of channels that are sensitive to the surface/cloud top emissivity signal was made using the following criteria. First, the transmittance $\tau(v)$ of the atmospheric layer between 65 mb (observation altitude) and 400 mb (average cloud altitude retrieved for the JAIVEx April 27 case) was computed. Then, the channel selection was made by analyzing the $\tau(v)$ spectrum so that the selected channel v^* satisfied the following rules:

$\tau(v^*) > 0.4$;
$\tau(v^*)$ is a point of a local maximum for $\tau(v)$ within the 10 cm^{-1} wide surrounding spectral window;
The estimated value of $\varepsilon^*_{CLD}(v)$ is in the 0 to 1 range.

Missed channels were filled with a linear interpolation between selected ones in order to obtain a smooth spectrum of the effective cloud emissivity. As a final step, the channel mask used for retrieval was applied to the computed spectra of $\varepsilon^*_{CLD}(v)$; channels with v in the 1000–1180 cm^{-1}

(O_3 band), 1240–1310 cm^{-1} (NO_2 and SO_2 lines), and v > 1600 cm^{-1} spectral regions were excluded from consideration.

3.2.3 Results

Figure 11 shows the analyzed transmittance spectrum $\tau(v)$ and corresponding channels selected for the estimation of $\varepsilon^*_{CLD}(v)$. The first 10 observed NAST-I cloudy radiances are also shown (in units of 0.01* $mW/cm^2cm^{-1}sr$ to fit on the plot) in order to see the observed scene variability and the correspondence between transmittance/radiance line signatures.

Figure 12 presents the mean effective cloud emissivity spectrum and its variability, obtained by averaging over 6264 NAST-I radiances for the April 27 case. The specific $\varepsilon^*_{CLD}(v)$ spectra, computed from the radiances in Figure 12, are also shown there.

The first six Empirical Orthogonal Functions (EOFs) of the cloud emissivity, calculated by singular vector decomposition of the corresponding covariance matrix, are presented in

Figure 13. It is worth noting that the first EOF is almost constant through all wavenumbers. This finding means that estimated $\varepsilon^*_{CLD}(v)$ spectra have very similar spectral shape (at least, to first order), and differ only by a constant bias from each other.

Figure 14 shows the accuracy of the EOF-fit for the obtained spectra of the effective cloud emissivity. It can be seen that first 4-6 principal components are enough to reach the 0.01-level of accuracy for the representation of $\varepsilon^*_{CLD}(v)$.

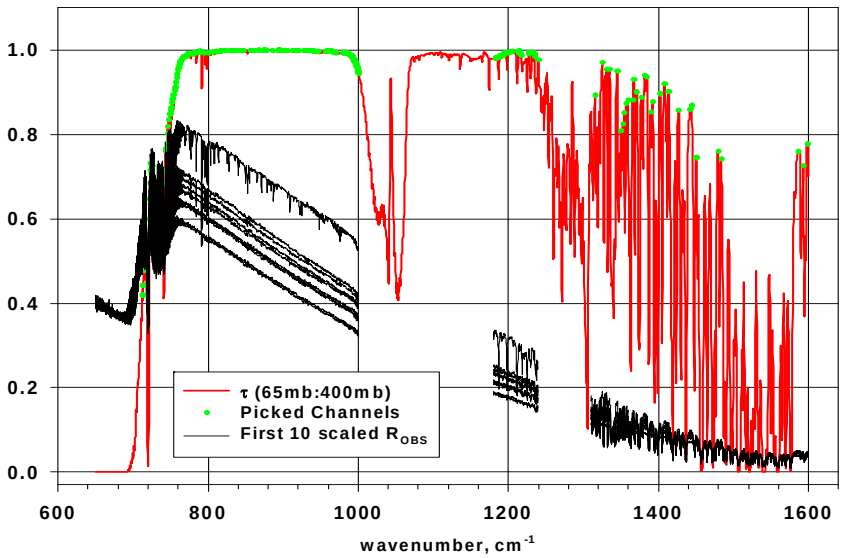

Figure 11. Transmittance of the atmospheric layer from 65 to 400 mb *(red line)*, channels selected for the cloud emissivity calculations *(green dots)*, and first 10 observed NAST-I cloudy radiances, scaled to 0.01*mW/cm^2-cm^{-1}-sr *(black lines)* as an example.

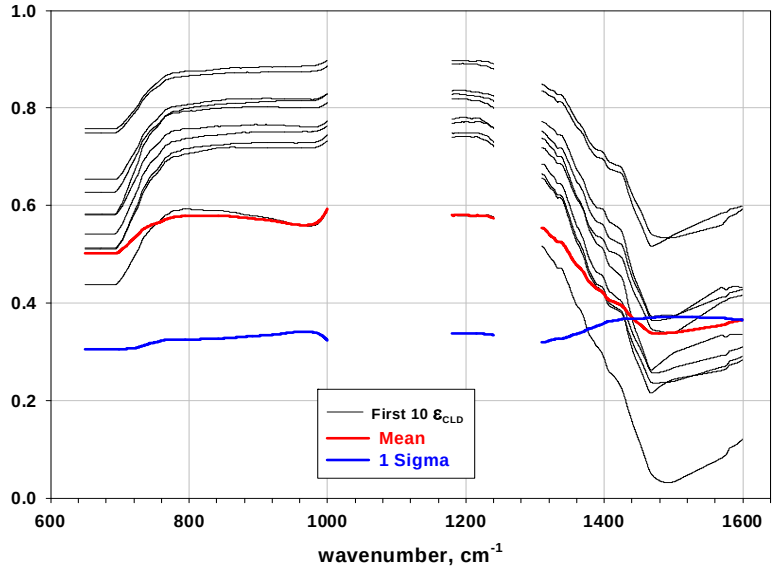

Figure 12. Mean spectrum of the effective cloud emissivity $\varepsilon^{*}_{CLD}(\nu)$ *(red line)* and its variability *(blue line)*, obtained by averaging over 6264 estimations from the NAST-I JAIVEx data, case April 27, 2007. Black lines are examples of the individual spectra for $\varepsilon^{*}_{CLD}(\nu)$, computed from the spectra shown in Figure 11.

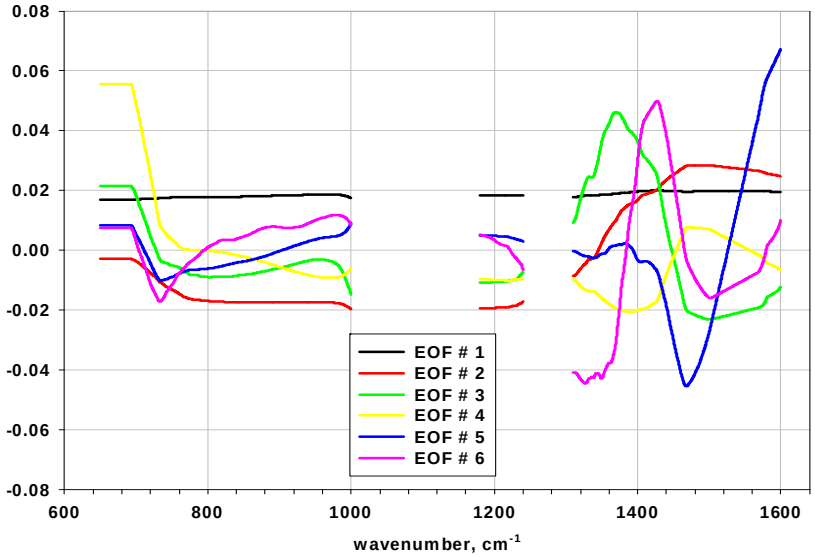

Figure 13. First 6 principal components for the effective cloud emissivity.

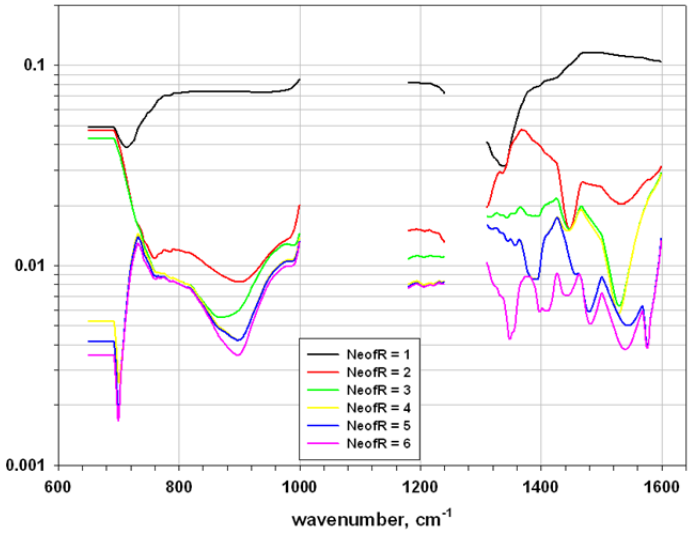

Figure 14. The accuracy of the EOF-fit for the effective cloud emissivity as a function of a number of principal components used.

3.3 Line-by-Line Radiative Transfer Model Calculations

3.3.1 Measurements for Model Verification

The Hyper-Cam was set up on an optics table directly under the open lidar hatch on a clear day, June 24, 2010. The Hyper-Cam configuration was such that it was looking straight up at the sky, the resolution was set at 1 cm^{-1}, and the integration time was set at 250 µs. The Hyper-Cam instrument settings are shown in Table 5. Thirty-one interferograms were averaged to produce every datacube, thus reducing the noise. This averaging was done on both the blackbodies and the sky measurements. Thirty-one was chosen because this was the upper limit.

Table 5. Hyper-Cam instrument settings for June 24, 2010 sky test.

Blackbody 1 set point	1.0°C
Blackbody 2 set point	50.0°C
Resolution	1 cm^{-1}
Integration time	250µs
FPA	100 x 100
Interferograms averaged per measurement	31
Acquisition time (for 31 interferograms)	12 minutes

Data acquisition commenced on June 24 at about 8:00 EDT, which is 1200 UTC, the time of the upper air data balloon launch at Peachtree City, which is south of Atlanta. The 355 nm aerosol lidar system was also operated so as to check for any sub-visual cirrus, which would affect the sky radiance and cause a difference between measured and modeled values, if such cirrus were present.

The IR image of the sky at 1075 cm^{-1} is shown in Figure 15. The image in the left panel is the radiance image, and the image in right panel is the radiance image after a bad pixel map has been applied. A 17x15 window of 255 pixels was chosen for analysis, as shown by the red box in the right panel of Figure 15.

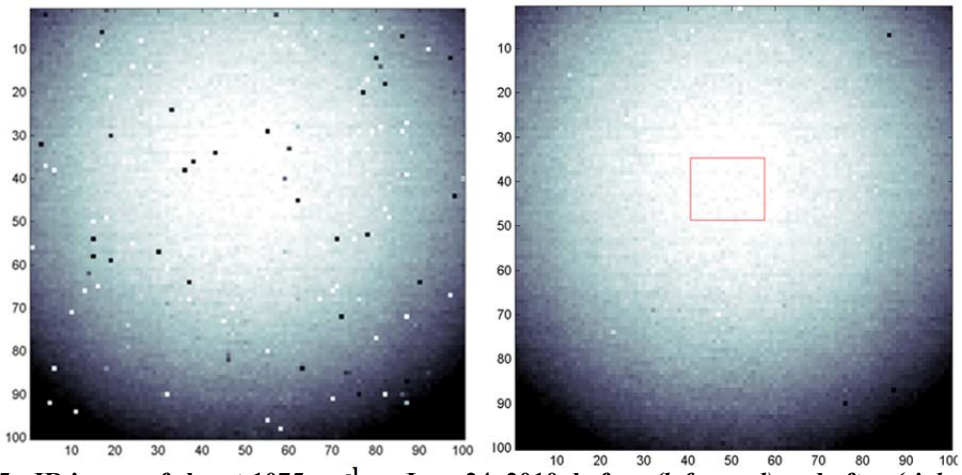

Figure 15: IR image of sky at 1075 cm^{-1} on June 24, 2010, before *(left panel)* and after *(right panel)* a bad pixel map is applied. The red box surrounds the pixels used in the analysis. (radiance units W/m^{2}cm^{-1}sr)

Note the ring that appears in the infrared images in Figure 15. This is due to the off-axis wavelength shift of the sensor. Because we only consider the center pixels for analysis we have not corrected for this effect.

The average radiance of all the pixels in the red box in the right panel of Figure 15 is shown in Figure 16.

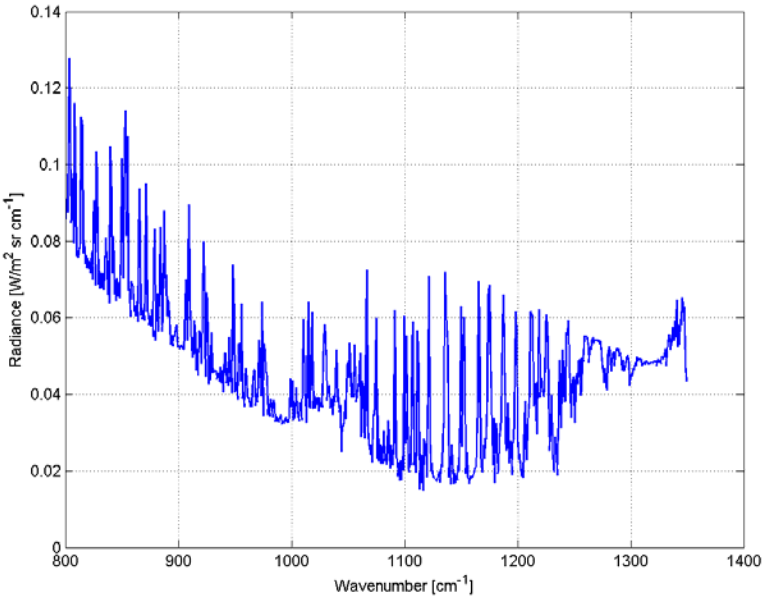

Figure 16: Sky radiance (average of 255 pixels).

The lidar data showed that the sky was in fact very clear. The range-corrected profile shown below, in Figure 17, is a one-minute average. The profile basically follows the exponential falloff of air density with altitude, with the exception of some small layers of aerosol in the 2500 – 4000 meter range. There is no evidence of cirrus, which was our main concern.

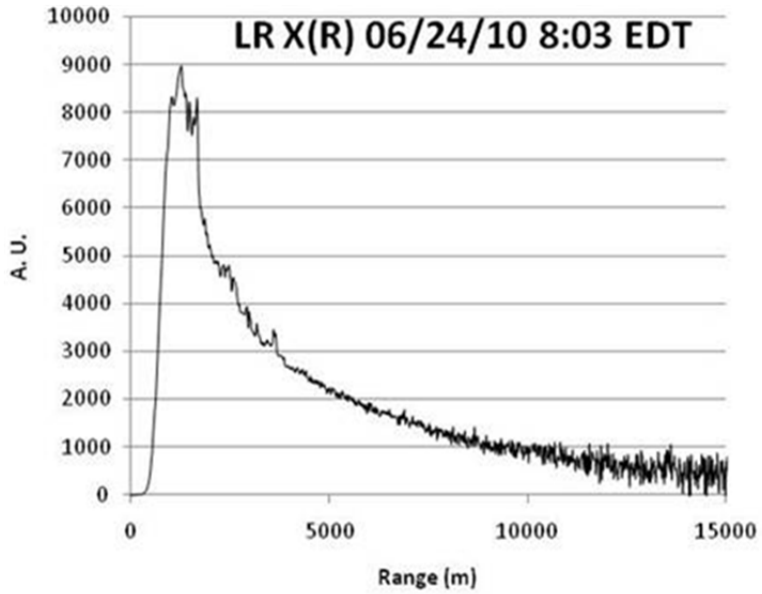

Figure 17: A one-minute average of the sky showing the exponential falloff of air density with altitude.

The lidar data can also be presented as a time-height plot, as shown in Figure 18. Again, faint aerosol layers can be discerned but no clouds (note that the time base is incorrect in this plot; the lidar was operated for approximately one hour).

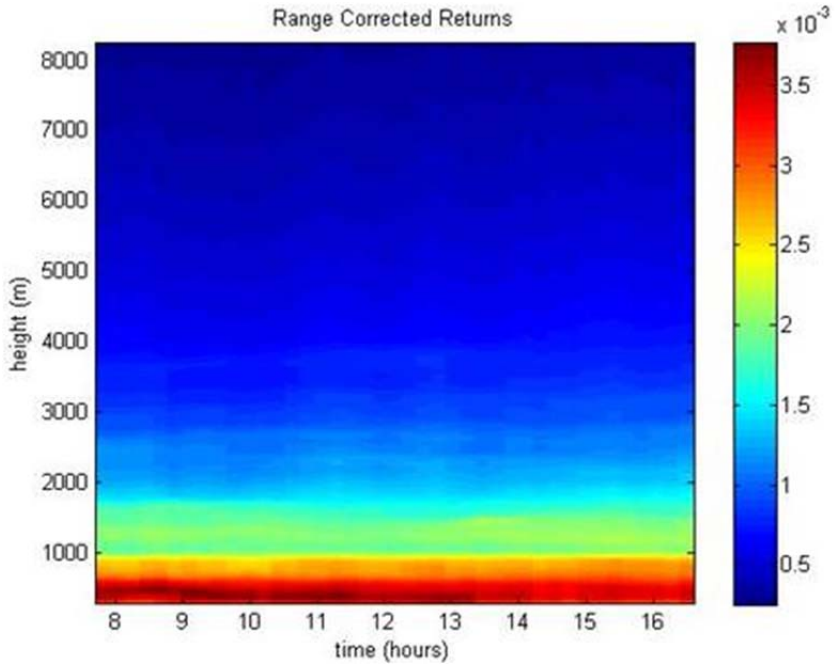

Figure 18: A time-height plot showing aerosol layers, but no clouds.

3.3.2 Fast Model Development

A fast model was developed to enable retrievals of atmospheric temperature and moisture from the Hyper-Cam measurements. The model uses the 0.5 spectral resolution AERI Fast Model (AFM), as its basis, with the result being converted to any of the Hyper-Cam's selectable spectral

resolutions via a double FFT process. Specifically, the AERI (Atmospheric Emitted Radiance Interferometer) fast model apodized radiance spectrum is converted to an interferogram through an FFT of the radiance spectrum. Next, the interferogram is deapodized by dividing the interferogram by the AFM apodization function. Finally the unapodized interferogram is truncated at the maximum optical path difference associated with the spectral resolution of the Hyper-Cam observations.

Figure 19 shows a comparison of the Hyper-Cam observed radiance spectrum for June 24, 2010 with radiances calculated by FLI-FM and LBLRTM for two different spectral resolutions. The FLI-FM results appear to compare with the observed spectrum with the same degree of accuracy as the time-consuming line-by-line calculation. To illustrate this agreement further, Figure 20 shows the difference between the calculated spectra and the Hyper-Cam observed radiance spectrum for the window 900-950 cm^{-1} region of the spectrum. Here it is seen that the spectrum calculated using FLI-FM is nearly as good as the LBLRTM calculation for the spectral resolution of the radiance observation (maxOPD = 0.6 cm). It is also noteworthy that the standard deviation between the LBLRTM calculation for the observed spectral resolution of 0.833 cm^{-1} (i.e. maxOPD = 0.6 cm) is significantly smaller than that for half observation spectral resolution (i.e. maxOPD = 0.3 cm), indicating that there is little self apodization being produced by any misalignment of the Hyper-Cam optics or the instrument's finite field of view.

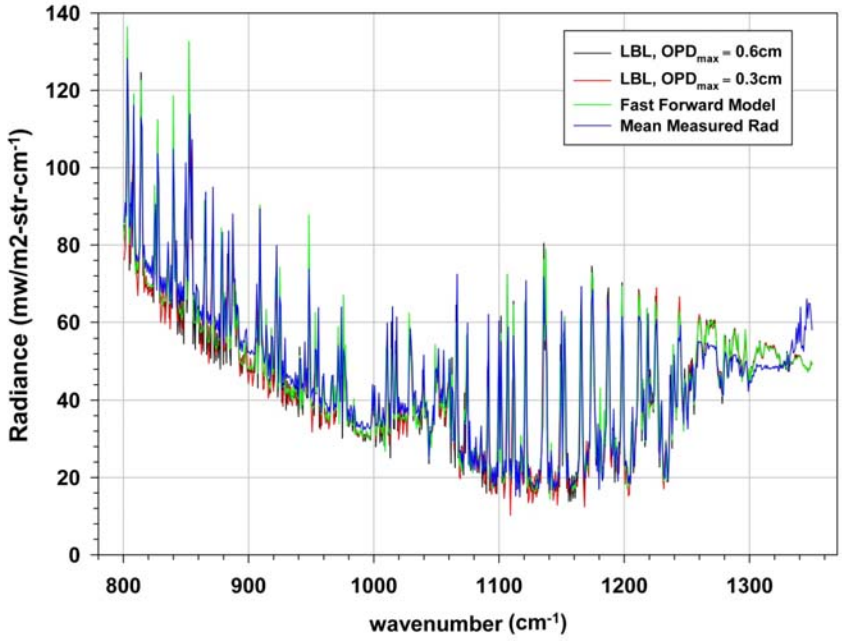

Figure 19: Comparison of the Hyper-Cam observed radiance spectrum for June 24, 2010 with radiances calculated by FLI-FM and LBLRTM for two different spectral resolutions.

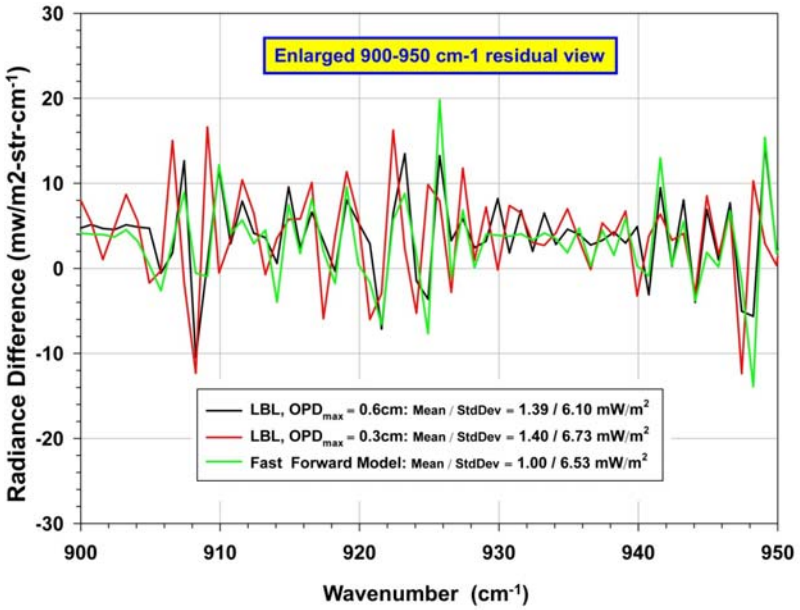

Figure 20: The difference between calculated spectra and the Hyper-Cam observed radiance spectrum for the window 900-950 cm^{-1} region of the spectrum.

3.4 FLI-FM, Version 2

The FLI Forward Model (FLI-FM) was updated to version 2 (FLI-FM2) during Year 3. The fast computations of FLI-radiance calculated with FLI-FM are based on the pre-calculated optical depth (OD) look-up-table. A newer version of the table was prepared in FLI-FM2, which implements the following improvements:

1. The wavenumber range was extended to 625–2475 cm^{-1} (before it was equal to 650–1650 cm^{-1}).

2. The look-up-table is now computed for six atmospheric models: tropical, midlatitude summer, midlatitude winter, polar summer, polar winter, and the US standard atmosphere. It accounts for seasonal/latitudinal atmospheric state variations more accurately. Before it was completed only for the US standard atmosphere.

3. Monochromatic optical depths pre-computed with LBLRTM (resolution 10^{-4} cm^{-1}) have been converted into transmittances for each layer and then convolved with a double Fourier transform into resolution 10^{-2} cm^{-1} (FLI "monochromatic" resolution). Before, optical depths had been simply averaged (boxcar) to the lower resolution.

4. The fact that the atmospheric state is defined on *levels*, but optical depths/transmittance are *layer* characteristics, results in the situation where varying one parameter (say, the temperature on some level) changes the optical characteristics of two layers: one below and one above of this level. The new table version includes both bottom and top Jacobians (derivatives) of the transmittance, $\tau(\nu)$. Before, only one (bottom) derivative had been saved. The Jacobian is computed for temperature and water vapor at all levels (0–95 km).

Time-consuming LBLRTM calculations to implement these improvements were performed. Figure 21, Figure 22, and Figure 23 show transmittance and its temperature and water vapor derivatives for layers with boundary levels 0–1 km, 5–6 km, and 10–11 km, respectively, as an example of the updated version of the look-up table. These changes have been adopted and incorporated into the FLI Forward Model.

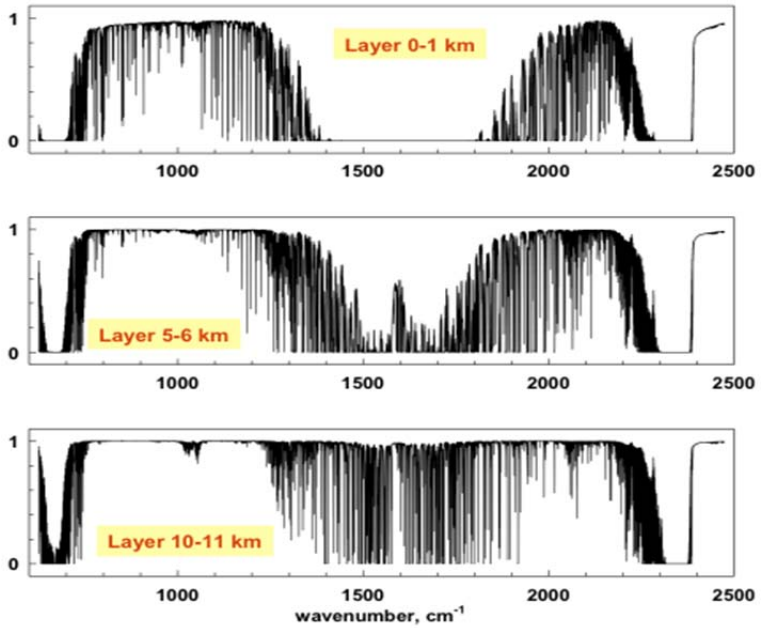

Figure 21. Layer transmittance, $\tau(\nu)$, for three indicated atmospheric layers; only every 20th point from the new look-up-table is shown for graphic purposes.

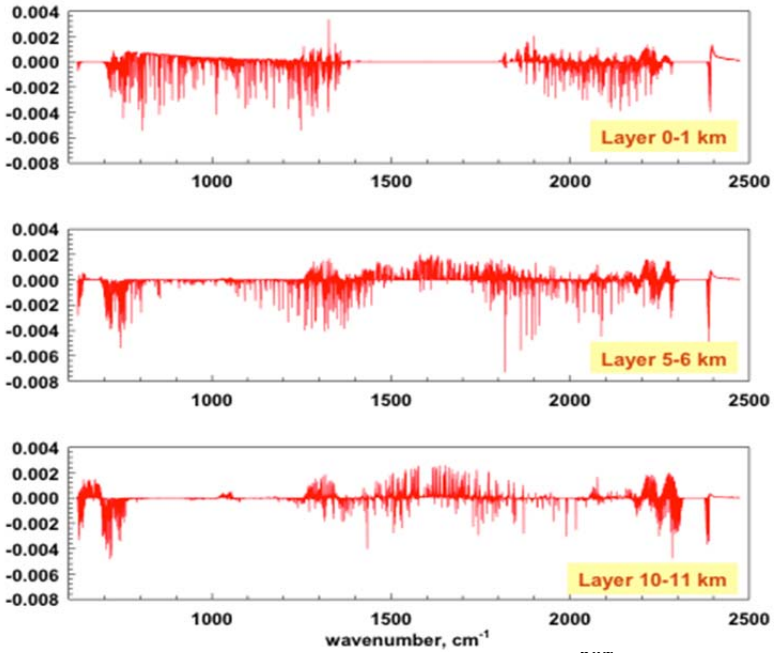

Figure 22. Temperature derivative of layer transmittance, $\delta\tau(\nu)/\delta T^{BOT}$, for three atmospheric layers. Unit is K^{-1}; only every 20th point from the new look-up-table is shown for graphic purposes.

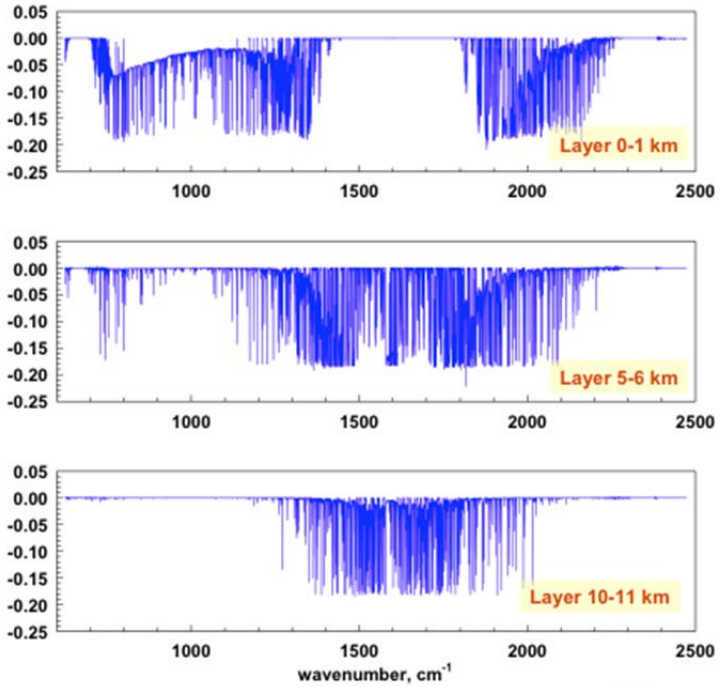

Figure 23. Water vapor derivative of layer transmittance, $\delta\tau(v)/\delta(lbQ^{BOT})$, for three atmospheric layers. H_2O unit is vmr; only every 20th point from the new look-up-table is shown for graphic purposes.

The model updates lead to better performance of the FLI-FM in terms of its agreement with LBLRTM. Figure 24 shows transmittances computed with the updated FLI Forward Model for some of the atmospheric layers. Figure 25 presents the difference between spectra computed with LBLRTM and FLI-FM2 (abbreviated LBL and FLI, respectively, in the legend) in both brightness temperature and radiance units. One can note that the residual does not exceed 0.3 K through almost the entire wavenumber range, with the exception being the ozone band between 1000 and 1100 cm^{-1}. This exception may be explained by the fact that the ozone is a fixed gas in FLI-FM, i.e. its spectral dependence on the input temperature profile is not taken into account. Finally, Figure 26 presents a direct comparison of the residual differences between spectra calculated by LBLRTM and both FLI-FM and FLI-FM2 in radiance units. This figure shows the improved performance of FLI-FM2 quantitatively; note that residuals have decreased dramatically. It is also important to note the extended wavelength range; the red line in Figure 26 ends at 1300 cm^{-1}.

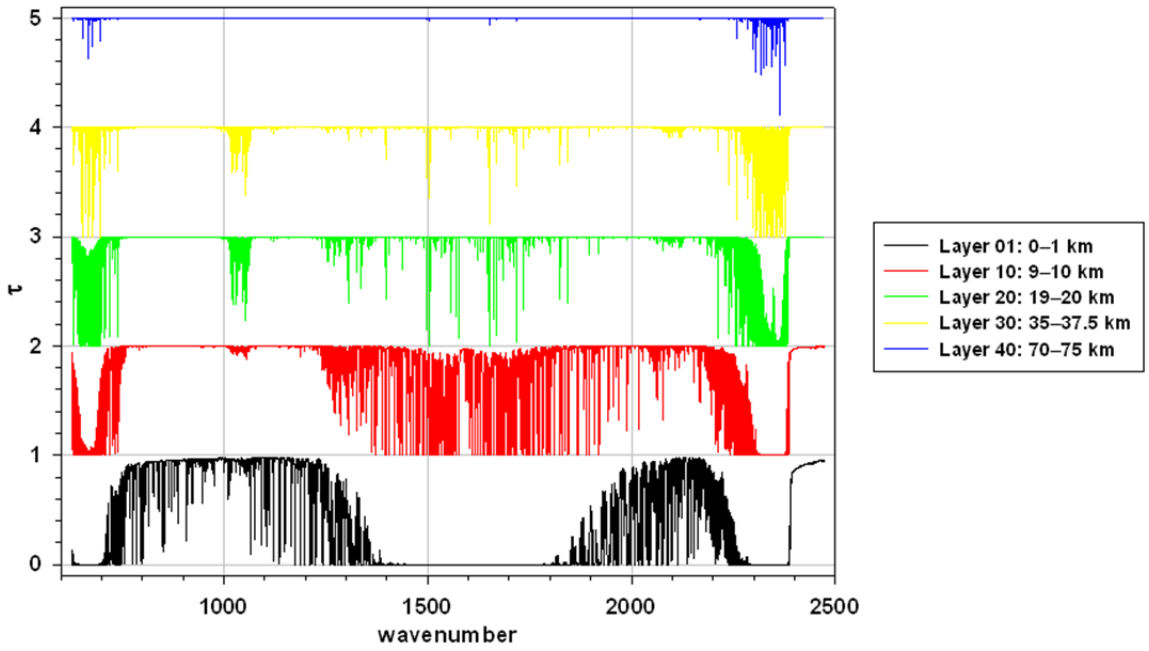

Figure 24. Layer transmittances computed with FLI Forward Model, version 2.

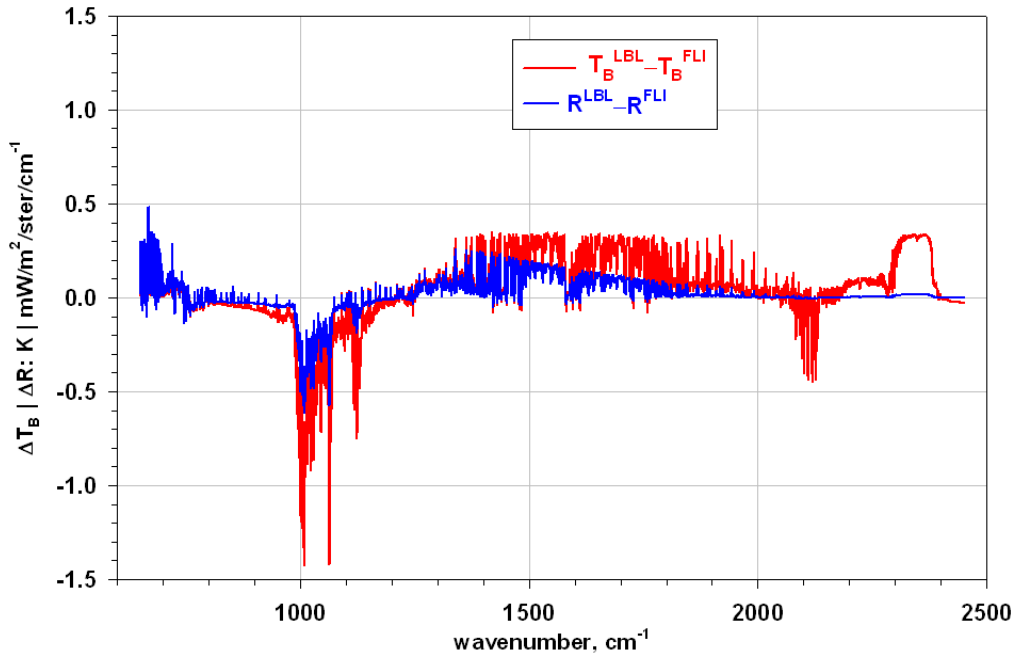

Figure 25. Residuals (LBL – FLI) for the same atmospheric state in both brightness temperature *(red)* and radiance *(blue)* units.

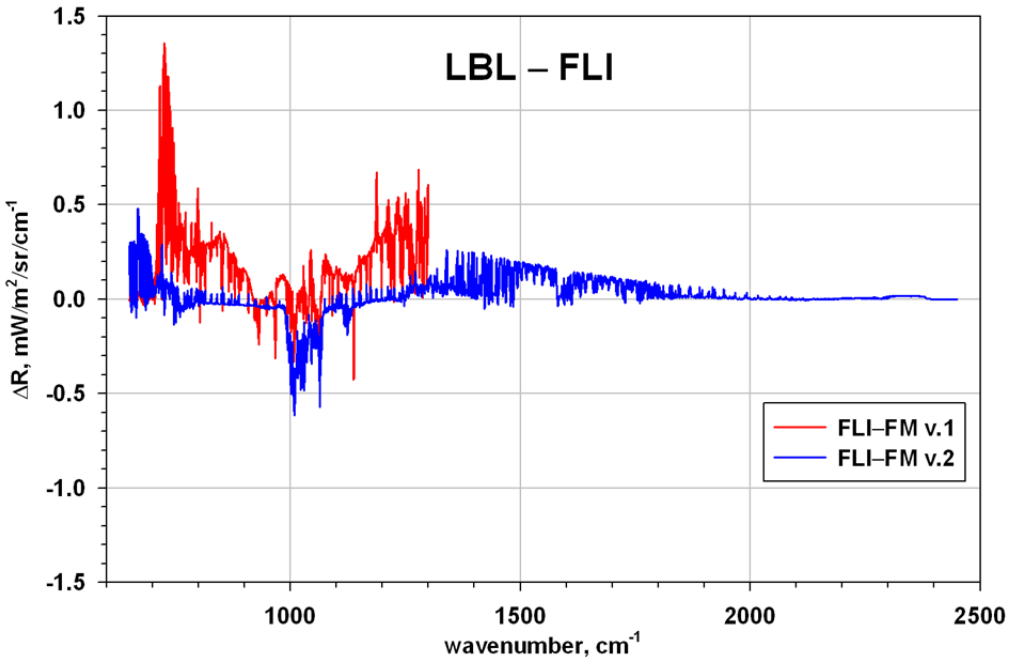

Figure 26. Residuals (LBL – FLI) for the same atmospheric state in radiance units only calculated from LBLRTM – FLI-FM version 1 *(red)* and LBLRTM – FLI-FM version 2 *(blue)*.

4 Wake Vortices

The formation and evolution of aircraft wake vortices was reviewed in the final report for an early phase of the FLI project [15]. Two potential detection mechanisms were described: 1) detection of temperature anomalies such as cool vortex cores; and 2) detection of entrained exhaust gasses such as water vapor, CO_2, CO, NO_x, and VOCs.

The vortex parameters (circulation, core size, spacing, descent rate, and decay rate) depend on weather conditions as well as the type of aircraft, its weight, and its airspeed. In Phase 2 of the FLI program, the Burnham-Hallock (BH) model was used to model the physical characteristics of vortices [24]. The model calculations were performed over ranges of vortex parameters rather than for specific scenarios. The radiometric wake vortex model was updated to accommodate input parameters for specific cases in coordination with the broader wake vortex community.

Data were collected at Atlanta's Hartsfield-Jackson International Airport to investigate these mechanisms. Cool vortex cores were not detected, and new simulations have shown that the radiometric signatures of wake vortex temperature structures are quite small. The lack of detection validates the model, albeit without truth data. However, exhaust plumes have been detected in the hyperspectral imagery.

Through both modeling and data analysis of images with vortices, we have already concluded that the signal of the wake vortices is too small to detect with the currently available Hyper-Cam instrument. The research team still believes it would be valuable to run the Hyper-Cam and other hyperspectral instrumentation next to a WindTracer Lidar at an airport facility if the opportunity ever arieses, because truth data was unavailable for all of the work to date. Therefore, it is not possible to know if or when wake vortices were within the instrument's field of view.

4.1 Wake Vortex Models

Hampton University created a Terminal Area Simulation System (TASS) Large Eddy Simulation run for an A319 case in level flight, but it did not include water vapor. This data set (3-D) was used at 5 time slices (10 second intervals) in conjunction with the FLI-FM model. Matlab code and Fortran code were written to perform these analyses. FLI spectra were simulated for a wake vortex condition produced by a numerical model for an Airbus-319 aircraft. Simulations were produced for level flight at 1000 m and with variations in temperature, moisture, and distance to the vortex from the aircraft. These simulations were used to provide an initial estimate of the radiance signal expected from the Hyper-Cam prior to any Hartsfield-Jackson International Airport (ATL) and San Francisco International Airport (SFO) field experiments viewing wake vortices. Figure 27 shows the temperature structure produced for the wake vortex as simulated by the NASA numerical model. As can be seen from this model there is significant temperature variation that may be detectable by a FLI instrument if the noise floor is low enough to detect the signal. The requirements for such an instrument are given in Section 11.

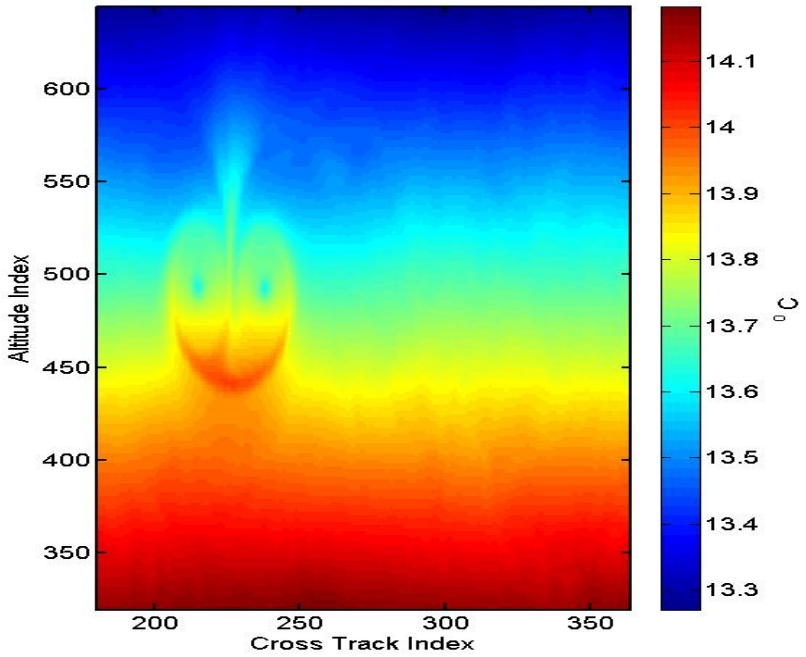

Figure 27: Temperature associated with a wake vortex produced at 1000 meters by an airbus-319 aircraft at 20.0 seconds. The Cross Track Index is distance in meters.

During Year 1, considerable discussion took place to prioritize wake vortex model simulations being performed by Dr. Fred Proctor and Taumi Daniels. There was already one simulation for the A319 aircraft, which is on the lighter side of heavy commercial aircraft. A decision was made to pursue simulation of a heavy aircraft typical of what was observed during the Hyper-Cam measurements to be conducted at ATL. After considering the data limitations available for the model runs, it was decided to perform the next simulation for a 747 heavy aircraft. It was also conveyed to Dr. Proctor that both temperature and water vapor are needed as output from the model in order to properly simulate the potential detection simulations capability of a FLI (or in the ATL case, Hyper-Cam) measurement. These updated models were used in the simulations described in this section.

Further simulations by Hampton University examine changes based on temperature differences across the wake vortex. For the A319 TASS simulation, a pair of wake vortices was generated in a 3-D space. Temperature and wind fields at ten second intervals were used as input to a FLI-like model. For the results below, 100 cases for the single pixel were simulated, each with the temperature decreasing by a fixed amount. All other parameters were held constant (namely water vapor mixing ratio, distance to vortex, and altitude of wake vortices and aircraft). Each of the 100 cases results in a unique spectrum over the 833 to 1250 cm^{-1} spectral region. As the initial case was generated using ambient temperature (at the same altitude), it can be considered the null case, and is subsequently subtracted from the other 99 cases. For a wake vortex core to wall temperature difference of 2 K, the resulting radiances can be converted to brightness temperatures. The null (no wake vortex) brightness temperatures are subtracted resulting in the values shown in Figure 28 below.

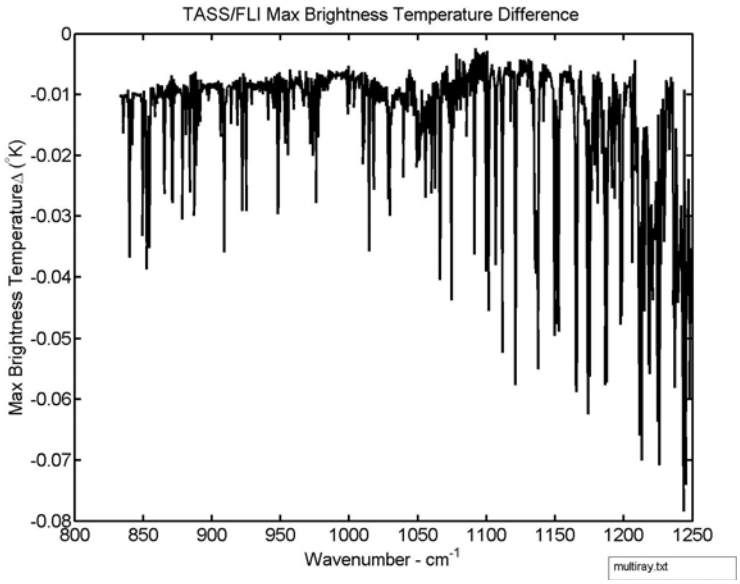

Figure 28. The maximum brightness temperature difference expected to be observed by the Hyper-Cam.

As can be seen, this simulated maximum brightness temperature signal is well below the noise level of the Hyper-Cam instrument (the signal is one order of magnitude less than that which is observable, see Appendix A). The IR long wave window region has a fairly flat response and < 0.1 K brightness temperature variation can be expected for a 2 K core to wall wake vortex temperature gradient, the maximum response being observed at the spectral location of the water vapor line centers. Thus, the wake vortex signal is difficult to see within the spectra range of the Hyper-Cam instrument unless the temperature variation is also associated with a variation of the water vapor mixing ratio, which was held constant for this simulation.

As a check on this simulation, Figure 29 shows the sensitivity of the ground-based Hyper-Cam spectral measurements to a 1 K temperature variation within a 1-meter path length as a function of Hyper-Cam distance from the vortex.

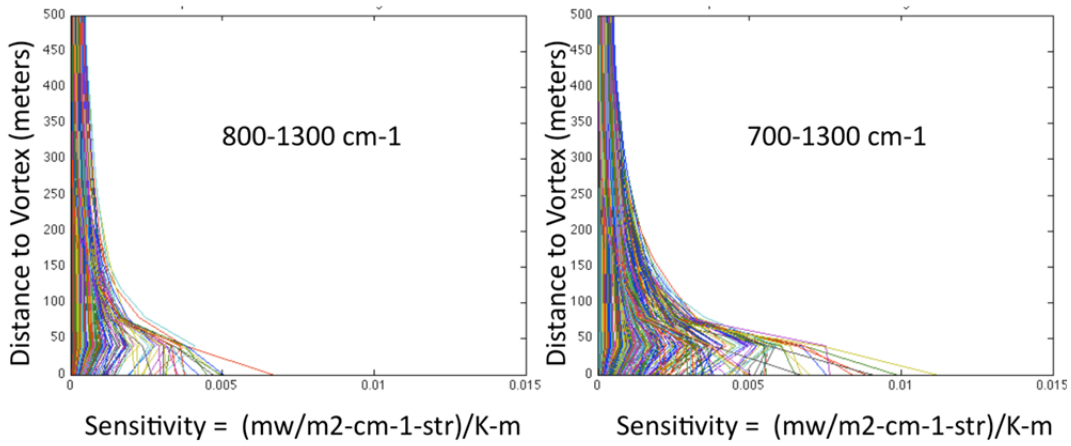

Figure 29: The sensitivity of ground-based Hyper-Cam spectral radiances to atmospheric temperature variations of 1 K within a 1-meter layer, as a function of distance from the instrument. Each curve shown represents a different spectral channel.

The results shown in Figure 29 are in good quantitative agreement with those shown in Figure 28. It is also shown that if the Hyper-Cam spectral response could be extended to obtain CO_2 channel measurements within the 700 – 800 cm^{-1} spectral region, the sensitivity would be doubled. However, the results presented in Figure 28 and Figure 29 indicate that it is very difficult to see wake vortices with the Hyper-Cam if the radiance signal is produced solely by temperature variations. It is possible that water vapor variations produced by the wake vortex may produce radiance signal variations much larger than those shown here for temperature alone. The impact of water vapor, and other trace gases associated with the wake vortex, needs to be investigated before any conclusions can be made regarding the Hyper-Cam's ability to sense wake vortices.

TASS model data for the A319 aircraft at 1-km altitude was used for simulation of the wake vortices as input to the FLI model. For these test cases, the relative humidity was varied, producing water vapor mixing ratio variations for a constant temperature (i.e. the US Standard Atmosphere). Relative humidity is based on a saturation water vapor mixing ratio (computed at 1-km altitude and temperature 281K) of about 3 g/Kg. The separation distance from the aircraft to the wake vortex for the single pixel study was 1 km. Results of the simulations are shown in Figure 30.

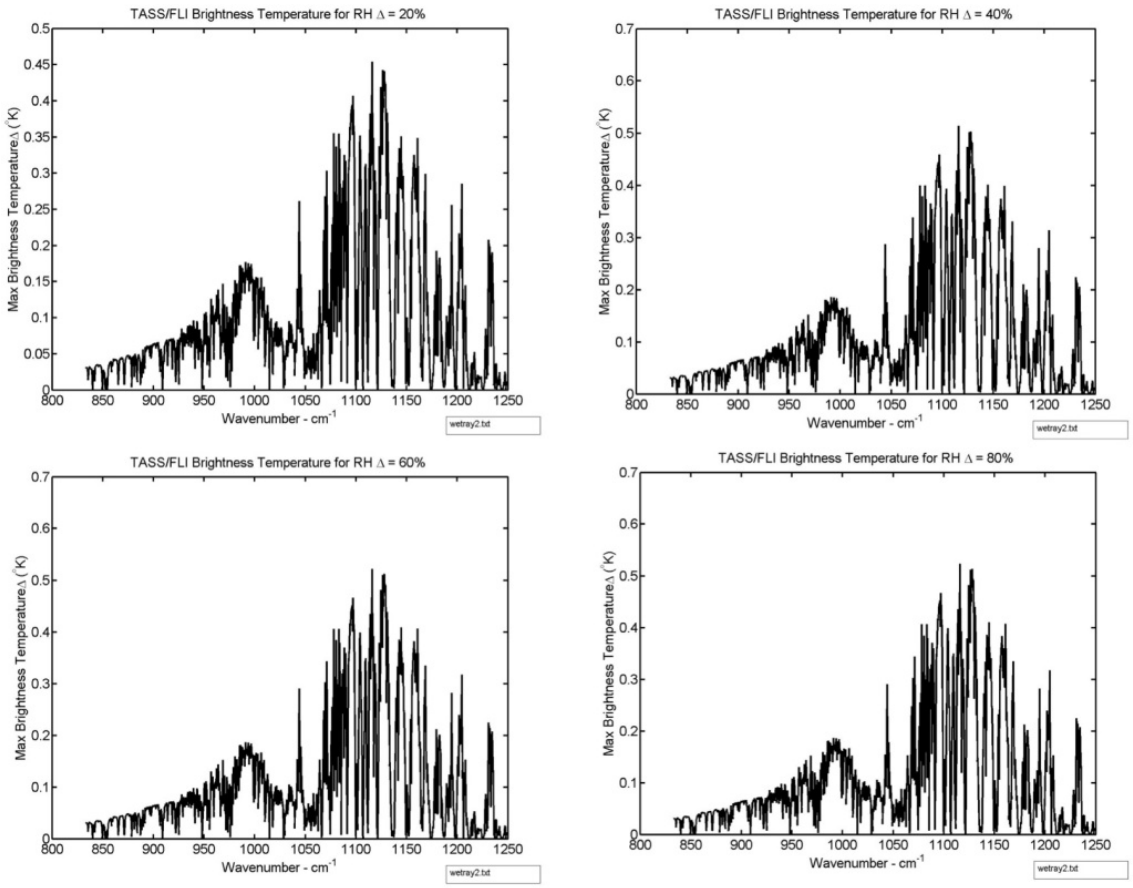

Figure 30: TASS wake vortex radiance simulations for different relative humidity conditions.

The water vapor radiance variability is significantly larger than the expected nominal noise of a FLI system (i.e. NEdT = 0.1 K). Also, an imaging FTS should provide a spatially coherent image of vortices (in this head-on configuration) which is not represented by this single pixel parameterization. The next step is to consider multiple pixels to simulate the image that would be provided by a FLI instrument.

Taumi Daniels completed a PhD thesis on the detection of wake turbulence using infrared radiance measurements in March 2012 [23]. The following models, through Figure 33, are highlights from this thesis. Simulations of the atmospheric temperature, moisture, and exhaust gas conditions associated with wake vortices from commercial jet aircraft were simulated using TASS. LBLRTM was used to simulate measurements of the infrared radiance spectrum (650 – 3350 cm^{-1} @ 0.5 cm^{-1} spectral resolution) that would be measured with a spectrometer when viewing the atmospheric disturbance created by the wake of a Boeing 747 jet aircraft. As can be seen in Figure 31, there is a small, but evident, temperature and moisture structure signature of the wake vortex disturbance.

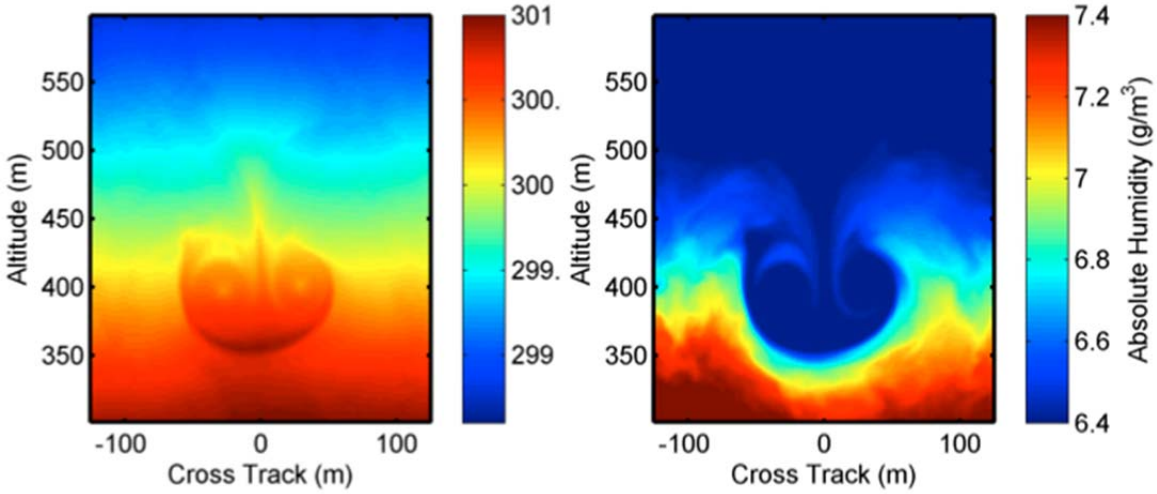

Figure 31. The temperature *(left panel)* and moisture *(*right *panel)* distribution associated with the wake of a Boeing 747 jet aircraft.

Computations for the standard deviation of the spectral radiance disturbance produced by the wake vortex measured by a ground based spectrometer viewing the wake are shown in Figure 32. The natural elevation angle dependence of the radiance emission has been removed to more clearly isolate the wake vortex signal.

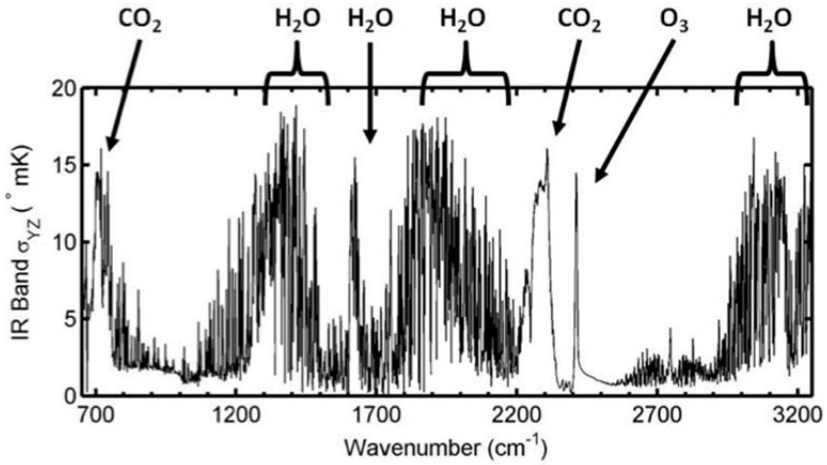

Figure 32. The standard deviation of the radiance observed across the field of regard of an imaging spectrometer associated with the temperature and moisture disturbances shown in Figure 31.

As shown, the wake vortex causes the radiance to vary across the instrument's field of regard with a standard deviation as high as 0.02 K, dependent upon the spectral frequency being observed. The CO_2 radiance signatures are due to the wake vortex atmospheric temperature disturbance, whereas the water vapor radiance signatures are due to the combined effects of the temperature and water vapor mixing ratio disturbances shown in Figure 31. Furthermore, it is shown that the wake vortex radiance signatures occur over broad spectral bands of carbon dioxide and water vapor emission, which is important for optimizing the signal-to-noise of a spectral radiometer designed for detecting wake vortex turbulence.

The measurements of the radiance associated with wake vortices generated by commercial jet aircraft were conducted both at Madison, Wisconsin (June, 2008) and Atlanta, Georgia (July through September 2010) using the Telops Mid-wave Hyper-Cam and Long-wave Hyper-Cam instruments, respectively. Extensive analyses of the data collected did not reveal any detectable radiance signal of the wake vortices being observed. Note, however, that winds in Madison were extremely high and likely prevented vortices from forming, and that the Atlanta data acquisition activity was meant as a preparation activity for a formal data acquisition activity to understand requirements and settings.

Figure 33 illustrates one reason for this lack of success from these experimental measurements. The spectral bands of the Telops Long-wave and Mid-wave Hyper-Cam instruments are shown in the top diagram. The optimal band pass for an imaging radiometer designed to detect wake turbulence is shown in the lower diagram of this figure. As can be seen, both the Long-wave and Mid-wave Hyper-Cam instruments operate across spectral bands where the wake vortex radiance signal is a minimum. Furthermore, the noise level of the Hyper-Cam measurements is more than two orders of magnitude larger than the wake vortex signal for the spectral bands observed (see Appendix A). Note that data were collected in Madison with a broadband spectrometer that covered the optimal band pass, but again, the winds were so high that vortices likely did not form or were blown out of the field of view before forming. Also, these tests were ground based, and the optimal band pass shown on the bottom plot of Figure 33 are for flight altitudes. The optimal band pass for a slant path from ground level will be described at the end of this section.

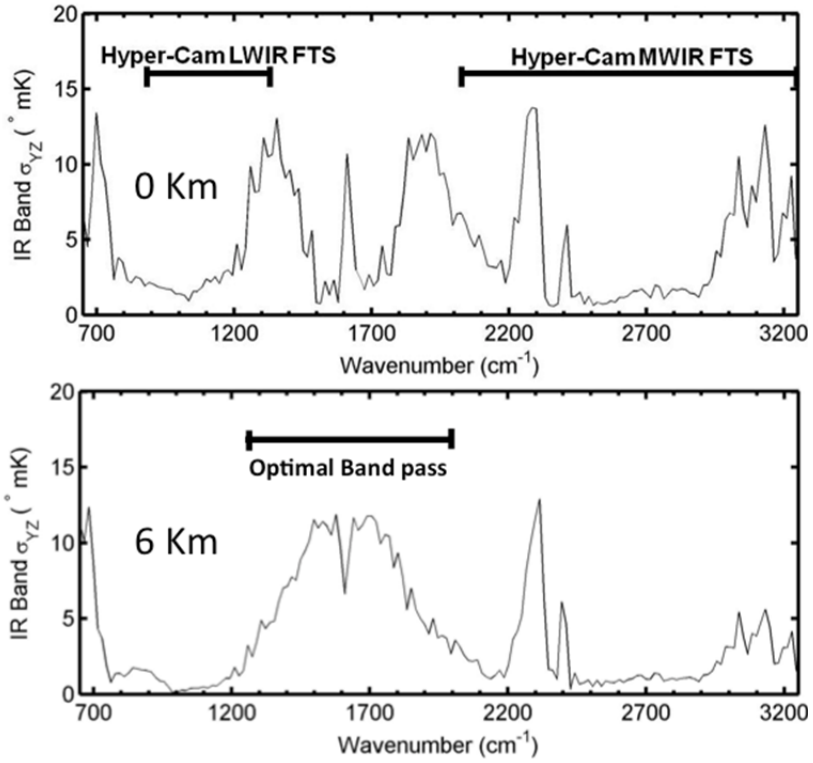

Figure 33. The standard deviation of the radiance spectrum (natural elevation angle dependence removed) as would be observed with a spectral resolution imaging spectrometer operating at a spectral resolution of 16 cm^{-1} at two different aircraft altitudes, 0 km and 6 km.

Figure 33 demonstrates that it should be possible to detect wake vortex turbulence, and presumably mountain lee wave and clear air turbulence if an appropriate sensor may be identified. Instrument requirements based upon the above models will be defined in Section 11.

Wake vortex radiance simulations were also conducted with FLI-FM2 to estimate the magnitude of the signal from a broadband instrument sensitive in the shortwave through long-wave spectral regions. The temperature and water vapor 3-D fields used in the simulations were prepared with TASS at NASA Langley Research Center (the same TASS model was used for the LBLRTM simulations above). The full TASS domain size is 800 m by 600 m by 600 m in the along-track (X), cross-track (Y), and vertical directions (Z), respectively. The spatial grid resolution was 1.5 m in the cross-track Y-Z plane and 2.0 m in the along-track direction, resulting in 404 x 404 x 404 pixels. Temporal development of the wake vortex was represented by seven data cubes, starting from $t = 0$ s and ending at $t = 60$ s, with a 10 s time increment.

The observer point was located on the ground level, at a distance about 700 m from the front cross-track Y-Z plane of data. The viewing elevation angle, β, for the center image pixel was equal to 30°. The detector matrix was assumed to have 25 x 25 pixels in the vertical and horizontal directions, with a full angular field of view 12° x 12° (± 6° from the center pixel), i.e. the pixel angular size is 0.5° (~10 mrad).

The instrument FOV, being projected to the TASS front cross-track plane, results in observation of an area that has a 300–500 meter altitude range with ± 84 m span in the horizontal direction, which corresponds to a simulated wake vortex location in the center of the image.

The referenced atmosphere was built from the mean temperature and water vapor vertical profiles, *T(H)* and *Q(H),* respectively, obtained by averaging over the horizontal X-Y plane plus averaging over all seven time moments. These mean vertical profiles are shown in Figure 34.

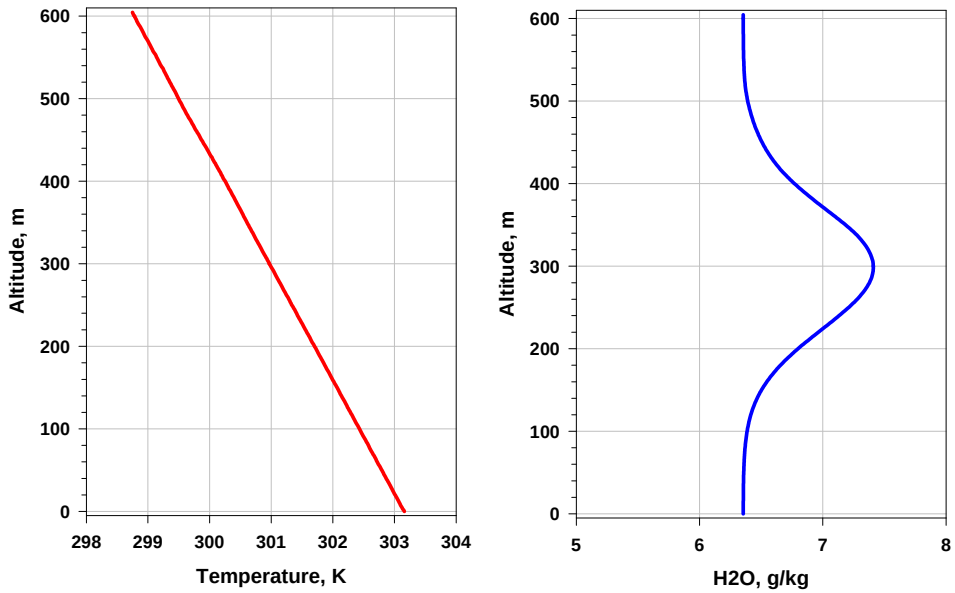

Figure 34. Total mean temperature and water vapor vertical profiles from TASS data.

The temporal variability of the horizontally averaged profiles caused by the wake vortex is presented in Figure 35 and Figure 36 for *T(H)* and *Q(H)* respectively. Because deviations of each cube mean profile from the total mean are comparatively small, the left panels in Figure 35 and Figure 36 show their difference, while the right panels present one-sigma profiles for each altitude level.

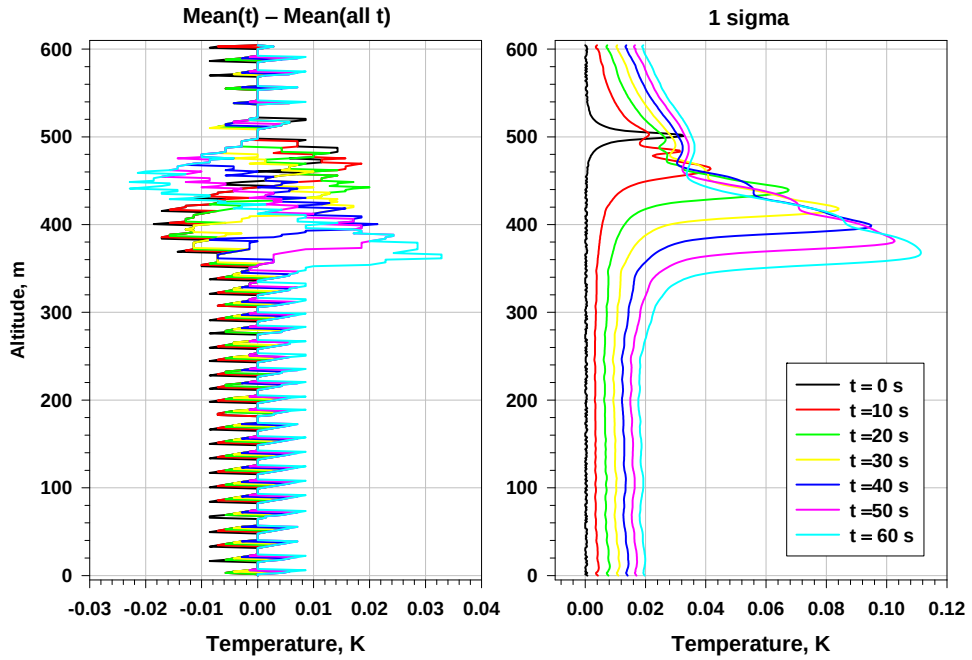

Figure 35. Deviation of the mean temperature vertical profile at the moment *t* from the total mean profile *(left* panel*)*, and temperature horizontal variability for each altitude level *(right panel)*.

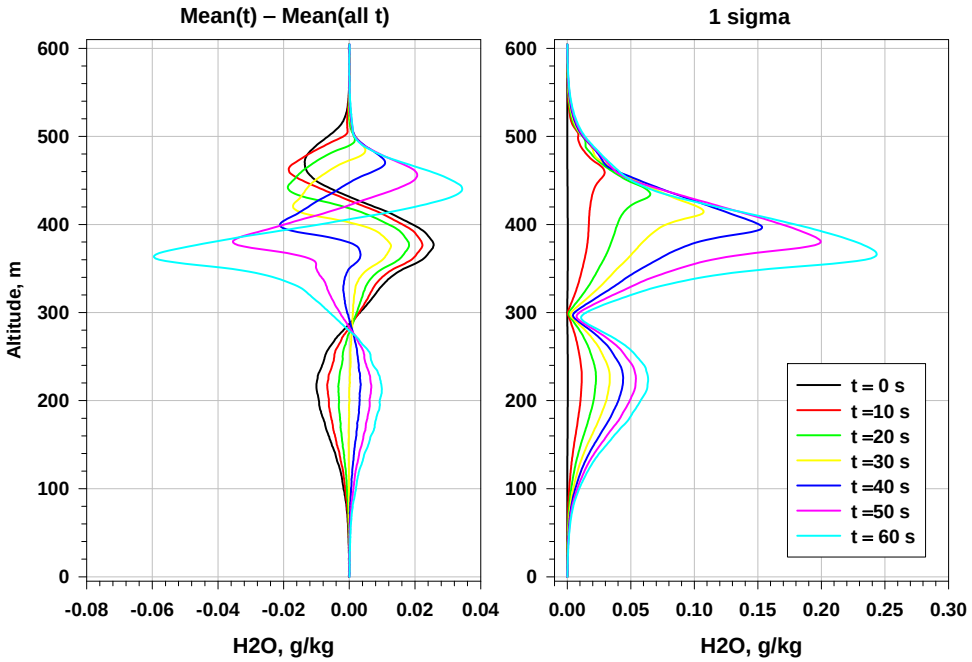

Figure 36. Deviation of the mean water vapor vertical profile at the moment *t* from the total mean profile *(left panel)*, and water vapor horizontal variability for each altitude level *(right panel)*.

Because TASS data continues only up to an altitude of 600 m, and the whole atmospheric profile is needed to perform radiative transfer calculations, the special *TASS Referenced Atmosphere* was constructed by smooth merging the TASS mean profiles with the US Standard Atmosphere. Figure 37 shows how this merging has been performed. For the temperature profile, the TASS vertical temperature gradient was kept up to an altitude of 12 km (tropopause), and then the standard profile was added. For the water vapor profile, the TASS mean profile was merged with the standard profile at the altitude of 2 km by interpolation.

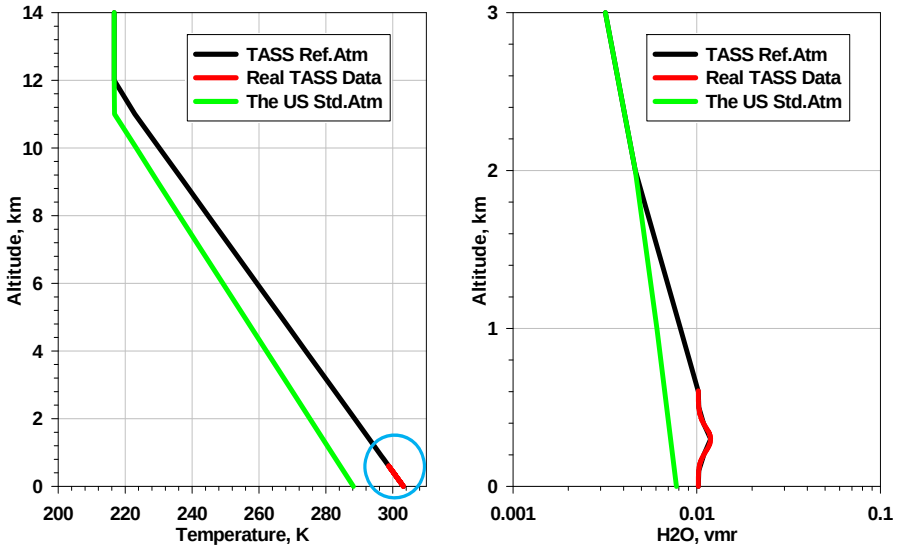

Figure 37. TASS Referenced Atmosphere (black) obtained by merging actual TASS mean profiles *(red)* with the US Standard Atmosphere *(green).*

Radiative transfer calculations were then performed with FLI-FM2. The wavenumber range 2200–2400 cm^{-1} was chosen for the simulation. Initial high-resolution spectra were computed with a 0.25 cm^{-1} wavenumber increment. Gaussian apodization with an interferometer equivalent maxOPD = 2 cm was applied as the FLI-FM2 monochromatic radiance convolution. Then, the broadband signal was obtained by simple averaging over the entire wavenumber range. Spectra were computed for each pixel and each time moment, which resulted in 25 x 25 x 7 = 4375 "wake vortex" spectra total.

In addition, one more cube of 25 x 25 = 625 spectra total was computed for the TASS Referenced Atmosphere to present background radiances $R_0(\nu, \alpha, \beta)$, where (α, β) are azimuth and elevation angle pixel coordinates. A wake vortex signal S was estimated as the radiance difference in both high resolution and broadband domains:

$$S(t,\alpha,\beta) = \frac{1}{\nu_2 - \nu_1}\int_{\nu_1}^{\nu_2}\{R(t,\nu,\alpha,\beta) - R_0(\nu,\alpha,\beta)\}d\nu \qquad (4.1.1)$$

It should be noted that path RT-integration through the TASS data cube was done with a TASS vertical resolution increment to account for the wake vortex signal with as high accuracy as possible. Background radiances were computed the same way; the only difference is that TASS data were replaced with the TASS Referenced Atmosphere for part of the path going through the

TASS cube location. Therefore, elevation/azimuth/path radiance dependence was accounted for with absolute accuracy.

Figure 38 shows the brightness temperature spectrum for the central pixel ($\alpha = 0°$, $\beta = 30°$) and TASS Referenced Atmosphere, with 0.25 cm^{-1} spectral resolution.

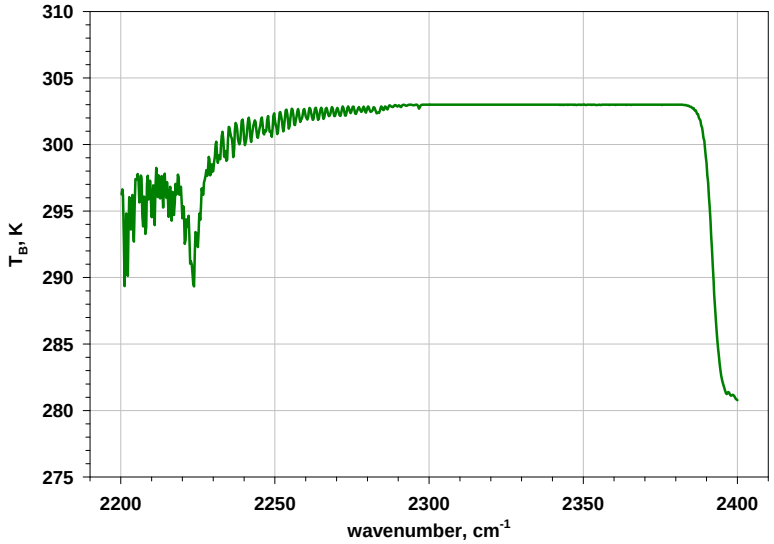

Figure 38. Brightness temperature spectrum for the central pixel *($\alpha = 0°$, $\beta = 30°$)*, TASS Referenced Atmosphere.

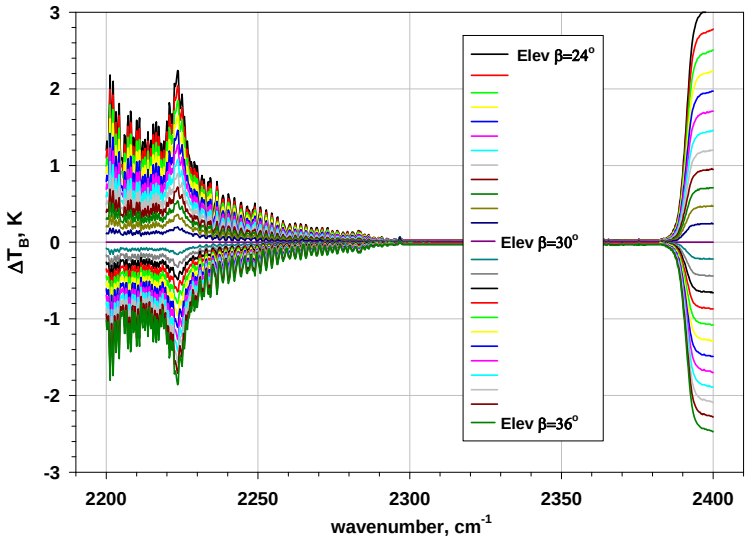

Figure 39. Radiance dependence on elevation angle *R(β) – R(β = 30°)*, TASS Referenced Atmosphere, brightness temperature units.

Figure 39 shows the radiance dependence on elevation angle, which can reach ~2 K in this spectral region and for the given observation geometry. Radiance dependence on azimuth angle has been found to be negligible under the same measurement conditions.

Figure 40 shows the high-resolution spectral dependence of the wake vortex signal, i.e. the statistics of the difference between perturbed and background radiances, obtained by averaging

over all 25 x 25 x 7 radiances. The signal is very weak (less than 0.01 K), while the measured value is about 300 K (see Figure 38).

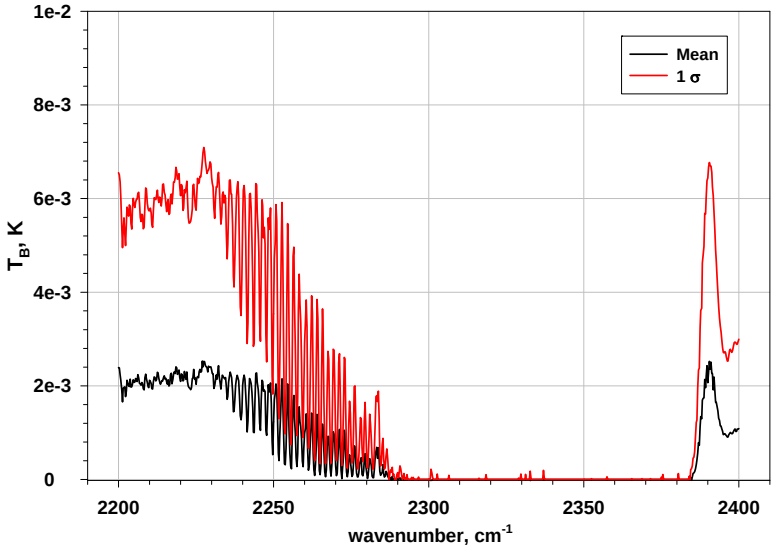

Figure 40. Statistics (mean and 1 σ) of the difference between wake vortex perturbed and background radiances, obtained by averaging over all pixels and time moments, brightness temperature units.

Temporal development of the wake vortex is presented in Figure 41. It shows the broadband (i.e. averaged over 2200 – 2400 cm^{-1}) difference between perturbed and background radiances for the whole field of view and all time moments separately. This figure demonstrates that the wake vortex signal can reach 0.01 K one minute after its generation.

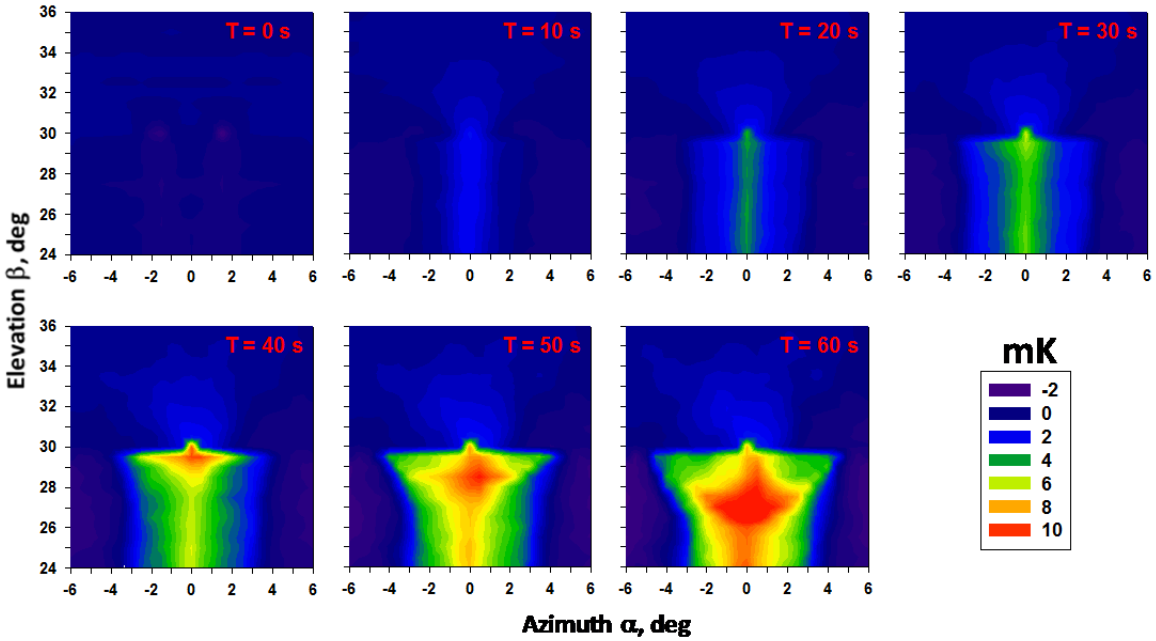

Figure 41. Evolution and magnitude of wake vortex signal as it would be seen by broadband instrument in the 2200 – 2400 cm^{-1} spectral region.

Wake vortex radiance simulations using the updated FLI-FM2 were then extended to the LW and MW bands. The ultimate goal of these simulations is to find the optimal channels for a broadband spectrometer where the wake vortex signal has a maximum value. The same TASS wake vortex temperature and water vapor 3-D fields were used. The geometry of the observations was changed slightly in order to get most of the wake vortex signal into the field of view. Figure 42 compares the field of view used in the SW-simulations with the new one. The expected wake vortex signal for a broadband spectrometer with 50 cm^{-1} width channels is shown in Figure 43. Two more bands located at about 700 cm^{-1} and 1250 cm^{-1} were found where the wake vortex signal is a maximum. These bands are in addition to the 2000 – 2200 cm^{-1} SW region explored earlier. Figure 44 shows images of a wake vortex, one minute after its generation and at the three optimal bands, respectively.

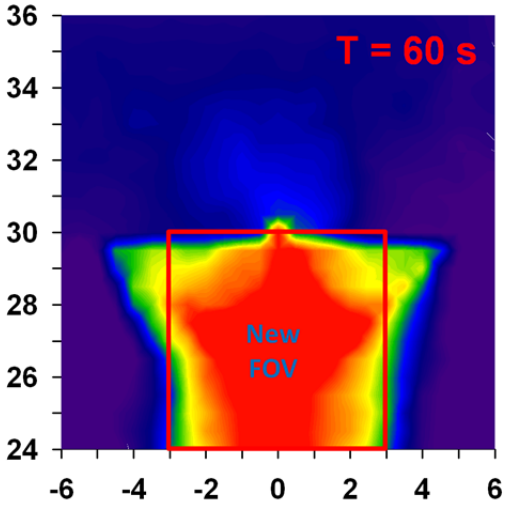

Figure 42. Updated FOV for MW and LW wake vortex simulations, represented by red box.

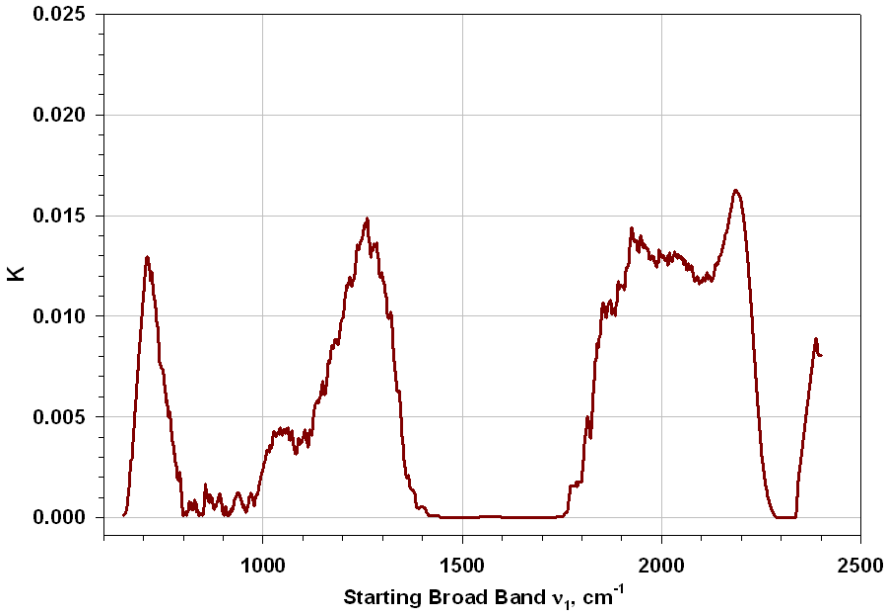

Figure 43. Brightness temperature RMS difference between wake vortex perturbed and referenced atmospheric state for a broadband spectrometer with 50 cm^{-1} width channels.

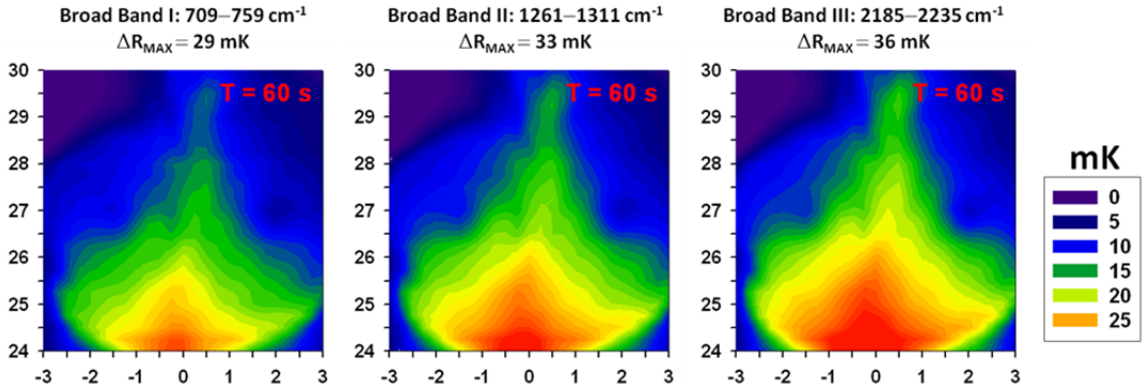

Figure 44. Wake vortex signal at LW, MW, and SW optimal bands.

The reader may note that the optimal band passes for detection of wake vortices identified by the LBLRTM and FLI-FM2 simulations do not seem agree. The LBLRTM simulation shown in Figure 33 indicates an optimal band pass of 1300 – 2000 cm^{-1}, and the FLI-FM2 simulation shown in Figure 43 indicates three optimal band passes of 700 cm^{-1}, 1250 cm^{-1}, and 2000 – 2200 cm^{-1}. However, there are two plots in Figure 33; the top plot shows the LBLRTM simulation at 0 km elevation, and the bottom plot shows the LBLRTM simulation at 6 km elevation. The optimal band pass drawn on Figure 33 is for the 6 km elevation. The FLI-FM2 models were performed at 0 km elevation only. For the 0 km simulations, the observer is on the ground and looking at a slant path through layers of atmosphere. For the 6 km simulation, the observer is at 6 km and is above these layers, looking horizontally. If one compares only the top plot of Figure 33 with Figure 43, they are very much in agreement, except for a peak at ~1600 cm^{-1}, which is probably due to differences in FFT-transfer, applied apodization, and broadband averaging between LBLRTM and FLI-FM2.

The conclusion that the optimal band passes are different for a wake vortex signal simulated along a slant path from ground versus a horizontal path at flight altitude is an important consideration when setting the requirements of a FLI sensor. However, for both elevations, there is a peak signal in the range of 1250 – 2000 cm^{-1}. Therefore, if a broadband radiometer with one band from 1250 - 2000 cm^{-1} could be identified, it would be optimal, as it could be used for wake vortex detection regardless of observer altitude. However, the noise floor would need to be much lower than currently available technology. The Suomi NPP CrIS was sent into space, and its detectors have noise levels representative of state of the art in current detector technology. The CrIS has a noise level of 0.06K, or 60 mK, which is still not low enough to detect the wake vortex signal. The noise level of this sensor must also be considered; the sensor requirements are summarized in Section 11.

4.2 Wake Vortex Measurements

In October 2009, GTRI first contacted personnel at Hartsfield-Jackson International Airport (ATL) to begin discussions regarding ground-based wake vortex field testing. The discussions continued with meetings between GTRI and ATL personnel in November and December 2009.

The purpose of these tests was to optimize test procedures for attempting to image wake vortices with the Hyper-Cam in anticipation of a full-scale data collection activity at San Francisco

International Airport (SFO). A runway was identified at ATL (27 R, boxed in red on Figure 45) as well as a location for our equipment (see starred area on Figure 45). The equipment location is outside the ATL fence, on private property owned by the Jacoby Development Corporation. ATL personnel facilitated a meeting between GTRI and Jacoby personnel, and they also offered to facilitate interactions/paperwork submission with the FAA and with airlines to enable GTRI to conduct the tests at this site.

Figure 45: An aerial view of the runway and equipment location for wake vortex testing.

Jacoby granted GTRI permission to use their land for testing. A site visit was held on March 4, 2010 with GTRI, ATL (Rob Rau), and Jacoby (Todd Addison) personnel in attendance. The site is approximately 25 minutes driving time south of GTRI, allowing for easy set up and tear down, as necessitated by weather or other factors. It was determined that no paperwork needed to be filed with the FAA for us to use this site, based on permissions that Jacoby already had in place for their development of the site. GTRI was allowed to have a ~10x10 tent to keep direct sun off of the instruments.

The first data collection activity at ATL was completed July 23, 2010. The Hyper-Cam was set up at the end of a runway, facing the direction of oncoming landing aircraft. The Hyper-Cam was oriented facing east, so as incoming aircraft landed, they passed over the test site and through the field of view.

The Hyper-Cam has an IFOV of 0.35 mrad and a variable window size of up to 320 x 256 pixels. For the July field test, reduced window sizes were used in order to decrease the recording time. The resolution of the Hyper-Cam was varied; sets of measurements were recorded at 1, 4, and 16 cm^{-1} resolutions. The Hyper-Cam was aimed eastward toward the landing aircraft; the setup is illustrated in Figure 46. The Hyper-Cam was inclined upwards to capture the flights, and the elevation angles, along with other instrument settings, are given in Table 6.

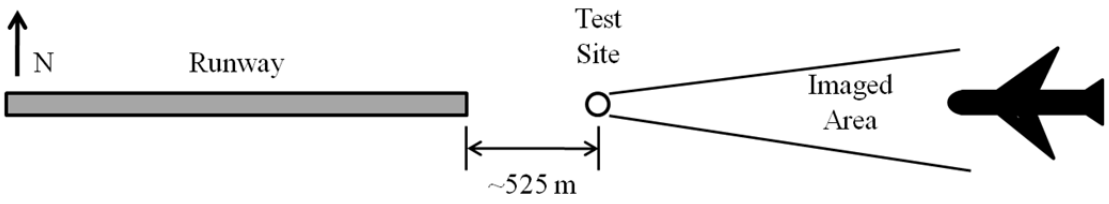

Figure 46. The test setup just off runway 26R at Hartsfield-Jackson International Airport in Atlanta, GA.

Table 6. Hyper-Cam instrument settings for July 23, 2010 ATL field test.

Acquisition Run Number	Start Time (EDT)	Elevation Angle (degrees)	Resolution (cm^{-1})	Window Size
1	8:25 AM	10	4	200 x 150
2	8:29	10	4	200 x 150
3	8:34	10	4	150 x 75
4	8:35	10	4	150 x 75
5	8:38	10	4	150 x 75
6	8:39	10	4	150 x 75
7	8:43	10	1	200 x 75
8	8:45	10	1	200 x 75
9	8:46	10	1	200 x 75
10	9:04	10	16	200 x 75
11	9:05	10	16	200 x 75
12	9:07	19	16	200 x 75
13	9:18	19	4	200 x 75

The second field test at Hartsfield-Jackson International Airport was conducted on August 27, 2010. However, on this day, because of local wind conditions, the aircraft were not landing in the same pattern as shown in Figure 46. Instead of landing from the East over the test site, the aircraft were taking off from the West, slightly south of the test site. Therefore, instead of looking directly at oncoming aircraft, the hyperspectral datacubes were collected viewing aircraft from the side at an angle; this difference in viewing angle is shown in Figure 47. Twenty-two measurement runs were made over the time in which over forty takeoffs occurred.

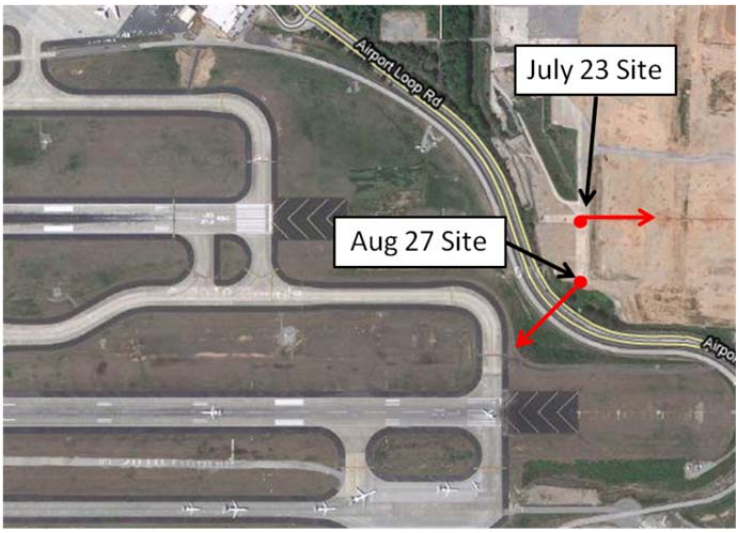

Figure 47. The locations of the Hyper-Cam in July and in August. The red arrows indicate the Hyper-Cam's viewing direction.

The third and final field test was conducted on September 22, 2010. The test site setup was identical to the data collection activity conducted on July 23, 2010, shown in Figure 46. A photo from this field test is shown in Figure 48.

Figure 48. September 2010 ATL field test setup with Hyper-Cam.

Data from several flights were collected, as well as data looking straight up to obtain a zenith sky measurement. For this field test, 16 cm^{-1} resolution datacubes were collected with a window size of 320 x 256 (the full FOV).

Lidar and METAR data were also collected at the Georgia Tech Campus in conjunction with the ATL measurements. The July 23 data run started off with a raw METAR at 11:53 AM GMT of METAR KFTY 231153Z 00000KT 6SM HZ CLR 27/23 A3013 RMK AO2 SLP190 70001 T02670233 10278 20250 53017, which shows that winds were calm (00000KT), there was a bit of haze (HZ), but the skies were clear of clouds (CLR). The METAR that was recorded the

closest to the end of the run, at 1:53 PM GMT, METAR KFTY 231353Z 02003KT 10SM CLR 31/24 A3014 RMK AO2 SLP194 T03060239 shows that winds (02003KT) had picked up a little with a speed of 3 knots (03) in the north-northeasterly direction (020 signifying 20 degrees which is labeled as being in the NNE direction), the skies remained clear (CLR) until the end of the run and the haze (HZ) disappeared.

The July 23 Range-Corrected Backscatter plot in Figure 49 shows clear skies, free of cirrus clouds, up to 8km. There is a small amount of returns (approximately 14 x 10^{-4}), corresponding to trace amounts of aerosols, from 0-1 km and then even fewer returns from 1-4 km.

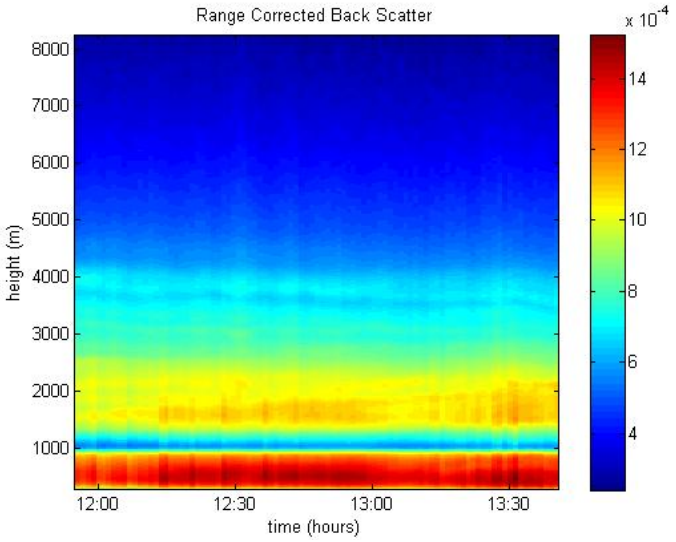

Figure 49: Range Corrected Backscatter plot for the UV Lidar, July 23, 2010.

4.3 Wake Vortex Analysis

The first detection mechanism investigated for wake vortices was brightness temperature differences caused by the temperature structure of the vortices. Previous reports had suggested that such contrasts would be measureable in the LWIR spectral region [16]; however, simulations described in Section 4.1 of this report show that the signal is too low to be detected by the Hyper-Cam. It is possible that water vapor variations produced by the wake vortex may produce radiance signal variations much larger than those shown here for temperature alone. The impact of water vapor and other trace gases associated with the wake vortex needed to be investigated before any conclusions can be made regarding the Hyper-Cam's ability to sense wake vortices. For these reasons, a detection mechanism based on entrained exhaust gasses was attempted. Much of the following section is from an SPIE paper by FLI team members [20], which is included as an appendix to this report.

4.3.1 Detection Algorithms for Entrained Exhaust Gases

As wake vortices form and then descend, there is no *a priori* way to tell where in the field of view they exist. They could form below the captured scene or be carried away by crosswinds and not be captured at all. With no way to determine where in the scene the vortices are located, a search methodology was developed which exploits the fact that vortices tend to entrain exhaust gases, such as CO_2, CO, NO_x, and H_2O [15]. The spectra of these gases, if they exist in the datacubes,

are in mixed pixels that may show spectral influences from all scene elements, including the gas of interest, the background, and the intervening atmosphere. Because these gases are in the exhaust, if they can be detected immediately upon exiting the aircraft engine, it could be possible to follow the gases through the next datacubes in the sequence of measurements as they either become entrained in a vortex or disperse into the atmosphere.

Gas detection algorithms investigated in this program included the Spectral Angle Mapper (SAM) and the Clutter Matched Filter (CMF) [25]; the Matched (MF) and Adaptive Matched Filter (AMF), and the Adaptive Coherence/Cosine Estimator (ACE) [26], [27]. All of the algorithms depend on finding a correlation or covariance in the data. The SAM algorithm finds the correlation between the target gas spectrum and every pixel in the datacube; a SAM result near 1 strongly indicates that a gas is present. All other algorithms depend on the covariance of the data, e.g. how much each pixel varies spectrally with the others. They are variants of the Generalized Likelihood Ratio Test [26] [27]. The Matched Filter, the Adaptive Matched Filter, and the Adaptive Coherence/Cosine Estimator were chosen as the most appropriate for the entrained gasses.

These gas detection algorithms depend on *a priori* knowledge of the gas spectrum under search, i.e. the target gas spectrum. Under a controlled gas release, gas constituents, abundances, temperatures, and concentrations are known. However, in the data sets under investigation, these characteristics must be estimated. To model the target gas spectrum effectively, the background and the atmosphere must also be considered. Therefore, the online tool Spectral Calc [28], which accesses the HITRAN database, was utilized to model the target gas. Many methods of modeling the target gas were investigated, including:

1. Creating the gas spectrum with the Spectral Calc atmospheric path radiance tool, then downsampling this spectrum to match the resolution needed. This spectrum then becomes the target gas.
2. Creating the gas spectrum with the Spectral Calc gas cell radiance tool, then downsampling this spectrum to match the resolution needed. This spectrum then becomes the target gas.
3. Creating the gas spectrum with the Spectral Calc gas cell radiance tool, smoothing it with a Lorentzian or Gaussian function with a width equal to the resolution needed, then downsampling this spectrum to match the resolution needed. This spectrum then becomes the target gas.
4. Creating the gas spectrum with the Spectral Calc gas cell radiance tool, using Spectral Calc's built in Gaussian smoother to smooth it, then downsampling this spectrum to match the resolution needed. This spectrum becomes then becomes the target gas.
5. Creating the gas spectrum in the same manner as 2 through 4, only the final spectrum is added to an average of the background from the actual datacube. Each horizontal strip of sky is averaged independently.

The gases searched for were H_2O, CO_2, NO_2, and HNO_3. As the largest component of the exhaust, water vapor at 425 K was chosen as the first target. The temperature was based on a derivation of aircraft exhaust temperature following the method described by Mattingly [29].

The best results were obtained when the gas cell spectrum was smoothed with the Spectral Calc Gaussian smoother, and the result added to the background averages. This process is thus

described in more detail here. The gas cell radiance spectrum was downloaded from Spectral Calc after having been smoothed with the Gaussian and the resulting spectrum was interpolated to match the resolution needed for each datacube that was collected. This result was combined with the measured data in the following manner. First, the datacube following the passage of the aircraft was divided into horizontal strips of sky and the radiance of each strip was averaged. These averages were done for each piece of sky independently, because the radiance of the sky is expected to change with elevation angle. This method of averaging the radiance for horizontal strips of sky is similar to the Directional Mean Filter [30], with the exception that we limited the direction of our background average to the horizontal. The resulting radiances give a measure of the background atmospheric conditions as a function of elevation angle at the time of measurement. Next, the gas cell data was added to each resulting radiance average; the gas cell data was added because in this case, the hot engine exhaust was expected to act as an emitter against the cold sky. This method gives the semi-empirically modeled target gas spectrum for each elevation angle.

A median filter was used on these images to eliminate noise. The result of the median filter was an image where every pixel takes the value of the median value of the 3 x 3 block of pixels around it in the original image. This filtering serves to eliminate pixels that score positively but have no positive scoring pixels around them, and are more likely false detections.

Originally, the CMF and the SAM algorithms were going to be run on the data from the September field test at ATL. These data were selected because the Hyper-Cam was allowed to run continuously for every flight instead of being started and stopped before and after each aircraft landing. However, this entire data set was collected at 16 cm^{-1} resolution. Also, only the data collected at zero zenith angle had valid calibration files; the sets angled to catch the cross-section of any falling vortices had blackbody files that were somehow corrupted. Therefore, the July dataset was analyzed more extensively. The July dataset had seven flights collected at 4 cm^{-1} resolution. The drawback with this set is that the Hyper-Cam did not run continuously, so the recording of vortex formation may have been cut off by the end of the measurement.

Two datacubes from the July dataset showed potential detection of exhaust plumes in the sense that the high-scoring pixels from the algorithm tests were located in an area of the image consistent with being part of an exhaust plume. One of the datasets was recorded at 4 cm^{-1} resolution, and results from its analysis are shown here. Water vapor was searched for in the cube following the passage of the aircraft and in all other succeeding cubes until that run ended. The visible image and a radiance image of the aircraft itself are displayed in Figure 50.

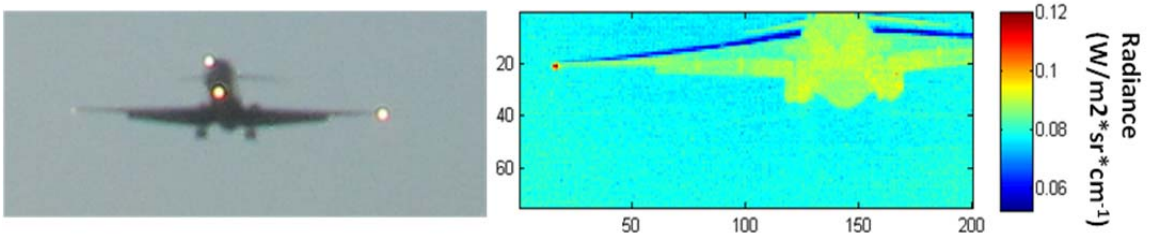

Figure 50. The visible image of the aircraft that passed through the FOV *(left)*, and the radiance image of the same aircraft *(right).*

The three algorithms that were run on the cube following the passage of the aircraft (cube 1452) were the MF, AMF, and ACE. Water vapor was the target spectrum. The radiance image of the entire datacube is shown in Figure 51, and the results of the algorithms are shown in Figure 52 through Figure 54.

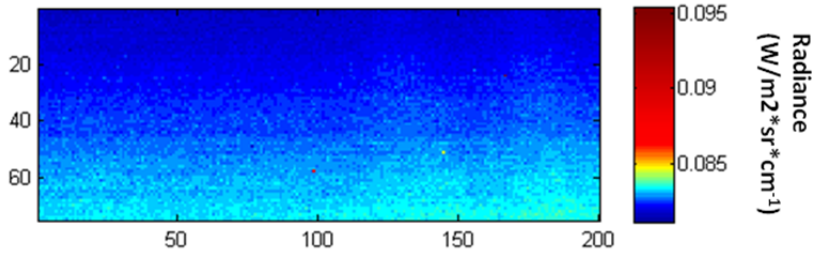

Figure 51. Average radiance of entire datacube 1452.

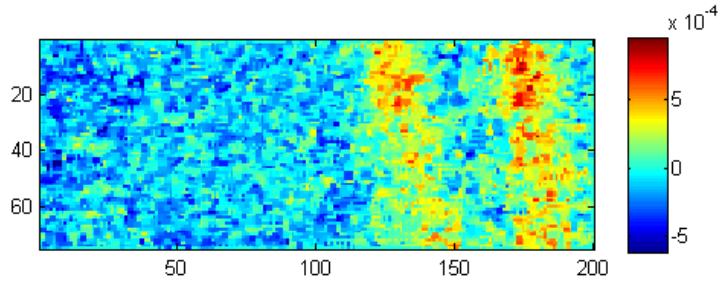

Figure 52. The MF results on datacube 1452.

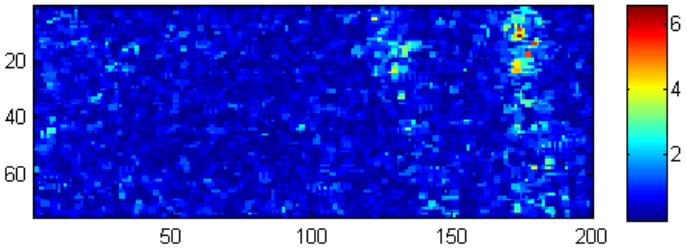

Figure 53. The AMF results on datacube 1452.

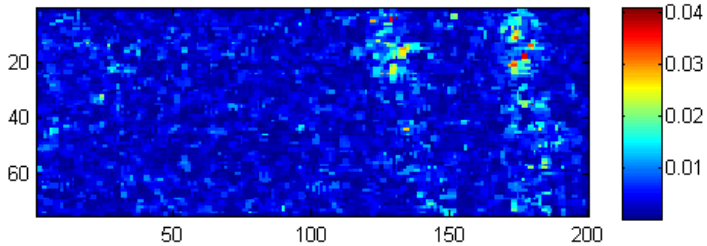

Figure 54. The ACE results on datacube 1452.

The target in all three runs is water vapor, and two trails in the air behind the aircraft are definitely detected; however, whether or not the algorithms are detecting water or anomalies is debatable. Nevertheless, there are two distinct trails, on the right side of all three images above that are not present in the radiance image of Figure 51.

All the algorithms depend on some kind of comparison of the target spectrum with the "demeaned data." This demeaned data is the spectrum of each pixel with the background

subtracted out. The average background is computed for every row of sky, since the sky radiance changes greatly with increasing viewing angle. Once the vapor trails were located, the algorithms were re-run, but when computing the average background for the demeaned data, only columns 1 – 90 (left side) were used so that we ensured no plume was present in our background average. The results of these tests are shown in Figure 55 through Figure 57.

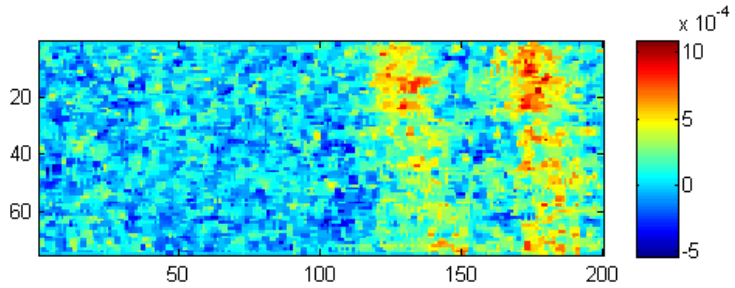

Figure 55. The MF results on datacube 1452, using only columns 1 – 90 as background in the calculation.

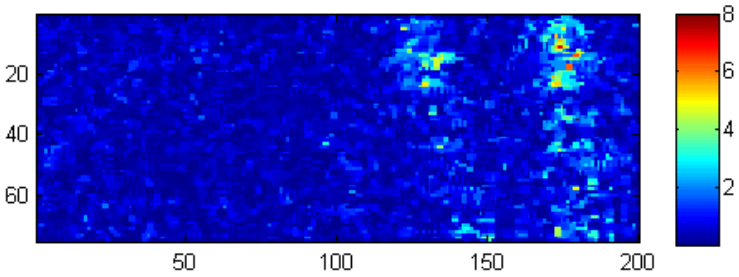

Figure 56. The AMF results on datacube 1452, using only columns 1 – 90 as background in the calculation.

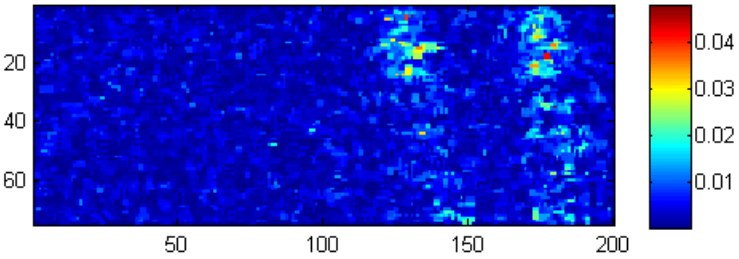

Figure 57. The ACE results on datacube 1452, using only columns 1 – 90 as background in the calculation.

Comparison of Figure 52 through Figure 54 to Figure 55 through Figure 57 shows improvement in the performance of all detectors when the plume-free background is used as an average. However, one still cannot say definitively whether water vapor is being detected. Therefore, we compared the spectrum of a pixel that scored high for all three algorithms to a pixel that was definitely only background. While there were differences in the observed spectra, they were at locations that could not be correlated with the water vapor spectrum.

The evolution of the water vapor trails can be studied by analyzing successive datacubes. The results shown in Figure 58 though Figure 63 are for water vapor, searched for with an AMF, to which a median filter has been applied.

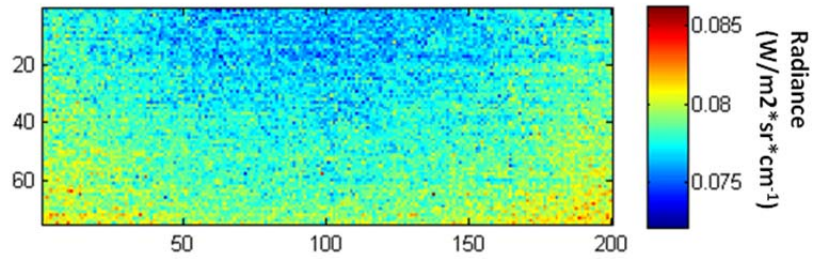

Figure 58. The radiance image of the datacube following the passage of the aircraft.

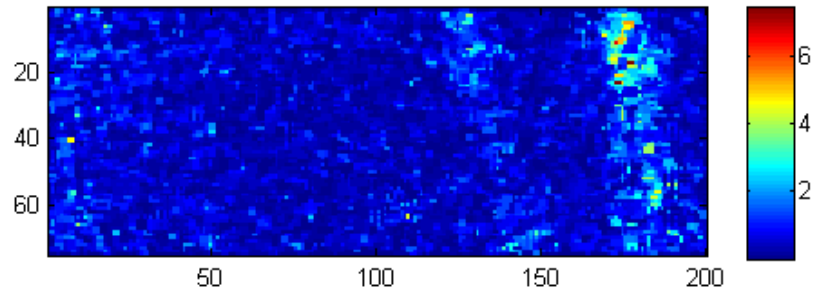

Figure 59. The adaptive matched filter results 1 second after the passage of the aircraft.

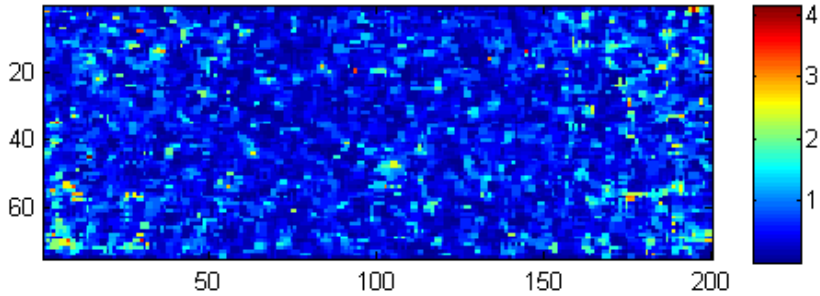

Figure 60. The adaptive matched filter results 5 seconds after the passage of the aircraft.

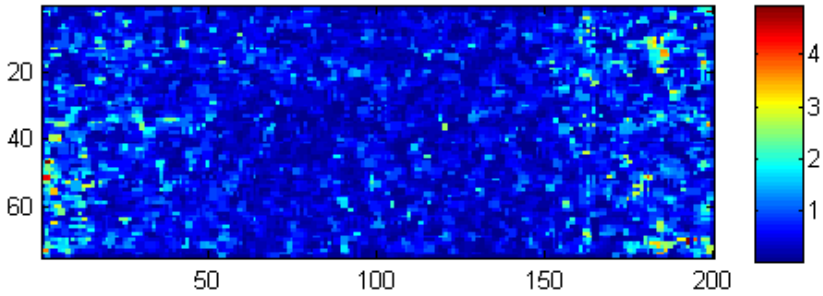

Figure 61. The adaptive matched filter results 10 seconds after the passage of the aircraft.

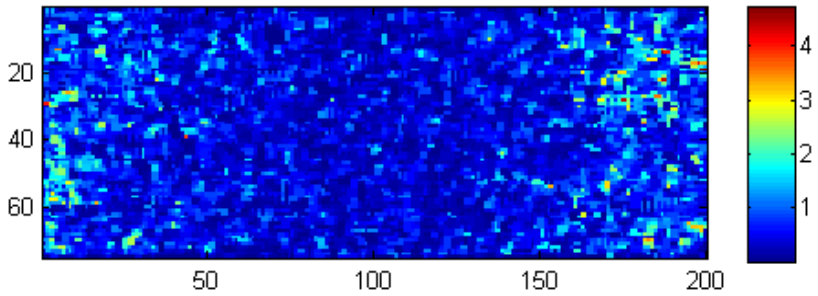

Figure 62. The adaptive matched filter results 15 seconds after the passage of the aircraft.

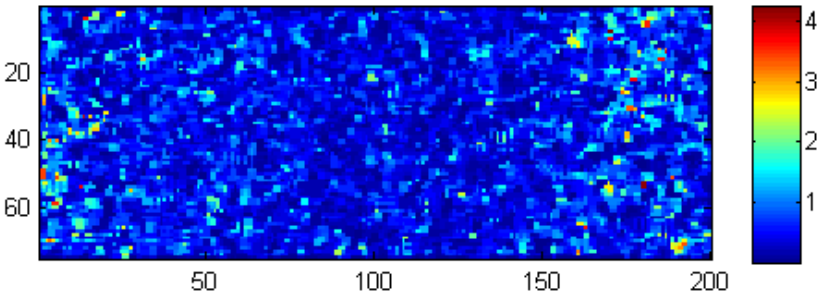

Figure 63. The adaptive matched filter results 20 seconds after the passage of the aircraft.

Figure 58 though Figure 63 demonstrate that the water vapor trails dissipate quickly, probably because the air behind the aircraft is very turbulent. However, the vapor can still be detected for a few seconds on the right side of the image, where the trails once were. We also analyzed a datacube before the aircraft entered the field of view, and the right side of that image scores higher as well. It may be that, due to the high volume of air traffic at ATL (there was a landing approximately every two minutes), the background has enhanced water vapor due to the exhaust from a nearly constant stream of incoming aircraft, making detection more difficult.

Questions arose as to whether the detection algorithms were acting as gas detectors or anomaly detectors. Therefore, a more in-depth look at the algorithms themselves was undertaken. Tests were run in which random targets were used instead of the actual gases, in an attempt to see whether or not the plumes could be detected. These random targets were modeled as vectors of zeros with ones inserted at random wavenumbers. In the instance of the MF, the random target was found in the area of the plume, which would lead one to believe that it is detecting an anomaly and not necessarily the gas itself. Something is being detected in the aircraft exhaust, but whether or not this can be identified as a specific gas is not clear. Thus, a methodology was developed to see if, once detected, the anomaly could be identified in a second step by comparison of its spectrum to that of a background pixel.

Gas detection algorithms run on ATL data using a plume-free background as an average showed improvement in performance; however, water vapor could still not be identified. In order to attempt to identify water vapor in the plume, the pixels in a 6-pixel high by 4-pixel wide region of plume that scored highly for all detection algorithms were averaged and labeled as plume. Then, the same 6-pixel high strip of sky was taken from a datacube that was recorded two frames before the airplane entered the field of view. These pixels, once averaged, were labeled as background. The plume and background plots are shown in Figure 64.

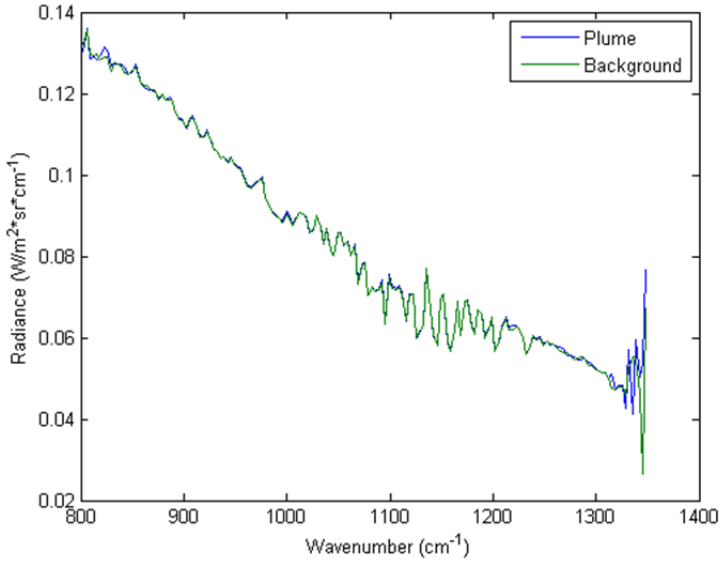

Figure 64. The radiance of the averaged plume pixels, plotted with the radiance of the averaged background pixels.

No obvious differences between the two spectra can be seen in Figure 64; therefore, to see if any differences do exist and where, the background was subtracted from the plume and the residuals plotted in Figure 65.

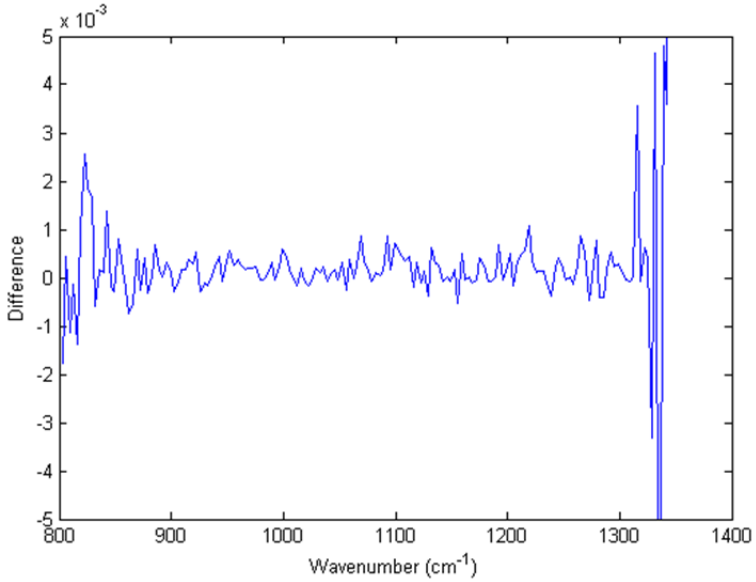

Figure 65. The difference of the plume and background.

The differences seen in Figure 65 are small and are not correlated with spectral features of the water vapor spectrum. It has not been possible to identify particular gases by the methods described here.

4.3.2 Principal Component Analysis

In addition to the methodology described above, Principal Component Analysis (PCA) on the data cubes from July 23, 2010 was also performed. After applying the bad pixel correction, these

difference images were examined visually for any potential wake signatures. Figure 66 through Figure 68 are sample images from the PCA reconstruction or filtering technique are shown below for each of the three resolutions collected on that day. This method revealed no detection of wake vortex signatures.

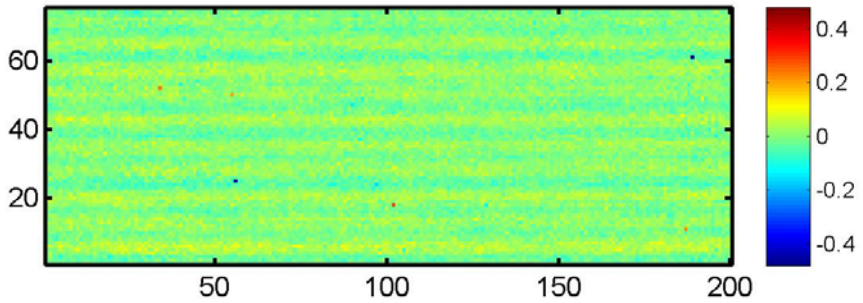

Figure 66. PCA filtered difference image integrated over 980 to 1100 wavenumber range, calculated for a 1 cm^{-1} resolution datacube.

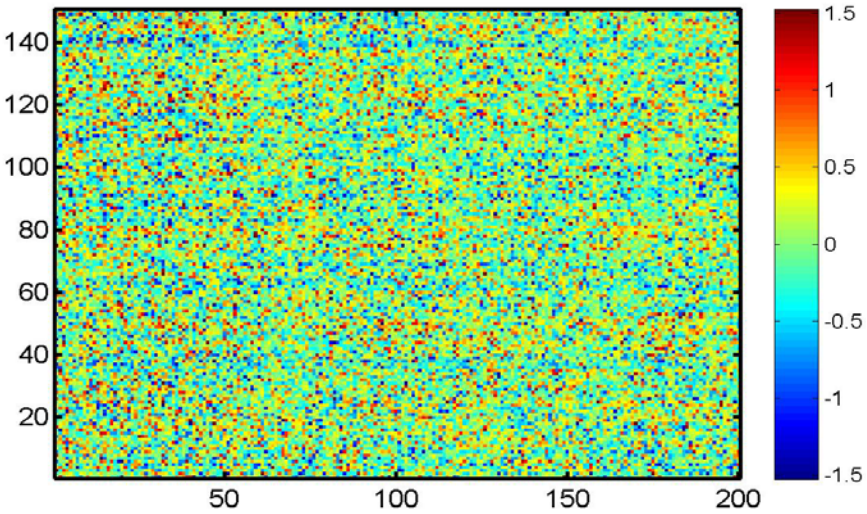

Figure 67. PCA filtered difference image integrated over 1100 to 1350 wavenumber range, calculated for a 4 cm^{-1} resolution datacube.

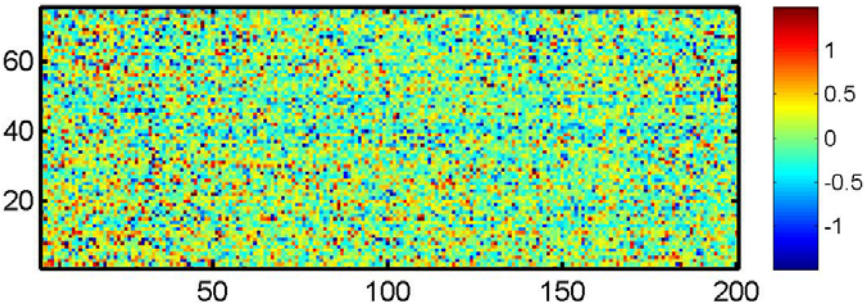

Figure 68. PCA filtered difference image integrated over 1100 to 1350 wavenumber range, calculated for a 16 cm^{-1} resolution datacube.

4.3.3 Wake Vortex Data Analysis Conclusions

While PCA and several other common methodologies were unsuccessful at identifying wake vortices, the investigations described here led to development of a novel methodology for the

detection of aircraft exhaust trails in hyperspectral data, as well as other mixed pixel gas data that has the sky as a background. The best method found is as follows:

1. Create the target gas spectrum with the Spectral Calc gas cell radiance tool, using Spectral Calc's built-in Gaussian smoother to smooth it.
2. Downsample this spectrum to match the resolution needed for the Telops datacube under study.
3. Calculate the average radiance of each strip of sky.
4. Add the target gas spectrum to the average sky radiance to create a semi-empirical target model.
5. Run the MF, AMF, or ACE algorithm, searching for the semi-empirical target gas model.
6. Display the result as a scaled image.
7. Eliminate any part of the cube that shows possible detection in the image.
8. Re-calculate the background average calculated in step 3, but do not include the parts of the image eliminated in step 7 in the average.
9. Add the target gas spectrum to the new plume-free average sky radiance to create a semi-empirical target model.
10. Re-run the MF, AMF, or ACE algorithm, searching for the semi-empirical target gas model.
11. Display the result as a scaled image.
12. Repeat this process for as many datacubes in the time series that show positive indication of detection in the event the gases become entrained in a vortex.

From the results shown, it is inconclusive as to whether the exhaust gases are actually being detected or some other disturbance is being seen. Additionally, if the exhaust is indeed being detected, the results indicate that the detection is short-lived, because the same results cannot be repeated in successive datacubes of this dataset. The method presented demonstrates a novel, and apparently effective, method to search for mixed pixel targets when the sky is the background, but we are constrained by the small radiometric signals of the trails. The method developed for mixed pixel target detection in a sky background was summarized in a SPIE proceedings paper [20], which is also given in an appendix of this report. Although truth data were not available, upward-looking hyperspectral imaging in the 800 to 1200 cm^{-1} region does not appear to be a robust means of detecting wake vortices.

5 Mountain Wave Turbulence

In early 2011, a Shift in Focus occurred due to changes in priority away from wake vortices and terminal area hazards. This shift moved the focus of the project from what was wake vortices to mountain wave turbulence, and moved the data collection activity from SFO to the CU-Boulder Mountain Research Station (MRS) in Nederland, CO. MRS experiences mountain waves and mountain wave turbulence in the fall and winter months, which affect flights into Denver International Airport (DEN), therefore it is an ideal location for collecting data on mountain waves and turbulence. The mountain wave turbulence data collection and analysis comprised the majority of Year 3's efforts.

The two main objectives of this test were as follows:

1. Observe slowly varying radiance patterns associated with standing waves.
2. Observe short-term fluctuations associated with turbulence.

These objectives required that long data sets (approximately thirty minutes) at as high as possible temporal resolution be collected of the sky by interferometric means. This collection activity utilized both the Telops Hyper-Cam and a Designs and Prototypes (D&P) TurboFT spectrometer, both operating in continuous mode simultaneously for approximately thirty minutes for each data collection event. Each sensor provides unique information about the sky; the Hyper-Cam collects LWIR hyperspectral image data of the scene, while the TurboFT has the capability to collect approximately 100 spectra per second in the 2–16 micron region. Both sensors have on-board blackbodies, which allow for calibrated radiance in the field. The two sensors were co-located on a custom-built mount which allowed boresighting of the sensors for the test so that they would be observing the same area of sky throughout each measurement period.

The Hyper-Cam data addressed the first objective in that the long data sets could capture slowly varying radiance, while the TurboFT data addressed the second objective in that the high temporal resolution and broader spectrum can capture short-term fluctuations.

5.1 Preliminary Tests and Data Analysis

5.1.1 Background

In a previous phase of this program, FLI simulations were conducted using three-dimensional temperature and water vapor fields associated with clear air turbulence. Techniques for determining the distance and warning time to an aircraft encounter with clear air turbulence were defined. The spectral resolution, range, and instrument noise requirements were defined for a FLI to be used to detect CAT and to determine its distance from the aircraft (i.e., warning time) by both the temperature and water vapor radiance signal techniques. The information in this section (5.1.1 only) is repeated from [15] except for the MODTRAN run at the end of this section to provide the reader with the relevant background.

A high spectral resolution spherical shell radiative transfer model, based on Line by Line Radiative Transfer Model (LBLRTM) molecular optical depths, was developed to study phenomena at some distance from the aircraft. A pictorial display of the path seen by a FLI aboard an aircraft is shown in Figure 69.

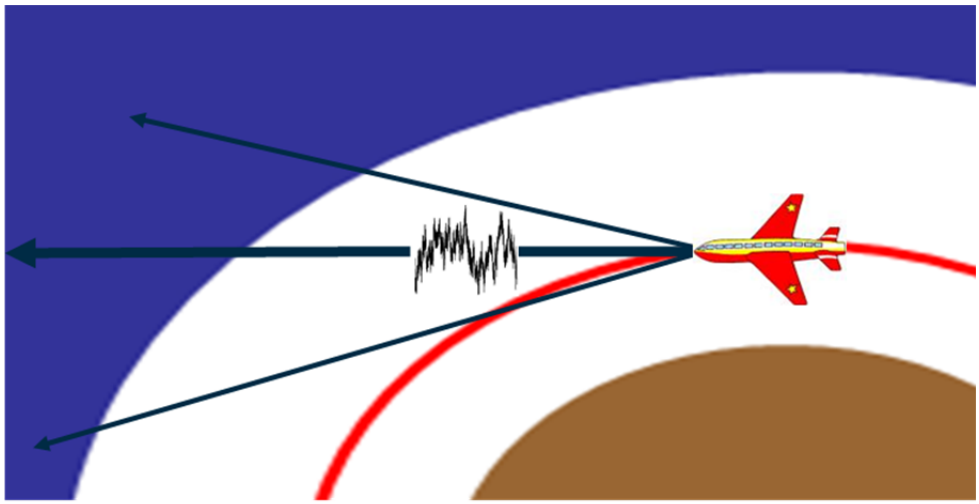

Figure 69. Path viewed by a forward-looking optical instrument aboard an aircraft.

The model takes the analytical form:

$$R(v, A, h_0) = \int_0^{TOA} B[\nu, T(s)] * [-\frac{\partial \tau(\nu, s, A)}{\partial s}] ds \tag{5.1.1}$$

where ν is wavenumber, A is the atmospheric state consisting of pressure (p), temperature (T), absorbing constituents (i.e., H_2O, CO_2, O_3, N_2O, CO, CH_4, O_2, NO, SO_2, NO_2, NH_3, HNO_3, clouds, and aerosols), h_o is the height of the aircraft, and B is the Planck function. The transmittance of the atmosphere between the aircraft and any position along the viewed path, s, is

$$\tau(\nu, s, A) = \int_0^s \exp[-\sigma(\nu, s', A)] ds' \tag{5.1.2}$$

where σ is the optical depth. The coordinate along the viewed path, s, is

$$s(h) = \sqrt{(r_e + h)^2 - (r_e + h_0)^2} \tag{5.1.3}$$

where h is height and r_e is the radius of the Earth.

Figure 70 below shows the results of applying this model to the US Standard Atmosphere to simulate what an FLI would see in clear air when flying on an aircraft at three different altitudes.

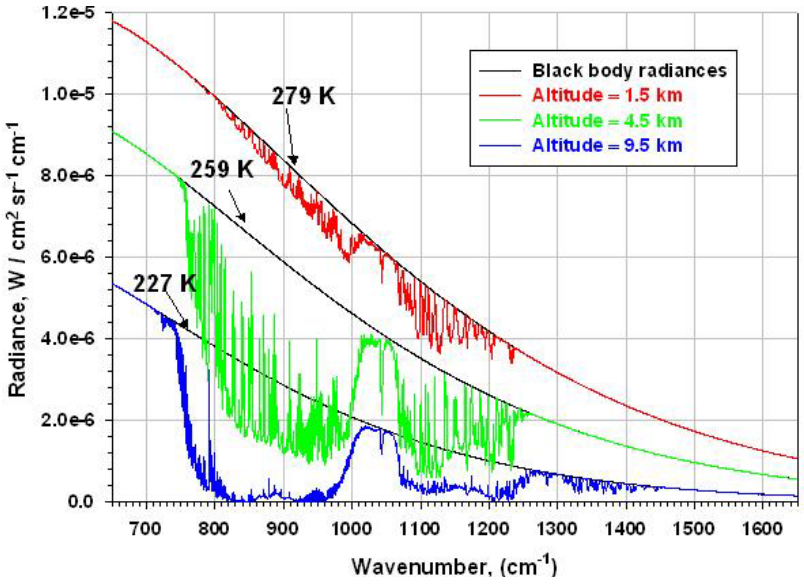

Figure 70. The spectral radiance which would be observed by an FLI looking through the US Standard Atmosphere for aircraft altitudes of 1.5, 4.5, and 9.5 km. A Norton-Beer Weak Apodization was applied to interferograms simulated to a maximum optical path difference of 1.0 cm (i.e. an unapodized spectral resolution of 0.5 cm^{-1}).

The spectrum corresponds to a near isothermal spectrum (i.e. a Planck function) for the relatively opaque 15-μm CO_2 band, 650-750 cm^{-1}. A near Planck radiance distribution is also observed for the strong water vapor absorption region, beyond a lower wave number limit ranging from 1250 – 1500 cm^{-1}, dependent upon instrument altitude. The strong emission by Ozone within the 1000 – 1100 cm^{-1} region can also be seen in Figure 70, with the amplitude of this emission band increasing with altitude as a result of the increase in Ozone concentration and the rapid decrease of the water vapor concentration with altitude. The strong absorption/emission by methane and nitrous oxide near 1305 cm^{-1} can also be seen from the fact that the spectral radiance distribution approaches a Planck radiance spectrum as the altitude of the sensor decreases.

Figure 71 shows the relative contribution from the atmosphere (assuming US Standard Atmospheric conditions) as a function of distance from the aircraft. Contributions greater than 100% are a consequence of ringing in the spectrum that remains after the weak apodization process that was performed. The higher the aircraft, the greater the contribution from spherical shells at greater distances from the aircraft. For the sensing of turbulence from the 15-μm CO_2 band, most of the signal (> 60 %) is confined to the first 5-km shell ahead of the aircraft for wave numbers smaller than 722 cm^{-1}, decreasing with increasing wave number. In the "window" region of the spectrum, 800 – 1200 cm^{-1}, the FLI observes contributions from the atmosphere at distances greater than 80 km when flying at high altitude (e.g., 9.5 km). This distance makes it useful for the detection of hazardous aerosol (e.g. volcanic ash clouds) contributions, providing avoidance warning times in excess of 5 minutes for a fast flying commercial jet aircraft. At middle and low atmospheric altitudes (e.g. 4.5 km and 1.5 km), the visibility of clouds and aerosol layers with distance decreases, being greatest for a narrow spectral region near 1000 cm^{-1} and the 1100 – 1150 cm^{-1} region of the spectrum. In addition, high spectral resolution is needed to optimize the FLI instrument sensitivity to contributions of radiance far from the aircraft, which results from being able to sense the radiation between the water vapor absorption lines within the "window" region of the spectrum.

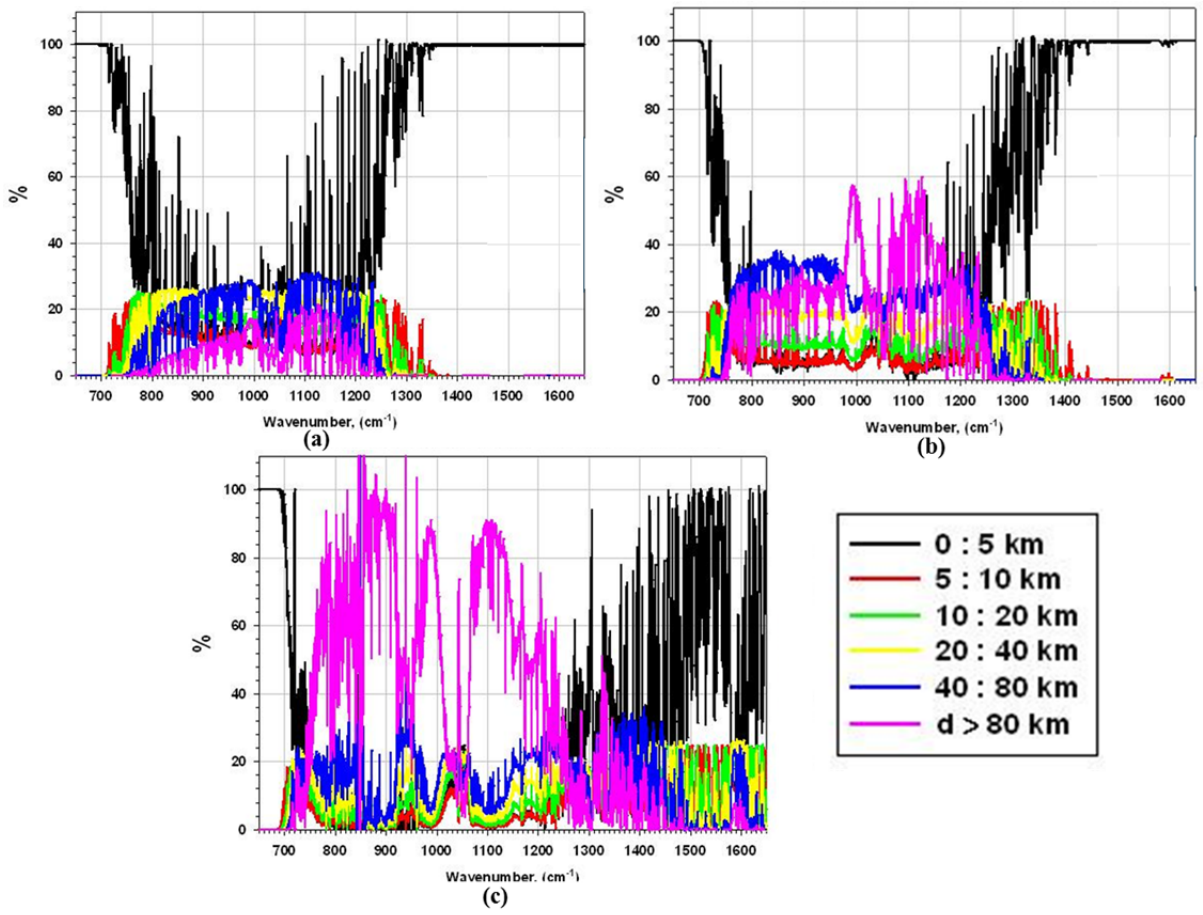

Figure 71. Contribution to the total radiance from various spherical shells along the atmospheric path observed looking forward from an aircraft at three different altitudes: (*a*) 1.5 km (~850 mb), (*b*) 4.5 km (~580 mb), and (*c*) 9.5 km (~280 mb).

Figure 69, Figure 70, and Figure 71 assumed horizontal paths at different altitudes because during the previous phase of the FLI program, flight tests were anticipated. However, due to the high cost of flight tests, only ground-based measurements were performed during this phase. The radiance measured along a horizontal path (i.e. a flight measurement scenario) will be different than the radiance measured along a slant path to space (i.e. a ground-based measurement scenario). Therefore, path radiances were predicted using MODTRAN with a Midlatitude Winter atmosphere for a ground-based sensor at 2.9 km elevation, which corresponds to the elevation of the dining hall at MRS. These radiances were computed at five different elevation angles, from 0° (horizontal) to 90° (zenith) in 30° increments, with a 15° elevation angle added because this is very close to the elevation angle which was measured at MRS. These radiances are shown in Figure 72.

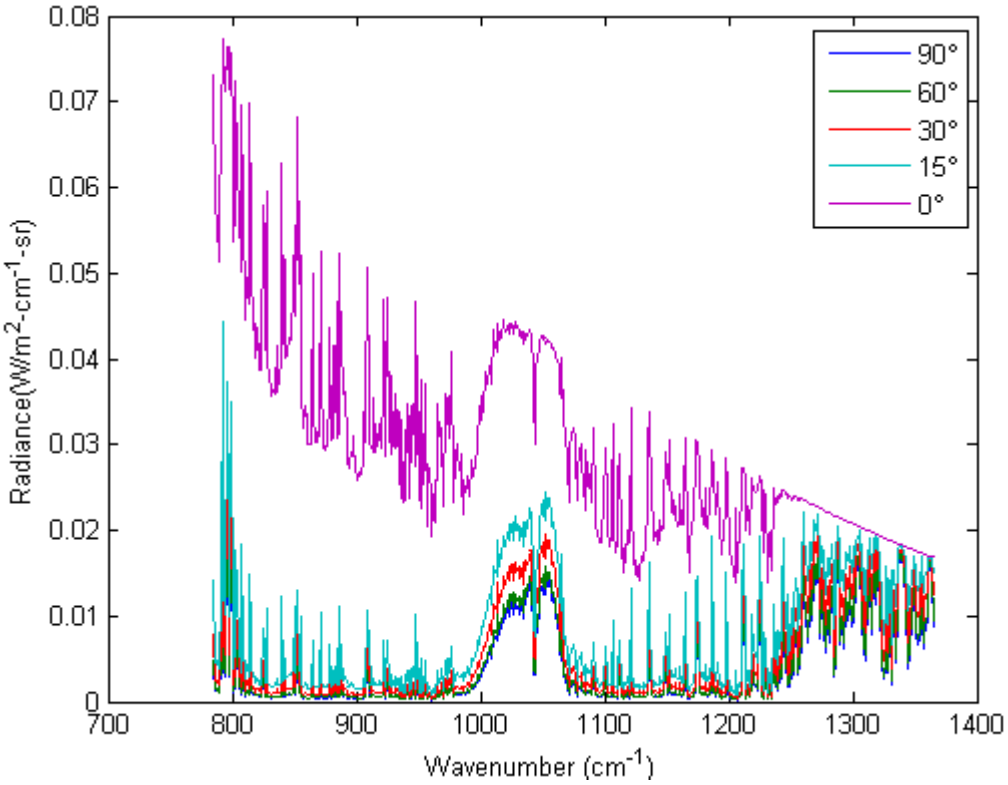

Figure 72. MODTRAN predicted path radiance for a slant path to space, from 2.9 km elevation, at five different elevation angles.

We cannot directly compare Figure 69 and Figure 72 because the simulations were done with two models (LBLRTM vs. MODTRAN) and for two atmospheres (US Standard vs. Midlatitude Winter). One can still observe that the predicted radiances in Figure 72 are much lower than those shown in Figure 69 (the units in Figure 72 are W/m^2-cm^{-1}-sr, to be consistent with Hyper-Cam data reported in remaining sections of this report). Additionally, the radiances for a horizontal path are included in Figure 72 (magenta line), and is much higher than all other elevation angles. The radiance decreases with increasing altitude *and* increasing elevation angle due to the atmospheric attenuation. This MODTRAN simulation shows that, going into the MRS test, there would be challenges due to the limitations of ground-based viewing geometries. This limitation was taken into consideration in the preliminary mountain wave simulations which are described in Section 5.1.5. Despite the lower radiance signals expected for ground-based slant paths versus horizontal paths at flight altitudes, the simulations which follow did show radiance signals that should have been observable with the Hyper-Cam.

5.1.2 D&P Sky Measurements

During the Phase 2 FLI program, radiometric observation of mountain lee waves (an example of orographic turbulence) was demonstrated with the D&P spectrometer in Boulder, CO, with fluctuations in several spectral regions that were well above the noise level [16] (see Appendix A for plots of D&P noise level). These data were analyzed further during this project in anticipation of the MRS field test. For comparison, additional D&P sky data were collected in Atlanta under clear sky conditions.

A data collection activity was conducted on the morning of April 29, 2011, under clear sky conditions with the D&P TurboFT Spectrometer. The test was made to mimic two D&P measurements from the Boulder Field Test at the NCAR Foothills Laboratory in January 2008, during a previous phase of this project. Two sky radiance measurements were made in April 2011, one at a 5 degree elevation angle and one looking vertically. These measurements, recorded from the roof of the Baker Building in Atlanta, GA, were conducted so that the data could be evaluated to see if the sky radiance time series behavior differs from the Boulder data. In addition, a run was made looking only at a blackbody, to ensure that any fluctuations in the sky data are indeed due to the sky radiance and not an artifact of the instrument. Table 7 summarizes the instrument settings and other details during the test.

Table 7. D&P instrument settings for April 29, 2011 sky test.

	Five Degree Elevation Test	Zenith Test	Blackbody Test
Resolution (cm^{-1})	4	4	4
Number Coadds for Calibration Files	1,000	1,000	1,000
Number Coadds for Sample Files	24	24	24

The instrument temperature set point was changed as the ambient temperature increased throughout the morning and into the afternoon; the closer the set point was to ambient, the steadier it remained throughout all test runs. This temperature was monitored throughout the tests and remained steady for all of them; this was important to consider as any indication of instrument drift requires re-calibration. The first sky zenith test was stopped after nine minutes when clouds began to develop. Another run was made early in the afternoon, after the clouds had dissipated and the sun had moved farther west in the sky.

Both sky measurements were conducted with a 1.2 degree field of view fore-optic, which was what was used in the 2008 tests. The standard optic has a 4.8 degree field of view; this optic was only used for the blackbody calibration and the blackbody test, because the blackbody attaches directly to this optic only.

Figure 73 shows the setup for the five degree elevation angle measurements. For these measurements, the tripod was simply tilted up slightly. An inclinometer was used to ensure the 5 degree elevation.

Figure 73. The D&P test setup for the five degree elevation sky measurements.

For the sky measurements at the zenith, the tripod was leveled and pointed at a gold mirror that was inclined at 45 degrees. A level was used to ensure that the center of the optic and the center of the gold mirror were properly aligned. This setup is shown in Figure 74.

Figure 74. The D&P test setup for the zenith sky measurements.

As a check to ensure that there was no instrument drift that was causing any of the fluctuations in sky radiance observations, the calibration blackbody was measured as a sample. The blackbody temperature was set at 24.4°C, which was close to ambient.

The data obtained from this field test proved to be very noisy due to RFI on the roof of the building. Therefore, the test was repeated on July 12, 2011 at the Bradley Observatory on the Agnes Scott College campus. This location was expected to have much lower RFI, and the observatory has a lidar that was operational during the test to ensure that the sky was cloud-free.

The D&P settings were identical to those shown in Table 7; however, the 5 degree elevation runs were not made due to the appearance of clouds during the test. There were unfortunately similar data issues with this test as well and the data were not very useful. The results of this test indicated that the D&P was in need of refurbishment; it was sent back to the manufacturer is September 2011 in anticipation of the MRS field test.

5.1.3 D&P Data Analysis of Previously Collected Data

STAR performed further analysis of sky radiance spectra that were recorded by GTRI personnel at the NCAR Foothills Laboratory in a previous phase of the program in January 2008 [16], in addition to the two data sets collected in Atlanta in 2011. The spectra were recorded with a D&P TurboFT spectroradiometer, which covers the 2 - 15 micron wavelength region (666–5,000 cm^{-1}) at 4 cm^{-1} resolution. Large sets of spectra were acquired, corresponding to long time series of data points at each wavenumber, and those time series provided the basis for the analyses presented here.

From Boulder, the data included Jan 14th, 15th, and 17th. The first day was calm, and for the data period shown in the plots, the device was pointing vertically. The second and third days were windy and mountain waves were present, and there were numerous instances of turbulence as measured by UAL 757s flying in and out of DEN. As a control, data were collected at GTRI on April 29, 2011. There was significant contamination in those data, so a second data set was collected on July 19, 2011. Unfortunately, these data had similar problems. In the following, a description of the data analysis methodology is presented, followed by a presentation of the analysis results.

For each of the data collection periods, the D&P sensor measured interferograms at a rate of approximately 96 samples/sec. Twenty four interferograms were averaged and then Fourier transformed to provide radiances as a function of time and wavelength (or wavenumber), as used below. The wavenumbers ranged from 630 to 3960 cm^{-1}. During processing, 5000 samples (approximately 1500 seconds, or 25 minutes) were analyzed at a time. This number of samples was somewhat arbitrary and was chosen as a balance between a long-enough time series and a set of data that could be processed in a reasonable amount of time. It should be noted that some data collection windows were shorter than 1500 seconds, so in those cases the data available were used. In other cases, more than 1500 seconds of data were collected at a time. In those situations, the data were separated into non-overlapping windows of 5000 samples. Henceforth, we refer to the 5000 sample-long (or less than 5000 if that was all that was available) data set as the analysis window.

Each window was broken into non-overlapping sub-windows of 512 points each, with the left-over data samples ignored. Over each of these sub-windows, a quadratic function was fitted to the data, and then subtracted from the data to give “trend removed” data. Probability distributions of the radiances over time were calculated and fitted with a Gaussian distribution. Since there should be a relatively large number of independent samples over the window, the Central Limit Theorem would predict a Gaussian distribution, especially for the trend-removed data. Correlation functions for each wavenumber were computed over the entire window. (The Mathematica correlation function was used for this computation.) Power spectra were also calculated for

specific wavenumbers of interest. The spectra were calculated for each sub-window and then frequency-averaged to give the spectrum for the given window. A von Karman turbulence model-plus noise and a quadratic function-plus noise were fitted to the spectra. The quadratic model was used to investigate whether there was any Brownian noise (f^{-2}) present in the data. Since the asymptotic form of the von Karman model has an $f^{-5/3}$ slope, Brownian noise with an f^{-2} slope can be confused with a true atmospheric structure. Brownian noise can result from averaging white noise.

5.1.3.1 Trend Removal

It was important to remove the trend prior to the calculations described above. When looking for turbulence signatures, one is typically investigating deviations from short-time/space scale phenomena; and hence, larger-scale (typically) non-turbulent phenomena should be excluded. Figure 75 and Figure 76 illustrate the results of the trend removal process. This is a more extreme case, showing a fairly significant variation in the radiance as a function of time, as seen in Figure 75. Recall that the sub-window used for trend removal is 512 points long, so even after the trend has been removed, some moderate-scale variations can still be seen (Figure 76). Figure 77 and Figure 78 show estimates of the probability distributions (histograms) for the original and trend removed data, respectively. In those figures, the red curve is a smoothed version of the histogram data, and the black curve is a Gaussian distribution with the mean and standard deviation coming from the histogram data. The bimodal structure seen in Figure 77 is due to the flattening of the radiance data at both ends, as seen in Figure 75. After the trend removal the data looks relatively consistent with a zero-mean Gaussian distribution, as seen in Figure 78.

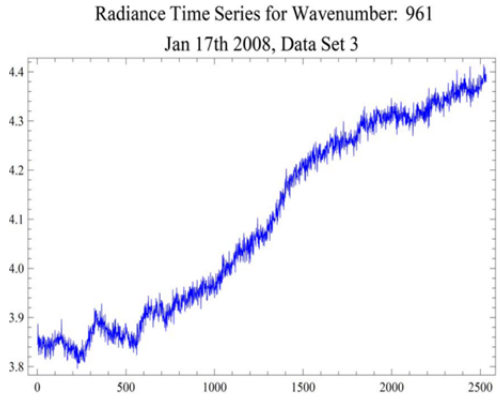

Figure 75. Radiance time series.

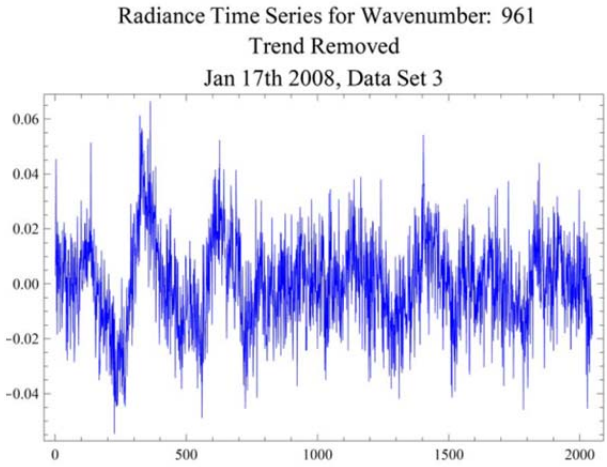

Figure 76. Same data as shown in Figure 75, after trend removal.

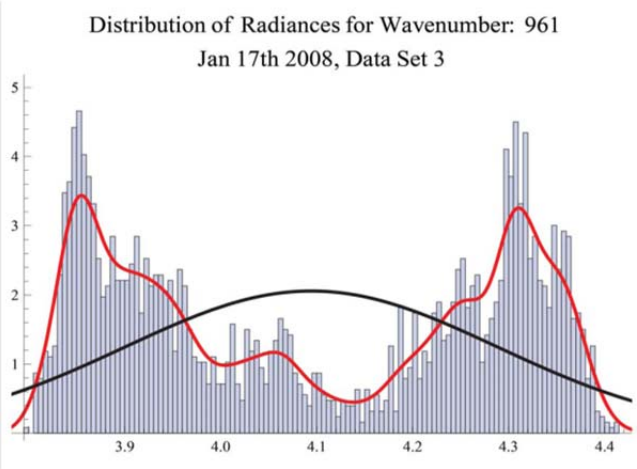

Figure 77. Probability distribution (histogram) for the data shown in Figure 75. The red curve is a smoothed version of the underlying histogram, and the black curve is a Gaussian distribution fit to the histogram.

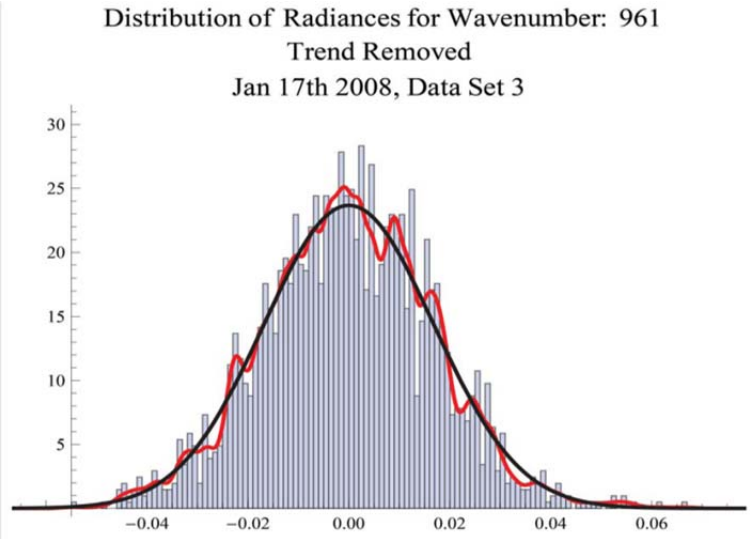

Figure 78. Probability distribution for the data shown in Figure 76, i.e. the trend-removed data.

The importance of removing a trend is clear from Figure 79, which shows the correlation function for the original (black curve) and trend removed (red curve) data. Note that the correlation function is normalized so that the value at zero lag is always one, hence the apparent jump in the red curve. It can be seen that the trend creates an artificial correlation in the data.

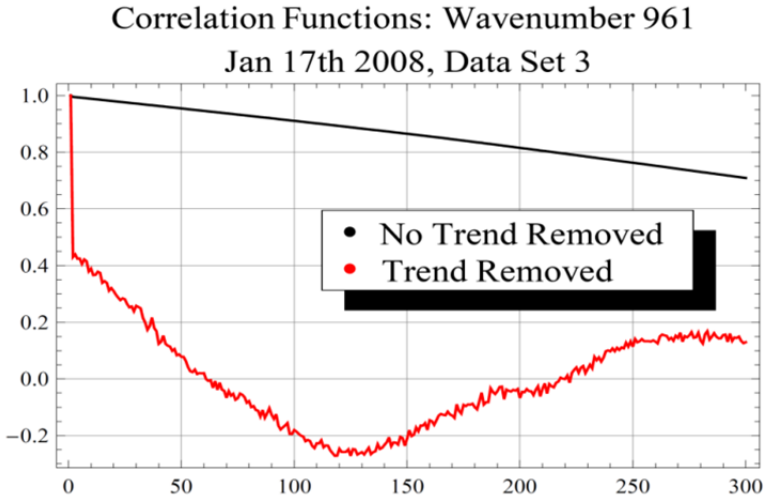

Figure 79. Correlation functions with and without trend removal.

Mathematically, this can be seen as follows. The normalized correlation function is given by

$$\rho(\tau) = \frac{\gamma(\tau)}{\gamma(0)} \tag{5.1.1}$$

where as an approximation,

$$\gamma(\tau) = \frac{1}{N}\sum_{i=1}^{N-\tau}(X_{i+\tau} - \bar{X}) - (X_i - \bar{X}) \tag{5.1.2}$$

Assume for simplicity that the mean $\bar{X}$ is zero, and that for not-too-large values of i, the data can be approximated by a linear function of i,

$$X_i = ai + b \tag{5.1.3}$$

This approximation means that

$$\gamma(\tau) = A\tau + B \tag{5.1.4}$$

where

$$A = \frac{a}{N}\sum_{i=1}^{N-\tau}(ai + b)^2 \tag{5.1.5}$$

and

$$B = \frac{1}{N}\sum_{i=1}^{N-\tau}(ai + b)^2 \tag{5.1.6}$$

Equation 5.1.1 implies that the correlation function in this case is a linear function of τ. We can further analyze this via a simple simulation. From the original radiance time series, a linear fit was calculated. We created a time series by adding the linear fit to a Gaussian noise sequence with mean and standard deviation calculated from the original time series. These quantities are shown in Figure 80, where the black curve is the original data (i.e. as seen in Figure 75), the red line is the linear fit to the original data, and the blue curve is the simulated data. Figure 81 shows the results of the analysis. The black and red curves are those from Figure 79, whereas the blue curve is the correlation function calculated from the simulated data. It can be seen that the correlation functions for both the original and simulated data are quite similar, and both are linear functions. This provides a good illustration of how trends can produce artificial correlations, and hence why it is important to remove such trends.

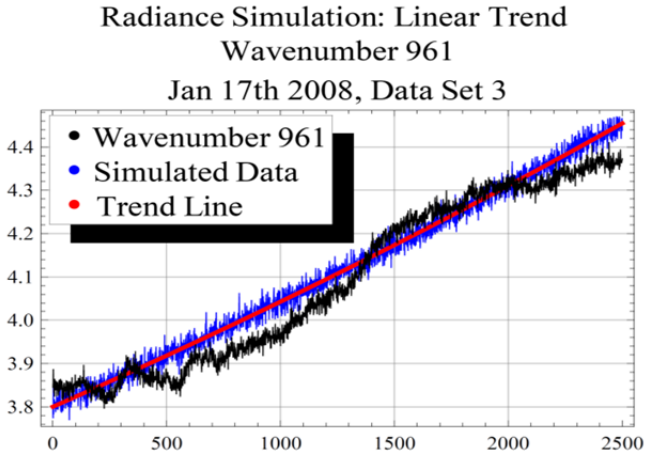

Figure 80. Black curve is radiance for wavenumber 961; Red curve is fitted linear trend; Blue curve is fitted linear trend with Gaussian noise (mean and std. deviation from radiance data).

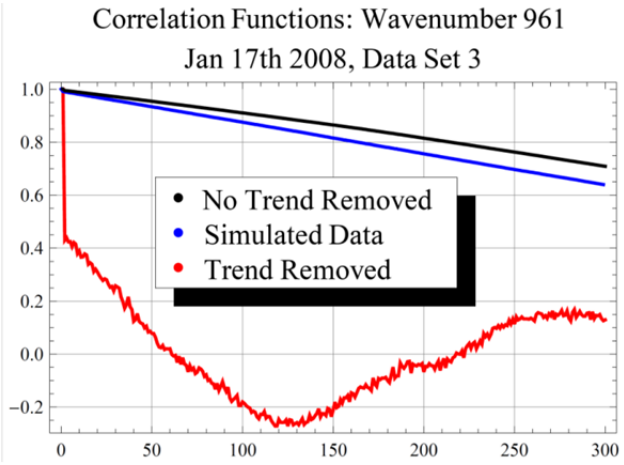

Figure 81. Black and red curves are as seen in Figure 79; blue curve is the correlation function for the simulated data (blue curve) from Figure 80.

Figure 82 and Figure 83 show the spectra calculated from the original and de-trended data, respectively. As mentioned above, the spectra were fit to a quadratic function plus noise (blue curves) and a von Karman function plus noise. As with the correlation functions, there is a dramatic difference at the low frequencies between the spectrum from the original and de-trended

data. This behavior is expected since removing a trend acts as a high-pass filter. Figure 84 is a direct comparison between the original and de-trended spectra. Figure 85 illustrates the original and de-trended spectra from a different wavenumber and from a different day. In this case, as can be seen in Figure 86 and Figure 87, there is not too much difference between the original and de-trended data, i.e. there is not much of a trend. From looking at numerous cases, it appears that trends are more prevalent in the lower wavenumber data.

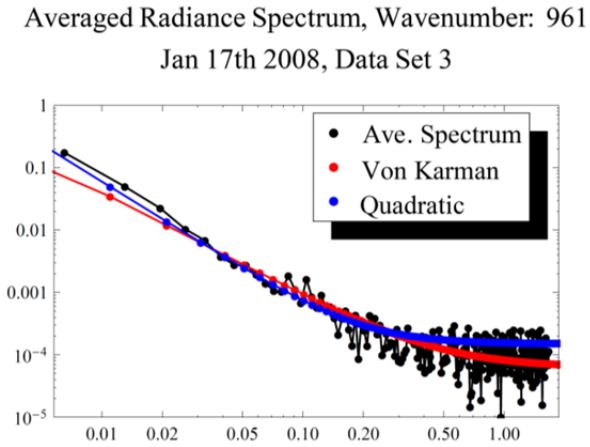

Figure 82. Power spectrum of radiance time series (black). The blue curve is the fit of a quadratic function plus noise to the data, and the red curve illustrates using a von Karman model plus noise.

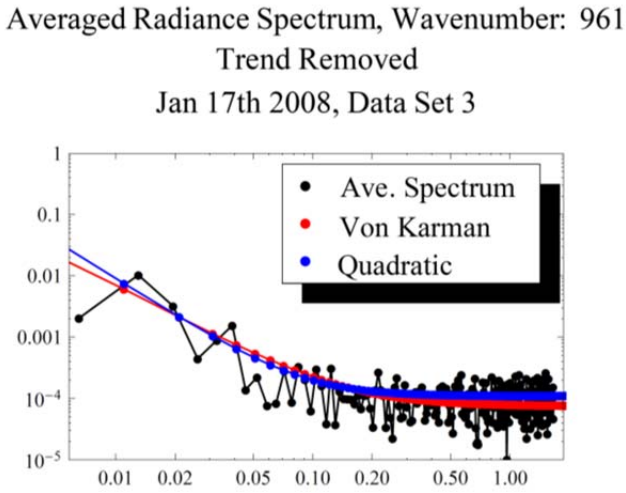

Figure 83. Same as Figure 82, but with trend-removed radiance data.

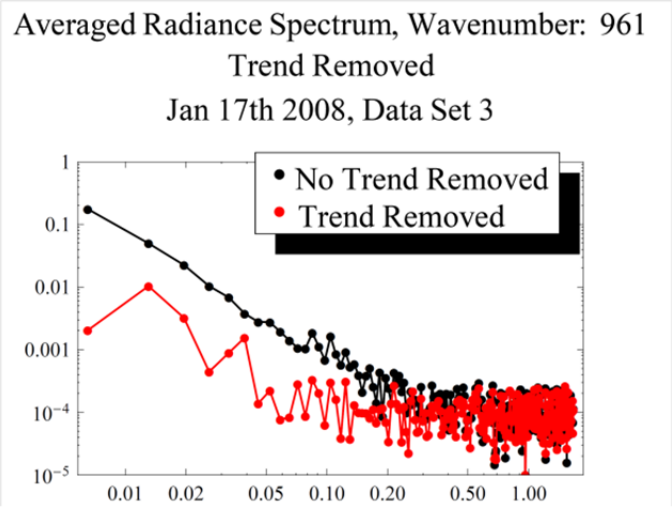

Figure 84. The effect of trend removal on the power spectra. Wavenumber 961 shown.

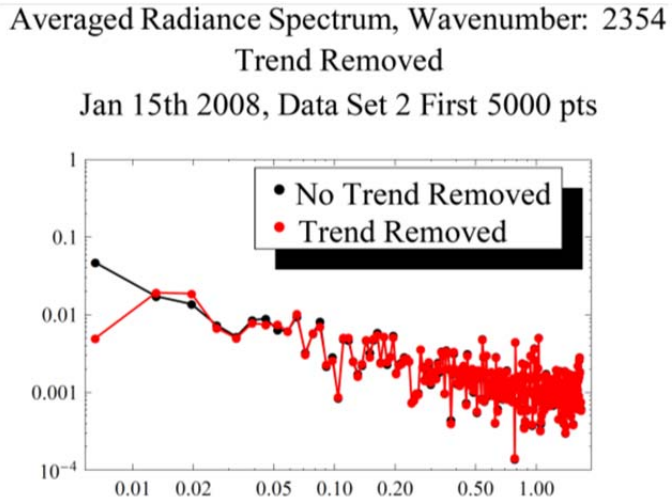

Figure 85. The effect of trend removal on the power spectra. Wavenumber 2354 shown. (Note that this is from a different day as the data shown above.)

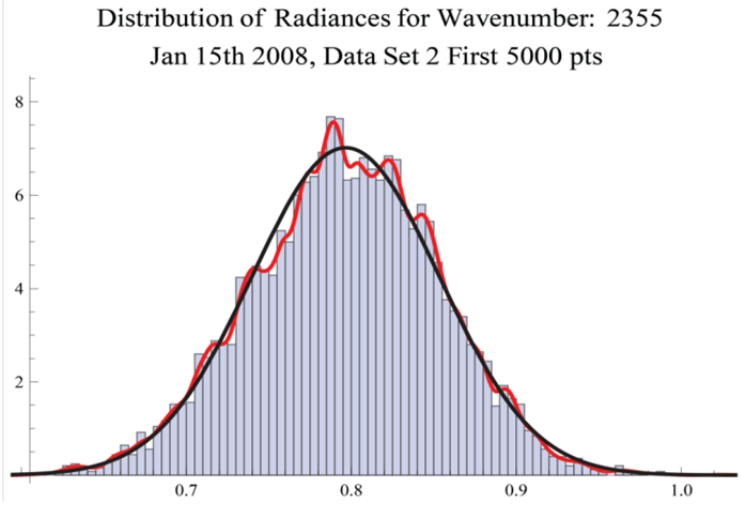

Figure 86. Probability plot for non-trend removed data used in Figure 85.

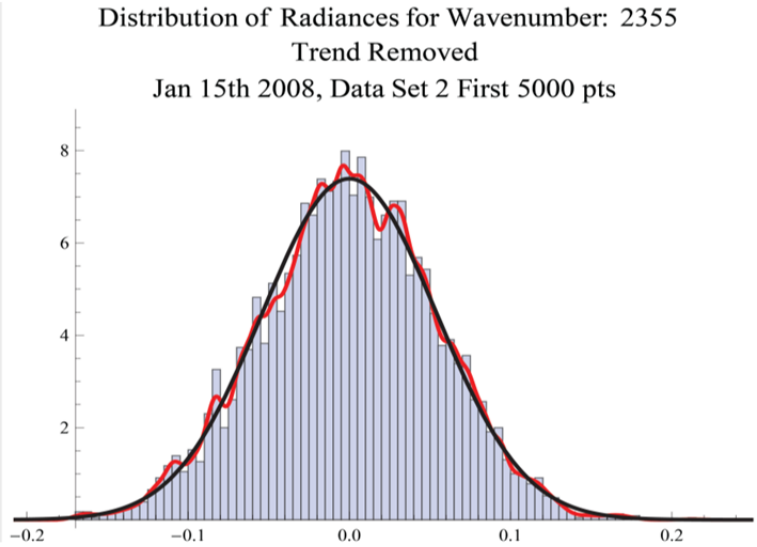

Figure 87. Probability plot for trend removed data used in Figure 85.

Another type of trend that was observed is a sinusoidal one, as seen in Figure 88. Figure 89 shows the result of the quadratic trend removal process, as described above. Another approach to trend removal is using Fourier methods; an example of which is as follows. A discrete cosine transform of the data was calculated and all the coefficients past the first 60 (arbitrary number), were set to zero. The inverse cosine transform was then applied to this new set of coefficients to generate a filtered time series. The results of this calculation are shown in Figure 90, where the red curve is the original time series, and the black curve is the Fourier-filtered data. The difference of these curves, the Fourier de-trended data, is shown in Figure 91, and a comparison of the two power spectra is given in Figure 92. Returning to the quadratic trend removal, Figure 93 illustrates the correlation functions for the original and quadratic de-trended data (seen in Figure 88 and Figure 89, respectively).

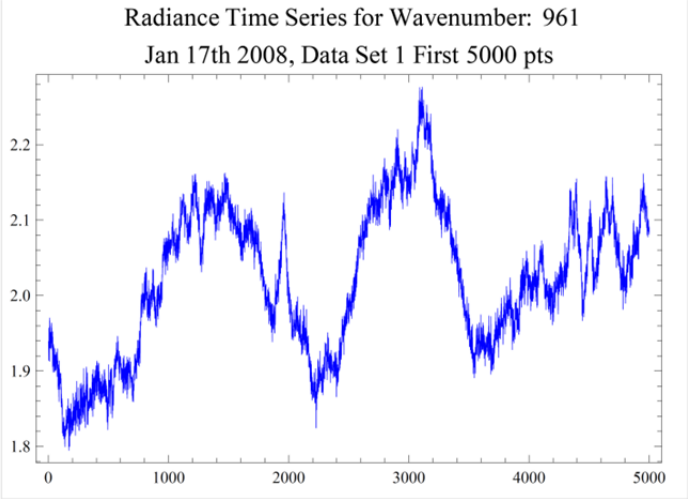

Figure 88. Original radiance data showing larger-scale sinusoidal trend.

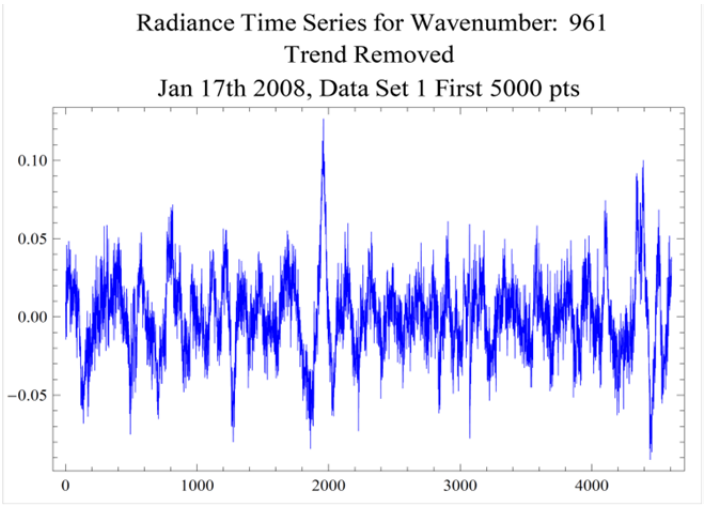

Figure 89. De-trended radiance data showing residual, smaller-scale sinusoidal trend. (Using quadratic trend removal, as above.)

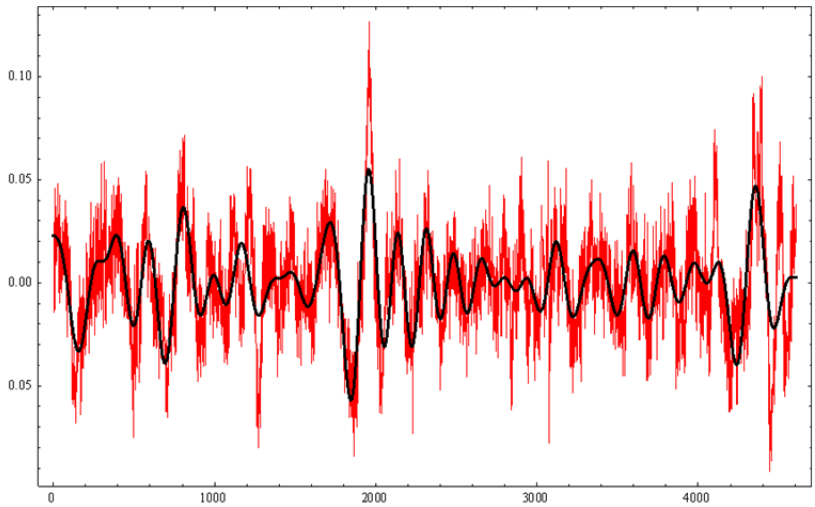

Figure 90. Using Fourier method for trend removal. Red curve is the original data as seen in Figure 88; black curve is trend from Fourier method.

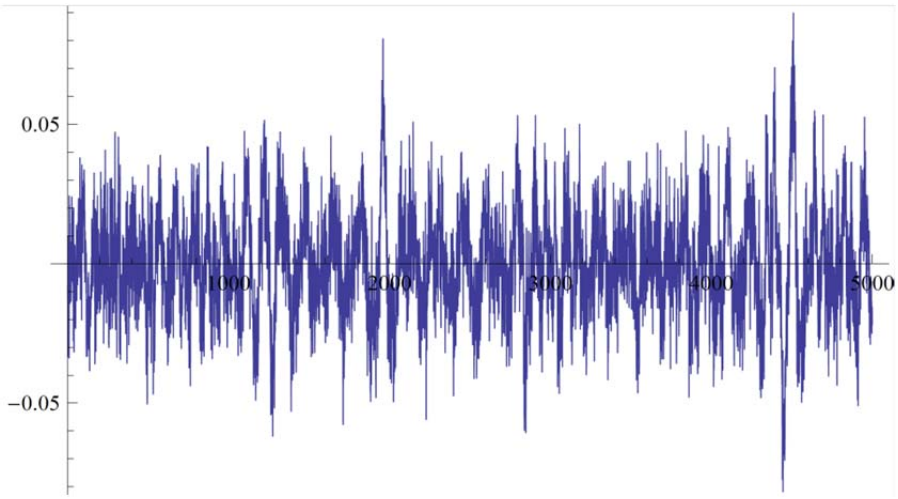

Figure 91. De-trended data – difference between red and black curves from Figure 90.

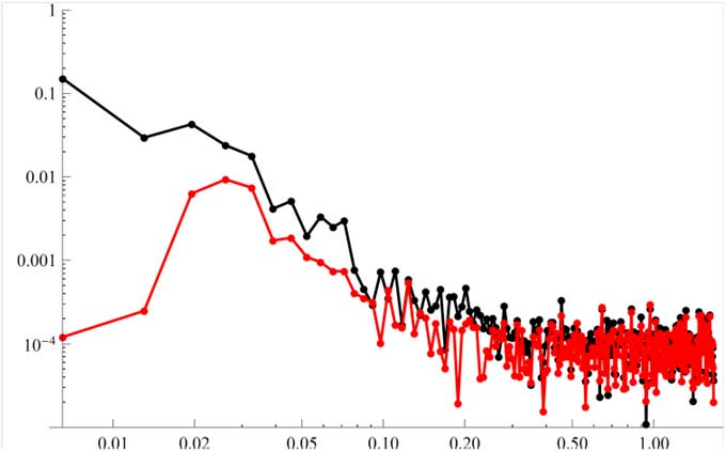

Figure 92. Spectra from original (black curve) and Fourier de-trended data (red curve).

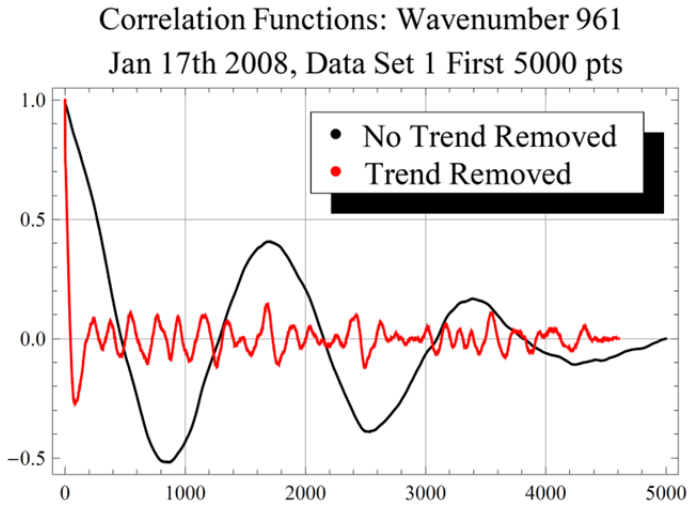

Figure 93. Correlation functions before and after quadratic trend removal, for the data shown in Figure 88 (original) and Figure 89 (de-trended).

As with the linear trend case, a closed-form correlation function can be computed for a sinusoidal trend. We use Equation 5.1.2 with

$$X_i = a\cos\left(2\pi\frac{i}{T}\right) \tag{5.1.7}$$

and

$$X_{i+t} = a\cos\left(2\pi\frac{i+\tau}{T}\right) \tag{5.1.8}$$

where T is the period of the sinusoidal trend. Using $\cos(A+B) = \cos A\cos B - \sin A\sin B$, we have

$$\gamma(\tau) = \frac{a^2}{N}\sum_{i=1}^{N-\tau}\left[\cos\left(2\pi\frac{\tau}{T}\right)\cos^2\left(2\pi\frac{i}{T}\right) - \sin\left(2\pi\frac{\tau}{T}\right)\cos\left(2\pi\frac{i}{T}\right)\sin\left(2\pi\frac{i}{T}\right)\right] \tag{5.1.9}$$

and

$$\gamma(0) = \frac{a^2}{N}\sum_{i=1}^{N}\cos^2\left(2\pi\frac{i}{T}\right) \tag{5.1.10}$$

The correlation function, given by Equation 5.1.1, can then be calculated. The parameters a and T were estimated by eye from the data shown in Figure 88 as 0.13 and 1800, respectively. Figure 94 gives the calculated correlation function. A comparison with the correlation function for the original data (cf. the black curve in Figure 93) shows a good match. This match indicates that the sinusoidal trend dominates the correlation function of the original data.

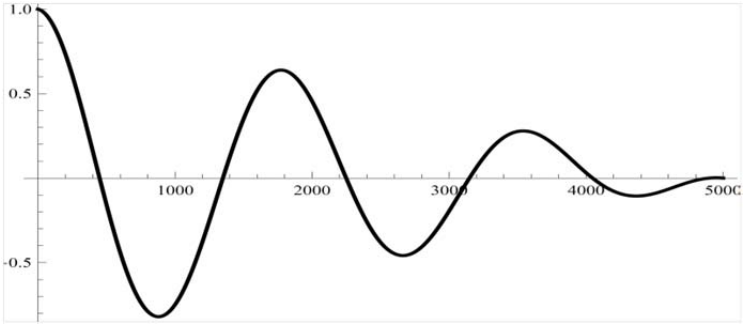

Figure 94. Correlation function for a cosine trend

Note that the cosine transform is the interferogram for the data, and hence the method just described is simply the application of a filter in the interferogram domain. Since performing Fourier transforms introduces artifacts, a preferable method would be to apply the filter in the original interferogram data and then transform to get a trend-removed radiance time series. For non-stationary data, a method preferable to the Fourier method is the application of a wavelet filter. In summary, we have seen how important trend removal is in investigating small-scale structures in the data, as the trends can dominate the statistical measures, i.e. correlation functions and spectra. Of course, the question arises, "What is the trend that *should* be removed?" Obviously, this is an arbitrary process: Is a low-order polynomial or sinusoidal trend appropriate?

Over what sub-window lengths should the trend be calculated? Unfortunately, there is no one-size-fits all method, and it is then left to the analyst to decide. Typically, the statistical measures are calculated and then the analyst's intuition is brought to bear. Often, this process reveals artifacts in the data or in the pre-processing methods. This same issue is discussed in a different context in the next section: fitting models to the radiance spectra.

5.1.3.2 Fitting Models to the Radiance Power Spectra

Figure 82 and Figure 83 show the results of fitting models to the radiance power spectrum. As mentioned above, the two models used are a quadratic function plus noise, $\phi_a(f) = af^{-2} + N$, and a model often used in turbulence analysis, the von Karman function plus noise,

$$\phi_{vk}(f) = 4\tau_{vk}\sigma^2\left[1 + \left(\frac{2\sqrt{\pi}\tau_{vk}\Gamma(1/3)}{\Gamma(5/6)}f\right)^2\right]^{-5/6} + N \qquad (5.1.11)$$

Where, τ_{vk} is a temporal scale, σ^2 is the variance of the radiance data. In this analysis, we are using the von Karman form for a scalar function. In the quadratic model there are two parameters to estimate, and in the von Karman model there are three.

We use Mathematica's *FindFit* routine to perform the fits. As in the trend removal process, there is some ambiguity in performing the fits; specifically, over what frequency points should the fit be performed? Since there is a well-defined noise floor (cf. Figure 82), and we include this as a fit parameter, we can use all the high-frequency points. Obviously, in the quadratic model case we do not want to use all the low frequency points – as the model grows without bound as $f \rightarrow 0$. (Recall, this is not intended to represent the physical phenomena, but rather to look for Brownian noise in the data.) As can be seen from Equation 5.1.8, the von Karman model reaches a constant as $f \rightarrow 0$, so we can use low-frequency points, but we must be careful when removing trends. As mentioned above, trend removal acts like a high-pass filter on the data, as can be seen in Figure 83, so we do not want to use all the low frequency points. So, how does one choose which spectral points to include in the model fitting? We would like to use as many points as possible, but at the same time we do not want to bias the fits.

Return to Figure 82. For that example we used the 10th through last points for the quadratic model and the 6th through last for the von Karman one. We see that the quadratic fit is better at the low-frequencies, but worse at the high-frequencies. Consider using 10th through last for both. As seen in Figure 95, now the von Karman model does a poorer job at both ends of the frequency range. If we expand the von Karman model in a power series around zero, the first two terms are a constant and a negative quadratic $(a - bf^2)$, which can be seen in Figure 95. Going the other way, Figure 96 shows the result of using the 2nd through last points in the fit. Obviously, neither model does a good job of fitting the higher-frequency points, but the von Karman is superior to the quadratic. It is not exactly clear why this fit did so poorly. One possibility is that the fitting routine is over-fitting to the lower-frequency (much larger in magnitude) points.

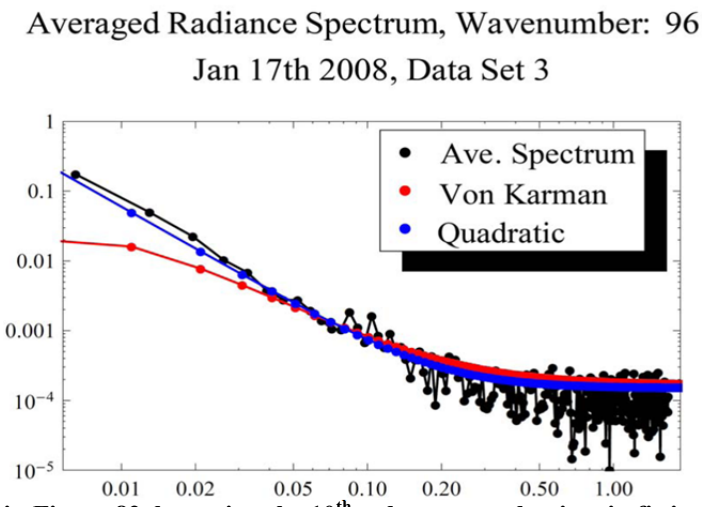

Figure 95. Same as in Figure 82, but using the 10th to last spectral points in fitting both models.

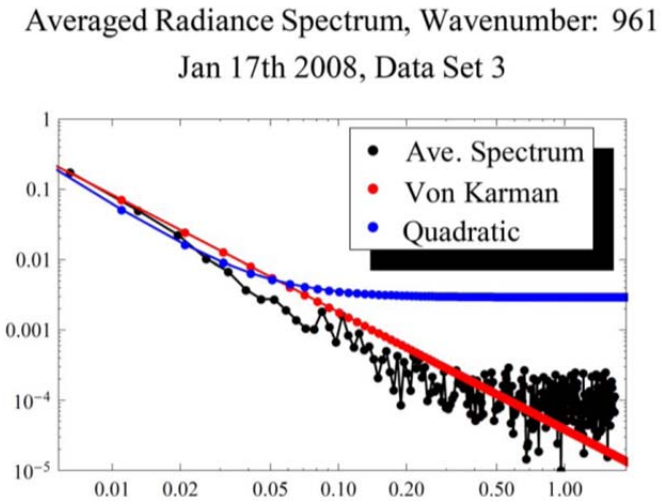

Figure 96. Same as in Figure 82, but using the 2nd to last spectral points in fitting both models.

Next, consider the de-trended data from Figure 83. In that case, we used the 10th through last and 4th through last for the quadratic and von Karman models, respectively, to get good fits. Figure 97 illustrates the results with using the 4th through last points for both models. In this case, the quadratic model does not do a good job fitting the data, similar to what happened with the original data. Using the 10th through last points for the von Karman model essentially is fitting the noise, as can be seen in Figure 98.

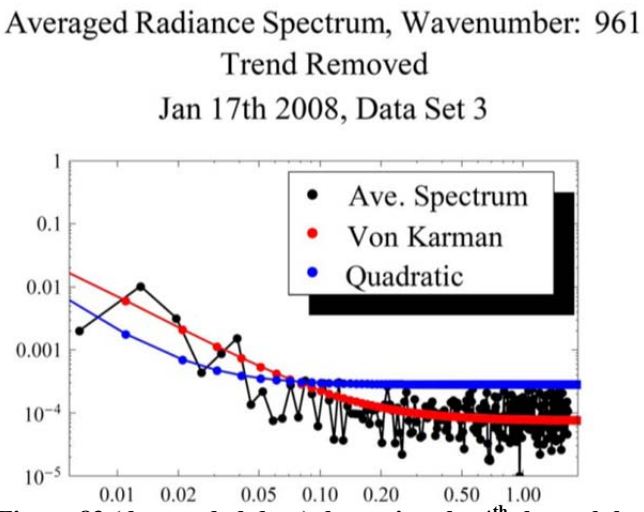

Figure 97. Same as in Figure 83 (de-trended data), but using the 4th through last points in the fits.

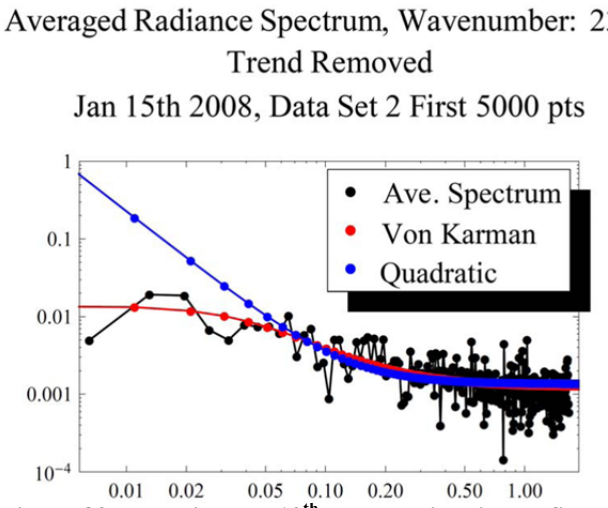

Figure 98. Same as in Figure 83, but using the 10th to last points in the fits.

We now turn to a case that was not dominated by a trend: wavenumber 2355 from the first 5000 points during Data Set 2 on 15 Jan 2008. First we look at the original data. Figure 99 shows the fits using the 4th through last for the von Karman model and 10th through last for the quadratic one. The fits to both models are very good over their full fitting domain. In Figure 100, we use the 2nd though last points for the von Karman fit, and get a very good fit over all these points. Using the 4th through last for the quadratic fit, as seen in Figure 101, does not perform as well as using the 10th through last. Next, we consider the de-trended data for this case. Figure 102 shows the comparable fits as used in Figure 99. As expected, the von Karman fit is quite good and the quadratic model does quite well over its set of fit points (10th through last). Since the de-trending mainly affected only the 1st frequency bin (cf. Figure 85), one would expect that changing the fitting domains, as was done for the original data, does not change the results in this case.

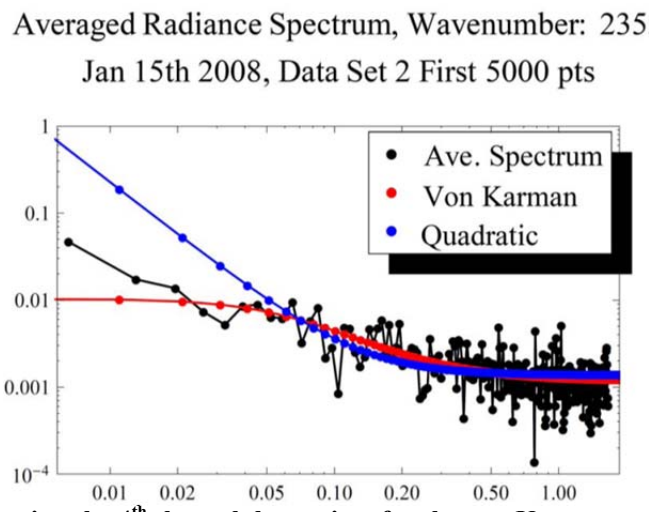

Figure 99. Model fits using the 4th through last points for the von Karman, and 10th through last for the quadratic.

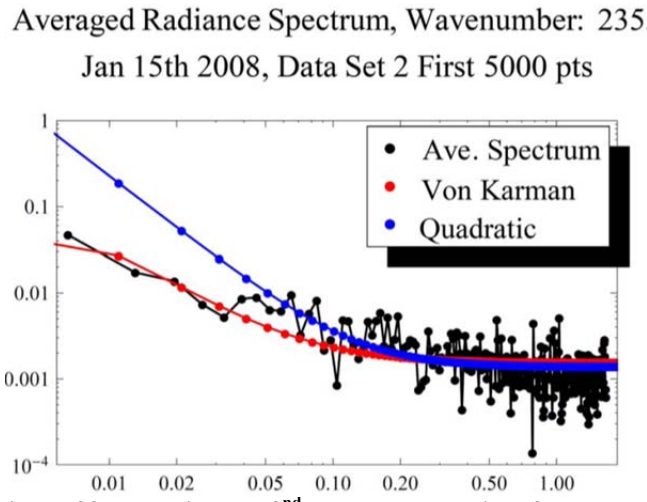

Figure 100. Same as Figure 99, but using the 2nd through last points for the von Karman fit.

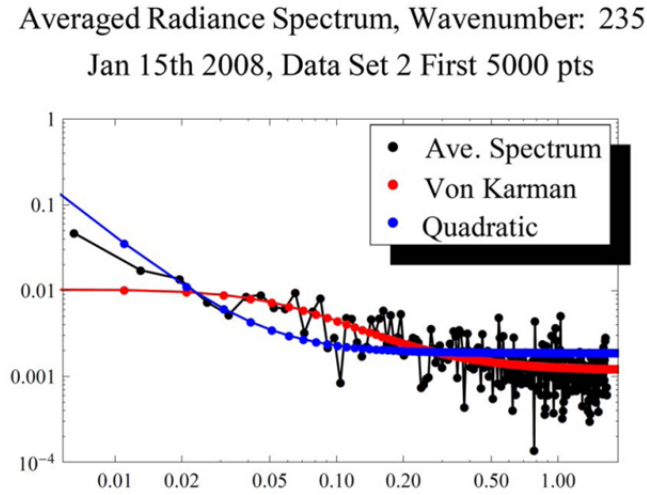

Figure 101. Same as Figure 99, but using the 4th through last points for both model fits.

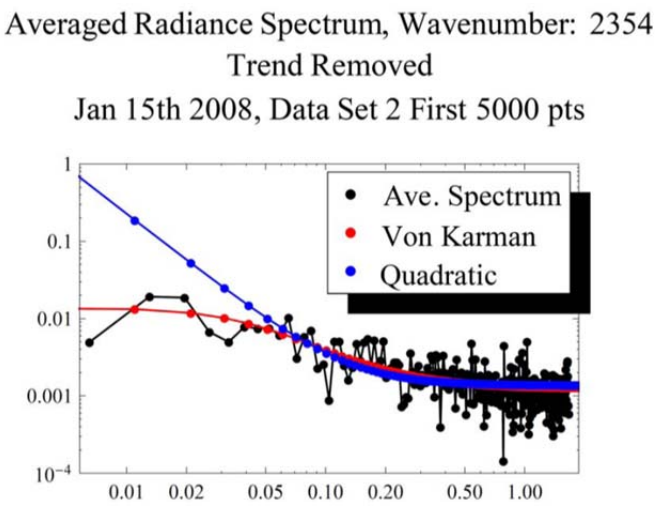

Figure 102. Same as Figure 99, but for the de-trended data.

In summary, we have seen that for the situation with a significant trend, the set of frequency points used in the fits has significant effects on the quality of the fit. This is especially true between the original and de-trended data. Moreover, as expected, data without much of a trend is less sensitive to the choice of points used in the fits. More importantly, the von Karman model provided much better fits to the data in the small-trend case than could the quadratic. This was not the situation for the data with the large linear trend, where we could get good fits with both models for the original and de-trended data. The situation with the case that had the large sinusoidal trend is similar, as can be seen from Figure 103 and Figure 104 (original and de-trended data), where the fit points for both models in both figures was the 10th through last. These issues with the fits could hint at an underlying data quality issue with data that has large trends.

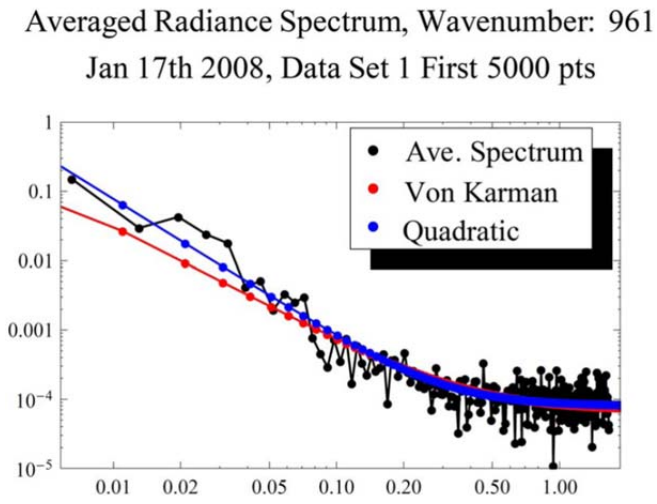

Figure 103. Spectrum and fits for the data shown in Figure 88 (large sinusoidal trend). Fit points are 10th through last for both models.

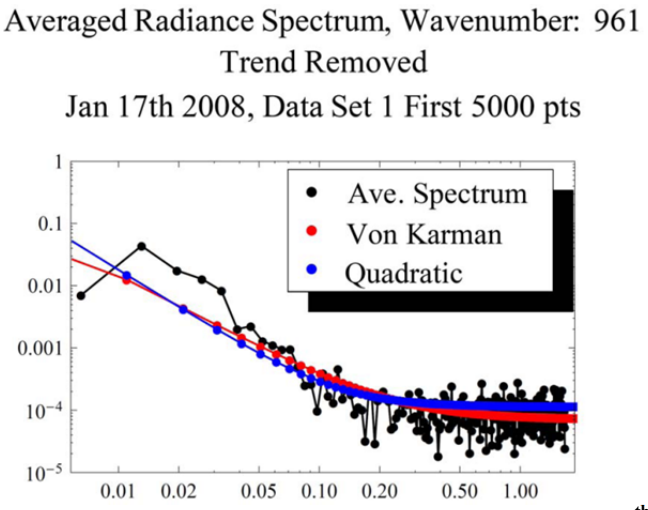

Figure 104. Same as in Figure 103 but for de-trended data. Fit points were 10th through last for both models.

5.1.3.3 Looking for Turbulence in the Radiance Data

Since there are over 1700 wavenumbers, trying to find cases that had good fits to the von Karman turbulence spectral model by looking at spectra is problematic. As a first-cut look through the data, the following methodology was used. If we consider pure noise, we would expect that the second and subsequent values in the correlation function would be very small. (Recall that due to normalization, the first point is always one.) On the other extreme, with highly correlated data, the second and subsequent points would be close to one. We have seen this with the artificial correlation due to trends. In the middle, as with smaller-scale turbulence, one would expect a somewhat smooth decay from larger correlation values to smaller ones. Hence, the quick-look method consisted of overlaying the 2nd, 10th, and 100th lags in the correlation domain and looking for this decaying structure. There are a few regions in the wavenumber domain where this structure is visible. In fact, the one around 900 cm^{-1} is where the large trends described above originate. Figure 106 shows the correlation values for the original data, where we can see the contaminating effects due to the trends. Looking at these types of plots with the original data was how the trends were first noticed. Figure 107 and Figure 108 show the same type of plots for the data set that had the large sinusoidal trends at small wavenumbers. The first figure is for the original data and the second is for the quadratic-fit method de-trended data. As opposed to the first case (cf. Figure 105 and Figure 106), where the quadratic trend removal makes for a significant difference, the same trend removal applied to the case with sinusoidal trends does not. Hence, using these plots is also helpful in finding other data issues, in this case a sinusoidal trend.

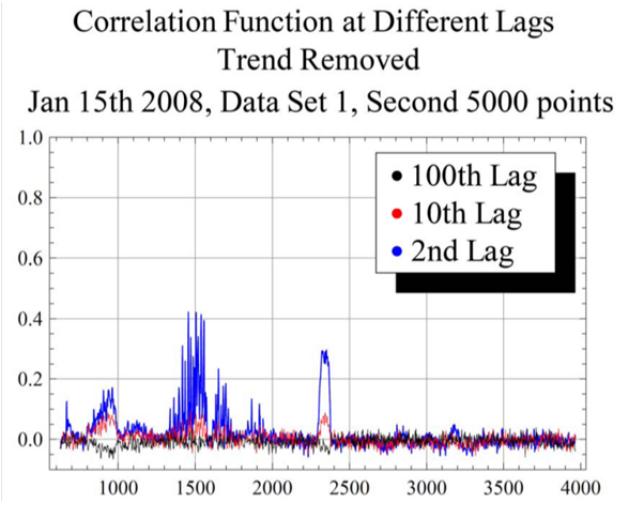

Figure 105. Correlation function at three different lags, for all wavenumbers, for de-trended data.

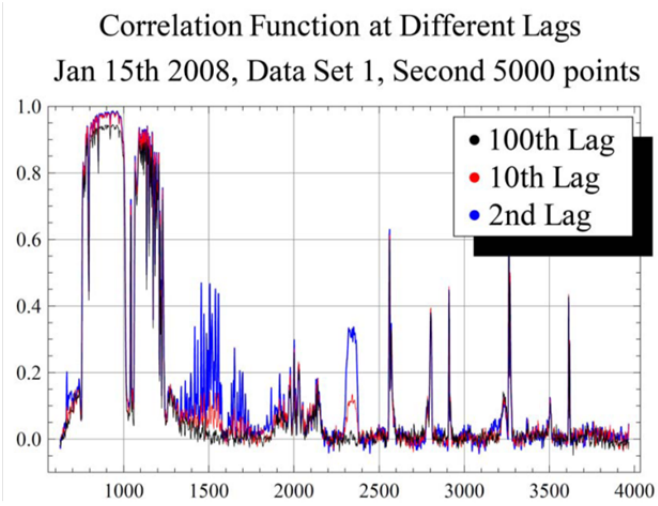

Figure 106. Same as Figure 105, but for the original data.

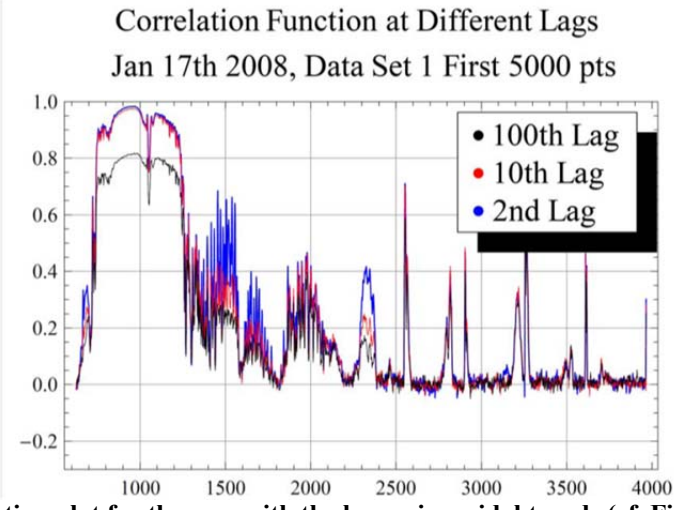

Figure 107. Correlation plot for the case with the large sinusoidal trends (cf. Figure 88).

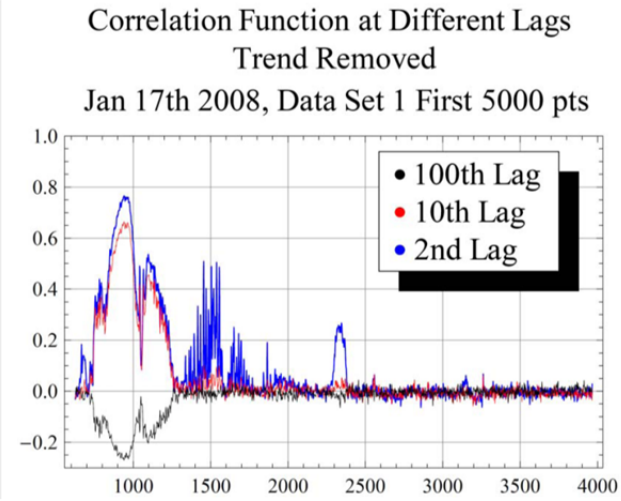

Figure 108. Same as Figure 107, but for the (quadratic) de-trended data.

Another way of looking for these correlation structures is to look at the full correlation function for all the lags. Figure 109 illustrates this for the original data from 15 Jan 2008 (Data Set 1) for all lags and for all wavenumbers. The color-coding uses hot colors for positive correlation and cool ones for negative. The data superimposed is the radiance for the first time sample and is presented for reference. The artificial correlation due to the trends is obvious at the smaller wavenumbers. Figure 110 shows the same type of presentation, but for the de-trended data. In this case, it is very difficult to see much in the way of interesting structure. However, if one looks very closely at the bottom of the plot, at around wavenumbers 900, 1500, and 2300, regions of elevated correlation can be seen. Figure 111 is the same data, but instead of showing all 5000 lags, it only shows the first 50. At this scale, the correlation structure is now revealed. This is why the 2, 10, and 100 lag plots were used for the initial investigations; it was much easier to find the "interesting" regions in these lags.

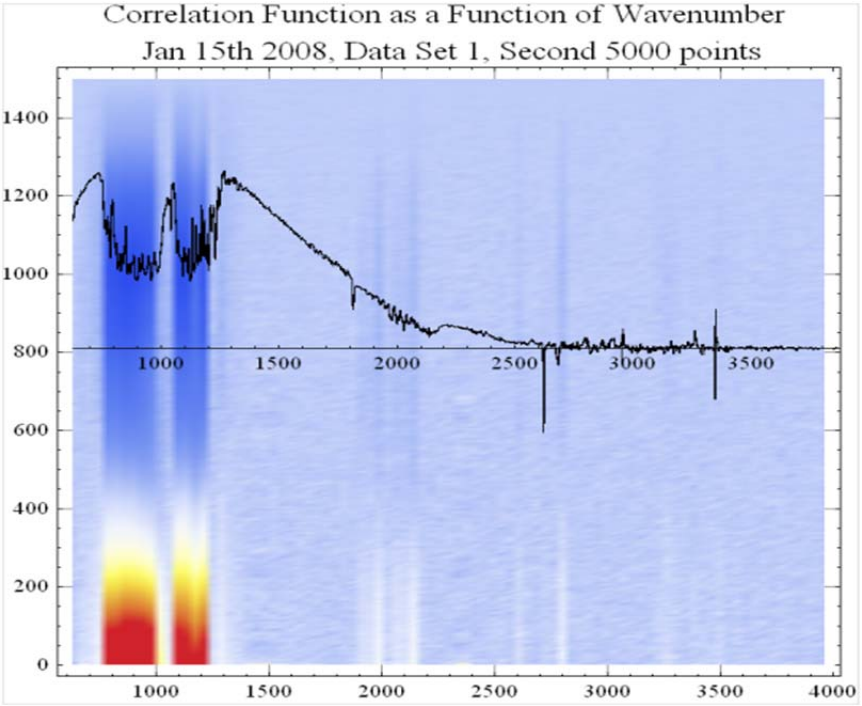

Figure 109. Correlation plot for all lags and all wavenumbers. The color scale uses hot colors for positive values and cool colors for negative ones.

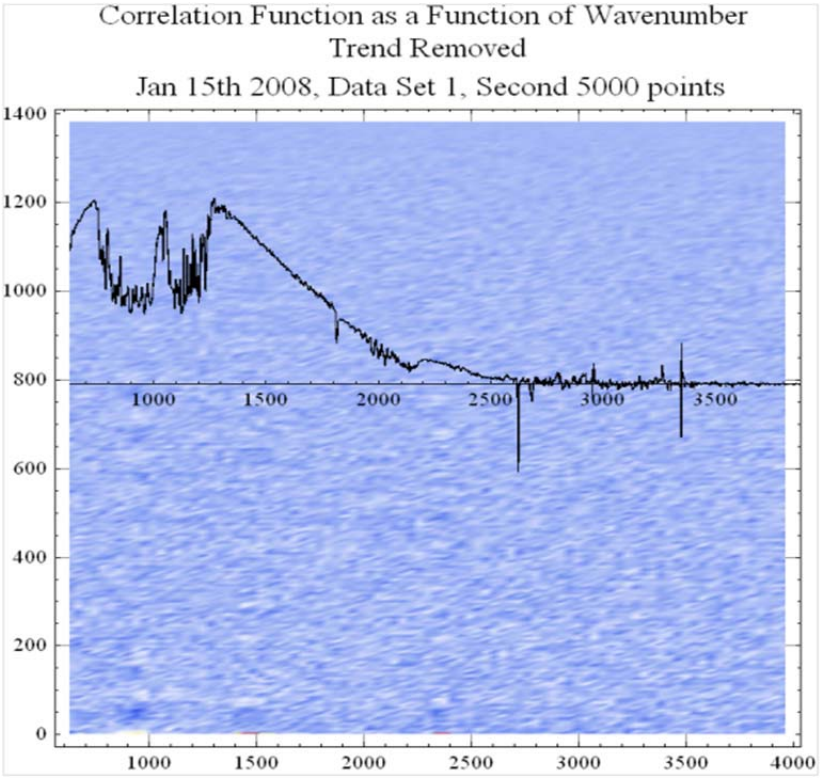

Figure 110. Same as Figure 109, but for de-trended data.

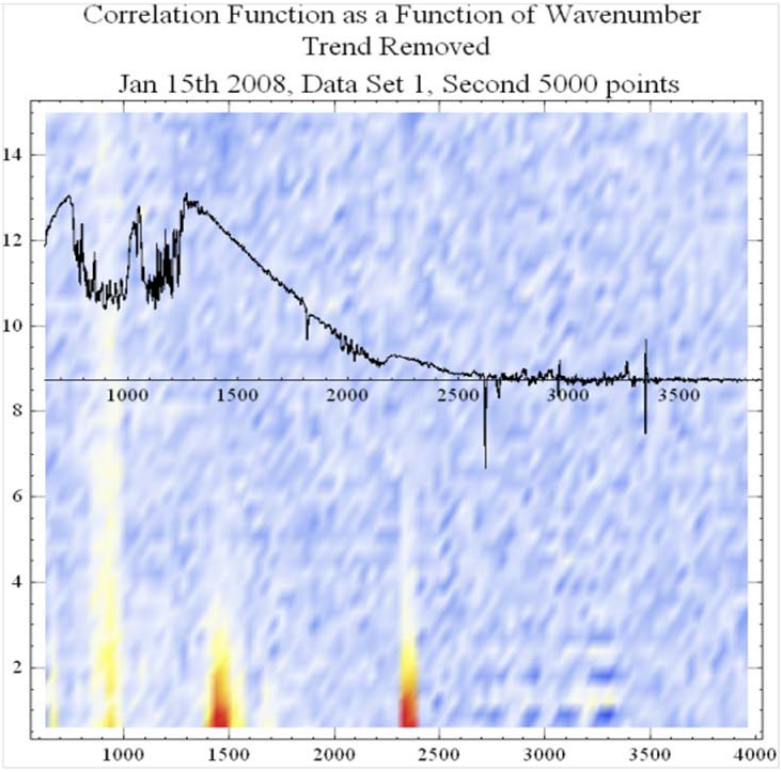

Figure 111. Same as in Figure 110, but only for the first 50 data samples (approximately 15 seconds).

5.1.3.4 Are We Seeing Turbulence?

The next question is, "Do the correlation function plots presented above imply that turbulence was being measured?" We can compare these plots for a day that was known to be turbulent, and one that was calm. Recall that January 15 and 17, 2008 were in the former category, and January 14, 2008 was in the latter. In the following, we present the correlation plots for the de-trended data covering two time periods on the 14th (Figure 112 and Figure 113), four on the 15th (Figure 114 through Figure 117), and two on the 17th (Figure 118 and Figure 119). Some of these plots have already been shown above, but we repeat them here so all the relevant figures are in the same place. The first, and most obvious difference is that there is no correlation structure in the 900 cm^{-1} region on January 14, whereas all the other cases do show a structure, except for January 15, 2008, Data Set 2, 1st 5000 points (Figure 116). Second, the magnitude of the correlations seen in the 1500 and 2300 cm^{-1} regions is larger on the turbulent days than on the calm day. However, the differences are not dramatic.

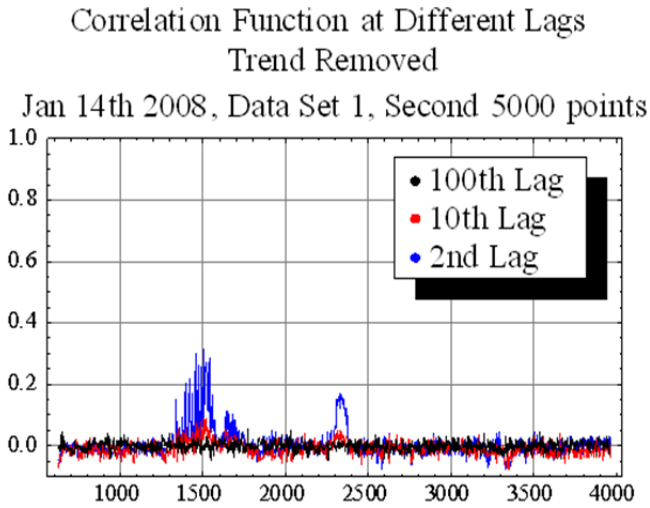

Figure 112. Correlation plot for 14 Jan 2008, Data Set 1, second 5000 points.

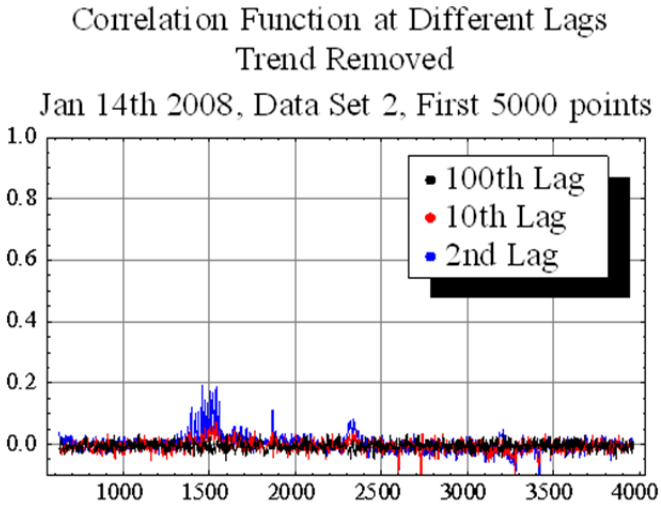

Figure 113. Correlation plot for 14 Jan 2008, Data Set 2.

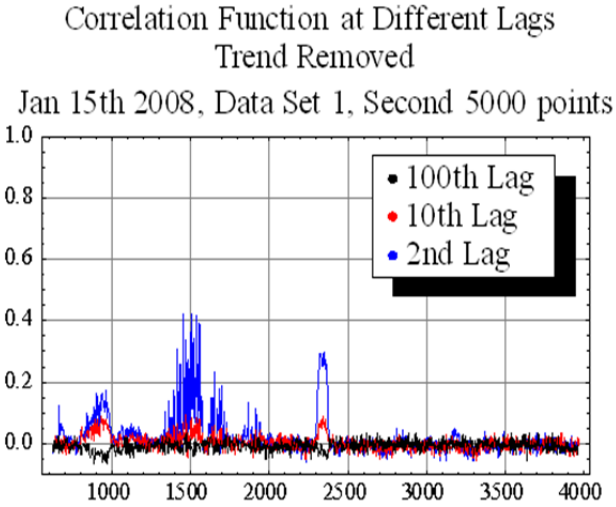

Figure 114. Correlation plot from 15 Jan 2008, Data Set 1, second 5000 points.

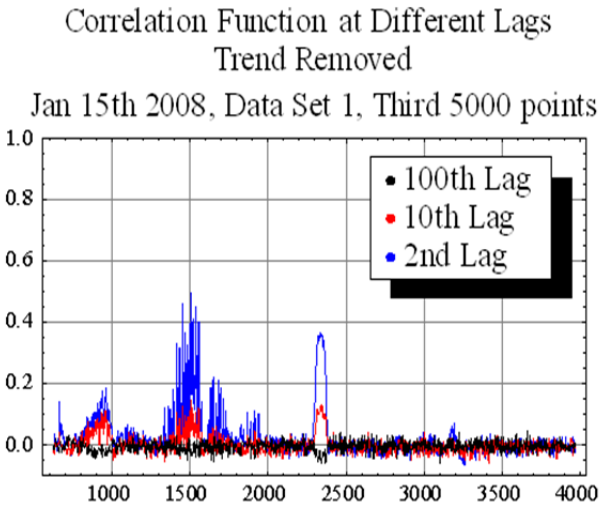

Figure 115. Correlation plot from 15 Jan 2008, Data Set 1, third 5000 points

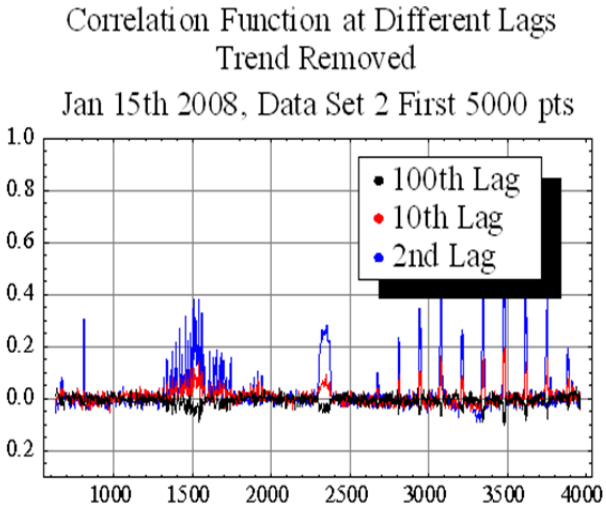

Figure 116. Correlation plot from 15 Jan 2008, Data Set 2, first 5000 points.

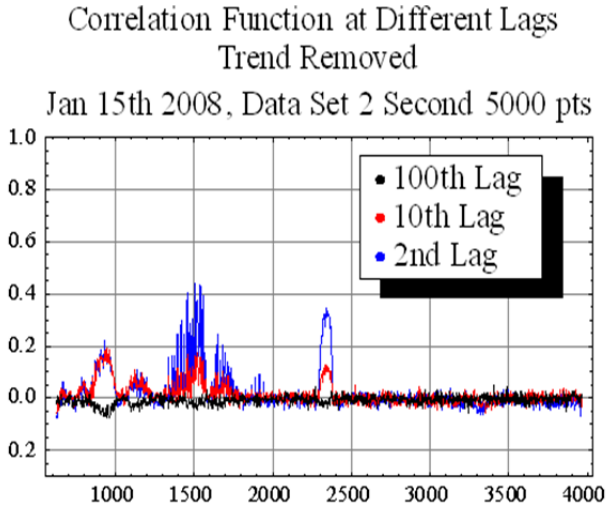

Figure 117. Correlation plot from 15 Jan 2008, Data Set 2, second 5000 points.

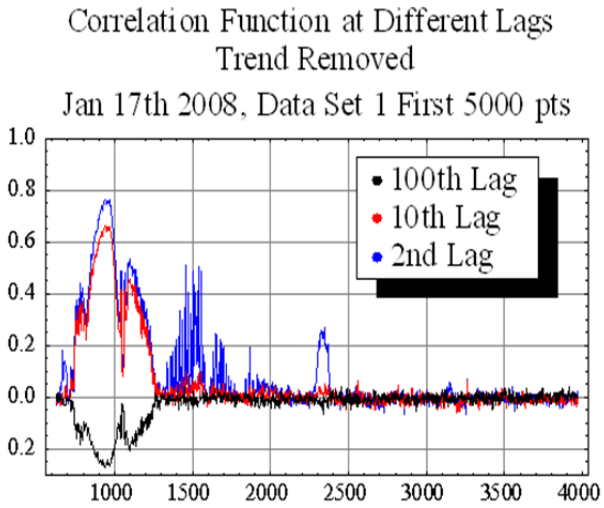

Figure 118. Correlation plot from 17 Jan 2008, Data Set 1, first 5000 points.

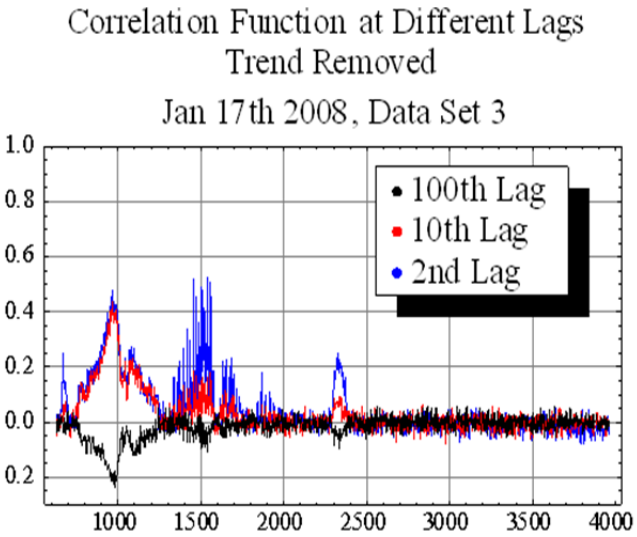

Figure 119. Correlation plot from 17 Jan 2008, Data Set 3.

Next, consider power spectra and model fits for selected wavenumbers on the three days. (As with the correlation plots, some of the subsequent spectral plots have been shown above, but we include them here for ease of comparison.) We have chosen wavenumbers that correspond to the three regions of interest: around 900, 1500, and 2350 cm^{-1}. In each case, the von Karman model is fit from the 2nd through last frequency points, and the quadratic model uses the 10th through last. First, consider spectra from January 14, 2008, Data Set 1. From the correlation plots (Figure 112 and Figure 113), it can be seen that the data around 900 cm^{-1} is noise-dominated, and so there is no need to look at spectral plots in that range (except to verify that the data is noise-like) – there is no information contained in them. However, the spectra from wavenumbers 1504 and 2355, seen in Figure 120 and Figure 121, do show a good match to the von Karman model. The 1504 wavenumber power spectrum has an order of magnitude worth of data above the noise floor, whereas the 2355 wavenumber power spectrum is less pronounced. As might be expected from the correlation plot for January 14, 2008, Data Set 2 (Figure 113), there is not much signature above the noise in the power spectrum. (Note that the scales for these and the subsequent power spectral plots are not necessarily the same. It is best to consider the height of the low frequency

portions above the noise floor seen in the higher frequencies.) The data from wavenumber 2355 is noise-dominated, whereas there is a very weak signature at wavenumber 1520 (Figure 122), although it could easily be argued that this is not statistically significant.

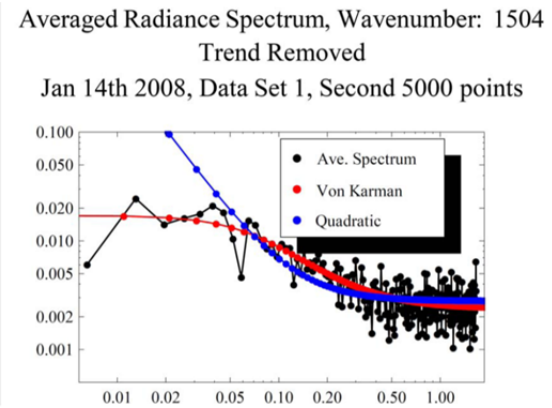

Figure 120. Power spectrum and fits for wavenumber 1504 from 14 Jan 2008, Data Set 1, 2nd 5000 points.

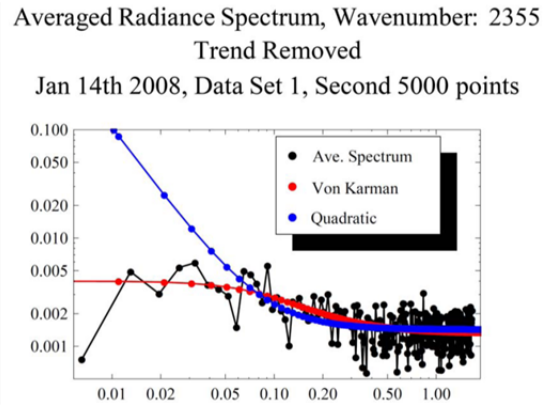

Figure 121. Power spectrum and fits for wavenumber 2355 from 14 Jan 2008, Data Set 1, 2nd 5000 points.

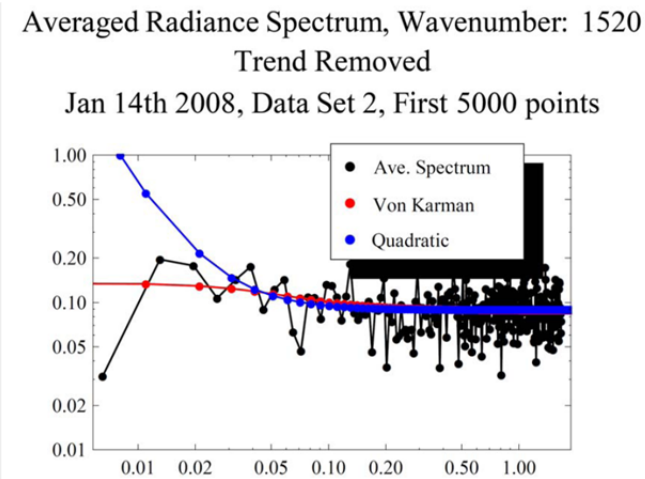

Figure 122. Power spectrum and fits for wavenumber 1520 from 14 Jan 2008, Data Set 2, 1st 5000 points.

The term "statistically significant" in this context is explained as such: As we have seen above, the distribution functions for the de-trended radiances are well-matched to a Gaussian one. If one takes the power spectrum of Gaussian-distributed data, it has an exponential distribution. (Do not confuse what we are discussing here with "Gaussian white noise." In the latter case, the data are uncorrelated, whereas in this case they can be.) That is, at each frequency, the power spectral level is distributed exponentially. Specifically, if we had multiple independent radiance time series that came from the same Gaussian distribution, then the spectral level at each frequency would represent a sample from an exponential distribution with mean and standard deviation values equal to the spectral level (definition of an exponential distribution). Unfortunately, this means that the power spectrum at each frequency has 100% noise – the standard deviation is equal to the mean. Therefore, at the lower frequencies, where the spectral level is higher, the errors are larger in magnitude (though not in percentage). It is important to note that in this context, the term "noise" refers to atmospheric fluctuations, not instrument errors. The latter is typically uncorrelated, and gives rise to the white spectrum at the higher frequencies. (We are speaking theoretically here: we are not considering the case where there are correlated sources of error as we have seen above with trends.) In the power spectra presented here, spectral averaging was performed (i.e. 9 spectra were averaged for a 5000 point window), and so the standard deviation is less than the mean. Nevertheless, one must be cautious in the interpretation of power spectra, and the associated fits, given the previous discussion.

Consider now the data from January 15, 2008. As mentioned above, on this day there were numerous pilot and automated reports of turbulence over the mountains and on the lee-side of the mountains. We look at four time periods on this day: Data Set 1, 2nd and 3rd 5000 points (Figure 123 through Figure 128); and Data Set 2, 1st and 2nd 5000 points (Figure 129 through Figure 132). As seen in the correlation plots, there is more "activity" in the wavenumber regions of interest. Most of the spectra are similar in that there is approximately an order of magnitude of signal above the noise, and there are good fits to the von Karman model. Comparing similar plots from the 17th (Figure 133 through Figure 136), we see consistent findings with the other days. A good comparison between January 14th and January 15th is seen in Figure 121 and Figure 128. Both are for wavenumber 2355 and are on the same scale. It can be seen that the data from the 15th shows much more pronounced spectral amplitude at the lower frequencies. Both cases illustrate good fits to the von Karman model. Is this a sign of more turbulence on the 15th? The evidence seems consistent with that hypothesis, but at it is not conclusive.

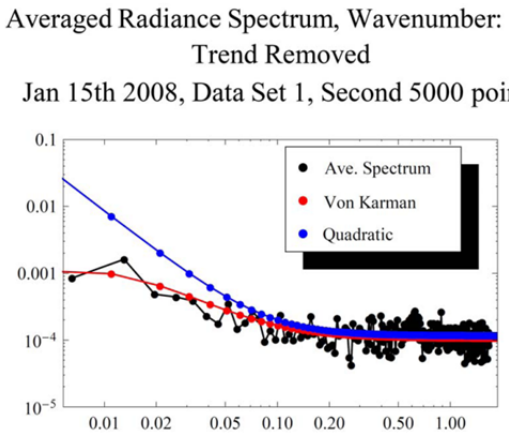

Figure 123. Power spectrum and fits for wavenumber 961 from 15 Jan 2008, Data Set 1, 2nd 5000 points.

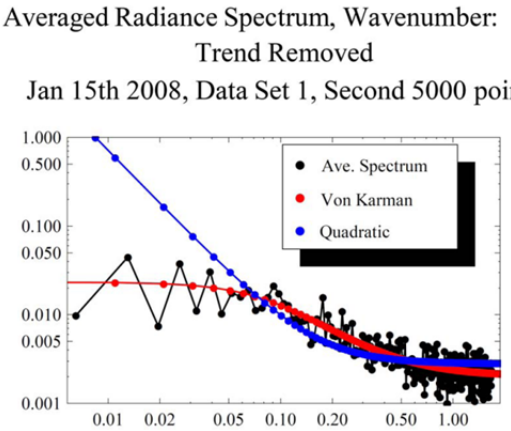

Figure 124. Power spectrum and fits for wavenumber 1504 from 15 Jan 2008, Data Set 1, 2nd 5000 points.

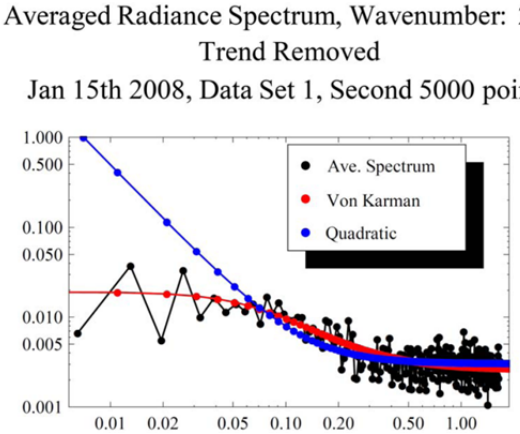

Figure 125. Power spectrum and fits for wavenumber 2355 from 15 Jan 2008, Data Set 1, 2nd 5000 points.

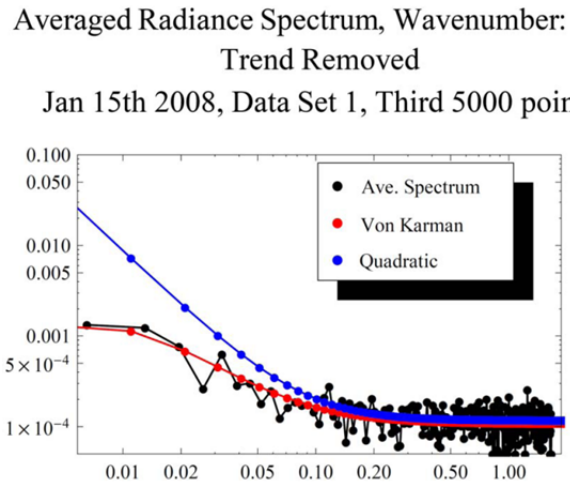

Figure 126. Power spectrum and fits for wavenumber 961 from 15 Jan 2008, Data Set 1, 3rd 5000 points.

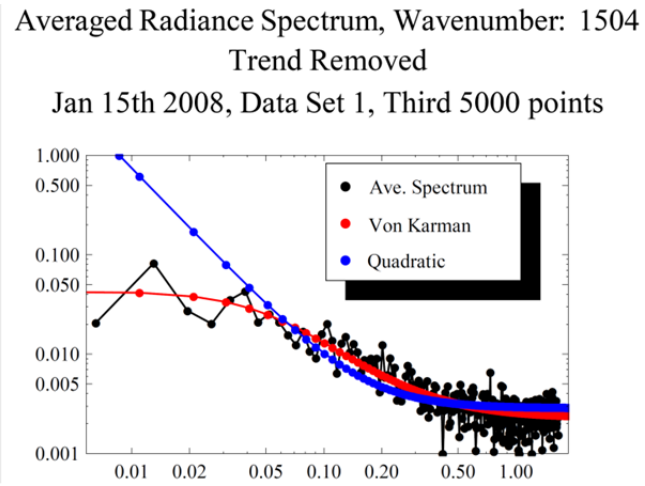

Figure 127. Power spectrum and fits for wavenumber 1504 from 15 Jan 2008, Data Set 1, 3rd 5000 points.

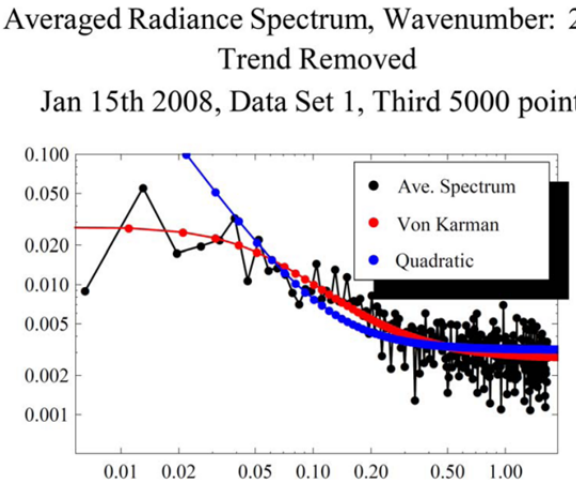

Figure 128. Power spectrum and fits for wavenumber 2355 from 15 Jan 2008, Data Set 1, 3rd 5000 points.

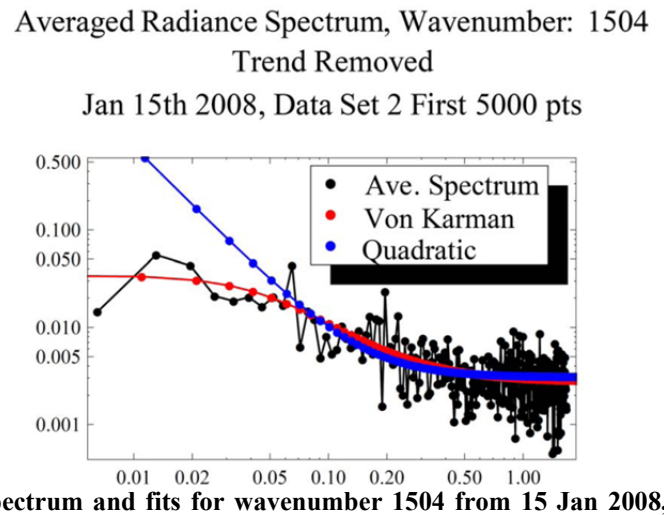

Figure 129. Power spectrum and fits for wavenumber 1504 from 15 Jan 2008, Data Set 2, 1st 5000 points.

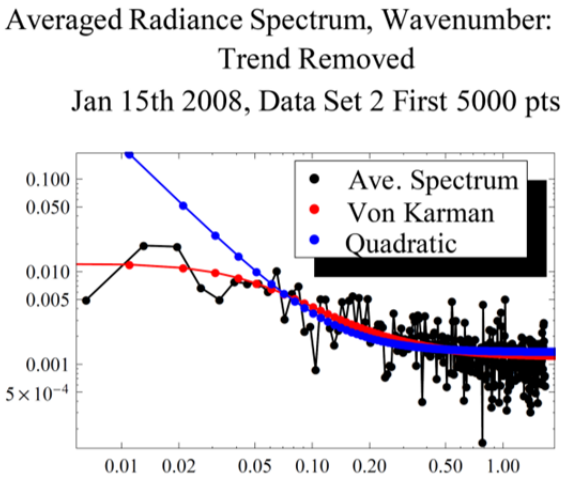

Figure 130. Power spectrum and fits for wavenumber 2355 from 15 Jan 2008, Data Set 2, 1st 5000 points.

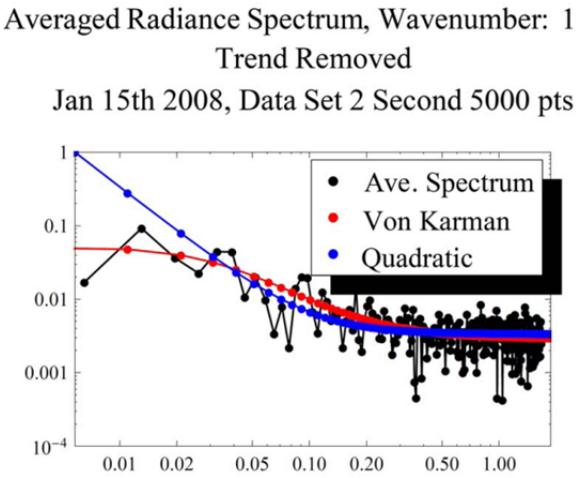

Figure 131. Power spectrum and fits for wavenumber 1504 from 15 Jan 2008, Data Set 2, 2nd 5000 points.

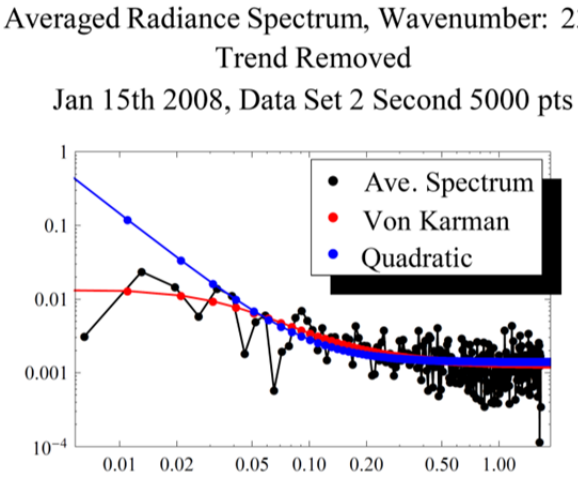

Figure 132. Power spectrum and fits for wavenumber 2354 from 15 Jan 2008, Data Set 2, 2nd 5000 points.

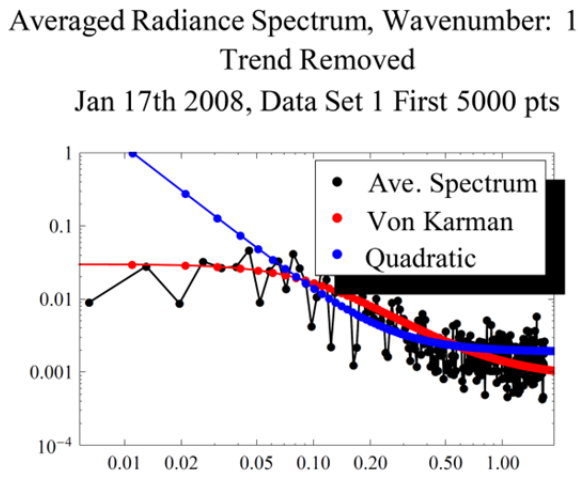

Figure 133. Power spectrum and fits for wavenumber 1504 from 17 Jan 2008, Data Set 1, 1st 5000 points.

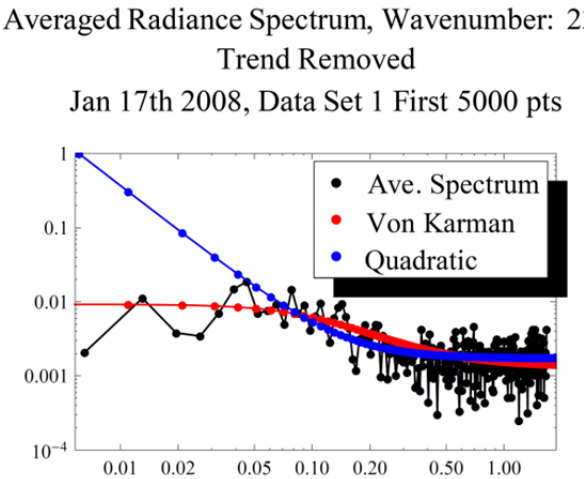

Figure 134. Power spectrum and fits for wavenumber 2354 from 17 Jan 2008, Data Set 1, 1st 5000 points.

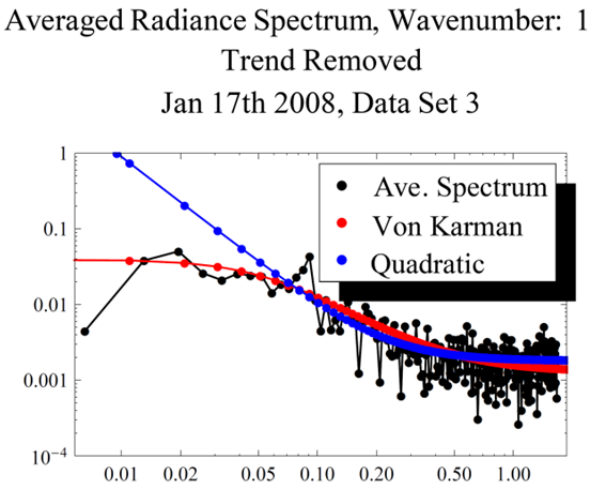

Figure 135. Power spectrum and fits for wavenumber 1504 from 17 Jan 2008, Data Set 3.

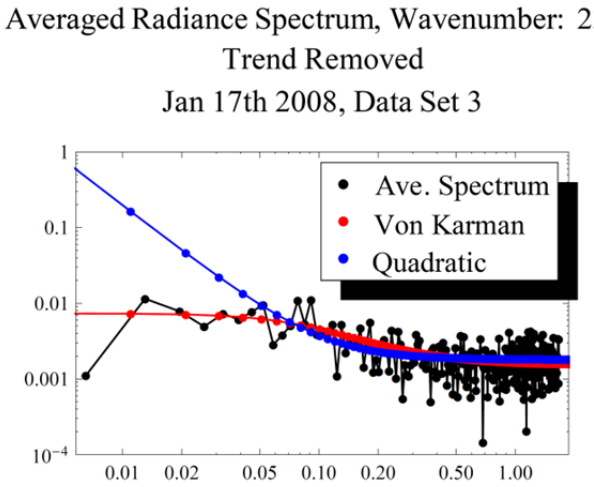

Figure 136. Power spectrum and fits for wavenumber 2354 from 17 Jan 2008, Data Set 3.

5.1.4 WRF Model: March 6, 2004

WRF data (temperature and H_2O profiles), generated for an actual lee wave turbulence event on March 6, 2004, were used in all simulations conducted in anticipation of the MRS field test. For the WRF data used, the center of turbulence is assumed to be located at 39.5°N, 105.0°W, and at an altitude of 5 km, where the largest perturbations of the air's vertical velocity and water vapor were observed (see Figure 137).

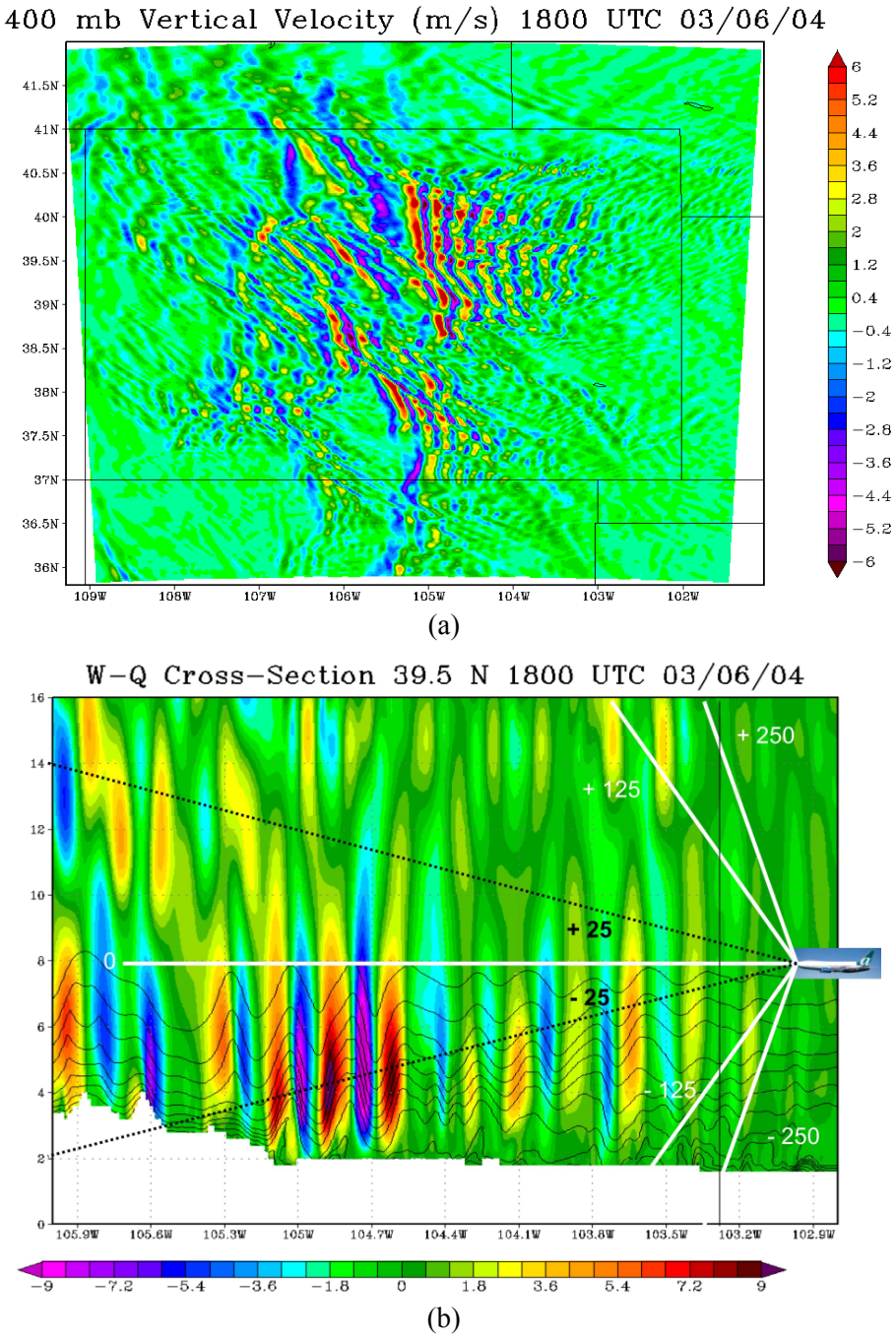

Figure 137. Horizontal (a) and vertical (b) cross-sections of vertical velocity and H_2O respectively for the lee wave turbulence, March 6, 2004.

5.1.5 FLI-FM Simulations

FLI Hyper-Cam imagery was simulated with FLI-FM in order to develop testing requirements for the MRS field experiment. These requirements include determination of spectral resolution and viewing geometry dependence. This simulation involved using WRF data (temperature and H_2O profiles) generated for an actual lee wave turbulence event and radiosonde data to simulate the anticipated experimental observations.

5.1.5.1 Spectral Resolution Dependence

FLI-FM calculations using the March 6, 2004 WRF model were performed for a limited portion of the Hyper-Cam array for its apodized spectral resolutions of 1, 4, and 16 cm^{-1}. The viewing point was located at 40.03253°N, 105.53775°W, and 2.9 km elevation to match the exact coordinates of the MRS field experiment. The image size was assumed to be 5 x 25 vertical/horizontal pixels with a single pixel angular size equal to 0.01 rad (~0.57°). Thus, the full angular image size is equal to 0.05 x 0.25 rad (~2.9° x 14.3°) in vertical/horizontal directions respectively.

FLI radiances were simulated for a northward and a westward viewing Hyper-Cam at the three spectral resolutions and at five distances from the turbulence center and the brightness temperature computed. In the following figures, *D* is this distance and is measured in terms of D_0, the maximum distance from the observer to the turbulence center.

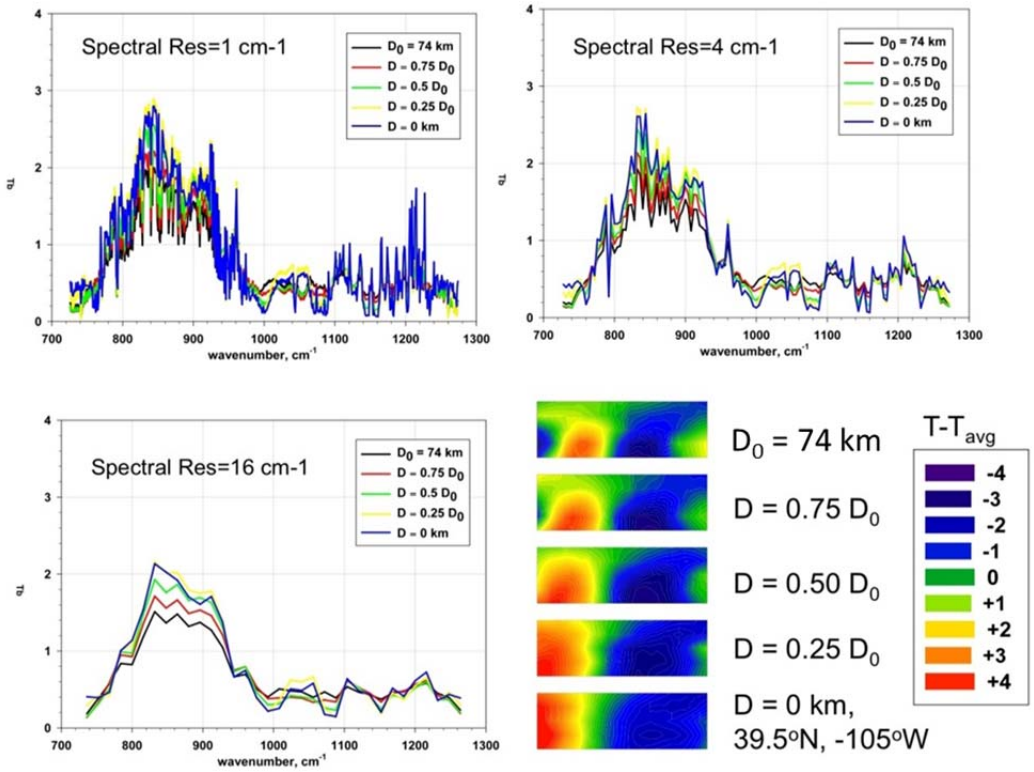

Figure 138. Spectral resolution dependence on lee-wave turbulence signal for a northward viewing Hyper-Cam. Lower right hand panel shows an image of the turbulence as would be viewed at 835 cm^{-1} by the Hyper-Cam operated at the lowest spectral resolution of 16 cm^{-1}.

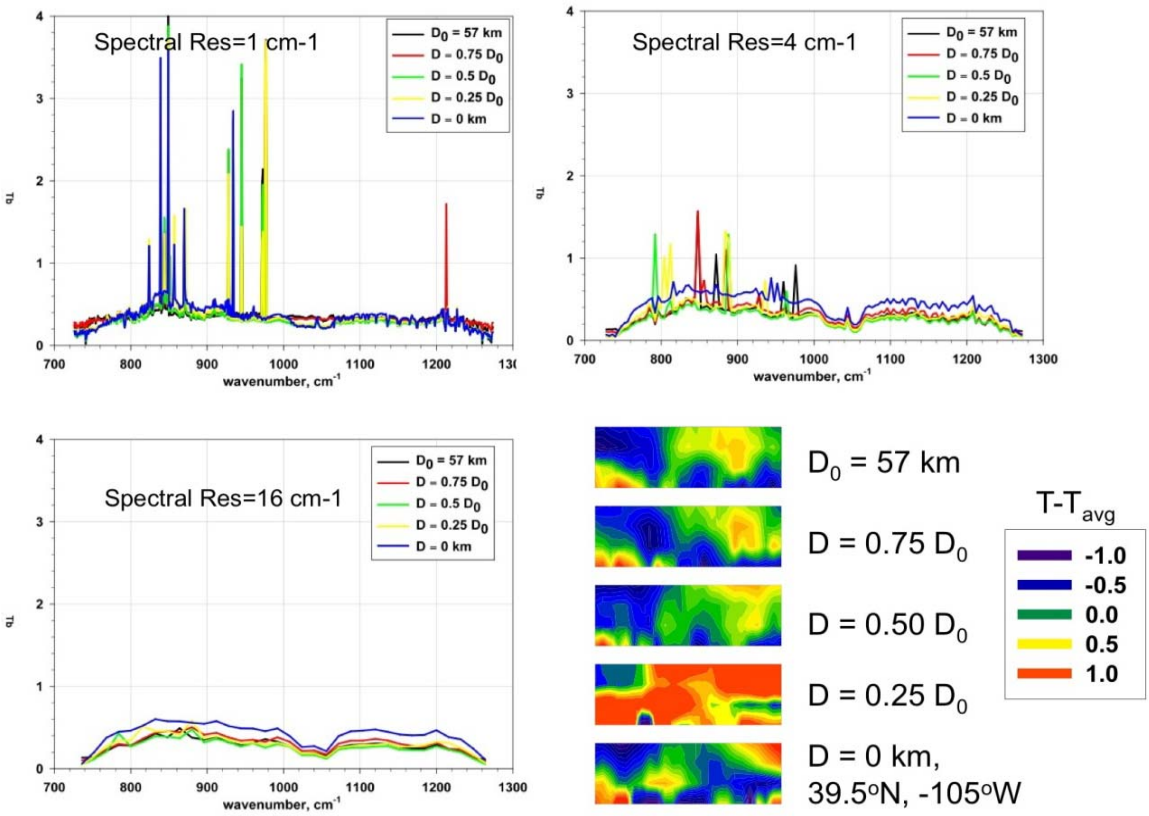

Figure 139. Spectral resolution dependence on lee-wave turbulence signal for a westward viewing Hyper-Cam. Lower right hand panel shows an image of the turbulence as would be viewed at 835 cm^{-1} by a Hyper-Cam operated at the lowest spectral resolution of 16 cm^{-1}.

As shown in Figure 138 and Figure 139, the wavenumber channels near 835 cm^{-1} have the highest variance due to lee wave turbulence, regardless of spectral resolution. It can also be seen that the northward viewing instrument, which resolves the wave amplitude, has a signal about four times larger than a westward viewing instrument that is looking into the wave train, and therefore is only sensitive to the turbulence along the axis of the lee wave train. The important conclusion to be drawn from these calculations is that the Hyper-Cam should be able to detect lee wave turbulence, even when operated at its lowest spectral resolution.

5.1.5.2 Elevation Angle and Distance Dependence

Next, the standard deviations for the five elevation angles and 25 azimuth angles (i.e. the 5 x 25 pixel image) for the five distances from the center of the lee waves were computed. The central pixel (3, 13) of the image was directed straight to the SSE (local azimuth angle 157.5°, clockwise from North) with an elevation angle +5° above the horizontal. The elevation angle was chosen so that the bottom rays in the image do not touch the surface (the real terrain height of WRF data is taken into account). These simulations used the March 6, 2004 WRF model.

One hundred twenty-five FLI radiances total were computed with FLI-FM in the range 800–1300 cm^{-1} with 1 cm^{-1} spectral resolution and no apodization applied. For a given spectral

channel, the statistics were computed by averaging over all 125 image pixels in three different ways:

1. The mean brightness temperature and its standard deviation were computed (Figure 140 and Figure 141);
2. The standard deviation for the brightness temperature when the corresponding mean vertical profile, obtained by averaging over azimuth angles, was subtracted (Figure 142, this variability is referred under as ΔBT_{VER}*);* and
3. The standard deviation for brightness temperature over the image when the left neighboring column was subtracted (Figure 143, this variability is referred under as ΔBT_{HOR}).

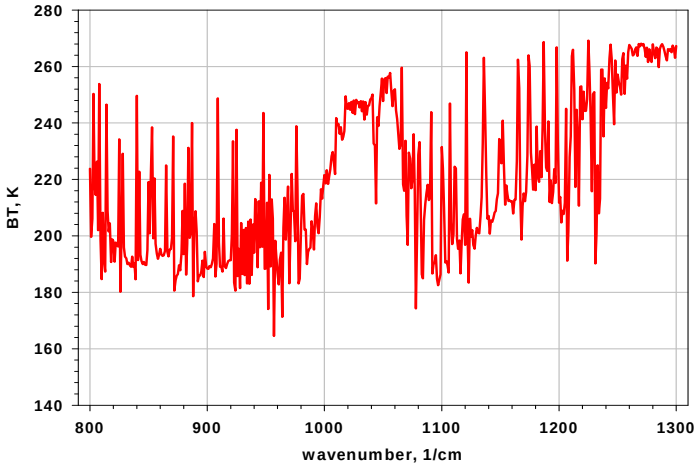

Figure 140. Mean brightness temperature spectrum, averaged over all image pixels.

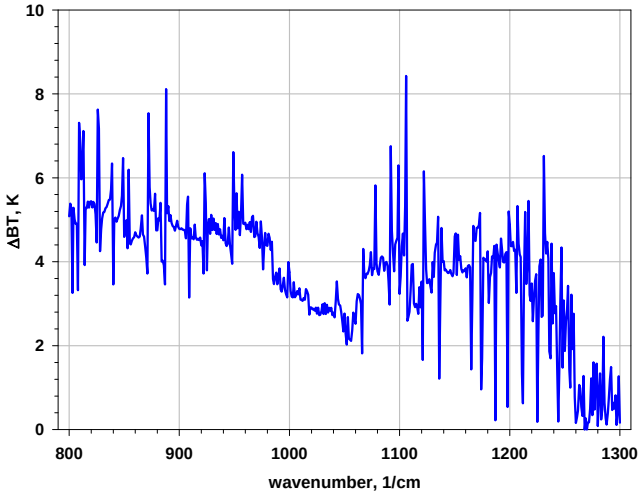

Figure 141. Standard deviation from the mean brightness temperature spectrum.

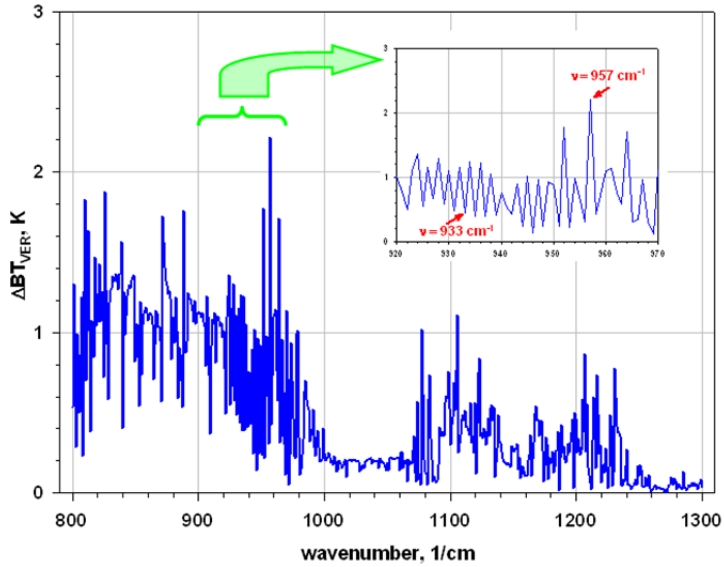

Figure 142. Standard deviation of the quantity ΔBT_{VER} (see text). The enlarged plot shows channels chosen for visualization.

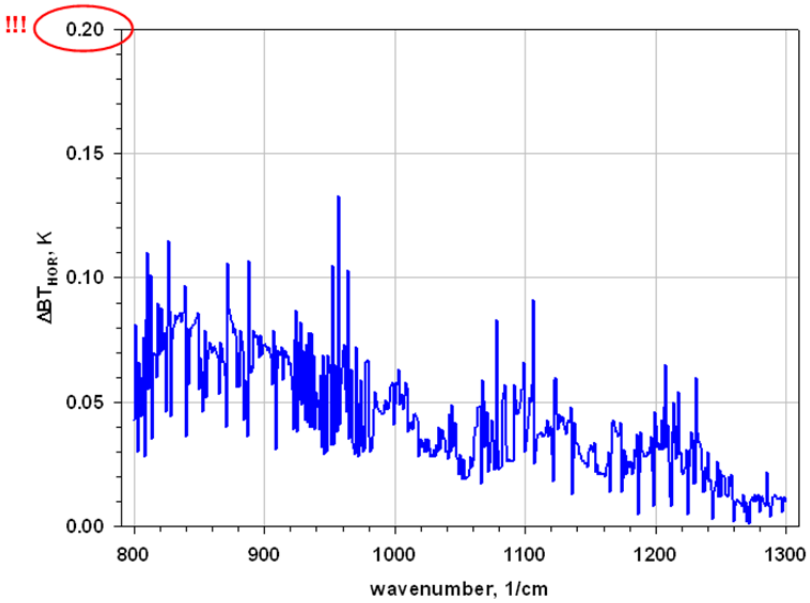

Figure 143. Standard deviation of the quantity ΔBT_{HOR} (see text).

Although ΔBT_{HOR} is about one order of magnitude lower than ΔBT_{VER}, as shown in Figure 142 and Figure 143, the two results highly correlate with each other and their spectral dependence is very similar (Figure 144). It was found that an on-line spectral channel Δ = 957 cm^{-1} (H_2O) has the maximum variability for both ΔBTs. Figure 145 shows images for this channel processed in the three ways as described above. Despite the high correlation between standard deviations for both ΔBT_{HOR} and ΔBT_{VER}, the images of these quantities look very different and have a significantly different BT scale. For comparison, Figure 146 shows the same panels for spectral channel Δ = 933 cm^{-1}, which is representative of an off-line window frequency showing "regular" variability. One can note that the value of the signal on all three panels varies in wide limits (see

corresponding legends), depending on whether an on-line or off-line channel is selected, but the corresponding pictures (i.e. relative variations) look almost the same.

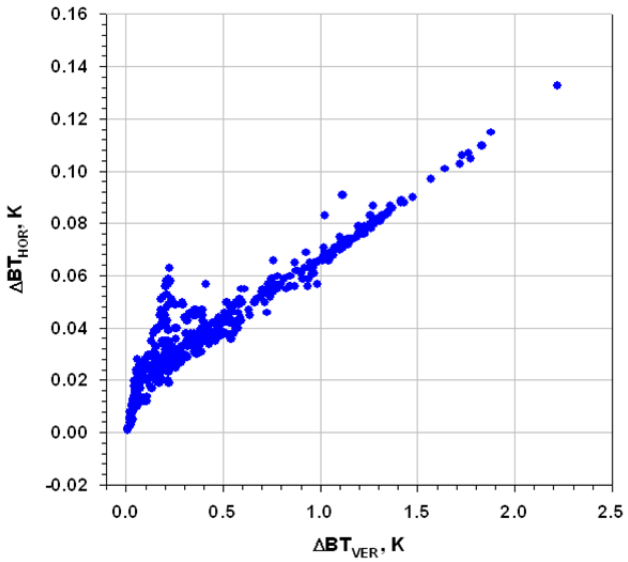

Figure 144. **Standard deviation of ΔBT_{HOR} versus standard deviation of ΔBT_{VER}.**

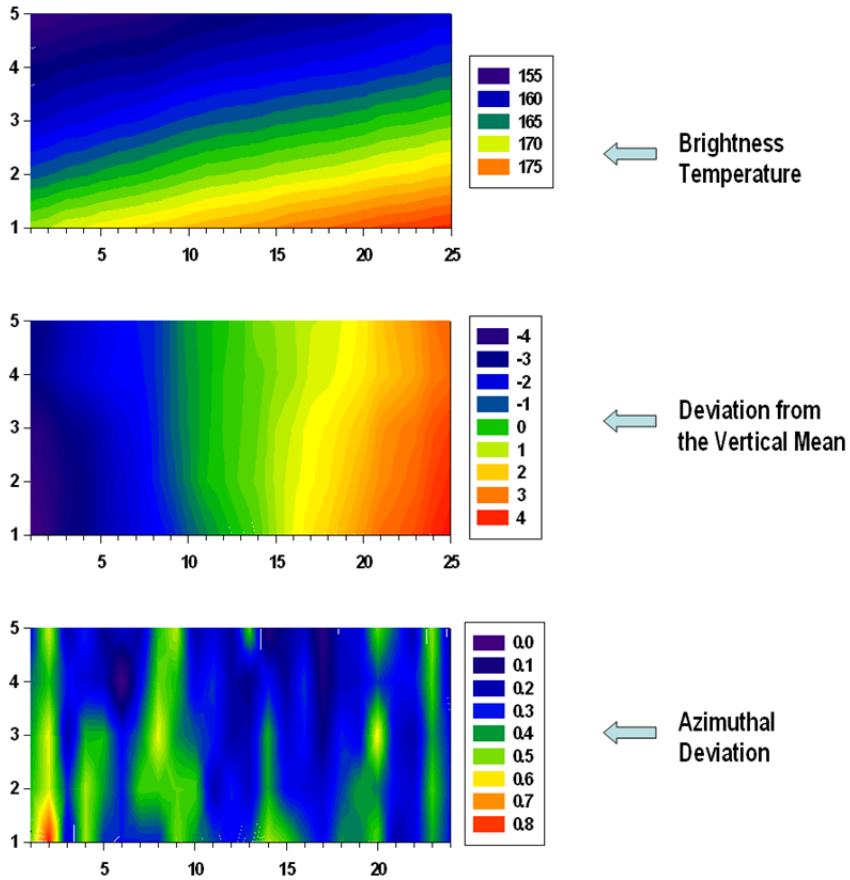

Figure 145. **Imagery for the on-line 957 cm^{-1} spectral channel, which has maximum variability for both ΔBT.**

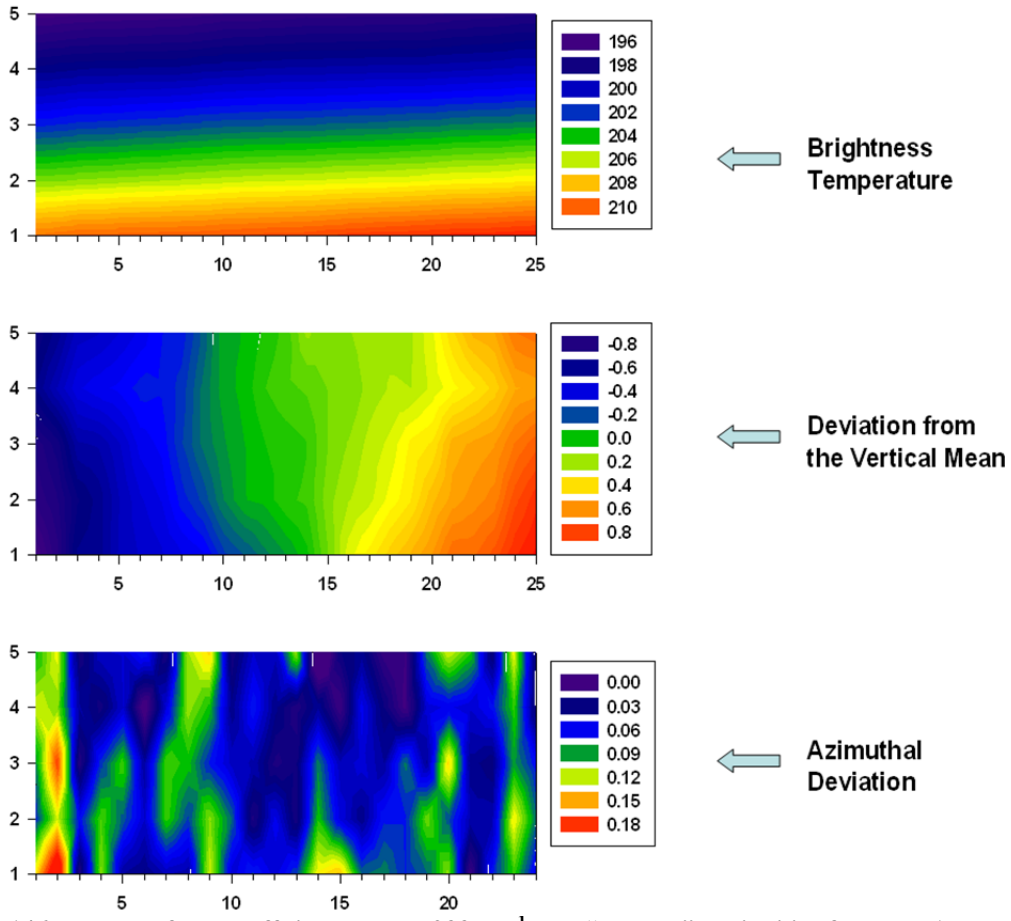

Figure 146. Imagery for the off-line channel 933 cm^{-1}: the "regular" variability for both *ΔBT*.

These simulations show that the FLI has the potential to observe the varying atmospheric state (temperature and H_2O) associated with mountain waves.

The simulations were then performed with the same March 6, 2004 WRF model for seven observer locations total, for a larger 35 x 35 pixel image. The first observer location was directly under the center of turbulence (the elevation angle for the central image pixel is equal to 90°). The next three observer locations were east of the turbulence center, while the main looking direction was to the west, with elevation angles equal to 60°, 30°, and 12° respectively. Finally, the last three observer locations were north of the turbulence center and the main looking direction is to the south with the same set of 3 elevation angles. Observer coordinates were chosen in such a way that the central ray of the image went exactly through the center of turbulence. Thus, the smaller elevation angle corresponds to the larger distances to the turbulence center and vice versa. West/south-looking directions allowed viewing of the turbulence from different sides: either ahead or from the side of an aircraft path.

Each simulated image contains 35 x 35 rays around the main viewing direction. The angular size of each pixel was set to 0.01 rad, which corresponds approximately to a 20° full field of view

(± 10° from the main viewing direction, horizontally and vertically). Table 8 and Figure 147 below explain the viewing geometry of the simulations.

Table 8. Viewing geometry for the simulations.

Location #	Central viewing azimuth angle, α_0 (degrees)	Central viewing zenith angle, β_0 (degrees)	Observer Latitude (°N)	Observer Longitude (°W)	Distance to turbulent center (km)	Wavenumber of max RMS (cm^{-1})
1	--	90	39.5	105.0	2.0	1093
2	270 (West)	60	39.5	104.99	2.31	1213
3	270 (West)	30	39.5	104.96	4.0	957
4	270 (West)	12	39.5	104.87	9.62	957
5	180 (South)	60	39.51	105.0	2.31	1247
6	180 (South)	30	39.53	105.0	4.0	1078
7	180 (South)	12	39.60	105.0	9.62	888

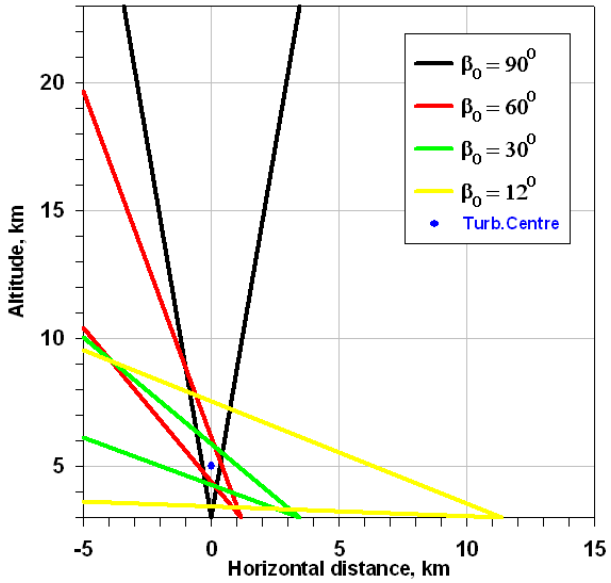

Figure 147. Layout of the viewing geometry fields of view for the simulations.

FLI radiances were computed with FLI-FM in the 800-1300 cm^{-1} range with spectral resolution equal to 1 cm^{-1}, and strong Gaussian apodization was applied for an interferometer with assumed maxOPD = 0.5 cm. Brightness temperature radiances were used for further analysis.

For each observer location, two atmospheric states were used for the simulations (when doing ray tracing for imagery). The first one was the actual WRF data (with lee wave turbulent perturbations), while the second one was an averaged "calm" atmospheric state for that day, obtained by horizontal averaging of WRF data. Corresponding sets of spectra are $R_{PERT}(\nu,\alpha,\beta,n)$ and $R_0(\nu,\alpha,\beta,n)$, where R is the brightness temperature in K, ν is the wavenumber, α and β are the horizontal/ vertical pixels of each image, and n = 1:7 is the observer location index (from Table 8). We analyze the value of $\Delta R = R_{PERT} - R_0$ to simulate the difference between calm and turbulent conditions.

Figure 148 through Figure 154 show statistics of the signal obtained by averaging over all α and β for each of the seven observer locations separately. The upper panel is the mean value of the referenced spectra R_0; the middle panel is the mean value of the difference $\Delta R = R_{PERT} - R_0$, and the bottom panel is the RMS-difference for ΔR. The green arrows on the bottom panels show channels for which the RMS-difference is maximum (Table 8 shows these channel wavenumbers in the rightmost column). The full images of ΔR for the same selected channels are shown in Figure 155 through Figure 161.

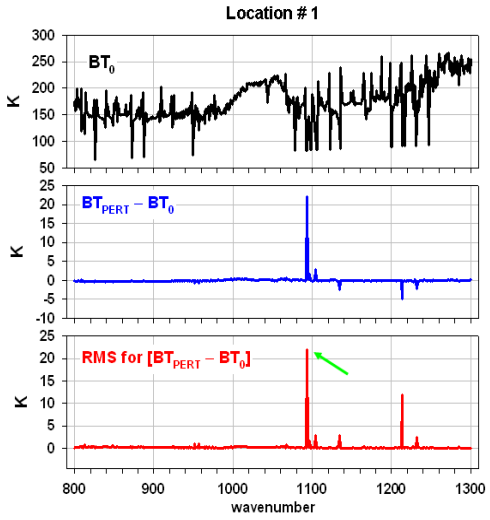

Figure 148. Statistics of the radiance signal at observer location no. 1.

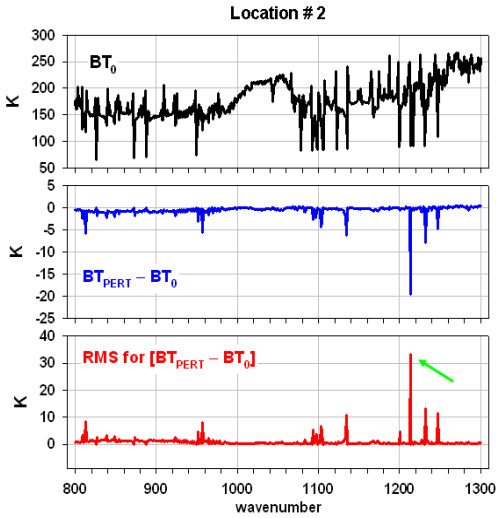

Figure 149. Statistics of the radiance signal at observer location no. 2.

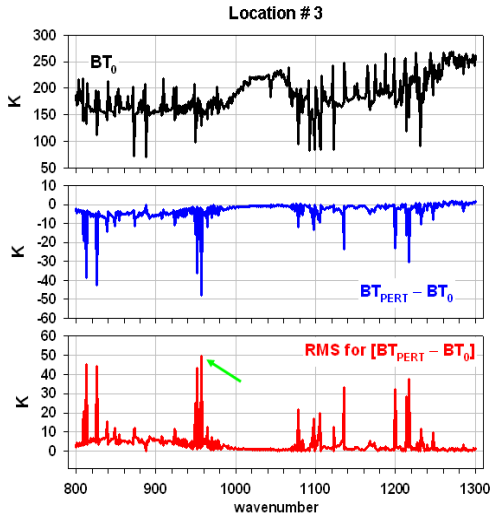

Figure 150. Statistics of the radiance signal at observer location no. 3.

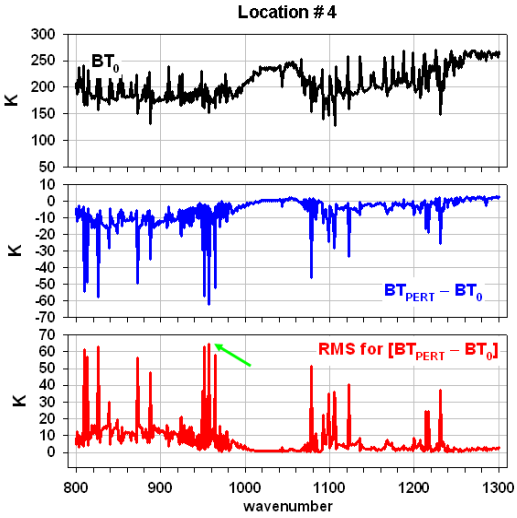

Figure 151. Statistics of the radiance signal at observer location no. 4.

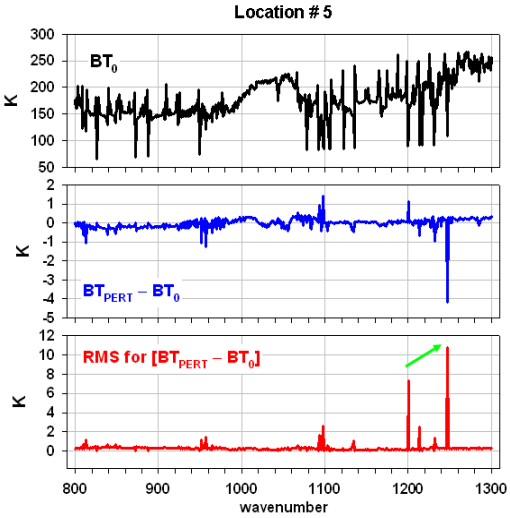

Figure 152. Statistics of the radiance signal at observer location no. 5.

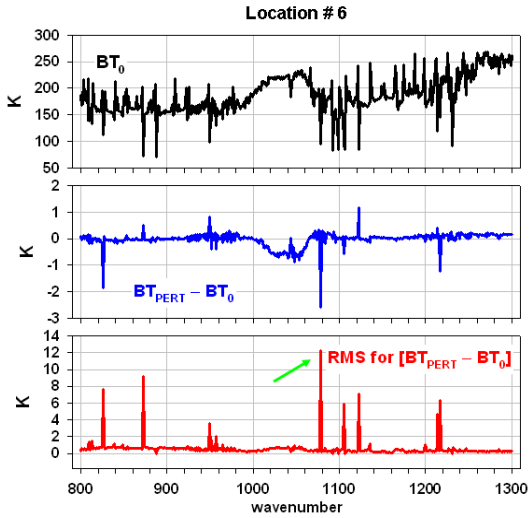

Figure 153. Statistics of the radiance signal at observer location no. 6.

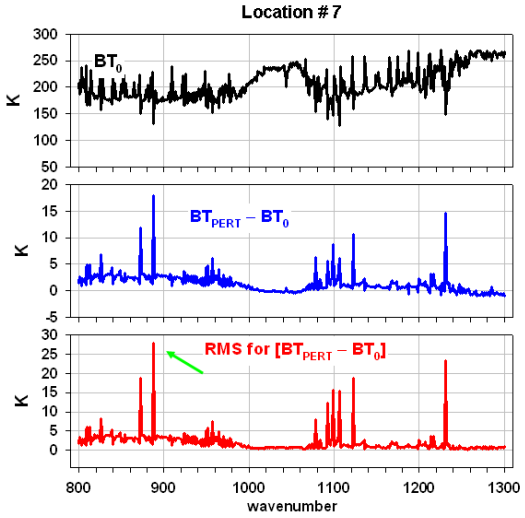

Figure 154. Statistics of the radiance signal at observer location no. 7.

Figure 155 through Figure 161 below show the images of $\Delta R = R_{PERT} - R_0$ for the channels shown by green arrows on Figure 148 through Figure 154 (which represent maximum RMS) for seven observer locations. Legends to the right of the images provide the color scale of the brightness temperature differences, K.

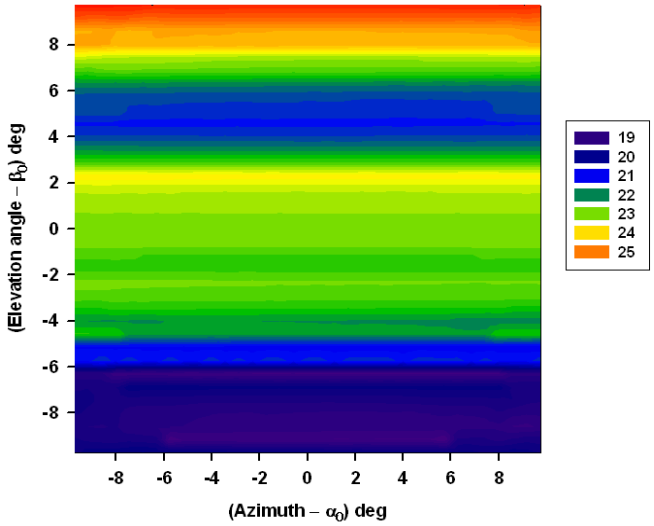

Figure 155. Modeled BTD image at observer location no. 1, α_0 = 270° (West), β_0 = 90°.

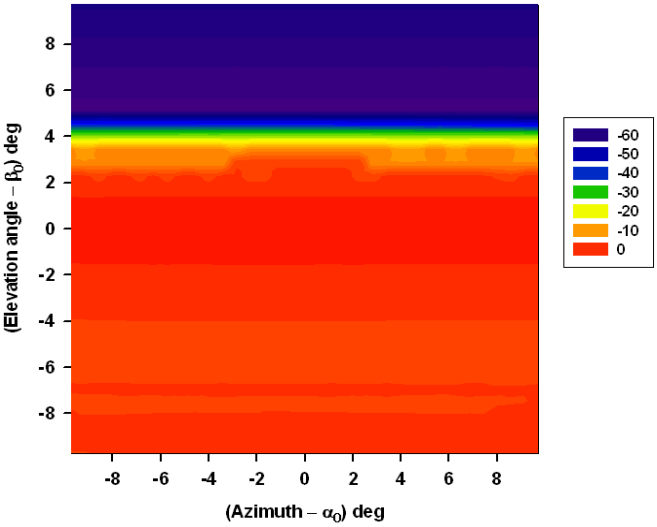

Figure 156. Modeled BTD image at observer location no. 2, α_0 = 270° (West), β_0 = 60°.

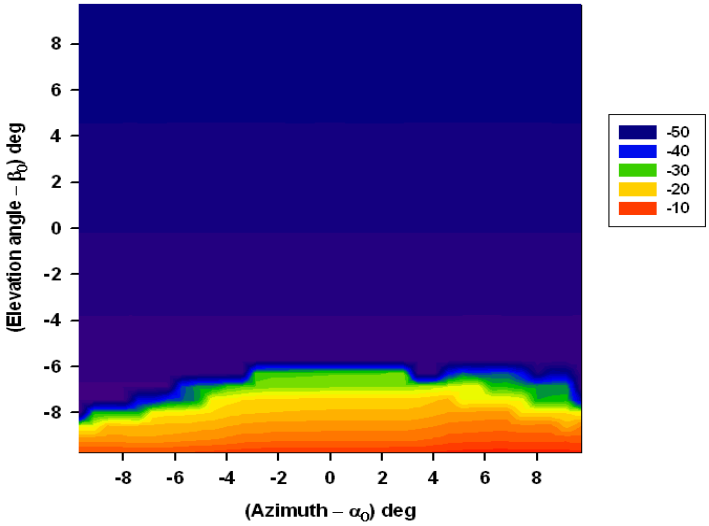

Figure 157. Modeled BTD image at observer location no. 3, α_0 = 270° (West), β_0 = 30°.

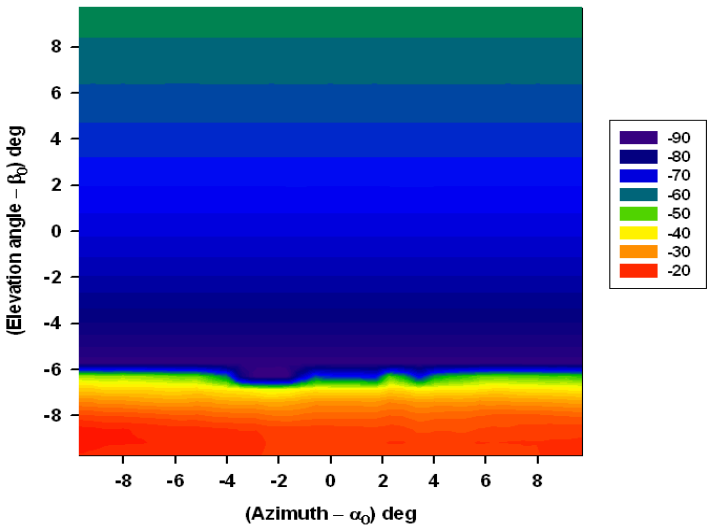

Figure 158. Modeled BTD image at observer location no. 4 , α_0 = 270° (West), β_0 = 12°.

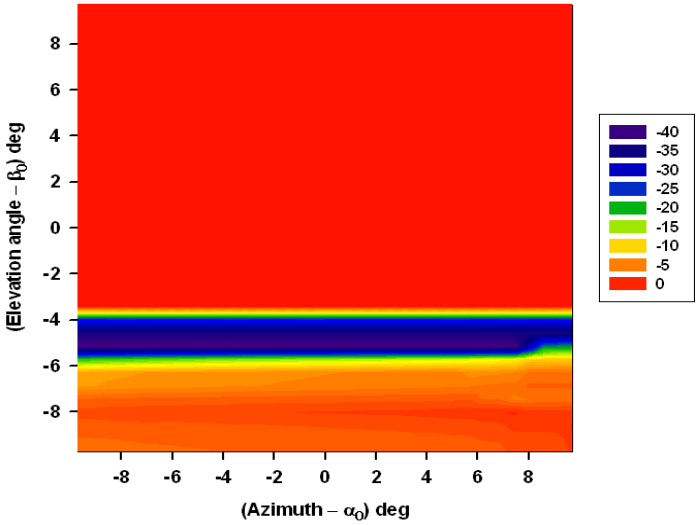

Figure 159. Modeled BTD image at observer location no. 5, α_0 = 180° (South), β_0 = 60°.

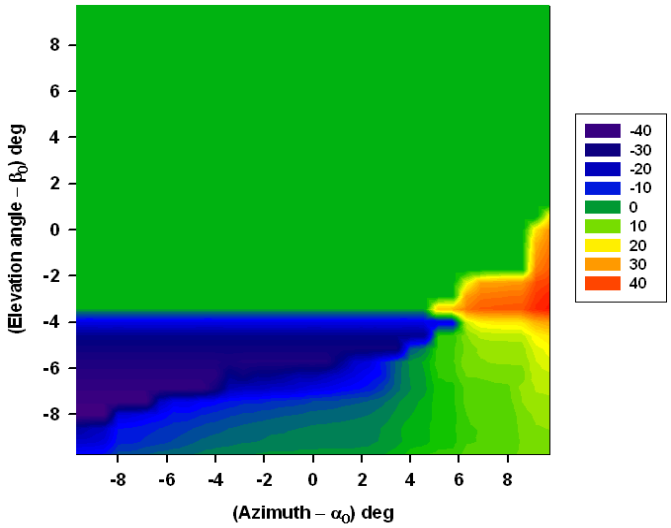

Figure 160. Modeled BTD image at observer location no. 6, α_0 = 180° (South), β_0 = 30°.

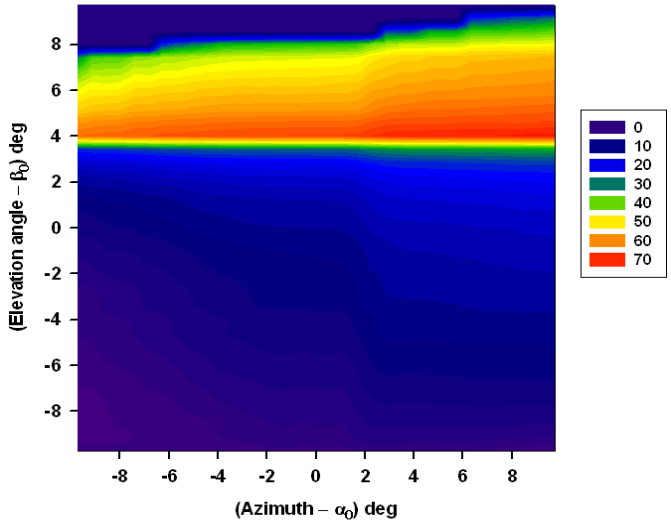

Figure 161. Modeled BTD image at observer location no. 7, α_0 = 180° (South), β_0 = 12°.

As can be seen from Figure 148 through Figure 161, the lee wave mountain turbulence produces strong signals in comparison with the radiance computed for a background calm atmospheric state. The maximum signal is observed on the water lines and it is obviously caused by updrafts/downdrafts providing sharp water vapor variations. Note that by analyzing ΔR, the angular variations of radiances caused by different ray trajectories in the field of view are significantly reduced. The actual images of ΔR and selected channels (Figure 155 through Figure 161) depend mainly on the viewing geometry and on how much of the lee wave is in the instrument's FOV. The simulation results indicate that mountain wave turbulence should be detectable with the Hyper-Cam at the Colorado MRS, if the WRF model is an accurate representation of conditions and the simulation is an accurate representation of what can be observed. After the field test, it was determined that the high signals observed were most likely an artifact of the model itself; this is discussed in further detail in Section 5.5.

Another simulation was made at the same observation point with the March 6, 2004 WRF model. The image size in this case was set at 25 vertical x 35 horizontal pixels with a single pixel angular size of 0.01 rad (~0.57°); the full angular image size was equal to 0.25 x 0.35 rad (~14.3° x 20.1°) in vertical/azimuthal directions respectively. The image central pixel (13, 18) was always directed straight to the east (local azimuth angle 90° from the North clockwise), i.e. to the center of the observed lee wave. The viewing elevation angles considered (measured at the central pixel of the array) were 90°, 60°, 45°, 30°, and 15° above the horizon. Eight hundred and seventy five (25*35) FLI radiance spectra were computed with the FLI-FM for each of the five different viewing angles. The wavenumber range was 650 – 1650 cm^{-1} with a spectral resolution of 16 cm^{-1} and no apodization applied.

For each spectral channel, the RMS (root mean square) and peak-to-peak differences were computed over all 875 image pixels for each measurement frame. Each radiance spectrum was subtracted from the azimuthal (horizontal) radiance mean spectrum. The results are presented in terms of brightness temperature. These statistics are shown in Figure 162 and Figure 163. One can note that although the spectral shapes of both statistical characteristics are similar, the peak-to-peak values are about order of magnitude greater than the RMS values (e.g. 12K and 1K,

respectively). It is also worth to noting that RMS difference regularly increases with decreasing elevation angle due to longer path through the lee wave turbulence-disturbed atmospheric state. Similar statistical displays were produced from the actual Hyper-Cam data in order to be able assess, in real-time, the lee wave information content of the measurements. These statistics are shown in Section 5.3.5.

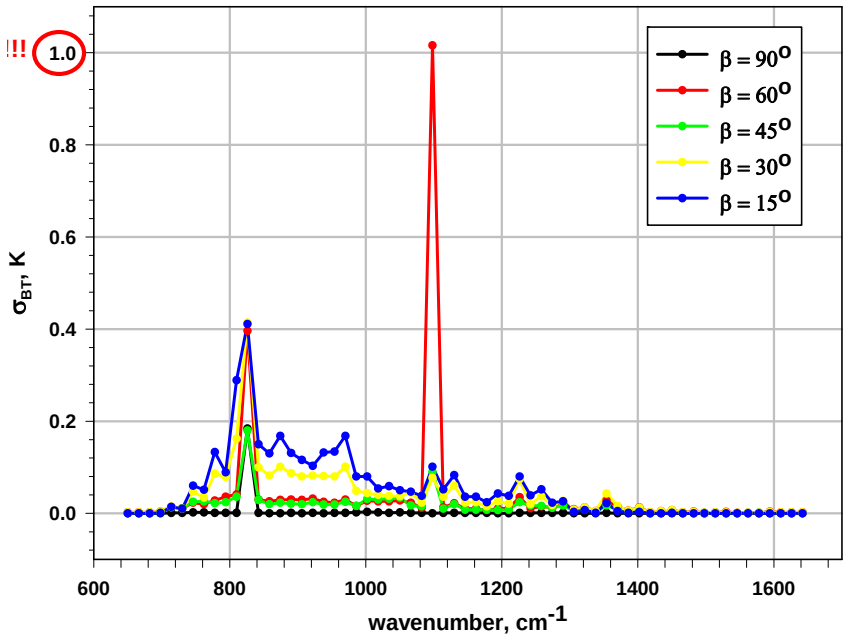

Figure 162. Brightness temperature RMS difference over all image pixels when mean azimuthal brightness temperature is subtracted.

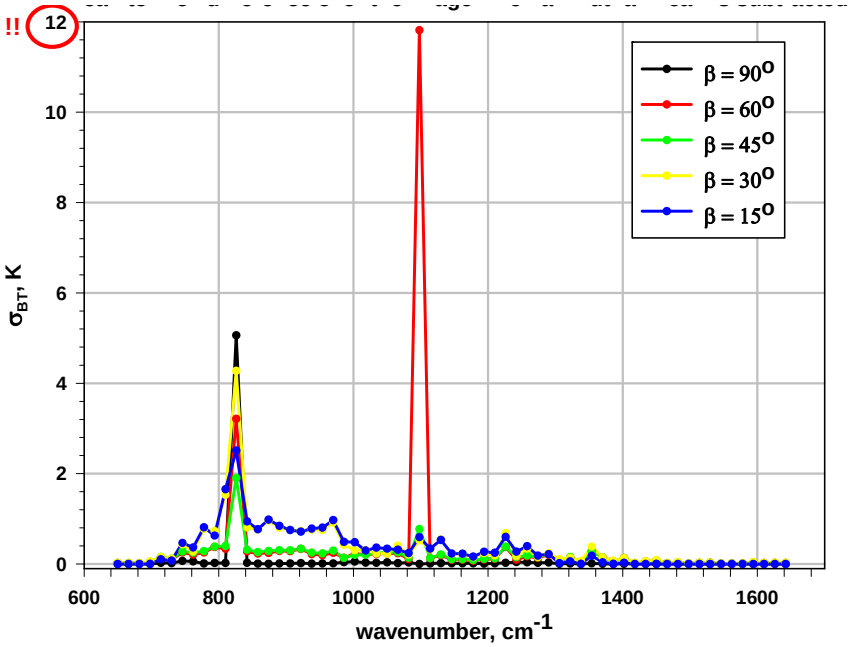

Figure 163. Brightness temperature peak-to-peak difference over all image pixels when mean azimuthal brightness temperature is subtracted.

The maximum signal is observed at v_{MAX} = 826 cm^{-1} for all elevation angles except β_0 = 60°, for which v_{MAX} = 1098 cm^{-1}, which might be explained by the fact that in the later case (β_0 = 60°), the center of the lee wave is located directly in the field of view, while for other elevation angles we observe less turbulent atmospheric regions surrounding the region of lee wave turbulence.

Figure 164 through Figure 168 show the expected signal (BTD from the azimuthal mean) for all five chosen elevation angles and for the channels with maximum BT variations across the field of view. Note that the scale is limited to ± 0.5 K in order to accentuate the smaller and larger signals beyond these limits; this scale is well the Hyper-Cam noise limits (see Appendix A, which shows noise floor at 16 cm^{-1} resolution is equivalent to 0.16 K BTD at 300 K). The results of these simulations show that large signals (i.e. 1 K or more) should be observed for the case of a well-developed mountain-generated turbulent wave.

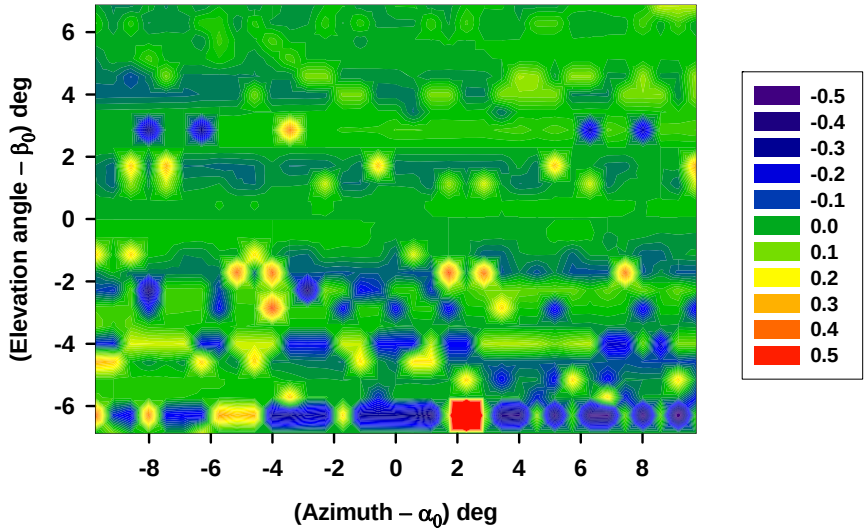

Figure 164. BTD from the azimuthal mean for v = 826 cm^{-1} and β_0 = 90°.

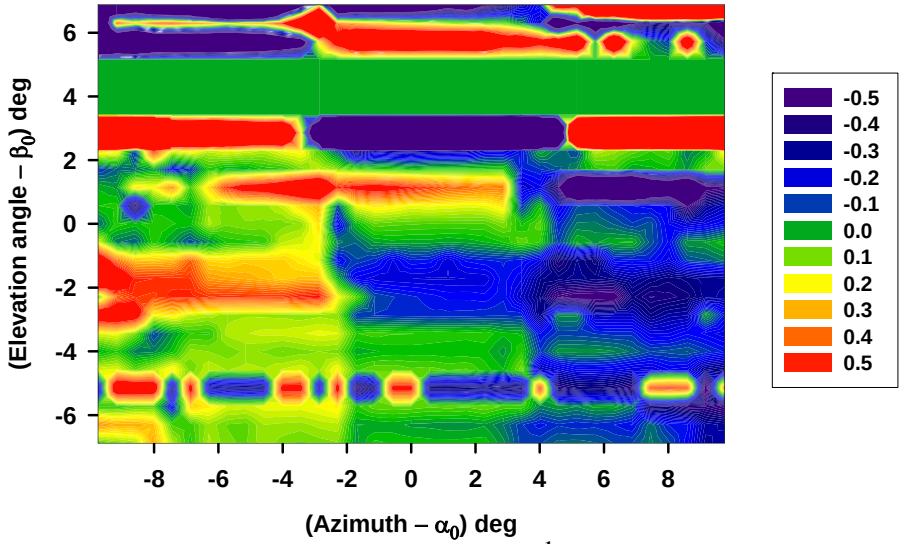

Figure 165. BTD from the azimuthal mean for v = 1098 cm^{-1} and β_0 = 60°.

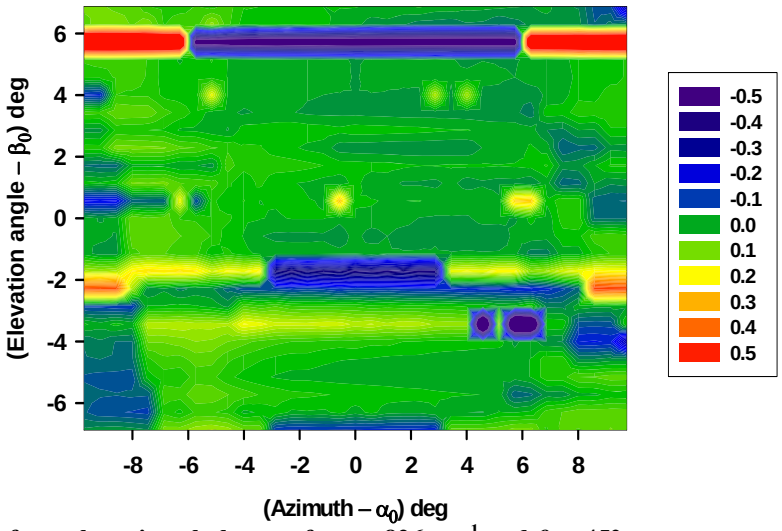

Figure 166. BTD from the azimuthal mean for $\nu = 826$ cm^{-1} and $\beta_0 = 45°$.

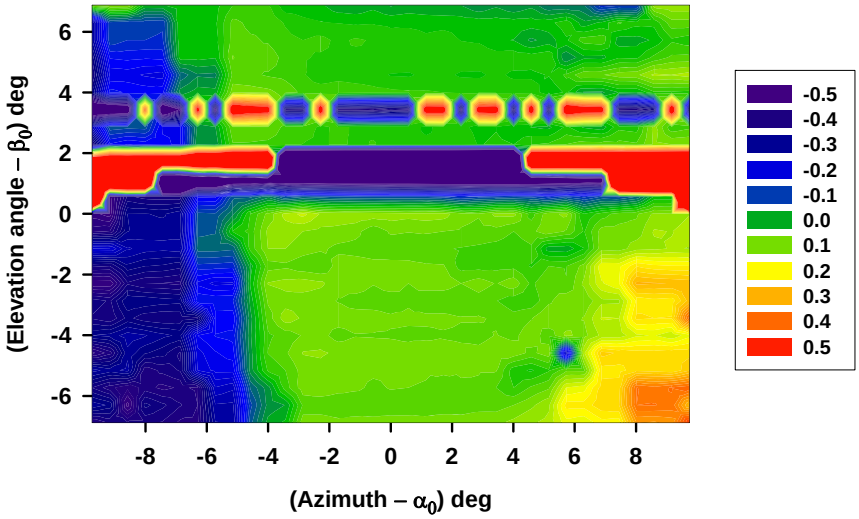

Figure 167. BTD from the azimuthal mean for $\nu = 826$ cm^{-1} and $\beta_0 = 30°$.

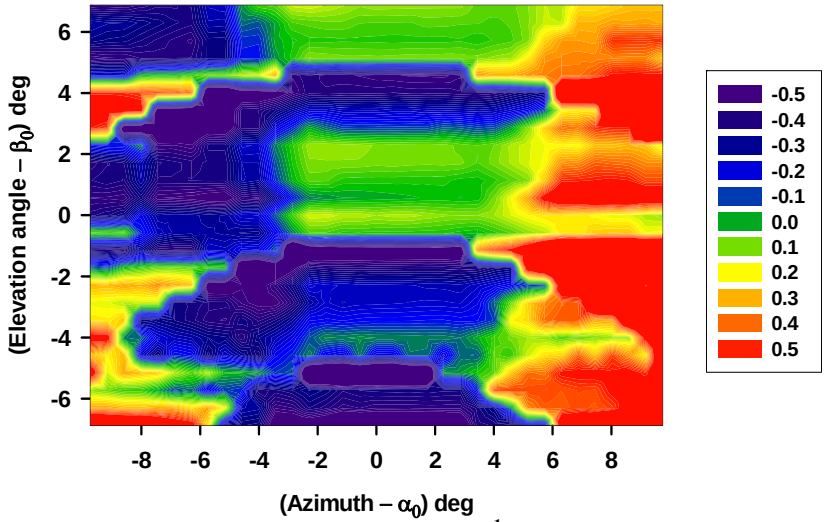

Figure 168. BTD from the azimuthal mean for $\nu = 826$ cm^{-1} and $\beta_0 = 15°$.

5.2 Mountain Research Station Data Collection Activity

The Mountain Research Station (MRS) is an interdisciplinary research facility of the Institute of Arctic and Alpine Research, University of Colorado, located on the front range of the Rocky Mountains. Research at the MRS is primarily performed by investigators not formally associated with the MRS. The support facilities of the MRS include laboratories, offices, classrooms, cabins, a dining hall, and a bathhouse. Laboratories include the Kiowa wet-chemistry lab, several plant, soil, and chemistry labs within the larger John W. Marr Laboratory Building, and the Tundra Lab located at 3500 m elevation on Niwot Ridge.

The test site at MRS was located at an elevation of 2,900 m (9,500 ft), approximately 76 km (47 mi) WNW of Denver International Airport (DEN). This elevation and clear line of sight towards the airport was an ideal location for observing mountain waves that form over the Rockies. Figure 169 shows a simple graphical representation of the viewing geometry from the MRS test location to the atmosphere above DEN. Details on the test location are given in 5.2.2, the MRS Data Acquisition section.

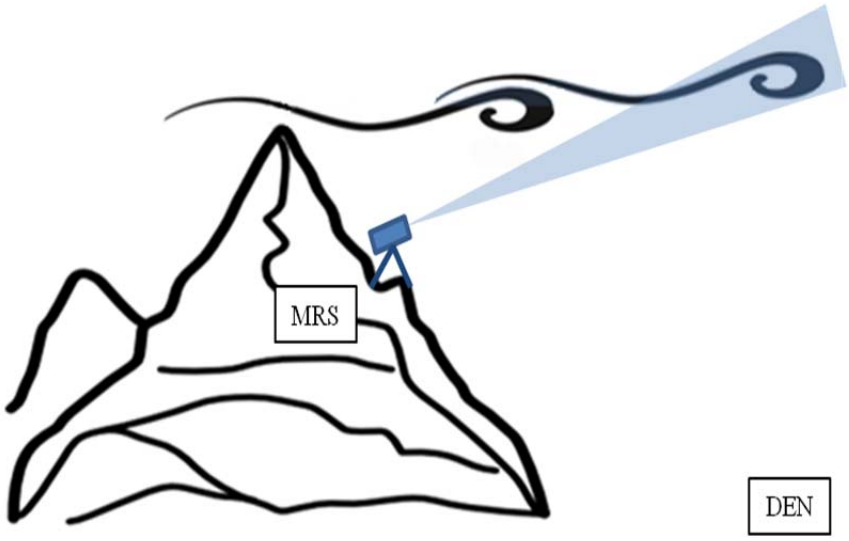

Figure 169. Representation of test location at MRS looking at atmosphere over DEN.

5.2.1 MRS Data Collection Preparations

As mentioned above, the University of Colorado's Mountain Research Station (MRS) includes three sites with buildings including the base camp (elevation 9,500 ft.), the Tundra Lab (11,600 ft.), and the C1 site at an intermediate elevation. On March 14, 2011, two of the research team members visited the MRS near Ward, CO, to investigate potential viewing sites for radiometric observations of mountain waves and associated air turbulence. Each site has differing clear-viewing directions and difficulties of access. All sites have electrical power. The highest site, the Tundra Lab, has an unimpeded 180-degree view from the east to the south and around to the west. Lower sites have east and west views, and the base camp has a clear view of Pikes Peak, as well as a view to the east. The Tundra Lab provides panoramic viewing but is accessible only by tracked snow vehicle for much of the year. The base camp also has Internet access and is served by both UPS and FedEx. A photograph of the Tundra Lab and its location relative to Boulder, CO is given in Figure 170.

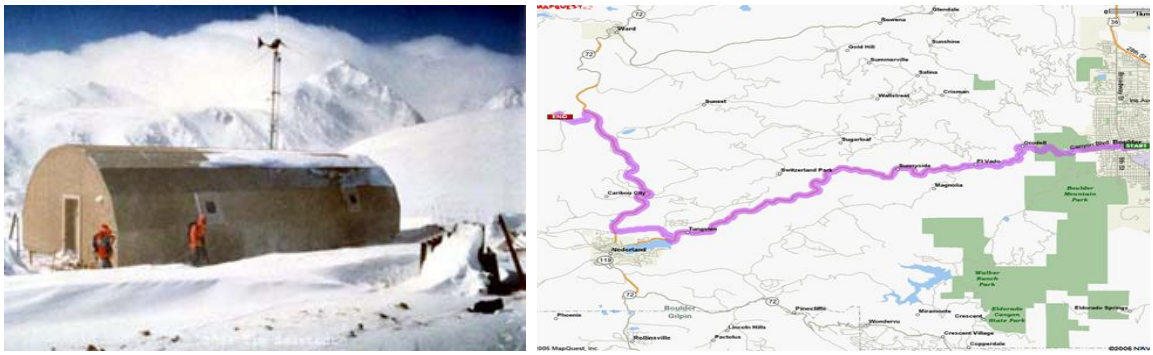

Figure 170. Mountain Research Station Tundra Site *(left)* and Map from Boulder, CO *(right).*

The attractive features of the MRS for the FLI project are that it provides long, near-horizontal views from several sites that all have plenty of electric power, and that the base camp has all utilities and amenities including high-speed internet and living quarters. The road to the base camp is kept plowed all winter. The rooftop platform on the base camp building is reached by a combination of an extension ladder and a steel stairway, as shown in Figure 171, below.

Figure 171. Rooftop platform on base camp building and access ladder/stairs.

The platform provides excellent views to the south and east, but it is small and it is already in use by two other sets of instruments. Furthermore, it would provide no shelter for our instruments, and the access method would make it very difficult to install the Hyper-Cam. Nevertheless, it is shown here to illustrate the viewing available at MRS. Figure 172 is a photo of Pikes Peak, which is a 14,110 ft. peak 86 miles SSE of the MRS.

Figure 172. Pike's Peak, at a distance of 86 miles from the MRS.

After touring the base camp, we travelled by snow vehicle to the C1 site, where again we were shown a rooftop on a small shelter where we could mount equipment on tripods. The C1 buildings are in the background of the vehicle photo shown in Figure 173.

Figure 173. **The snow vehicle at the C1 site.**

On the way back, we investigated an open clearing as a potential site. Several photos are shown below to illustrate the views that the site provides. Long views to both east and west are available in the clearing and at nearby locations. Electric power is available. Snow does not accumulate here due to high winds, which makes it an inhospitable place to work.

Figure 174. **View to the west from clearing, Kiowa Peak (13,156 ft. elevation).**

Figure 175. **View to the east from clearing.**

The annual weather cycle at MRS constrained the test dates and locations. Mountain waves are a winter phenomenon [31]. During summer, the road to the C1 and Tundra Lab sites is open for wheeled vehicles. After a snowpack has formed in the winter, access to the higher elevations is provided by the snow vehicle. At an intermediate time, there is not enough snow for the tracked vehicle and access is not available, except to the base camp. During September-October, it is usually possible to drive to the C1 site. The upshot of these considerations is that the best test dates are late October to early November.

Figure 176. **Leanne West and Kurt Chowanski, Kiowa Peak ~6 miles to the west.**

We discussed the site visit and test dates with Larry Cornman of the STAR Institute and Bob Sharman, who confirmed the wintertime nature of mountain waves and made several points:

- Mountain waves can be forecast no more than three days in advance.
- Turbulence associated with mountain waves is over the terrain, not east of it. (It propagates upward.)
- Looking south might be good because our line of site would cross flights paths into DEN.
- Mountain waves persist all day, so aircraft data and PIREPS constitute good truth data.
- We can get turbulence data from http://weather.aero/. NCAR archives actual airline turbulence data.
- Bob and Larry spoke about using NCAR's connections in the airline industry to obtain additional PIREPS and aircraft turbulence data to support the MSR measurements, for example by getting United Airlines on board.
- Large waves condense out the water vapor, which could present a problem for a clear line of sight, but perhaps we could look horizontally through a dry slot.

In addition, the location of the tests, on the front range of the Rocky Mountains, was important for acquiring truth data due to the amount of air traffic in the area: flights into, out of, and at cruise altitudes over the Denver International Airport. The large amount of air traffic meant that pilot reports (PIREPS) and automated reports from United Airlines (UAL) 757 and Delta Airlines (DL) 737 aircraft were available as "ground truth" for the turbulence detection efforts.

The UAL and DL aircraft are equipped with instruments to estimate and automatically report eddy dissipation rates (EDR) to the one-third power. These reports consist of peak and mean value of the EDR over the previous one minute (in cruise). These reports cover "none" to "extreme" levels of turbulence, and they were used as verification data. The truth data allows for the evaluation of both true detections and false alarms by the sensor and algorithms. Pilot reports, on the other hand, are more subjective in nature. PIREPS are not always given for turbulence

encounters (even severe ones); they rarely provide for null turbulence; the reported time and position can be in error; and the intensity level of the turbulence reported by the pilot is a subjective measure of the actual intensity level. Nevertheless, these data, when available, are still valuable in the verification process. Figure 177 shows the flight tracks of the EDR-equipped UAL 757s over a 24-hour period. There are many flights in the Colorado area. Figure 178 shows the same data for the DL 737 aircraft. While there are fewer DL flights over Colorado, data from these aircraft were helpful in the verification process.

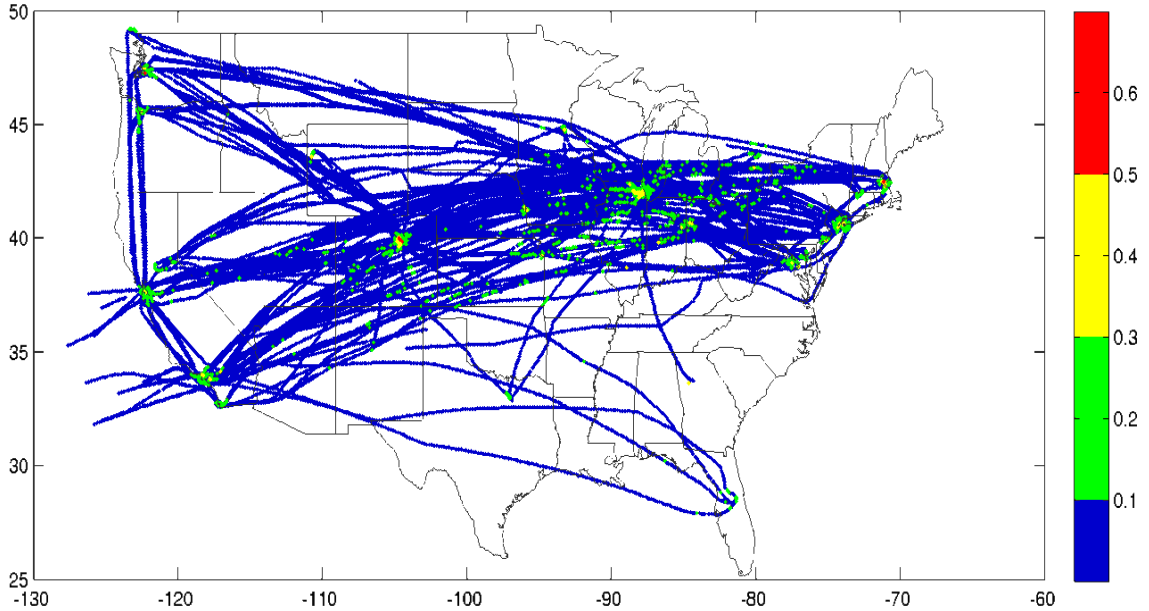

Figure 177. UAL 757 reports over a 24 hour period.

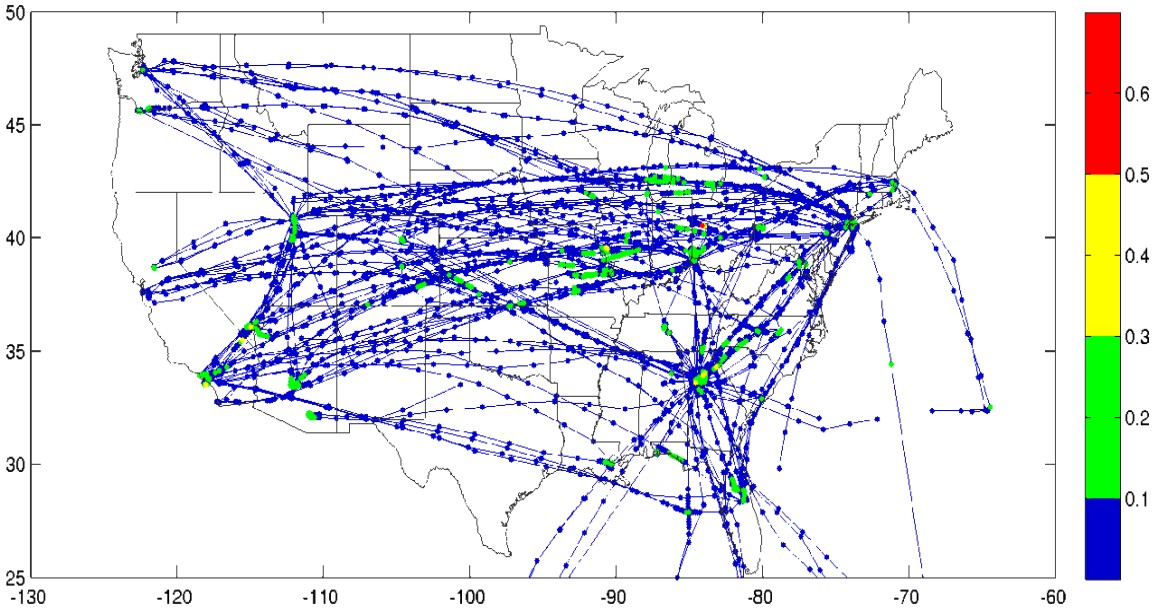

Figure 178. DAL 737 reports over a 24 hour period.

Our test plan for the mountain wave measurements in Colorado included two radiometric instruments, the D&P TurboFT spectroradiometer and the Telops Hyper-Cam imaging interferometric radiometer. During the test plan review on August 24, 2011, the procedure for pointing the D&P and the Telops instruments in the same direction was identified as an issue. A consensus emerged that the instruments should be on a common mount and boresighted. This decision had several implications, one of which was that the D&P must operate in the same outdoor environment as the Hyper-Cam. The manufacturer's specified operating temperature range for the D&P is about 60 – 90°F, so a temperature-controlled shelter was designed and constructed for the D&P. The shelter design also considered:

1. Both instruments can currently be mounted individually on heavy-duty tripods, with dovetail slides. It was desirable to retain this tripod mounting capability.
2. The D&P is very susceptible to electromagnetic interference (EMI), so the shelter should provide EMI shielding for it.
3. The shelter must provide access to the D&P's built-in aiming sight, the liquid nitrogen refill port, and the calibration blackbody.

To meet all of these requirements, we purchased a commercial enclosure made of lightweight aluminum, along with a thermostatically-controlled forced-air heater for the interior of the enclosure and foam insulation to line the interior of the enclosure. This combination of components provides both thermal stability and EMI shielding.

We modeled all of these elements, along with the D&P spectrometer itself in SolidWorks mechanical design software. A cutaway drawing of the system is shown in the Figure 179. The blue box in the figure is the enclosure heater. Access to the D&P is provided by means of the hinged lid, and a viewing port on the front provides a view of the outside world.

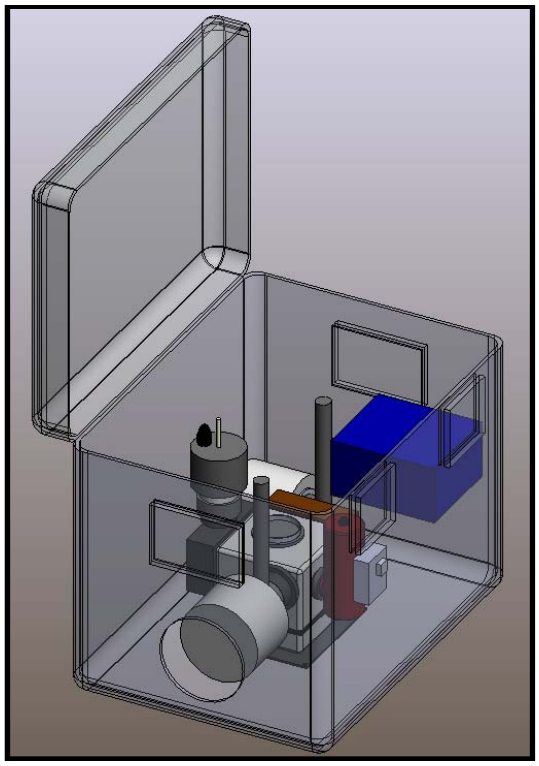

Figure 179. SolidWorks illustration of the D&P instrument installed in its shelter with the heater (blue box).

The D&P was bolted through the bottom of the enclosure to a base plate. The base plate allows for the system to be mounted on a tripod or in an over-and-under mount with the Hyper-Cam. The base plate also provides a mount for a turning mirror to the front of the system (not shown). By using the mirror, we can aim the D&P field of view vertically, which is another capability that was identified during the test plan review. A boresighted camera was added to the enclosure to provide a more convenient aiming procedure and visible images.

For the D&P/Hyper-Cam common mount, the desirability of an over-and-under configuration was also discussed during the test plan review with the following requirements:

1. Both instruments should attach with the same dovetail slides that are used on the tripods.
2. The mount must provide access to the Hyper-Cam visible camera focus knob.
3. The mount must provide for boresight adjustment.
4. The mount must provide elevation angles in the range 0 – 60 degrees.
5. The mechanical design should include consideration of ease of assembly and teardown, minimizing weight, and disassembly for shipping.

A low-cost means of achieving all of these requirements is illustrated in Figure 180. The entire framework is fabricated from bolted Uni-Strut members and gussets. The Hyper-Cam mounts on the bottom, and the D&P shelter mounts on the top because it is lighter and access to the D&P is required for liquid nitrogen. The elevation axis is at the center of gravity of the moving parts, and an elevation lock is provided. This mount enabled the field test team to aim the instrument out a window in the dining hall at MRS, as required.

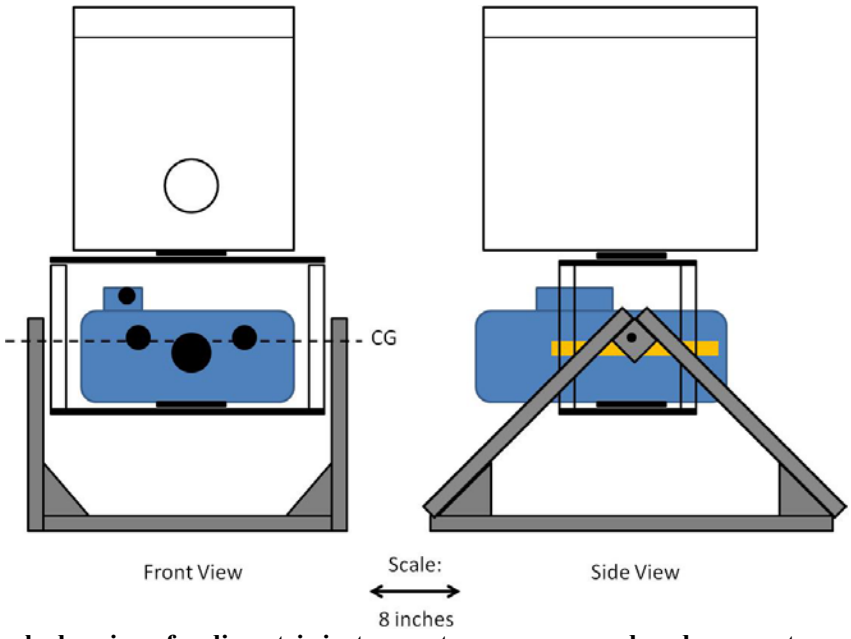

Figure 180. Scale drawing of radiometric instruments on an over-and-under mount.

A SolidWorks representation of the mount with the D&P in a temperature-controlled box with the Hyper-Cam mounted below is shown in Figure 181.

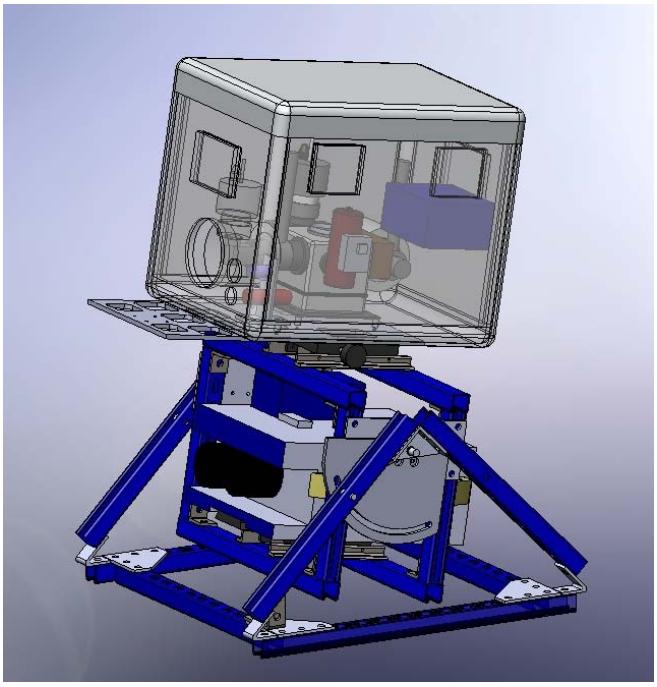

Figure 181. A SolidWorks representation of the mount with the Hyper-Cam and D&P installed.

Note the location of the rotation axis in Figure 181; this rotation enables the operator to adjust the elevation angle while maintaining boresight of the two sensors. The alignment of the boresight was tested by setting up two light bulbs at a 19-inch vertical spacing, which is equivalent to the distance between the D&P's and Hyper-Cam's optical axes. Near perfect alignment was observed, even after a complete teardown and re-assembly.

The mount itself is shown below in Figure 182; the D&P is encased in the aluminum enclosure and the Hyper-Cam is mounted below.

Figure 182. The final mount for the D&P and Hyper-Cam.

In addition to the construction of the enclosures and mounts in preparation for the field test, the sensors themselves were checked. Ten-meter cables were ordered from Telops for the Hyper-Cam. This longer length enables the user to not be right next to the instrument while running it. The operation was tested with the longer cable and the wide-FOV lens (25.6° x 30.6° FOV when the entire FPA is used). The lens was delivered with the original Hyper-Cam order but had not been used in a field test until the November 2011 MRS experiment.

The D&P was sent back to the manufacturer in early September 2011 for a refurbishment. This service included re-conditioning the detector, re-pumping the Dewar, and a check of all systems. The detector was re-aligned and the signal restored to that of a new instrument. Despite this refurbishment, we still experienced problems with a loose wire that caused errors in the collected data. The data issues are described in 5.3.3, the Data Analysis section.

The D&P enclosure was tested in an environmental chamber on the Georgia Tech campus. The chamber has a controller that reports several temperatures in real time, as well as a graph showing their time history. These temperatures are as follows:

Set Point:	the temperature that the operator has selected for the chamber,
D (Duct) A – T:	the air temperature in the duct leading to the chamber, and
R (Room) A – T:	the air temperature in the chamber.

The room temperature was about 7 °C at the start of the test. However, the duct air temperature was about –1 °C, and all of the cold air emerged forcefully from a ceiling vent in one corner of the room. The D&P system was installed on a table near the ceiling vent. The heater thermostat in the enclosure was set to 21 °C, the lid closed, and the enclosure placed under the blast of –1 °C air. All temperature monitoring was done with the D&P; it reports box temperature and the

instrument temperature continuously on the GUI, and it also records these values in file headers during data acquisition.

The four temperatures monitored by the D&P are ambient temperate (Tbox), instrument temperature (Tinst), blackbody temperature (Tbb), and laser diode temperature (Tld). Those recordings, along with comments, are included in Table 9 and Figure 183. All temperatures are in degrees Celsius.

Table 9. D&P monitored temperatures (°C).

Elapsed Time (minutes)	Tbox	Tinst	Tbb	Tld	Comment
0	22.0	18.9	13.3	24.8	
5	21.1	19.4	19.0	24.5	
11	19.4	19.0	18.8	24.7	
13	19.4	19.0	18.5	24.7	Heater unplugged
15	19.4	18.9	18.2	24.7	Cold air blower unexpectedly turned off
20	19.2	18.9	17.6	24.7	
25	19.0	18.9	17.1	24.7	Cold air blower unexpectedly turned on
30	18.8.	18.9	16.7	24.7	
33	18.7	18.9	16.4	24.7	Heater plugged back in
38	18.1	18.8	15.8	24.7	Heater temp. set to ~38 °C, turns on
40	19.9	19.5	16.3	24.7	
42	24.5	20.1	20.1	24.9	
44	25.9	20.3	22.9	24.9	Though Tbox–Tinst >5 °C, no alarm
47	26.3	20.4	24.9	24.9	

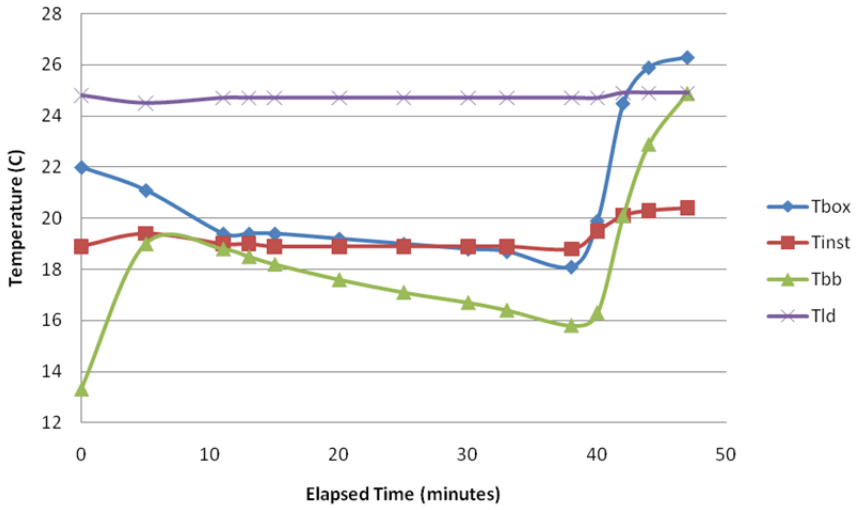

Figure 183. The D&P temperature readings during the time of the test.

From the table and graph we note several things:

1. When being blasted with –1 °C air, the box lost heat at a rate that corresponds to somewhere from 2 to 4 °C in 30 minutes.
2. During the time interval from 10 to 40 minutes, Tinst was constant.
3. When the heater came on, it caused a temperature rise of ~8 °C in 5 minutes.
4. The sudden, large change in Tbox caused a change of >1 °C in Tinst.

The conclusions from this test were as follows:

1. The D&P enclosure allowed easy access for filling the cryostat with LN2.
2. The D&P enclosure allowed easy access for changing the fore-optics and installing the insulating sleeve.
3. The heater had plenty of power.
4. Hot air from the heater did not cause adhesion or melting problems for the box's insulation.
5. The thermostat set point was inaccurate (set at 21 °C, but it never came on).
6. The thermostat ΔT was very large, ~8 °C.
7. We needed to provide better temperature control in the box.

The results of the D&P enclosure test required that a better temperature controller be incorporated into the box. The new components were purchased and a new controller installed for the heater. These tests were repeated and the new heater performed as needed.

5.2.2 MRS Data Acquisition

Knowing that weather is very unpredictable with any type of lead time, the STAR team was watching for weather patterns that indicated high winds/turbulence. With only 3 days' notice, the GTRI team went to MRS based on STAR's prediction that high winds were likely. We conducted the field campaign during four days in November 2011. Several sites at elevations higher than the main lab were selected for possible locations for the data collection; however, due to snow cover and an inoperational Sno-Cat at the time of the test, the data collection was confined to the dining hall and parking lot at MRS. However, this restriction did not inhibit the data collection; looking out of an open window from the second floor of the dining hall provided a clear view of the sky over the tree line in the direction of Denver (shown in Figure 184), even though the instruments were below the tree line. Data collection activities are outlined below in Table 10 and Table 11.

Figure 184. Instrument set-up looking out the open window of the MRS dining hall (*left panel*), and instruments looking ESE toward Denver (right *panel*).

Table 10. Data Collection Matrix, Atmospheric Observations.

Time (UTC)	Azimuth (deg)	Elevation (deg)	Hyper-Cam FOV	Run Number	Duration (min)	D&P	Hyper-Cam	Hyper-Cam Resolution (cm^{-1})	Location
Wednesday, November 16									
18:57	113	10.1	WFOV	5	30	Yes	Yes	16	Inside
19:40	113	29.4	WFOV	6	30	Yes	Yes	16	Inside
20:58	148	40	WFOV	7	30	Yes	Yes	16	Inside
22:29	148	40	WFOV	9	30	Yes	Yes	1	Inside
23:14	148	40	WFOV	10	30	Yes	Yes	16	Inside
Thursday, November 17									
15:53	?	?	WFOV	1	30	No	Yes	16	Inside
17:45	164	10.6	WFOV	2	30	Yes	Yes	16	Inside
18:12	112	10.1	WFOV	3	30	Yes	Yes	16	Inside
18:48	112	4	NFOV	4	30	Yes	Yes	16	Inside
20:26	164	13.5	NFOV	5	30	Yes	Yes	16	Inside
21:05	164	39	NFOV	6	30	Yes	Yes	16	Inside
21:38	164	39	WFOV	7	30	Yes	Yes	16	Inside
22:12	164	25	WFOV	8	30	Yes	Yes	16	Inside
22:49	176	18	WFOV	9	30	Yes	Yes	16	Inside
Friday, November 18									
15:45	0	88.5	WFOV	1	30	No	Yes	16	Outside
16:38	0	88.5	WFOV	2	30	No	Yes	4	Outside
17:45	112	12	WFOV	3	30	Yes	Yes	16	Outside
18:20	112	31.5	WFOV	4	30	Yes	Yes	16	Inside
18:55	117	31.5	WFOV	5	30	Yes	Yes	16	Inside
19:40	117	19	WFOV	6	30	Yes	Yes	32	Inside
20:54	258	24	WFOV	7	10	Yes	Yes	16	Inside
21:17	85	20	WFOV	8	30	Yes	Yes	1	Inside
21:52	123	11.5	WFOV	9	33	Yes	Yes	1	Inside
Sunday, November 20									
16:14	175	31	WFOV	1	30	No	Yes	16	Inside
16:51	190	30	WFOV	2	30	No	Yes	16	Inside
17:35	113	13	WFOV	3	30	Yes	Yes	16	Inside

Table 11. Data Collection Matrix, Surface Emissivity Observations, Resolution = 1 cm^{-1} for all runs.

Time (UTC)	Scene	Run	Distance to Scene (m)	Viewing azimuth (deg)	Air Temp (°C)	Object	Object Temp Before (°C)	Object Temp After (°C)
17:06	powdery snow	1	5.9	87	1.2	gold plate	1.9	1.4
						dry concrete	1.6	1.9
						wet concrete	1.4	1.2
						disturbed snow	0.2	0.2
						undisturbed snow	0	0.2
17:12	powdery snow	2	5.9	87	2.3	gold plate	1.4	1.4
						dry concrete	1.9	1.7
						wet concrete	1.2	1.4
						disturbed snow	0.2	0.2
						undisturbed snow	0.2	0
17:16	powdery snow	3	5.9	87	2.2	gold plate	1.4	1.2
						dry concrete	1.7	1.4
						wet concrete	1.4	0.9
						disturbed snow	0.2	0.3
						undisturbed snow	0	0
17:20	powdery snow	4	5.9	87	2.1	gold plate	1.2	1.3
						dry concrete	1.4	1.7
						wet concrete	0.9	1.2
						disturbed snow	0.3	0.3
						undisturbed snow	0	0.2
17:33	snow bank	1	28.7	185	2.5	gold plate	0.2	0.8
						snow	-1.2	-1.7
xx	ice/snow	1	21.4	218	xx	gold plate	-0.2	-0.7
						compact snow	-2.3	-2.5
						powdery snow	-3.5	-3.0
						ice patch	-1.8	-1.8
xx	rock/snow	1	9	178	1.3	gold plate	-0.7	-0.5
						powdery snow	-2.1	-1.9
						ice patch	-0.7	-0.9

The weather conditions on Thursday, November 17 were exactly as desired – lenticular clouds (indicating mountain waves; see Figure 185) with clear skies otherwise and many PIREPS indicating turbulence. We collected several hours of data in many directions, including the direction of reported turbulence.

Figure 185. Lenticular clouds, Thursday November 17, 2011.

Winds were calmer, but still present on Friday. Saturday was snowy and overcast, so we took the opportunity to collect data for runway surface emissivity. Sunday was calm, but cloudy with a few patches of clear sky. We collected data before needing to pack the instruments, trying to replicate some of the viewing angles from Thursday. The D&P was experiencing issues both Saturday and Sunday. The Hyper-Cam worked well the entire test.

Approximately 13 hours of data were collected in all. During the field activity, data was copied to external hard drives to ensure multiple copies of the data were available. Supporting data collected includes meteorological data from C1 (provided by MRS), radiosonde data, MODIS data, EDRs, and PIREPS. Samples of MODIS data from November 17 and PIREPs data from November 16 are given in Figure 186 and Figure 187, respectively. In these examples, the MODIS data show the mountain waves, and the PIREPS show moderate to light turbulence.

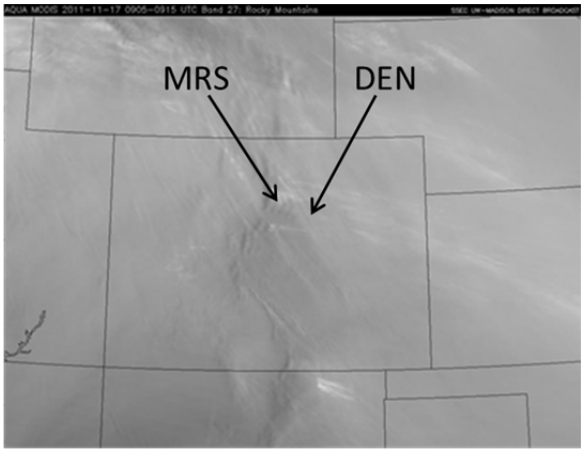

Figure 186. Aqua MODIS water vapor channel data; November 17, 2011; mountain waves visible. Band 27 (6.535 – 6.895 micron).

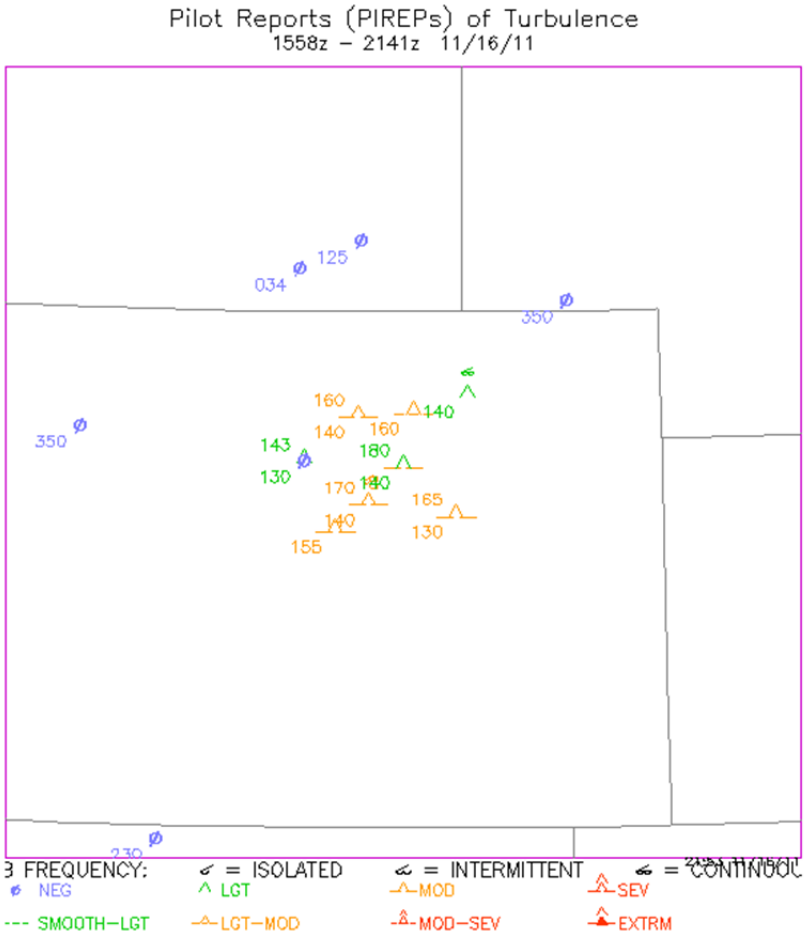

Figure 187. PIREPs data from November 16, 2011; moderate turbulence reported.

Code has been developed to read the PIREPS data, which were provided by UCAR in netCDF format. These data were converted to Excel with Matlab to make it easier to read. The data chosen to include in the Excel spreadsheets distributed to team members only included PIREPS with data in the turbulence fields and PIREPS from times during the test. The spreadsheets were then sorted according to severity of turbulence; 5 (Moderate to Severe) was the highest turbulence intensity reported during the time of the data collect. These spreadsheets were then utilized to determine which data runs had the best chance of having captured turbulent events. The latitude and longitude of the PIREPS observation must be correlated to the viewing angle of the Hyper-Cam and D&P during different measurement runs. Additionally, the Eddy Dissipation Rate (EDR) reports were compared with these PIREPS.

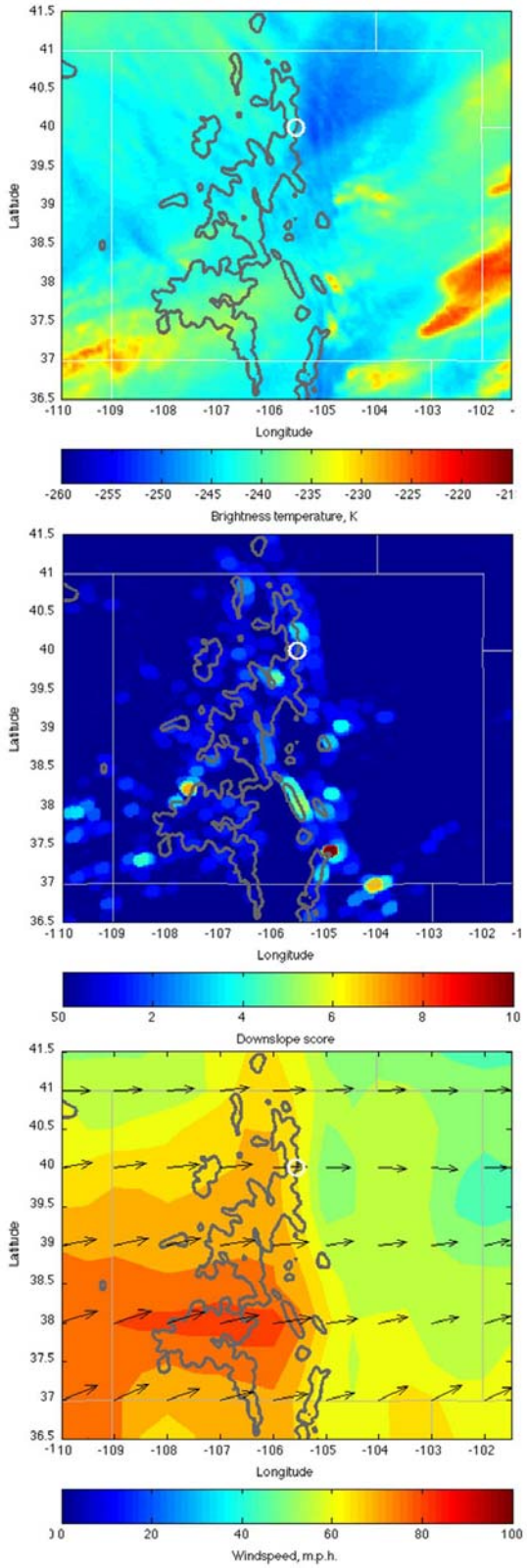

Figure 188. GOES water vapor channel *(top panel)*, experimental downslope wind product *(middle panel)*, and model wind at 500 hPa *(*bottom *panel)*, November 18, 2011. Colorbar scales and units for each are beneath each subfigure.

5.3 Mountain Research Station Data Analysis

Hyper-Cam and D&P data were analyzed in detail in an attempt to reveal mountain lee wave turbulence and associated CAT. A variety of analysis techniques have been applied to the data. Turbulence should cause fluctuations in temperature and water vapor structures due to updrafts and downdrafts associated with mountain waves that are visible in the LWIR.

5.3.1 Hyper-Cam/D&P Data Comparison

The Hyper-Cam and D&P instruments were boresighted and operated simultaneously, so we are able to check the agreement between their radiance measurements. The radiance of Hyper-Cam pixel (176, 120) was used for this comparison, because that pixel location was determined to be the D&P aimpoint during an onsite alignment check. D&P data were recorded at 4 cm^{-1} resolution, and unfortunately only one Hyper-Cam run was recorded at this resolution, during a time when the the D&P was not operating. Hyper-Cam 1 cm^{-1} resolution data shown in Figure 189 was downsampled to match the D&P 4 cm^{-1} resolution data.

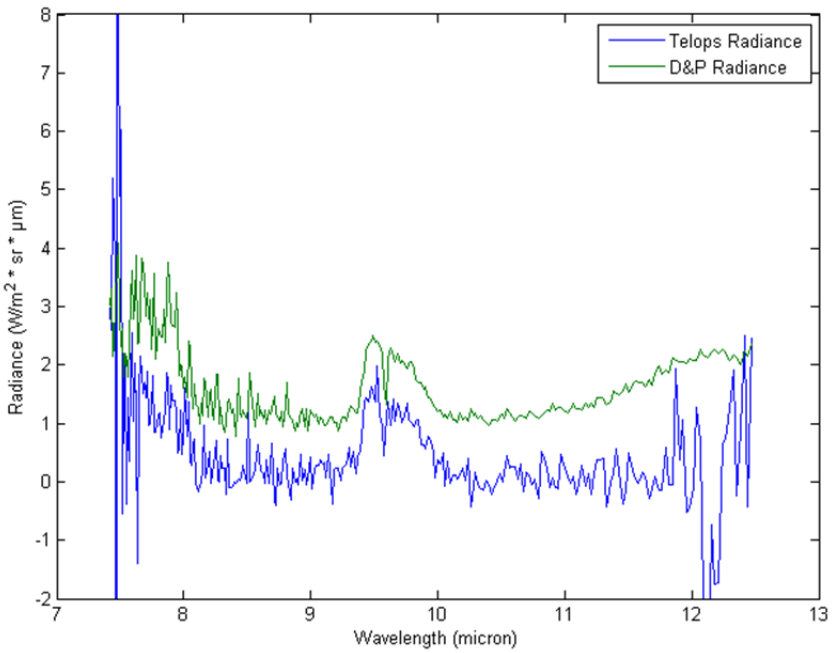

Figure 189. Telops radiance (1 cm^{-1} resolution) vs. D&P radiance (4 cm^{-1} resolution).

The data shown in Figure 189 were measured at MRS on November 16 at 22:31 UTC and the sky viewing direction for this data run was 148° azimuth, 40° elevation. Figure 189 shows the radiance spectra have the same shape, but the Hyper-Cam radiance is lower than the D&P radiance.

5.3.2 D&P Calibration Issues

The D&P experienced problems in the field during the latter portion of the acquisition activity. It was operative during the day with lenticular clouds, November 17. It was operative intermittently after that, but the blackbodies were not responding, so the later data is not calibrated.

An unexpected result was seen while investigating the D&P data from the MRS data collection. Sample interferograms were collected at 4 coadds and blackbody interferograms were collected at 1,000 coadds, meaning that each resulting spectrum is the average of 4 or 1,000 spectra, respectively. When each interferogram was viewed separately, it was noted that for both the sample and cold blackbody data, every even interferogram in the sequence exhibited a waviness about zero OPD. This phenomenon was not seen in the warm blackbody data. A normal interferogram and a wavy interferogram are shown in Figure 190.

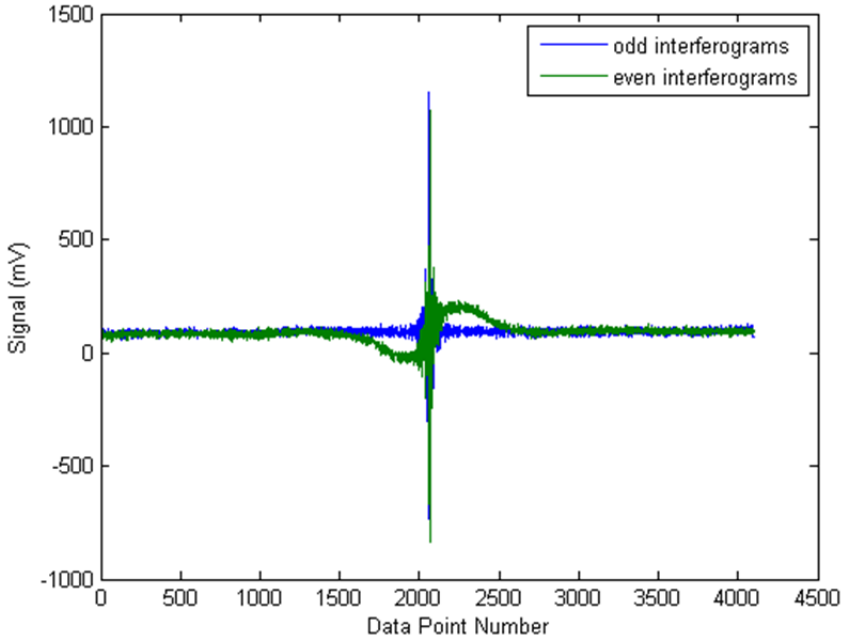

Figure 190. D&P interferograms. The green interferogram exhibits waviness about zero OPD that is seen in all even-numbered interferograms.

These data were sent to D&P in an effort to understand what the source of this result could be, and Winthrop Wadsworth of D&P provided an explanation. There is a slight mismatch in the frequency content of the two orientations of the rotor that produces the four interferograms per revolution. One set of two interferograms is produced when the rotor is parallel to the beamsplitter, and the other set of two is produced when the rotor is perpendicular to the beamsplitter. There is an AC couple in the signal chain that takes out a low frequency signal from the rotor that is due to blocking the IR beam in between interferograms. It is adjusted to minimize this low frequency signal without affecting the long wavelength end of the spectra. The waviness is in the even-numbered interferograms, but it is not of concern because the signal is not in the frequency range of the IR spectrum. The effect shows up more on lower temperature spectra because it has a fixed amplitude, so it is a higher percentage of the signal when looking at lower signal amplitudes. Because the waviness in the interferogram is outside the frequency range of our spectra, it should not affect our data.

5.3.3 Analysis of D&P Data

STAR identified several issues with data discontinuities and spikes in the D&P data; however, a plan was developed to mitigate these issues in subsequent analysis. Prior to the MRS field test,

the D&P instrument had been sent back to the manufacturer for refurbishment to make sure it was in good condition; many of the issues, however, were not noticed until the analysis.

An investigation was undertaken into data quality issues related to the D&P radiometer data taken at the MRS. Two separate issues were seen: data spikes and data gaps. Figure 191 illustrates both of these problems. The data gaps in this image are seen as data discontinuities – not spikes. These occur because the radiance level (or calibration) changes over time, so if the sensor is not collecting data for a while, and then comes back, a discontinuity in the radiance can occur. A good example of this can be seen around sample 15000 in Figure 191. The large discontinuities seen in this figure are not of major concern, because they occur between datasets. Each dataset was not only separated in time from the next but also was recorded at different azimuth/elevation angles. The smaller data gaps within each dataset are not apparent in this figure but are explained in more detail within this section; the data spikes are quite obvious in this figure. The major concern is that when calculating statistical characteristics of the data, such as correlation functions or power spectra, these data quality problems can have significant effects. Two approaches are possible. For the data gaps, one may just use segments of the data that are continuous, or have very short temporal gaps. For the spikes, one may use a spike removal algorithm.

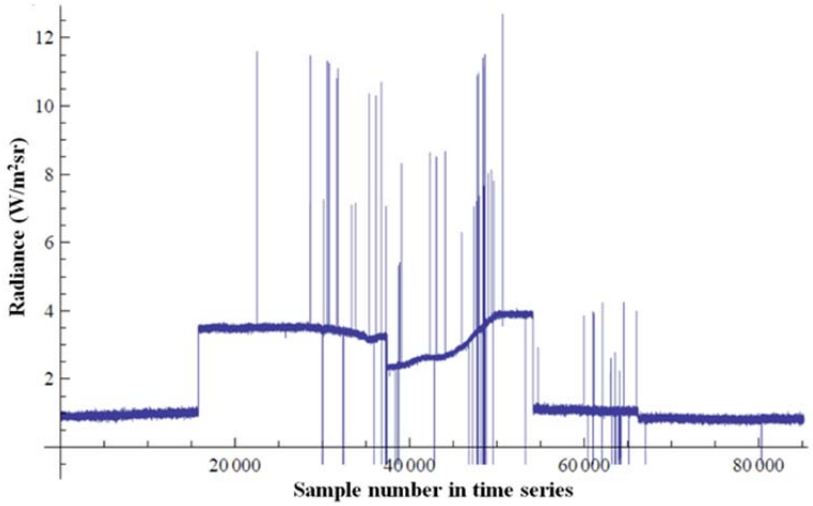

Figure 191. Example of spikes in the radiance time series (ν = 936 cm^{-1}).

Figure 192 is similar to Figure 191, except that radiance is shown at 1501 cm^{-1}, instead of 936 cm^{-1}. These data are over the same time period, so we can see that the temporal discontinuities are quite different at different wavenumbers. However, the spikes are still visible.

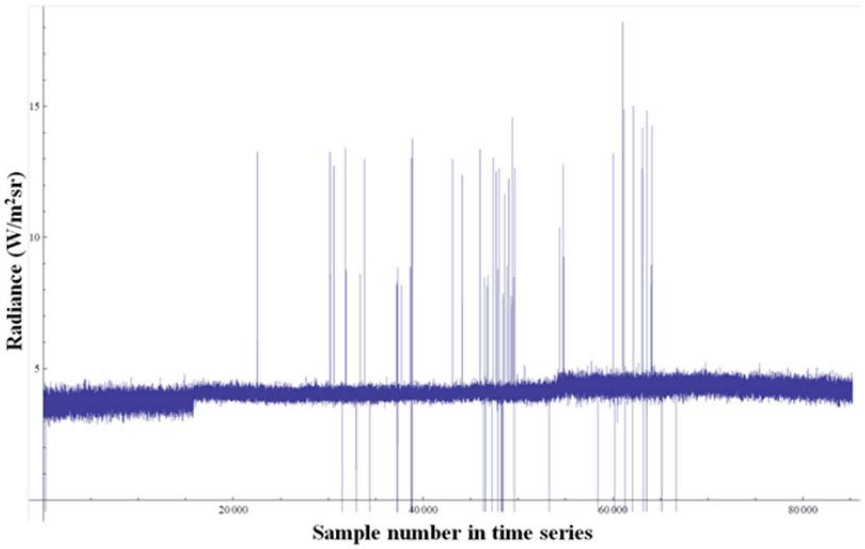

Figure 192. Same as previous figure, but for ν = 1501 cm^{-1}.

Figure 193 and Figure 194 illustrate these differences over wavenumber. Figure 193 shows every 5th wavenumber over the first 300 wavenumbers. The color-coding is such that the "hotter" colors show more deviation and the black regions are ones where the deviations are above a chosen threshold. Figure 194 is similar, except that every 10th wavenumber over the first 1000 (out of a total of 1728) are shown. At higher wavenumbers, there are numerous large variations just due to the radiances being noise-dominated. The larger radiance jumps in the temporal discontinuities can be seen as the vertical black stripes. Certain wavenumbers also exhibit large variations as a function of time. These can be seen as the horizontal black stripes.

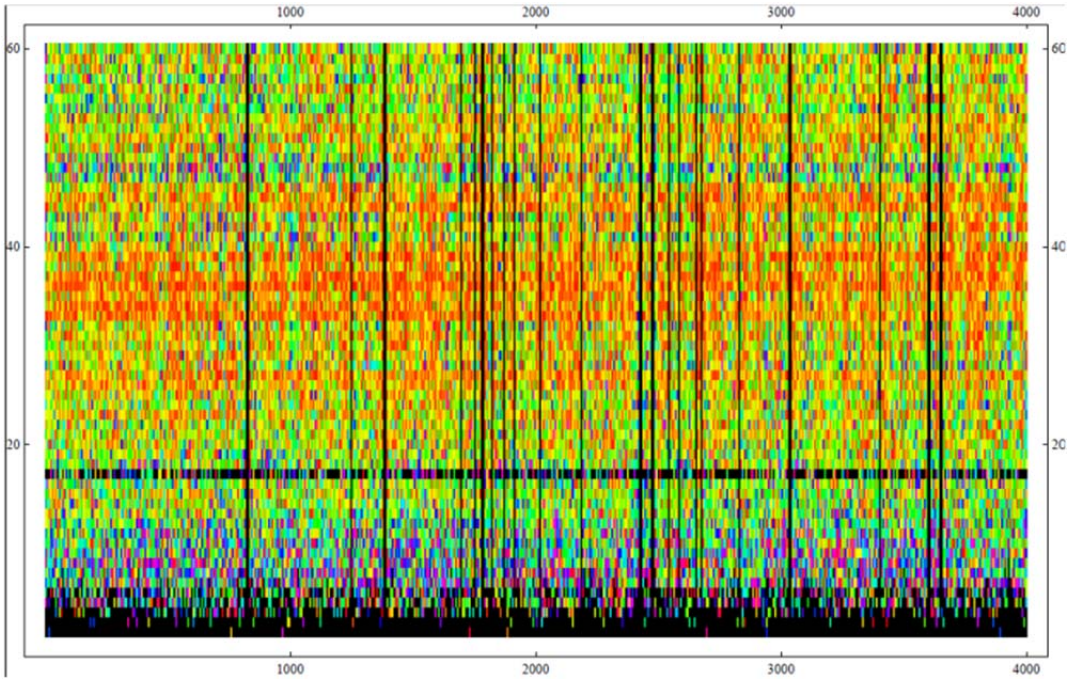

Figure 193. Sample-to-sample differences in the radiance time series. The vertical axis index corresponds to every fifth wavenumber index for the first 300 wavenumbers; the horizontal axis index corresponds to the sample number index in the time series.

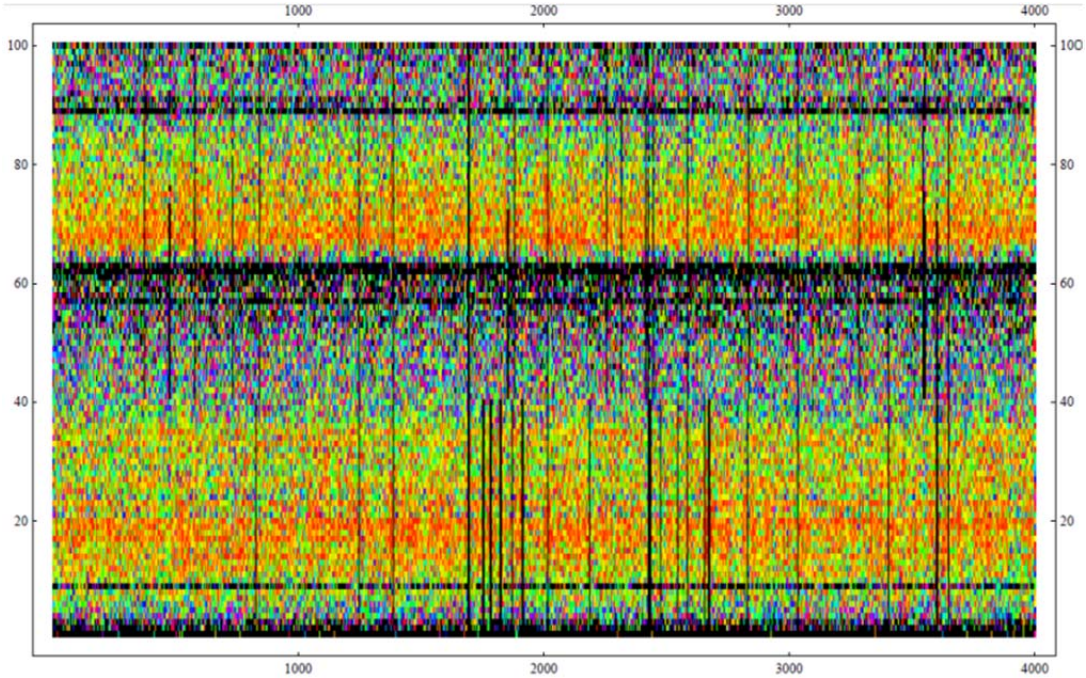

Figure 194. Same as previous figure, but the vertical axis index corresponds to every tenth wavenumber index for the first 1000 wavenumbers; the horizontal axis index corresponds to the sample number index in the time series.

Figure 195 shows the result of a simple spike detection and mitigation algorithm. The original data is in black and the "fixed" data is in red. The technique uses the deviation from a local median, normalized by the local median deviation, to create a standardized variable. These values are then compared against a threshold to determine if the datum is a "spike." If it is a spike, then it is replaced by the local median, which appears to work well for this data, although more testing and perhaps some refinement is needed.

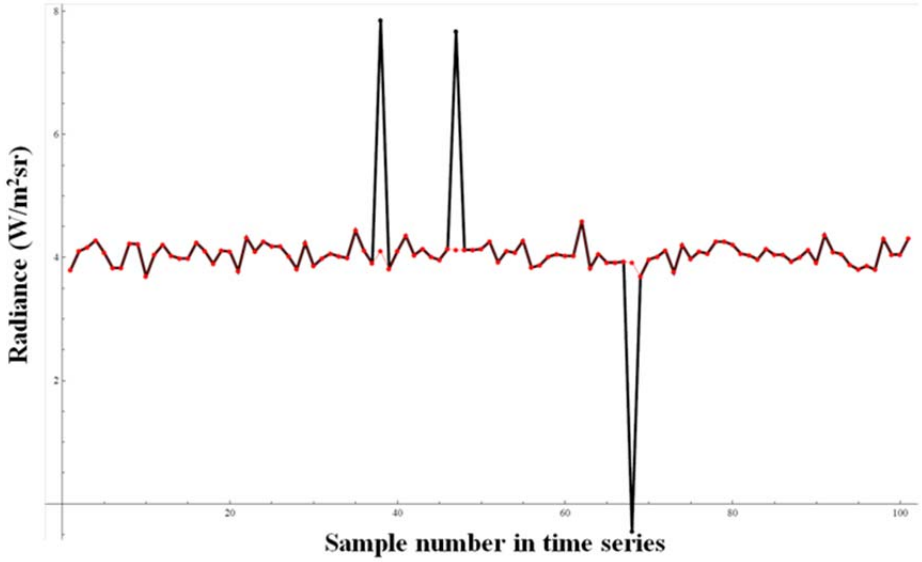

Figure 195. Spike removal example.

Figure 196 shows the temporal differences (i.e. the sample-to-sample difference) as a function of sample number. It can be seen that most of the temporal differences are small and clustered around the nominal sampling interval. However, some large deviations are apparent, and it appears that the deviations get worse towards the end of the recording interval. This deviation may be the result of a problem with wiring in the sensor, something that was not noticed until after the data collection. Figure 197 is similar to Figure 196, except that the vertical scale only goes from zero to one to give better resolution around the "nominal" sampling interval. Figure 198 is similar to Figure 197, except that a small set of temporal samples (around the large jump towards the right-hand side of Figure 196) is shown. It can be seen that the time gaps are bifurcated in an odd fashion, something that is quite apparent in Figure 199, which is a further blow-up of Figure 198. This problem in the data sampling interval indicates the sensor is not stable.

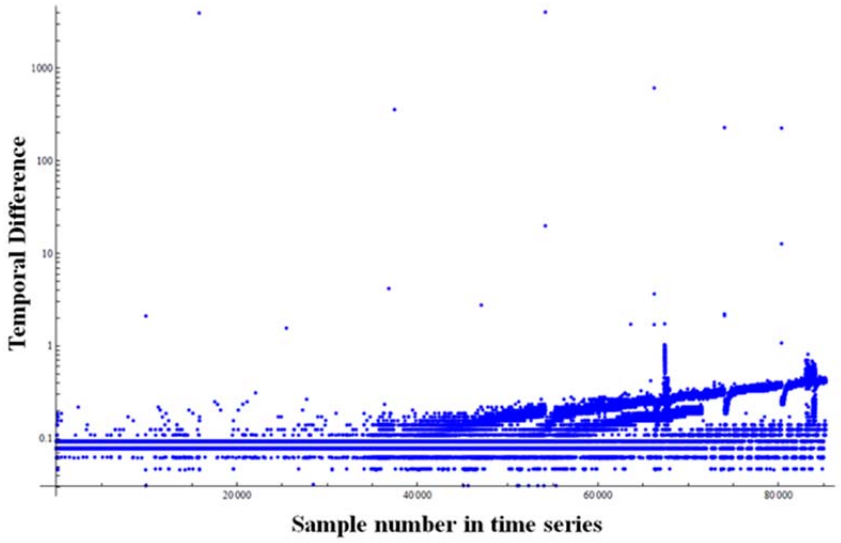

Figure 196. Time gaps as a function of sample number.

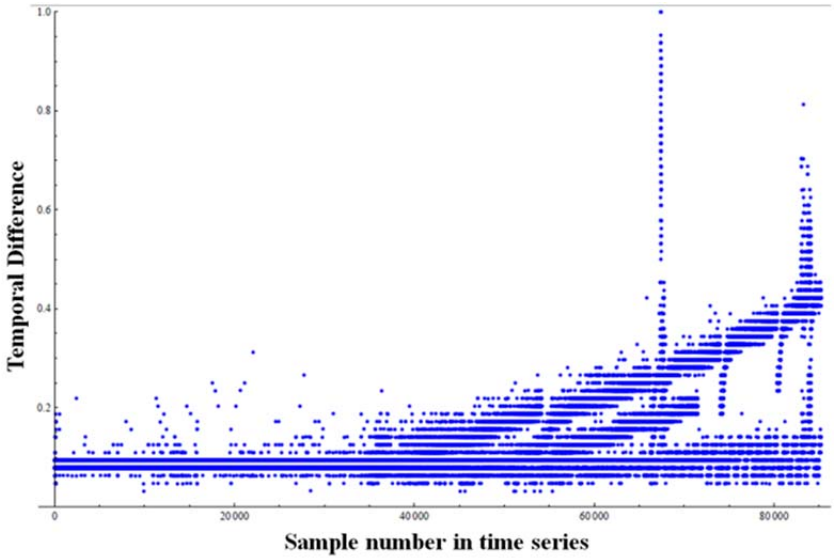

Figure 197. Same as previous figure, but linear vertical scale – and limited to zero to one.

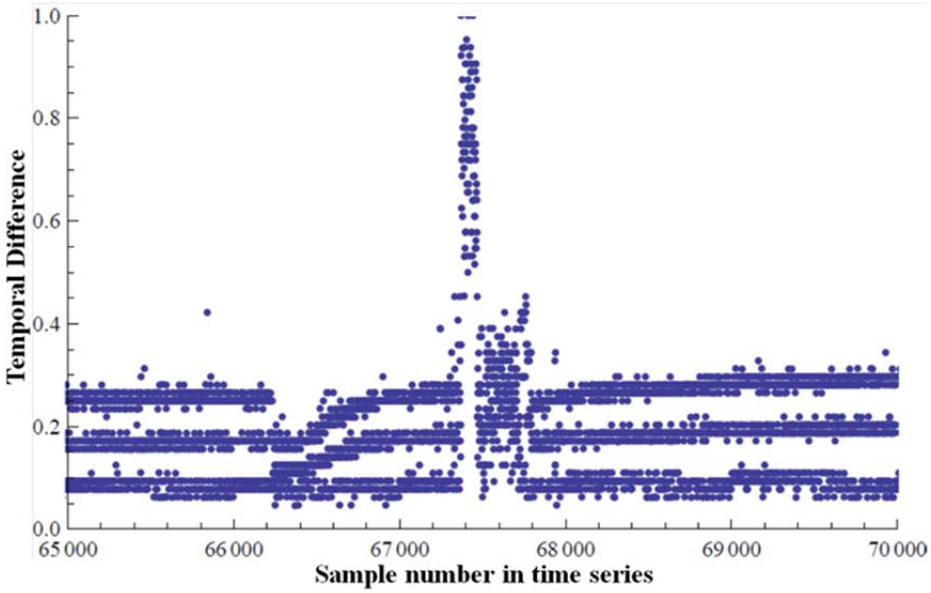

Figure 198. Same as the previous figure, but zoomed in on samples 65000 to 70000.

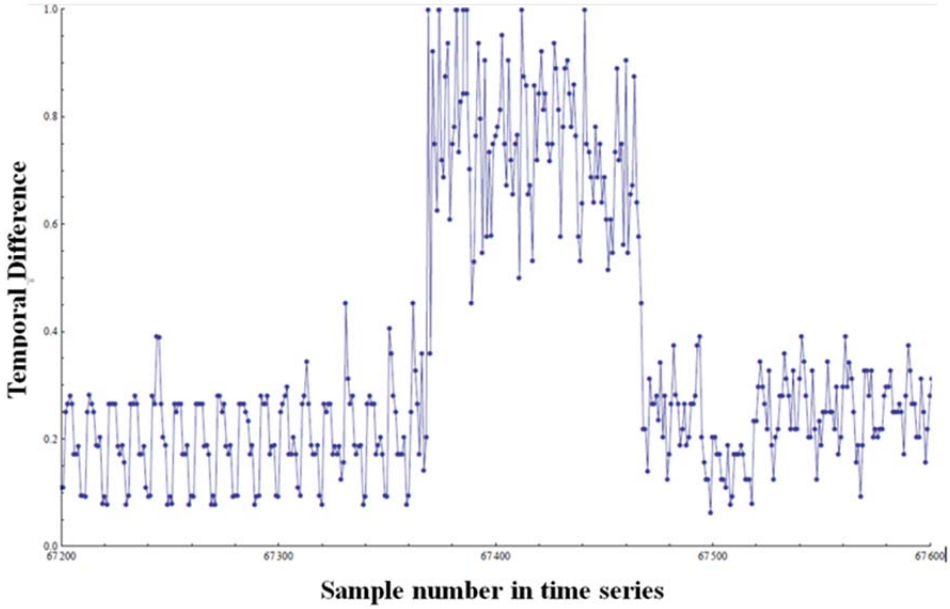

Figure 199. Same as previous figure, but zoomed in from 67200 to 67600.

Finally, Figure 200 illustrates the sample-to-sample temporal deviations (log scale) on the vertical axis versus the sample-to-sample radiance differences. This analysis was performed to see if there is a correlation between the two different data quality issues. Most of the points are in the lower left-hand corner, which indicate the variation in the sensor-sampling interval mentioned above. The single point spikes are seen along the bottom of the figure, and the large temporal deviation is seen in the upper portion. The deviations are well-separated is good because this means that the mitigation methods mentioned previously (spike removal and using regions that do not contain large temporal gaps) are feasible.

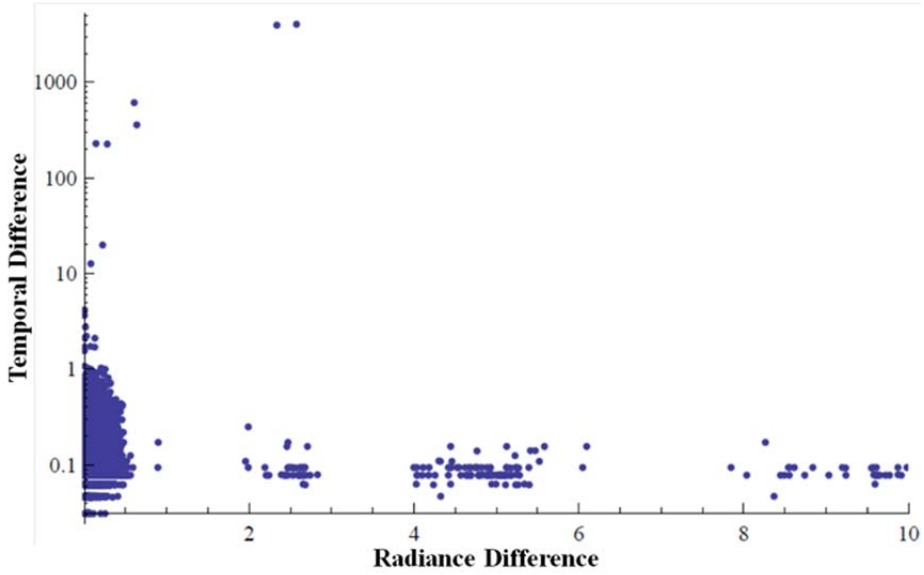

Figure 200. Temporal versus radiance differences.

As mentioned above, the spike removal algorithm did a good job of removing the spikes. The next step was to deal with the uneven sampling rate. Two approaches were investigated:

1. The use of spectral analysis methods that can handle unevenly spaced samples; and
2. The removal of samples that were locally discontinuous, followed by the methods in (1).

Figure 201 shows the sample-to-sample differences over the sample range 84000 to 85200 on November 17, 2011. Figure 202 shows the distribution of differences over the same sample range. Compare this to Figure 203, which shows the distribution for 37500 to 46000. There is a much wider distribution of sampling rates in the 84000 to 85200 period. (See also Figure 196 and Figure 197.) By locally discontinuous, we do not mean the large changes as seen in the middle of Figure 199, but rather those seen in Figure 204. This latter figure shows that the sampling rate was nominally around 0.25 seconds, but every 10^{th} sample there is a two-point discontinuity in the rate. The two-point discontinuity is not a universal feature of the data, as three-point ones were also seen. Figure 205 and Figure 206 show mixed two- and three-point, and three-point behavior, respectively, as well as illustrate much larger discontinuities than seen in Figure 204. Also associated with these discontinuities is a repeated data (radiance) value at the beginning of the sampling discontinuity. This repeated value can be seen in Figure 207, where the sampling rate (offset by -0.25 sec.) is shown in black, and sample-to-sample (spike-removed/trend-removed) radiance differences are shown in red. The repeated radiance values show up as zeroes. (The offset is merely a convenience to help illustrate the location of the zeroes relative to the discontinuities.) The two repeated radiance values are aligned with the beginning of the two-point sampling rate discontinuity. Figure 208 is an interesting case in that the temporal discontinuities are not associated with repeated radiance values. Figure 209 illustrates three-point temporal discontinuities where there were still only two repeated samples. In each of these three cases, the temporal discontinuities were at every 10^{th} point; this is a dominant feature, though not the rule, as can be seen in Figure 210, which shows the log of the number of samples between repeated data values.

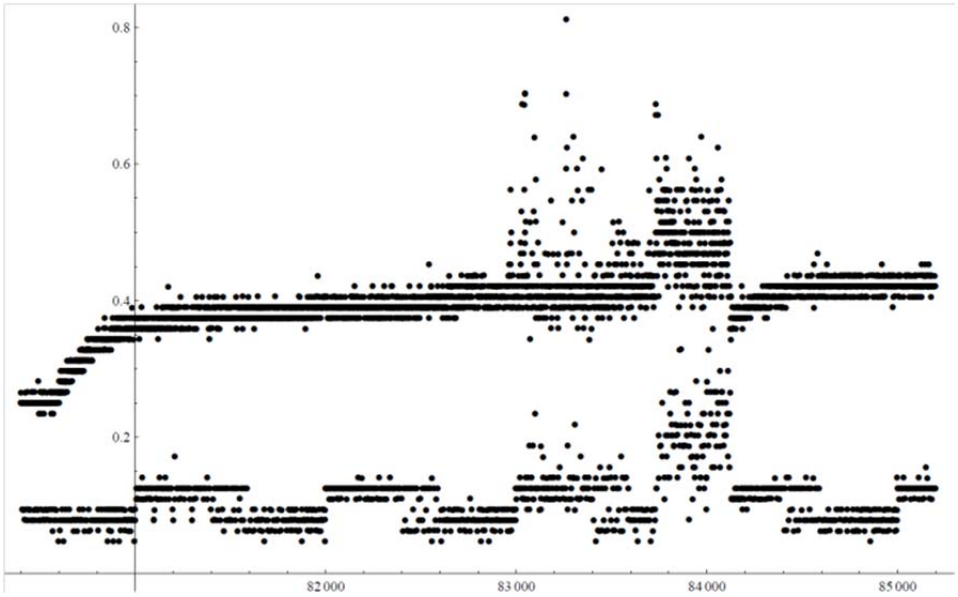

Figure 201. Sample-to-sample temporal differences for the sampling period 80400 to 85200.

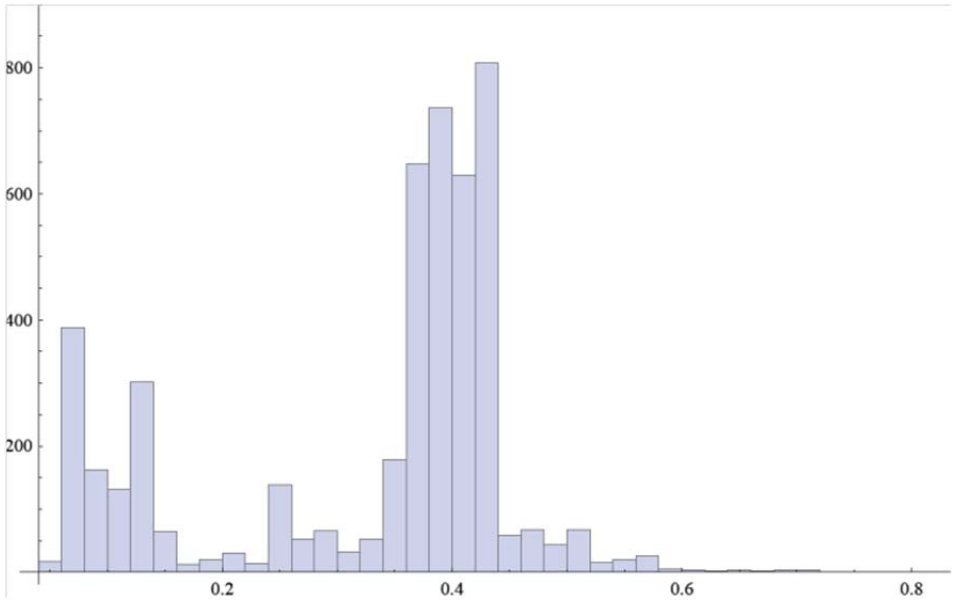

Figure 202. Histogram of sample-to-sample time differences for samples 80400 to 85200.

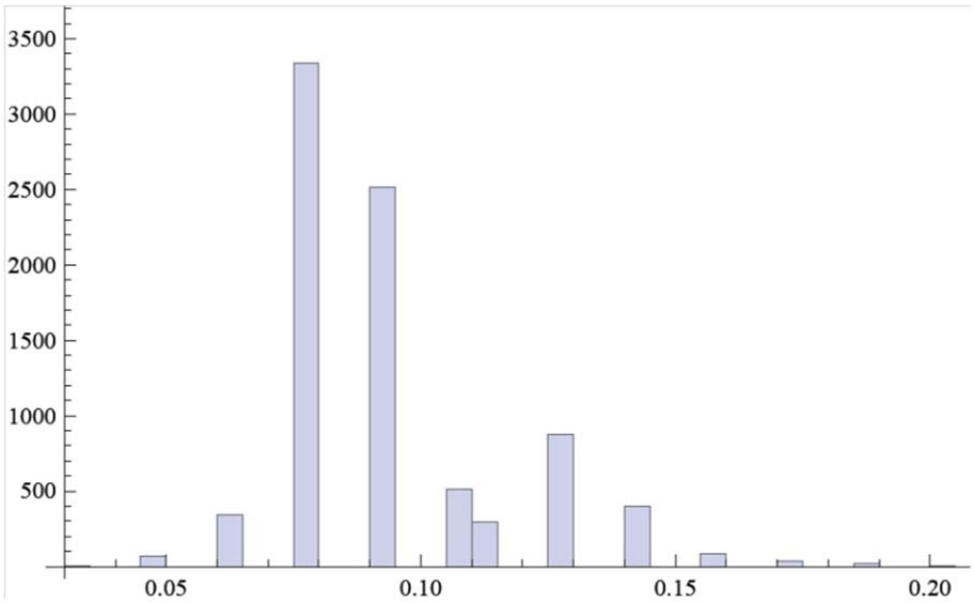

Figure 203. Same as Figure 202, but for the sample range 37500 to 46000.

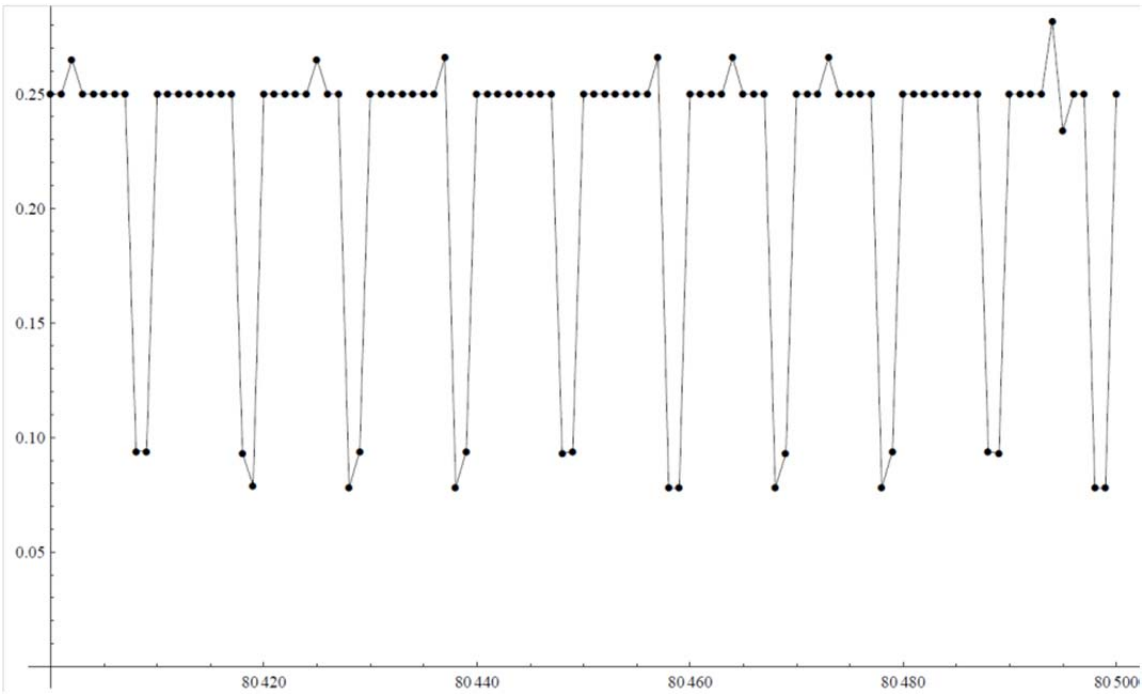

Figure 204. Sample-to-sample temporal differences, showing "local" discontinuities in the sampling rate. Note that the predominant discontinuity is two samples long for samples in the 80400 to 80500 period.

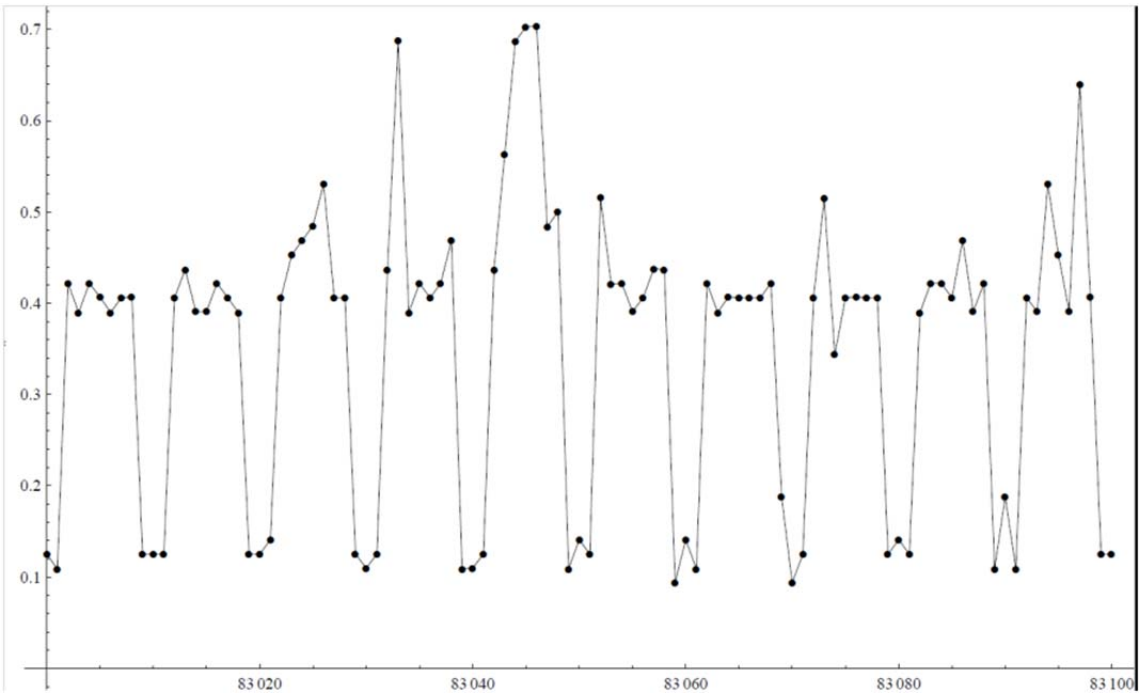

Figure 205. Same as in Figure 204 but for the sample range 83000 to 83100. Note the much larger discontinuities in sampling rates, as well as the three-point discontinuities.

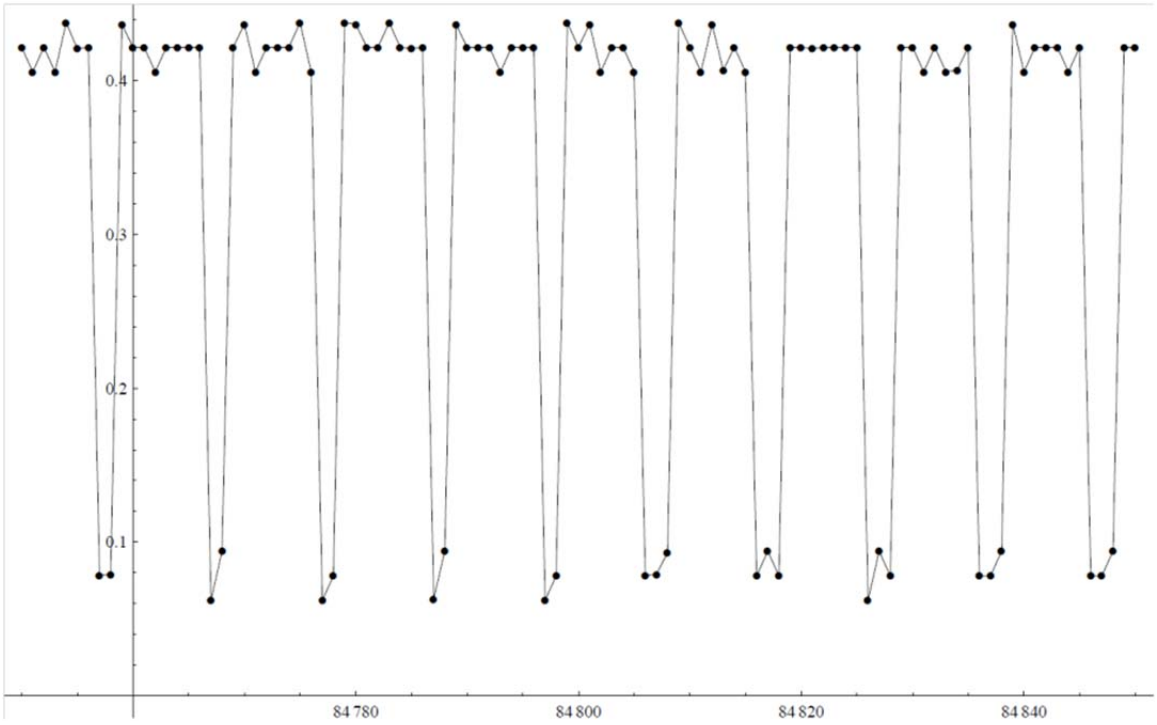

Figure 206. Same as in Figure 204, but showing a mixture of two- and three-point discontinuities in the sampling rate. Sample interval is 84750 to 84850.

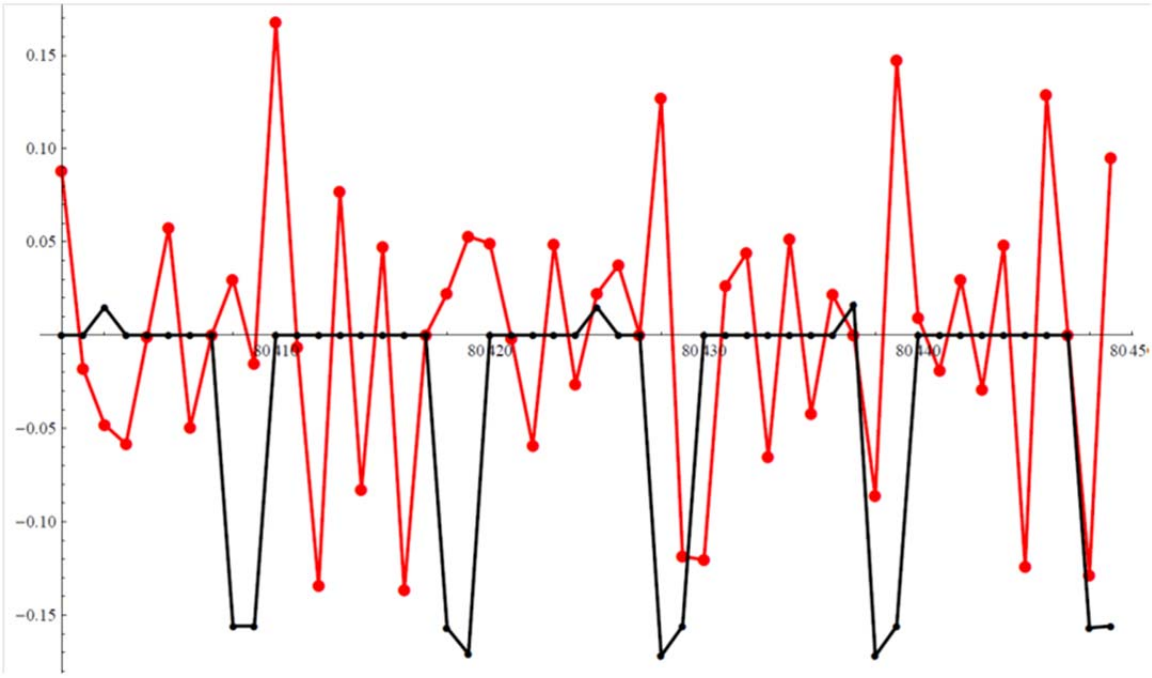

Figure 207. Sample-to-sample temporal differences (offset by -0.25 sec) in black, with sample-to-sample data difference values in red. Note the repeated data values are the zeros at the beginning of each discontinuity in sampling rate. The sample range is 80400 to 80450.

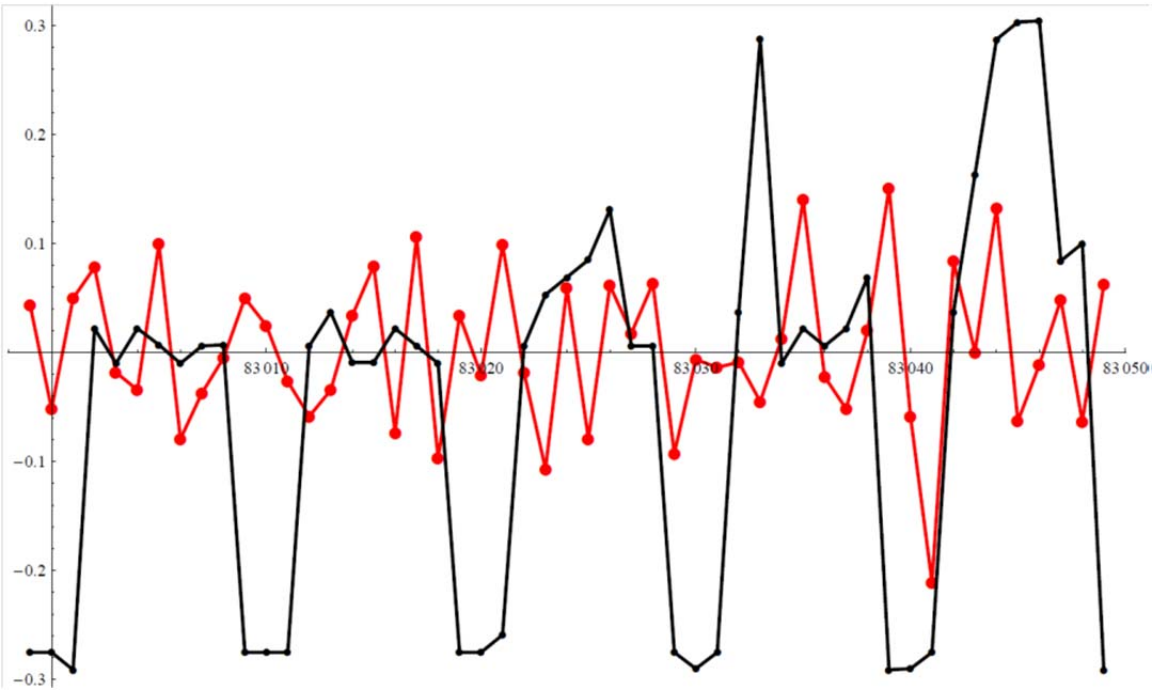

Figure 208. Same as Figure 207, except that in this case the temporal discontinuities are not associated with repeated values. The sample range is 83000 to 83050. (Offset for sample-to-sample temporal differences is -0.4 in this case.)

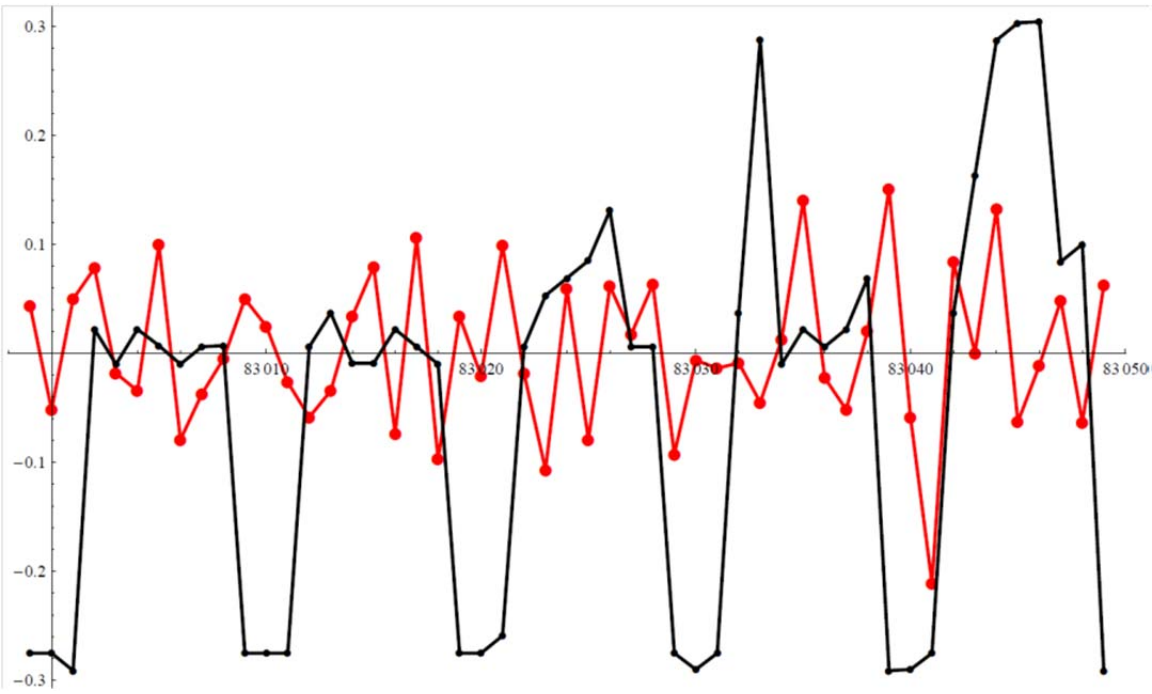

Figure 209. Same as Figure 207, but for a three-point discontinuity case. The sample range is 84800 to 84850. (Offset for sample-to-sample temporal differences is -0.42 in this case.)

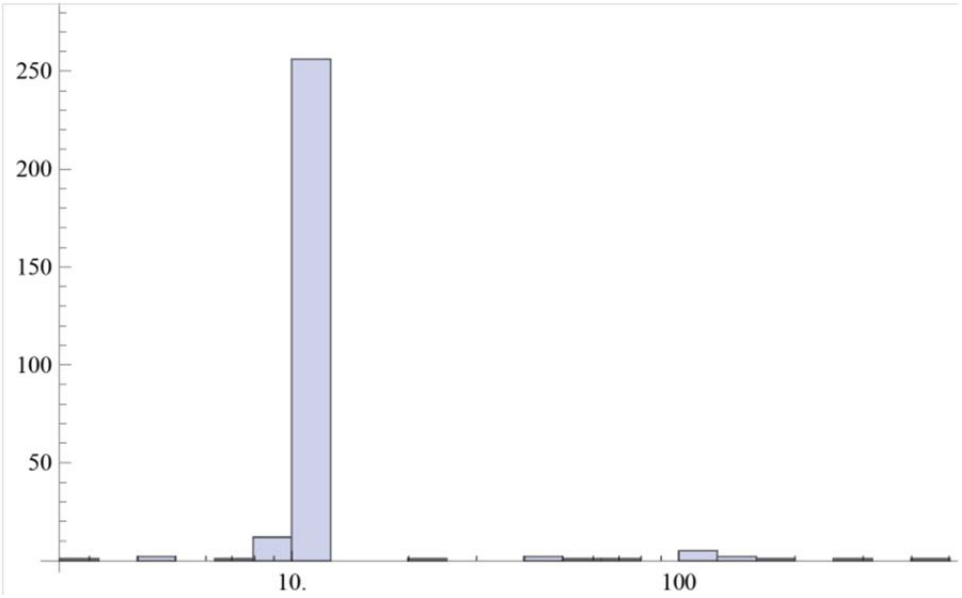

Figure 210. Log-histogram of the number of samples between repeated data values.

As mentioned above, there were two approaches taken to dealing with the uneven sampling rates. Both relied on a method to compute a power spectrum, or more precisely a periodogram estimate of the power spectrum, that accommodates uneven sampling. This method is known in the literature as the Lomb-Scargle Periodogram. The standard Fourier periodogram is the dot product of the data vector with sines and cosines at different frequencies, i.e. the Discrete Fourier Transform (DFT). The Fast Fourier Transform (FFT) is a very efficient implementation of this type of periodogram, but requires constant sampling rates. For a Gaussian random process, the

standard periodogram is exponentially-distributed. The Lomb-Scargle periodogram maintains the same statistical distribution and is also equivalent to a least-squares fitting of the data to sinusoids. It also reduces to the standard periodogram when the data is evenly spaced. These facts make the Lomb-Scargle periodogram a very attractive method for spectral analysis of unevenly-spaced data.

The Lomb-Scargle periodogram for data *X(t)* is given by,

$$P(\omega) = \frac{1}{2}\left[\frac{\left[\sum_{i=1}^{N} X_i \cos\omega(t_i - \tau(\omega))\right]^2}{\sum_{i=1}^{N} X_i \cos^2\omega(t_i - \tau(\omega))} + \frac{\left[\sum_{i=1}^{N} X_i \sin\omega(t_i - \tau(\omega))\right]^2}{\sum_{i=1}^{N} X_i \sin^2\omega(t_i - \tau(\omega))}\right] \quad (5.3.1)$$

Where,

$$\tau(\omega) = \frac{1}{2\omega}\tan^{-1}\left[\frac{\sum_{i=1}^{N} \sin 2\omega t_i}{\sum_{i=1}^{N} \cos 2\omega t_i}\right] \quad (5.3.2)$$

It should be noted that this periodogram can be calculated for any set of frequencies $\omega = 2\pi f$; that is, it is not restricted to $f_i = i/N\Delta t$ as in the FFT. This means that we can oversample the frequencies. Of course, one can do this for a standard DFT for equally spaced samples; but since the FFT implementation of the DFT is the predominant tool in spectral analysis, we use this method for comparison. For the FFT, however, the only way to increase the frequency resolution (for a fixed sampling rate) is to increase the number of samples.

The first approach used in dealing with the unevenly spaced data was to apply the Lomb-Scargle periodogram directly to the radiance data. These results (in red) are compared to the standard periodogram (black), as seen in Figure 211, Figure 212, and Figure 213. Since the choice of frequencies to use in the Lomb-Scargle periodogram is somewhat arbitrary, we chose to use the same frequencies as in the Fourier spectrum, but oversampled by a factor of two. Since the data are not evenly sampled, we chose Δt to be the median of the sample-to-sample time differences.

Figure 211, Figure 212, and Figure 213 show the Fourier and Lomb-Scargle periodograms at 913 cm^{-1} and the sample periods 80400–80900, 83000–83500, and 84000–84500, respectively. It can be seen that the Fourier and Lomb-Scargle spectra are fairly similar to each other in each case, and all are noise-like. As mentioned above, for both of these types of spectra the power at each frequency is distributed exponentially, which means that the standard deviation of the power at each frequency is equal to that power level, i.e. 100% error. To improve the estimates, spectral averaging is required. Figure 214 shows the result of averaging nine spectra over the full 80400–85200 period. As with the individual spectra, the data are noise-like; however, a few systematic differences between the two types of spectra can be seen (e.g. at 0.06 Hz and 0.2–0.3 Hz). Of course, averaging nine spectra only reduces the standard deviation by $1/\sqrt{9} = 1/3$, which still means a 33% error. Hence, one must be cautious in making specific statements about the differences in the two types of spectra; nevertheless, they are different.

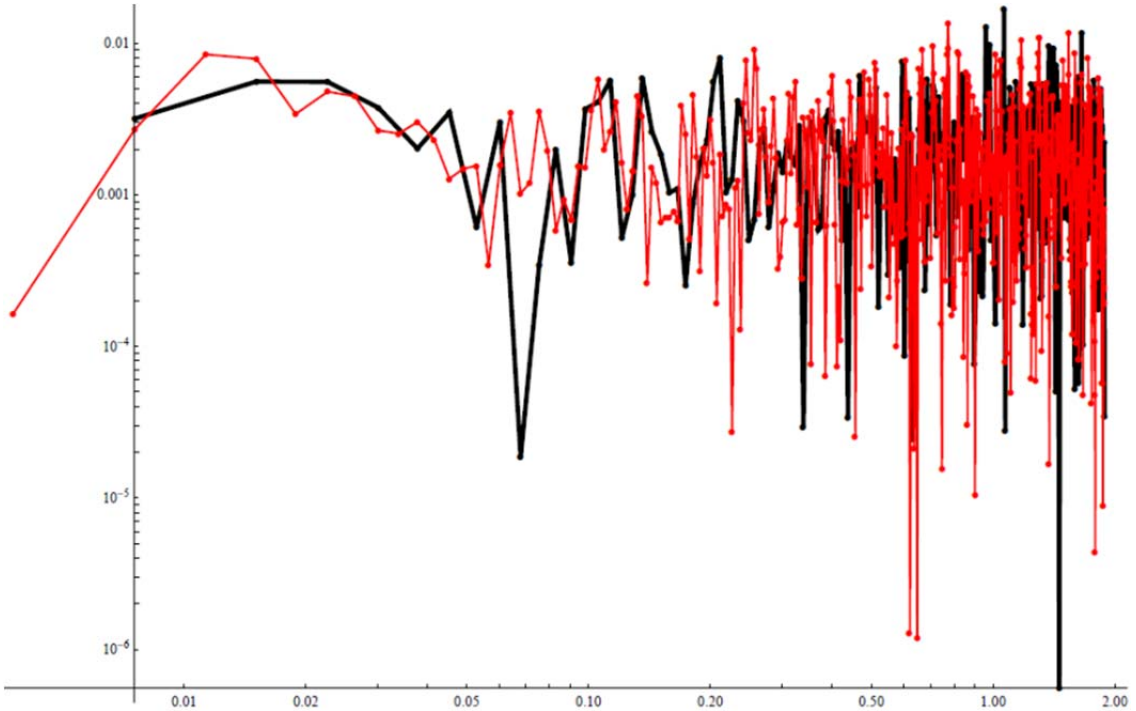

Figure 211. Lomb-Scargle periodogram *(red)* and standard Fourier periodogram *(black)* the sample interval 80400 to 80900, v = 913 cm^{-1}. The Lomb-Scargle periodogram has been oversampled by a factor of two over the Fourier one.

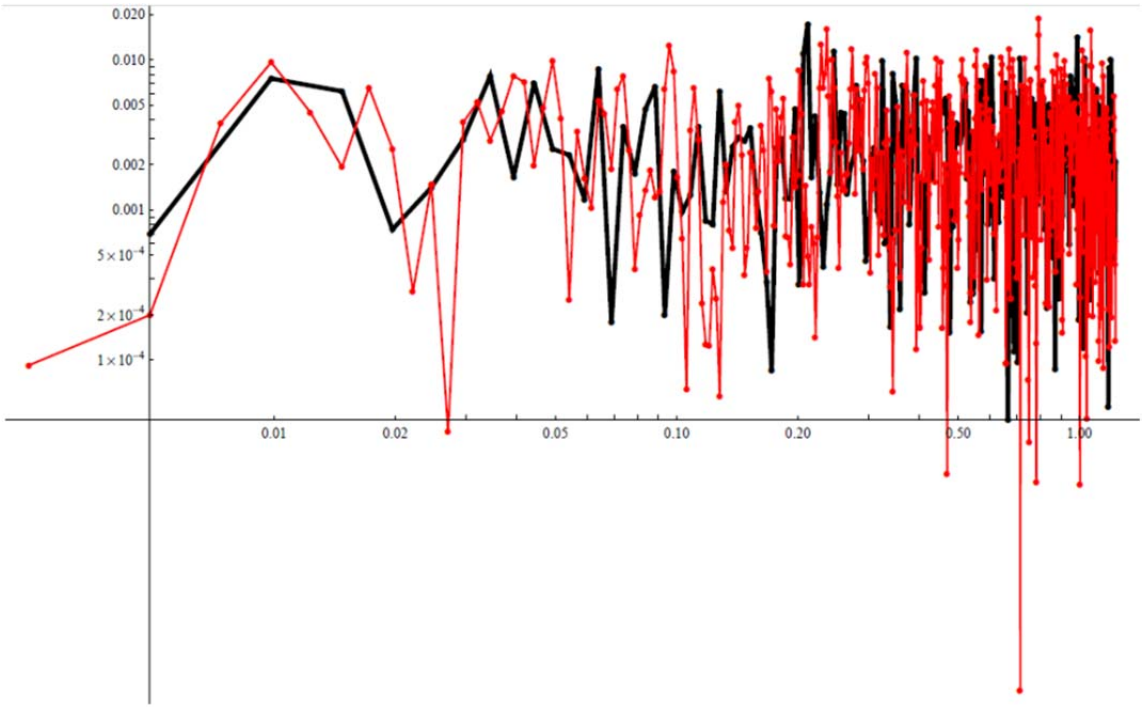

Figure 212. Same as Figure 211, but for the sample interval 83000 to 83500.

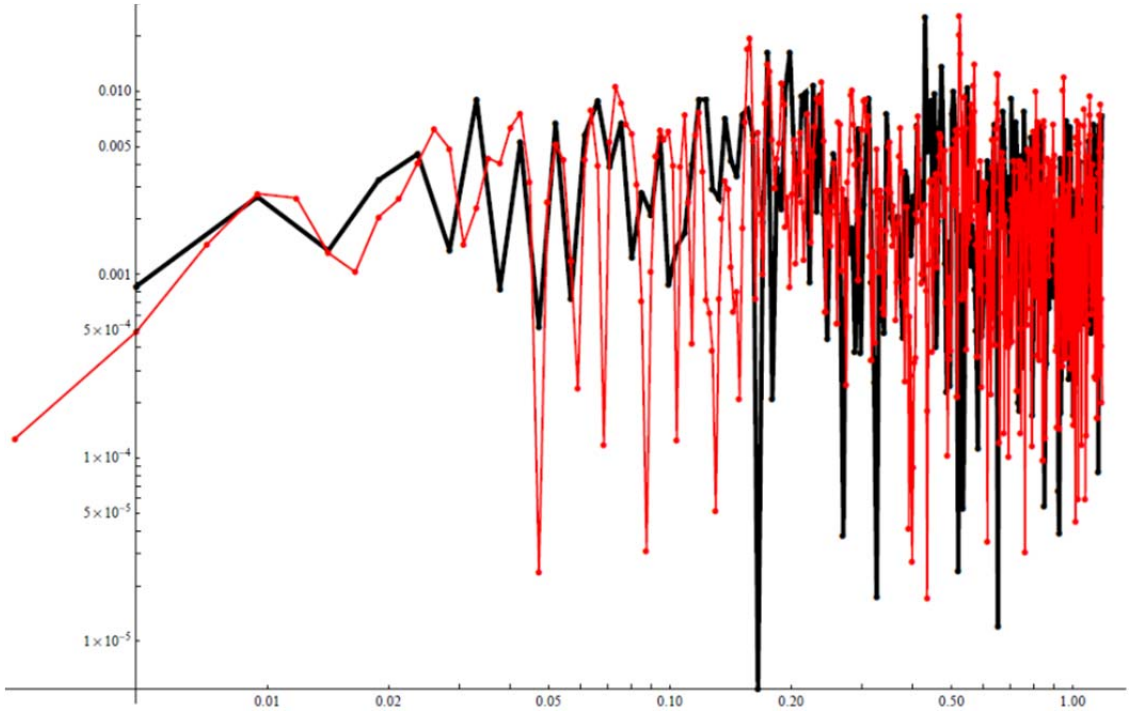

Figure 213. Same as Figure 211, but for the sample interval 84000 to 84500.

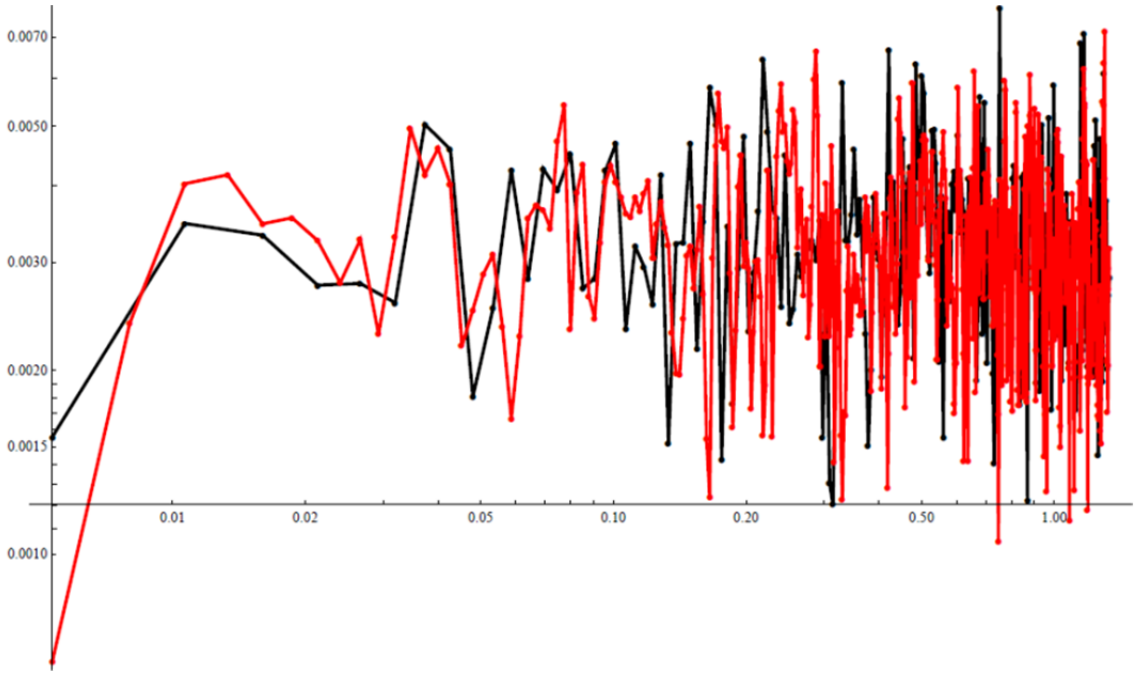

Figure 214. Same as Figure 211, but for spectra averaged over the whole 80400 to 85200 range. (Note the change in scale from the un-averaged spectra.)

The second approach in dealing with the uneven sampling rate is to remove the sampling outliers and then process the data with the Lomb-Scargle periodogram. We used the same spike-removal algorithm to remove the "spikes" in the sample-to-sample temporal differences. The results of

this removal is seen in Figure 215, Figure 216, and Figure 217, which show the sample-to-sample temporal differences (black) and the "fixed" time differences for the periods 80400–80500, 83000 –83100, and 84750–84850, respectively. This approach does an excellent job of removing the temporal "spikes." Figure 218, Figure 219, and Figure 220 show the spike- and trend-removed radiances (black) and the "fixed" data for the same sample ranges. As we saw above, in the first and third sample periods, (with two- and three-point discontinuities, respectively), the temporal discontinuities were associated with repeated radiance values, and the fixed data now steps over those data points. We note, however, that the temporal spikes in some cases are also associated with data spikes, but not always. The second time period is more complicated. In the left-hand side of Figure 216, there are two temporal discontinuities that do not correspond to the otherwise regular 10-point repeating pattern. The spike removal algorithm does pick these discontinuities out, and as can be seen in Figure 219, these samples are associated with some odd features in the radiance data.

Figure 221 through Figure 224 are the "fixed" data versions of Figure 211 through Figure 214. In black are the same Fourier spectra as shown before, and the blue curves are the Lomb-Scargle periodograms for the "fixed" data. Figure 225 compares the averaged Lomb-Scargle periodogram with the averaged "fixed" Lomb-Scargle periodogram. As with the "un-fixed" spectra, one can see some systematic differences in these spectra (e.g. 0.01–0.02 Hz, 0.04 and 0.08 Hz).

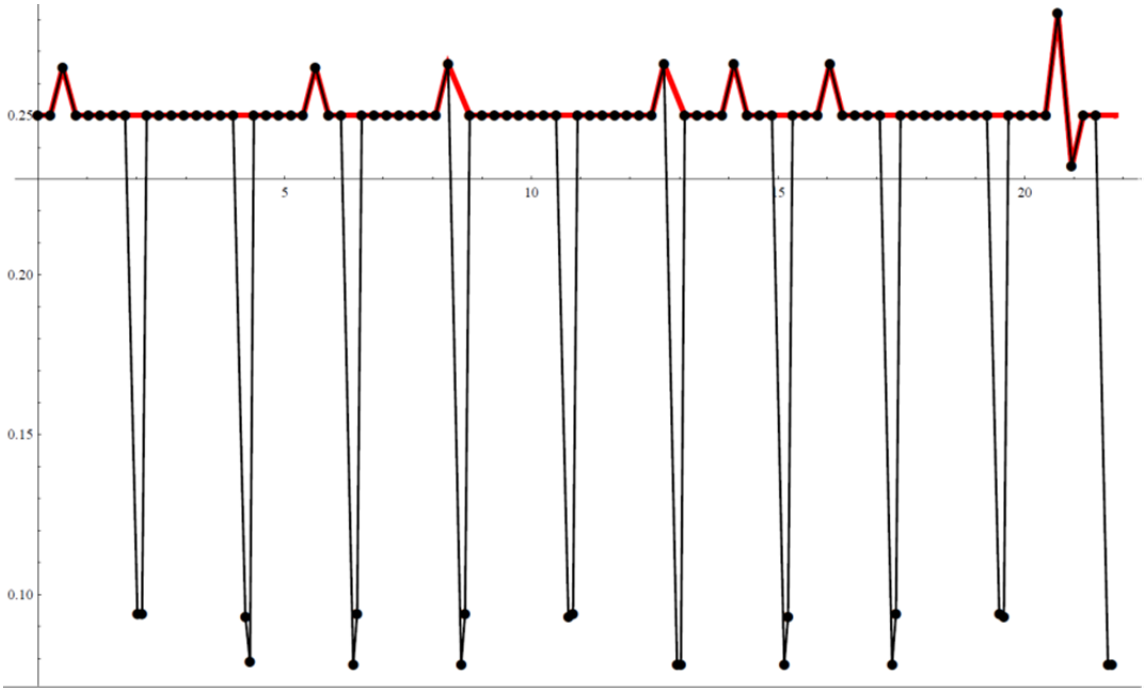

Figure 215. Sample-to-sample time differences and "fixed" time differences for the period 80400 to 80500. (Abscissa is time in seconds from sample 80400.)

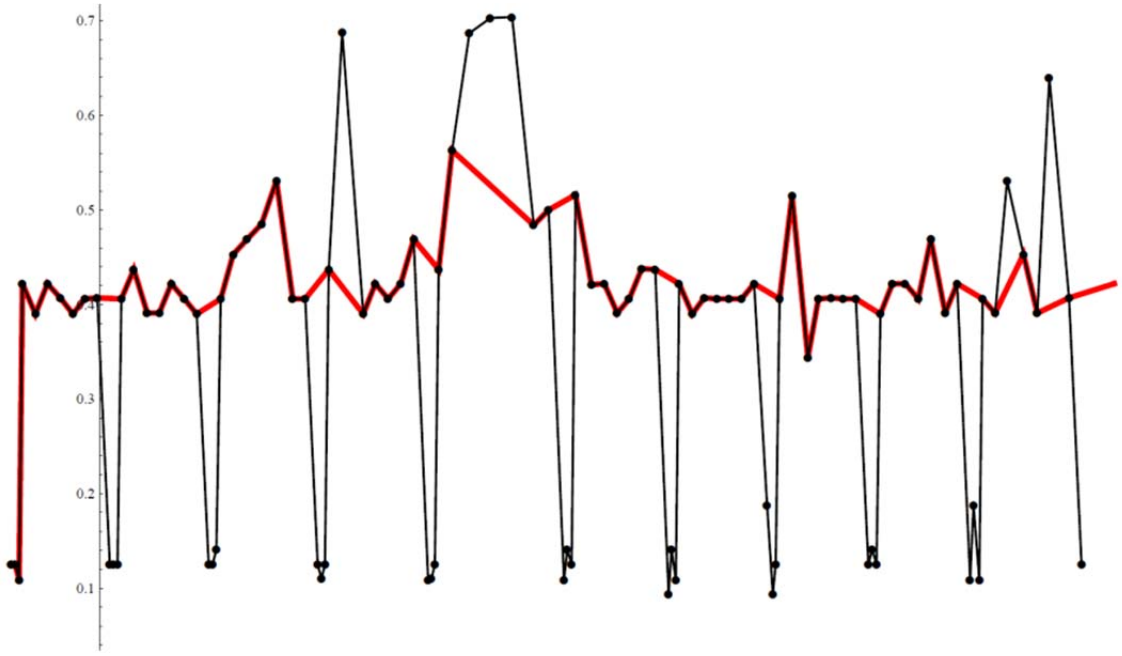

Figure 216. Same as Figure 215, but for the period 83000 to 83100.

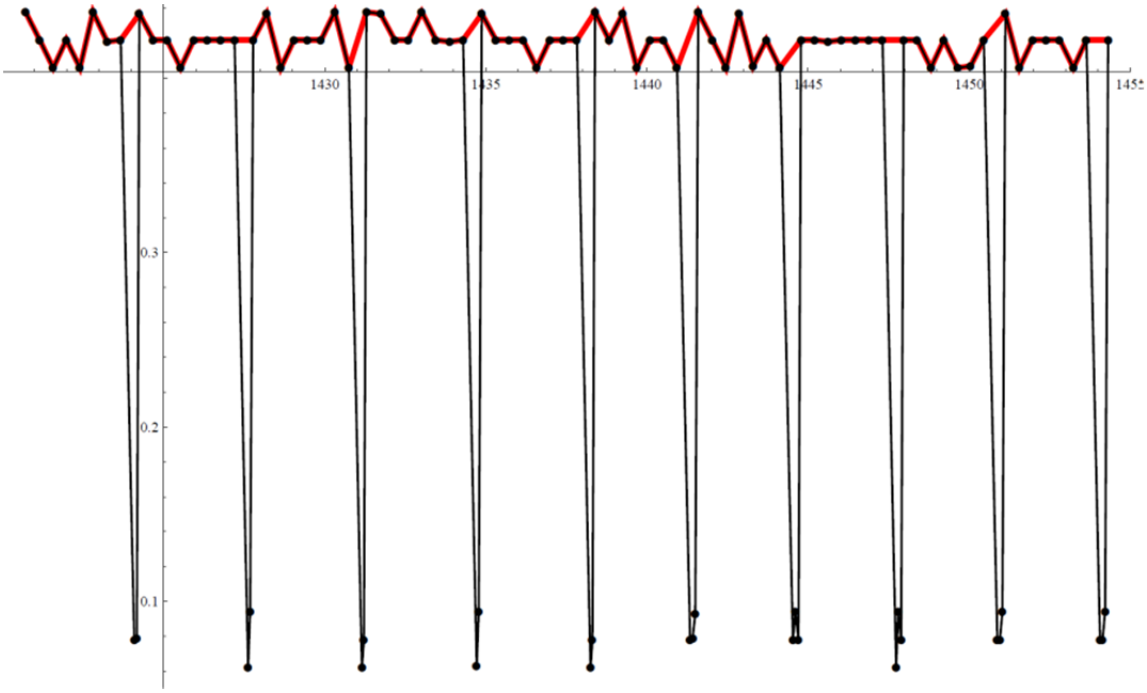

Figure 217. Same as Figure 215, but for the period 84750 to 84850.

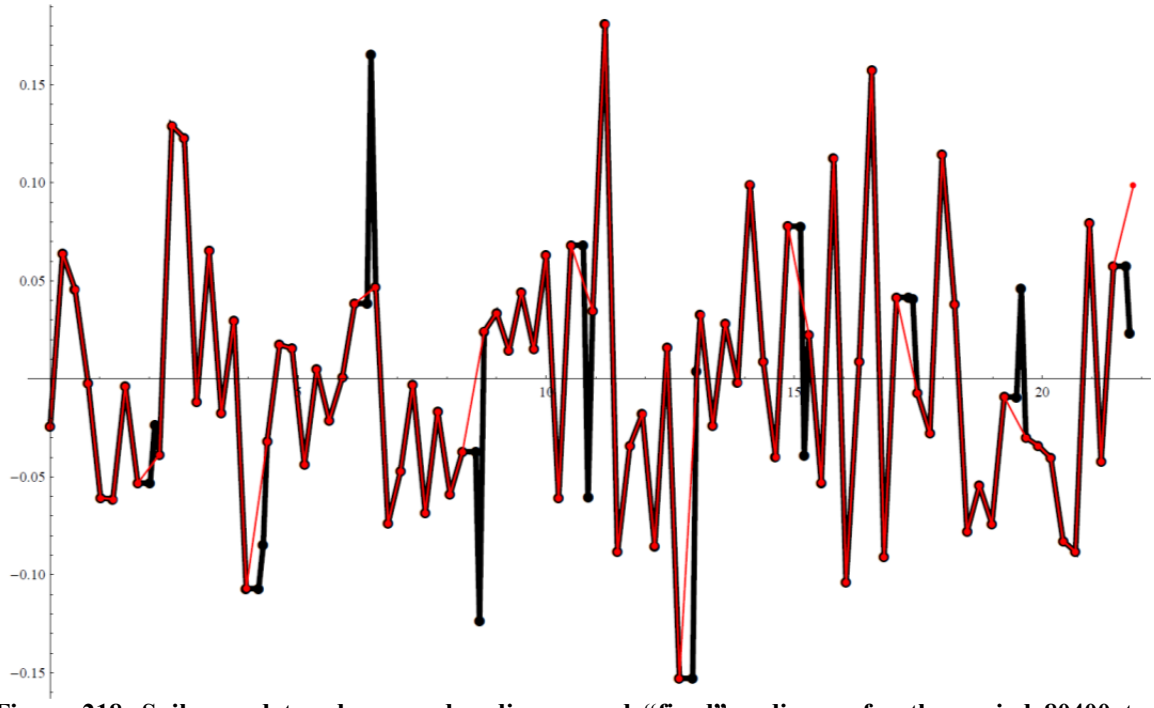

Figure 218. Spike- and trend-removed radiances and "fixed" radiances for the period 80400 to 80500. (Abscissa is time in seconds from sample 80400.)

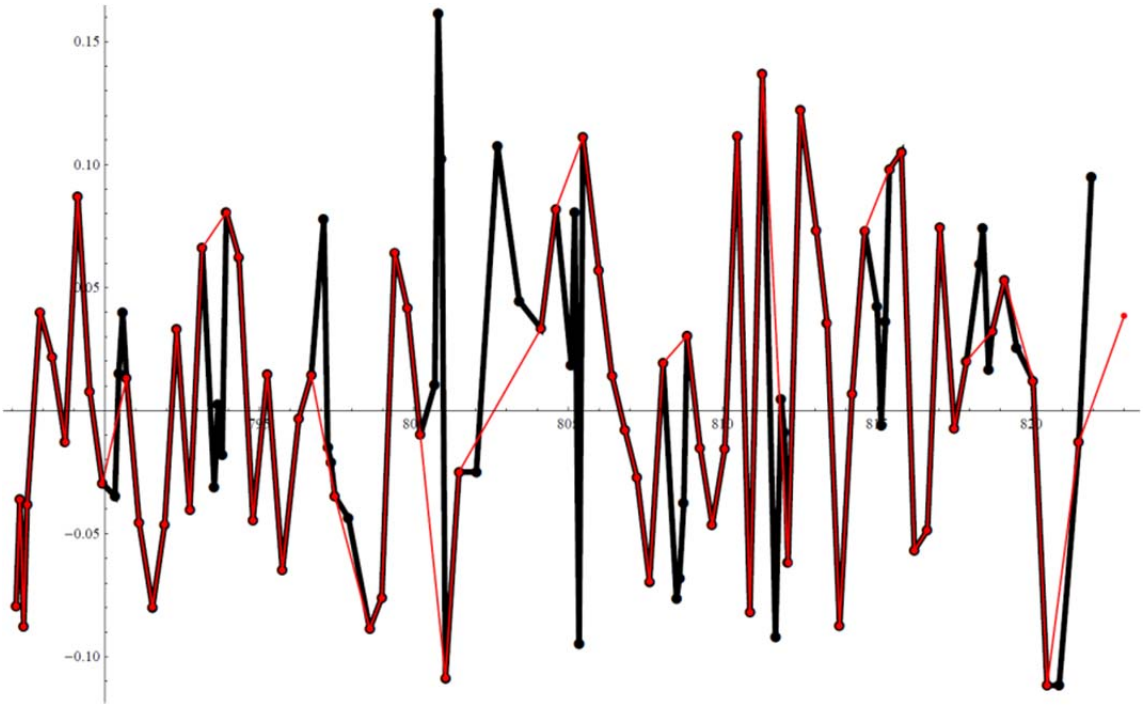

Figure 219. Same as Figure 218, but for the period 83000 to 83100.

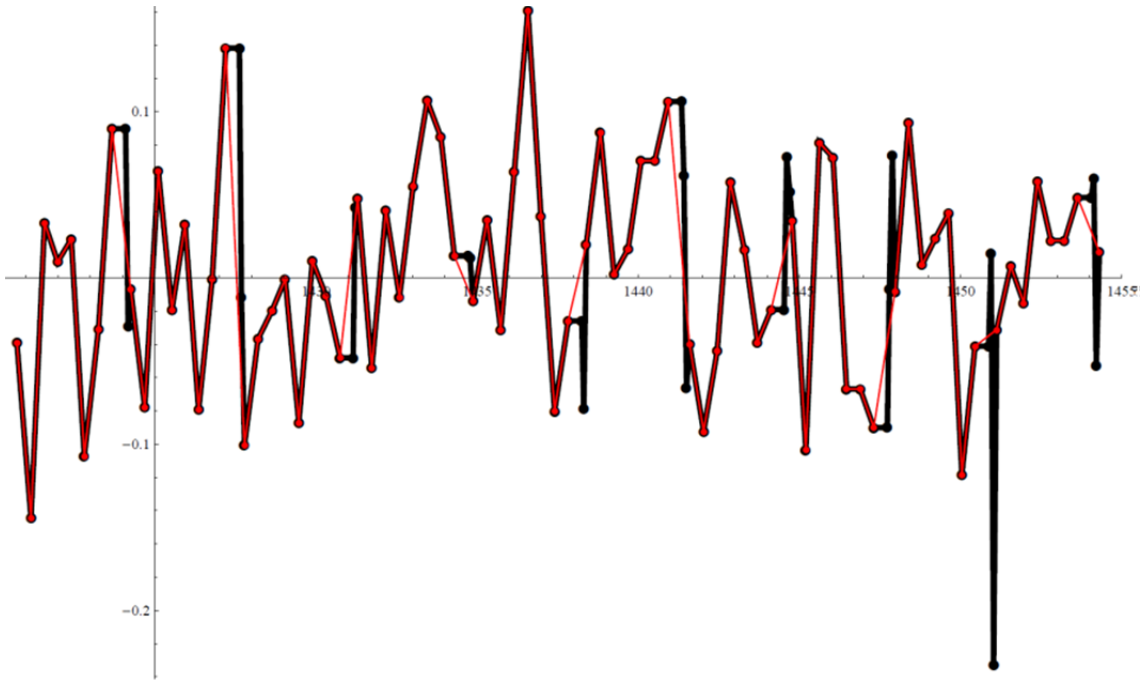

Figure 220. Same as Figure 218, except for the period 84750 to 84850.

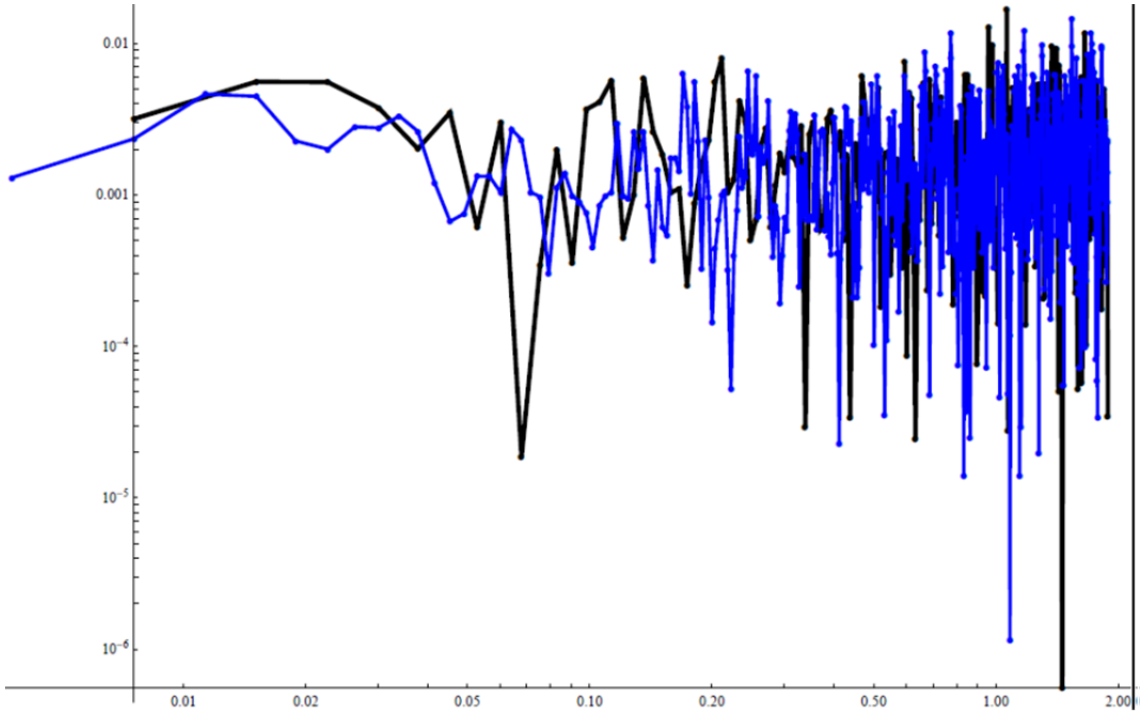

Figure 221. Same as Figure 211, but for the "fixed" data *(blue).*

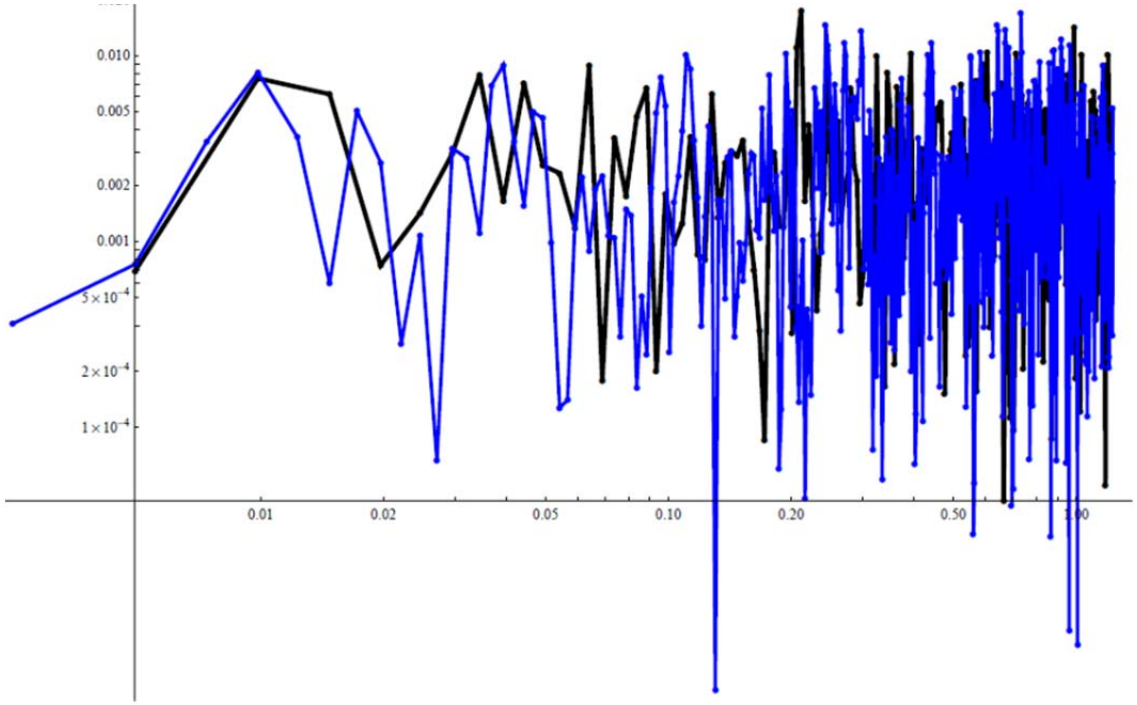

Figure 222. Same as Figure 212 but for the "fixed" data *(blue).*

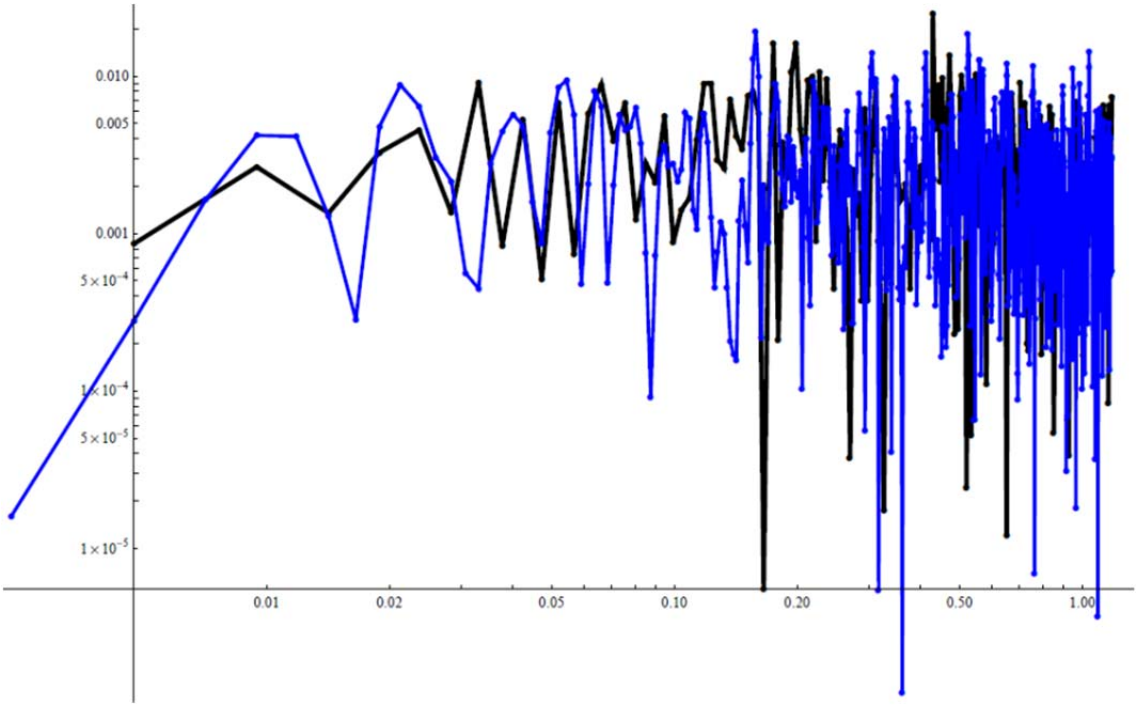

Figure 223. Same as Figure 213, but for the "fixed" data *(blue).*

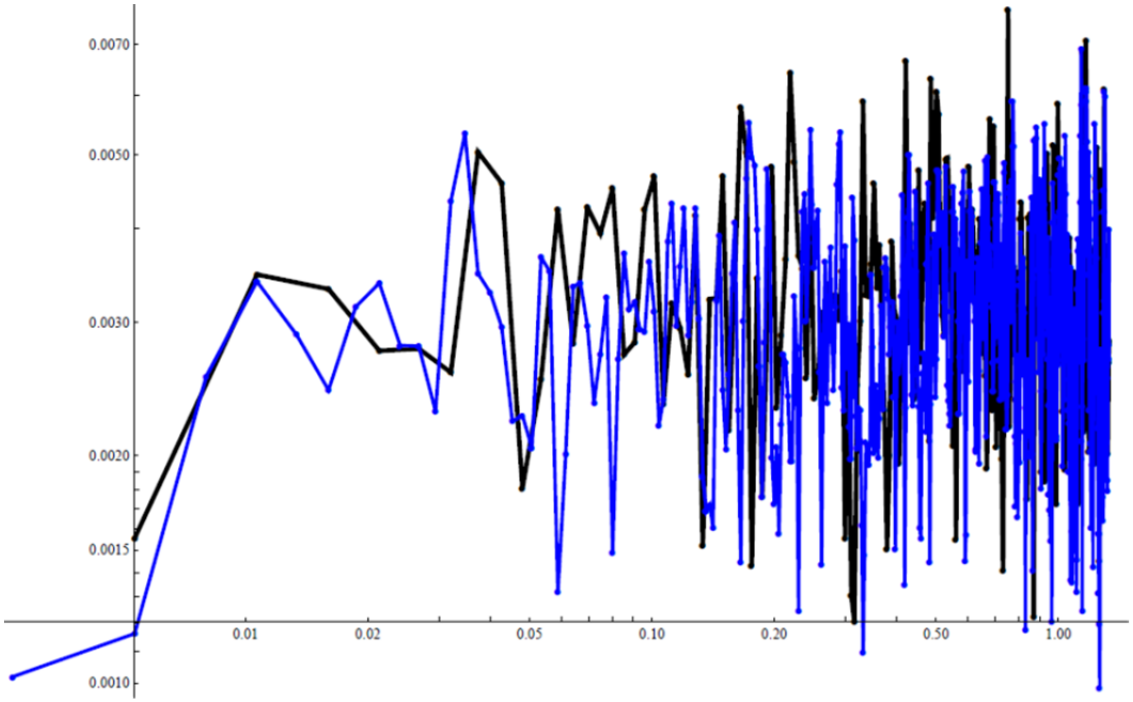

Figure 224. Same as Figure 214, but for the "fixed" data *(blue).*

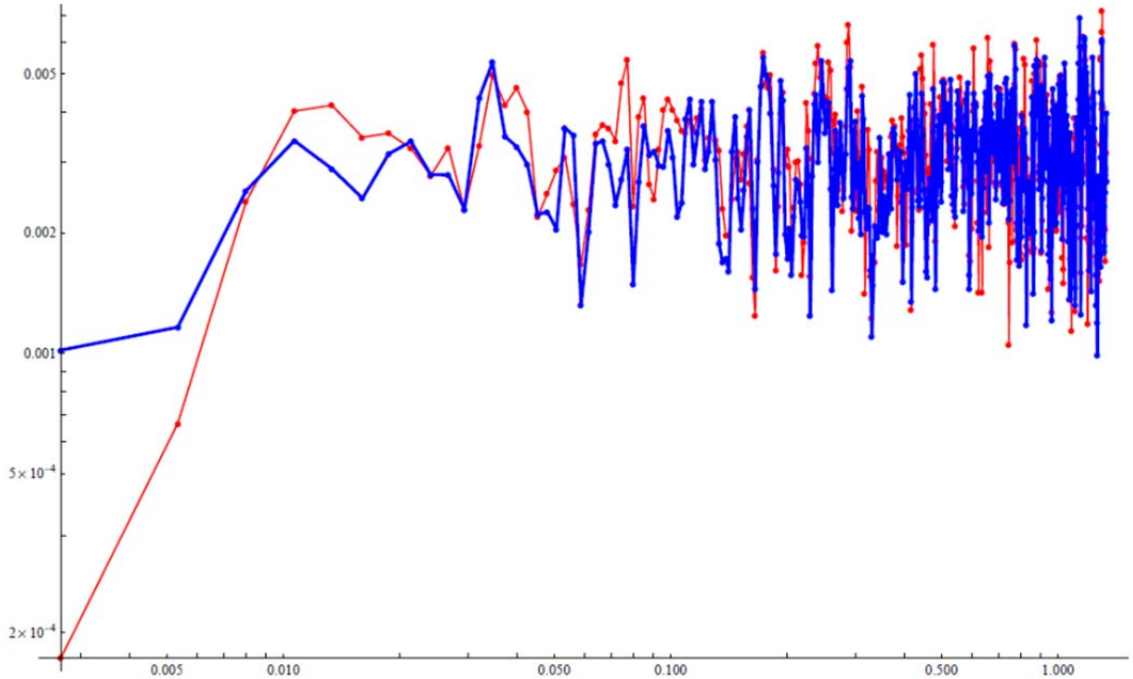

Figure 225. Averaged Lomb *(red)* and Averaged "fixed" Lomb *(blue)* periodogram for the sampling interval 80400 to 85200.

5.3.4 Investigation of "Amoeba" Pattern in Hyper-Cam Data

Figure 226 shows results of the Hyper-Cam viewing the atmosphere at a low elevation angle from MRS on November 16 and 17. The upper left-hand image is that of the uncalibrated radiance when viewing one of the on-board blackbodies. There is a pattern in the instrument response of the focal plane detector array, called the "amoeba" pattern due to its shape. This artifact in the

spatial characteristics of the signal should not appear in the calibrated signal. However, one can see from the brightness temperature standard deviation plots for November 16 and 17 that this amoeba pattern seems to be present in the calibrated sky scene data, regardless of day or viewing angle. In Figure 226, the upper left panel is the uncalibrated detector output when viewing the ambient calibration blackbody whereas the other three panels show the standard deviation of brightness temperature when viewing the sky at a low elevation angle. The outline of trees can be seen in the field of view; they were fluctuating spatially due to high winds.

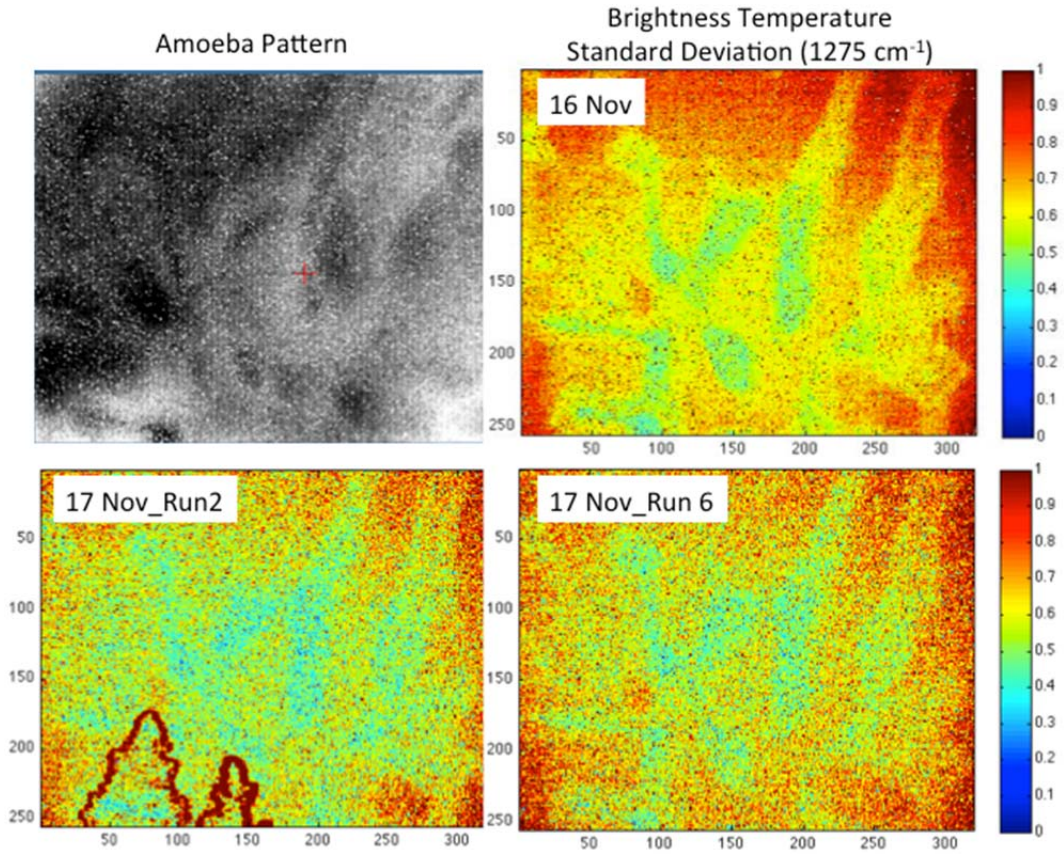

Figure 226. Images of "amoeba" pattern in Hyper-Cam radiance for November 16 and 17, 2011.

The temporal variability of the signal was investigated over 14 data cubes (# 8940–8953) from the November 17, 2011, Run 2 dataset. We computed the mean radiance, $R_0(v,x,y)$, by averaging over 14 cubes for each wavenumber, v, and each image pixel, (x,y). This mean radiance was then subtracted from the actual measured data. The obtained difference, ΔR, is the signal that is being analyzed.

Figure 227 shows the spectrum of the standard deviation of ΔR averaged over all image pixels (320 x 160) for each data cube separately (represented by different colored lines). This figure therefore presents the total variability of the scene, which allows one to detect the spectral channels that vary most during the observation. The first and last 3 channels have been excluded from consideration since they suffer from wrap-around effect (i.e. the measured spectra are not apodized).

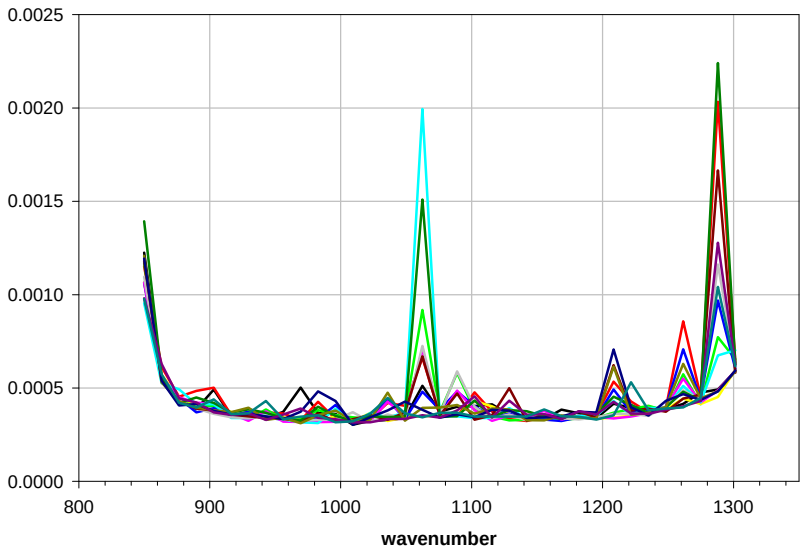

Figure 227. Standard deviation for radiance perturbations averaged over 320 x 160 image pixels, separately for 14 data cubes processed (November 17, 2011, cubes 8940–8953).

Figure 228 shows an image of the standard deviation of ΔR for channel v = 849.9 cm^{-1}, the channel which showed the highest variability across image pixels. The image looks very similar to the "amoeba" pattern described above and shown in Figure 226. It confirms the necessity to understand the calibration issues.

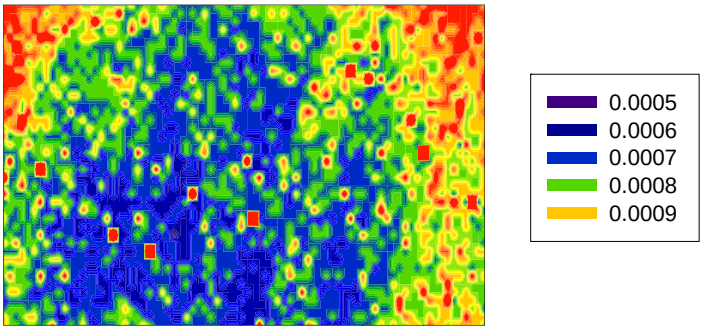

Figure 228. Standard deviation for radiance perturbations for channel #4 (v = 849.9 cm^{-1}) that shows the highest variability across image pixels.

The Telops Reveal Pro software that is used to control the Hyper-Cam during a measurement shows a real time update of the infrared image of the scene. As the screen updates, the software cycles through the wavenumber dimension of the hyperspectral data cube and randomly selects a radiance image to show on the display. This amoeba pattern is present on the display during calibration of the sensor when looking at the blackbodies. The presence of the pattern is not of concern here, as it is most likely representative of the detector response and should be removed during calibration. Why then, is it also apparent in the real-time display of the infrared scene? Further investigation revealed the answer.

The Telops Reveal Pro software does a "quick calibration" on the data cubes for the display. The actual calibration, using the two blackbody measurements to calculate a gain/offset file to calibrate the entire set of measurements, is performed in the separate Telops program Reveal

Calibrate. This calibration is a post-process step that, for the data taken at MRS, took approximately three weeks to complete. For the most part, the calibrated radiance data obtained from this process does not show these amoeba patterns, and this is confirmed by comparing a blackbody interferogram image to a calibrated radiance image (i.e. the blackbody was measured as though it were the scene). Figure 229 shows the "amoeba" is calibrated out when comparing images of blackbody measurements before and after calibration.

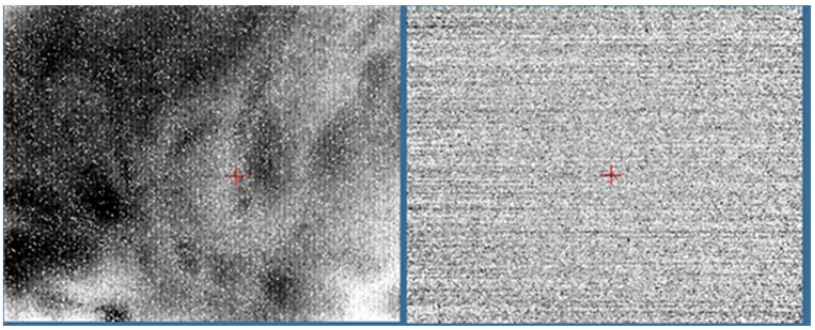

Figure 229. The interferogram image *(left panel)* and the radiance image *(right panel)* of the blackbody.

There were occasions where the amoeba pattern was still seen in the radiance data as calibrated by post-processing. As the pattern is essentially the detector response, it should certainly be gone after this more thorough calibration. For the data where these patterns exist in the radiance data, the source of the problem is attributed to a lost calibration. The MRS datasets were taken in thirty minute intervals; blackbody calibrations were performed between each set. Therefore, one must assume that there is no sensor drift or changes in ambient condition during the thirty minutes that the data were taken. The Telops monitored values during a calibration and measurement are shown in Table 12. The data in Table 12 was from cube 8940 of the November 17, Run 2 dataset.

Table 12. Telops monitored values during two blackbody and one scene measurement (all temperatures in Kelvin).

	Blackbody 1	Blackbody 2	cube 8940
FTSTemperatureMeasured	301.14	301.15	301.95
IRLensTemperatureMeasured	301.43	301.44	301.42
FPATemperatureMeasured	66.7	66.7	66.75
AmbientTemperature	279.77	279.88	286.86
EntranceWindowTemperature	285.82	285.87	290.46
BeamsplitterTemperature	299.49	299.5	300.6
FTSAmbientTemperature	300.01	300.06	301.38
IRLens1Temperature	301.01	301.02	301.24
CoolerColdFingerTemperature	306.36	306.42	310.77
CoolerCompressorTemperature	321.72	321.72	321.72
IRLensTubeTemperature	302.71	302.73	302.52
EnclosureAmbientTemperature	297.44	297.39	300.98
Ambient RH %	20	20	14

The two blackbody measurements were used to calibrate cube 8940. Note in Table 12 that there are several instances that indicated the sensor has drifted and the ambient conditions had changed. Cube 8940 was recorded 44 minutes after the blackbodies, and the calibration was no longer valid. Therefore, if the amoeba patterns are present in calibrated radiance data, the assumption is that it is due to a bad calibration and is not a sensor defect.

This assumption was verified by Christoph Borel of the Air Force Institute of Technology (AFIT) in his presentation entitled, "Data processing and temperature-emissivity separation for tower based imaging Fourier transform spectrometer data" at the 2012 Telops Scientific Workshop. AFIT uses both the mid-wave and long-wave versions of the Hyper-Cam for testing temperature and emissivity (T&E) separation algorithms and analysis of combustion events, among other things, and for the most part, they do their own calibration rather than use the Telops-provided Reveal Calibrate. Dr. Borel's presentation on T&E separation included a discussion of calibration, which included calculations of gains and offsets, bad pixel replacement, and flat-field correction. His figures of gain/offset maps were essentially our "amoeba" pattern. AFIT has termed this phenomenon the "Moiré" pattern, and as hypothesized, it represents the non-uniformity of the detector and can be calibrated out by measuring two blackbodies and generating gains and offsets to apply to scene interferograms.

5.3.5 Temporal Variability Analysis Theory

The algorithm used to identify potential turbulence in the Hyper-Cam data is based on the assumption that the natural (i.e. non-turbulent) azimuthal variations of observed radiances are negligible in comparison with natural variations due to the elevation angle. Thus, the average over 320 horizontal pixels generates a vertical profile of mean radiance that can be subtracted from observed data to reveal atmospheric inhomogeneity associated with mountain wave turbulence. It should be noted that all Hyper-Cam data are corrected for bad pixels; two methods are given in the following section. Results from the fourteen data cubes analyzed from November 17 are shown here as well to illustrate the theoretical development of the variability analysis; detailed results on entire datasets are given in following sections.

Temporal variability of the scene during one run is estimated by performing statistics over all data cubes for a given run after subtracting the row mean radiance for each cube/channel separately (to eliminate the radiance dependence on the viewing elevation angle). The computation of temporal variability ends up with one cube of data, which contains the estimated standard deviation for each pixel/channel separately.

Figure 230 presents the vertical dependence of the observed radiances, obtained by horizontal averaging, for each of the 35 spectral channels (4 through 38). Figure 231 presents the corresponding vertical variability of the observed channel radiances around these means.

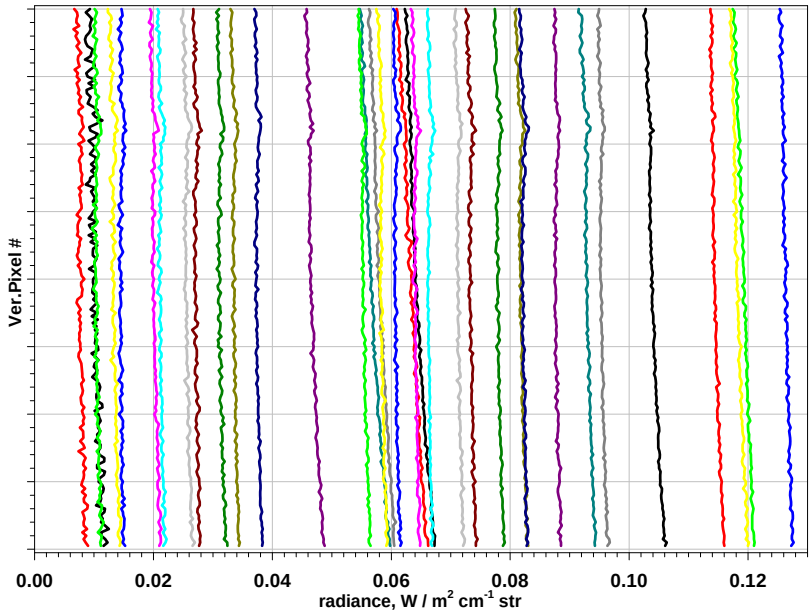

Figure 230. Mean vertical radiances; each successive channel shifted by 0.003 along the x-axis.

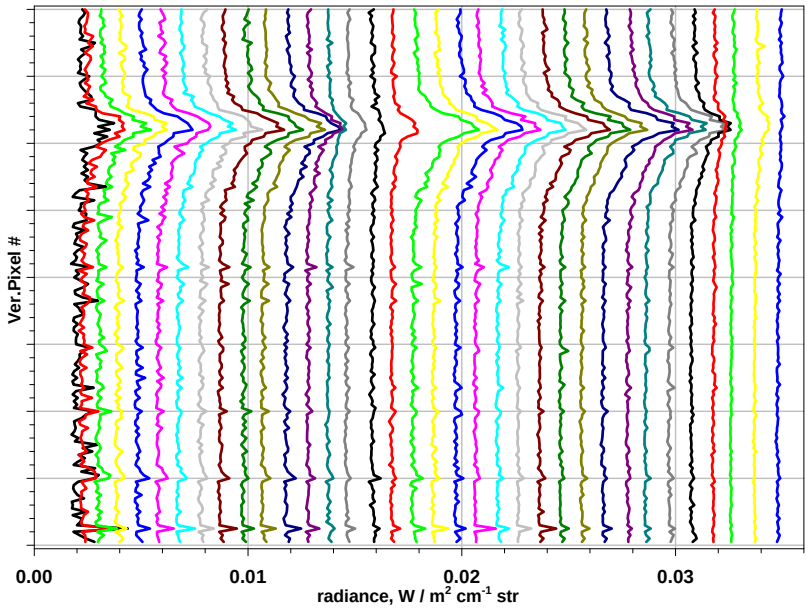

Figure 231. Standard deviation for vertically averaged radiances; each channel shifted by 0.001 along the x-axis.

From Figure 231, we can definitely see that something unusual appears in the upper part of the image (high variability in almost all channels).

After the azimuthal average observed spectrum was calculated, it was subtracted from the actual radiances. Thus, for a given channel and given cube of data (i.e. time of observation) we can compute the RMS difference of the resulting deviations over the whole image matrix, which is 160 vertical x 320 horizontal pixels. This spectral deviation, shown separately for each of the 14 times that data cubes were available, is shown in Figure 232. When we average this RMS difference over all 14 observed cubes, we can find those channels of highest time variability. The

result of this averaging is presented in Figure 233. As can be seen, channels 5 (~863.18 cm^{-1}) and 28 (~1168.61 cm^{-1}) show the most time variability, which in turn might be associated with mountain wave turbulence activity.

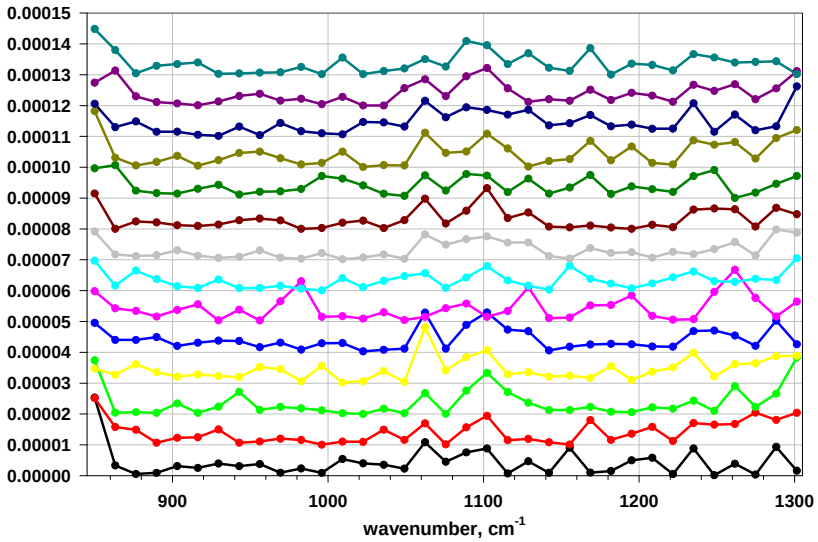

Figure 232. Spectral RMS difference over 320 x 160 image pixels for channels 4 – 38 and 14 consecutive data cubes (from the bottom to the top; each successive curve is shifted by +1.0e-5 $W/m^2cm^{-1}sr$ along the Y-axis).

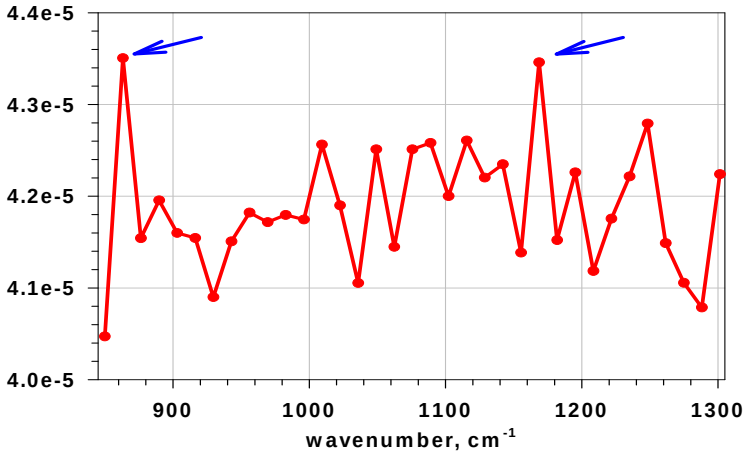

Figure 233. Time variability (averaging over 14 observed data cubes) of the difference between observed and azimuthal (horizontal) mean radiance. Blue arrows indicate channels with maximal time variability, as shown in Figure 234 and Figure 235.

The time development of the observed radiance disturbances for channels 5 and 28 is shown in Figure 234 and Figure 235, respectively. Although all previous statistical results have been obtained taking into account quality control (i.e. bad pixel replacement) described in the following section, the images in Figure 234 and Figure 235 show all pixels without regard to their quality control status, and results are displayed as 4 x 4 pixel averages for easier visualization. Also, the color scale is the same for all images, and it spans from –10 K to +10 K BTD, which is a measurable value range. Finally, it should be pointed out that the bright red spot visible at the upper left corner of all panels is caused by a cloud in the field of view. The dark blue stripe

starting right after the red spot and spanning the whole azimuth range is most likely an artifact resulting from the abnormally high radiances due to cloud emission.

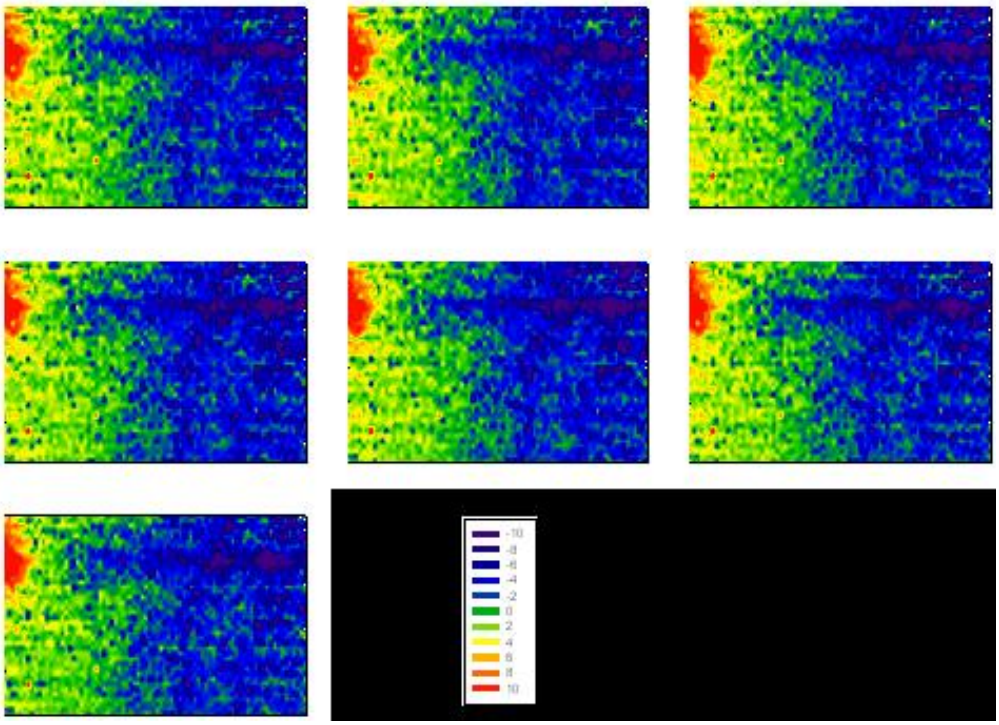

Figure 234. Time development (every odd data cube from 1 to 14) of the BTD deviations from the vertical mean for observed Telops channel # 5, ~863.18 cm^{-1}.

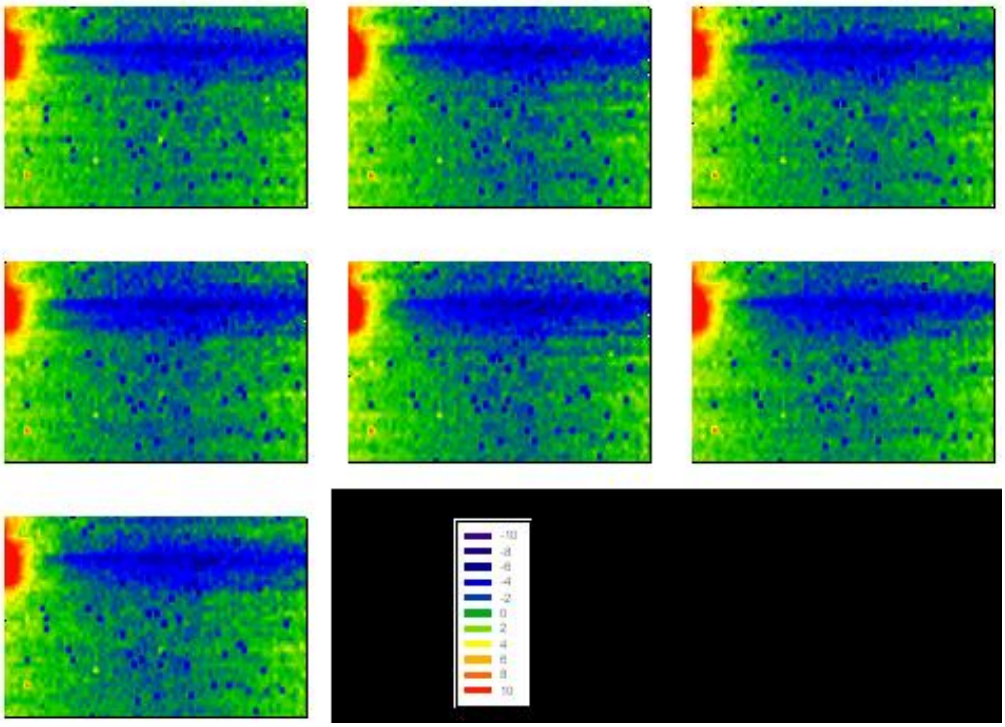

Figure 235. Time development (every odd data cube from 1 to 14) of the BTD deviation from the vertical mean for observed Telops channel # 28, ~1168.61 cm^{-1}.

5.3.6 Bad Pixel Map Creation

It should be noted that in order to exclude "bad" (i.e. low responsivity) pixel observations, some data quality control needs to be performed. As is shown later in Figure 278, it is unlikely that either observed or simulated radiances exceed 0.04 $W/m^2cm^{-1}sr$. All pixels for which the observed radiance exceeds this threshold value in one or more channels have therefore been excluded from the overall statistics. The threshold value of 0.04 was chosen after LBLRTM simulations and based on the first look of the MRS data as described previously. However, it should be noted that not all pixels marked as "bad" after this procedure are necessarily really bad pixels of the instrument, because the rule "<0.04" marks any accidental artifacts in the field of view (e.g. trees or the dining hall window frame, etc). Since the bad pixel map is defined for each run separately, we were able to compute the frequency of bad mapping, i.e. how many times each pixel is classified as bad one over all 7 runs. This frequency is shown in Figure 236: green pixels are bad in 4 runs out of 7 total; light blue, red, and black pixels are repeated as bad in 5, 6, and 7 (all) runs correspondingly. These 97 + 63 + 63 + 645 = 868 pixels can be considered to be bad within the instrument detector array. Although the numbers of "bad" pixels which happen only in one, two, or three runs are much larger (6766, 11893, and 3088, respectively), they are mostly caused by the natural artifacts mentioned above, and for this reason are not shown in Figure 236. To illustrate this point, Figure 237 shows bad pixels observed in 2 runs out of 7. Thus, the simple rule "<0.04" works properly for identifying both bad pixels and naturally produced high radiance values. Those high radiance measurement pixels have been excluded from further consideration and do not distort the processing designed to detect lee wave turbulence.

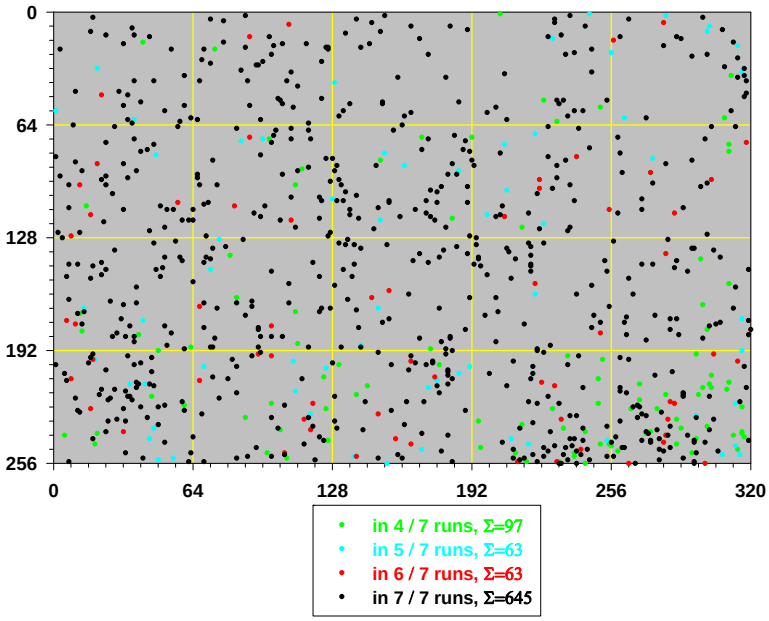

Figure 236. Frequency of pixels marked as bad over seven processed runs.

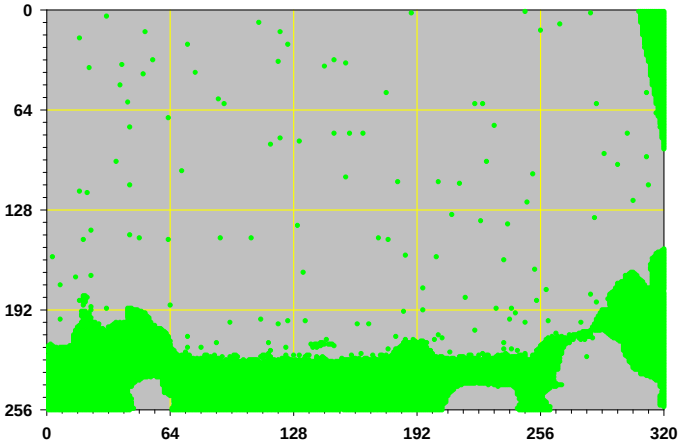

Figure 237. Bad pixels with frequency = 2 over seven runs, caused mostly by the artifacts in the field of view.

5.3.7 Cloud Detection/Removal Algorithms

Methods for accounting for the influence of clouds on FLI spectra were investigated and developed. These methods are needed in order to detect the relatively small atmospheric turbulence signals in the FLI radiance spectra. Three different techniques were defined:

1. Cloud clearing: The time and/or spatial variation of radiance associated with cloud amount variations are used to separate the radiance coming from the clear air from that coming from the cloudy portions of the instrument's field of view.

2. Cloud correcting: The cloud contribution to the observed radiance is estimated via a radiative transfer calculation in which the cloud emissivity spectrum and cloud distance from the instrument are estimated using the ratio of effective cloud amounts computed for two different spectral channels, one of which is a relatively clean atmospheric window transparent to the atmosphere between the instrument and the cloud, and another semi-transparent channel which is subject to the absorption of the atmospheric gas between the instrument and the cloud. The correct distance between the instrument and the cloud is specified as that distance in which the cloud amounts computed for both the transparent and semi-transparent spectral regions are the same.

3. Cloud detecting: The spectral features of clouds and clear sky are exploited to determine which parts of the scene are cloud and which are sky.

"Cloud detecting" is a quick method of determination of cloud cover using information inherent in the scene. The "cloud clearing" technique assumes that the clouds are broken and that local variations of the observed radiance are due to variations in the cloud fractional coverage rather than to variations in the cloud height or their optical properties. The cloud clearing process only requires the radiance observations (i.e. no ancillary data or time consuming radiative transfer calculations are required). However, the technique does not work in a completely overcast sky condition. The cloud correction technique works for any cloud amount condition, including a dense overcast, but requires ancillary information on the temperature and moisture structure of

the atmosphere, as well as time-consuming radiative transfer calculations. As a result, the ultimate solution is a combination of these algorithms.

5.3.7.1 Cloud Clearing

The radiance measured by a spectrometer whose field of view contains a broken and or semi-transparent cloud can be expressed as

$$R(\nu,t) = N \times R_{CLD}(\nu,t) + (1-N) \times R_{CLR}(\nu,t) \tag{5.3.3}$$

where $R_{CLD}(\nu,t)$ is the radiance coming from the cloud filled portion of the sensor's field of view at spectral wavenumber ν and time t, $R_{CLR}(\nu,t)$ is the radiance coming from the clear air within the sensor's field of view, and N is the product of the fraction of cloud cover and the emissivity of the cloud. The clear air radiance can then be solved from the radiance observations at two different times, t_1 and t_2, if it can be assumed that the clear air radiance (i.e. atmospheric profiles) and the cloud altitude and optical properties are the same for the radiances measured at the two different times. The solution is:

$$R_{CLR}(\nu,t) = \frac{R(\nu,t_1) - N^* \times R(\nu,t_2)}{1-N^*} \tag{5.3.4}$$

where:

$$N^* = \frac{R(w,t_1) - R_{CLR}(w)}{R(w,t_2) - R_{CLR}(w)} \tag{5.3.5}$$

In Equation 5.3.5 the wavenumber w is a reference channel window region wavenumber (or average of wavenumbers) where the clear air radiance, $R_{CLR}(w)$, is known from either surrounding time clear air window radiance observations or estimated from a clear sky radiative transfer calculation. Because the clear sky window radiance is very small (near zero from aircraft or high altitude observatory levels) compared to the spectral atmospheric radiances used for atmospheric turbulence detection, the result is not very sensitive to the accuracy of the assumed clear window radiance, $R_{CLR}(w)$. By using an average of radiance measurements over the large number of window wavenumbers within the spectrum, the impact of instrumental noise on the result can also be reduced.

Figure 238 and Figure 239 show results obtained from ground-based ASSIST measurements obtained during the Chemistry and Physics Atmospheric Boundary Layer Experiment (CAPABLE) conducted during the June–August 2010 time period. The ASSIST data was transformed to the 16 cm^{-1} spectral resolution of the Hyper-Cam. The results shown are for two different days during CAPABLE, June 23 and July 6–7, 2010. As can be seen in the upper left-hand panel of each figure, clouds existed during both of these measurement days, with the heaviest cloud occurring near the end of June 23, 2010.

The upper-left hand panel of each figure shows the radiance for the 1100–1150 cm^{-1} transparent window used as the reference channel to calculate the N^* parameter used to cloud-clear the Hyper-Cam spectrum. Radiance is very small for this relatively transparent window, and the clear air radiance can be easily inferred by time interpolation of these clear air radiances across the obvious cloud contaminated fields of view. This reference channel clear air radiance is then used to define N^* using Equation 5.3.5 which is used in Equation 5.3.4 to define

the clear air radiance for all the cloud-contaminated fields of view. Since the error in the calculated clear air radiance tends towards infinity as N^* approaches unity, only values with an $N^* < 0.75$ are retained, and the missing data are filled in by time interpolation of the acceptable clear air radiance values. In these cases, almost all the results shown are actual clear air radiance values, rather than being the result of time interpolation.

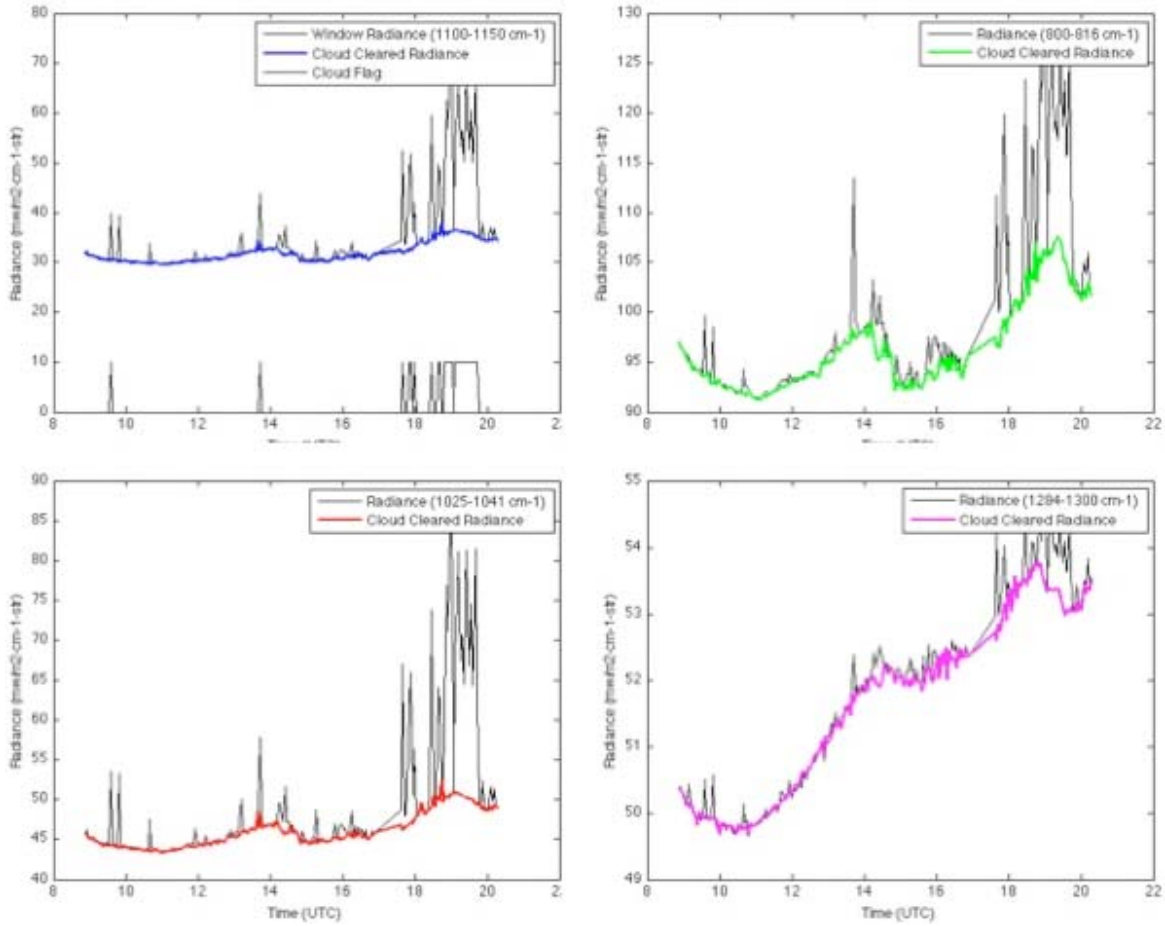

Figure 238. Cloud-clearing results for June 23, 2010. The upper left panel shows the reference window region and cloud flag while the upper right, lower left, and lower right hand panels show the cloud-cleared results for the 800-816 cm^{-1} long-wave water vapor absorption region, the 1025–1041 cm^{-1} ozone absorption region, and the 1284–1300 cm^{-1} shortwave water vapor region.

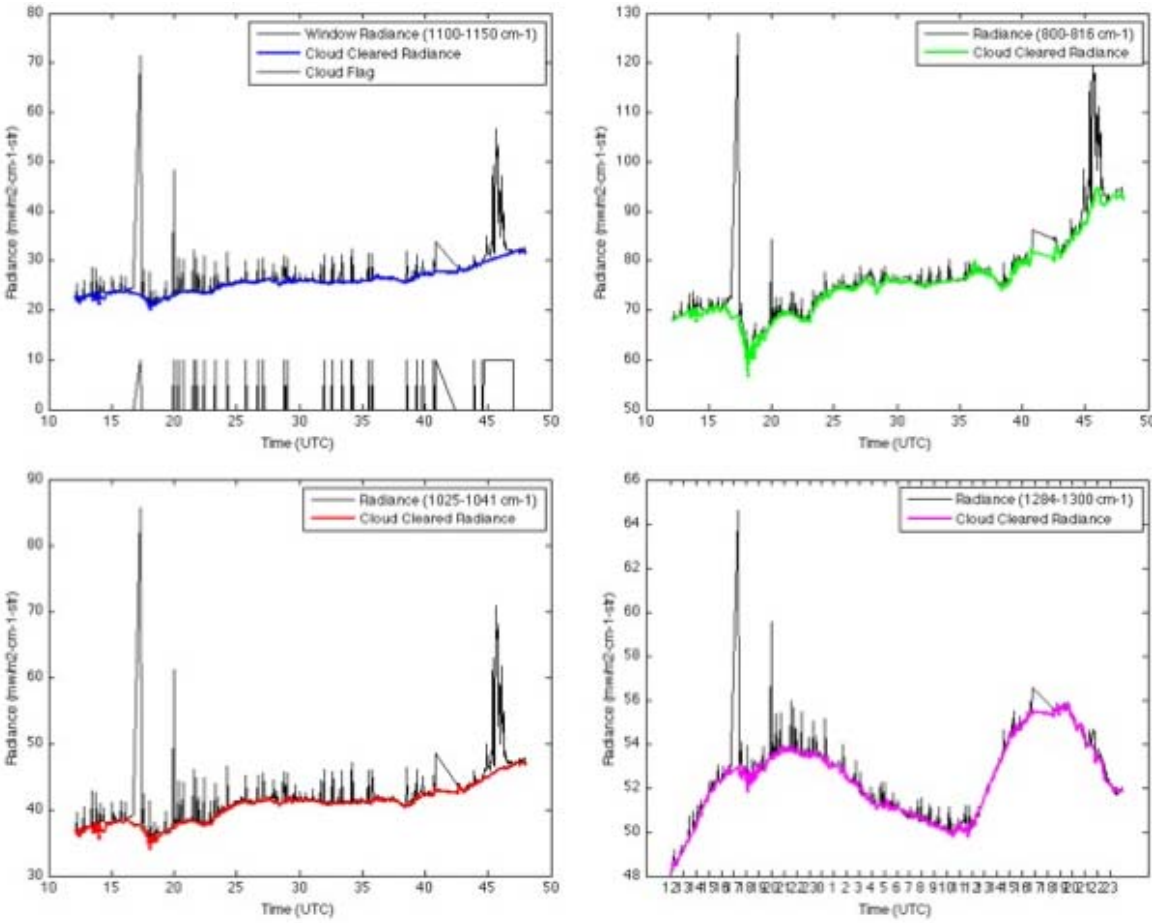

Figure 239. Cloud-clearing results for July 6-7, 2010. The upper left panel shows the reference window region and cloud flag while the upper right, lower left, and lower right hand panels show the cloud-cleared results for the 800–816 cm^{-1} long-wave water vapor absorption region, the 1025–1041 cm^{-1} ozone absorption region, and the 1284–1300 cm^{-1} shortwave water vapor region.

5.3.7.2 Cloud Correcting

As defined in the previous section, the radiance measured by a spectrometer whose field of view contains a broken and/or semi-transparent cloud was given in Equation 5.3.3. The cloud amount can then be solved from the radiance observations for two different spectral regions, *v* and *w*. The solution is

$$N(v,t) = \frac{R(v,t) - R_{CLR}(v)}{R_{CLD}(v,t,d) - R_{CLR}(v)} \tag{5.3.6}$$

And

$$N(w,t) = \frac{R(w,t) - R_{CLR}(w)}{R_{CLD}(w,t,d) - R_{CLR}(w)} \tag{5.3.7}$$

In Equation 5.3.7 the wavenumber *w* is the channel window region and the wavenumber *v* refers to the semi-transparent spectra channel. The clear window radiance, $R_{CLR}(w)$ is known from either surrounding time cloud-cleared window radiance observations or estimated from a clear sky radiative transfer calculation based on forecast model atmospheric profiles, and R_{CLD} is the radiance calculated from the forecast model atmospheric profiles for an opaque cloud placed at

various distances from the instrument, *d*. Because the clear sky window radiance is very small (near zero from aircraft or high altitude observatory levels) compared to the spectral atmospheric radiances used for atmospheric turbulence detection, the result is not very sensitive to the accuracy of the assumed clear window radiance, $R_{CLR}(w)$. For the Hyper-Cam, operating at 16 cm^{-1} spectral resolution, w = 1075–1091 cm^{-1} and v = 1251–1283cm^{-1}. The second channel is mainly sensitive to methane, which is a fairly uniformly mixed gas, so that the ratio of the calculated cloud amount in this band relative to the window region should be proportional to the distance of the observed cloud from the instrument (i.e. the difference between the observed cloud radiance and the clear radiance in the methane channel depends upon the optical depth of methane between the cloud and the instrument). It is noted that in the calculation of *N*, the clear radiance in the numerator is taken as the pre-derived clear air radiance obtained by the *N** method described in the previous Cloud Clearing section. However, since the cloud radiance is calculated using model forecast atmospheric profiles, the clear air radiance for the denominator of the equation is specified using a clear sky radiance calculation based on the same model profiles used to calculate the cloud radiance. This is important to alleviate any systematic discrepancies between observed and calculated radiance due to radiative transfer model or atmospheric state errors.

The cloud distance and effective cloud amount are calculated using:

$$R_{CLR}(v) = R(v,t) + N\{R_{CLR}(v) - R_{CLD}(v,t,d)\} \tag{5.3.8}$$

Here, both the clear air and the cloudy radiance are obtained from radiative transfer calculations so that their difference becomes zero for cloud distances which cannot be seen by any particular spectral channel due to strong atmospheric absorption.

Figure 240 shows an example result for a very cloudy condition observed from ground-based ASSIST measurements during the Chemistry and Physics Atmospheric Boundary Layer Experiment (CAPABLE) conducted during the June – August 2010 time period. The ASSIST data were transformed to the 16 cm^{-1} spectral resolution of the Hyper-Cam. As can be seen from the upper left-hand panel, clouds existed throughout much of the day, with the heaviest cloud occurring during the first half of the day.

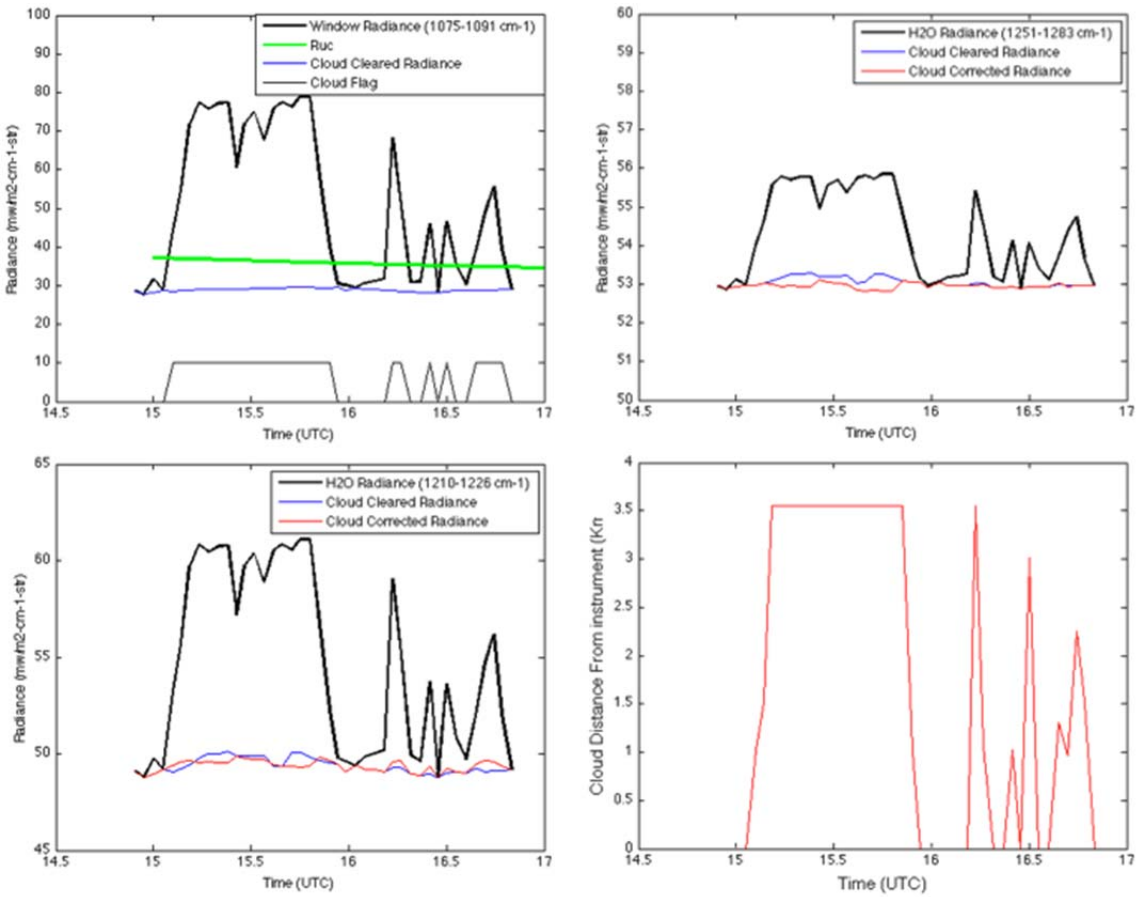

Figure 240. Cloud-correction results for June 22, 2010. The upper left panel shows the reference window region and cloud flag while the upper right and lower left show the cloud-cleared and cloud-corrected results for the 1251–1283 cm^{-1} methane and 1210–1216 cm^{-1} water vapor absorption regions, respectively. The derived distance to cloud is shown in the lower right hand panel.

5.3.7.3 Cloud Detecting

Data from the MRS November 17, 2011, Run 4 dataset was used to illustrate the development of the Cloud Detecting Algorithm. Detailed results of the temporal variability analysis for this dataset are given in the following section. The cloudy area brightness temperature was estimated to be about 240 K. We performed computations for cloud brightness temperatures from 215 K to 250 K with 5 K increments to see how this threshold value affects the temporal variability pictures. A cloud mask was applied in such a way that all pixels with radiance values higher than R (T_{CLD} = 215, 250, 5 K) have been excluded from the consideration, which leads to a different number of pixels averaged over 1007 data cubes total. For example, as can be seen in Figure 241, the upper and bottom thirds of the whole frame are always excluded, while for the central 1/3 of the frame the number of averaged pixels is changing from 1007 (always clear) to 0 (always cloudy) from left to right. The number of averaged pixels depends also on the given value of threshold cloud temperature.

The temporal variability results, with cloud contributions over a threshold value (T_{CLD} = 240 K) eliminated, are presented in Figure 241. Eight channels with central wavenumbers from 863 cm^{-1}

to 1115 cm^{-1} are shown in brightness temperature units, with the same color scale 0 – 4 K for each panel.

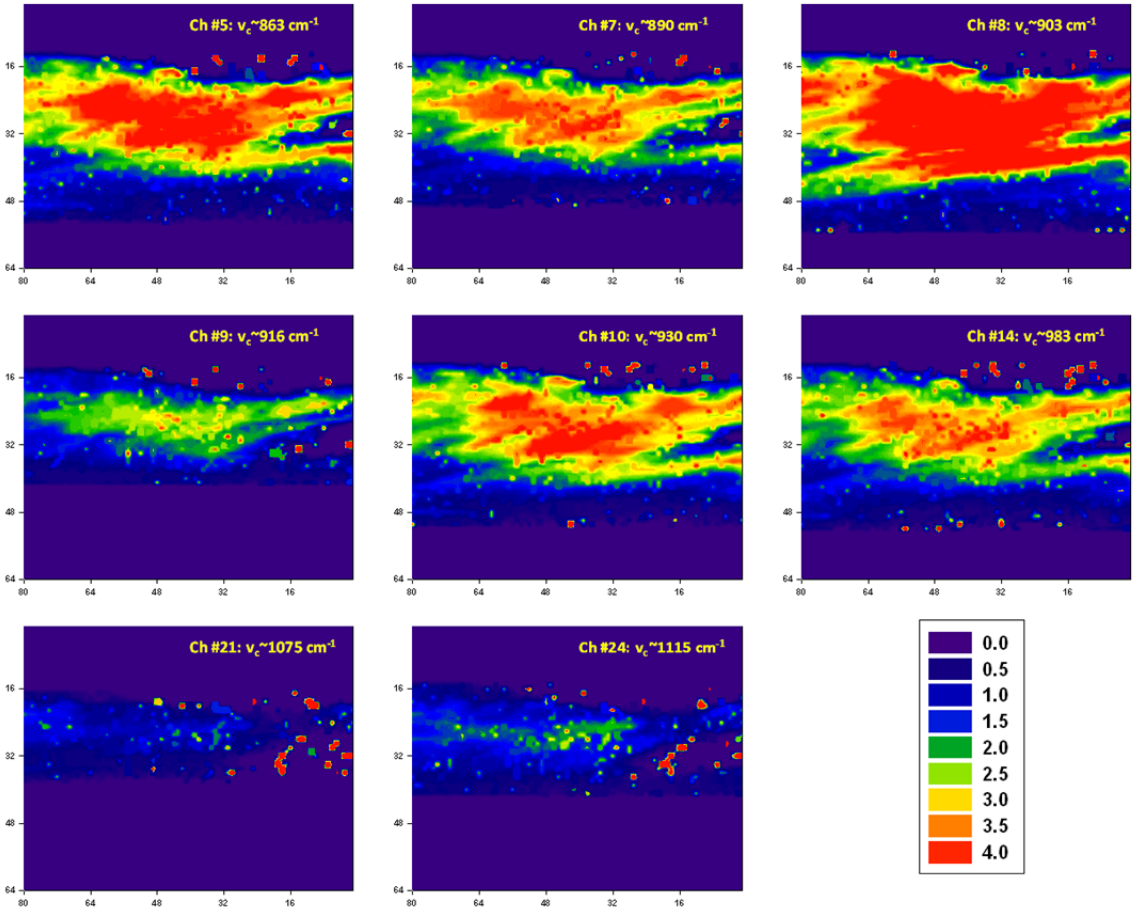

Figure 241. The temporal variability of the scene when cloudy pixels T_{CLD} > 240 K are eliminated. Unit is brightness temperature, the same color scale 0–4 K is used for all panels.

The temporal variability when T_{CLD} varies from 215 K to 250 K is presented in Figure 242 for the transparent channel #8. One can note that even as low as 215 K there is cloud signal. For comparison, Figure 243 shows temporal variability for the opaque channel #18 (O_3 band, ~1035 cm^{-1}). The panels shown are for threshold values of T_{CLD} = 260 K, 265 K, and 270 K. There is no signal for $T_{CLD} \leq$ 255 K in this channel. Note also that the color scale is a factor of 2 smaller (0 – 2 K) in Figure 243 than in previous figures.

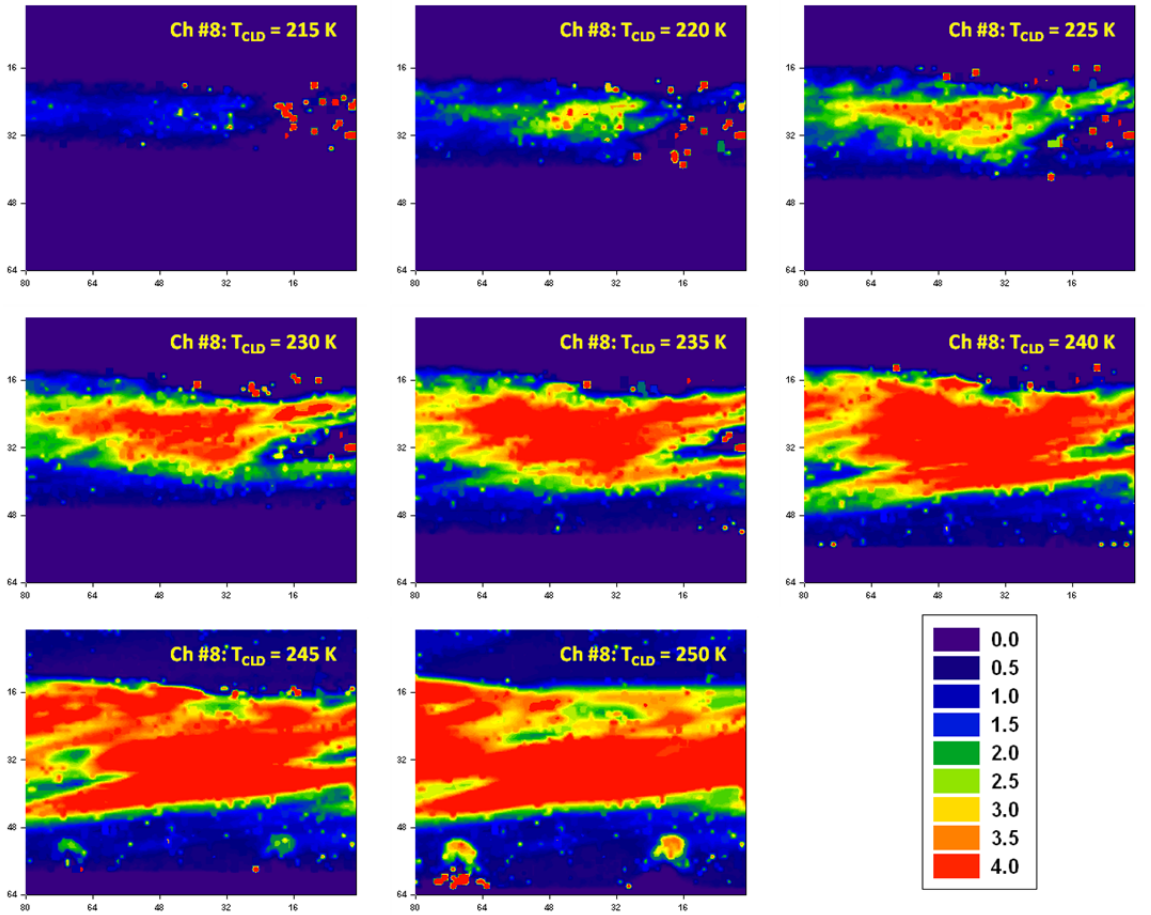

Figure 242. The temporal variability of the scene for the transparent channel #8 (~903 cm^{-1}) when different cloud brightness temperature threshold values are applied (215 K to 250K, increment 5 K); November 17, Run 4.

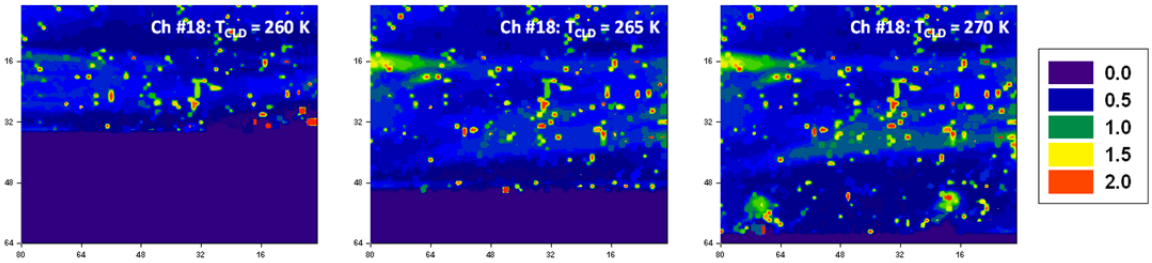

Figure 243. The temporal variability of the scene for the opaque channel #18 (~1035 cm^{-1}) when different cloud brightness temperature threshold values are applied (260, 265, 270 K); November 17, Run 4. Note that color scale is a factor of two smaller (0 – 2 K) than the previous figures. There are no pixels for $T_{CLD} \leq 255$ K.

A second method was developed to exclude cloudy pixels based on comparison of sky radiance and cloud radiance as shown in Figure 244; the spectra shown are from the same row of pixels so that the elevation angle for both would be the same and not create a difference in magnitude. These spectra are at 16 cm^{-1} resolution, so the narrow spectral lines characteristic of a sky spectrum cannot be seen in the measured sky radiance; however, there is enough difference in the

two spectra so that a determination of sky or "other" can be made for every pixel in the scene. The cloud spectrum exhibits much higher radiance than the sky spectrum; additionally it has fewer spectral features and follows more closely the trend of a blackbody.

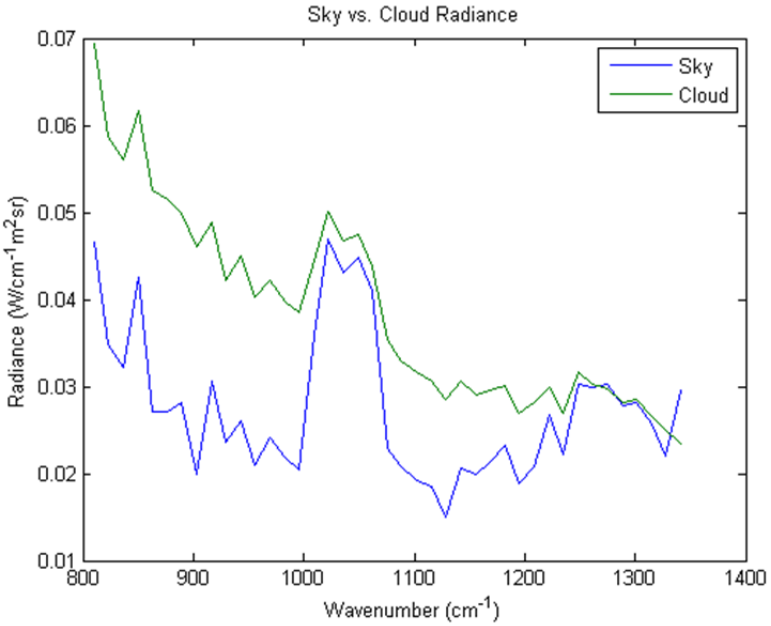

Figure 244. The radiance from a sky pixel compared to the radiance from a cloud pixel.

In order to determine the areas of clear sky, the following procedure was followed. Channel #8 (903.02 cm^{-1}) from each data cube in time was chosen to be the frame that exhibited a substantial difference between sky and cloud spectra. Channel #35 (1261.67 cm^{-1}) from each data cube in time was chosen to be the frame that exhibited the most similarity between sky and cloud spectra. For every time in the series, channel #35 was subtracted from channel #8. A binary image was created for every time step, whereby if the result of the subtraction was positive, a one was assigned to the pixel, and if the result of the subtraction were negative, a zero was assigned to the pixel. By overlaying these binary images over the difference images described in the previous section, everything but clear sky should be masked, which aids in the determination of whether variability can be attributed to temporal changes in cloud position. Variability images from the beginning and end of the time series, both unmasked and masked, are shown in Figure 245.

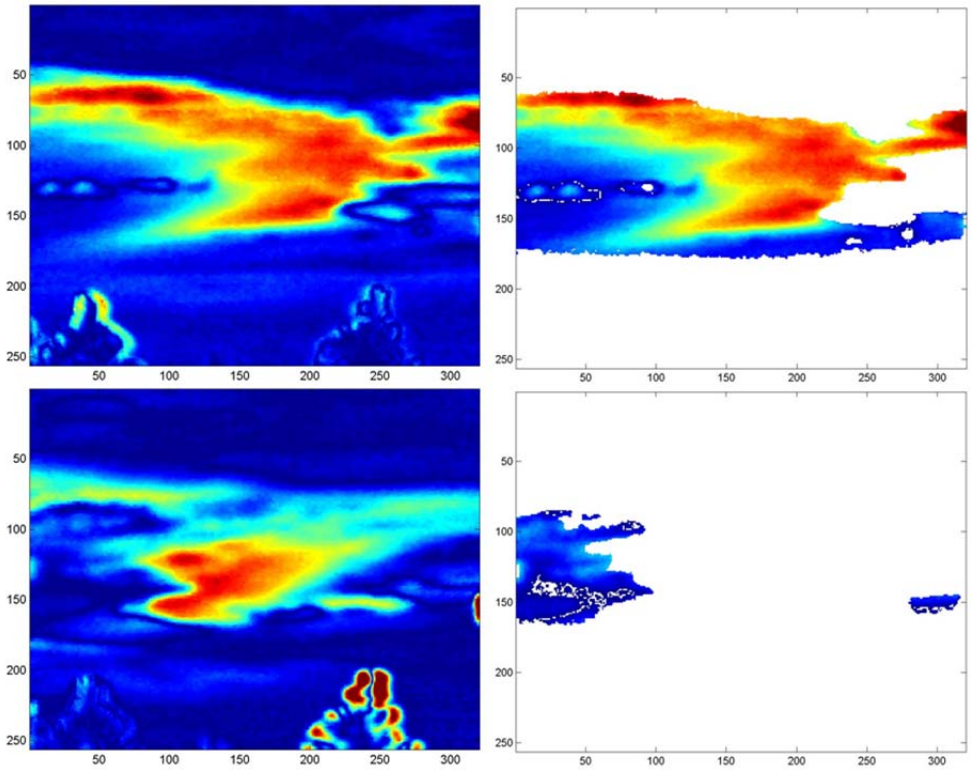

Figure 245. The variance in radiance at the beginning of the thirty minute run *(top two images)* vs. the variance in radiance at the end of the thirty minute run *(bottom two images).* The images on the right have been masked by the cloud removal test.

This simple algorithm to test for sky also masks clear sky at the horizon as the atmosphere here is more opaque and its radiance looks more like a blackbody. Therefore, a second test was developed that would compare the relative change in radiance between channel #8 (903.02 cm^{-1}) and channel #9 (916.30 cm^{-1}). As shown in Figure 246, both sky spectra, regardless of elevation angle, exhibit a much greater change between the two wavenumbers than the cloud spectrum.

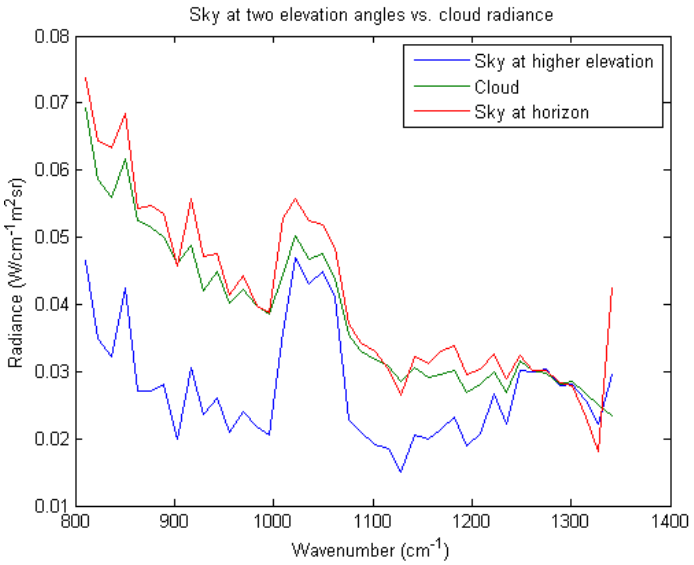

Figure 246. The radiance from sky pixels at two elevations compared to the radiance of a cloud pixel.

The relative difference of the local radiance between 903.02 cm^{-1} and 916.30 cm^{-1} of the three spectra in Figure 246 is 8.133 x 10^{-4} W/m^2sr in the case of the sky at the high elevation, 2.410 x 10^{-4} W/m^2sr in the case of the cloud, and 7.681 x 10^{-4} W/m^2sr in the case of the sky at the horizon. Because the sky radiance changes approximately three times faster in the case of both sky spectra, this derivative is checked in addition to the radiance difference between 903.02 cm^{-1} and 1261.67 cm^{-1}. Variability images from the beginning and end of the time series, both unmasked and masked with the new constraint are shown in Figure 247.

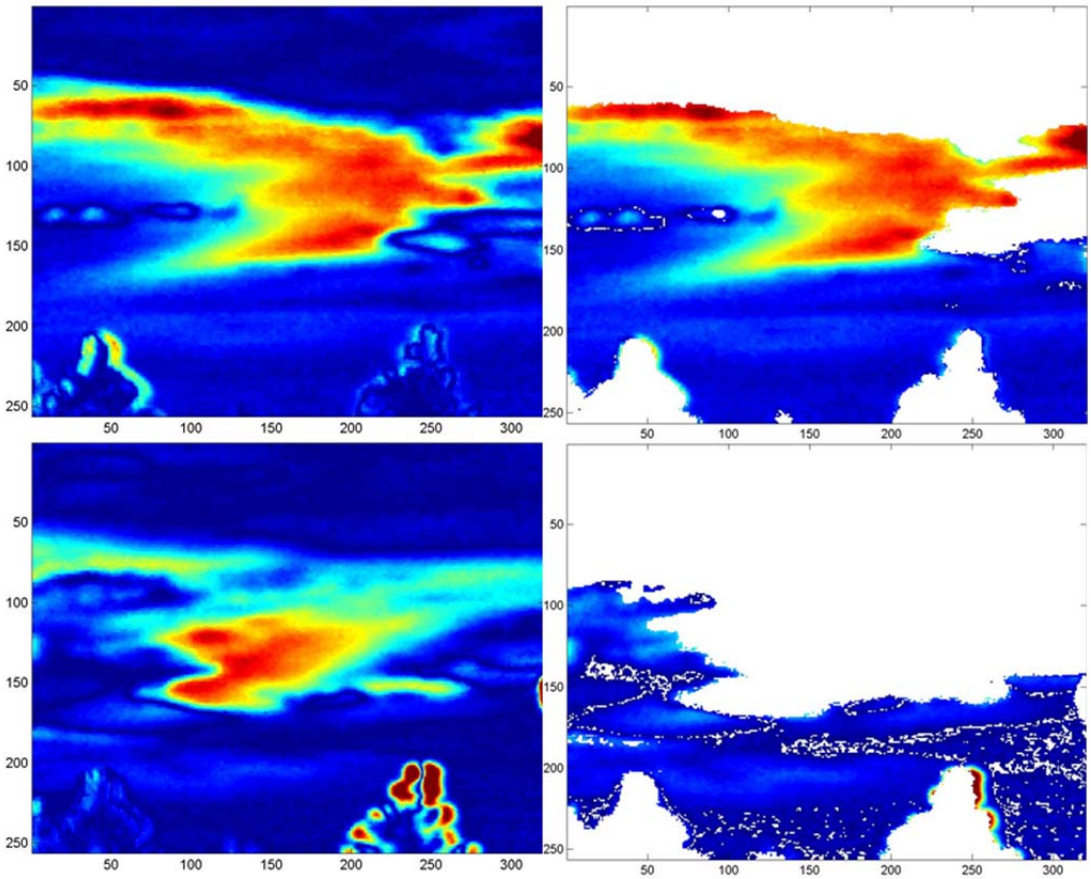

Figure 247. The variance in radiance at the beginning of the thirty minute run *(top two images)* vs. the variance in radiance at the end of the thirty minute run *(bottom two images).* The images on the right have been masked by the cloud removal test as in Figure 245, but with the additional constraint of checking the change in radiance between 903.02 cm^{-1} and 916.30 cm^{-1}.

5.3.8 Temporal Variability Analysis Results

Hyper-Cam calibrated data for November 16, 2011, Run 1 (cubes 1917 to 2534, 618 total) with 16 cm^{-1} spectral resolution were processed first, following the methodology outlined in the Temporal Variability Analysis Theory Section. After generating a bad pixel map for this run by excluding pixels for which calibrated radiances in all channels were larger than 0.04 $W/m^2cm^{-1}sr$, about 2000 pixels were classified as bad out of 320*256 = 81920 total. Again, horizontal mean radiances were obtained by row averaging (excluding pixels marked as bad). These mean radiances were then subtracted from the measured radiance, separately for each spectral channel and data cube. After that, the temporal variability of the signal was computed as the standard deviation of the resulting radiance differences by averaging over all 618 cubes. The last step was

done separately for each spectral channel and image pixel. Finally, the data cube of this temporal variability, with dimensions 320 x 256 x 618, was analyzed.

To estimate which channel exhibited the highest temporal variability, averaging over all image pixels for a given channel was performed. Figure 248 shows the spectral dependence of these statistics on the corresponding mean, minimum, and maximum values. Note that the first and last three channels have been excluded from consideration since they obviously suffer from the wrap-around effect. From Figure 248, channels #4 and #5 (~850 cm^{-1} and 863 cm^{-1}) have been selected for display as these channels show the highest temporal variability. The corresponding full-size images of temporal variability for these two channels are shown in Figure 249.

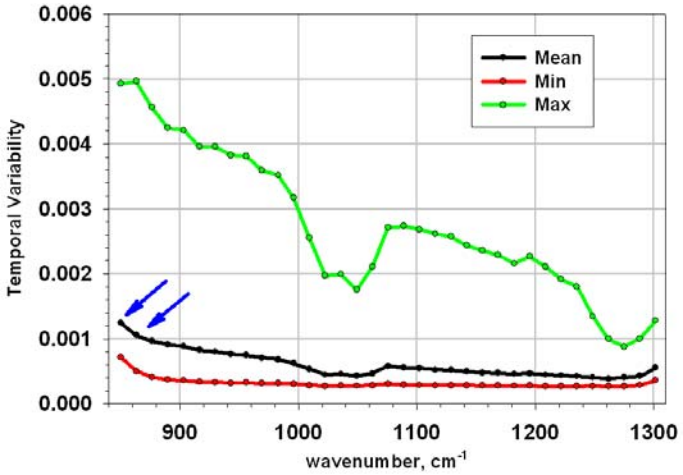

Figure 248. Statistics for temporal variability of the signal obtained by averaging over all image pixels for each channel. Blue arrows indicate the two channels shown in the full-size images in Figure 249.

The temporal variability is relatively large; the full-scale range shown in Figure 249 is from $2x10^{-4}$ to $2x10^{-3}$ $W/m^2cm^{-1}sr$. The relatively high variability in the upper left-hand corner of the image is due to the lost calibration amoeba pattern discussed previously. The red spots in the lower left corner are due to a tree in the field of view, where an arbitrary high variability value was assigned. On the upper right-hand side of the tree, there are two areas where the temporal variability is comparatively high. These areas were later confirmed to be due to clouds.

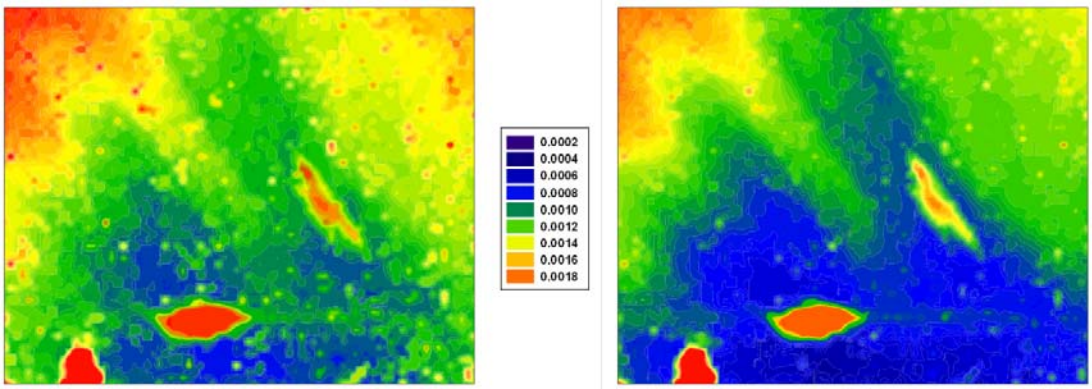

Figure 249. Full-size image of temporal variability for channels #4 *(left panel)* and #5 *(right panel)* that have maximum values of the signal.

Images were then created for each channel for every data cube in sequence. An example of three images from the fourth channel is shown in Figure 250. Note that all three images have the same color scale, and different features appear in the images as the sequence continues. Unfortunately there are no webcam images for this run, so it is unknown whether or not the features seen in Figure 250 are clouds.

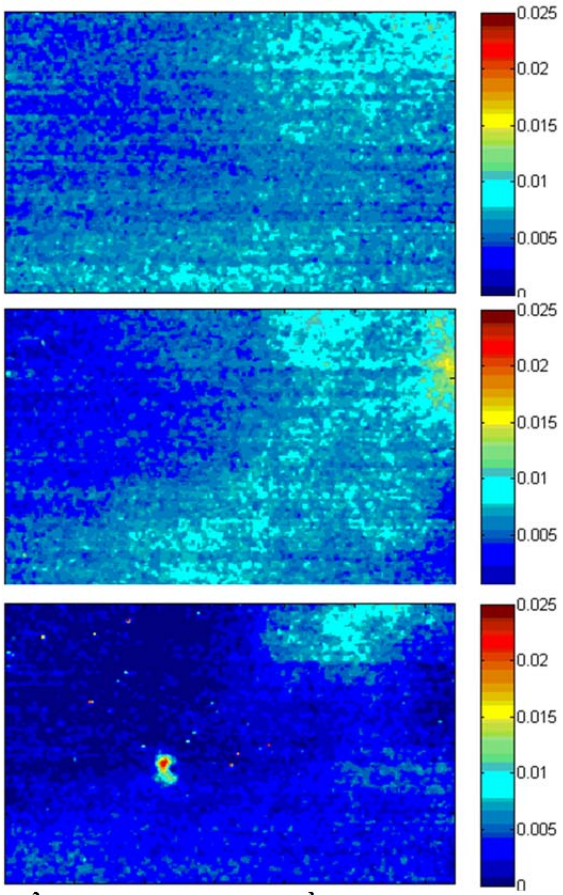

Figure 250. Radiance (W/m^{2}sr) imagery at 850 cm^{-1} from November 16, 2011, Run 1. Each frame (from top to bottom) was recorded at 18:13:45, 18:23:03, and 18:26:37 UTC, respectively.

This data set lacked not only webcam imagery to verify or exclude the existence of clouds, but also D&P data and pilot reports of turbulence in the area. Therefore, going forward, we decided to focus on several runs from November 17, 2011. On this day, we could see lenticular clouds; also, there were several PIREPS of turbulence, and we have complete data, including simultaneous Hyper-Cam, webcam, and D&P datasets.

Six processed runs from November 16 and 17 contain 1000+ data cubes each, so the temporal interval is about twice as long as November 16 Run 1 (618 cubes). The computation of temporal variability ends up with one cube of data that is the variability (i.e. standard deviation of the radiance) for each pixel/channel separately.

Averaging this resulting cube over all pixels for a given channel helps to determine which channels have the highest sensitivity to turbulence. Figure 251 shows this spectral dependence for all 7 runs processed, from this we again conclude that channel #4 (~850 cm^{-1}) shows the most

variability. Corresponding images of temporal variability at this channel for all runs in radiance units are shown in Figure 252. Note that while making the images in Figure 252, the bad pixel values have been replaced either with the average over good pixels in ± 2 surrounding area or with a zero value when an insufficient number of valid radiances are observed. Also note that the "amoeba" pattern is present in this data.

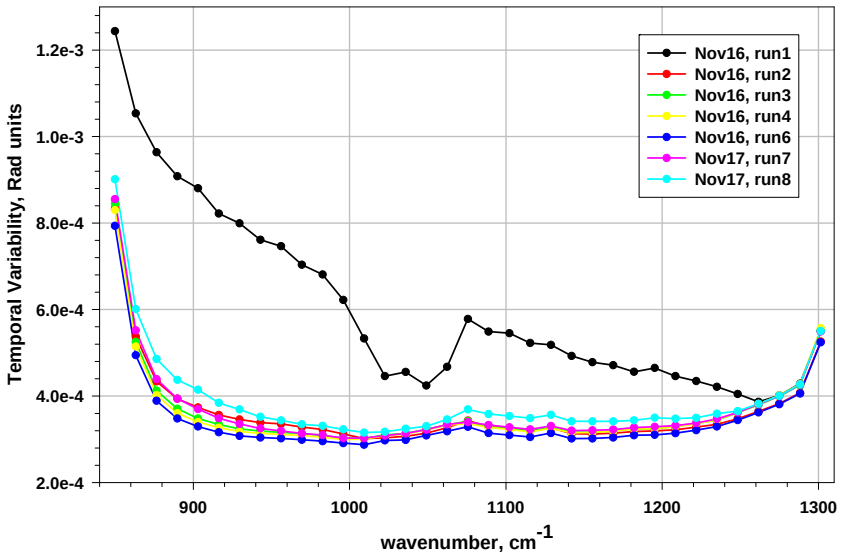

Figure 251. Spectral dependence of the temporal variability of the scene obtained by averaging over all image pixels for given channel, 7 runs.

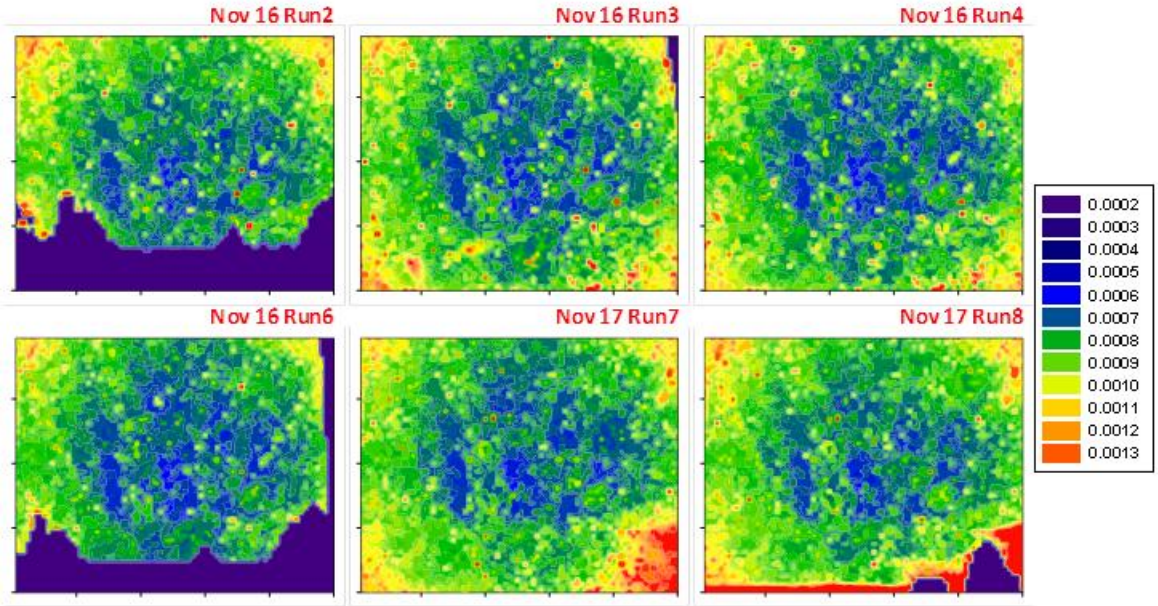

Figure 252. Image of temporal variability (radiance units) for channel #4, that have maximum values of the signal, 6 runs.

November 17, Run 4 data was the next run analyzed and was chosen because the field of regard was positioned directly under a lenticular cloud. During this time series, clouds were crossing the instrument FOV, which resulted in significantly larger disturbances of the measured signal than

was observed in all runs processed before. This disturbance is clearly seen in Figure 253, which shows the spectral dependence of temporal variability of the signal in radiance units for all eight runs processed to the point of the November 17, Run 4 analysis. Averaging the standard deviation over all pixels, separately for each spectral channel, provides the spectral dependence of the computed temporal variability. Figure 254 shows the same quantity in brightness temperature units for November 17, Run 4 only. Corresponding images of temporal variability for channels 4 and 23 are shown in Figure 255 and Figure 256.

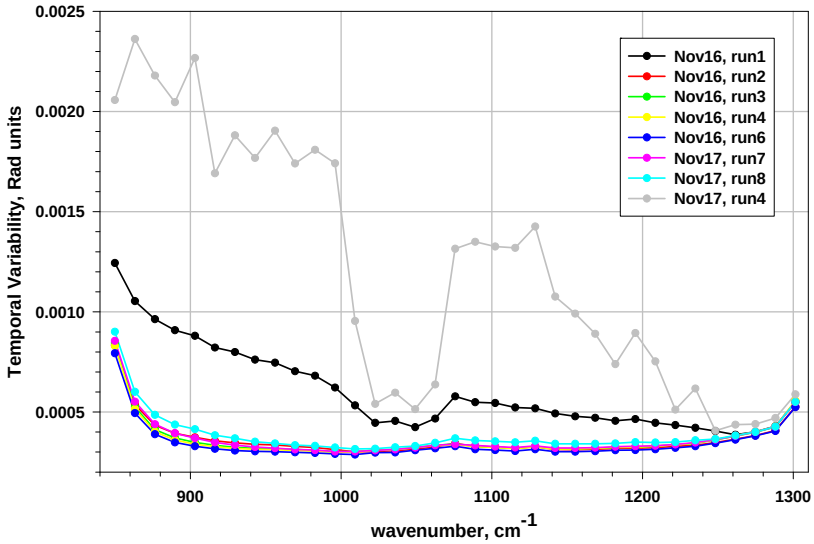

Figure 253. Spectral dependence of the temporal variability of the scene obtained by averaging over all image pixels for a given channel, 8 runs total, radiance units.

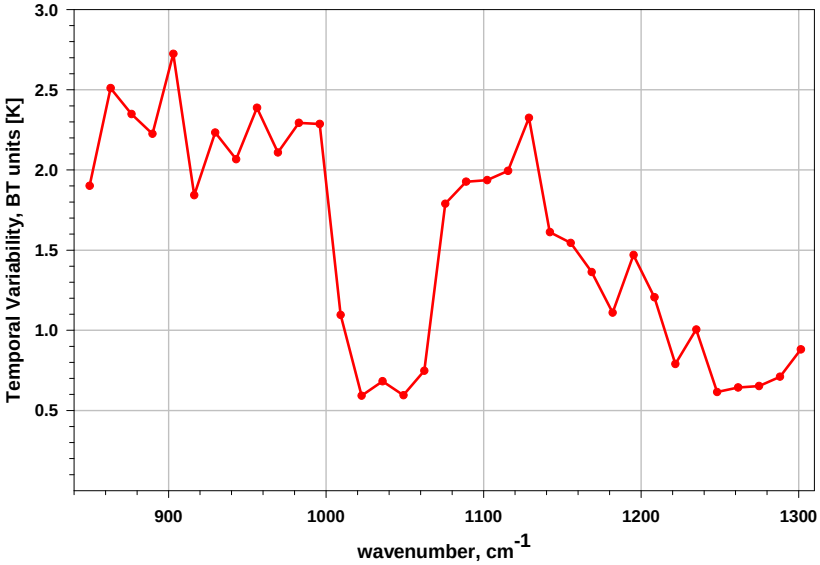

Figure 254. Spectral dependence of the temporal variability of the scene obtained by averaging over all image pixels for given channel, November 17, Run 4, brightness temperature units.

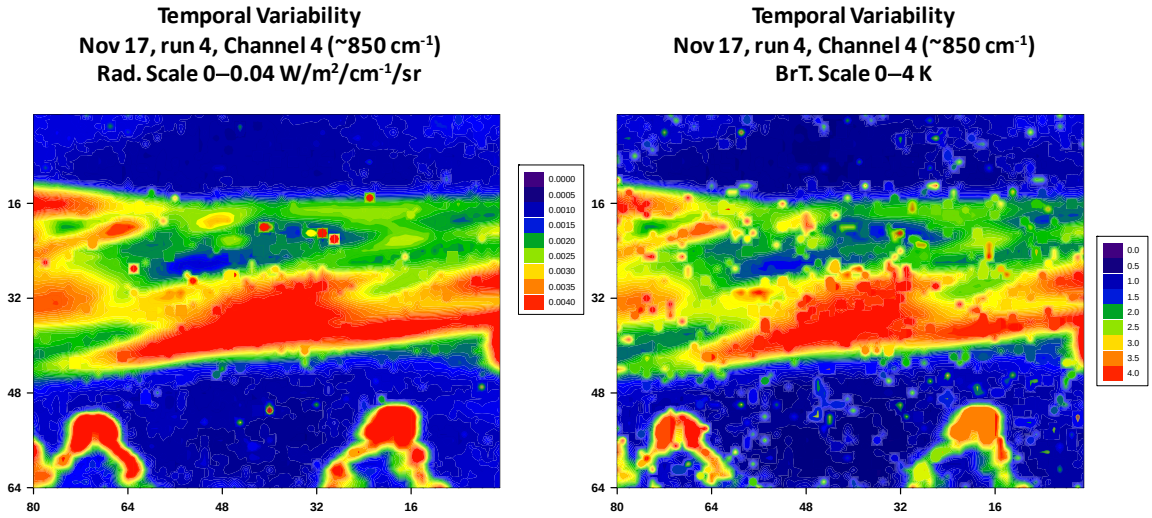

Figure 255. Image of temporal variability for channel 4, radiance units *(left panel)* and brightness temperature units *(*right *panel)*, November 17, Run 4.

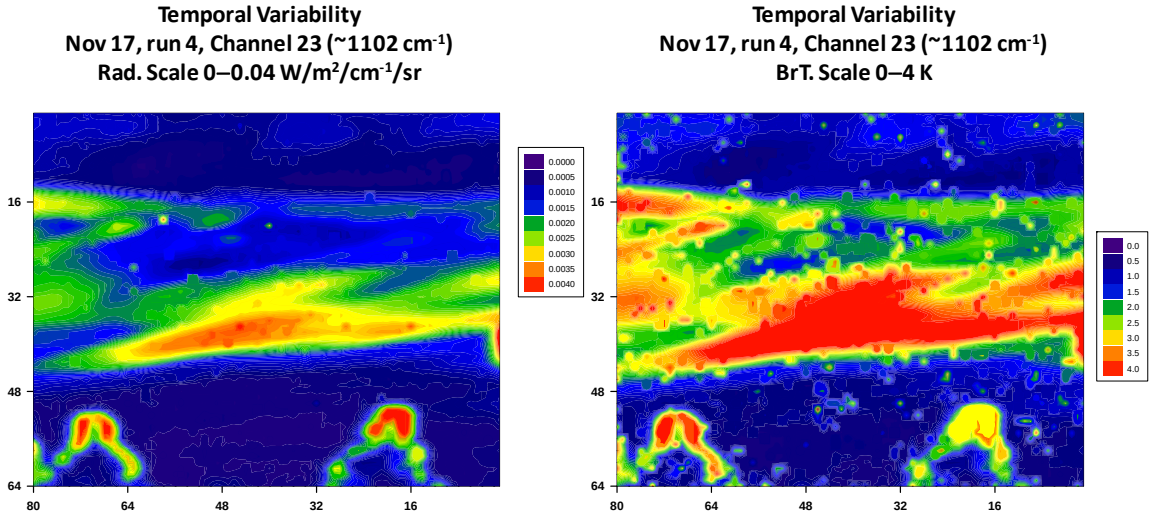

Figure 256. Image of temporal variability for channel #23 in radiance units *(left panel)* and brightness temperature units *(right panel)*, November 17, run4.

The most visible patterns seen in the previous figures are caused by cloud motion across the FOV during time series of measurements; the clouds can be seen in the radiance imagery shown in Figure 257.

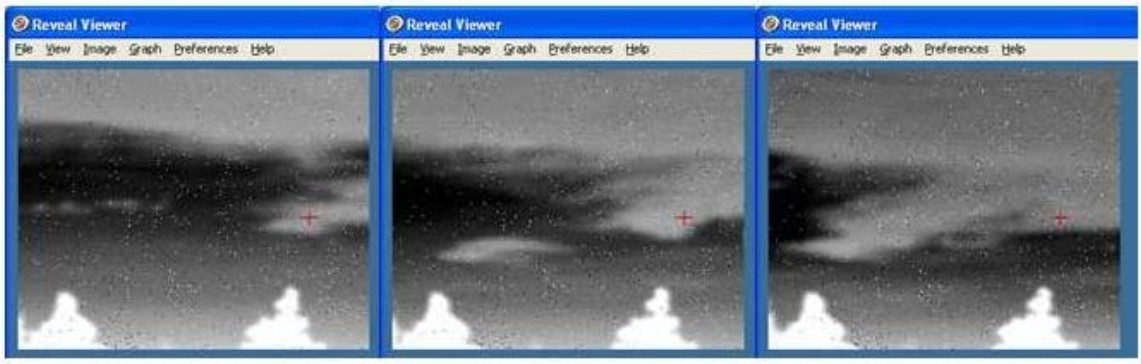

Figure 257. From left to right: channel #5 from the first, middle, and last cubes of data, November 17, run 4.

Despite cloud cover, some interesting features were observed on the edges and in gaps between the clouds. The temporal variability had been computed over all good pixels, including cloudy ones. Therefore, the "Cloud Detecting" methodology for excluding cloudy pixels from the statistical averaging described in the previous section was implemented.

Once the algorithms were implemented and upon closer inspection, the variability seen appears to be due to a thick haze at the horizon. When the haze at the horizon is compared with a clear day, it seems to be thicker and could be leading to the variability; the radiance of the sky for a clear vs. the cloudy day is shown in Figure 258. The box in the left-hand image is roughly the same FOV as the image on the right. The haze in the radiance images and the cloud removal analysis performed lead us to believe that the variability in the imagery was not due to mountain waves.

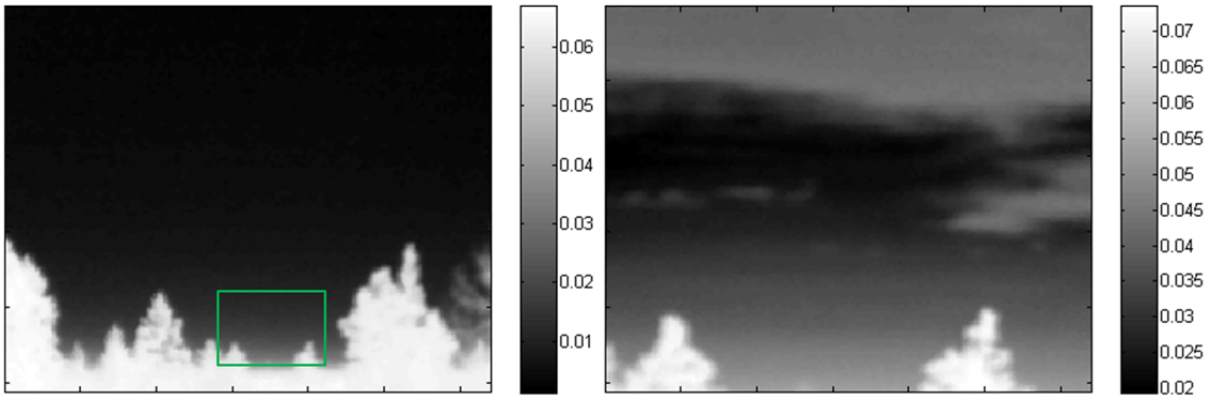

Figure 258. LWIR imagery from November 16 (a clear day) vs. November 17 (a cloudy day). Radiance in W/m^{2}sr, at 926.6 cm^{-1}.

It was determined that November 17, Run 4 data were too cloudy to discern the source of any variability in the scene. Thus, the eighth dataset from November 17 was investigated for any signs of variability next. This dataset was chosen for the following reasons:

1. The webcam imagery from that time frame indicated minimal cloud coverage.

2. There were four PIREPS of turbulence in the vicinity of MRS: three moderate and one light. Two of these moderate reports identified the type of turbulence as mountain wave. The other two reports did not indicate the type.

The data from Run 8 did not show any evidence of turbulence as indicated by variability in the scene. Therefore, two other analyses were performed on these data: gas detection and anomaly detection. These methodologies are described in the following two sections.

5.3.9 Gas Detection Algorithm Analysis

Temperature and moisture variations are associated with mountain waves. In Year 2 of this program, hyperspectral gas detection algorithms were used in an attempt to detect wake vortices based upon the exhaust gases they entrain [20]. The Adaptive Cosine/Coherence Estimator (ACE) had proven to be effective and was thus used to search for water vapor in the MRS dataset. A water vapor spectrum was defined as the target under search.

Radiosonde data from November 18, 00 Z was the closest in time to the Run 8 dataset (beginning at 22:12 UTC, November 17). The water vapor target was modeled at two different altitudes; these were chosen based on radiosondes only and not on the altitude of any PIREPS. The underlying assumption here is that if turbulence PIREPS exist in the general vicinity of MRS then turbulence should exist in our dataset. The Denver radiosonde temperature, relative humidity, and mixing ratio data from November 18, 00Z, are shown in Figure 259.

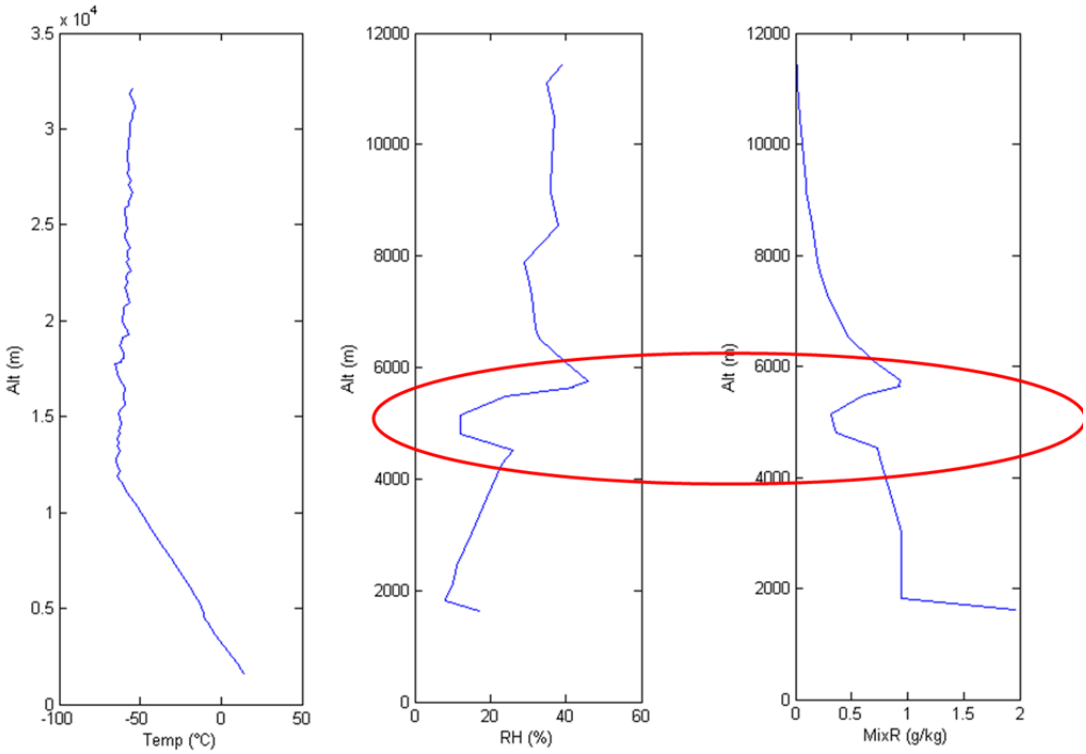

Figure 259. Denver, CO radiosonde data (November 18 2011 00Z). The dry slot is circled in red. Note the different scale on the altitude axis of the temperature plot.

A dry slot can be seen in the relative humidity and mixing ratio data that exist at an altitude between 5141 and 5761 meters. The temperature and pressure were extracted for these altitudes, and then the ACE detector was run on all 1,019 data cubes from Run 8 twice, once with each of the modeled water vapor spectra. The two sets of ACE results for water vapor at each altitude were investigated for possible differences by subtracting the results of the two sets; however, there was no indication of any turbulent event using the algorithms and parameters we tested.

Because of small signals (i.e. water vapor at low temperatures) and atmospheric composition (i.e. searching along a long atmospheric path full of water vapor), the detection of temporal anomalies could be of more use than the ACE detector as a preliminary step. If anomalies are detected, they could be investigated further by then looking at the spectra of the pixels that show anomalous behavior. Two temporal anomaly detectors were investigated and are described in the following section.

5.3.10 Temporal Anomaly Detection Analysis

Temporal anomaly detectors based upon the algorithms developed by Heinz [32] were implemented on the MRS data. The two algorithms are the TSAD (Temporal-Spectral Anomaly Detector) and the TSCD (Temporal-Spectral Covariance Detector). The TSAD is a ratio of anomalies at each time, while the TSCD is a ratio of the covariances at each time. Thus, a TSCD value of about 1 corresponds to the negligible temporal changes in the scene; otherwise, the temporal anomalies may be detected. One of the advantages of the TSCD analysis technique is that it gathers information over the entire measured spectrum.

The spectral data must first be de-meaned, and it should be noted that the global mean is not used. Instead, means are calculated independently from horizontal strips of sky due to varying sky radiance with viewing elevation angle (which was implemented during the wake vortex part of this program). This mean calculation was the only change made to Heinz's algorithms, which were then run on data cubes from Run 8 from November 17. A median filter was applied to all results to accentuate groups of highly scoring pixels while eliminating those with no neighbors.

When the TSAD and TSCD results were made into a movie, a flashing blob appeared near the bottom center of the frame. This corresponds to the approximate center of the entire frame, since the bottom was cut out of analysis (it contained trees). The flashing is not regular in frequency, but occurs every 1, 2, 3, or 4 frames; each frame is separated by 2 seconds in real time. The TSAD showed a similar result. To check if this phenomenon was perhaps an artifact of the Telops measurement, the TSAD and TSCD algorithms were run on another clear dataset from a different day. The dataset chosen was Run 5 from November 18. The artifact is apparent in the Run 5 analysis as well; therefore, we believe it may be an artifact of the measurement and the data might require more pre-processing or different analysis to identify temporal anomalies.

For confirmation of the blinking phenomena observed in the TSCD results, the algorithm was also implemented in a comparison of this algorithm to the temporal variability analysis described in previous sections. Figure 260 shows cross-data cube TSCD images for the first 15 cubes (from 14076 with 14075 to 14090 with 14089), November 17, Run 8. One may note changes in TSCD coefficients for some moments (for example, left center and right bottom panels). We have already reported temporal variability for this run obtained by averaging over all cubes (about 30

min of observations), which is shown in Figure 252 and again in Figure 261 for the November 17, Run 8 run only. In this image, the 100 x 100 pixel red square marks the area of interest for the TSCD analysis.

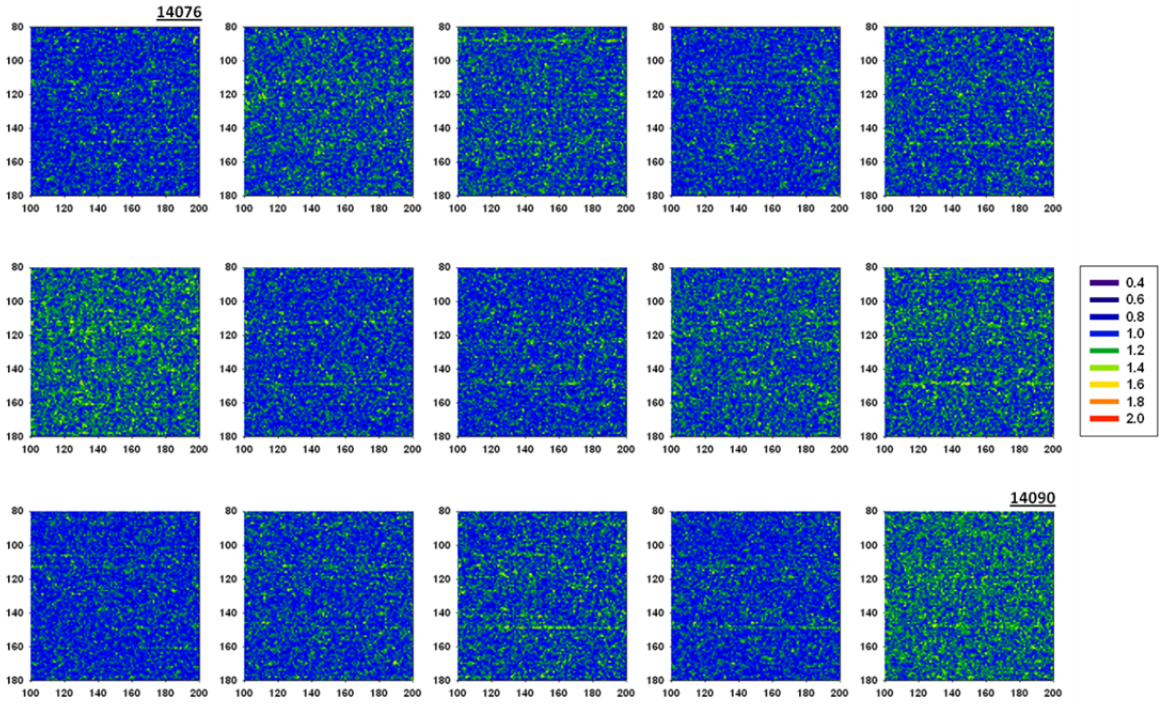

Figure 260. TSCD images for the first 15 data cubes, November 17, Run 8.

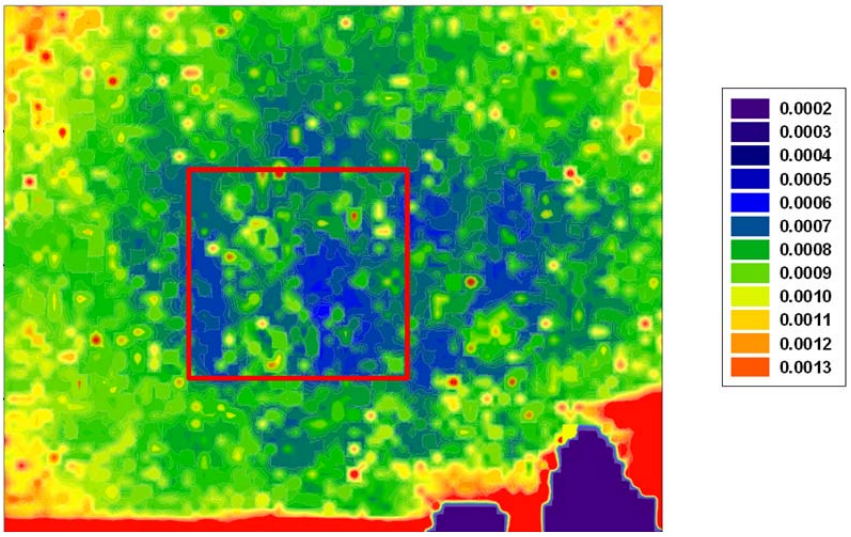

Figure 261. Temporal variability for November 17, Run 8 over all data cubes (~30 min), channel #4. The area of interest is marked with a red square.

Note that in addition to the window size, the temporal variability image in Figure 261 is for an entire 30 minute dataset while the TSCD analysis results shown in Figure 260 were only computed for 2 minutes of observations; also the results shown in Figure 261 were computed for a 4 x 4 pixel average while the results shown in Figure 260 have no spatial averaging. Therefore,

for a direct comparison of the TSCD and the temporal variability methods, we also redid the temporal variability analysis, but for the first 70 data cubes only and with no spatial averaging. The resulting image for the same channel 4, but for 70 data cubes only, is shown in Figure 262.

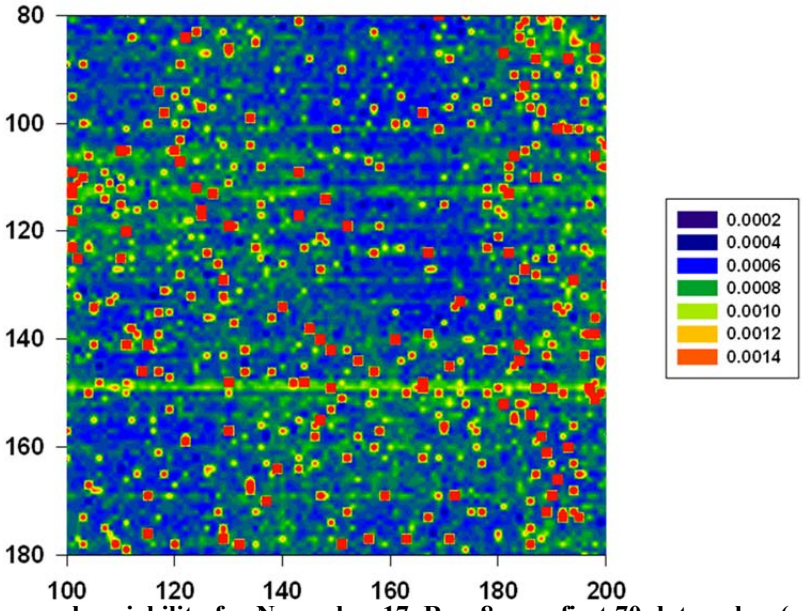

Figure 262. Temporal variability for November 17, Run 8 over first 70 data cubes (~2 min), channel #4.

Red dots are associated with bad pixels (i.e. low responsivity detector elements). The horizontal lines, seen in Figure 262, and also noticeable in Figure 260, are aircraft contrails, as verified by the visual camera images taken during this run. Comparing Figure 261 and Figure 262 indicates that the overall period of time averaged is critical for temporal variability estimates. Also, the TCSD technique yields results similar to those obtained with the original elevation angle normalized pixel radiance temporal standard deviation technique.

The individual frames from November 17, Run 8, did show one interesting result in both the TSAD and TSCD analysis. This anomaly occurred at frame 332 in the Run 8 series, which corresponds to data cubes 14408 and 14409. These images are shown in Figure 263 and Figure 264.

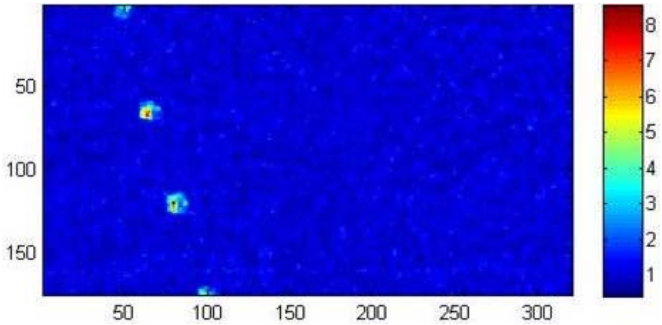

Figure 263. TSAD Result, November 17 Run8, frame 332 in time series.

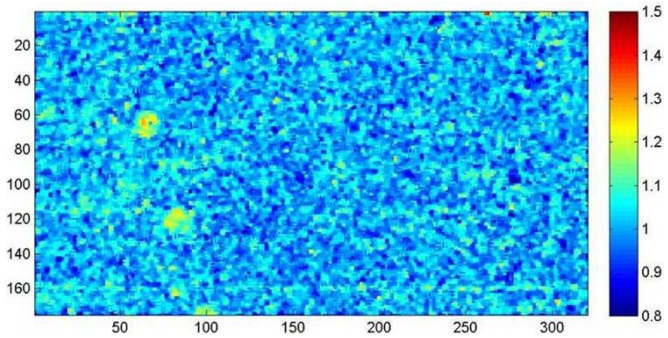

Figure 264. TSCD result, November 17 Run 8, frame 332 in time series.

It is unknown to what the circles correspond. There have been other data in which birds passing through the field of view have been identified, but they appear as streaks. The radiance data at several wavenumbers from this time are shown in Figure 265.

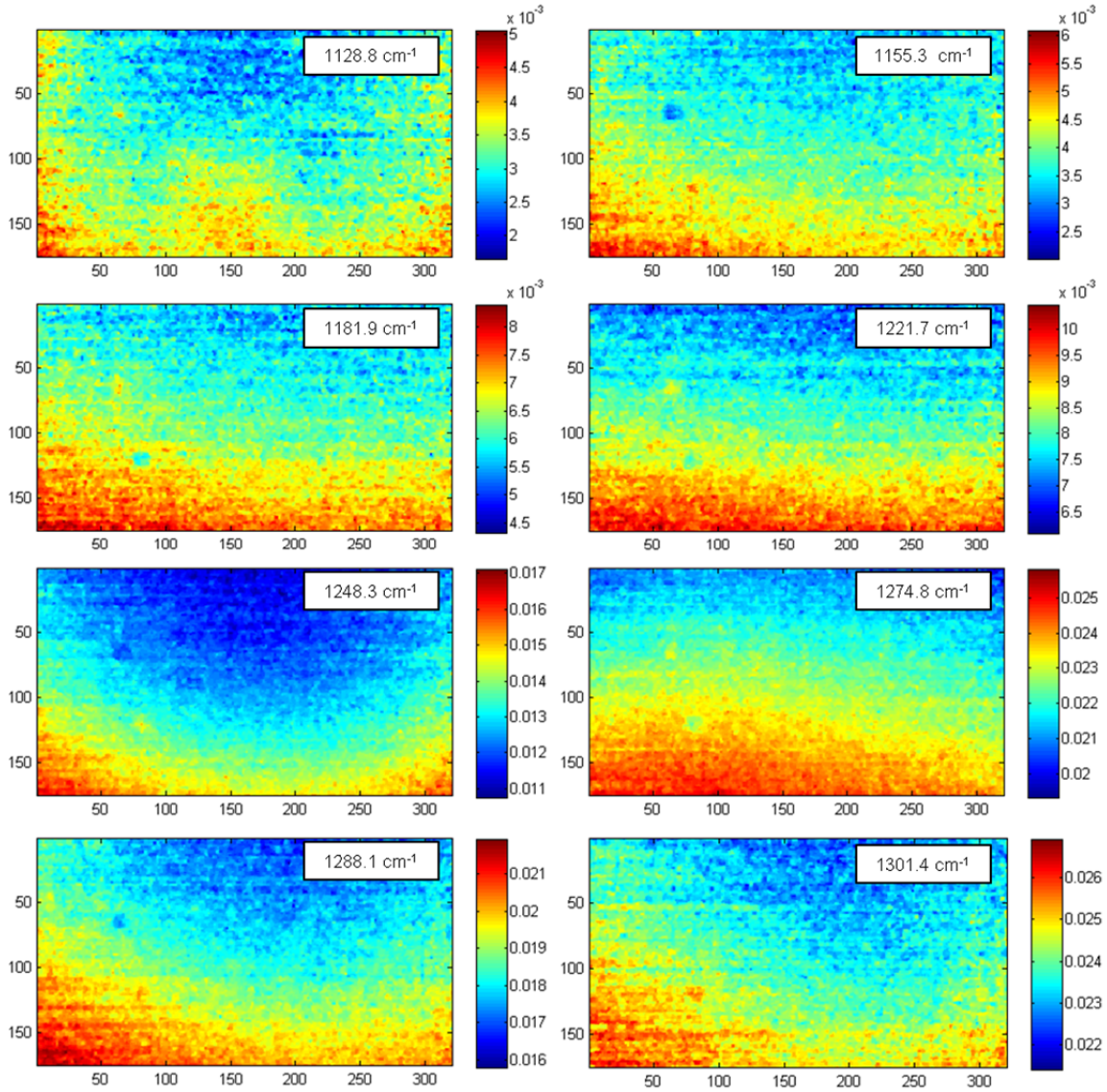

Figure 265. Radiance (W/m^{2}sr) at several wavenumbers from data cube 14408.

The radiance of the spots, at most wavenumbers, is less than the radiance of the rest of the sky at that altitude. For this reason, the fact that they are regularly spaced, and by comparison with the visible webcam movies, we do not believe they are clouds. The spots are not evident at any other wavenumbers.

Attention then shifted to MRS data from November 17, Run 5, because it was relatively cloud free and there were PIREPs in the vicinity during the run. This was also the run for which a WRF model was created. A band-averaged radiance image from the first datacube is shown in Figure 266; this figure shows that there is clear sky in approximately the upper 100 rows of the image. This region of sky stayed relatively clear for the entire 30 minute run. The analysis that follows was done on these top 100 rows.

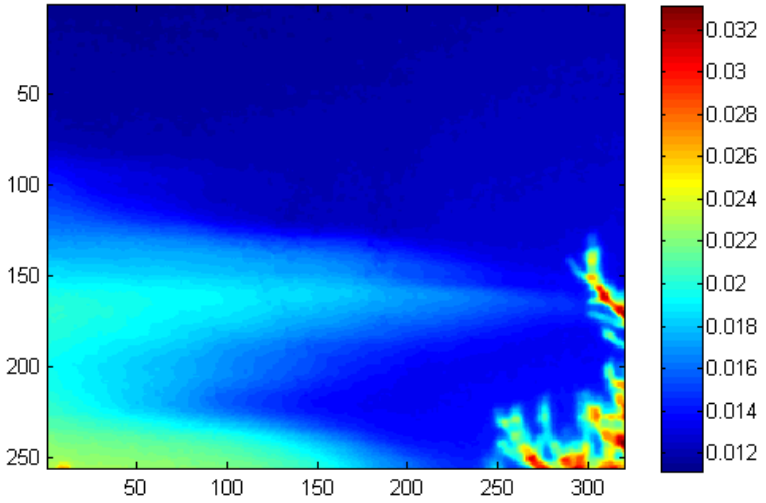

Figure 266. Average radiance of first datacube in Novenber 17, Run 5 set, units W/m^{2}cm^{-1}sr.

Run 5 consists of 1037 Hyper-Cam datacubes; over 20,000 images from this dataset were processed. The radiance at several bands is shown below in Figure 267 for "Datacube 100" in the time series and in Figure 268 for "Datacube 898" in the time series. "Datacube 100" represents results from a randomly selected time that is typical of most of the results. "Datacube 898" represents results of a time that showed anomalous behavior. In these data, the anomalies to which we refer are represented by areas of similarly colored pixels. For a uniform background, such as sky, we would expect the distribution of color to be fairly uniform in azimuth with some random variation for noise in the sensor. Therefore, pixels of similar values that are clustered, or not randomly distributed in the spatial dimension, could be indicative of an anomaly. These clusters, or "blobs", appear in the variability analysis presented in Figure 270 and Figure 274. However; note that all images are scaled into 256 color bins, so even narrow distributions in pixel values in an image will show up as different colors.

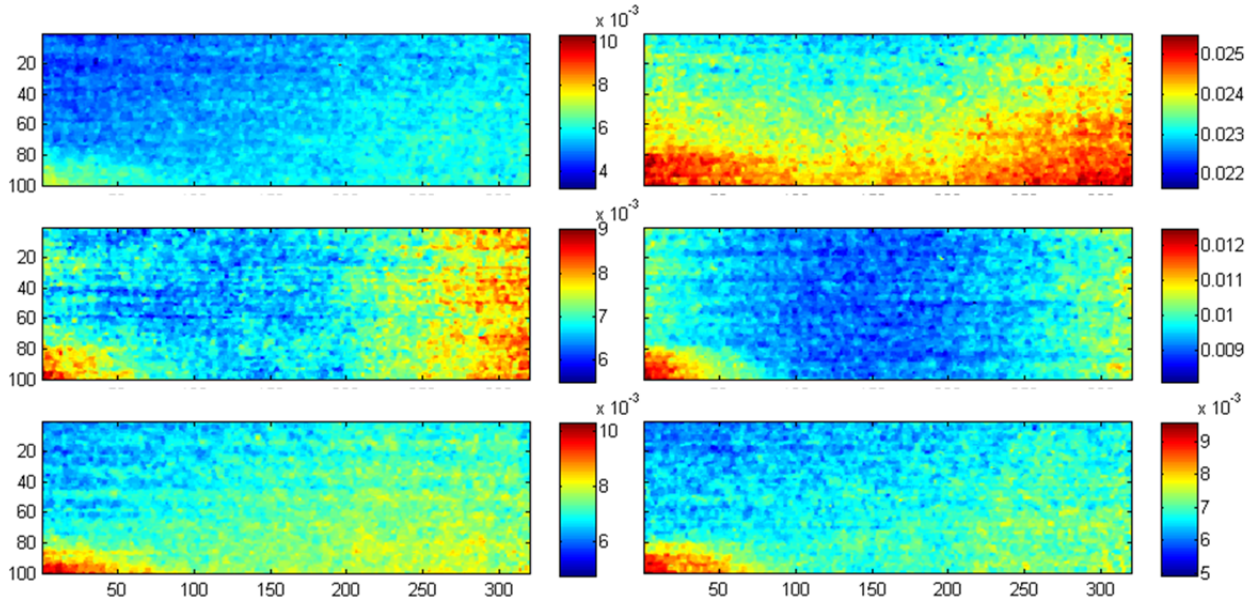

Figure 267. Radiance images at: *Top:* Frame 12 (956.14 cm^{-1}) and Frame 17 (1022.53 cm^{-1}), *Middle:* Frame 15 (995.97 cm^{-1}) and Frame 31 (1208.45 cm^{-1}), and *Bottom:* Frame 21 (1075.65 cm^{-1}) and Frame 22 (1088.93 cm^{-1}). All at time step 100. Radiance units W/m^{2}cm^{-1}sr.

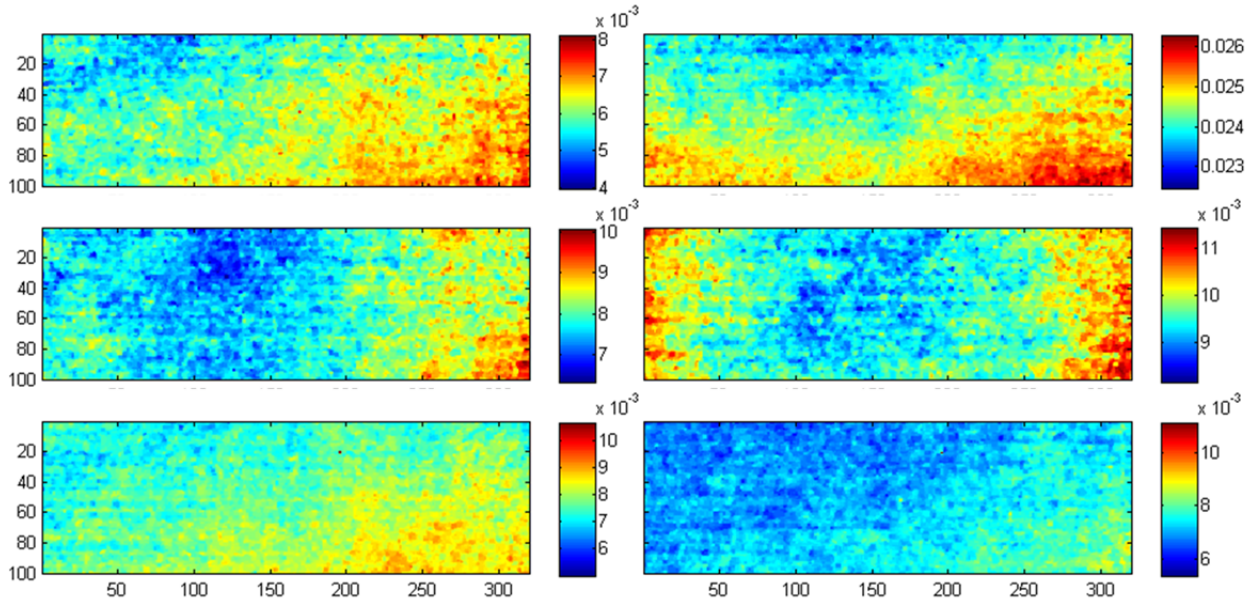

Figure 268. Same as Figure 267, but at time step 898.

The radiance imagery does not show anything very interesting at either time step. Next, we show the difference from the mean for all times for each respective spectral waveband. That is, the mean was calculated at each pixel *(x, y)* for all *t*; the results are shown at $t = 100$ (Figure 269) and $t = 898$ (Figure 270).

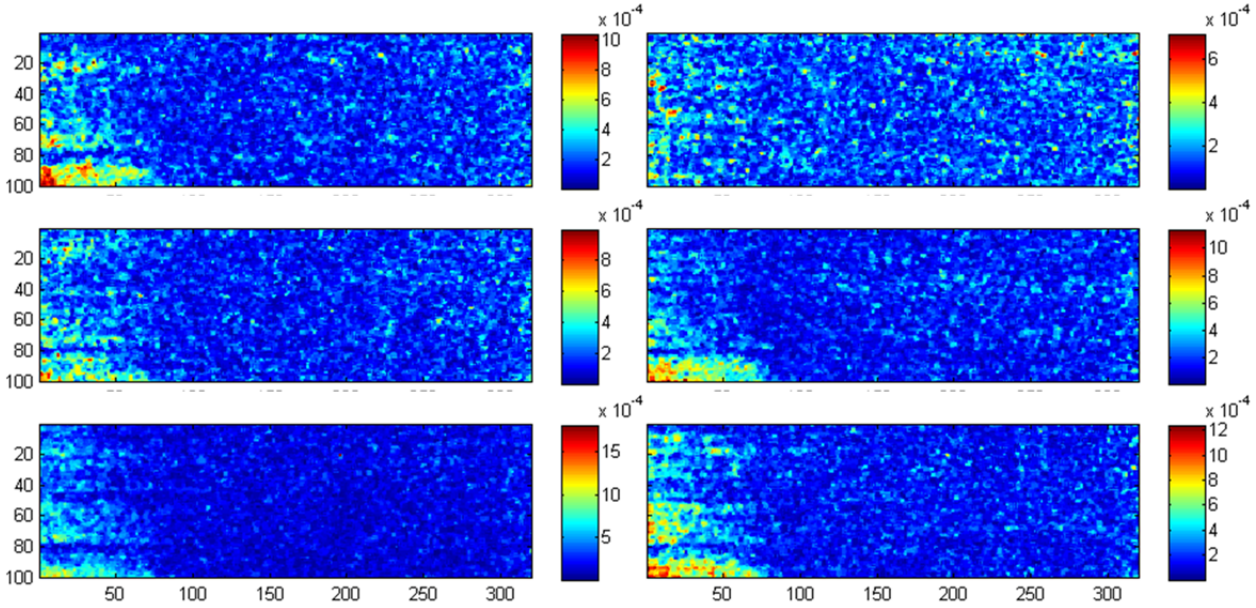

Figure 269. Difference from the mean at: *Top*: Frame 12 (956.14 cm-1) and Frame 17 (1022.53 cm-1), *Middle*: Frame 15 (995.97 cm-1) and Frame 31 (1208.45 cm-1), and *Bottom*: Frame 21 (1075.65 cm-1) and Frame 22 (1088.93 cm-1). All at time step 100. Radiance units W/m^{2}cm^{-1}sr.

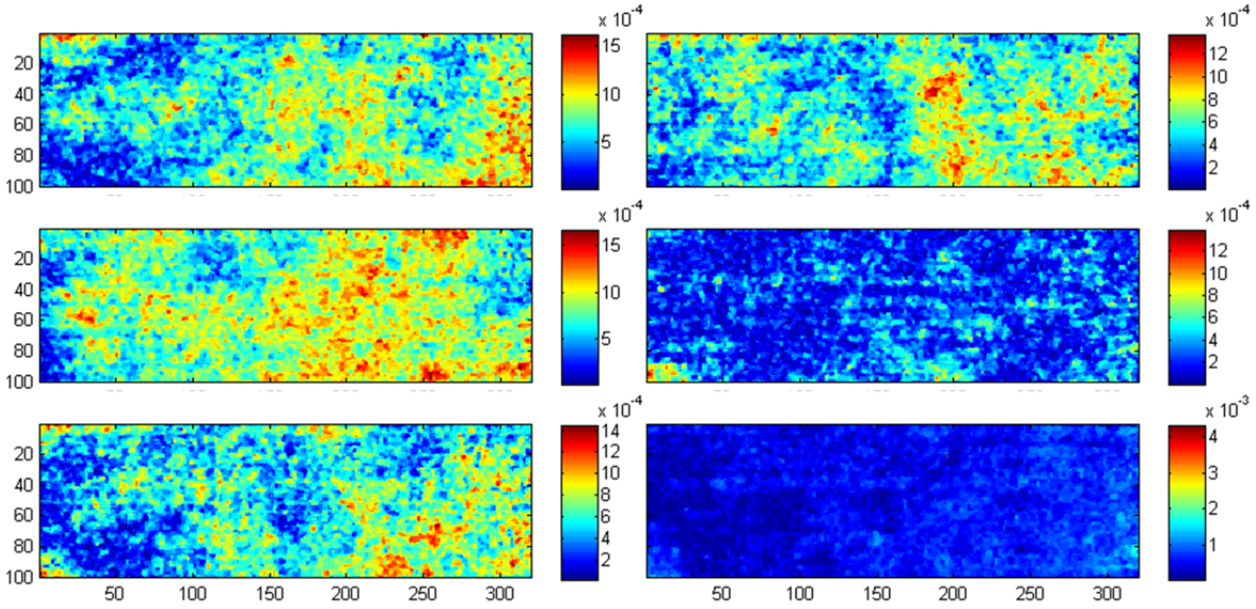

Figure 270. Same as Figure 269, but at time step 898.

Figure 269 and Figure 270 give representations of the time variability at several spectral wavebands in the time series. While no evidence of anomalous behavior is evident at time step 100 (Figure 269), we can begin to see anomalies at time step 898.

The following two figures show simple band ratios at t = 100 (Figure 271) and t = 898 (Figure 272). The top, middle, and bottom panels correspond to the ratios of the radiance images in the top, middle, and bottom panels of Figure 267 and Figure 268, respectively.

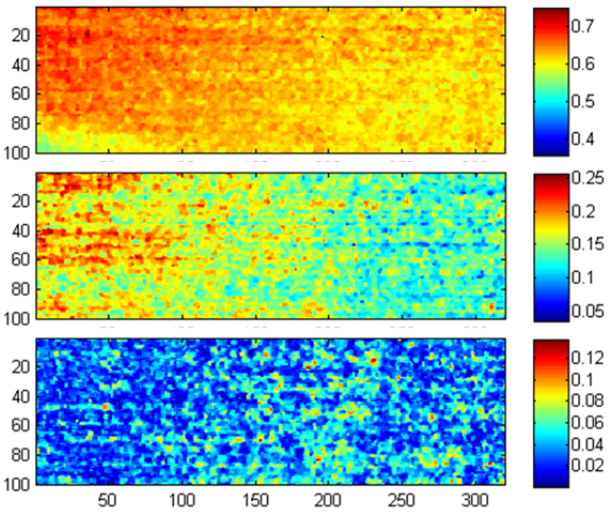

Figure 271. Ratio of radiances for bands: *Top*: Frame 12 (956.14 cm-1) and Frame 17 (1022.53 cm-1), *Middle*: Frame 15 (995.97 cm-1) and Frame 31 (1208.45 cm-1), and *Bottom*: Frame 21 (1075.65 cm-1) and Frame 22 (1088.93 cm-1). All at time step 100. Radiance units W/m2cm-1sr.

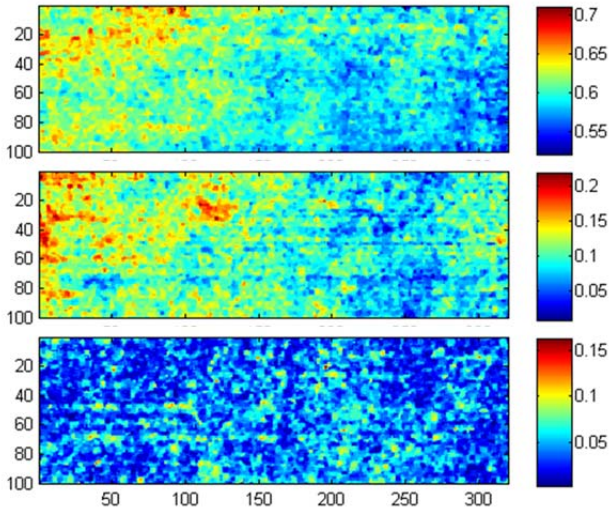

Figure 272. Same as Figure 271, but for time step 898.

Finally, the following two figures show the difference from the mean of the band ratios at t = 100 (Figure 273) and t = 898 (Figure 274).

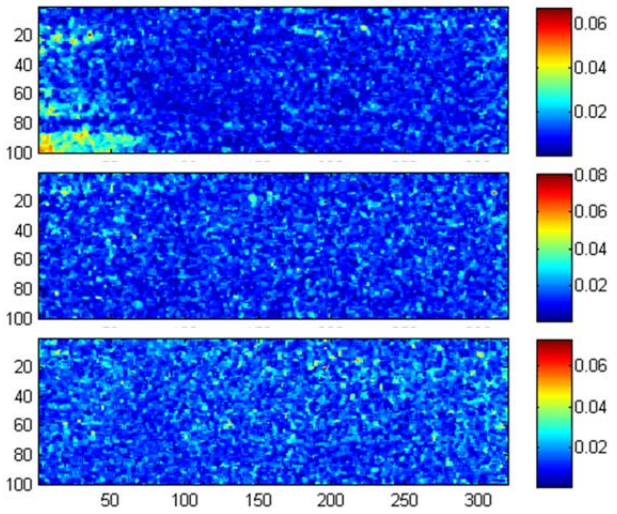

Figure 273. Difference from mean of the band ratios shown in Figure 271.

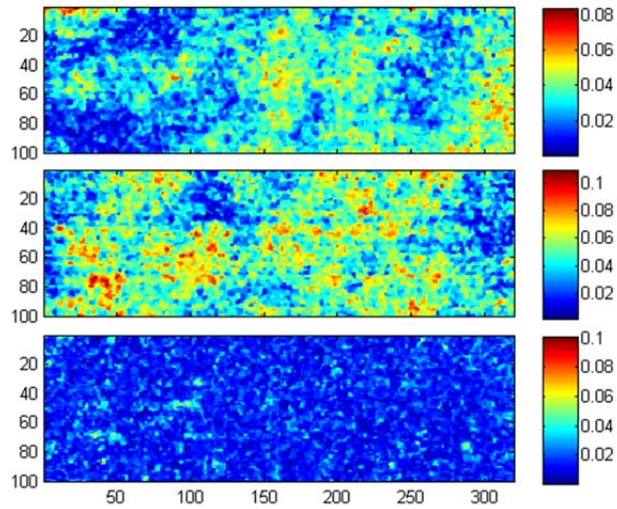

Figure 274. Difference from mean of the band ratios shown in Figure 272.

While the figures shown above indicate there is something anomalous at time step 898, the magnitude of the variability does not appear to be significant. These anomalies could be an artifact of a bad calibration or corrupted data and do not necessarily indicate the presence of turbulence. These anomalies do not appear at time steps 897 or 899.

Note that we do not believe the blobs that show up in the analysis are related to the amoeba patterns we have described in previous reports. The amoeba patterns are apparent in uncalibrated data because they represent the raw response on the detector. An interferogram image from the datacube at time step 898 is shown in Figure 275; note that the raw signal "amoebas" do not seem occur at the same locations as the anomaly "blobs."

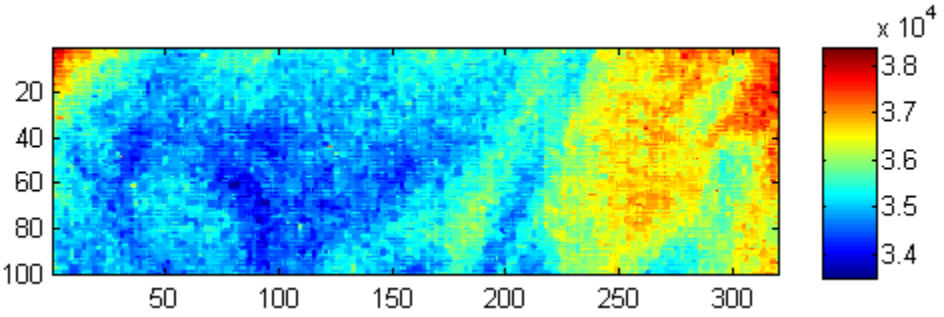

Figure 275. Interferogram image from the datacube at time step 898. The image is a "slice" of the interferogram at OPD position 100 (near center burst). The color scale is in raw intensity counts.

5.4 Mountain Research Station Data: Simulated vs. Observed

Radiance signals due to mountain lee wave turbulence were simulated for comparison with actual measurements obtained during the MRS field experiment in November 2011. In addition, the viewing geometry and spectral resolution of the simulations were chosen to match as closely as possible to the actual conditions of the measurements. The simulated radiances were processed the same way as measured ones, i.e. temporal variability of the signal was estimated.

5.4.1 LBLRTM Simulation Using Denver Radiosonde Data

Fourteen data cubes from the November 17, 2011 measurements were analyzed. That day of observation was clear and very windy, and pilot reports revealed turbulent conditions during the observation time. The analysis had two main goals:

1. To compare observed data with simulated radiances;
2. To visualize observed data after processing, aiming for evidence of the mountain lee wave turbulence.

The 14 Hyper-Cam data cubes each consist of 256 vertical by 320 horizontal spatial pixels, for each of which the radiance had been measured in 41 channels from ~810 cm^{-1} to ~1341 cm^{-1} with 16 cm^{-1} spectral resolution. The first and last three channels were excluded from the analysis since they suffer from rapid fall-off of detector responsivity. The bottom 96 rows of each image were excluded from the analysis too, because nearby trees were in the instrument's field of view (FOV). Thus, the processed data cubes contain a total of 160 x 320 x 35 x 14 radiance spectra. The total time period of processed observations was about one minute.

The angular size of the FOV was assumed to be 20° x 25° in vertical/horizontal directions, respectively, which corresponds to approximately 0.078° angular size for the image pixels. The bottom row had an elevation angle 0° above the horizon. Figure 276 shows the observation geometry as FOV size in vertical/horizontal projections as a function of the distance from the point of observation. The MRS altitude is ~9,500 feet.

In order to validate the radiometric calibration of the observed data, comparisons were made with LBLRTM simulations. The closest radiosonde temperature and water vapor profiles (Denver) for November 17, 12Z, and November 18, 00Z, were averaged to approximate the observation time of about 1 PM MST. Concentrations of other gases needed for the radiative calculations were

taken from the US-1976 standard atmosphere, excepting CO_2, which was set to 385 ppm. The resulting radiosonde temperature and water vapor profiles used in the simulations are shown in Figure 277. LBLRTM simulations were performed for ten elevation angles ranging from ~8° to 19.5° with an increment of ~1.25°, which correspond to Hyper-Cam measurement rows 97–256. For the comparison of observed and calculated radiances, 16 consecutive rows from the actual observations are merged into a single bin, starting from row 97 (i.e. exactly the piece of data picked for analysis). The ten radiances simulated using LBLRTM were compared with averages over the same 16-row-wide-bin observed radiances.

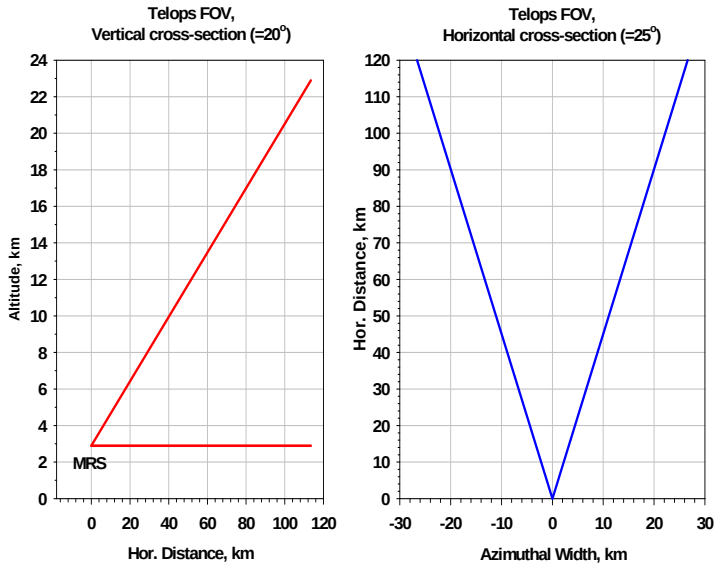

Figure 276. The Hyper-Cam observation geometry, November 17, 2011.

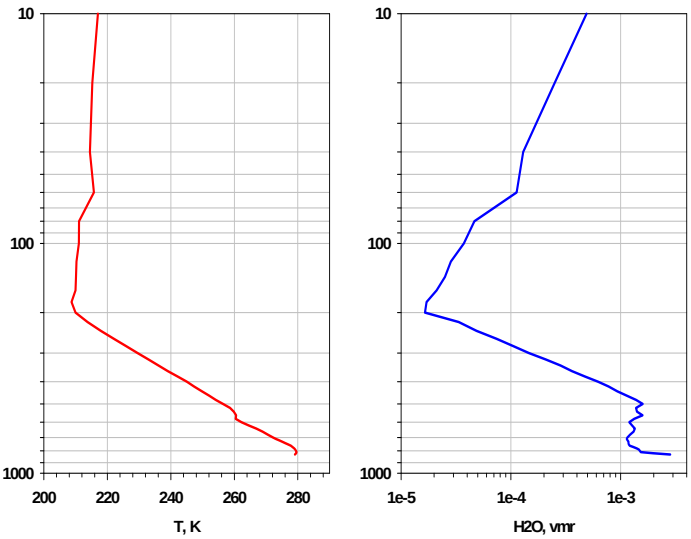

Figure 277. The atmospheric state, averaged over the two closest times, from the closest radiosonde launch site (Denver).

The result of this comparison (together with variability of observed data over the corresponding means at 16 row-bins) is presented in Figure 278. One can note the relative agreement in the spectral shape of the observed and simulated radiances, although there are many regions

(e.g. 960 cm^{-1}, 1020 cm^{-1}, 1105 cm^{-1}, 1260 cm^{-1}, and 1300 cm^{-1}) where there is considerable disagreement in the spectral variation of the observed and calculated radiance spectra. Also, there is considerable disagreement in the absolute magnitude of the radiances with the observed radiances being generally higher than the simulated radiances, except in the water vapor absorption region near 1300 cm^{-1}. These systematic differences may be due to a combination of absolute calibration uncertainty and the use of an average Denver radiosonde to represent the atmospheric state at the time of the observations. The disagreement in absolute values for the O_3 band (~1050 cm^{-1} centered) is explained by using the US-1976 standard ozone profile, since no in-situ observations of ozone were available.

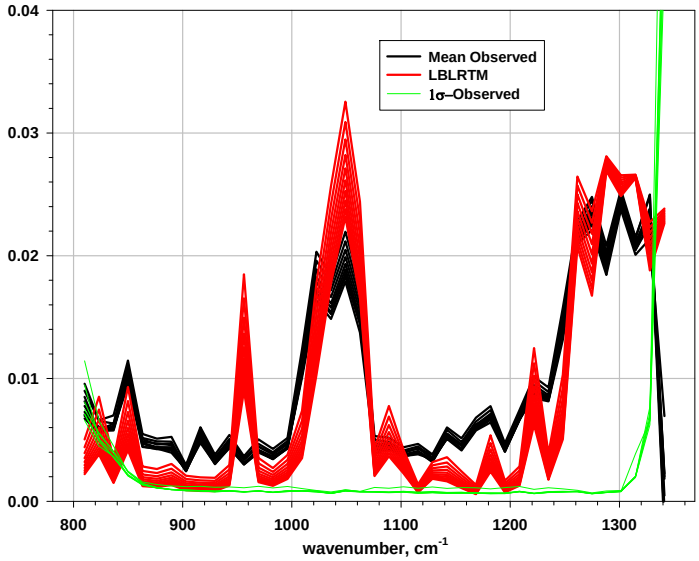

Figure 278. Comparison of the mean observed *(black)*, LBLRTM-simulated *(red)*, and the standard deviation *(green)* of the observed radiances around their means for ten elevation angles.

5.4.2 FLI-FM Simulation with March 6, 2004 WRF Model

For the first comparison, highly spatial and temporal resolved data were not available; therefore, atmospheric states obtained with a WRF model for a lee wave turbulent event on March 6, 2004 (described in Section 5.1.4) were used. As with previous simulations, the arbitrary "center" of turbulence was assumed to be located approximately at 39.5°N, 105.0°W. Because of lack of time resolution, temporal variability of the signal was created by changing the observer point of view (i.e. different parts of WRF data cube are then observed for each observer location). For the simulations, the observer altitude was equal to 2.75 km (~MRS altitude), the observer latitude was fixed at 39.5°N, and the observer longitude was variable in range from 105.5075°W to 105.0°W with a 0.07025° increment. Thus, simulations were performed for eight locations total, with the distance to the "center" of turbulence varying from ~45 km to 0 km with an increment of about 6.5 km. However, because lee waves are *atmospheric standing waves*, it is hard to define the time increment that corresponds to the observer position increment used.

The instrument field of view was assumed to be 5° in both horizontal and vertical directions, with 15 x 15 pixels. The central pixel for all locations had an elevation angle of 13.5° and its azimuthal direction was directly to the east, towards the turbulence center. Thus, 15 x 15 x 8 = 1800 spectra total were computed and combined into eight data cubes, similar to Hyper-Cam output. The 35

channel radiances for a Hyper-Cam 16 cm^{-1} resolution datacube were obtained by boxcar averaging the FLI-FM2 high resolution unapodized spectra in the range ~800-1300 cm^{-1}. The three first and three last Hyper-Cam channels (there are 41 total) are not considered here because it was found earlier that they suffer from a wrap-around effect of the spectral convolution.

Figure 279 and Figure 280 show the mean radiance and its standard deviation for the central pixel (8, 8) of the image, obtained by averaging over eight different observer locations (considered to be equivalent to eight time moments) in radiance and brightness temperature units.

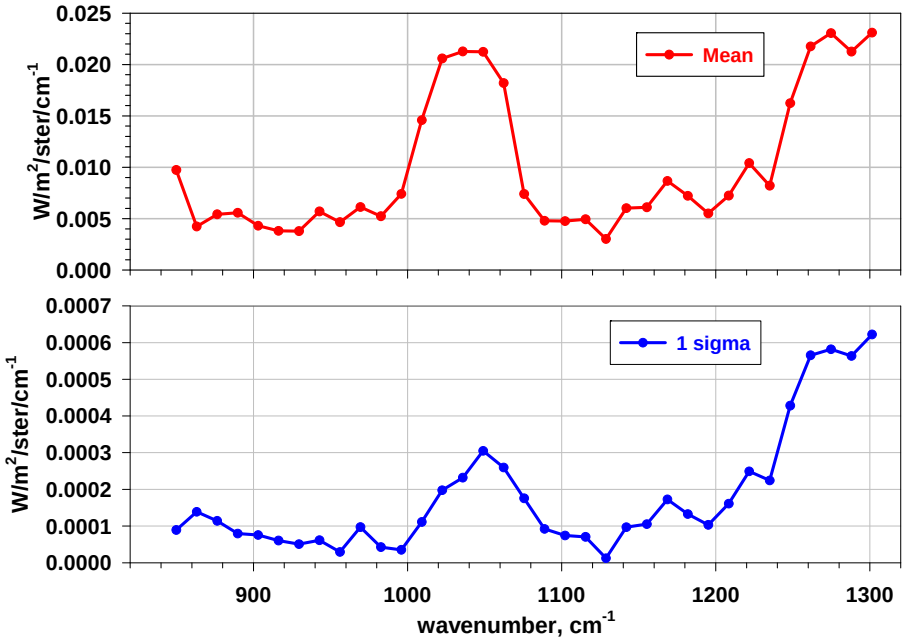

Figure 279. Mean radiance and its standard deviation for the central image pixel, obtained by averaging over 8 observer locations.

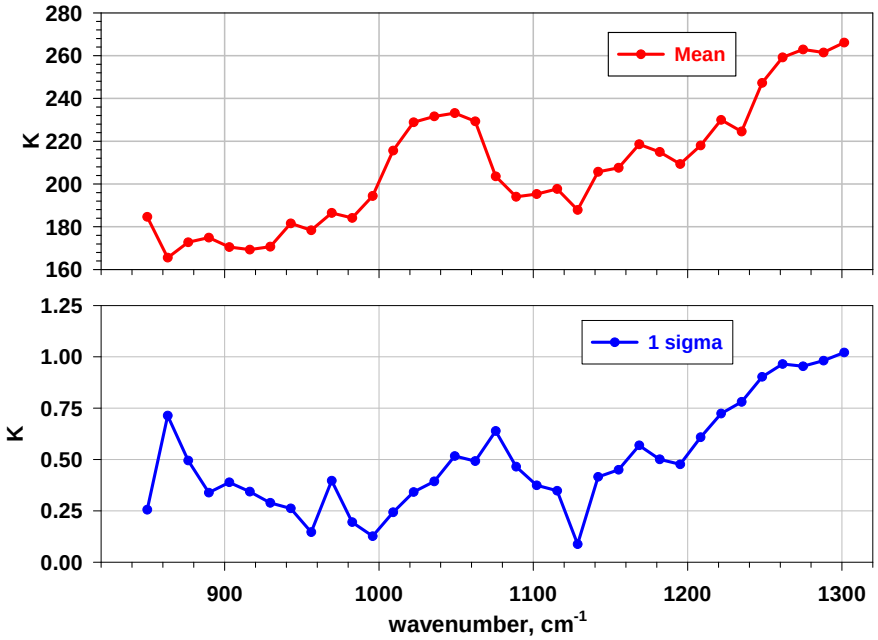

Figure 280. The same as Figure 279, but in brightness temperature units.

The highest signal and variability are observed in the ozone band 1000–1080 cm^{-1} and water channels $\nu > 1250$ cm^{-1}. While high variation in water channels is expected and not surprising, the variations at the ozone band need some additional comments. Since ozone is a fixed gas in FLI-FM2, variations there can be explained by atmospheric temperature variations only. Thus, simulations show significant sensitivity (i.e. a standard deviation greater than the instrument noise: 0.16 K BTD at 300K, see Appendix A) to temperature and water vapor turbulence.

Figure 281 presents the spectral temporal variability of simulated radiances in comparison with those obtained from actual measurements. The temporal variability was estimated the same way for simulated and measured data (i.e. by averaging over all image pixels and observer locations, in order to define the most sensitive channels). In general, the simulated radiances display less variability than the measured ones. This is expected since the simulated radiances are free of measurement noise and cloud contamination. As can be seen, the spectral features of the atmospheric turbulence are masked by the instrument and cloud noise, except possibly for the water channels $\nu > 1250$ cm^{-1}. The masking of turbulence signals by instrument and cloud noise is most noticeable for the ozone absorption band (1000–1100 cm^{-1}). The fact that November 16, Run 1 (black curve) has a much larger temporal variability than the other runs shown, except for in the central region of the ozone absorption band, is probably the result of larger cloud contamination in this run than for in the others runs shown in Figure 281. The enhanced absorption by ozone in the path between the instrument and the cloud reduces the instrument's sensitivity to cloud variability in this spectral region, causing the decrease in radiance variability within this band, as shown in Figure 281.

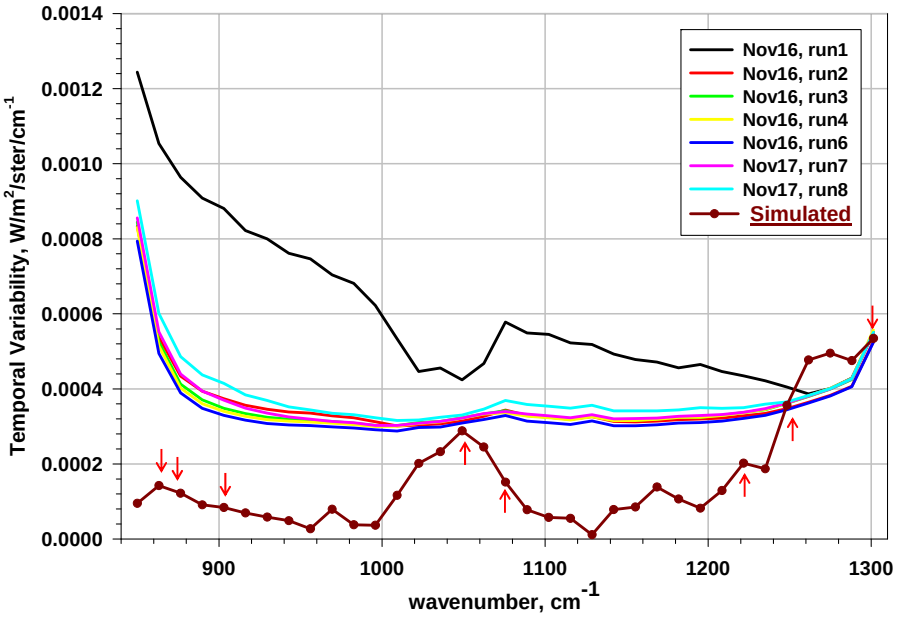

Figure 281. The temporal variability of simulated radiances (dark red curve with symbols) in comparison with that obtained from observations of several runs. Red arrows indicate channels for which full-size images of temporal variability are shown on the next figure.

Figure 282 presents full-size images of temporal variability of the simulated radiances for the channels marked with red arrows in Figure 281, which show the highest signal in the brightness temperature domain. The signal is in the 0.5–0.8 K range, as obtained from simulations.

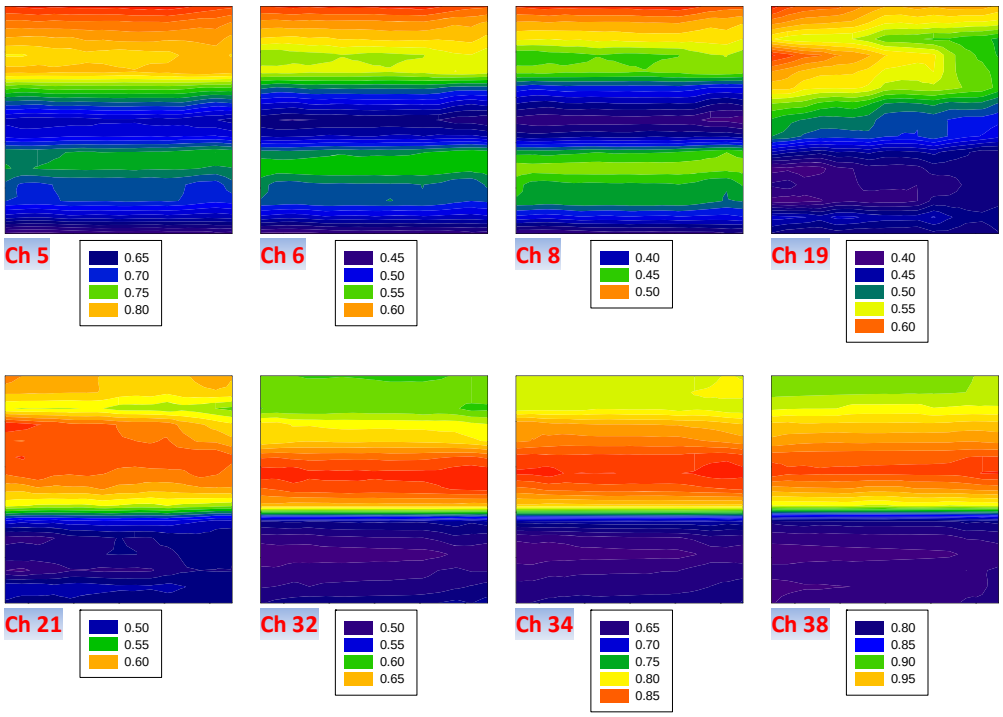

Figure 282. Full-size images of the signal temporal variability, obtained from simulations (brightness temperature units, K). Note that color scale is slightly different for different channels.

5.4.3 FLI-FM2 Simulations with November 17, 2011 WRF Model

Because the simulations described in the previous sections were modeled from either incomplete or incorrect meteorological data, it was determined it would be worthwhile to create a WRF model for the exact time and location of the MRS test for comparison with the measured Hyper-Cam data. November 17, 2011 was a day in which lenticular clouds were present and PIREPs documented mountain wave turbulence. The optimum time and location of the WRF model were identified by the following criteria:

1. Relatively cloud-free sky in Telops Hyper-Cam field of view for measurements recorded during that time.

2. Turbulence PIREPs reported in general vicinity of viewing direction during time of run.

Three runs on November 17 were cloud free; the PIREPS during these three runs and field of view of the sensor were plotted in Google Earth. Figure 283 below shows a view of Colorado with the MRS test observation point and PIREPs that were reported during the time of each of the three runs. Only the FOV of the Hyper-Cam during Run 5 is shown on this plot because it was the only run in which the sensor was aiming in the direction of a PIREP.

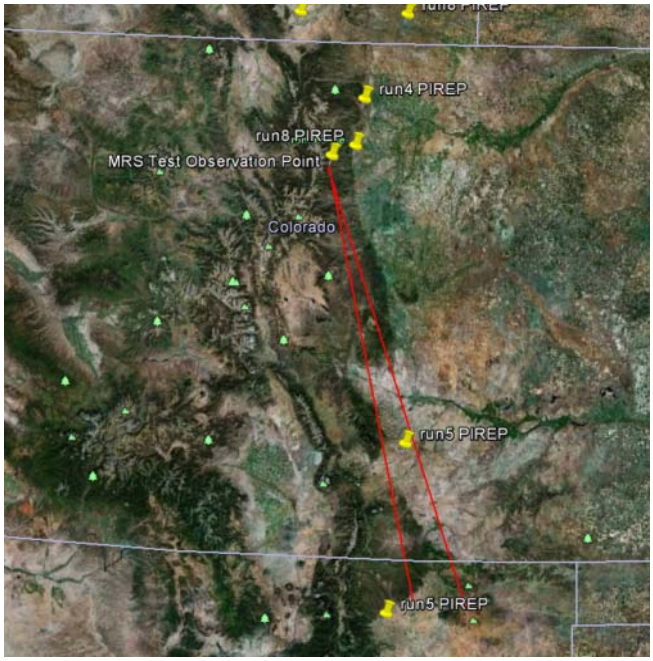

Figure 283. Google Earth view of Colorado with PIREPs (*yellow markers*) and Hyper-Cam FOV (*red lines*) plotted.

5.4.3.1 New WRF Model: November 17, 2011

The WRF configuration was identical to that described in Frehlich et al [33]. An example set of figures showing various atmospheric parameters at 20:00 UTC the day of the data collection is displayed in the following charts.

To understand how the modeled data are represented spatially, consider only the east-west red band drawn in Figure 285 and its associated figures (Figure 286 to Figure 292). The red line, drawn at an altitude of 12 km, forms an upper altitude bound on the vertical plane running east-west as the line shows. It is this 'window' or plane that is depicted in Figure 286 through Figure 292. Each of those charts contains modeled data up to 12 km ASL along the east-west path, with the MRS test site roughly in the middle of the east-west (and later, north-south) red band. In each 'ground-level' plot showing the Rocky Mountains in profile, the MRS site is marked with a blue cross. The elevation angles of the Hyper-Cam are likewise marked by blue lines. An important note is that the FOV azimuthal angles are not depicted in the modeled data charts (because they lie outside of the image plane). Analysis of the WRF model at each 15-minute interval in the set of five received reveals little difference in most atmospheric parameters over this 75-minute period, indicating the usefulness of this model for all data collected on the 17th.

The modeled data shown above and the other datasets produced by STAR apply to specific latitude or longitude bands, as indicated in Figure 285 and Figure 293. In addition to these charts GTRI has received grid-point data permitting the creating of similar models along any line-of-sight across Colorado's geography. These grid-points allowed GTRI to create a map of weather conditions for azimuth lines bisecting the Hyper-Cam FOV during the three runs depicted in Figure 283. These modeled data, after identification and summation, help indicate the expected spatial radiance patterns in our collected dataset.

Figure 294 (temperature and wind vectors), Figure 296 (relative humidity), and Figure 298 (graphical turbulence) from the north-south line-of-sight set are most useful for informing expectations as we continued to process the data collected that day. High winds and temperature variations created a dynamic, highly varying sky background. Relative humidity variations are traceable using H_2O vapor detection algorithms, and the predicted turbulence of Figure 298 helps us understand when the varying atmospheric conditions plotted conspire to create the desired effect.

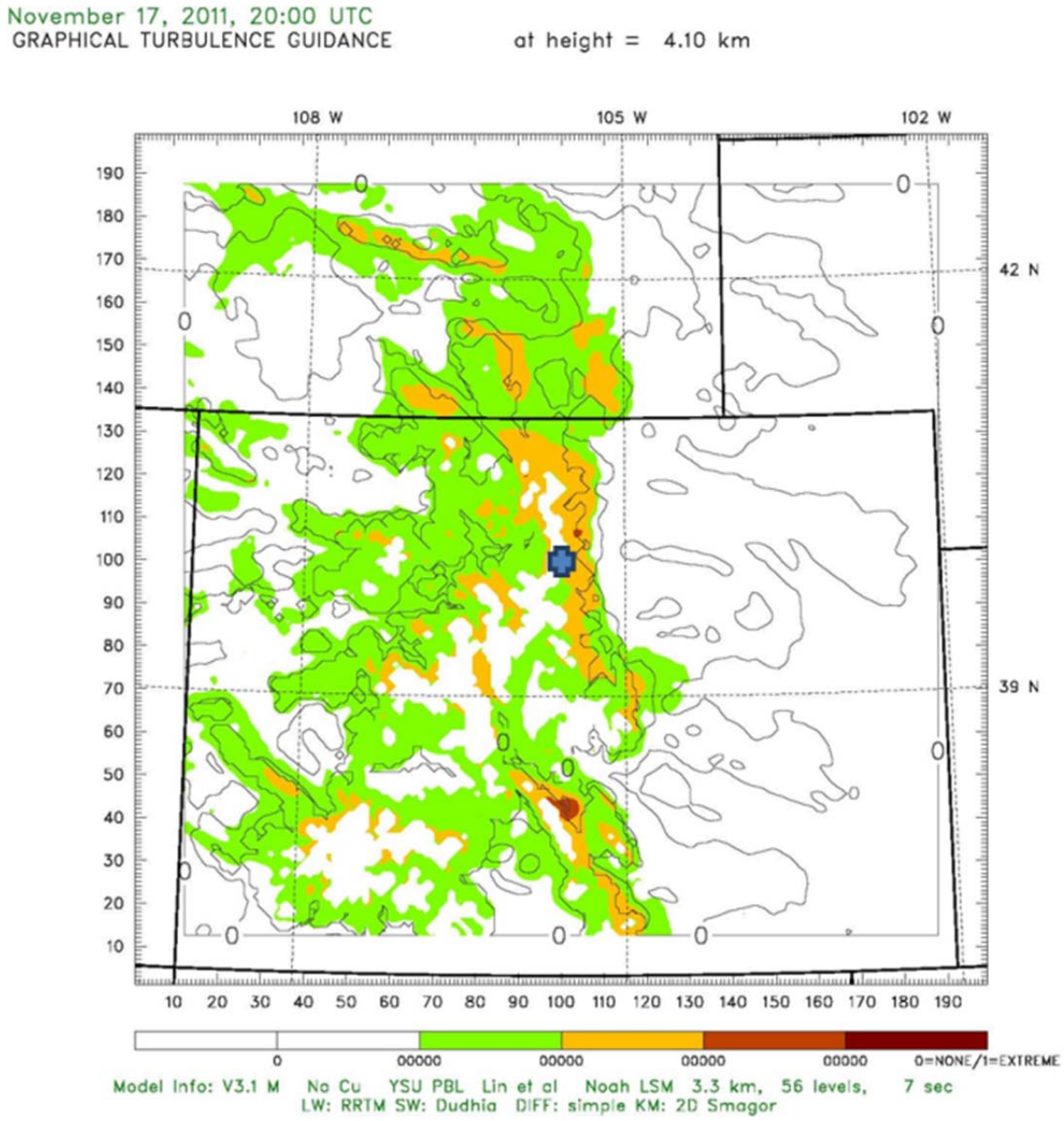

Figure 284. In this map of turbulence at 4.1km elevation, the blue cross marks the MRS test location.

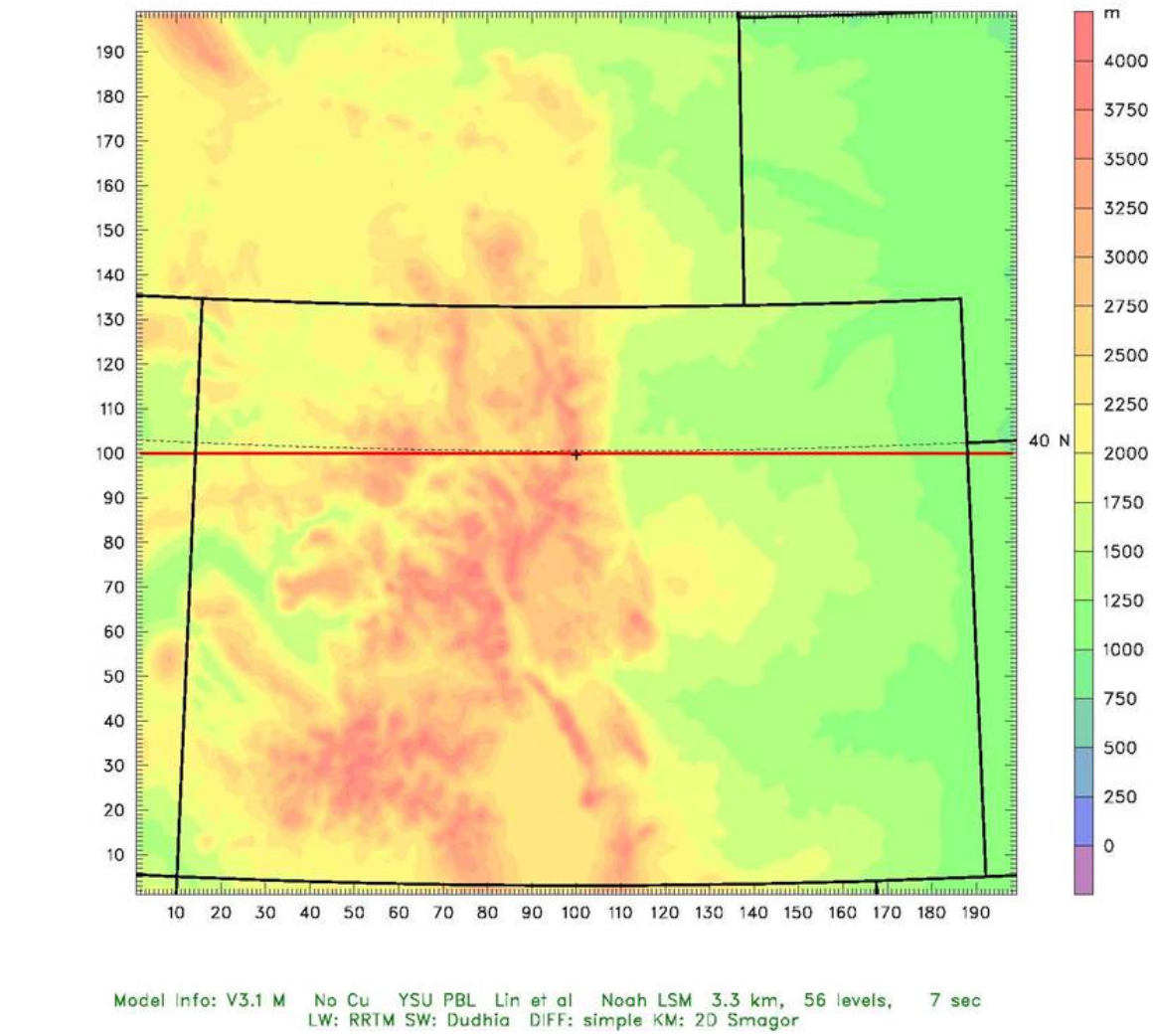

Figure 285. The red East-West line indicates the line along which are modeled the atmospheric conditions in the following figures.

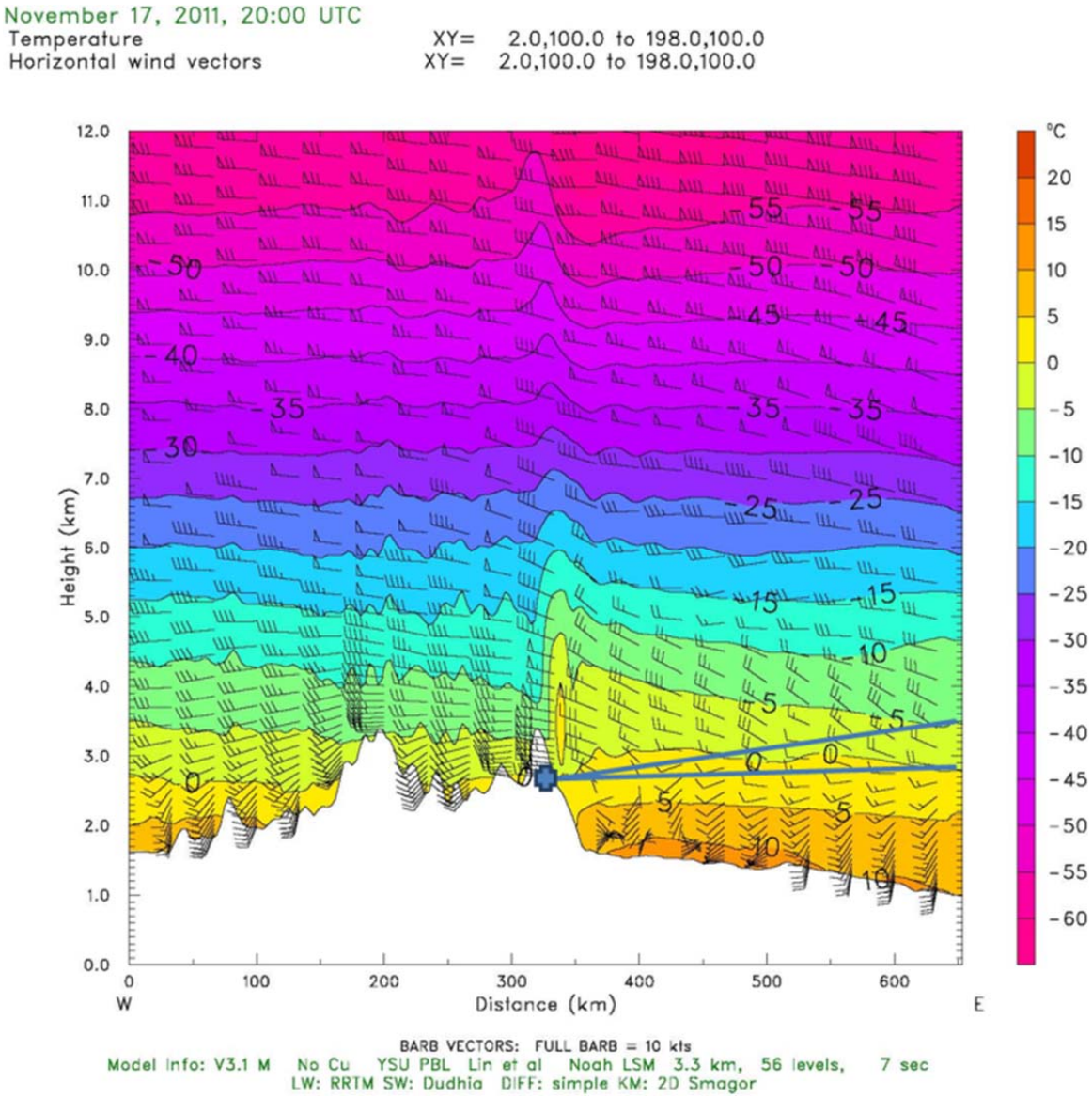

Figure 286. In this figure the blue cross marks the MRS test location and the elevation lines indicate the upper and lower elevation angles in the Hyper-Cam FOV of Run 5 collected on November 17th.

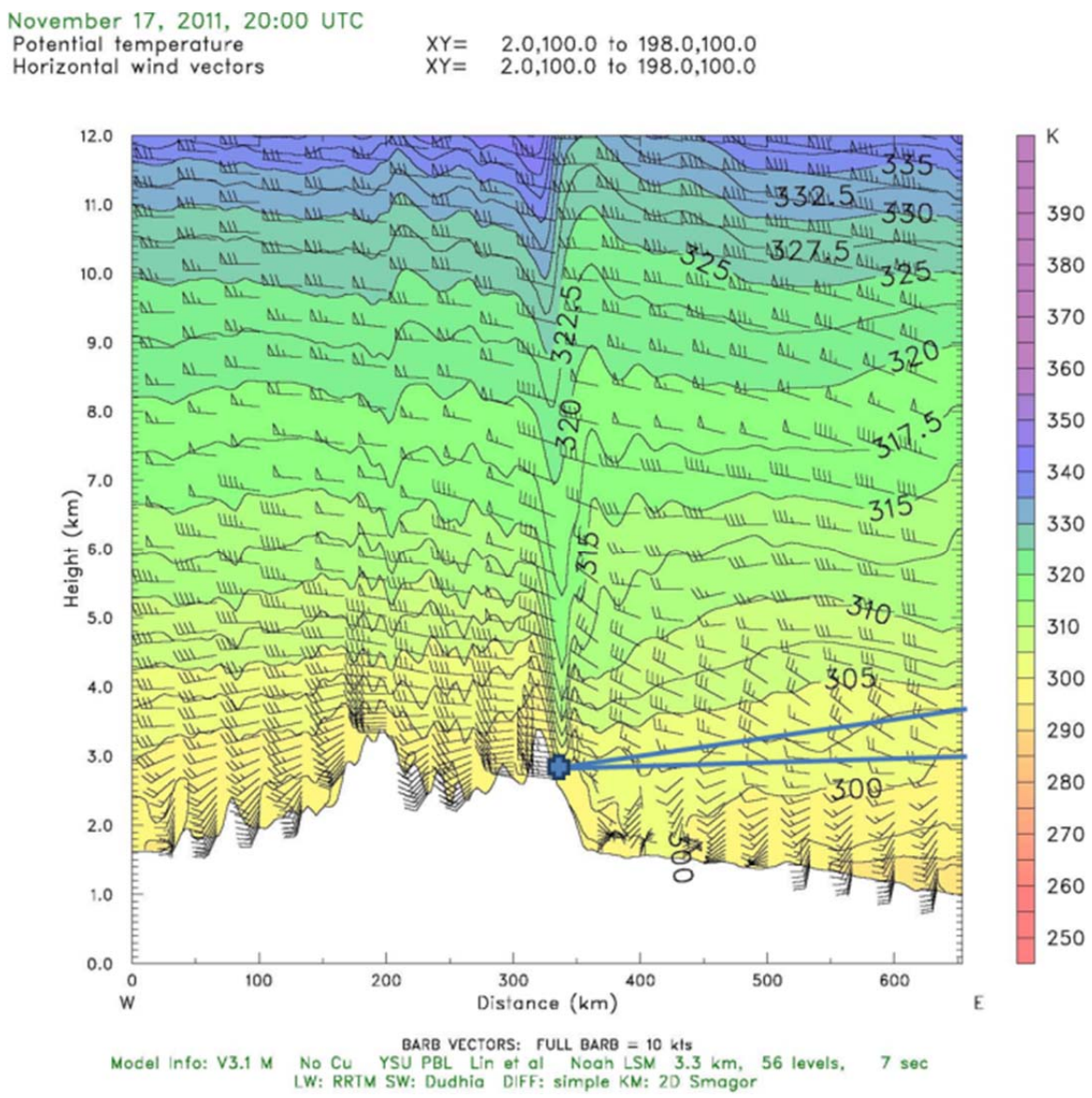

Figure 287. Potential temperature for the same East-West viewing line.

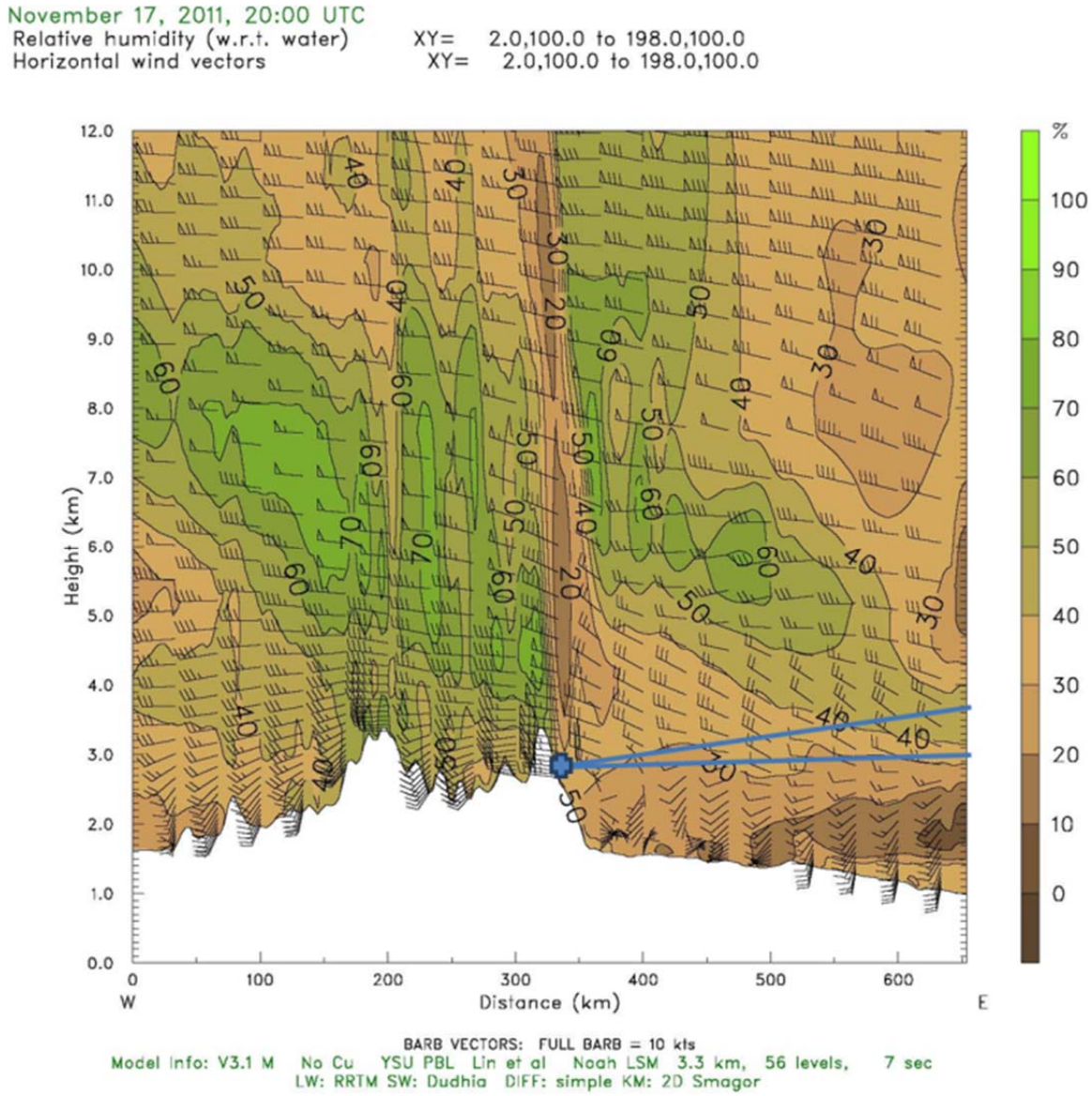

Figure 288. Relative humidity for the same East-West viewing line.

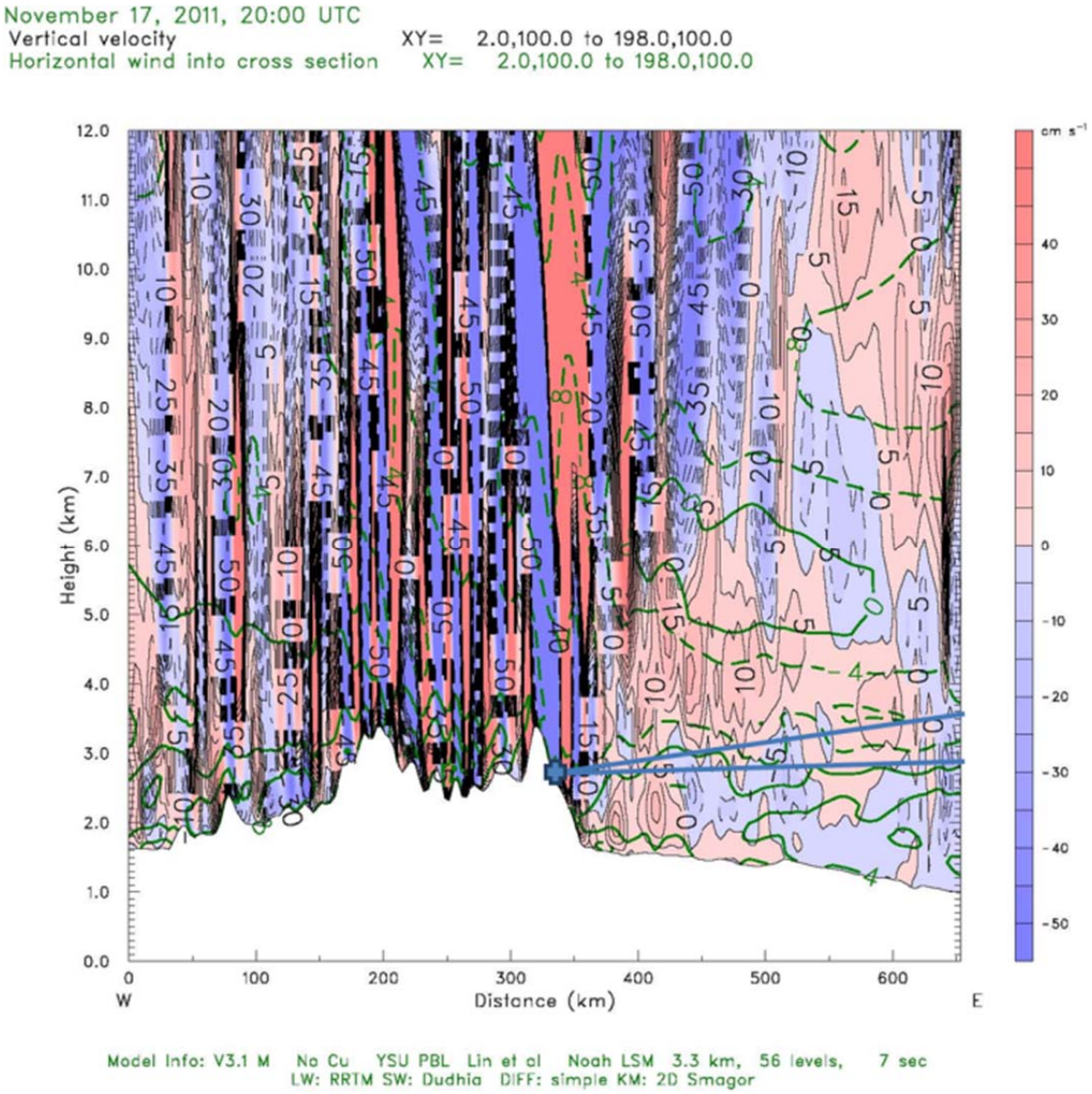

Figure 289. Vertical wind velocity for the same East-West viewing line.

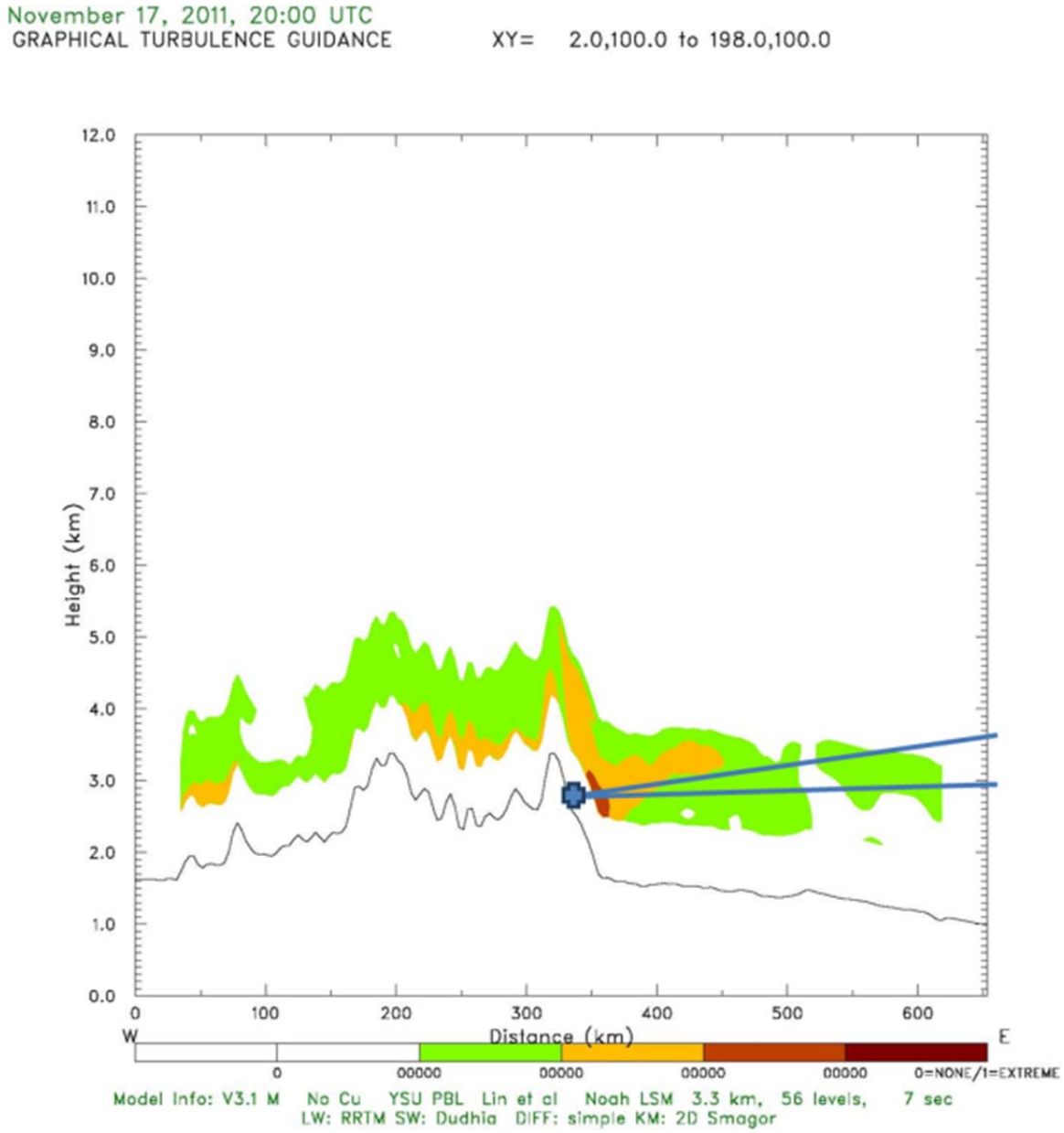

Figure 290. Predicted turbulence for same East-West viewing line.

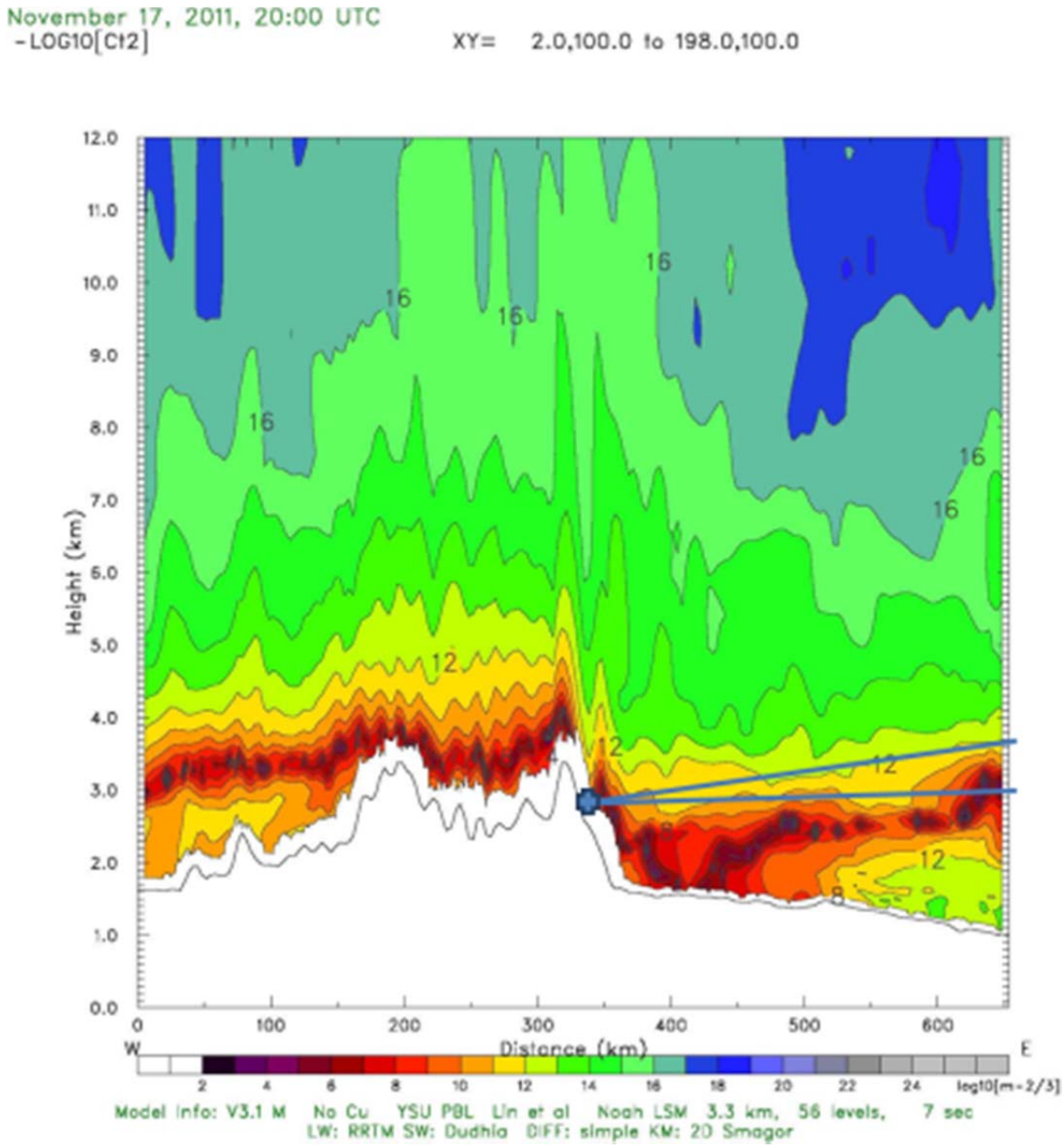

Figure 291. Predicted Turbulence Indicator for the same East-West viewing line.

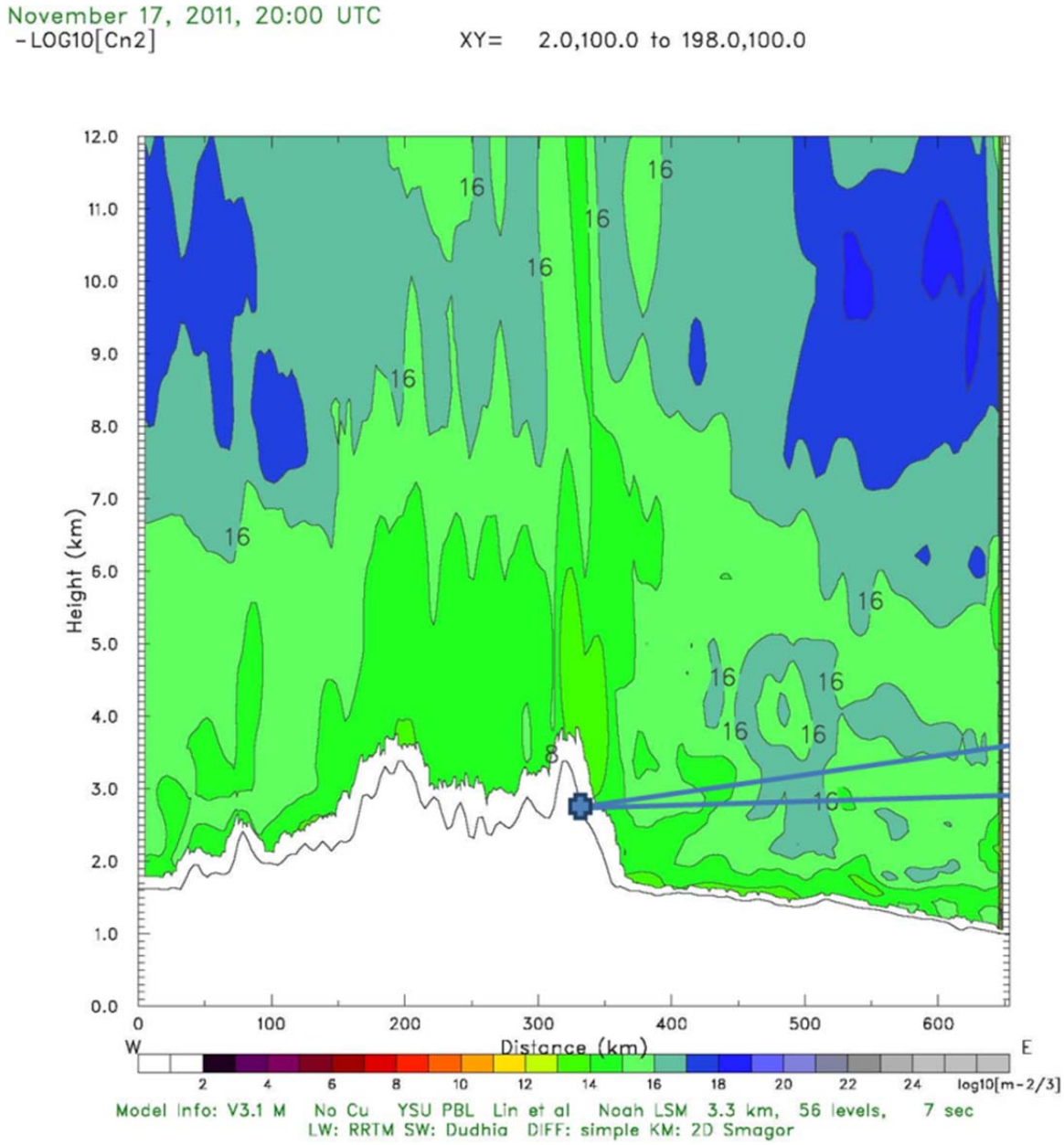

Figure 292. Logarithmic plot of C_n^2 structure constant.

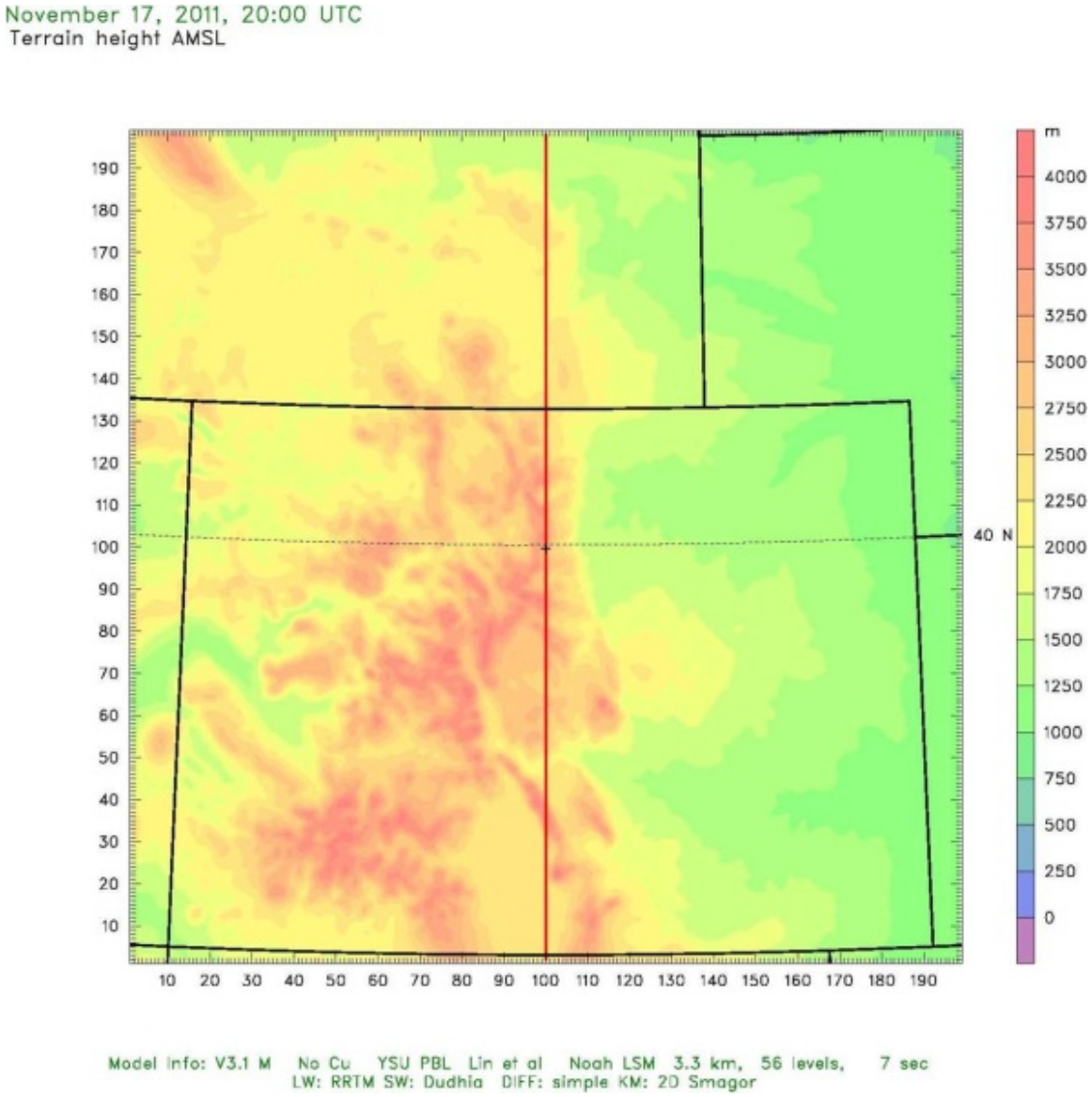

Figure 293. Down-looking view of North-South line intersecting the MRS site. The following charts display predicted data along this longitude line.

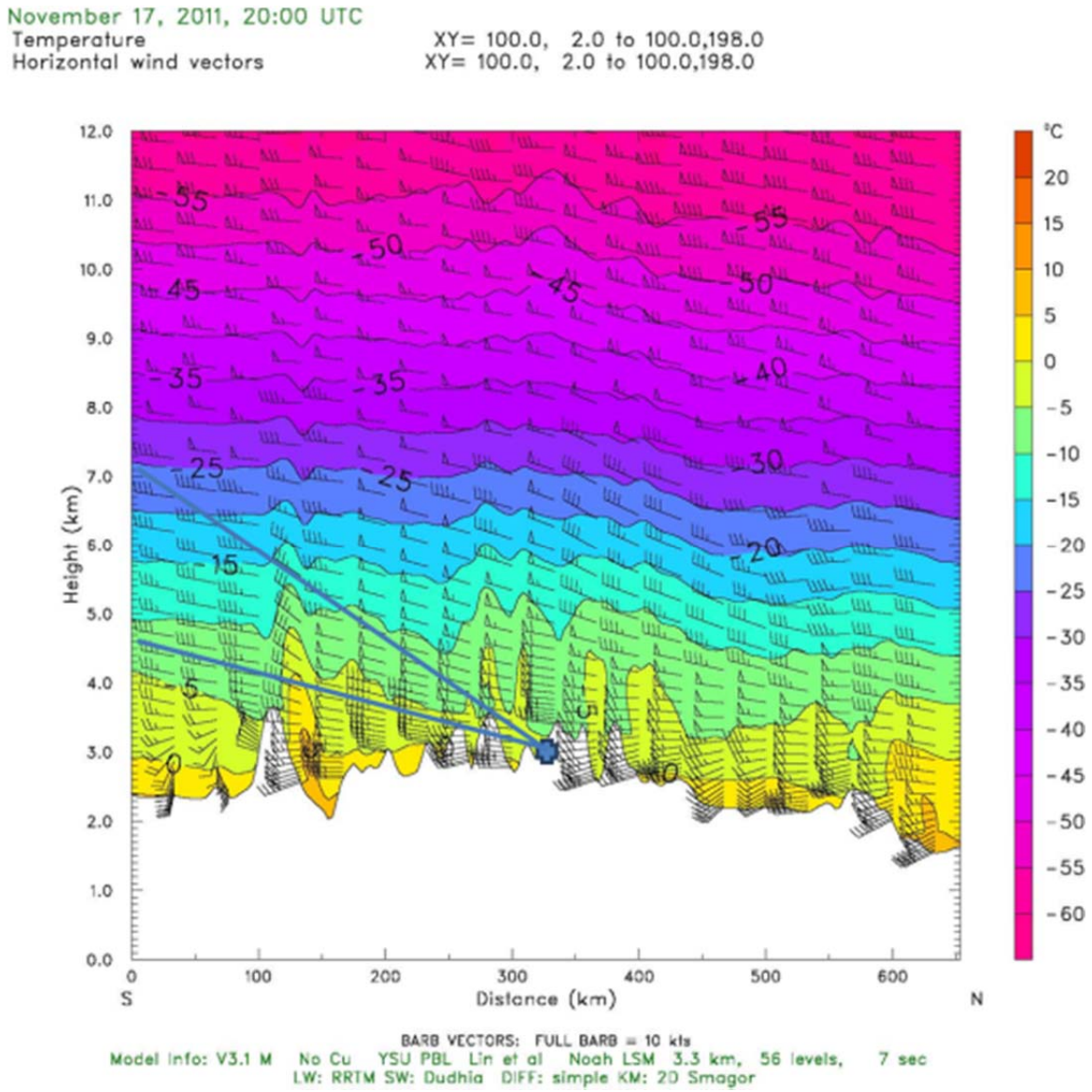

Figure 294. Modeled air temperature and wind vectors. The blue lines again indicate the elevation angles bounding the Hyper-Cam field-of-view, this time for Run 8 looking SSE.

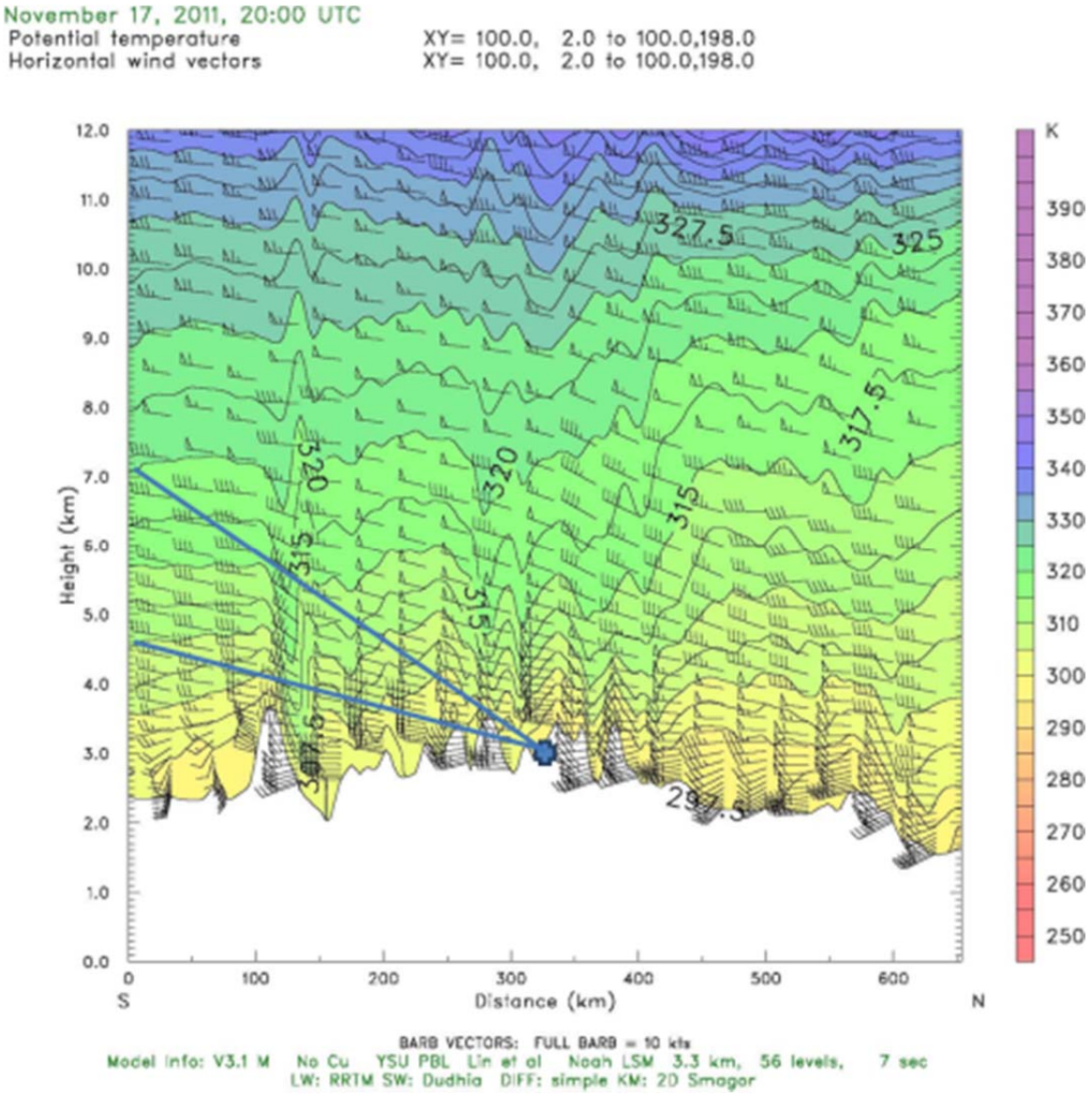

Figure 295. Potential temperature for the same North-South viewing line.

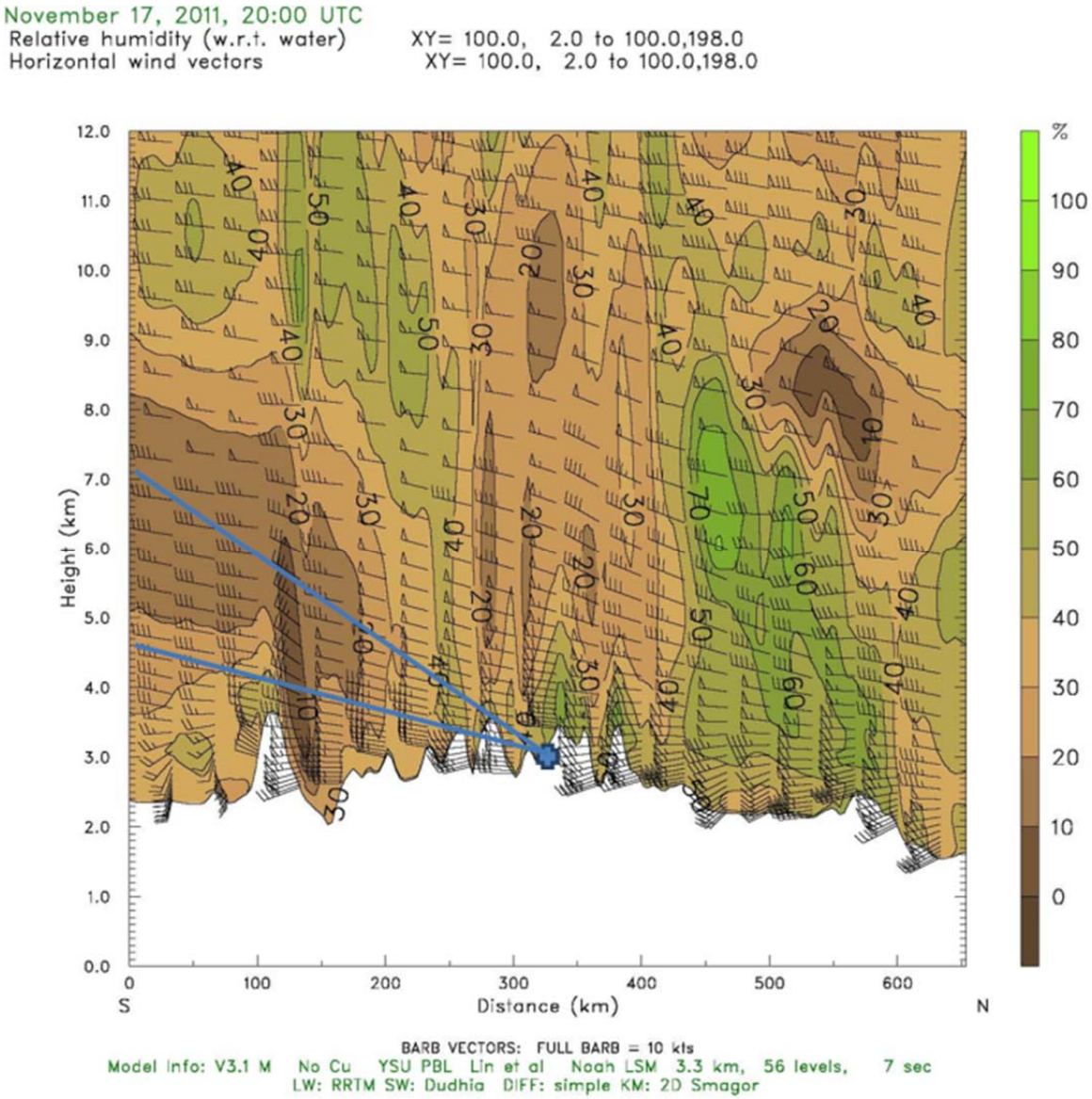

Figure 296. Relative humidity along the same North-South viewing line.

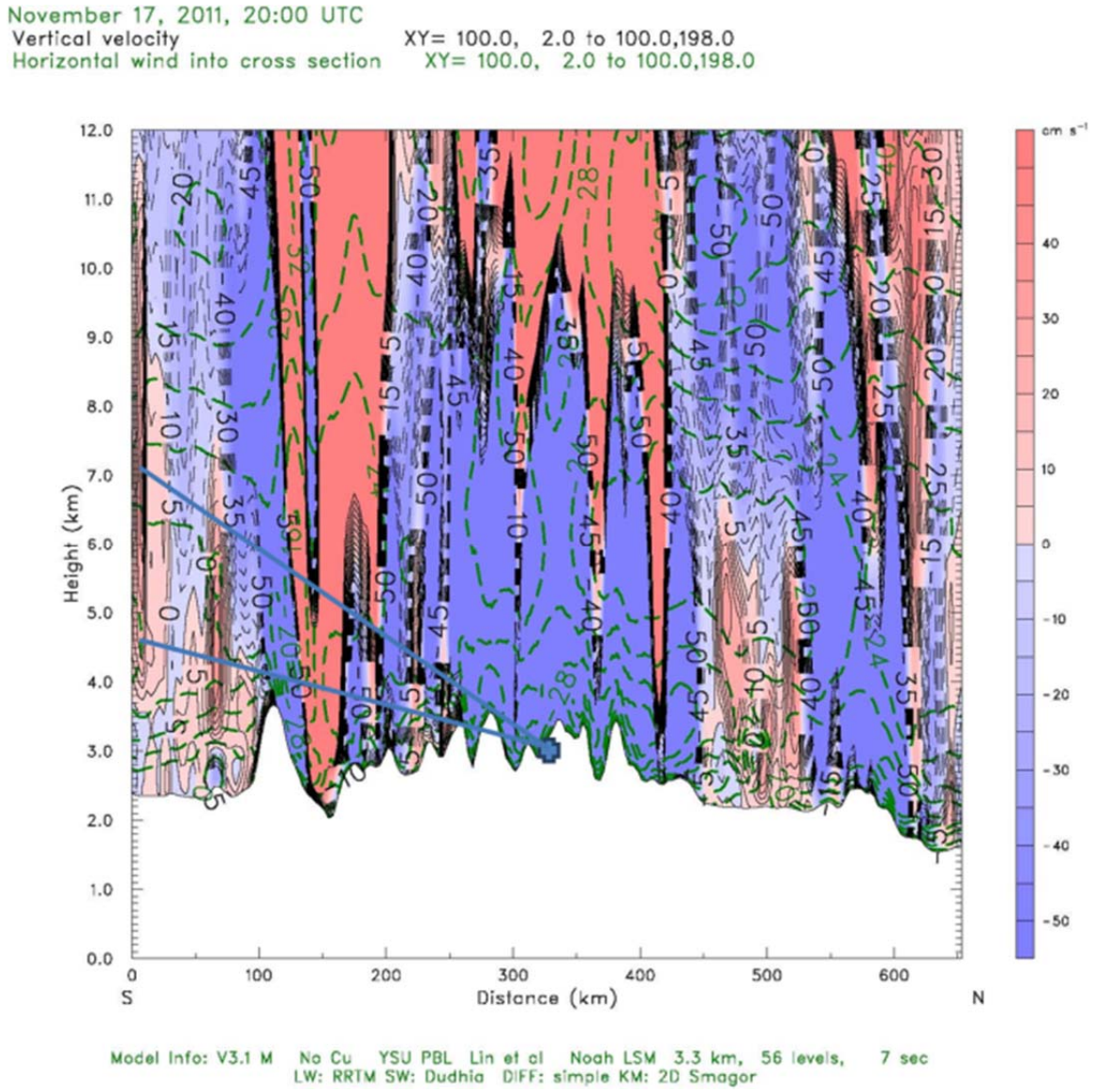

Figure 297. Vertical wind velocity along the same North-South viewing line.

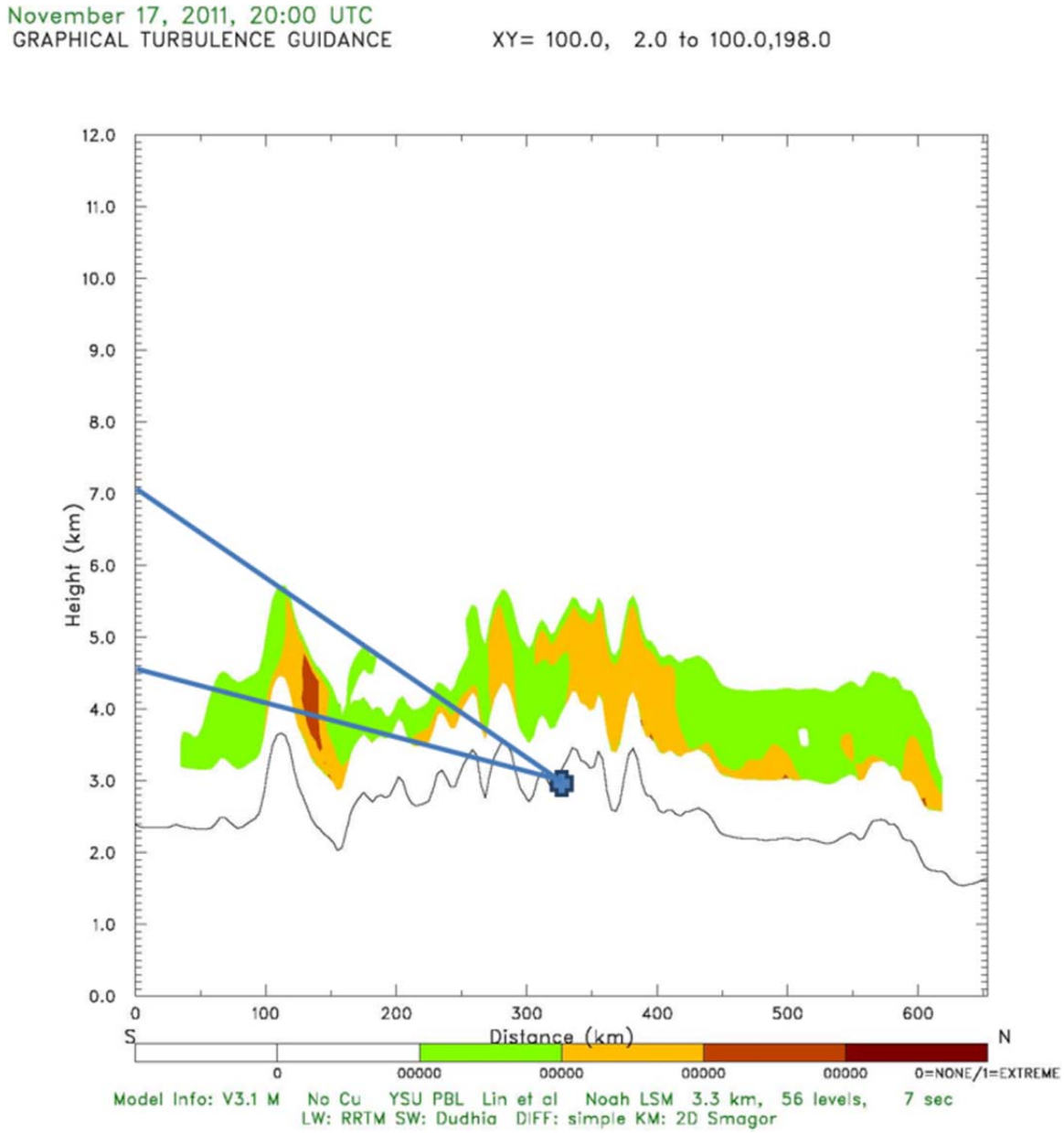

Figure 298. Predicted turbulence along same North-South line through the test site.

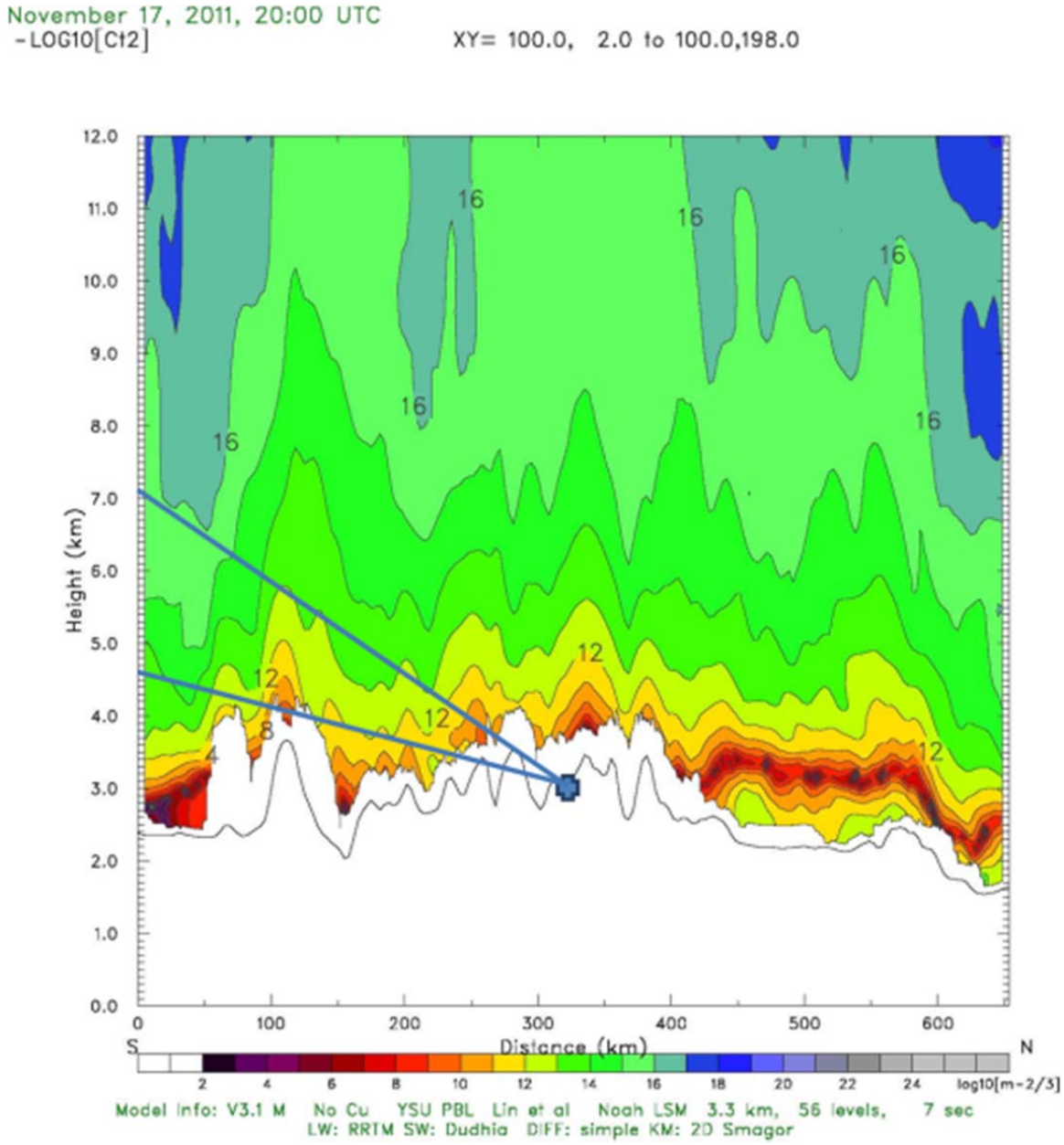

Figure 299. Predicted turbulence indicator for the same North-South view line.

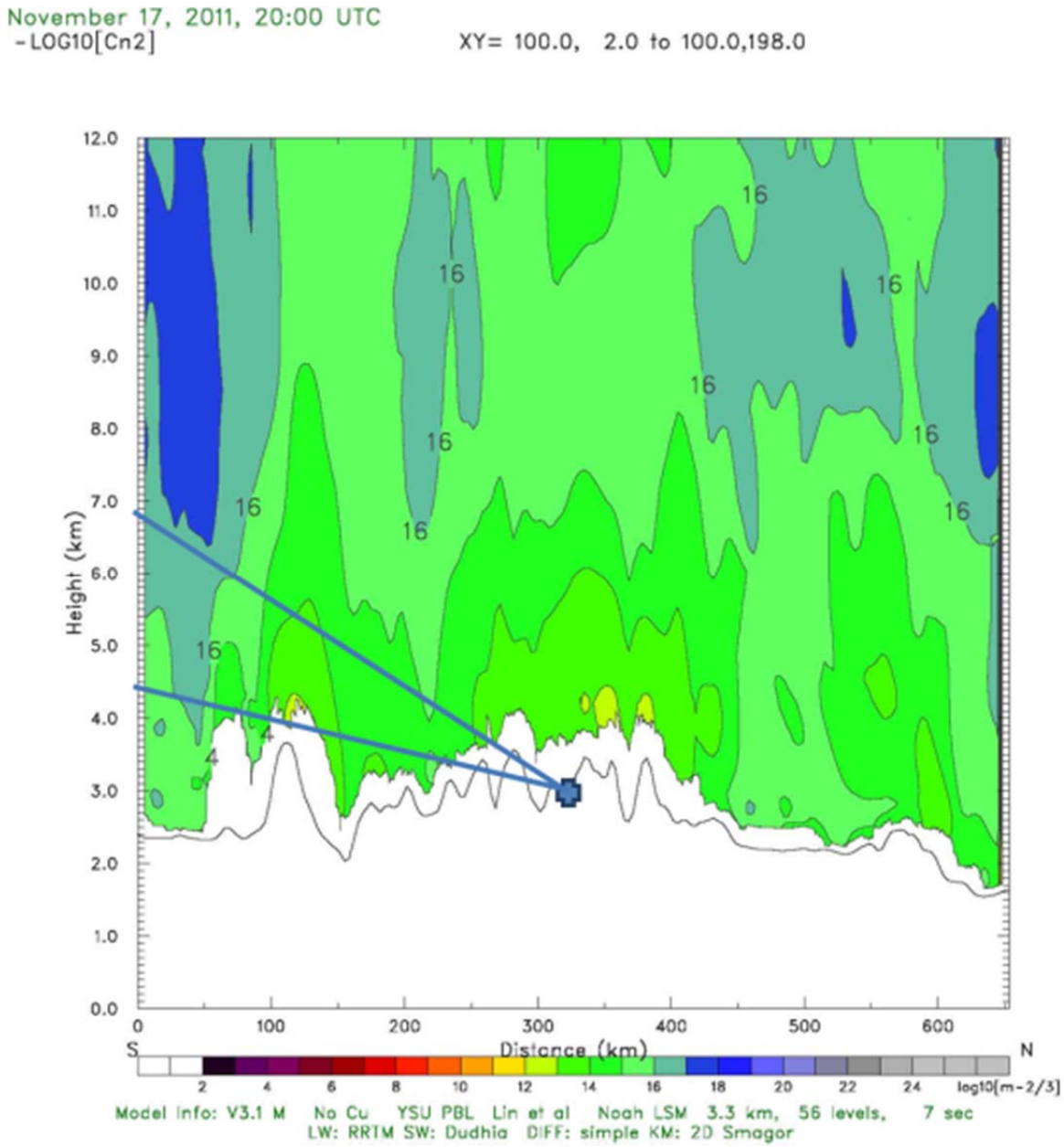

Figure 300. Predicted atmospheric structure constant C_n^2.

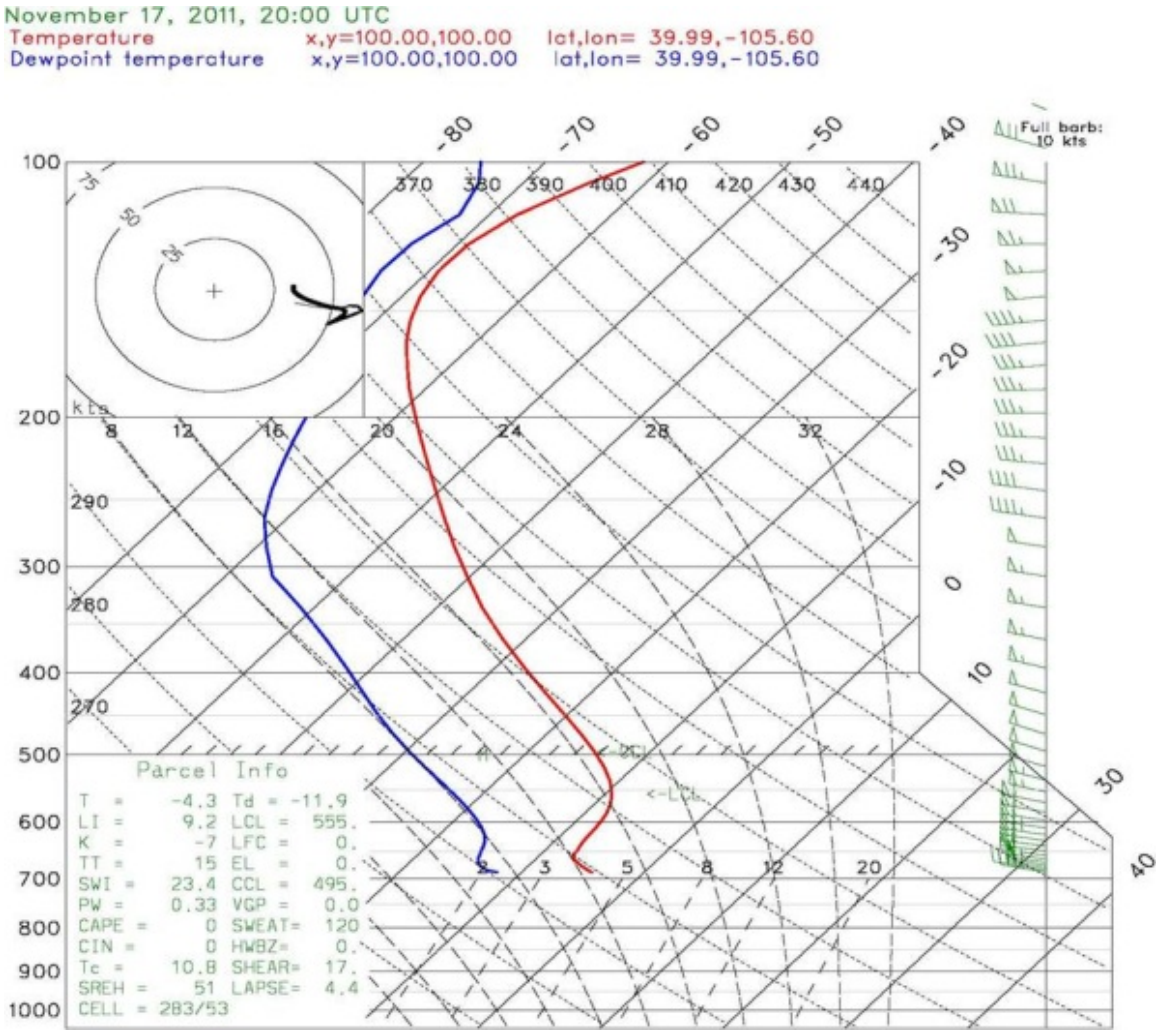

Figure 301. Dew Point Indicator for test location and time.

5.4.3.2 Observer Geometry and Hyper-Cam FOV in WRF Data Cubes

The WRF data cube had 198 x 198 x 64 voxels in longitude-latitude-altitude dimensions which correspond to the boundaries given in Table 13. The altitude levels started at 1km, increased to 6 km in 100 meter increments, and then continued to 21 km in 500 meter increments.

In addition, WRF data cubes were available for five time moments from 20.00 to 21.00 UTC. The observation point, which corresponds to the actual test location at MRS, is given in Table 13. The instrument viewing geometry, which was set up to correspond to November 17, 2011, Run 5, is also given in Table 13.

Table 13. Simulation set-up details

WRF Data Cube Geographic Boundaries	
WRF Min Latitude	36.878° N
WRF Max Latitude	43.036° N
WRF Min Longitude	109.775° W
WRF Min Longitude	101.423° W
Observation Point	
Observer Altitude	2.9 km
Observer Latitude	40.0323° N
Observer Longitude	105.5356° W
Instrument Viewing Geometry	
Central pixel azimuth angle	164° (SSE)
Central pixel elevation angle	13.5°
FOV pixel size (hor x ver)	320 x 256
FOV angular size (hor x ver)	6.4° x 5.1°

Figure 302 and Figure 303 below show the horizontal and vertical projections of the given FOV in comparison with the WRF data cube boundaries. One can see that only a small part of the entire WRF cube gets into the instrument FOV for the given viewing geometry. For example, the right panel of Figure 303, which shows the vertical projection of the FOV, demonstrates that only the first 60/100 km of the highest/lowest rays are in the WRF data cube while the corresponding ray total lengths are about 300/400 km, respectively, extending from the surface to the top of the atmosphere (=90 km here). However, the atmosphere's density falls off exponentially with a scale height of about 7 km. Therefore, only about 5% of the atmosphere is above 20 km, and the WRF model includes about 95% of the atmosphere. For completeness, a standard atmosphere is defined above this altitude and it is described in the following section. It should also be noted that the 320 x 256 image pixel resolution for the simulations appears to be a bit excessive, especially taking into account that the WRF data cube vertical resolution is only 100 m, at best.

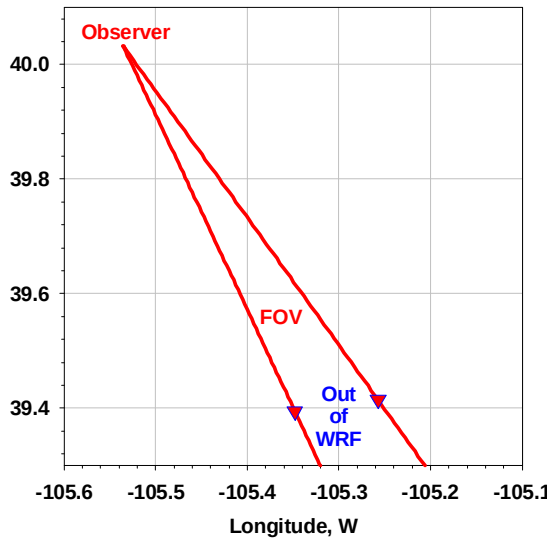

Figure 302. FOV in lat/lon coordinates (horizontal projection) for November 17, Run 5 observations.

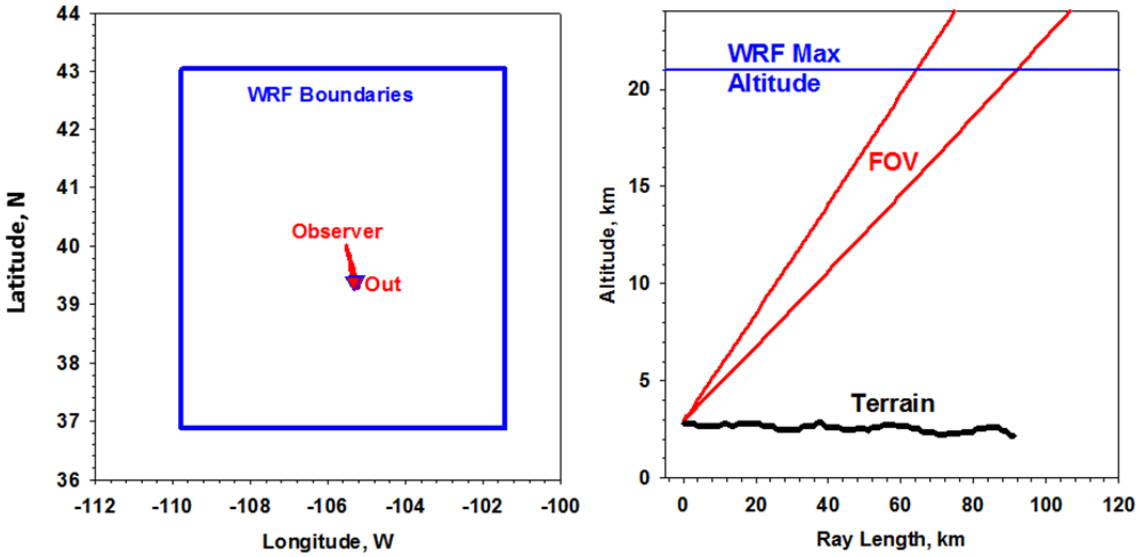

Figure 303. Horizontal Hyper-Cam FOV in WRF data cube boundary *(left panel)*; vertical projection of Hyper-Cam FOV *(right panel)*. Hyper-Cam FOV projections are in red; WRF data cube boundaries are in blue.

5.4.3.3 The Local Standard Atmosphere

It was necessary to define a Local Standard Atmosphere (LSA) for two main reasons:

1. To enable radiative transfer integration up to the top of the atmosphere when the ray goes beyond the WRF data cube, and
2. To estimate "the unperturbed signal" that would be observed without atmospheric perturbations caused by the mountain waves.

The LSA was determined as follows: in the WRF altitude range 1-21 km the standard temperature and water vapor profiles were computed by averaging over all corresponding WRF altitude levels

(i.e., over 198 x 198 voxels for each altitude), and then the US standard atmosphere was added above. The agreement between these two sources is shown in Figure 304 and Figure 305.

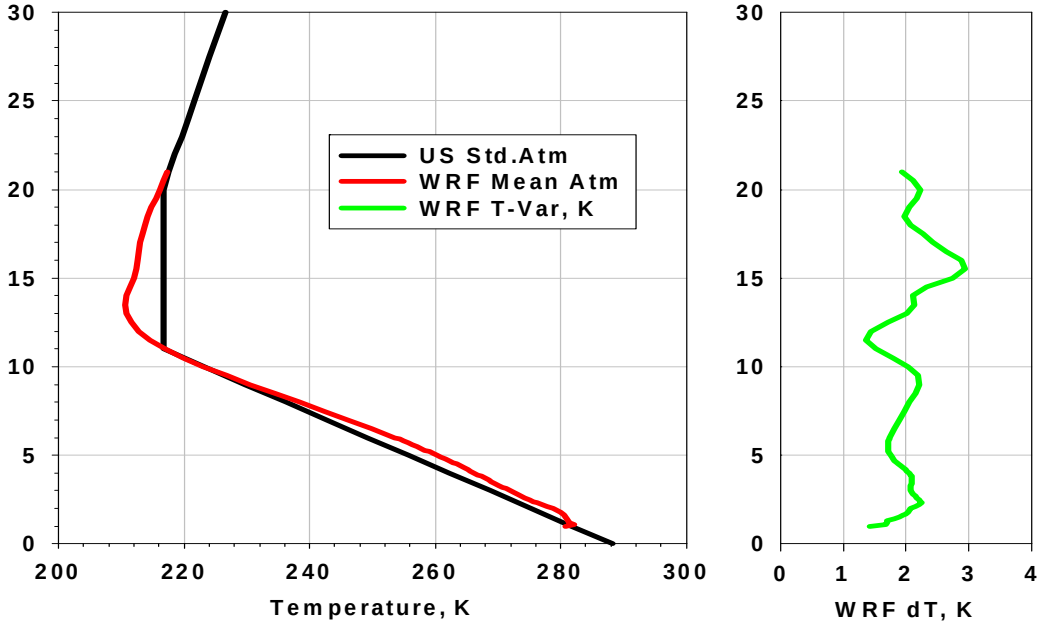

Figure 304. The LSA temperature profile was set to be equal to averaged WRF temperature below 21 km (red line) and the US standard atmosphere above (black line). The green line shows WRF temperature variability (i.e., one standard deviation from the WRF mean).

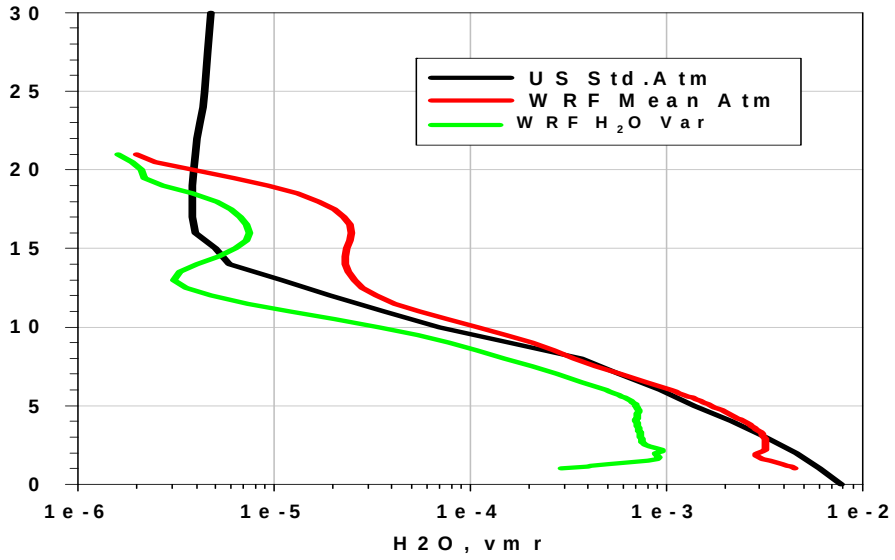

Figure 305. Same as Figure 304, but for water vapor.

Figure 306 and Figure 307 show the deviation of the temperature and H_2O from the LSA along the ray for three pixels: the bottom central pixel, the central pixel, and top central voxel. WRF data cube t_1 = 20.00 UTC.

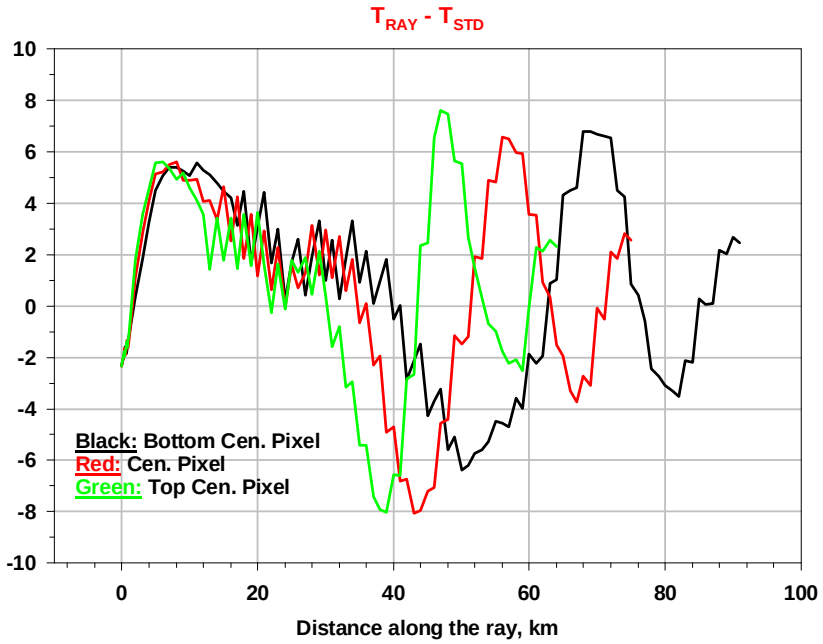

Figure 306. Temperature deviation from LSA for the three pixels.

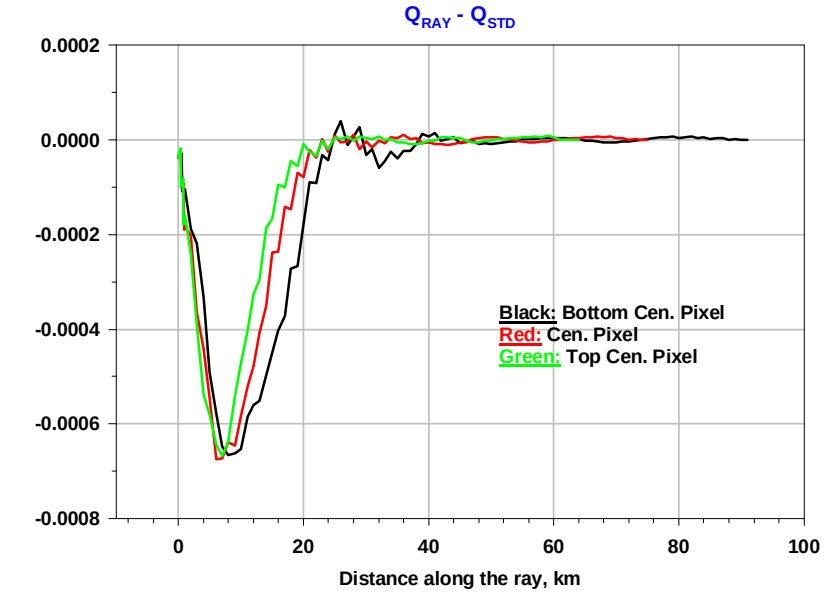

Figure 307. H_2O deviation (vmr) from the LSA for the three pixels.

5.4.3.4 Simulation Results

Radiances were computed with FLI-FM2 for the five time moments that were available from the input WRF data set: 20.00 UTC, 20.15 UTC, 20.30 UTC, 20.45 UTC, and 21.00 UTC (time stamps t_1 to t_5 respectively). Radiances were also computed for the same viewing geometry but for the Local Standard Atmosphere (marked t_0) as a reference to an "unperturbed" atmospheric state. Thus, there are 6 radiance sets total, each of which contains 320 x 256 spectra (full image pixel resolution) degraded to 41 Hyper-Cam channels (spectral resolution ~ 16 cm^{-1}). The radiance unit is equal to $mW/(m^2\text{-}sr\text{-}cm^{-1})$.

To estimate a turbulence signal, two kinds of RMS differences (obtained by summing the deviations squared over all 81,920 image pixels) were computed:

1. The difference between perturbed and unperturbed radiances, and
2. The differences between perturbed radiances at the different times.

The latter one is most interesting in terms of comparison with what could actually be observed with the MRS measurements. As an example, Figure 308 presents the RMS radiance (for all channels) between t_1 and t_0 and between t_4 and t_0 (both are variability from the "unperturbed" radiances), and t_4 and t_1, which is the signal temporal variability. As can be seen in the figure, the maximum difference from the unperturbed radiances (computed for the LSA) is about 1.0 mW/m^2-sr-cm^{-1}, while the temporal variability is about 10 times less, i.e., 0.1 mW/m^2-sr-cm^{-1}. It should be noted that the FLI-FM has no ozone variability in its current version (i.e., the optical depth look-up-table was pre-computed for the same standard ozone profile). Thus, the variability in the ozone band channels (~1020-1080 cm^{-1}) is mostly due to the temperature variations in the WRF part of the ray since the incoming radiance outside of the WRF cube is the same for all times, from t_0 to t_5.

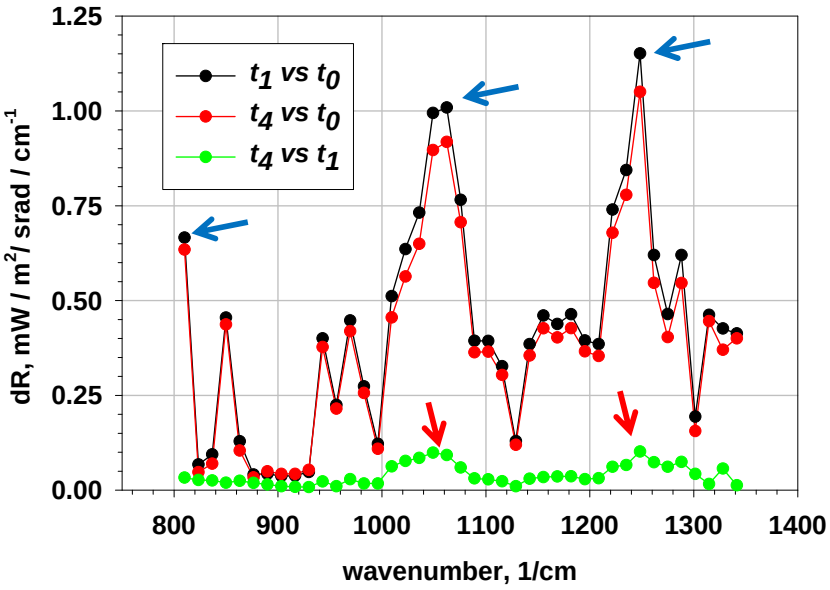

Figure 308. RMS difference for deviation from unperturbed radiances (black and red) and for temporal variability (green), computed for 320 x 256 image pixels. The arrows indicate the channels shown in the following figures at full image resolution.

Figure 309 through Figure 313 show full-size images of the radiance difference for those channels where the corresponding RMS is a maximum. The images have been spatially averaged with a 4x4 pixel window for illustrative purposes only; the numerical results have full resolution.

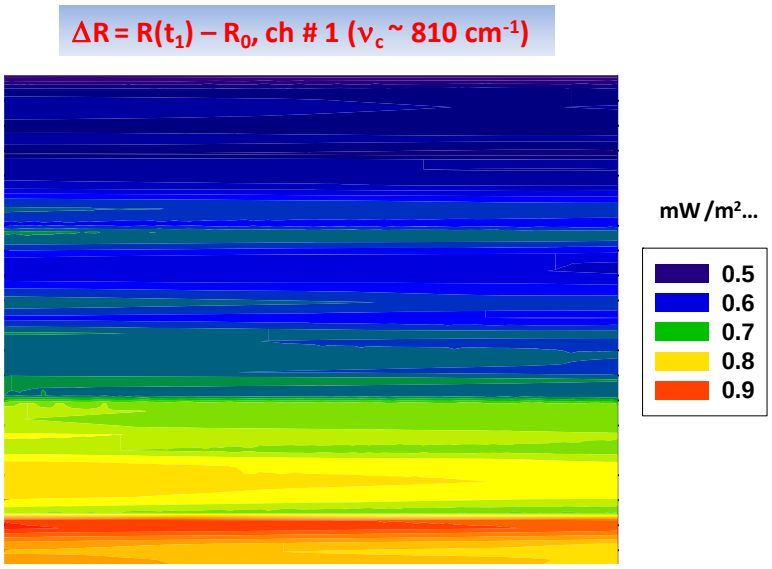

Figure 309. Full-size image of *R(t$_1$)* - *R(t$_0$)*, Hyper-Cam channel # 1.

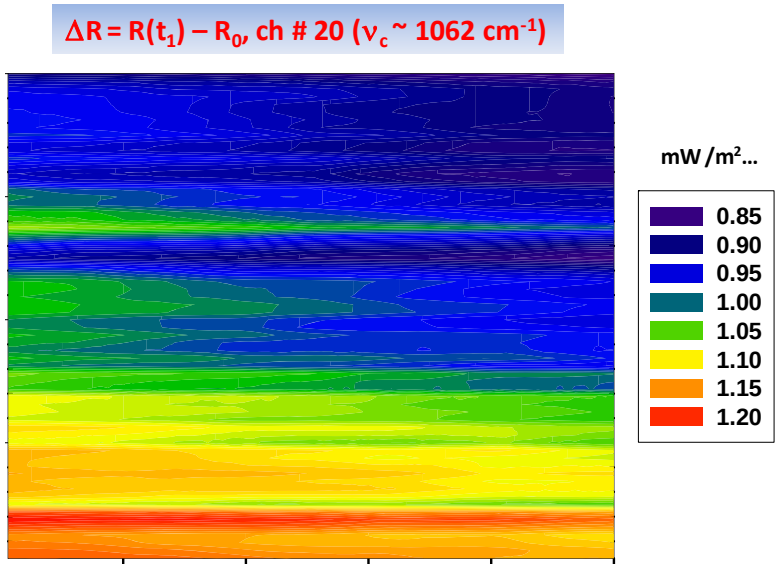

Figure 310. Full-size image of *R(t$_1$)* - *R(t$_0$)*, Hyper-Cam channel # 20.

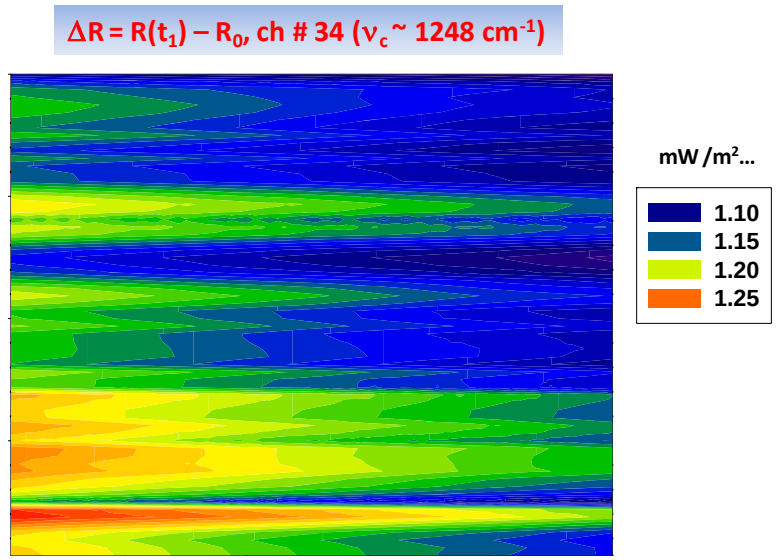

Figure 311. Full-size image of *R(t$_1$)* - *R(t$_0$)*, Hyper-Cam channel # 34.

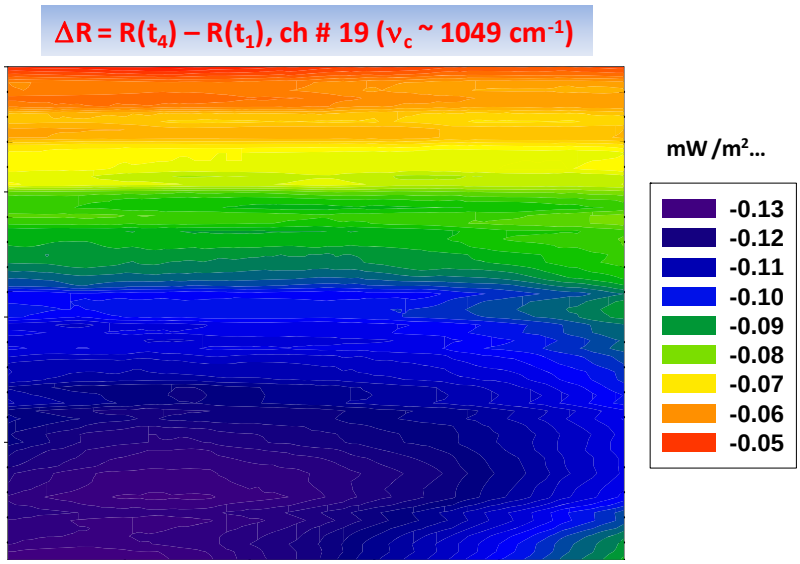

Figure 312. Full-size image of *R(t$_4$)* - *R(t$_1$)*, Hyper-Cam channel # 19 *(*temporal *variability!).*

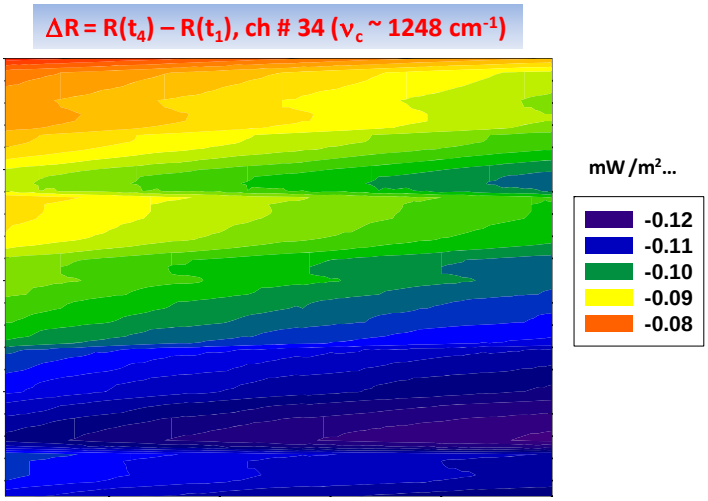

Figure 313. Full-size image of *R(t₄) - R(t₁)*, Hyper-Cam channel # 34 *(temporal variability!).*

5.5 Why Were We Unable to Detect Turbulence?

At 16 cm^{-1} resolution, the NESR is approximately 0.25 mW/m2-sr-cm^{-1} (see Appendix A), which is higher than the signal seen in the simulated time variability shown in Figure 312 and Figure 313. Unfortunately, this indicates that the Hyper-Cam is not sensitive enough to see the signal for this particular case.

Simulations run prior to the MRS field test indicated that we should have been able to see the turbulence with the Hyper-Cam. It has been noted that the high simulated signals could have been an artifact of the modeling. However, it could be possible that during the field test at MRS, we never collected any Hyper-Cam data of mountain wave disturbances that were high enough in severity to be observed. All simulations performed prior to the test were for the March 6, 2004 severe turbulence WRF model. During the test, there were no mountain wave turbulence PIREPs higher than "Moderate," and the EDRs did not show any unusual activity. Mountain waves are standing waves and vary only slowly with time, but temperature and water vapor concentration are not homogeneous at any given altitude when the wave pattern is present, and it is that disturbance that leads to the radiance variations across a scene as shown in previous simulations. On the other hand, there is always some turbulence associated with the mountain waves.

The plan was to separate the standing wave pattern from the turbulence on the basis of the time scales. The D&P was going to get the fast variations caused by turbulence, and our earlier Boulder work led credence to that idea [34]. During the test, the D&P was tempermental and sometimes non-functional despite having been sent for an overhaul prior to the test, and the Hyper-Cam could not see evidence of the standing wave pattern. We know we had standing wave patterns because of the presence of lenticular clouds and the satellite image. Turbulence severity is undetermined, but likely not what we hoped.

We knew that the analysis of ground-based measurements would be more challenging than flight-based measurements due to the reduced radiance signal for a slant path to space (see Section 5.1.1, in particular, Figure 69 and Figure 72). Despite the smaller expected signal, we did not believe it would be so small that it would be unobservable. We believed the radiance signal

would still be above the noise level of the Hyper-Cam because the FLI-FM simulations indicated it would. As the simulations were performed for a ground-based slant path, they inherently take transmission through layers of atmosphere into account. They may have over-predicted the signals due to the manner in which the turbulent signal was modeled. When modeling turbulence as a difference between a perturbed state and a standard atmosphere, a temperature offset will always exist, and will cause a constant bias between the two atmospheric states. For the simulations, the difference between perturbed radiances at different *times* (i.e. the standard atmosphere has *not* been subtracted) shows actual signal due to scene variability. The differences between perturbed and unperturbed radiances are mostly due to how the standard atmosphere was defined. The actual scene variability is represented by the temporal variability shown in the green data in Figure 308, and is unfortunately below the noise level of the Hyper-Cam.

6 Runway Surface Conditions and Obstructions

Emissivity images, obtained from an aircraft-mounted Forward Looking Interferometer (FLI), are intended to be used to alert the pilot of hazardous landing runway surface conditions and enable the determination of runway friction and associated stopping distance for a particular aircraft. This hazard detection technique is based on the fact that different surfaces have different emissivity spectra in the LWIR spectral region, where the FLI operates, as shown in Figure 314.

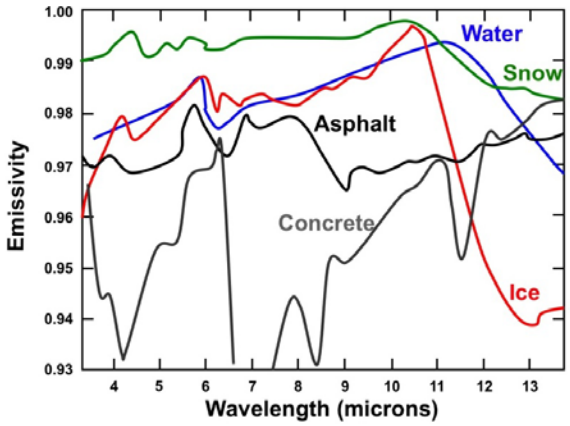

Figure 314. Spectral emissivity of runway surface materials and water, ice, and snow.

In a previous phase of the FLI program, the ice versus water difference was shown by their indices of refraction [15]. Figure 315 and Figure 316 below are reproduced from the referenced report. The real (reflection) and imaginary (absorption) parts of the index of refraction differ in the infrared. Kirchhoff's Law states that absorption and emission terms are equivalent; thus the imaginary component of the index of refraction influences the emissivity of the surface.

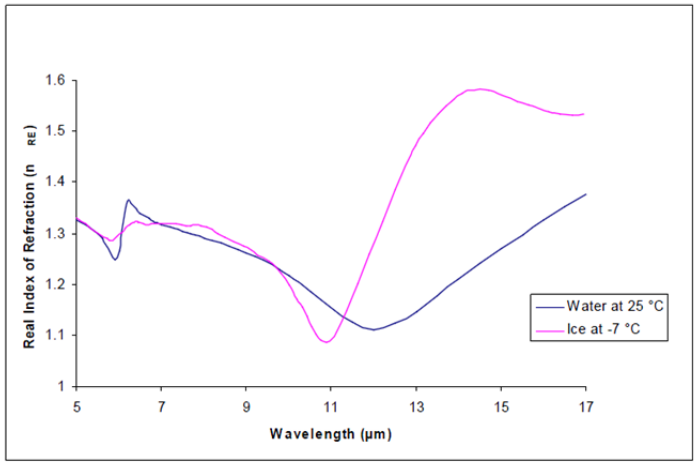

Figure 315. Real index of refraction of water and ice in the infrared [2] [3].

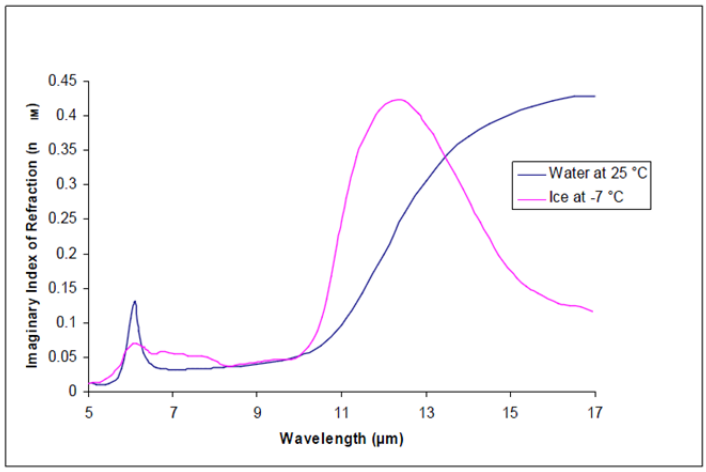

Figure 316. Imaginary index of refraction for water and ice in the infrared [2] [3].

As a secondary priority, runway obstructions such as wildlife were studied briefly. Ground-based measurements of animals were conducted with another LWIR imager. The following sections outline the governing equations for determination of emissivity of surface conditions, followed by measurements and the development of a hazardous surface condition training set. The wildlife runway obscuration is discussed briefly, last.

6.1 Governing Equations for Emissivity Determination

The radiance as measured by the Telops Hyper-Cam can be written as:

$$R_{sens}(\nu) = R_{surf}(\nu)\tau(\nu) + R_p(\nu) \tag{6.1.1a}$$

$$R_{sens}(\nu) = [R_e(\nu) + R_r(\nu)]\tau(\nu) + R_p \tag{6.1.1b}$$

Where R_{sens} is the at-sensor radiance, R_{surf} is the at-surface radiance, R_e is the radiance emitted by the surface, R_r is the radiance reflected by the surface, τ is the atmospheric transmission, and R_p is the path radiance. Equation 6.1.1 has been written in two parts to explicitly show that $R_{surf} = R_e + R_r$.

It is assumed that the atmospheric transmittance of the short path between the Hyper-Cam and the surface is unity, which is particularly true for the atmospheric window region (8–12 μm) observed with the Hyper-Cam. Therefore, with $\tau \sim 1$ and $R_p \sim 0$ for short path lengths, then R_{sens} in Equation 6.1.1 is simply the sum of the emitted and reflected radiance at the surface, i.e.:

$$R_{sens}(\nu) = R_e(\nu) + (\nu) = R_{surf}(\nu); \;\; \tau \sim 1, R_p \sim 0 \tag{6.1.2}$$

The emitted and reflected component of the radiance in Equations 6.1.1b and 6.1.2 can be written as:

$$R_e(\nu) = \varepsilon(\nu) B(\nu, T) \tag{6.1.3a}$$

$$R_r(\nu) = \rho(\nu) R_i(\nu) = (1 - \varepsilon(\nu)) R_i(\nu) \tag{6.1.3b}$$

Where ε is the emissivity of the surface, $B(T)$ is the Planck function computed at the temperature of the surface, ρ is the reflectivity of the surface, and R_i is the radiance incident on the surface. Note in Equation 6.1.3b that the reflectivity of the surface has been replaced by 1 – emissivity, following Kirchhoff's Law. Because we are looking at rough surfaces such as concrete, the incident radiation comes from the entire sky dome, and ε is the total hemispherical emissivity.

Equation 6.2 can now be rewritten in terms of the variables in Equations 6.1.3a and 6.1.3b:

$$R_{sens}(\nu) = \varepsilon(\nu) B(\nu, T) + (1 - \varepsilon(\nu)) R_i(\nu) \tag{6.1.4}$$

Solving for emissivity, we get:

$$\varepsilon(\nu) = \frac{R_{sens}(\nu) - R_i(\nu)}{B(\nu, T) - R_i(\nu)} \tag{6.1.5}$$

The radiance observed does not represent the angularly integrated sky radiance being reflected by the surface. In order to account for this angular dependence, a diffuse gold plate is placed within the Field of Regard (FOR) of the Hyper-Cam measurements. Since gold is a nearly perfect reflector at infrared wavelengths, surface measurements for those pixels whose FOV were filled with the gold plate provided measurements of the diffuse sky radiance needed for the computation of emissivity from the radiance for pixels viewing the surrounding surfaces. In order to estimate the diffuse sky radiance for those pixels not viewing the gold plate, a spectral diffusivity factor to be multiplied by the observed sky radiance was defined from those pixels viewing the gold plate. The diffuse sky radiance, R_{DSKY}, for each wavelength was computed from the observed gold plate radiance, R_G, using Equation 6.1.4.

$$R_{DKSY}(\nu,\theta) = \frac{R_G(\nu) - \varepsilon_G B(\nu, T_G)}{1 - \varepsilon_G} \tag{6.1.6}$$

where ε_G and T_G are the emissivity and temperature of the gold plate, respectively. Note that the emissivity of the gold plate is not dependent on wavenumber; because it is very low (~0.03) and constant over the wavelength range we use the value calibrated by Labsphere.

The surface skin temperature is defined as the value that minimizes the local spectral variance in the emissivity calculated using Equation 6.1.5. The emissivity calculated according to Equation 6.1.5 exhibits excessive local spectral variance for an incorrect surface skin temperature since atmospheric emission line features observed in the sky radiance propagate into the calculated surface emissivity spectrum [35]. Since the local spectral variance of the true surface emissivity is small compared to that produced by atmospheric emission line features, the correct surface skin temperature must be that which produces minimal local spectral variance in the derived surface emissivity spectrum. The local variance of the surface emissivity spectrum is calculated as the standard deviation of the spectral derivatives of emissivity around every spectral point. The correct surface skin temperature, and associated surface emissivity spectrum, is assumed to be that which has the minimum local spectral variance of the calculated surface emissivity. Kanani et al [36] represent the smoothness of the emissivity, *Sm(T)* as a minimization of the following function with respect to temperature:

$$Sm(T) = \int \left| \frac{d\varepsilon(T_S)}{d\nu} \right| d\nu \tag{6.1.7}$$

6.1.1 Constraints on Emissivity Determination

The MLEV (Minimization of Local Emissivity Variance) method has been successfully used on datasets collected under the FLI program which will be described in the next section. This method allows us to determine the surface temperature and emissivity if we know both the at-sensor radiance and the incident radiance. However, all analysis which produced good results thus far has been constrained by the following:

1. There must be a Lambertian reflector (we use a roughened gold plate) in the scene in order to measure the reflected radiance component, integrated over the sky dome.
2. The path length between sensor and scene must be relatively short so that path radiance and atmospheric transmission can be neglected.

In all datasets where we were able to obtain good results with the MLEV method, the incident radiance was obtained from the gold plate measurement. We believe we have been unable to get emissivity results without the gold plate measurement for the following reasons:

1. As described above, one of the reasons why the MLEV method works so well is that it minimizes the high spectral variance in the incident radiance spectrum. If the measurement of the gold standard is flawed slightly (or, if the estimation of the incident radiance is inaccurate), it can have significant effects on the resulting emissivity calculation, because the assumptions under which the algorithm was created are now violated. This is probably one of the reasons why our attempts at estimating the reflected component were unsuccessful. This effect is shown quantitatively in Figure 317: when the radiance of the gold standard was changed by 1%, and the resulting emissivity of the

surface changed by up to 400%. This large error is due to the fact that the MLEV algorithm is no longer converging; because it does not converge, the 400% change is not really an accurate representation of the error. There is actually no error that can be measured, because there is no solution. The corresponding is shown in Figure 317.

2. As shown in Equation 6.1.5, the surface emissivity is not proportional to the incident radiance. Therefore, one cannot expect to obtain the apparent surface emissivity (i.e., the magnitude is incorrect but the general shape of the emissivity curve is maintained) by neglecting the L_i term when classifying various materials. This also explains why attempts to constrain the emissivity (e.g. don't allow values over one, or set the maximum value at some predetermined wavenumber) were unsuccessful.

3. Using a measurement of sky radiance recorded with the Hyper-Cam as incident radiance is not accurate because the measurement is too directional. The benefit of the gold plate is that it is diffuse and therefore provides an accurate representation of background radiance from the entire dome above the horizon.

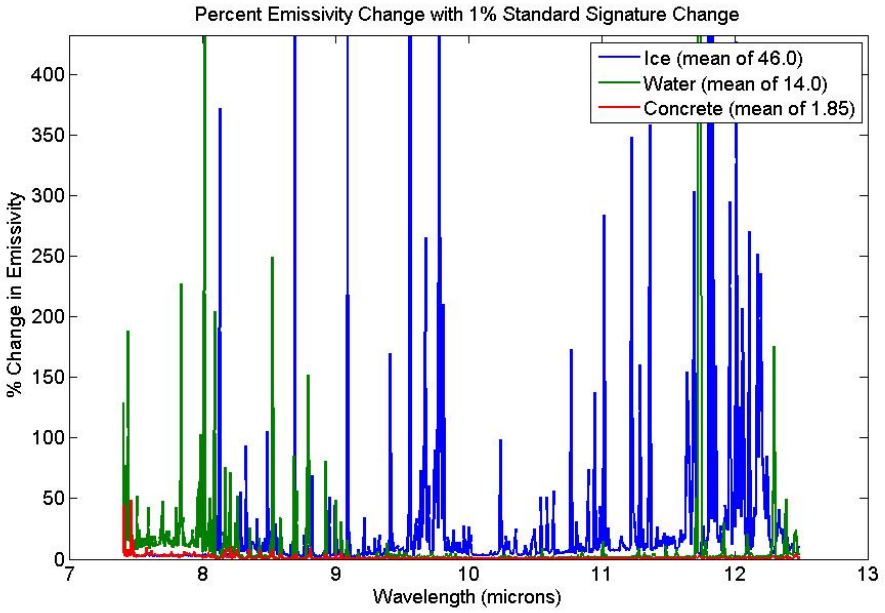

Figure 317. Percent change in material emissivity due to 1% change in gold standard signature. Note the average value of each material given as part of the figure legend.

The ultimate goal is to find the emissivity of the surface, but as shown in Equation 6.1.5, to compute it accurately we need the at sensor radiance, the radiance incident on the surface, and the surface temperature for computation of the Planck function. Of these three variables, the only thing we will have in a practical FLI application is the at sensor radiance, because it is what a radiometric sensor measures. The incident radiance must be measured by the gold plate or another diffuse target of very low emissivity, and the surface temperature must be measured by contact measurement (for an accurate measurement with an IR radiometer one would need to input the target emissivity, which is unknown).

6.1.2 In-Scene Atmospheric Compensation

The ISAC (In-Scene Atmospheric Compensation) method [37] was identified because for a practical FLI application (in addition to not having a gold plate in the scene), the path lengths might be long enough such that the assumption of $\tau \sim 1$ and $R_p \sim 0$ might be invalid. The ISAC methodology uses the statistics of the data in the scene itself to estimate the transmission and path radiance.

A blackbody has an emissivity of 1 and it reflects nothing; therefore, for blackbody-like surfaces, $R_e = B(T)$ and $R_r = 0$. We can then rewrite the radiative transfer equation for these surfaces (Equation 6.1.1) as:

$$R_{sens}(\nu) = B(\nu, T)\tau(\nu) + R_p(\nu) \tag{6.1.8}$$

Assuming that most pixels in the scene are blackbody-like (i.e. $\varepsilon \sim 1.0$) is valid for the satellite observations for which the algorithm was developed. In our case, the concrete runways are not blackbody-like, but given enough other background pixels, such as grass, we believe the algorithm is worth investigation. Equation 6.1.8 is the equation of the best-fit line with slope equal to atmospheric transmission and the intercept equal to path radiance, if one plots measured radiance, R_{sens}, vs. the theoretical Planck, B, for every pixel. The theoretical Planck function is computed for the temperature at the wavenumber index where the brightness temperature of the entire datacube is found to have a maximum value. Because each Telops datacube can have up to 320 x 256 (81,920) pixels, depending on the scene, there should be enough blackbody-like pixels to fit a line to a scatterplot. The authors of the ISAC method recommend fitting the line to the top of the plot, since the blackbody-like pixels will lie there. This analysis is done for every wavenumber in the cube; a unique scatterplot is created at each wavenumber, thus producing τ and R_P as a function of wavenumber.

Once τ and R_p are determined from the line parameters, the surface radiance can be found by solving Equation 6.1.1a:

$$R_{surf}(\nu) = \frac{R_{sens}(\nu) - R_p(\nu)}{\tau(\nu)} \tag{6.1.9}$$

The ISAC algorithm thus provides a method to determine the at-surface radiance from the data itself; however, how does one determine the emissivity? The at-surface radiance still depends on both the emitted and reflected components of radiance, i.e.:

$$R_{surf}(\nu) = \varepsilon(\nu)B(\nu, T) + (1 - \varepsilon(\nu))R_i(\nu) \tag{6.1.10}$$

Setting Equation 6.1.9 equal to Equation 6.1.10 and solving for emissivity does not produce as clean a result as shown in Equation 6.1.5; instead, when τ and R_P must be considered, the emissivity becomes:

$$\varepsilon(\nu) = \left(\frac{L_{sens}(\nu) - L_p(\nu)}{\tau(\nu)} - L_i(\nu)\right)\left(\frac{1}{B(\nu,T) - L_i(\nu)}\right) \tag{6.11}$$

Note that, for $\tau \sim 1$ and $R_p \sim 0$, Equation 6.1.11 reduces to Equation 6.1.5, as it should, but we are still left with the same problem. The incident radiance and the at-surface temperature are still

unknown. We could again try to minimize the variance in emissivity spectra, but we still need a gold plate measurement in order to provide an accurate estimate of R_i. We have been unable to identify a replacement for the gold plate. The results of several measurements that were successful under the constraints described above are shown in the following section.

6.2 Surface Emissivity Measurements

Surface emissivity and skin temperature measurements were conducted with the Hyper-Cam spectrometer for multiple scenes representing hazardous runway conditions. Ground-based measurements taken under this program included ice; snow; wet/dry asphalt and concrete; and runway surroundings/hazards such as terrain, wildlife, and vehicles.

6.2.1 Staged Ice and Water: September 2010

An experiment was conducted under clear sky conditions in September 2010 to simulate the hyperspectral emissivity imaging of runways under different surface conditions. A parking deck located next to Baker Building on the Georgia Tech campus provided an ideal location; the top level was high enough to allow for a view of the sky almost to the horizon. Additionally, the concrete surface on one half of the deck was treated with a non-skid coating, allowing two surfaces to be imaged. The experimental setup is shown in Figure 318.

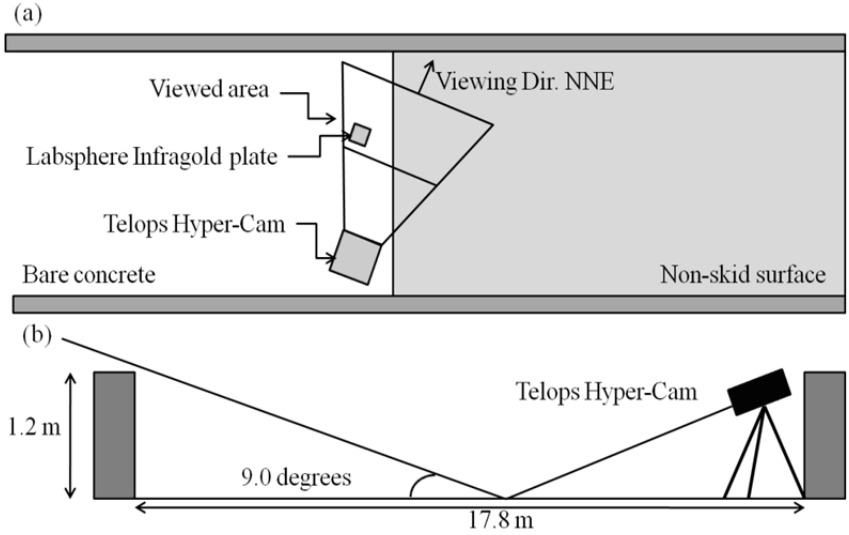

Figure 318. Parking deck set-up on Georgia Tech campus *(a)*; Elevation view of test set-up *(b)*

The Labsphere InfraGold plate [shown in Figure 318 (a)] has an emissivity of approximately 0.03 in the LWIR. The plate enables a measurement of the diffuse reflection of the downwelling radiance from the sky in the same scene as the surface targets. The Hyper-Cam was initially pointed down at the scene at a 9° declination angle. After each downward-looking scene image, the Hyper-Cam was then pointed up 9° at the sky to measure the specular sky radiance component. The elevation view is shown in Figure 318 (b). A diffusivity factor determined from the ratio of the gold target radiance to the sky radiance was applied to enable estimation of the surface emissivity and skin temperature for every pixel within the imaging array of the Hyper-Cam instrument. The FOR of the Hyper-Cam results from a 320 x 256 detector pixel array, with each pixel having a Field of View (FOV) of 0.35 mrad. The unapodized spectral resolution is 0.5 cm^{-1}. The radiance spectra were calibrated using two blackbody references, with

temperatures of 1.0 °C and 55.0 °C respectively. The sample integration time was 200 μs. Because the scene to be imaged was static, an average of ten interferograms per blackbody measurement and ten interferograms per scene measurement was made to reduce the effect of detector noise. The instrument settings are given in Table 14.

Table 14. Hyper-Cam instrument settings for parking deck test.

Interferograms Averaged per Blackbody	10
Interferograms Averaged per Scene	10
FOV	320 x 256
Resolution	1 cm^{-1}
Integration Time	200 μs
Cold Blackbody	1.0°C
Warm Blackbody	55.0°C

The surface scene consisted of wet, dry, and ice-covered concrete and wet, dry, and ice-covered non-skid surfaces (note that the concrete temperature was above freezing). The different surface conditions imaged are given in Table 15, where "bare concrete" refers to the concrete that has not been treated with the non-skid coating; "wet" or "dry" indicates whether water has been poured on the surface.

Table 15. Surface conditions measured during parking deck test.

Time	Scene	Bare Concrete Temp (°C)	Non-skid Concrete Temp (°C)	Gold Plate Temp (°C)
7:22AM	Dry surface conditions, before sunrise	Dry – 23.4, 22.3	Dry – 23.5, 23.5	24.2, 24.1
7:23AM	Sky scene	n/a	n/a	n/a
8:07AM	Dry surface conditions, sun is low in sky	Dry – 25.3, 25.5	Dry – 25.2, 25.3	25.8, 25.9
	Sky scene	n/a	n/a	n/a
8:52AM	Dry & Wet concrete surface scene	Wet - 25.2, 25.2 Dry – 26.7, 26.0, 26.2	Wet only – 24.9, 24.9	27.0
9:06AM	Sky scene	n/a	n/a	n/a
11:03AM	Dry concrete surface conditions	Dry – 35.3, 35.7	Dry – 36.3, 35.8	36.3
11:15AM	Sky scene	n/a	n/a	n/a
~11:45AM	Water and ice in scene (Ice cube 0.1°C, water 6.5°C)	Dry – 39.6, Wet – 33.6	Dry – 35.8, Wet – 18.1	38.0
12:14PM	Sky scene	n/a	n/a	n/a

The experiment was conducted to acquire Hyper-Cam data for a variety of possible runway surface conditions from which the surface emissivity, and in principle surface friction and aircraft stopping distance, can be determined. The wet concrete and non-skid concrete (referred to below as “asphalt”) conditions were observed for different surface temperature and water temperature contrast conditions (i.e. warm water over cold concrete and asphalt and cold water over warm concrete and asphalt, as provided by the melting of the ice).

6.2.1.1 Hyper-Cam Radiance Filtering

The first step in computing surface emissivity from the Hyper-Cam data was to filter detector noise. This filtering was performed by first identifying the bad (i.e. high noise) pixels in the array and then replacing them with an average of the surrounding good pixel values. Here, the bad

pixels were identified using the sky view data, which have a near-constant scene radiance. The algorithm consisted of considering an adjacent 3 x 3 array of data and identifying any outliers from all the differences between each pixel and all of its neighbors. Any pixel was identified as a "bad pixel" if its difference with all neighboring pixel values exceeded one standard deviation of the differences for all pixels within the 3 x 3 array. After the bad pixels were identified, the original sky-view and surface-view radiance values for the bad pixels were replaced with an average of all radiance values for good pixels surrounding the bad pixel.

6.2.1.2 Diffuse Sky Radiance Estimation

An average of this diffusivity factor for all pixels viewing the gold plate was used to estimate the diffuse sky radiance from the sky radiance observed for each pixel in the Hyper-Cam array. Figure 319 shows the average gold plate pixel spectral radiance, along with the sky radiance observed with the same pixels and the spectral diffusivity factor defined as the ratio of the gold plate and sky view radiance values.

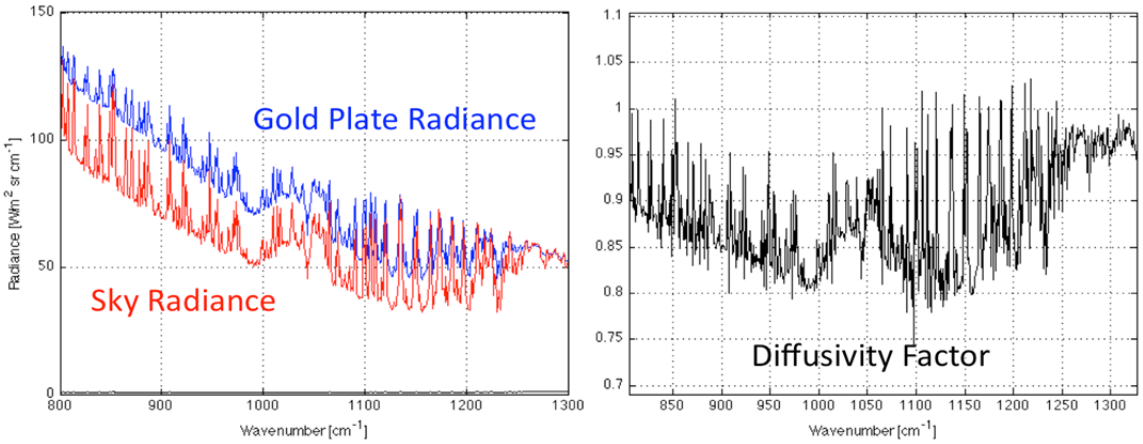

Figure 319. Average surface radiance spectra for pixels viewing the gold plate and average sky radiance for the same pixels viewing that viewed the gold plate.

6.2.1.3 Surface Temperature and Emissivity Determination

The surface temperature and associated spectral emissivity were derived by considering all temperatures within the range of 260 K to 360 K using a five-step iterative process. In the first step, an increment of 10 K was used to define the temperature that minimized the standard deviation of the local spectral derivative of the calculated surface spectral emissivity. Once this temperature was defined, then a 2° increment was used within a 20° interval centered on the first-defined surface temperature value. The iterative process was repeated a third, fourth, and final time, reducing the increment by a factor of 10 after each iteration, to provide a final surface temperature resolution of mK.

Figure 320 shows the spectral emissivities along with the derived surface skin temperatures. Significant differences are evident in the emissivities, depending on the surface condition, thereby providing a significant measure of the surface condition.

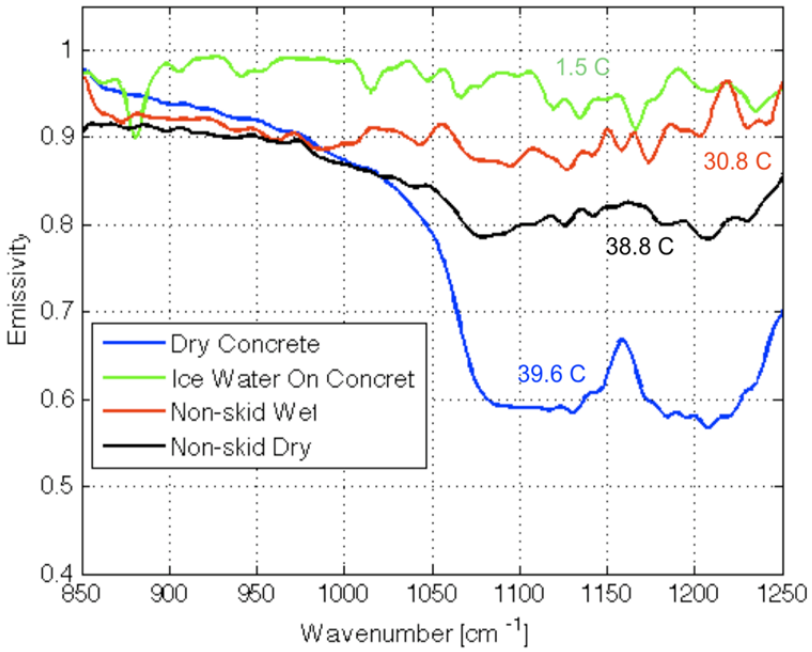

Figure 320. Spectral emissivity of different surface types (i.e. dry concrete, wet concrete, wet non-skid pavement, and dry non-skid pavement) retrieved from radiance spectra observed with the Hyper-Cam instrument

As can be seen, ice and water have very little spectral variation, whereas the dry concrete and non-skid surfaces provide large variations in spectral emissivity, dependent on their coverage with ice and/or water. Most interesting is the apparent accuracy of the surface skin temperature retrieved as that value which minimizes the local surface spectral emissivity variation. The in-situ measurements indicated the following surface temperatures: the dry concrete = 40 ºC (313 K); wet concrete = 34 ºC (307 K); dry non-skid pavement = 36 ºC (309 K); wet non-skid pavement = 18 ºC (291 K); ice = 0 ºC (273 K); and the ice water = 7 ºC (280 K). The retrieved surface temperatures shown in Figure 321 for these different surface conditions are in excellent agreement with these in-situ surface temperature measurements. It is clearly seen that the major spectral emissivity signal of different surface conditions is within the 1000–1250 cm^{-1} (8–10 μm) spectral region. It is this spectral region that is most useful for estimating runway surface condition and potentially aircraft stopping distance from FLI measurements.

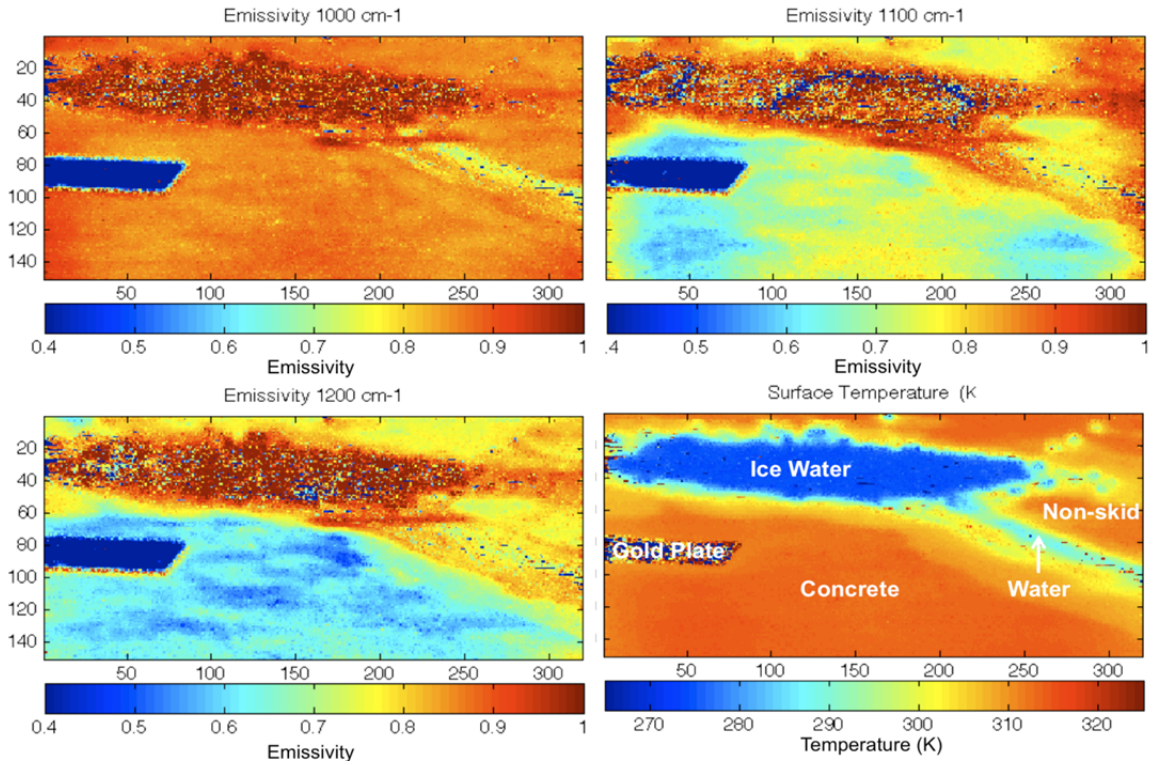

Figure 321. Derived surface emissivity for three wavelengths and the derived surface skin temperature (lower right hand panel). The dark spots are missing data due to the fact that a local emissivity variance minimum was not found in the retrieval process.

6.2.2 Naturally Occurring Ice: January 2011

Atlanta was hit with a rare snowstorm on the night of January 9, 2011; subsequent freezing temperatures all week led to ice on the roads for days. The parking lot south of GTRI's Baker Building provided an excellent location for a Hyper-Cam data collection. There were several surfaces which simulated different runway conditions: bare asphalt; wet asphalt; ice; and snow. The Hyper-Cam data were collected on January 13, 2011, four days after the snowfall, so it should be noted that the snow had developed a thick, icy crust. A photograph of the scene is shown in Figure 322.

Figure 322. Parking lot south of the Baker Building, GTRI, on January 13, 2011.

The ice in the foreground of Figure 322 was beginning to turn slushy at the edges. However, beyond the bare asphalt the sheet of ice was still very solid. That area was selected for subsequent analysis. The asphalt in the middle of Figure 322 was wet and dry in patches; it was difficult to see the difference in either visible or IR images and so several sections of pixels were chosen for analysis. The data were collected at 4 cm^{-1} resolution, and the Labsphere Infragold plate was placed in the scene and the temperature recorded.

As described previously, when the temperature that minimizes the local variance in emissivity is found, it is recorded as the apparent temperature and it used to recalculate the emissivity. The temperatures and emissivities for the ice and snow data were obtained in this manner. The results of the radiance measurements and emissivity derivations are shown in the figures below.

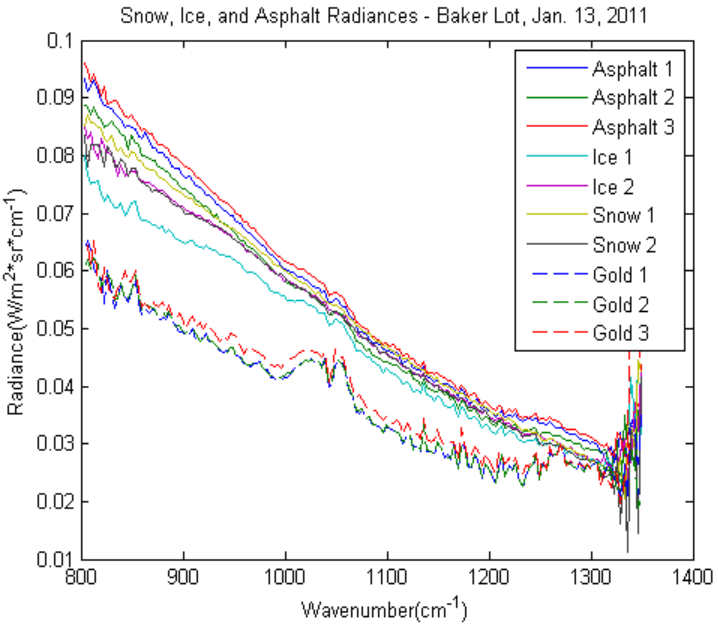

Figure 323. Radiances as measured by the Telops Hyper-Cam of surfaces on the Baker parking lot on January 13, 2011.

The three gold sample spectra in Figure 323 represent the diffusely reflected downwelling radiance. The radiances of all other materials in this figure (asphalt, ice, and snow) contain some of that reflected component, which had not yet been subtracted out. After the reflected component is subtracted, the emissivities for each material were calculated by the minimizing the variance in emissivity. The retrieved temperatures are given in Table 16.

Table 16. Derived apparent sample temperatures.

Sample	Apparent Temperature (°C)
Asphalt 1	5.08
Asphalt 2	1.59
Asphalt 3	6.39
Ice 1	0.55
Ice 2	-0.53
Snow 1	-0.73
Snow 2	1.33

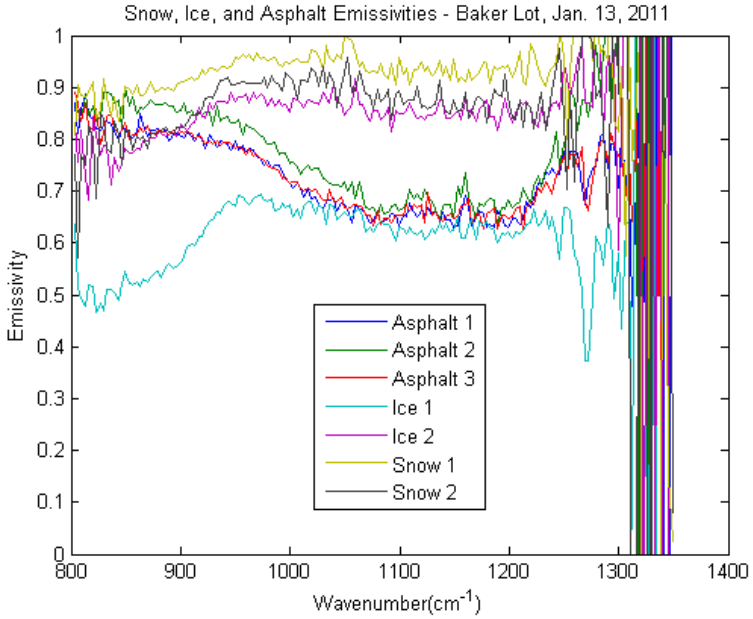

Figure 324. The emissivities of the surfaces on the Baker parking lot.

Figure 324 shows the emissivities calculated from the apparent temperatures in Table 16. The results, while somewhat noisy, clearly show a difference in the shape of the emissivity of asphalt versus snow or ice. Figure 325 shows this more clearly, where average spectra are shown for each material.

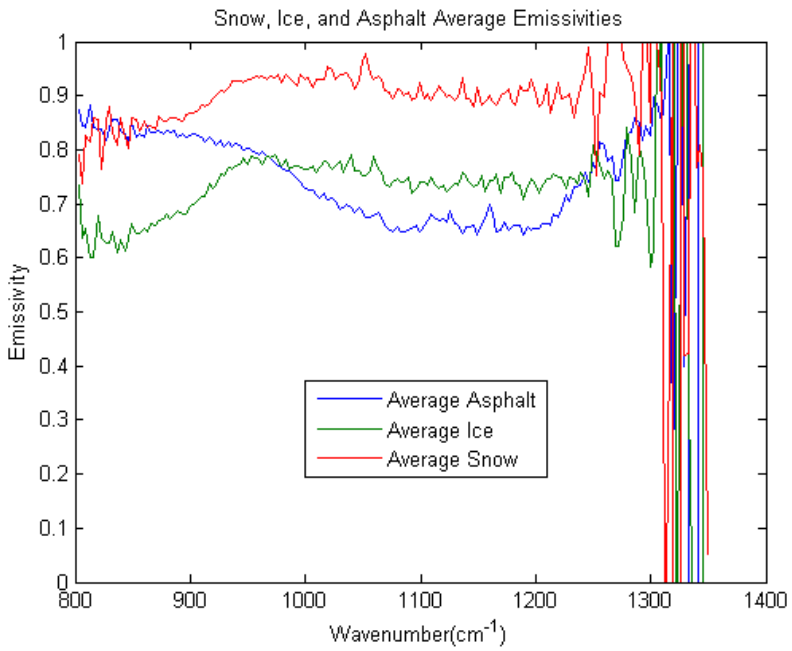

Figure 325. Average material emissivities.

The difference between the ice and snow emissivity spectra and the asphalt emissivity spectrum is clearly evident in Figure 325. As can be seen in Figure 323, none of the radiance spectra has a unique spectral feature that stands out from the rest. The feature in Figure 323 between 1000 and 1100 cm^{-1} that appears in the asphalt, ice, and snow radiance spectra is most likely due to the reflected sky radiance. These results are consistent with those from the September 2010 field measurements.

While the differences have been noted in Figure 325, it is also noted that the ice and snow spectra are very similar. As noted earlier, the snow was four days old and had developed a crust; this could account for the similarities. The difference in magnitude could be attributed to surface roughness and/or differences in viewing angle, because the snow was on a hill on the opposite side of the parking lot.

6.2.3 MRS Emissivity Measurements: November 2011

On November 19, 2011, there was an opportunity to measure the emissivity of natural snow and concrete in the MRS parking lot. An example of the results for one run is shown here. The technique for determining emissivity from the November 19 Telops Hyper-Cam data consisted of the following steps:

1. Ingest 1 cm^{-1} spectral resolution calibrated radiances and replacing bad pixel data with neighboring values;
2. Perform a 10 x 10 x 10 3-D boxcar smoothing of the data to minimize random noise;
3. Define the sky radiance from the radiance observed for the gold plate within the field of regard assuming that:

$$R_{SKY}(\nu) = R_M(\nu) - \frac{(1 - R_G) \times B(\nu, T_G)}{R_G} \tag{6.2.1}$$

Where $R_M(v)$ is the measured radiance, R_G is the reflectance of gold, assumed to be 0.99, and T_G is the temperature of the gold plate which was measured to be 274.6 K. $B(v,T_G)$ is the Planck radiance corresponding to the spectral frequency v and the temperature T_G;

4. Create a cube of spectral mean brightness temperature for spectral frequencies 800–1200 cm^{-1};
5. Compute the cube average spectral mean brightness temperature;
6. Define snow and concrete fields of view assuming that any spectral mean brightness less than the cube average was snow and any spectral mean brightness temperature greater than or equal to the cube average was concrete; and
7. Define the spectral emissivity, $\varepsilon(v)$, of the surface using the relation in Equation 6.1.5, where the surface temperature was measured to be 273.7 K for the snow and 275 K for the concrete within the Hyper-Cam's field of regard.

Figure 326 shows the results of a single run of Hyper-Cam measurements. Shown are the spectral mean brightness temperature and the emissivity for the 850, 1000, and 1150 cm^{-1} spectral channels, respectively. One can see that the mean brightness temperature is less than the physical temperature of the surface, dependent upon the surface emissivity. Although the surface temperature was assumed to be equal to the physical measurements taken in-situ for this case, in practice the physical temperature must also be retrieved simultaneously with the spectral emissivity for the runway friction determination application.

Figure 327 shows the cube average spectrum of emissivity derived for the snow and ice conditions. Surprisingly the snow spectral emissivity is considerably smaller than that for concrete, a result that requires further validation. The relatively low snow surface emissivity may be due to: (1) the off-axis angle of the measurements; (2) an unrepresentative temperature measured in-situ for the snow; and/or (3) an incorrect estimate of the gold plate reflectivity used to compute the sky radiance from the gold plate measurements.

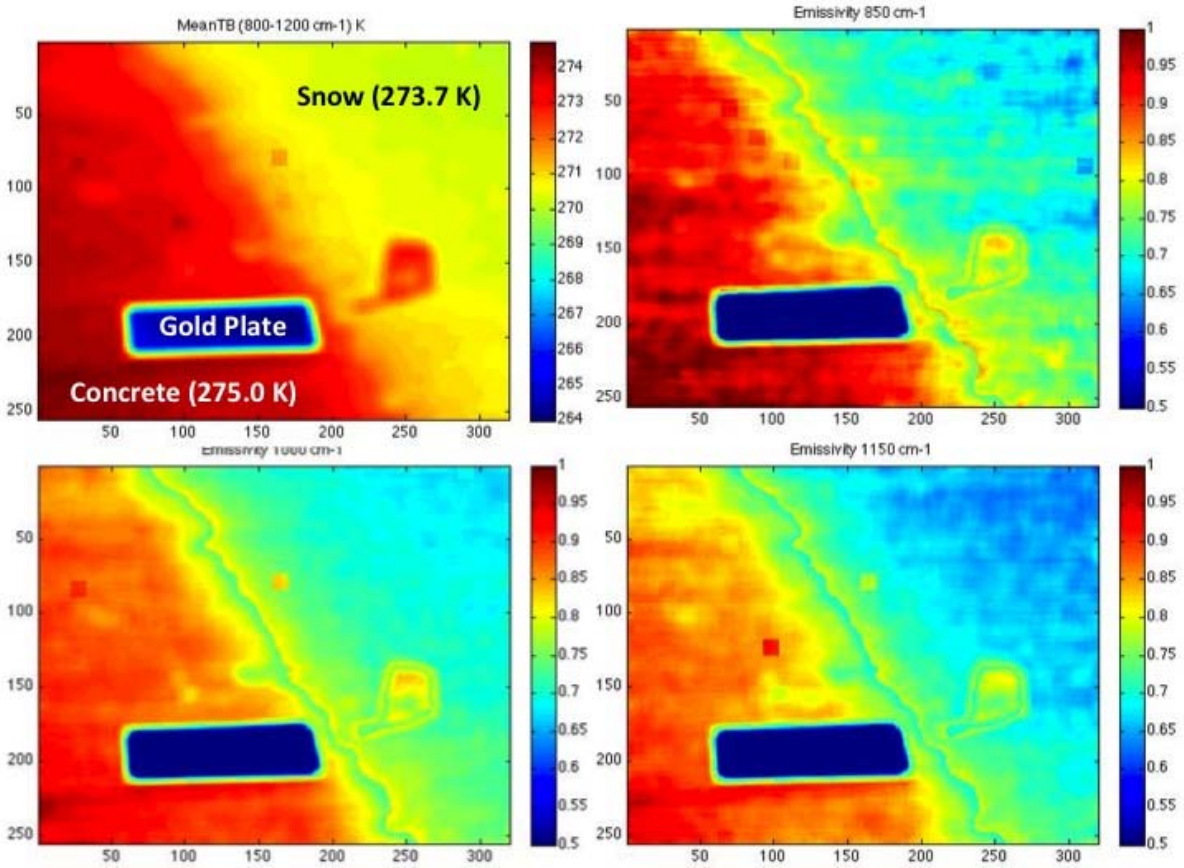

Figure 326. Hyper-Cam measurements for run "snow_scene_0000022941" taken on November 19, 2011 at the Mountain Research Station in Colorado. The upper left panel shows the spectral mean brightness temperature whereas the remaining three panels show the emissivity for the 850, 1000, and 1150 cm^{-1} channels, respectively.

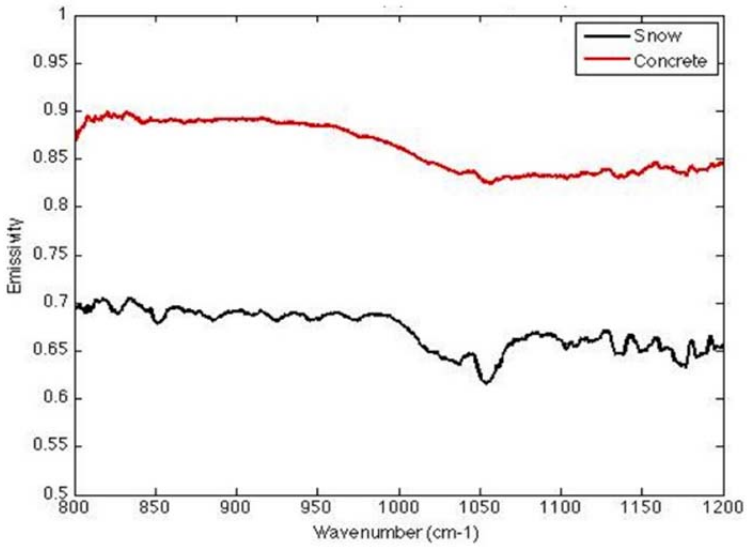

Figure 327. Cube average emissivity spectrum for snow and concrete.

6.2.4 Staged Ice and Water: Winter 2012

Hyper-Cam measurements of a second test on the parking deck on the Georgia Tech campus were made on November 20, 2012. The measurements were made to see if sky could be used as a substitute for the reflected component in the calculation of emissivity.

The field test was set up to look at a scene similar to the parking deck test from September 2010 (Section 6.2.1), where a scene was staged to look at dry and wet concrete and ice. In those measurements, the gold standard was placed in the scene because it is a diffuse and nearly perfect reflector of the background in the infrared. As previously described, the gold plate is necessary for retrieval of true emissivity because the radiance measured at the sensor is made up of both emitted and reflected radiance from the target. The development of a methodology for estimation of apparent emissivity when the reflected component is unknown is desirable. A potential method used sky spectra as an estimate of what would be reflected by the gold plate. However, after looking through all previously collected datasets, a datacube with enough foreground and sky could not be found. Therefore, in the November 20, 2012 test, the scene was staged to include the dry and wet concrete and ice, as well as enough sky for analysis.

A Google map view of the test site and set up is shown in Figure 328. During the test, the wide field of view optic (25.6° x 20.4°) was used and the Hyper-Cam was viewing west. There were no buildings in the field of view, only the parking deck scene and the sky.

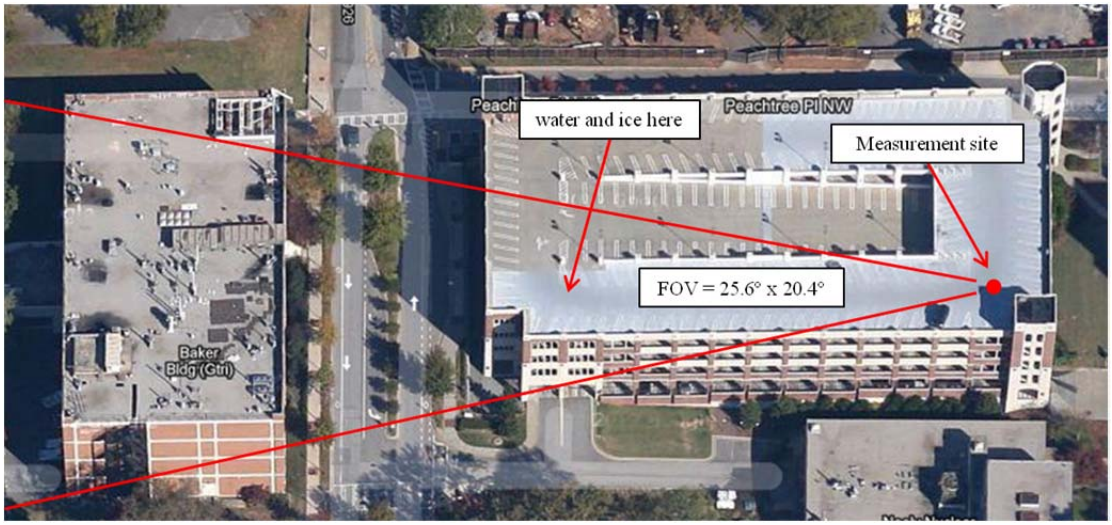

Figure 328. Emissivity test plan set-up.

A radiance image of one of the datacubes is shown below in Figure 329. This image is from a datacube recorded at 6:40 AM (EST), right before sunrise. All datacubes were collected at 1 cm^{-1} resolution because the Minimum Local Emissivity Variance (MLEV) method depends upon the narrow spectral lines that appear due to water and other molecules in the atmosphere. Note that the gold standard is still in the scene (in red box) for comparison of the apparent emissivity algorithms with the true calculation.

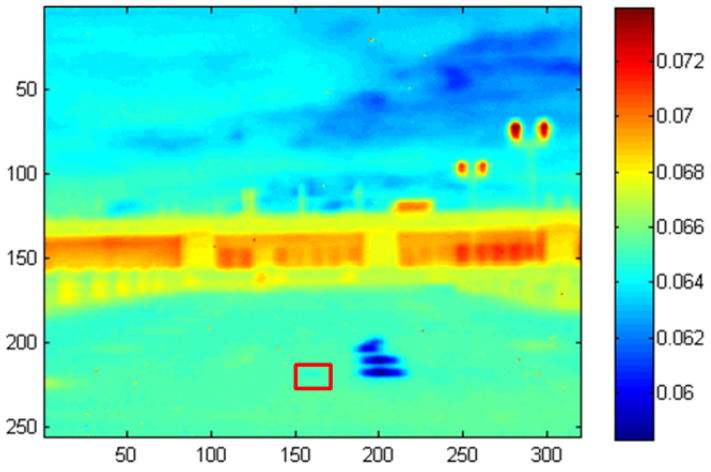

Figure 329. Radiance image of parking deck and sky at 6:40 AM EST. The radiance image is an average over all bands (excepting the first and last 50), Radiance units W/cm^{-1}m^{2}sr.

A second set of Hyper-Cam measurements on the parking deck on the Georgia Tech campus were made on December 19, 2012. These measurements were conducted in the exact same manner as the measurements made in November 2012 so are not described again. The only difference was that the December test was planned for a clear day (in November it was cloudy), and the narrow FOV optic was used to increase the spatial resolution. The set-up is shown below in Figure 330. The FOV from the November test and the FOV from the December test are shown in this figure and are represented by solid and dashed red lines, respectively. In November, the FOV was 25.6° x 20.4°, and in December the FOV was 6.4° x 5.1° (horizontal x vertical).

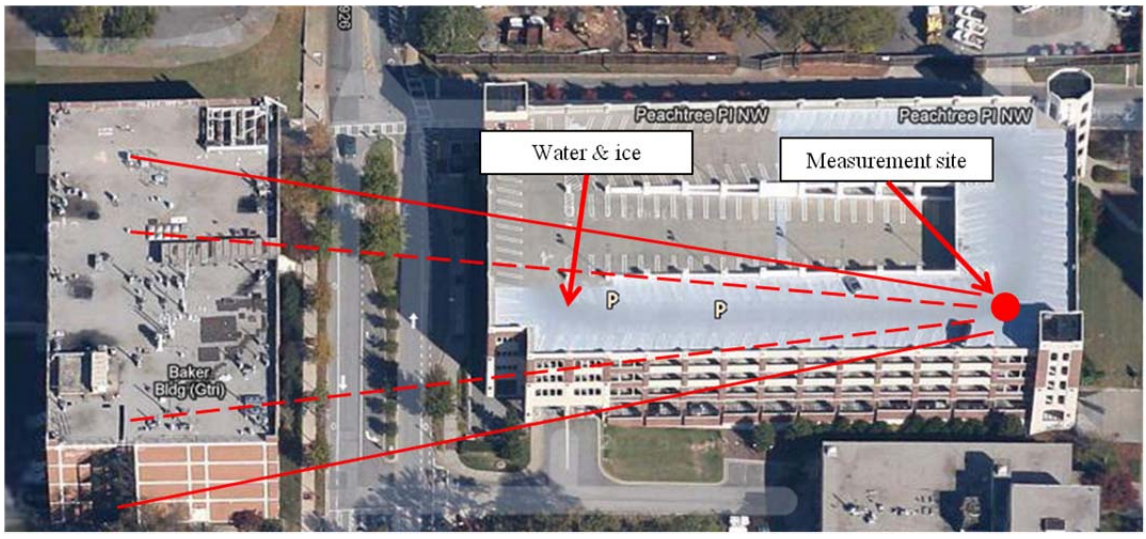

Figure 330. Emissivity test plan set-up. The solid lines represent the FOV used in the November test; the dashed lines represent the FOV used in the December test.

An averaged radiance image from the parking deck test conducted on December 19 is shown in Figure 331. In this scene, the Hyper-Cam is positioned on the parking deck looking sideways. Therefore, the scene is looking along the parking deck with a building behind it and the sky above. In this image, the ice and water are circled in yellow and red, respectively. The gold

reflectance standard was also in the scene; however, due to the narrow field of view there are not enough pixels on target to distinguish it in the image. The gold reflectance standard radiance is not crucial to the following analysis; the standard was placed in the scene only in case we wished to analyze the data as we have done previously. Therefore not having enough pixels on that target is not detrimental to the analysis.

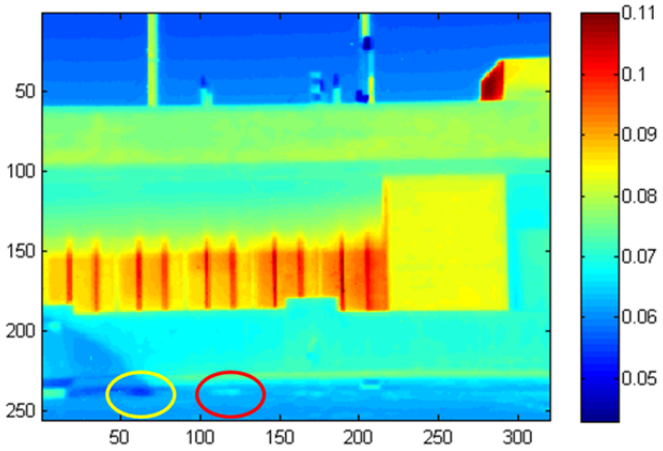

Figure 331. The averaged radiance datacube from the Dec 19 test. The ice is circled in yellow, and the water is circled in red. Radiance units W/m^{2}cm^{-1}sr.

As described, the purpose of this test was to see if the radiance of any sky pixels could be used as a substitute for the radiance of the gold plate pixels. This technique did not work, as we described in Section 6.1.1. Therefore, because this dataset had longer path lengths then all previous sets, we decided to test the ISAC method that was described in Section 6.1.2.

The first step of this method was to calculate the brightness temperatures for each datacube. This was done for one datacube from November 20 and one datacube from December 19. Note the sizes of both images were cropped in all three dimensions to save processing time. Then, the wavenumber index where the brightness temperature is a maximum value was found for both images. These maxima occurred at 1259.9 and 1257.4 cm^{-1} for the November 20 and December 19 images, respectively. The brightness temperature images are shown below in Figure 332.

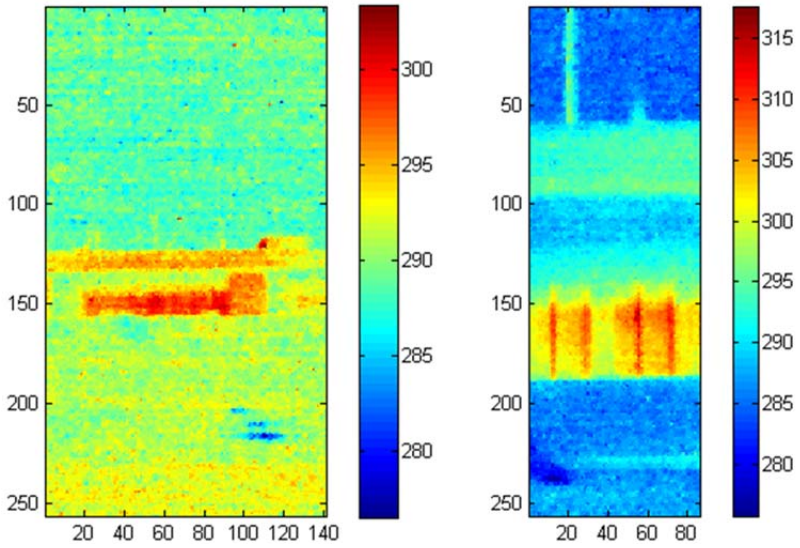

Figure 332. Maximum brightness temperature images for November 20 *(left)* and December 19 *(right)* datasets, brightness temperature in Kelvin.

After the maximum wavenumber index was found, the Planck function was calculated for all pixels for the brightness temperature at this index. This calculation was performed for the two images shown in Figure 332. Then, a scatterplot was created of the measured radiance vs. the calculated Planck function for all pixels in each image. These plots are shown below in Figure 333.

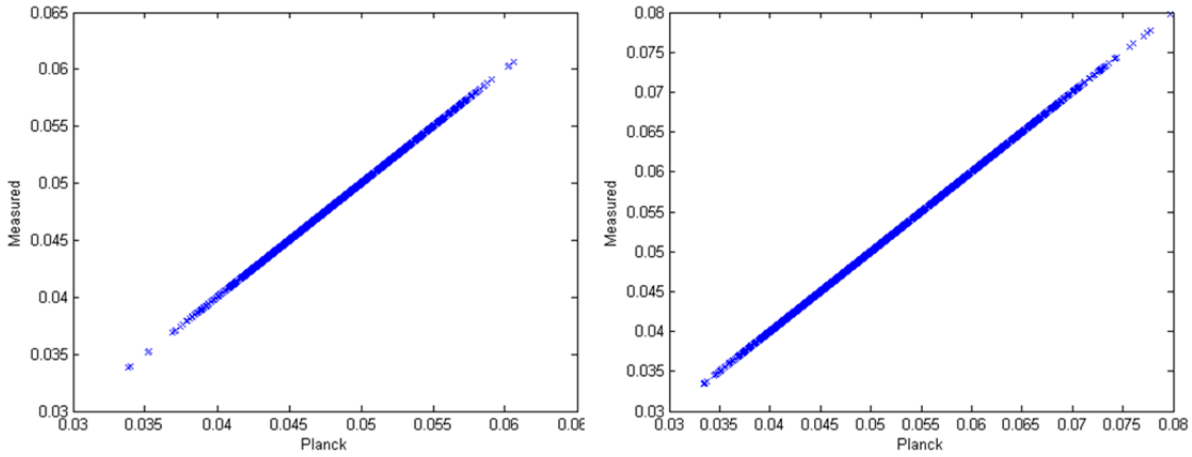

Figure 333. Scatterplot of measured radiance vs. Planck calculated radiance for November 20 *(left)* and December 19 *(right)* datasets. Data shown at 1259.9 and 1257.4 cm^{-1}, respectively. Radiance units W/m^{2}cm^{-1}sr.

The plots shown above indicate that the measured radiance is nearly equal to the Planck computed radiance for both November and December datasets. They are very close due to the manner in which the Planck radiance was computed; these plots show the measured vs. Planck radiance at the wavenumber index where the brightness temperature was found to be maximum. These scatterplots were then created for every wavenumber index in the datacube for the

brightness temperature at the maximum. Scatterplots at 965.7 cm-1 are shown below in Figure 334 for the two datasets.

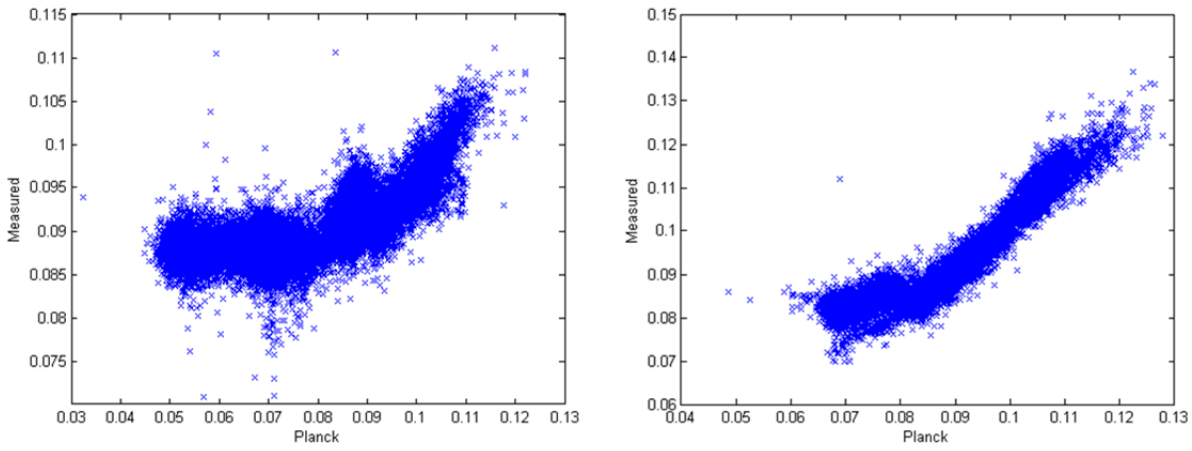

Figure 334. Scatterplot of measured radiance vs. Planck calculated radiance for November 20 (left) and December 19 (right) datasets. Data shown at 965.7 cm^{-1}. Radiance in $W/m^2cm^{-1}sr$.

Lines were fit to the top-most pixels in the scatterplots to find the atmospheric transmission and path radiance (see Equation 6.1.8). However, we were unable generate reasonable results. We believe that there were not enough blackbody-like pixels in this scene (mostly concrete, which has Reststrahlen feature), which we knew prior to the analysis but decided to try anyway. Another data collection was planned to collect more data to test the ISAC method; however, given that we could not find a way to eliminate the gold plate measurement, the data collection was cancelled.

6.3 Surface Emissivity Retrieval Algorithm

The radiative transfer equation governing the radiance spectrum observed with a FLI on an aircraft approaching an airport runway is

$$\begin{aligned} R(\nu,\theta) = {} & \varepsilon(\nu,\theta)B(\nu,T_S)\tau\left[(p_{aircraft},p),\nu,\theta\right] \\ & + \rho(\nu,\theta)\tau\left[(p_{aircraft},p),\nu,\theta\right]\int B(\nu,T)d\tau[(p_S,p),\nu,\theta] \\ & + \int B(\nu,T)d\tau\left[(p_{aircraft},p),\nu,\theta\right] \end{aligned} \tag{6.3.1}$$

Where the first term is the surface radiance reaching the FLI, the second term is the surface reflected downwelling atmospheric radiance reaching the FLI, and the last term is the atmospheric emission between the aircraft level and the surface received by the FLI.

The retrieval model used is a radiance eigenvector (EOF) regression model where the runway surface emissivity spectrum $\varepsilon(\nu,\theta)$ and skin temperature T_S are predicted from a linear combination of radiance eigenvector coefficients. The matrix of radiance eigenvectors was computed from a training set of simulated radiances.

LBLRTM was used to produce a statistical training set of spectra based upon the September 2010 surface emissivity measurements described in Section 6.2.1. Accurate line-by-line calculations provide us with more line signatures in the output spectrum due to the reflected term in

Equation 6.3.1, which in turn leads to more information content in the measurements, because it allows us to unlink the emissivity and skin temperature signals in the measured spectrum.

The surface emissivity spectrum for the training set of radiances was represented by a linear model as

$$\varepsilon(\nu_k) = \sum w_i \varepsilon^*_{i,k} \tag{6.3.2}$$

Where w_i are weights for the combination of five possible runway surface emissivity types, $\varepsilon^*_{i,k}$ (i.e. asphalt, concrete, water, ice, and snow) of Equation 6.3.2 and shown in Figure 335.

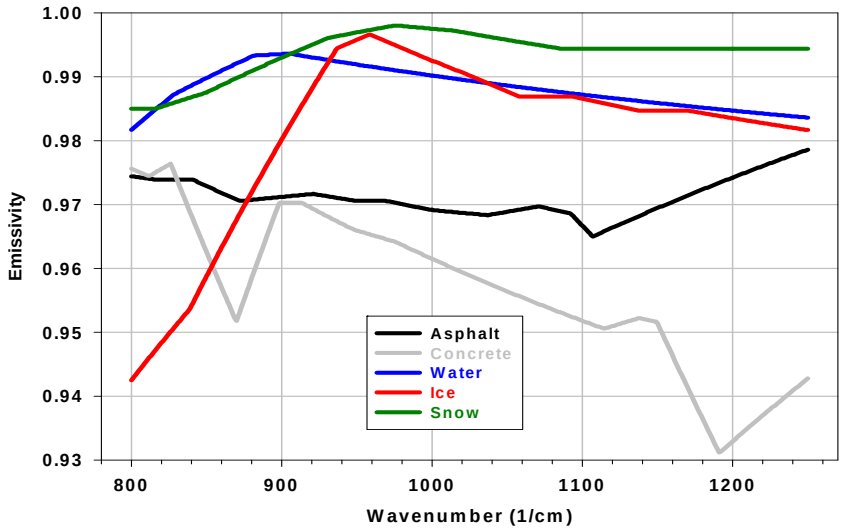

Figure 335. Spectral emissivities of different surface types assumed for development of the training set.

The radiance/emissivity training data set was generated using LBLRTM for the conditions where aircraft altitudes were 100 m, 300 m, and 500 m. The viewing angle was fixed and equal to 5.7 degrees below the horizon, which corresponds to 1 km, 3 km, and 5 km distances to the runway, respectively. For each altitude, the ground air temperature T_{air} was uniformly distributed within a 260 K to 320 K range, in 5 K increments. The surface temperature was randomly distributed around the ground air temperature by adding Gaussian noise with bias 0 K and sigma 3 K. The spectral range was 850–1200 cm^{-1} and the spectral resolution was 1 cm^{-1}. Different runway surface emissivity spectra were generated by selecting the w_i's from a uniform distribution of random numbers ranging between 0 and 1, with the results scaled so that the sum of the w_i's equaled unity. The emissivity weights were additionally constrained so that w(water) = 0 when the surface temperature was below 270 K, and the weights for ice and snow were set equal to zero when the surface temperature exceeded 275 K. A total of 500 randomly generated surface emissivity spectra and skin temperatures were used to produce FLI radiance spectra for each of the 13 ground air temperature conditions, yielding 6,500 different runway surface conditions for given aircraft altitude. Clear skies were assumed for all of this analysis. Empirical orthogonal functions were calculated from the training set of FLI radiances for each aircraft altitude separately.

The retrieval vector includes the surface temperature and 5 weights w_i for the emissivity spectrum of different surface types used. The same set of training radiances was used to check the accuracy of the retrieval, but artificial noise with NEdT = 0.1 K, 0.3 K, and 0.5 K was added to the original radiances for the retrieval. The accuracy of the retrieval significantly depends on the number of the radiance principal components (PC-scores) taken for prediction. Figure 336 shows the root mean square error of the retrieved surface temperature (averaged over 6500 trials for an aircraft altitude of 300 m) as a function of the number of PC-scores taken into account.

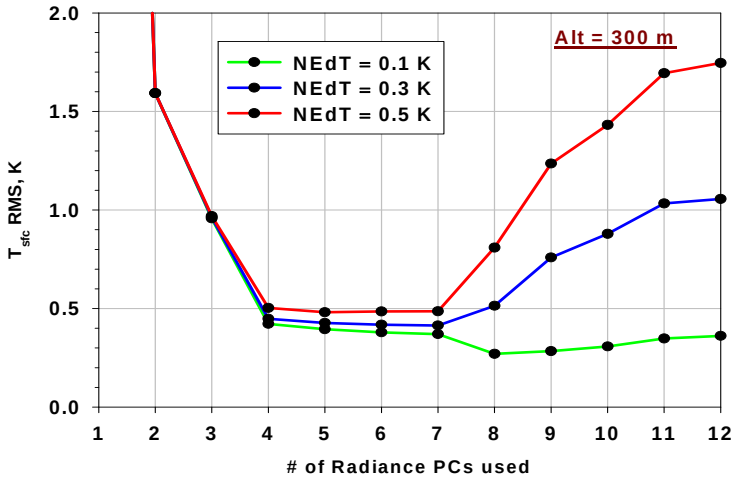

Figure 336. Root Mean Square Error of the retrieved surface temperature for the 6,500 simulated runway surface conditions and for three different radiometric measurement noise levels; aircraft altitude 300 m.

As follows from Figure 336, the optimal number of PCs ranges from 4 to 7 in terms of the best accuracy. The same range for the number of PCs is optimal to retrieve the weights of the emissivity spectra (with slight variations depending on noise level). It is worthwhile to note that the initial variability for the surface temperature in the set was ~18.5 K (260 – 320 K range for the ground air temperature T_{air} plus additional 3 K random variations for T_S around T_{air}), while the retrieved surface temperature is within a 0.5 K statistical agreement with the "true" one.

Figure 337 shows the root mean square error of the retrieved surface emissivity spectrum for all 6,500 surface temperature/emissivity cases and for the three aircraft altitudes. It can be seen that the emissivity error significantly depends on the noise level (it almost doubles for a radiometric brightness temperature error of 0.5 K as opposed to 0.1 K). The figure also shows that the emissivity error is slightly increasing with aircraft altitude.

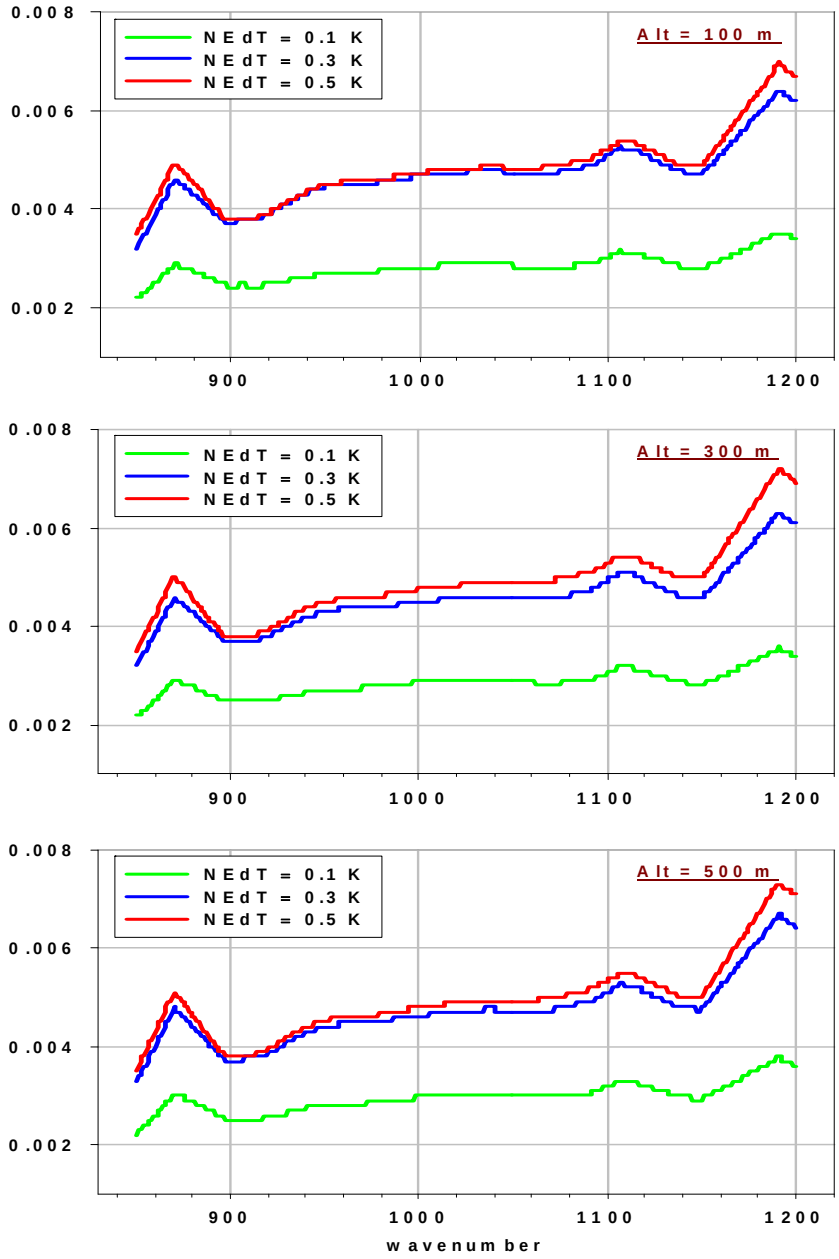

Figure 337. Root Mean Square Error (RMSE) of the retrieved surface emissivity spectra for the 6,500 simulated runway surface conditions, for three different radiometric measurement noise levels, and for three different aircraft altitudes

Following the development of the emissivity retrieval algorithm, it was then updated as follows:

1. Emissivity spectra retrieved from real measurements in Atlanta, in September 2010, were used to generate the random set of emissivity spectra;
2. More accurate computing of the downward radiance was accomplished; and
3. Specular surface reflectance was replaced with diffuse (Lambertian) reflectance.

The emissivity spectra retrieved from real measurements made with the Hyper-Cam in Atlanta are presented in Figure 320. Those spectra were used as a basis to generate random emissivity while checking the accuracy of the regression retrieval.

A second radiance/emissivity training data set was generated using LBLRTM. As noted above, the surface reflectance was changed from specular to diffuse. Figure 338 shows the difference in radiances due to this change. Although this difference is not large in comparison with the total signal, it has clear line structure, which helps to unlink surface temperature/emissivity coupling during retrieval.

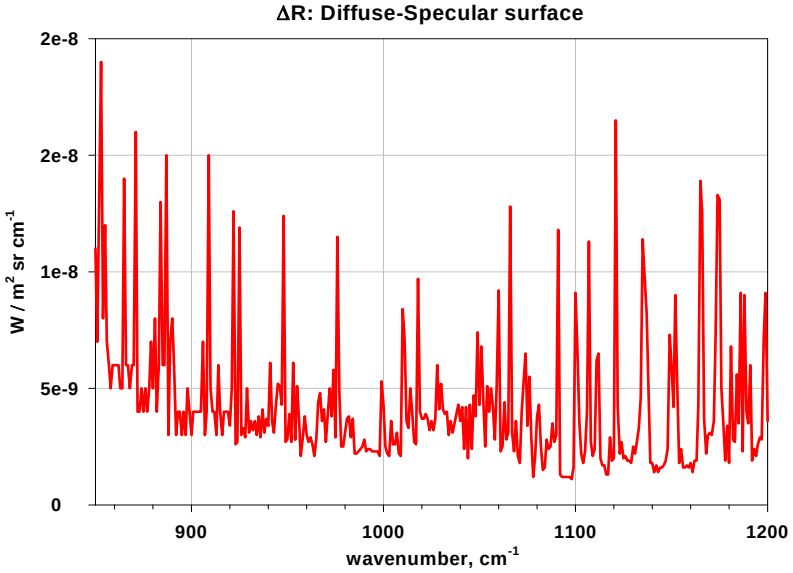

Figure 338. The difference in radiances for the same atmospheric state when the surface reflectance is specular or diffuse.

As before, the viewing angle was fixed and equal to 5.7 degrees below horizontal, which corresponds to 1 km, 3 km, and 5 km distances to the runway for aircraft altitudes of 100 m, 300 m, and 500 m, respectively. The spectral interval was the 850–1250 cm^{-1} range and the spectral resolution was 1 cm^{-1}. Different runway surface emissivity spectra were again generated by selecting the w_i's from a uniform distribution of random numbers ranging between 0 and 1 with the results scaled so that the sum of the w_i's equaled unity. The emissivity weights were additionally constrained as before so that w(wet) = 0 when the surface temperature was below 270 K, and the weight for icy concrete was set equal to zero when the surface temperature exceeded 275 K. A total of 500 randomly generated surface emissivity spectra and skin temperatures were used to produce FLI training spectra for a given aircraft altitude.

Figure 339 shows mean radiance values and standard deviations for the training set, for an aircraft altitude of 300 m. The downward radiance at the surface level is shown in Figure 340. As it is partially reflected, it contributes to the line structure of the total observed radiance.

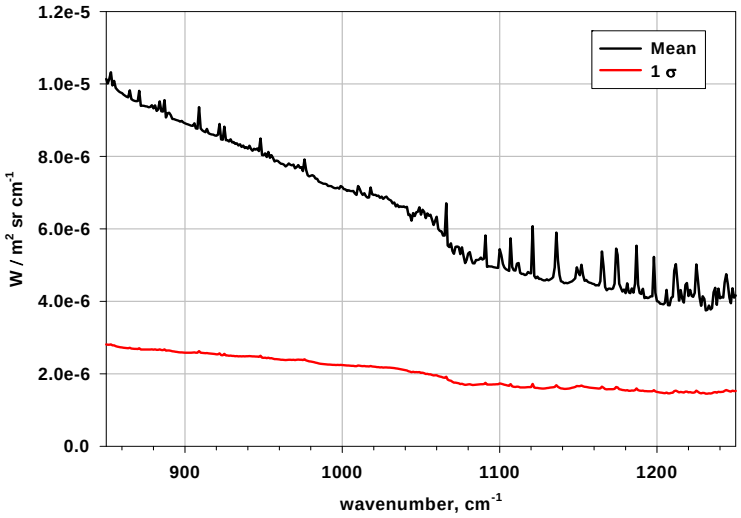

Figure 339. Mean and standard deviation for training set of radiances; aircraft altitude 300 m.

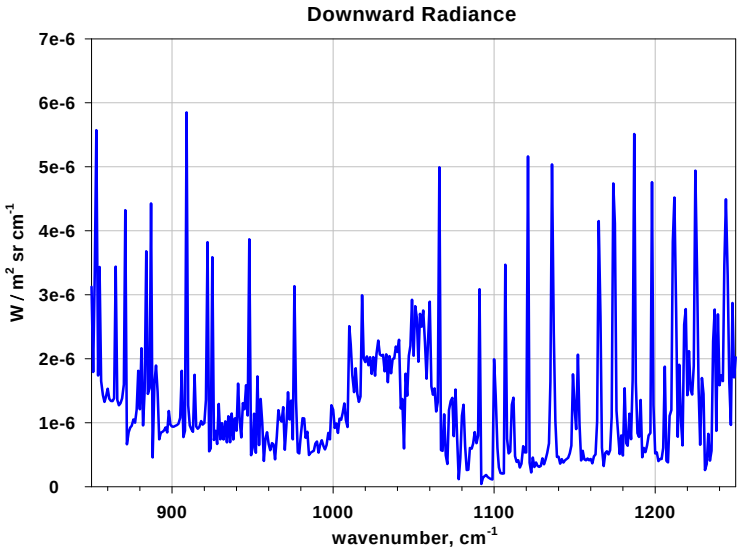

Figure 340. Downward radiance at the surface level.

The same set of training radiances was used to check the accuracy of the retrieval, but artificial noise with NEdT = 0.3 K, 0.5 K, and 1.0 K was added to the original radiances for the retrieval. Figure 341 below shows the root mean square error of the retrieved surface emissivity spectrum for an aircraft altitude of 300 m, averaged over 500 different runway conditions. Note that the total emissivity error over whole spectrum is about 1/100 of the added noise level, i.e. it is equal to ~0.003, ~0.005, and ~0.01 for NEdT = 0.3 K, 0.5 K, and 1.0 K, respectively.

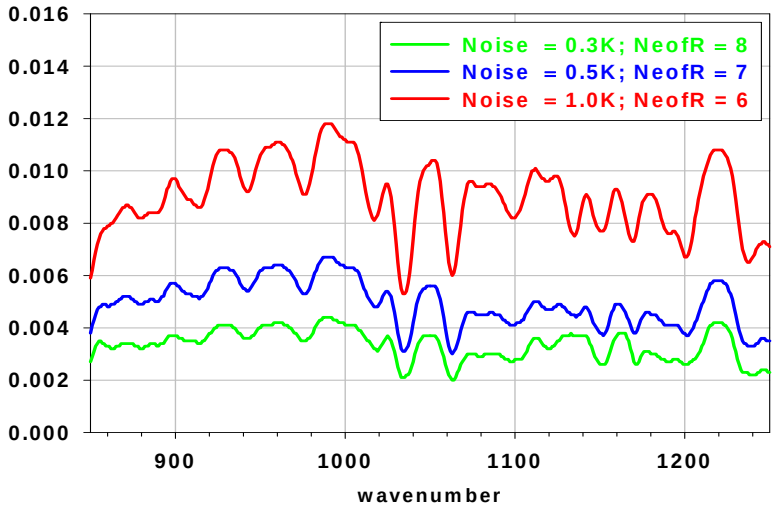

Figure 341. Root Mean Square Error (RMSE) of the retrieved emissivity averaged over 500 simulated runway surface conditions and for three different radiometric measurement noise levels; aircraft altitude 300 m.

6.4 Surface Emissivity Conclusions

The surface emissivity is a difficult property to calculate because it is difficult if not impossible to measure all variables at measurement time. It is true that for most materials the emission term dominates the at-surface radiance term; however, due to the spectral nature of incident radiance, it cannot be neglected. For emissivity calculation, we have shown that small errors in the input variables (of as little as 1%) lead to large errors in the output (up to 400%). The incident radiance is also a very difficult quantity to measure; it requires simultaneous measurement of a Lambertian reflector made of a low emissivity material and with known temperature. We used a roughened gold plate, which is standard practice, but it only exists in experimental set-ups.

Furthermore, consider the plot shown in Figure 342. It contains emissivity of water, ice, frost, snow, concrete, asphalt, and asphaltic concrete. These data were compiled from JPL's ASTER Spectral Library and the UCSB MODIS Emissivity Library. This figure is similar to Figure 314 in that the same types of materials have been plotted to show the emissivity differences among several materials representative of runway conditions. However, note the scale of each axis on both figures. In Figure 314, the wavelength axis is scaled between 3 and 14 μm, and the emissivity axis is scaled between 0.93 and 1.0. In Figure 342 the wavenumber axis is scaled between 800 and 1350 cm^{-1}, and the emissivity axis is scaled between 0.84 and 1.02. The wavenumber scale was chosen for this figure because it represents that which is observable with the Hyper-Cam; the scale corresponds to 8 to 12.5 μm.

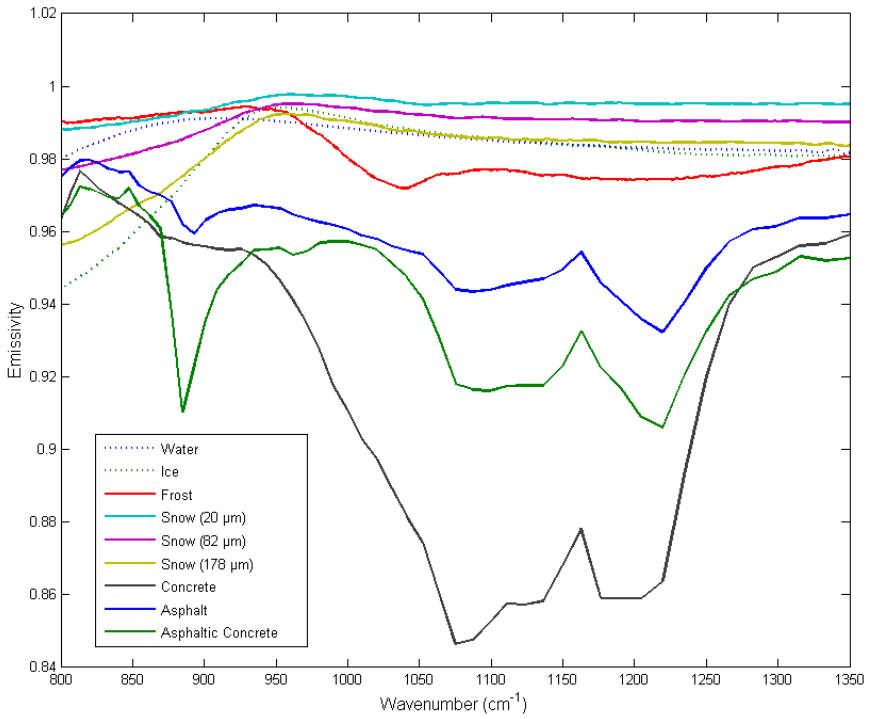

Figure 342. Spectral emissivity of materials representative of runway surfaces [38] [39].

We must consider not only the emissivity differences among the surfaces, but also emissivity differences among the surfaces in the waveband region that is observable with the Hyper-Cam when making conclusions about the emissivity measurements in the previous section. In the 800 to 1350 cm^{-1} region, the emissivity of ice, water, and snow are nearly identical. In Figure 314 there is a substantial separation between the emissivity spectra of ice and water between 11 and 14 µm, but this corresponds to ~715 to 910 cm^{-1}, and the Hyper-Cam range overlaps from 800 to 910 cm^{-1} only. If one looks at the "U" shape of the NESR of the Hyper-Cam at 1 cm^{-1} resolution (see Appendix A), it becomes apparent that most of the overlapping region is in the noise. Therefore, there are differences among the emissivity of the materials in the *stated* range of the Hyper-Cam, however, we must consider the differences among the emissivity of the materials in the *effective* range of the Hyper-Cam.

Despite the limitations, we have demonstrated that we can determine material emissivity with the MLEV method in staged scenes. However, the overall goal is to define the requirements for a FLI sensor. The MLEV method requires high spectral resolution, which means that if a FLI sensor were to use this algorithm, it would need to be a hyperspectral sensor. The hyperspectral measurements were to be used as a study to determine if certain bands could be identified that could be used to possibly set the requirements for a broadband, duel band, or multispectral sensor FLI sensor. We attempted to do band comparisons in the radiance domain, but due to different illumination conditions among different data sets, we realized the need to work in the emissivity domain. We were unable to identify an appropriate temperature and emissivity separation algorithm that had the potential to be effectively translated from a purely research demonstration to a real-world, real-time FLI sensor application.

One might note in Figure 314 that there are also differences among emissivity spectra in the mid-wave Infrared (3 – 5 μm) region. There are sensors that operate in this waveband; but, emissivity measurement in the MWIR presents new challenges: in particular, there is substantial contribution from direct solar irradiance that may dominate the calculation, and the minimization technique that works in the LWIR cannot be applied to the MWIR [36]. Kanani et al [36] recommend minimizing the emissivity variance in the LWIR, and once the temperature is determined, using this temperature to compute emissivity in the MWIR. This method would again require a hyperspectral sensor covering the two bands.

6.5 Runway Obscuration

As a part of funding for another project, the GTRI research team was able to acquire LWIR images of animals in various conditions at Yellowstone National Park in May 2010. The following images were not collected with the Hyper-Cam, but rather a Fluke Ti10 Thermal Imager. The specifications of the thermal imager are given below in Table 17. Note that the spectral band of this thermal imager is the same as the Hyper-Cam.

Table 17. Fluke Ti10 specifications.

Field of view	23° x 17°
Spatial resolution (IFOV)	2.5 mrad
Minimum focus distance	Thermal lens: 15 cm (6 in) Visible (visual) light lens: 46 cm (18 in)
Focus	Manual
Image frequency	9 Hz refresh rate
Detector type	160 X 120 focal plane array, uncooled microbolometer
Infrared lens type	20 mm F = 0.8 lens
Thermal sensitivity (NETD)	≤ 0.2 °C at 30 °C (150 mK)

The following images were collected with the Ti10 LWIR imager. Figure 343 and Figure 344 are of a wolf walking on the roads at Yellowstone at night. Figure 345 is of a deer at night in the visible and LWIR. Figure 346 is a herd of elk at night on the grass. Figure 347 is a herd of elk in the daytime on the grass. These images, while not taken with the Hyper-Cam, are representative of images that the Hyper-Cam would take since they are both imaging in the same spectral band. It is evident in these images that animals are distinct from the background in both the day and the night. The animals stand out from the background because they are much warmer than the background. Also note that the pavement is differentiated from the grassy surroundings because of the relative temperature differences.

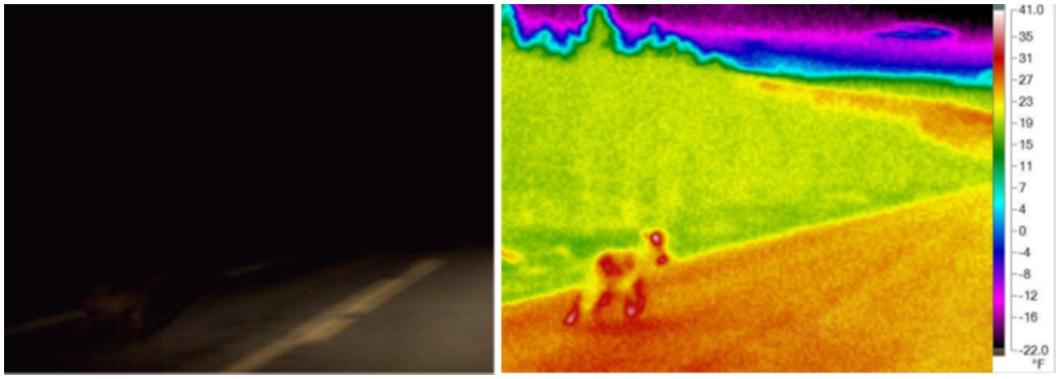

Figure 343. Grey Wolf at night on pavement, Yellowstone National Park: visible (*left*) , and LWIR (*right*).

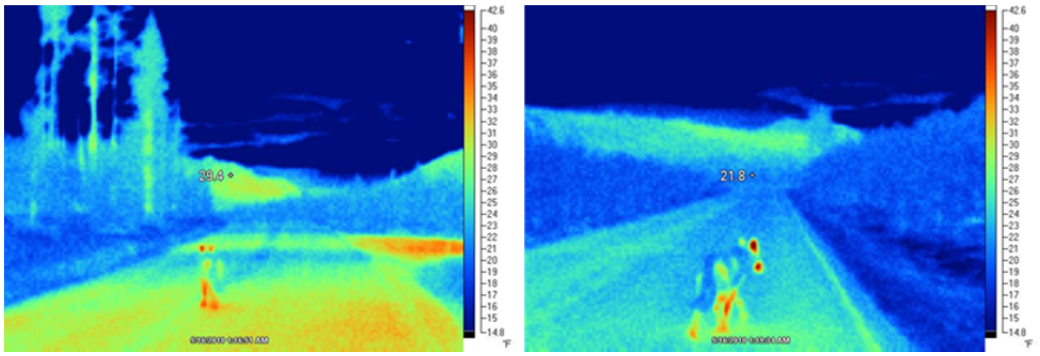

Figure 344: Wolf at night, on pavement. (visible images are not shown, they were black).

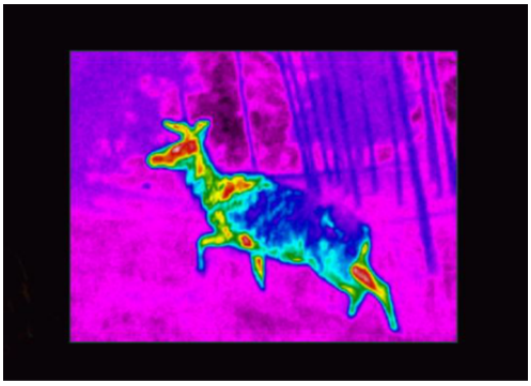

Figure 345. LWIR image of deer at night at YNP in central region of composite image (visible image is black border).

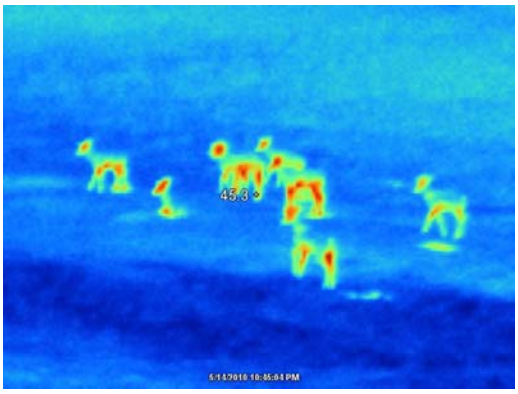

Figure 346: Elk at night in the distance, on grass.

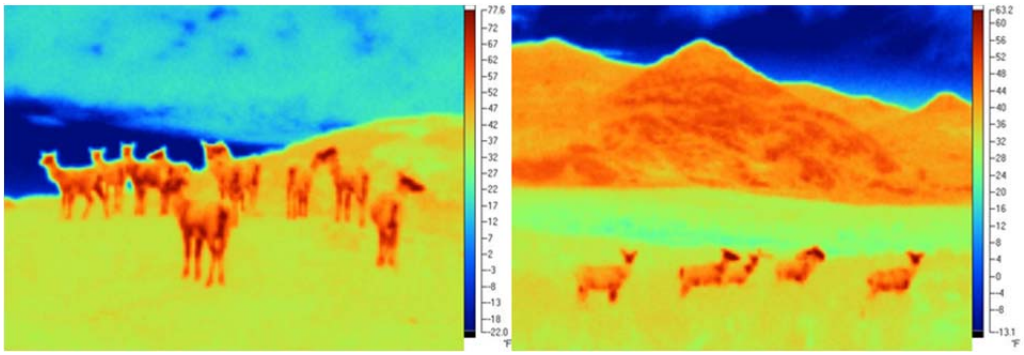

Figure 347: Elk in day in the distance, on grass.

7 Low Visibility

Based on the sensitivity studies in the previous Phase 1 FLI project, an imaging FLI spectrometer is expected to provide enhanced vision in the cockpit of an aircraft in low visibility conditions. The image quality can be greatly enhanced by using an algorithm that retrieves the background scene temperature distribution from the observed radiance spectra, and the algorithm is a simple linear operator that could provide real-time cockpit displays of the terminal area on approach.

The algorithm was demonstrated under a restricted set of aircraft altitude and atmospheric conditions. Further work was performed to demonstrate the robustness of the algorithm and to define the actual measurement and display characteristics of a practical system.

7.1 Low Visibility Measurements

Several data collection activities associated with low visibility conditions occurred. The first was on November 30, 2010. The Telops Hyper-Cam was set up on the fire escape of GTRI's Baker Building on the Georgia Tech campus to collect data in these low visibility conditions. The instrument settings from the activity are given in Table 18. However, during set up and calibration, the fog lifted. At the time of the measurement, only the tip of the Bank of America Building (the tallest building in the Atlanta skyline) was still obscured. A visible image of the Bank of America Building is shown in Figure 348.

Table 18. Hyper-Cam instrument settings for November 30, 2010 fog measurements.

Cold Blackbody Temperature	10.0 °C

Warm Blackbody Temperature	35.0 °C
Resolution	4 cm^{-1}
FPA Size	320 x 150
Integration Time	200 µs

Figure 348. Nov. 30, 2010 Visible Image of Bank of America Building taken with the Hyper-Cam.

Three additional Hyper-Cam data collections in three different visibility conditions were made from the fire escape of Baker Building, aimed toward the AT&T building (the building to the left of the Bank of America Building in Figure 348). The AT&T Building provided a background to see if any features could be seen in the LWIR through the fog. The data collections were made on January 18, 2011, at a visibility of 2 miles; on January 20, 2011, at a visibility of 6 miles; and on January 28, 2011, at a visibility of 10 miles. The visibility information was obtained for Atlanta, GA from www.wunderground.com. A Google map of Atlanta is shown in Figure 349 to show where the AT&T Building is relative to the GTRI measurement site.

The view off the fire escape on the clear day, January 28, is shown in Figure 350. Of the two buildings in the distance that can be seen in Figure 350, the one on the left, which is the AT&T Building, is the target. Figure 350 is compared with Figure 351, which was taken on January 18, 2011. Note that the two buildings in the distance are completely obscured in the reduced visibility condition of January 18. Also note from Figure 349 that the AT&T Building is approximately 1.4 km (0.87 mi) from the Baker building, therefore the visibility between the measurement site and the target building was much less than the 2-mile visibility listed on Weather Underground the morning of January 18. Weather data, such as temperature and relative humidity, were collected on site by GTRI. These conditions are given in Table 19.

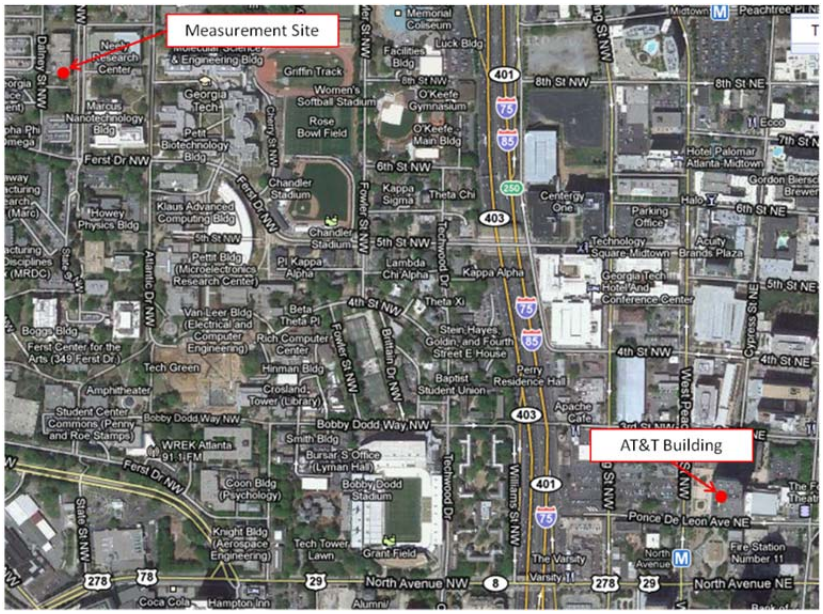

Figure 349. Google map view of Atlanta showing the AT&T Building relative to the measurement site.

Table 19. Temperature and relative humidity readings for the low visibility data collection activities.

Date	Temp (°C)	RH (%)
11/30/2010	23.09	48
01/18/2011	11.90	57
01/20/2011	13.91	49
01/28/2011	23.97	18
02/01/2011	10.53	69

Figure 350. The view from the Baker building fire escape on a clear day, January 28, 2011.

Figure 351. **The view from the Baker building fire escape in reduced visibility conditions, January 18, 2011.**

Hyper-Cam datacubes were collected on January 18 and 20, 2011 at 4 cm^{-1} and 56 cm^{-1} resolution. The lower 56 cm^{-1} resolution datacubes were collected in addition to the 4 cm^{-1} resolution datacubes in the event that the spectra from the 4 cm^{-1} datacubes were too noisy, however this was not the case and the results of the 4 cm^{-1} data are presented here. Figure 8 shows the IR imagery of the scene from all three days.

Figure 352. IR image at 1076 cm^{-1} of the scene on January 18, 2011, visibility 2 miles *(left panel)*. IR image at 1076 cm^{-1} of the scene on January 20, 2011, visibility 6 miles *(middle panel)*. IR image at 1076 cm^{-1} of the scene on January 28, 2011, visibility 10 miles *(right panel)*.

The left panel in Figure 352 is much noisier than the other two images; the sharpness increases with the visibility. The lack of contrast in the lower visibility images could lead to this graininess. The NESR's from sky pixels all three images are compared and are shown in Figure 353.

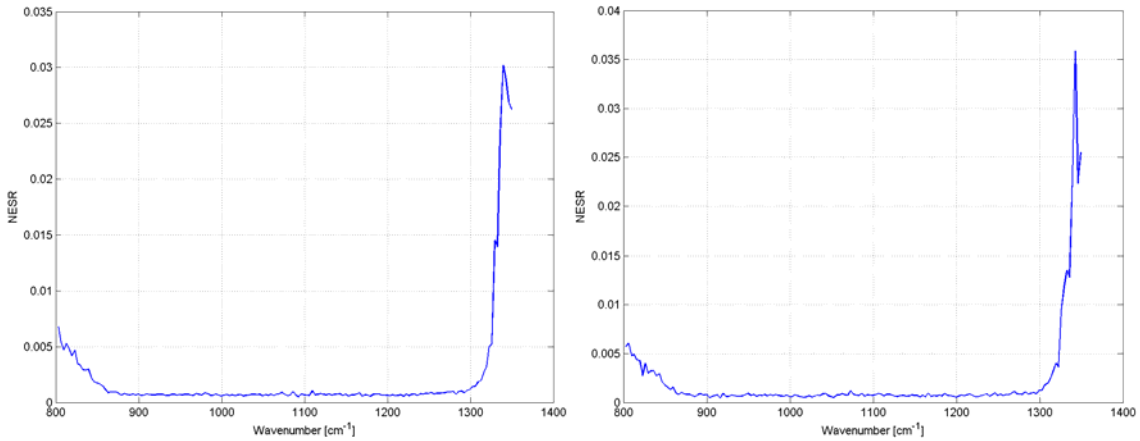

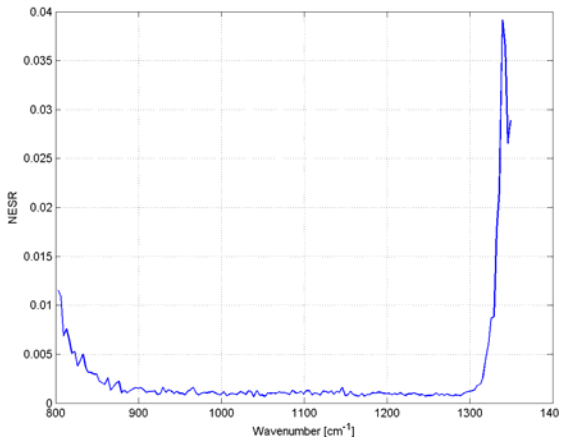

Figure 353. **NESR of selected sky pixels from January 18, 2011 *(top left panel)* January 20, 2011 *(top right panel)* January 28, 2011 *(bottom panel)*, Radiance units W/cm^{-1}m^{2}sr.**

Two different regions in each cube were then selected for radiance comparison: a sky region and a building background region. The results are shown in Figure 354.

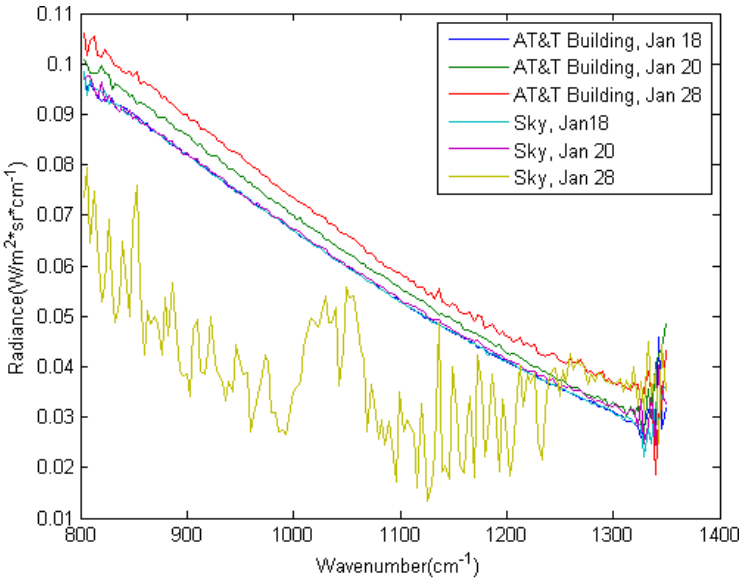

Figure 354. Radiance comparison of building and sky at three visibilities.

Several observations can be made from Figure 354. First, one may note that the radiance of the sky on January 18 and on January 20 (2 and 6 mi visibility, respectively) is nearly equivalent to the radiance of the AT&T Building background on January 18. In the lower visibility conditions, the building is completely obscured by the fog in the IR. The radiance spectra of sky itself from the two reduced visibility days are also relatively flat and featureless, in comparison with the measurement taken on January 28 under clear conditions. The sky measurement on January 28 has spectral features that are characteristic of a sky spectrum. Note also the difference in the sky spectrum versus the AT&T Building spectrum on January 28 under clear conditions. This day is the only day of the three where the building is clearly different than the sky. On January 20 (6 mile visibility), the radiance of the building background is only slightly higher. This data set

demonstrates that under reduced visibility conditions, the fog tends to obscure the background in the long-wave IR since the water is opaque in this region.

The weather on February 2, 2011 presented another excellent opportunity to collect Hyper-Cam data in reduced visibility conditions. This data collection, as opposed to the fog data collected in January, focused on imaging concrete and asphalt through fog at as close to an aircraft descent angle (3 degrees) as possible.

The Hyper-Cam was set up on the roof of the Centennial Research Building, which is next to the Baker Building at GTRI. Three different scenes were imaged from this roof: 1) looking east towards 10th Street; 2) looking south towards a parking lot on the Georgia Tech campus; and 3) looking southeast towards the roof of an adjacent parking deck. Figure 355 shows a Google map view of the test site and imaged scenes; Figure 356 through Figure 358 show the visible images of the imaged scenes.

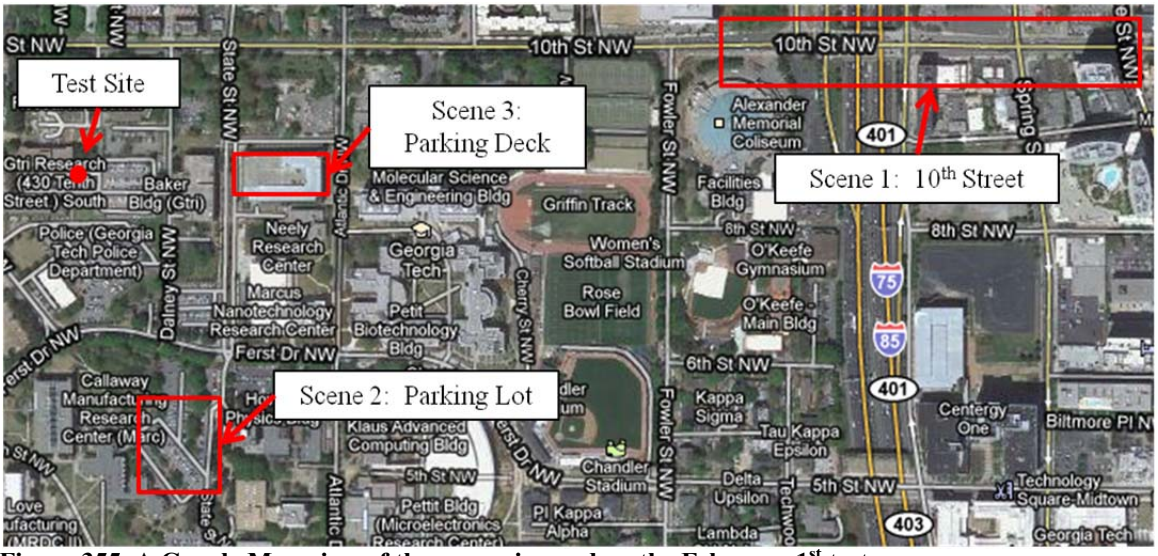

Figure 355. A Google Map view of the scenes imaged on the February 1st test.

Figure 356. Visible image of Scene 1, looking East to 10th St.

Figure 357. Visible image of Scene 2, looking South to parking lot.

Figure 358. Visible image of Scene 3, looking Southeast to parking deck.

Neither the Hyper-Cam's visible camera nor the Nikon could distinguish any features along 10th Street through the fog; the visible image from the Nikon is shown in Figure 356. However, during the test we could visually see the traffic lights, and this visual cue was used as a guide for orienting the Hyper-Cam. An attempt was made to record each datacube during red lights along 10th Street so that no cars would be moving through the scene. The data for all three scenes were recorded at 4 cm^{-1} and 56 cm^{-1} resolution. In addition, the parking deck of Scene 3 was recorded at 1 cm^{-1} resolution (a higher resolution and longer recording time were enabled since there were no cars moving on the deck). Scene 1 (10th Street) and Scene 2 (parking lot) were recorded at a Hyper-Cam declination angle of 3 degrees to mimic the angle at which aircraft land; Scene 3 (the parking deck) was recorded at a 5 degree declination angle.

After initial preview of these data sets by Hampton University, it was determined that data collected in thirty-minute intervals on the same day would be better suited for their analysis. The project team was unable to collect this sporadic weather condition during the remainder of the project.

8 Volcanic Ash

Approximately 60 volcanoes worldwide are active during a typical year, and in the North Pacific Region of the United States alone volcanic ash is present an average of 4 days a year where most jet aircraft fly [40]. The Geophysical Institute at the University of Alaska Fairbanks completed an extensive study of volcanic activity in the North Pacific. In this study, 100 years of volcanic eruption data was used to run thousands of PUFF model simulations of eruptions of volcanoes in the area. (PUFF is a model that simulates the movement of airborne volcanic ash in near real-time when an eruption has occurred [41]). The result was a reliable set of average data describing trends in ash migration from Northern Pacific volcanoes. They found that only 35% of volcanic eruptions in that area over the past 100 years caused ash to reach above 8km or about 26,250 feet [42].

Volcanic Clouds contain ash and gases that are hazardous to aviation. Significant damage to aircraft has occurred during encounters with ash, where the ash melts and fuses to the engine turbine blades causing engine failure in flight. The 2010 eruption of Iceland's Eyjafjallajokull is estimated to have cost the airline industry over two billion dollars.

The Norwegian Institute for Atmospheric Research holds the patent on an airborne passive IR radiometer originally developed by Dr. Alfredo Jose Prata when he was employed by the Commonwealth Scientific and Industrial Research Organisation (CSIRO) located in Melbourne, Australia. The system, named the Airborne Hazards Detection System (AHDS) uses a two-band detection technique similar to satellite detection techniques for volcanic ash. International patent WO 2011/135060 A1 was issued in November 2011 to Prata and Bernado for a "System and method for detecting adverse atmospheric conditions ahead of an aircraft" [1]. The patented system has multiple infrared cameras that detect IR radiance in different bands of IR light. The system warns and displays the position of the adverse condition so the aircraft may be re-routed. Similarly, a FLI system is able to perform this capability. A good working relationship exists with Prata.

9 In-Flight Icing

As reported in the FLI Phase 1 program [16], ice and liquid water have very different optical properties in the infrared molecular "window" region of the spectrum starting at 11 microns. As a result, it should be possible to use the FLI instrument to diagnose the existence of supercooled liquid water in clouds (i.e., detect water droplets at sub-freezing temperatures that causes airframe icing) and to discriminate between ice and water on surfaces, such as runways. However, this hazard was not investigated because flight tests were not conducted, and the area of greatest differentiation between the indices of refraction for ice and water occurs outside of the effective spectral range of the Telops LWIR instrument.

With the proper instruments available, the possible detection technique is described here. The temperature of the cloud can be observed as the brightness temperature measured with the FLI near 12 μm, where the cloud emissivity is a maximum, or assumed to be close to the outside air temperature observed independently by the aircraft measurement system. Figure 359 and Figure 360 show that the real (reflection) and imaginary (absorption) parts of the index of refraction for

water and ice differ greatly in the range of infrared wavelengths where atmospheric molecular absorption is a minimum (i.e., the molecular absorption "window" between 10 and 12 µm). In particular, when viewing cloud ice crystals, or an icy runway surface, with an FLI, the radiance observed will increase rapidly between 10.5 and 12 µm, whereas when viewing water droplets, or a wet surface, the radiance observed will be relatively constant between 10.5 and 11 µm with the strong increase in radiance occurring between 11 and 12 µm. Thus, it is the small spectral shift in the wavelength at which the radiance emission abruptly increases across the atmospheric "window" region that will allow the FLI to determine whether cloud icing conditions, or a hazardous icy runway, may be encountered by the aircraft. There is a precedent for this type of discrimination; two-band IR radiometers are commercially available for detecting "black ice" on highways (black ice is the term for a thin layer of ice that is difficult to detect visually).

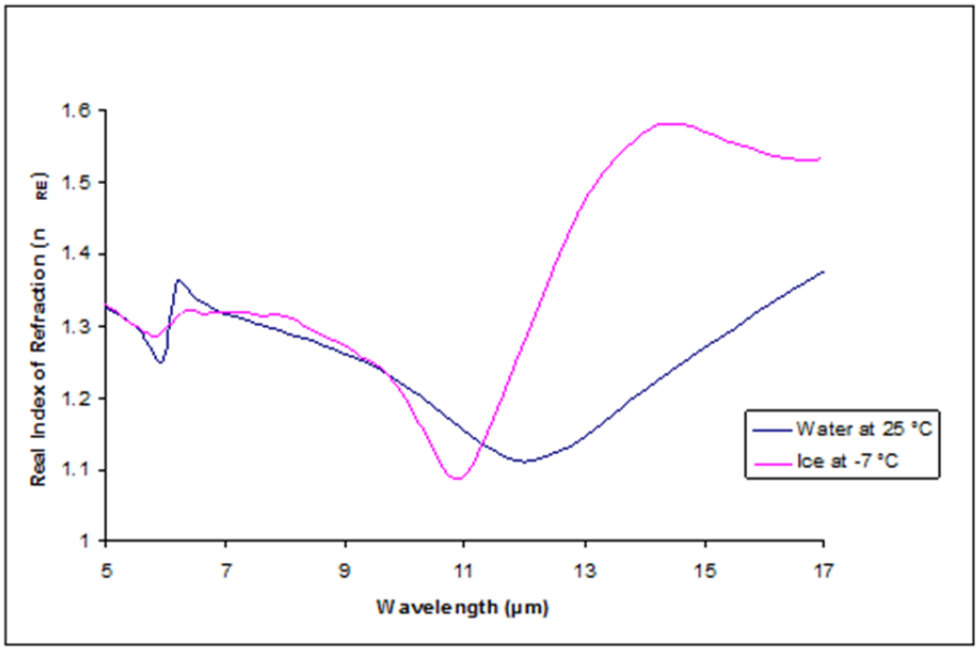

Figure 359. Real Index of Refraction for Water and Ice in Infrared. [43][44]

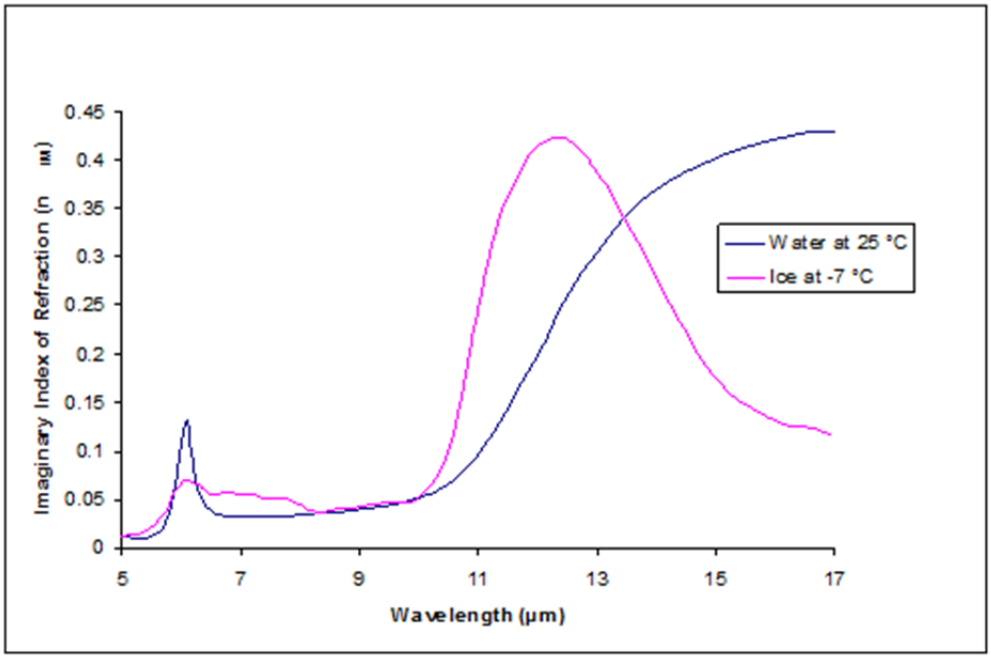

Figure 360. Imaginary Index of Refraction for Water and Ice in the Infrared. [43][44]

10 Distance to the Hazard

In previous reports, we have discussed the ability to determine the distance to the hazard. This ability relied on the collection of high spectral resolution data (1 cm^{-1}). Over the last year, we have shifted to lower spectral resolution data (16 cm^{-1}) to try to detect the signal of the hazards. As such, we have inherently lost the ability to determine the distance to the hazard using the CO_2 line structure. However, an additional dedicated detector with two narrowband filters that can look at the amplitudes of the CO_2 lines has been proposed. Note that these lines appear in the mid-wave infrared (MWIR) and at the edges of the long-wave infrared (LWIR) window. Detection in this phase has focused on the long-wave infrared (LWIR). Therefore this dedicated detector would be in the MWIR, while the hazard detection detector would be in the LWIR.

11 Defining a FLI Sensor Requirements

Unfortunately, known imaging instruments in the wavelength ranges of interest were not found to meet the needs of a FLI sensor for the detection of aviation hazards. Generally, optimal wavelength ranges for the various signals were different, and sometimes the same hazard has a different wavelength range depending on flight altitude. In addition, signal strengths were below the noise level of the instruments used for data collection.

11.1 Wake Vortices

Simulations of the atmospheric temperature, moisture, and exhaust gas conditions associated with wake vortices from commercial jet aircraft were simulated using TASS. Wake vortex signals were then simulated for several different flight altitudes both LBLRTM and FLI-FM2; the results are shown in Section 4.1. The results of each model agree and indicate that the noise level necessary for wake vortex detection is on the order of milli-Kelvin. The models show that the

optimal band passes are different for a wake vortex signal simulated along a slant path from ground versus a horizontal path at flight altitude. However, for both elevations, there is a peak signal in the range of 1250 – 2000 cm^{-1}. Therefore, if a broadband radiometer with one band from 1250 – 2000 cm^{-1} could be identified, it would be optimal, as it could be used for wake vortex detection regardless of observer altitude. Using a broad band (~750 cm^{-1}) imaging radiometer, operating in the 1250 – 2000 cm^{-1} band, which has a sensitivity on the order of 1 mK, the detection of wake vortices should be possible. Mid-wave sensors usually operate from ~3 – 5 μm, while long-wave sensors usually operate from ~8 – 12 μm. The 1250 – 2000 cm^{-1} band corresponds to 5 – 8 μm, which is in the opaque region; therefore, sensors do not really exist in this band. Also, the Suomi NPP CrIS was sent into space, and its detectors have noise levels representative of state of the art in current detector technology. The CrIS has a noise level of 0.06K, or 60 mK, which is still not low enough to detect the wake vortex signal.

11.2 Mountain Wave Turbulence

For cost reasons, the experiments conducted under this program were ground based, not airborne, and that limitation is probably a key reason that the FLI program has not yet demonstrated CAT detection. However, the FLI program did develop a greatly improved understanding of the radiometric signal strength of mountain wave patterns observable from a ground-based sensor. FLI-FM simulated the radiance signal expected of a mountain wave pattern in order to define instrument requirements for the Telops Hyper-Cam at the MRS field test. The simulations were created at different wavenumber resolutions and at different viewing geometries (i.e. elevation and azimuth angles from an observation point at MRS). These simulations were done for two WRF models: one for a severe turbulence case from 2004, and one created for a day with moderate turbulence reported during the time of the field test.

The simulations were very thorough but may have over-predicted the radiance signal due to the manner in which the turbulent atmosphere was modeled. A FLI-FM simulation which modeled the radiance signal as variability in time (rather than as a difference from a standard atmospheric state) indicated radiance signals on the order of 0.1 $mW/m^2\text{-}cm^{-1}\text{-}sr$ (see Figure 308). Because all simulations were done in anticipation of and for comparison with the MRS field test, we can only define FLI instrument requirements for a ground-based sensor operating in the long-wave infrared waveband. Throughout this report, we have often referred to a “turbulent signal” or “turbulent atmosphere” that the Hyper-Cam measures. Again, we must stress that the Hyper-Cam was never intended to measure the actual turbulence fluctuations, but the standing wave pattern that is associated with the mountain wave turbulence. The D&P is much faster, but non-imaging, and we had several issues with it during the data collection.

Therefore, we believe that a broadband imaging radiometer operating in the 8 – 12 μm region with a noise level on the order of 0.1 $mW/m^2\text{-}cm^{-1}\text{-}sr$ would be required to detect the radiance variability due to mountain waves from a ground-based platform. However, no simulations were created in other wavebands, so we cannot define an optimal waveband. We do not believe it would be appropriate to define the requirements for a FLI sensor until further simulations can be performed at different wavebands and for horizontal paths at different altitudes. Furthermore,

given the opportunity, it would be beneficial to repeat the MRS measurements at flight altitudes (flight test), or at least for horizontal paths at a much higher elevation.

11.3 Runway Surface Conditions

We have had success in classifying materials in staged scenes based upon their emissivity with the MLEV method. However, the successful analyses were performede on staged scenes, and a gold plate was always used to characterize the background. It is true that for most materials the emission term dominates the at-surface radiance term; however, due to the spectral nature of incident radiance, it cannot be neglected. We still have not found a substitute for the gold plate.

Additionally, the emissivities of ice and water are nearly identical in the waveband studied. As shown in Section 6.4, classification based on emissivity comparison might work better if the waveband were changed to 715 to 900 cm^{-1}. As noted in Section 6.4, the Hyper-Cam range of 800 – 1350 cm^{-1} is reduced when one considers that the sensor becomes noisy at either extreme of the spectral range (see Appendix A). However, changing the waveband under consideration to 715 to 900 cm^{-1}presents another problem: starting around 12 μm (i.e. wavenumbers less than 833 cm^{-1}), atmospheric transmission begins to drop off rapidly.

Therefore, we are unable to define instrument requirements for runway surface characterization at this time. However, we have demonstrated success with the MLEV algorithm. This algorithm requires high spectral resolution because it minimizes the high spectral variance that would propagate into the calculation of emissivity spectra from atmospheric lines if an incorrect surface temperature were used. To calculate emissivity for surface characterization would thus require a hyperspectral imaging sensor. A hyperspectral imaging sensor would not be appropriate for a FLI sensor because it is more than that which is required for all other hazards studied and it would take too long to collect the data in a real-world scenario. If certain bands could be identified in radiance spectra, then a multi-spectral system could be used. The hyperspectral measurements were to be used as a study to determine if certain bands could be identified that could be used to define these sensor requirements. We attempted to do band comparisons in the radiance domain, but due to different illumination conditions among different data sets, we realized the need to work in the emissivity domain. We were unable to identify an appropriate temperature and emissivity separation algorithm that had the potential to be effectively translated from a purely research demonstration to a real-world, real-time FLI sensor application.

11.4 Requirement Summary

The following table summarizes the sensor requirements for the aviation hazards studied.

Table 20. FLI Sensor Requirements for Hazard Detection

Hazard	Wavelength Region	Resolution	Sensitivity	Caveat
Wake Vortices	5 – 8 μm	Broadband	1 mK	5 – 8 μm is the opaque region of the atmosphere, and sensors do not exist for this range
Mountain Wave	LWIR window region (8 – 12 μm)	16 cm^{-1}	50 mK	Other wavelength regions cannot be excluded because

Turbulence				they were not studied during this program
Runway Surface Conditions	LWIR window region and beyond (11 – 17 μm for ice/water discrimination)	1 – 4 cm^{-1}		Cannot omit gold plate in calculation of absolute emissivity)
Runway Obscurations (animals)	LWIR or MWIR			Any thermal imager will work (does not require radiometric accuracy).
Low Visibility	LWIR	2.5 cm^{-1}		
Distance to Hazard	CO_2 lines in MWIR, edges of LWIR window	1 cm^{-1}		
Volcanic Ash	6 – 13 μm	Broadband microbolometer with narrowband (0.5 – 1.0 μm) filters	50 mK	This commercialized instrument uses five cameras with narrowband filters at specified bands (including SO_2) [1].
Icing	11 – 17 μm	4 cm^{-1} or less		Differences in slope of the indices of refraction will indicate differences in ice/water. Use this knowledge in conjunction with knowledge of temperature to indicate supercooled liquid.

12 Conclusions

The state of knowledge associated with the aviation hazards of wake vortices, clear air turbulence, and icing on runways has been greatly advanced. A greater understanding of the application/needs of real-world functionality, as well as signal strength, has been achieved through both models and simulations, in addition to analysis of experimental data.

Prior to the FLI program summarized here, radiometric efforts to detect aviation hazards were largely experimental, and they were limited by single-line-of sight broadband instruments. In general, the experiments were not adequately supported by simulation and modeling, and truth data were usually not recorded in the field, so it was not possible to know what the radiometers were looking at. Despite tantalizing results dating back to the late 1970s, radiometric detection of aviation hazards did not live up to its promise (the exception is volcanic ash detection research, which resulted in commercial instruments). In the FLI program, we investigated the use of imaging radiometers with high spectral resolution, using both modeling/simulation and field experiments, along with sophisticated data analysis techniques that were originally developed for analysis of data from space-based radiometers. By these means, we have greatly advanced the state of knowledge in this technical area. For cost reasons, the experiments were ground based, not airborne, and that limitation is probably a key reason that the FLI program has not yet demonstrated CAT detection. However, the FLI program did develop a greatly improved understanding of the radiometric signal strength of aviation hazards in a wide range of scenarios,

along with a much better understanding of the real-world functionality requirements for hazard detection instruments.

12.1 FLI Forward Model Updates

The fast computations of FLI simulated radiance with FLI-FM are based on the pre-calculated optical depth (OD) look-up-table. A newer version of the table was prepared in FLI-FM2 which implements the following improvements:

1. An extended wavenumber range (625–2475 cm^{-1} instead of 650–1650 cm^{-1}) has been implemented;

2. Six atmospheric models are incorporated instead of one.

3. LBLRTM pre-computed optical depths have been converted into transmittances for each layer and then convolved with a double Fourier transform (instead OD of boxcar averaged).

4. Bottom and top Jacobians (derivatives) of the transmittance $\tau(v)$ are included instead of bottom only.

The model updates lead to better performance of the FLI-FM2 in terms of its agreement with LBLRTM (refer back to Figure 25 and Figure 26).

Validation of the FLI Forward Model was not performed. However, a *verification* of FLI-FM2 for one particular case was completed through comparison of FLI-FM2 with LBLRTM. The small residuals, which did not exceed 0.3 K for most of the wavenumber range, calculated from the difference in transmittances computed with both FLI-FM2 and LBLRTM, indicate good agreement. The only exception was seen in the ozone band, which may be explained by the fact that the ozone is a fixed gas in FLI-FM2 and its spectral dependence on the input temperature is not taken into account.

A comparison of LBLRTM simulated radiances and MRS measured data was completed to check the radiometric calibration of the observed Hyper-Cam data. These results did not match well; there is relative agreement in the spectral shape of the observed and simulated radiances but there are many regions where there is considerable disagreement between the observed and calculated radiance spectra. Also, there is considerable disagreement in the absolute magnitude of the radiances with the observed radiances being generally higher than the simulated radiances, except in the water vapor absorption region near 1300 cm^{-1}.

These systematic differences may be explained by the following two points:

1. The use of an average Denver radiosonde to represent the atmospheric state at the time of the Telops observations.

2. The use of the US-1976 standard ozone profile since no in-situ observations of ozone were available.

True validation of the FLI-FM2 would require dedicated experiments with sondes and ozone profilers.

12.2 Wake Vortices

Daniels [23] simulated the atmospheric temperature, moisture, and exhaust gas conditions associated with wake vortices from commercial jet aircraft using TASS; Daniels then used LBLRTM to simulate measurements of the infrared radiance spectrum that would be measured with a spectrometer when viewing the atmospheric disturbance created by the wake of a Boeing 747 jet aircraft. The results indicate there is a small, but evident, temperature and moisture structure signature of the wake vortex disturbance.

Wake vortex radiance simulations were then conducted using FLI-FM2 to estimate the magnitude of and spectral location of the signal from a broadband instrument sensitive in the SW, MW, and LW spectral regions. Three regions were found where the wake vortex signal is a maximum; these are located at 700 cm^{-1}, 1250 cm^{-1}, and 2000–2200 cm^{-1}.

The measurements of the radiance associated with wake vortices generated by commercial jet aircraft were conducted both at Madison, Wisconsin (June, 2008) and Atlanta, Georgia (July through September 2010) using the Telops Mid-wave Hyper-Cam and Long-wave Hyper-Cam instruments, respectively. Analyses of the data collected did not reveal any detectable radiance signal of the wake vortices being observed. Note, however, that in Madison winds were extremely high and likely prevented vortices from forming, or moved them from the field of view before they formed, and that the Atlanta data acquisition activity was meant as preparation for a formal data acquisition activity to understand requirements and instrument settings. Seeing no observable signals in Atlanta preempted the formal acquisition activity.

12.3 Mountain Wave Turbulence

At 16 cm^{-1} resolution, the Hyper-Cam NESR is approximately 0.25 $mW/m^2\text{-}sr\text{-}cm^{-1}$ (see Appendix A), which is higher than the simulated turbulence radiance signal in time variability. Simulations run prior to the MRS field test indicated that we should have been able to see the turbulence with the Hyper-Cam. It has been noted that the high simulated signals could have been an artifact of the modeling. However, it could be possible that during the field test at MRS, we never collected any Hyper-Cam data of mountain wave disturbances that were high enough in severity to be observed. All simulations done prior to the test were for the March 6, 2004 severe turbulence WRF model. During the test, even though conditions for turbulence were predicted by STAR and Lenticular clouds indicative of mountain waves were present, there were no mountain wave turbulence PIREPs higher than “Moderate.” Mountain waves are standing waves and vary only slowly with time, but temperature and water vapor concentration are not homogeneous at any given altitude when the wave pattern is present, and it is that disturbance that leads to the radiance variations across a scene as shown in previous simulations.

The plan was to separate the standing wave pattern from the turbulence on the basis of the time scales. The D&P TurboFT was to be implemented to obtain the fast variations caused by turbulence, as indicated was possible in our earlier Boulder data collection activity [34]. The Telops Hyper-Cam was going to provide a two-dimensional image of the scene on a longer time

scale to view the standing mountain wave pattern. During the test, we experienced trouble with the D&P, and the Hyper-Cam could not see evidence of the standing wave pattern. We know we had standing wave patterns though because of the presence of lenticular clouds and satellite imagery. Turbulence is typically associated with mountain waves, but is not a given.

We knew that the analysis of ground-based measurements would be more challenging than flight-based measurements due to the reduced radiance signal for a slant path to space (see Section 5.1.1, in particular, Figure 69 and Figure 72). Despite the smaller expected signal, we did not believe it would be so small that it would be unobservable. We believed the radiance signal would still be above the noise level of the Hyper-Cam because the FLI-FM simulations indicated it would. As the simulations were performed for a ground-based slant path, they inherently take transmission through layers of atmosphere into account. They may have over-predicted the signals due to the manner in which the turbulent signal was modeled. When modeling turbulence as a difference between a perturbed state and a standard atmosphere, a temperature offset will always exist, and will cause a constant bias between the two atmospheric states. For the simulations, the difference between perturbed radiances at different *times* (i.e. the standard atmosphere has *not* been subtracted) shows actual signal due to scene variability. The differences between perturbed and unperturbed radiances are mostly due to how the standard atmosphere was defined.

We do believe that, given the opportunity, mountain wave turbulence measurements should be repeated at flight altitude. The FLI-FM models and simulations developed within this program indicate that the turbulent signal is too small to be seen with a Hyper-Cam, but these simulations were done *at ground level* in anticipation of and for comparison with MRS field test measurements. If the sensor were above the layers of atmosphere where attenuation will decrease the signal, it is possible the turbulent signal could be observed. Unfortunately, budgetary limitations prevented a flight test during this program.

12.4 Runway Surface Conditions

The ability to detect the surface emissivity for various types of runway surface conditions with a FLI is important for the determination of runway friction and aircraft stopping distance. However, surface emissivity is a difficult property to calculate because it is difficult if not impossible to measure all variables at measurement time. It is true that for most materials the emission term dominates the at-surface radiance term; however, due to the spectral nature of incident radiance, it cannot be neglected. The incident radiance a very difficult quantity to measure; it requires simultaneous measurement of a Lambertian reflector made of a low emissivity material and with known temperature. We used a roughened gold plate, which is standard practice, but it only exists in experimental set-ups; it is not practical for real-world scenarios.

We have had success in classifying materials in staged scenes based upon their emissivity with the MLEV method; however, we were unable to determine the surface emissivity without the gold plate measurement. Also, in defining requirements for a FLI sensor, for ice vs. water, classification based on emissivity comparison might work better if the waveband were changed to 715 to 900 cm^{-1}. Original plots showed that the 800-1350 cm^{-1} operating region of the Telops Hyper-Cam was appropriate, with the differences for ice and water appearing mainly in the 700-

800 cm^{-1} range; however the NESR of the Telops Hyper-Cam made measurements in that region not possible.

The hyperspectral measurements were to be used as a study to determine if certain bands could be identified that could be used to define FLI sensor requirements. We attempted to do band comparisons in the radiance domain, but due to different illumination conditions among different data sets, we realized the need to work in the emissivity domain. We were unable to identify an appropriate temperature and emissivity separation algorithm that had the potential to be effectively translated from a purely research demonstration to a real-world, real-time FLI sensor application.

12.5 Low Visibility

Based on the sensitivity studies in the previous Phase 1 FLI project, an imaging FLI spectrometer is expected to provide enhanced vision in the cockpit of an aircraft in low visibility conditions. An algorithm was demonstrated under a restricted set of aircraft altitude and atmospheric conditions. Data of varying visibility due to fog was collected in Atlanta on several occasions. However, after initial preview, it was determined that data collected in thirty-minute intervals on the same day would be better suited for the analysis. The project team was unable to collect this sporadic weather condition during the remainder of the project.

12.6 In-Flight Icing

In-flight icing could not be studied during this program, since no flight tests were conducted. However, previous investigations have shown that the indices of refraction for ice and water differ starting at 11 μm, therefore providing the opportunity for differentiation. That knowledge combined with the knowledge of the temperature of the cloud to diagnose the existence of supercooled liquid water in clouds could be used to detect water droplets at sub-freezing temperatures that causes airframe icing.

12.7 Volcanic Ash

Detection of volcanic ash has not been investigated by the FLI team since methods of modeling the movement of volcanic ash (PUFF model) and instruments for its detection (Airborne Hazards Detection System, Norwegian Institute for Atmospheric Research) were being commercialized at approximately the same time as this investigation. This report summarizes the literature and patents related to volcanic ash detection.

12.8 Distance to Hazard

The ability to determine the distance to a hazard relies on the collection of high spectral resolution data (1 cm-1). Because we have shifted to lower spectral resolution data (16 cm-1) to try to detect the signal of the hazards, we have inherently lost the ability to determine the distance to the hazard using the CO2 line structure. However, an additional dedicated detector with two narrowband filters that can look at the amplitudes of the CO2 lines has been proposed as the method of determining the distance to the hazard should the FLI instrument be developed.

12.9 Recommendations

For cost reasons, the experiments conducted under this program were ground based, not airborne, and that limitation is probably a key reason that the FLI program has not yet demonstrated CAT detection. However, the FLI program did develop a greatly improved understanding of the radiometric signal strength of aviation hazards in a wide range of scenarios. We do believe that, given the opportunity, mountain wave turbulence measurements should be repeated at flight altitude. The FLI-FM models and simulations developed within this program indicate that the turbulent signal is too small to be seen with a Hyper-Cam, but these simulations were done *at ground level* in anticipation of and for comparison with MRS field test measurements. If the sensor were above the layers of atmosphere where attenuation will decrease the signal, it is possible the turbulent signal could be observed. The increase in signal should be quantified by simulations prior to any flight testing.

In-flight icing is another hazard that could be studied in more detail with the ability to perform airborne data collection activities. Ground-based differentiation of water and ice is recommended prior to going airborne. This program investigated that capability under runway hazards, but the effective range of the Telops instrument ends at about the same wavelength as the beginning of the divergence of the water and ice indices of refraction. Therefore, the Telops instrument was unable to make the distinction consistently across multiple scenes, even though an algorithm could be tailored for a single scene. Single line-of-sight instruments exist in this range and may be adequate to make this determination effectively across multiple scenes.

Low visibility conditions could be further investigated as well. After an initial look at the data collected under this program, it was determined that data collected in thirty-minute intervals on the same day would be better suited for the analysis than what was collected. The project team was unable to collect this sporadic weather condition during the remainder of the project. However, if we had been able to, the algorithms developed by Hampton University could have been tested for effectiveness. Again, airborne tests would be ideal after some initial analysis of ground-based data.

13 Conferences, Papers, and Presentations

1. AvSafe 2009: GTRI personnel attended the Aviation Safety (AvSafe) Conference held in November 2009.
2. AMS 2010: Hampton University and STAR Institute personnel participated in the American Meteorological Society (AMS) Conference held January 17-21, 2010 in Atlanta, GA.
3. WakeNet 3: GTRI attended and presented at the WakeNet3 Workshop (Mar 29-30, 2010). While at the conference, we learned that ATL has an operational WindTracer Lidar. It would be good to work with the FAA and Volpe to use the lidar at ATL as truth data for the project. Steve Lang at the FAA and Frank Wang at Volpe are in charge of the WindTracer Lidar installation and operation. Steve Hannon who works for the manufacturer of the WindTracer gave an update on current locations of operation for WindTracer Lidars. The WindTracer at SFO is currently not operational but should be

repaired soon, STL is still operational, HOU no longer has one; HOU's WindTracer is the one that now resides in ATL.

4. L. West, G. Gimmestad, W. Smith, L. Cornman, S. Lane, S. Kireev, and T. Daniels, "Airborne Forward Looking Interferometer for the Detection of Terminal-Area Hazards," poster presented by G. Gimmestad at the AvSafe meeting; St. Louis, MO; May 2011.

5. S. Lane., L. West, G. Gimmestad, W. Smith, and S. Kireev; "Surface characterization measurements with the Hyper-Cam," Telops Scientific Workshop; Baltimore, MD; May 2011.

6. W. Smith, L. West, G. Gimmestad, and S. Lane, "Ultraspectral measurements of surface emissivity with an imaging interferometer spectrometer," in *Hyperspectral Imaging and Sounding of the Environment*, 2011, OSA Technical Digest (CD) (Optical Society of America, 2011), paper HTuC4. (see Appendix B)
   Special Note: This paper was among the top five downloaded HISE InfoBase papers in 2012.

7. S. E. Lane, L. L. West, G. G. Gimmestad, W. L. Smith, Sr., and E. M. Burdette, "Detection of aircraft exhaust in hyperspectral image data," in *Proc. SPIE. 8158, Imaging Spectrometry XVI*, 2011, doi: 10.1117/12.894078 (see Appendix C)

8. S. E. Lane, L. L. West, G. G. Gimmestad, S. Kireev, W. L. Smith, E. M. Burdette, T. Daniels, and L. Cornman, "Hyperspectral image turbulence measurements of the atmosphere," in *Proc. SPIE. 8355, Infrared Imaging Systems: Design, Analysis, Modeling, and Testing XXIII*, 2012, doi: 10.1117/12.919386 (see Appendix D)

9. P. R. Schaffner, T. S. Daniels, L. L. West, G. G. Gimmestad, S. E. Lane, E. M. Burdette, W. L Smith, S. Kireev, L. Cornman, R. D. Sharman, "Experimental validation of a forward looking interferometer for detection of clear air turbulence due to mountain waves," in *4th AIAA Atmospheric and Space Environments Conference*, 2012, doi: 10.2514/6.2012-2790 (see Appendix E)

10. T. S. Daniels, W. L Smith, and S. Kireev, "Recent Developments on Airborne Forward Looking Interferometer for the Detection of Wake Vortices," in *4th AIAA Atmospheric and Space Environments Conference*, 2012, doi: 10.2514/6.2012-2791

11. S. Lane., L. West, G. Gimmestad; W. Smith; and S. Kireev; "Analysis of atmospheric data collected over the Colorado Rockies"; Telops Scientific Workshop; Annapolis, MD; Sept 2012.

12. S. Lane., L. West, G. Gimmestad; W. Smith; e. Burdette, S. Kireev; and J.M. Cathcart, "Analysis of atmospheric data collected over the Colorado Rockies and Sky Radiance Measurements at Georgia Tech"; Telops Scientific Workshop; Quebec; Sept 2013.

14 References

[1] A. J. Prata and Cirilo Bernado, "System and method for detecting adverse atmospheric conditions ahead of an aircraft," WO2011135060 A1, November 3, 2011.

[2] Stephen G. Warren, "Optical Constants of Ice from the Ultraviolet to the Microwave," *Applied Optics*, vol. 23, no. 8, pp. 1206-25, April 1984.

[3] George M. Hale, "Optical Constants of Water in the 200-nm to 200-µm Wavelength Region," *Applied Optics*, vol. 12, no. 3, pp. 555-63, March 1973.

[4] P. M. Kuhn, I. G. Nolt, L. P. Stearns, and J. V. Radostitz, "Infrared passbands for clear-air-turbulence detection," *Optics Letters*, vol. 3, no. 4, pp. 130-132, 1978.

[5] E. A. Weaver et al., The 1979 Clear Air Turbulence Flight Test Program, 1979.

[6] P. C. Sinclair and P. M. Kuhn, "Infrared Detection of High Altitude Clear Air Turbulence," in *31st Aerospace Sciences Meeting and Exhibit*, Reno, NV, January 11-14, 1993.

[7] A. J. Prata and I. J. Barton, "Detection and Discrimination of Volcanic Ash Clouds by Infrared Radiaometry - I: Theory," in *Proceedings of the First International Symposium on Volcaninc Ash and Aviation Safety*, 1994, pp. 305-311.

[8] A. J. Prata and I. J. Barton, "Detection and Discrimination of Volcanic Ash Clouds by Infrared Radiometry – II: Experimental," in *Proceedings of the First Inernational Symposium on Volcanic Ash and Aviation Safety*, 1994, pp. 313-317.

[9] A. J. Prata, "Infrared radiative transfer calculations for volcanic ash clouds," *Geophysical Research Letters*, vol. 16, no. 11, pp. 1293-1296, November 1989.

[10] I. J. Barton, A. J. Prata, I. G. Watterson, and S. A. Young, "Identification of the Mount Hudson volcanic cloud over SE Australia," *Geophysical Research Letters*, vol. 19, no. 12, pp. 1211-1214, June 1992.

[11] A. J. Prata and I. J. Barton, "Airborne Hazard Detection System - Project Overview," CSIRO Atmospheric Research, October 1999.

[12] H. P. Adamson and C. F. Morrison, "Infrared Airborne and Ground Detection of Wake Vortices," in *Proceedings of the Aircraft Wake Vortices Conference*, 1991.

[13] "Infrared Detection of Wake Vortices," NASA Phase 1 SBIR contract to Turbulence Prediction Systems, George Green COTR, NAS1-19907, 1993.

[14] Gary G. Gimmestad, Chris D. Papanicolopoulos, Mark A. Richards, Donald L. Sherman, and Leanne L. West, "Feasibility Study of Radiometry for Airborne Detection of Aviation Hazards," Funded by

the Sensors Research Branch of the Airborne Systems Competency at NASA Langley Research Center, NASA/CR-2001-210855 under contract NAS1-99073, 2001.

[15] Leanne West, Gary Gimmestad, Bill Smith, and Stanislav Kireev, "Applications of a Forward-Looking Interferometer (FLI) for the On-board Detection of Aviation Weather Hazards," NASA/TP-2008-215536; Added to NTRS: 2008-12-10; Document ID: 20080045836; Report Number: L-19522, 2007.

[16] Leanne West et al., "Hazard Detection Analysis for a Forward-Looking Interferometer," Final Report NASA/ NNX07AN17A, 2008.

[17] Gary Gimmestad et al., "Airborne Forward-Looking Interferometer Turbulence Investigation," in *Proceedings of the 45th AIAA Aerospace Sciences Meeting*, Reno, NV, January 8, 2007.

[18] Leanne West et al., "Airborne Forward Looking Interferometer for the Detection of Terminal-Area Hazards: Annual Progress Report, Year 1," 2010.

[19] Leanne West et al., "Airborne Forward Looking Interferometer for the Detection of Terminal Area Hazards: Annual Progress Report, Year 2," 2011.

[20] Sarah Lane, Leanne West, Gary Gimmestad, William Smith, and Edward Burdette, "Detection of Aircraft Exhaust in Hyperspectral Image Data," in *Proc. SPIE 8158*, San Diego, CA, 2011.

[21] William Smith, Leanne West, Gary Gimmestad, and Sarah Lane, "Ultra-spectral measurements of surface emissivity with an imaging interferometer spectrometer," in *Hyperspectral Imaging and Sounding of the Environment*, Toronto, 2011.

[22] Leanne West et al., "Airborne Forward Looking Interferometer for the Detection of Terminal-Area Hazards: Annual Progress Report, Year 3," 2012.

[23] Taumi Daniels, "The Analysis of an Imaging Passive Infrared Fourier Transform Spectrometer for Airborne Detection of Wake Vortices," Hampton, VA, May 2012.

[24] Leanne L. West et al., "WAke Vortex Experiment (WAVEx) Field Measurement Test Plan," 2008.

[25] Alexandre Vallières et al., "Algorithms for Chemical Detection, Identification, and Quantification for Thermal Hyperspectral Imagers," in *Proc. SPIE 5995*, 2005.

[26] Dimitris Manolakis and Gary Shaw, "Detection Algorithms for Hyperspectral Imaging Applications," *IEEE Signal Processing Magazine*, vol. 19, no. 1, pp. 29-43, 2002.

[27] Eric Robert Larrieux, "Performance Evaluation of Chemical Plume Detection and Quantification Algorithms, Paper 18," 2009.

[28] Spectral Calc. [Online]. www.spectralcalc.com

[29] J. D. Mattingly, *Elements of Gas Turbine Propulsion*.: McGraw-Hill, 1996.

[30] Charlene E. Caefer et al., "Analysis of False Alarm Distributions in the Development and Evaluation of Hyperspectral Point Target Detection Algorithms," *Optical Engineering*, vol. 46, no. 7, 2007.

[31] J. K. Wolff and R. D. Sharman, "Climatology of Upper Level Turbulence over the Contiguous United States," *Journal of Applied Meteorology and Climatology*, vol. 47, pp. 2198-2214, 2008.

[32] Daniel C. Heinz, Charles E. Davidson, and Avishai Ben-David, "Temporal-Spectral Detection in Long-Wave IR Hyperspectral Imagery," *IEEE Sensors Journal*, vol. 10, no. 3, 2010.

[33] Rod Frehlich et al., "Estimates of Cn2 from Numerical Weather Prediction Model Output and Comparison with Thermosonde Data," *Journal of Applied Meteorology & Climatology*, vol. 49, no. 8, p. 1742, August 2010.

[34] L L West et al., "Hazard Detection Analysis for a Forward-Looking Interferometer," 2008.

[35] Hung-Lung. Huang et al., "Minimum Local Emissivity Variance Retrieval of Cloud Altitude and Effective Spectral Emissivity - Simulation and Initial Verification," *J. Appl. Meteor.*, vol. 43, pp. 795-809, 2004.

[36] Keyvan Kanani, Laurent Poutier, Françoise Nerry, and Marc-Philippe Stoll, "Directional Effects Consideration to Improve Out-doors Emissivity Retrieval in the 3-13 µm Domain," *Optics Express*, vol. 15, no. 19, pp. 12464-12482, 2007.

[37] Stephen J. Young, B. Robert Johnson, and John A. Hackwell, "An in-scene method for atmospheric compensation of thermal hyperspectral data," *Journal of Geophysical Research*, vol. 107, no. D24, 2002.

[38] NASA Jet Propulsion Laboratory, California Institute of Technology. ASTER Spectral Library. [Online]. http://speclib.jpl.nasa.gov/search-1

[39] Institute for Computational Earth System Science, University of California, Santa Barbara. MODIS UCSB Emissivity Library. [Online]. http://www.icess.ucsb.edu/modis/EMIS/html/em.html

[40] Tom Simkin. (1994) Volcanoes: Their Occurence and Geography. [Online]. http://vulcan.wr.usgs.gov/Glossary/Tephra/Bulletin2047/Simkin/abstract.html

[41] Craig Searcy, Ken Dean, and William Stringer, "PUFF: A Lagrangian Trajectory Volcanic Ash Tracking Model," *Journal of Volcanology and Geothermal Research*, vol. 80, pp. 1-16, 1998. [Online]. http://parc.arh.noaa.gov/puff/jvgr/puffpaper.html

[42] K. P. Papp, K. G. Dean, and J. Dehn, "Predicting Regions Susceptible to High Concentrations of Airborne Volcanic Ash in the North Pacific Region," *Journal of Volcanology and Geothermal*

Research, vol. 148, no. 3-4, pp. 395-314, 2005.

[43] Warren, Stephen G.; "Optical Constants of Ice from the Ultraviolet to the Microwave"; Applied Optics, Vol. 23, No. 8, 15 April 1984, pg. 1206-1225.

[44] Hale, George M.; "Optical Constants of Water in the 200-nm to 200-µm Wavelength Region"; Applied Optics, Vol. 12, No. 3, March 1973, pg. 555-563.

[45] Telops Inc., Telops Infrared Hyperspectral Imager Specification Sheet, 2008, "TEL-COMM-00040-g (high-res Hyper-Cam complete flyer).pdf".

[46] D&P Instruments. TurboFT Portable FT-IR Spectrometer Instruction Manual. [Online]. http://www.dpinstruments.com/papers/turbo_winxp.pdf

Appendix A: Instrument Characterization

Throughout this report, we have often referred to the "noise limit" or "noise floor" of the Hyper-Cam instrument as it relates to whether or not a simulated signal can be seen. Prior to the MRS field test, we had one measurement of NESR the Hyper-Cam system, which was calculated from a measurement of a uniform patch of sky at 1 cm^{-1} resolution and with 31 interferograms averaged. The plot is shown in Figure 361. This NESR was computed from the test described in Section 3.3.1.

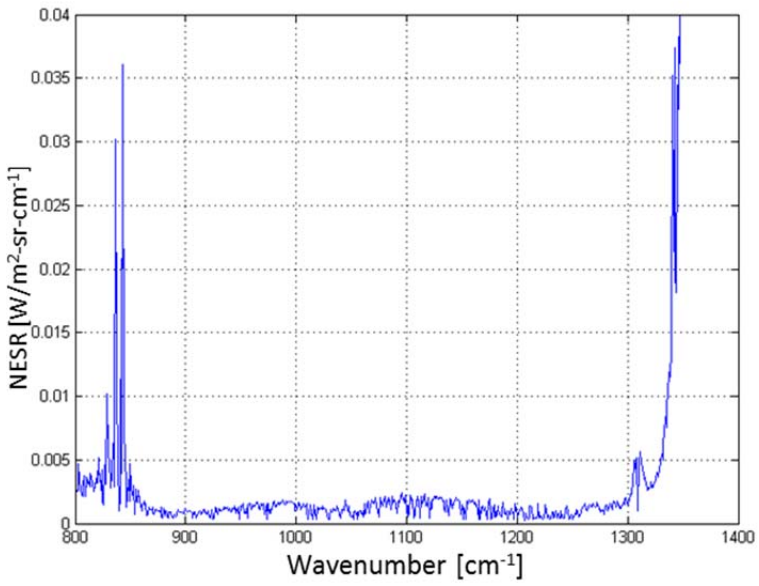

Figure 361. Telops Hyper-Cam NESR calculated from a uniform patch of sky.

However, the NESR will change for different resolutions, integration times, and averaging. Therefore, the above test should not be taken as representative of the expected NESR. Typical NESR at 16 cm^{-1}

resolution for different Hyper-Cam systems can be found in the Telops Hyper-Cam Specifications Flyer, and is 0.20 mW/m^2-sr-cm^{-1} at 10 μm (Long-wave Hyper-Cam), 0.04 mW/m^2-sr-cm^{-1} at 5 μm (Mid-wave Hyper-Cam), and 0.06 mW/m^2-sr-cm^{-1} at 5 μm (Mid-wave Extended Hyper-Cam) [43]. Note that the Mid-wave system used in the previous phase of this project was the 3 – 5 μm Mid-wave system, not the Mid-wave Extended, which has a range of 1.5 – 5 μm.

The NESR of our Hyper-Cam system was measured after the MRS test for three different resolutions, a 250 μs integration time, and no averaging. NESR should be calculated from a measurement of a blackbody at a uniform temperature which fills the FOV. Because the NESR changes with spectral resolution, we also needed to conduct this measurement at 16 cm^{-1} resolution, in order to compare with the simulated radiances as described in Section 5.4. For completeness, the NESR was calculated for 1, 4, and 16 cm^{-1} resolutions, which have all been used as set resolutions in Hyper-Cam tests throughout the FLI program.

We used measurements of the Hyper-Cam's own blackbody (at a set temperature) as a scene in order to estimate the NESR. During the test, the ambient air temperature in the room was approximately 24.8 °C; therefore, for calibration, the two blackbodies were set at 20.0 and 30.0 °C, while for the measurement, the second blackbody was set to 25.0 °C. The integration time for all tests was 250 μs, which matched the integration time used in the MRS tests. The order of measurement, which was repeated for each wavenumber resolution, was:

1. Calibration with BB1 set at 20.0 °C and BB2 set at 30.0 °C.
2. Measurement of BB2 set at 25.0 °C.
3. Calibration with BB1 set at 20.0 °C and BB2 set at 30.0 °C.

Time was given between each step for the temperature set point of BB2 to stabilize.

After calibration, each 25.0 °C blackbody radiance datacube was corrected for bad pixels. Then, the NESR was estimated by calculating the standard deviation of all pixels at each wavenumber. The resulting NESR plots for 1, 4, and 16 cm^{-1} resolution measurements are shown in the following three figures. Note the radiance units are in $mW/(m^2$-sr-$cm^{-1})$, for consistency with those reported in the simulated results of Section 5.4.

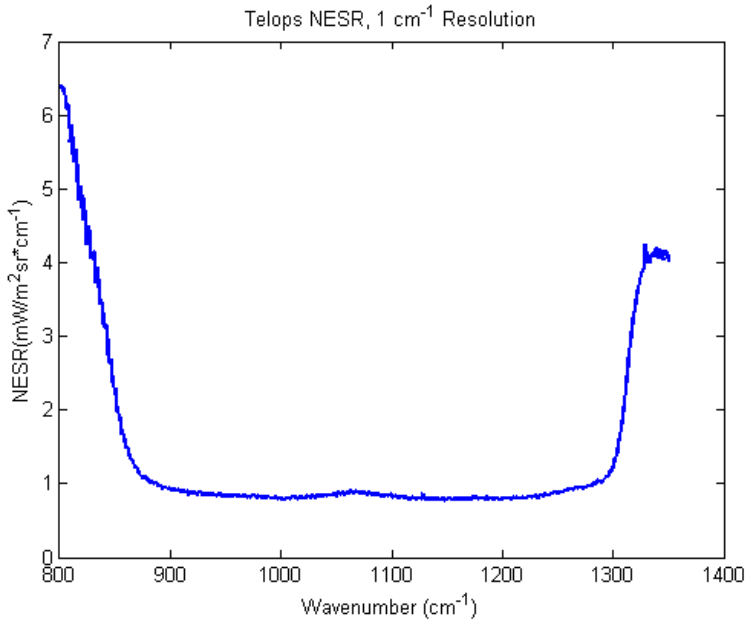

Figure 362. Telops Hyper-Cam NESR at 1 cm^{-1} resolution.

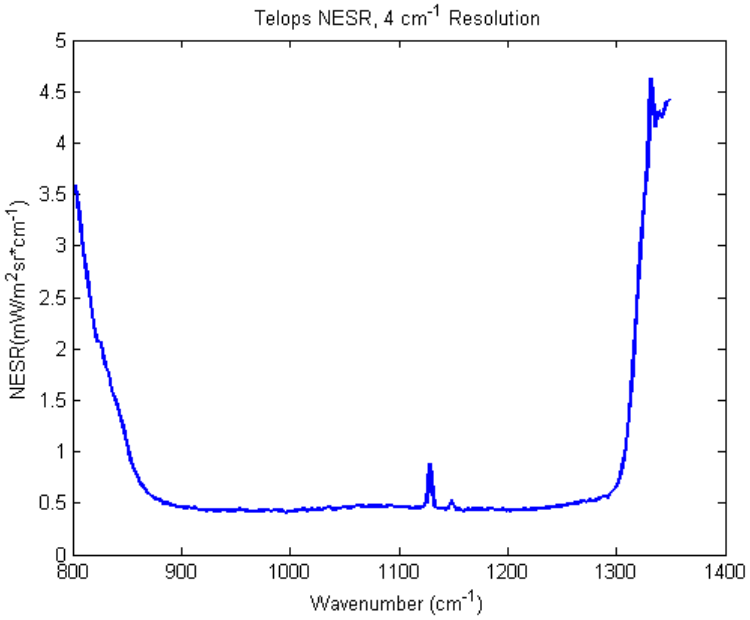

Figure 363. Telops Hyper-Cam NESR at 4 cm^{-1} resolution.

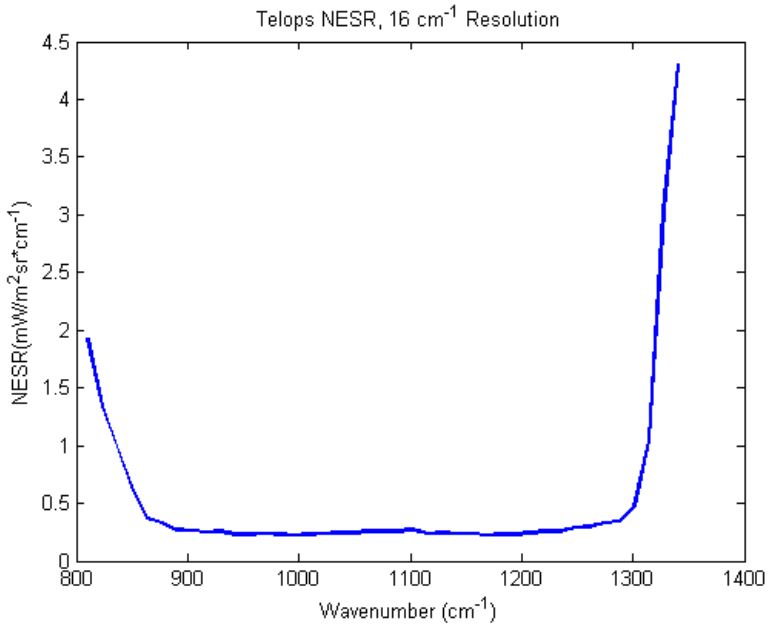

Figure 364. Telops Hyper-Cam NESR at 16 cm^{-1} resolution.

Figure 365 below shows the NESR at all three resolutions on the same plot. The two higher resolution NESRs were downsampled with Matlab's interp1 function to match the sampling interval of the 16 cm^{-1} datacube. Neglecting the first and last three channels in the 41 channel 16 cm^{-1} resolution datacube (as well as the spike seen in the 4 cm^{-1} resolution data), the 4 cm^{-1} resolution NESR is lower than the 1 cm^{-1} resolution NESR by a factor of 1.89 (approximately $\sqrt{4} = 2$), and the 16 cm^{-1} resolution NESR is lower than the 1 cm^{-1} resolution NESR by a factor of 3.37 (approximately $\sqrt{16} = 4$).

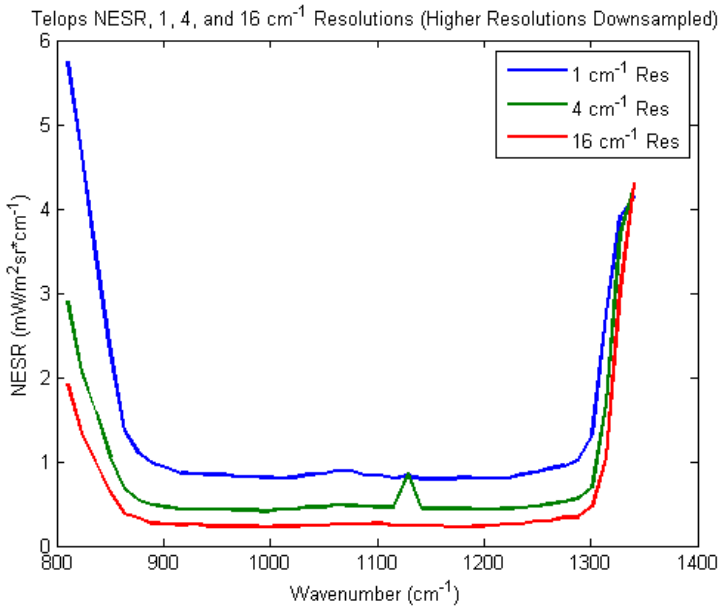

Figure 365. Telops Hyper-Cam NESR at all resolutions.

The important conclusion from this test is that it is a quantitative measure of the Hyper-Cam noise floor. However, the values are plotted in radiance units, and in this report, we often refer to brightness temperature differences. Therefore, both the NESR values (average, over Hyper-Cam wavenumber range) and its corresponding brightness temperature difference at 300 Kelvin are listed in Table 21.

Table 21. Hyper-Cam measured noise characteristics.

	NESR (mW/m^2-sr-cm^{-1})	BTD @ 300 K &1000 cm^{-1} (milli-Kelvin)
1 cm^{-1} Resolution	0.85	530
4 cm^{-1} Resolution	0.45	280
16 cm^{-1} Resolution	0.25	160

For completeness, we also measured the NESR of the D&P at 4 cm^{-1} resolution for 4 and 24 coadded spectra (these correspond to the settings used at MRS in 2011 and in Boulder in 2008, respectively). This was done in the same manner as the Hyper-Cam test except that the cold and warm blackbodies used for calibration were set at 15.0 °C and 35.0 °C, respectively; however, the blackbody for measurement was set at 25.0 °C as in the Hyper-Cam tests. The NESR plots are shown in in Figure 366. The D&P range is 625 – 3950 cm^{-1}; however, the wavenumber axis has been constrained to 600 – 2600 cm^{-1} in this figure; beyond that the noise is too high. Note the two "U" shapes typical of the NESR in the figure. This shape is due to the fact that the D&P TurboFT uses two detectors, a MCT detector is used for the LWIR (625 – 2000 cm^{-1}) and an InSb detector is used to extend the range to the SWIR and MWIR regions (3950 cm^{-1}) [44]. The detector change-over seems to be located at 1800 cm^{-1} in our sensor. The D&P TurboFT NESR in Figure 366 has the same units as that shown for the Hyper-Cam in Figure 365; the average NESR of the D&P in the effective Telops Hyper-Cam range (~900-1300 cm^{-1}) is nearly equivalent when one compares the Hyper-Cam 4 cm^{-1} resolution NESR (0.45 mW/m^2-sr-cm^{-1}) to the D&P 4 cm^{-1} resolution, 4 coadd NESR (0.41 mW/m^2-sr-cm^{-1}). The 4 coadded data were compared because that was the setting used at MRS.

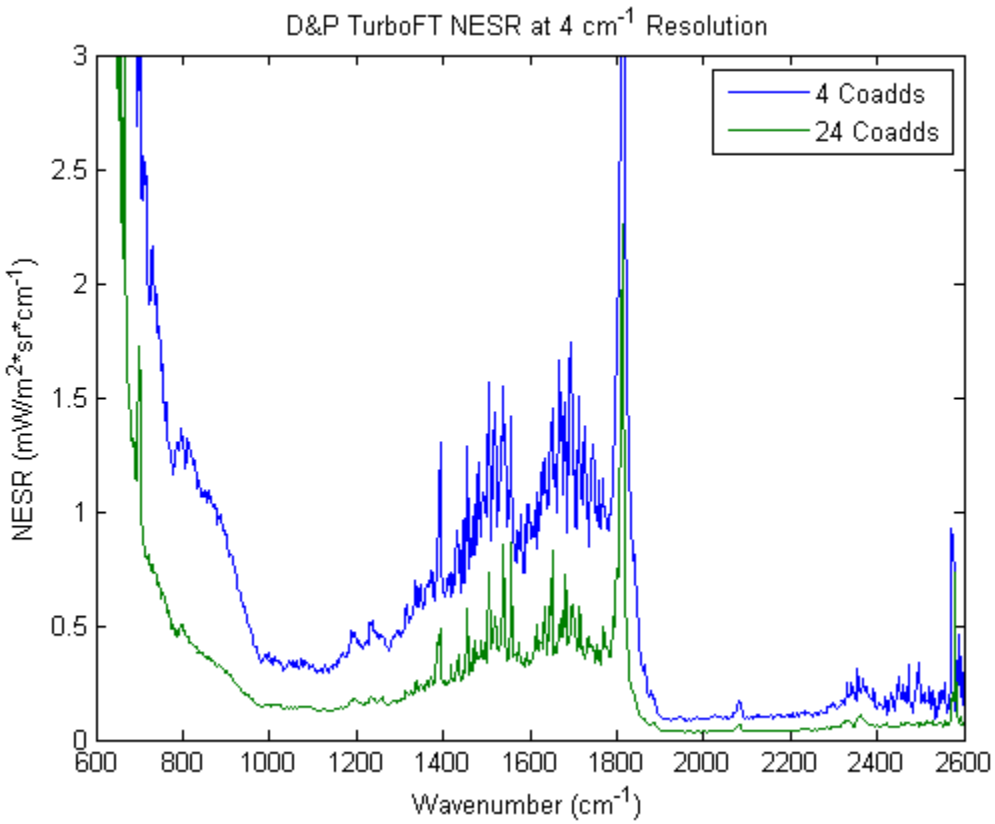

Figure 366. D&P TurboFT NESR.

The average D&P NESR values measured at different wavenumber regions are shown below in Table 22. The 900-1300 cm^{-1} region is in the LWIR (7.7 – 11.1 μm), and the 1900-2600 cm^{-1} region is in the MWIR (3.9 – 5.3 μm). The LWIR region was chosen based upon the effective waveband of the Telops Hyper-Cam, the MWIR region was chosen somewhat arbitrarily based upon where the D&P noise level is low (i.e. the bottom of the "U").

Table 22. D&P TurboFT measured noise statistics at 4 cm^{-1} Resolution

	NESR (mW/m^2-sr-cm^{-1})		BTD (milli-Kelvin)	
	900-1300 cm^{-1}	1900-2600 cm^{-1}	@ 300 K & 1000 cm^{-1}	@ 448 K & 2250 cm^{-1}
4 coadds	0.42	0.15	260	100
24 coadds	0.16	0.06	100	40

Appendix B: 2011 OSA Paper

Ultra-spectral measurements of surface emissivity with an imaging interferometer spectrometer

IN OSA HYPERSPECTRAL IMAGING AND SOUNDING OF THE ENVIRONMENT

TORONTO, CANADA

JULY 2011

Ultra-spectral measurements of surface emissivity with an imaging interferometer spectrometer

William Smith Sr.[1], Leanne West[2], Gary Gimmestad[2], and Sarah Lane[2]
[1] *Hampton University, Hampton VA*
2 Georgia Tech Research Institute, Atlanta GA
bill.l.smith@cox.net

Abstract: Surface emissivity and skin temperature measurements were conducted with the Telops Hyper-Cam imaging spectrometer for a scene consisting of wet, dry, and ice covered concrete and a wet, dry, and ice covered non-skid surface.
OCIS codes: 010.1615, 280.4991

1. Introduction

An experiment was conducted under clear sky conditions in September 2010 to simulate the ultra-spectral emissivity imaging of runways under different surface conditions. Emissivity images, obtained from an aircraft mounted Forward Looking Interferometer (FLI), are intended to be used to alert the pilot of hazardous landing runway surface conditions and enable the determination of runway friction and associated stopping distance for his particular aircraft. A parking deck on the Georgia Tech campus provided an ideal location; the fifth level was high enough to allow for a view of the horizon over surrounding buildings and trees. Additionally, the concrete surface was treated with a non-skid coating, but on only half the deck, allowing two surfaces to be imaged. The setup is shown in Figure 1.

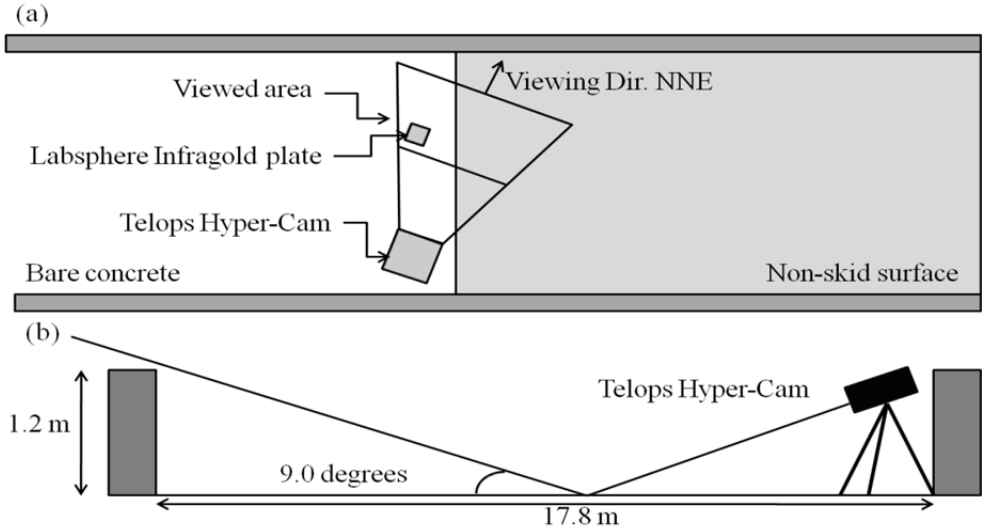

Figure 1. Parking deck setup on Georgia Tech campus, (a) Top View, (b) Side View

The roughened gold-coated surface that is shown in Figure 1 is an InfraGold target from Labsphere with an emissivity of approximately 0.01 in the longwave infrared. The target allows the measurement of the diffuse reflection of the downwelling radiance from the sky surrounding in the same scene as the surface targets. The Hyper-Cam was oriented down at the scene at a 9 ° declination angle. After each downward-looking scene image, the Hyper-Cam was oriented up 9 °at the sky to measure the sky radiance component. The elevation is shown in Figure 1 (b). A diffusivity factor determined from the ratio of the gold target radiance to the sky radiance was applied to enable surface emissivity and skin temperature to be estimated for every pixel within the imaging array of the Hyper-Cam instrument. The Field of Regard (FOR) of the Hyper-Cam consists of a 320 x 256 detector pixel array with each pixel having a Field of View (FOV) of 0.35 μrad. The unapodized spectral resolution is 0.5 cm^{-1}. The radiance spectra were calibrated using two blackbody references with temperatures of 1.0 C and 55.0 C. The sample integration time is 200 μs. Since the scene to be imaged was static, averages of ten interferograms per blackbody measurement and ten interferograms per scene measurement were made to reduce the effect of detector

noise. The surface scene consisted of wet, dry, and ice covered concrete and wet, dry, and ice covered non-skid surfaces.

2. Method

Governing Equations: The radiative transfer equation governing the radiance (R) as a function of wavenumber (ν) observed, with the Hyper-Cam placed a few feet above the surface, at the local zenith angle (θ) is

$$\mathbf{R(\nu,\theta) = \varepsilon(\nu,\theta)B(\nu,T_{sfc}) + \rho(\nu,\theta)\ Rsky(\nu,\theta),} \qquad \mathbf{(1)}$$

where the first term is the surface radiance reaching the Hyper-Cam and the second term is the surface reflected downwelling sky radiance reaching the Hyper-Cam. Here, $\varepsilon(\nu,\theta)$ is the surface emissivity, $B(\nu,T_{sfc})$ is the Planck radiance corresponding to the surface temperature, T_{sfc}, and $\rho(\nu,\theta)$ is the surface reflectivity. To arrive at equation (1), it is assumed that the atmospheric transmittance of the short path between the Hyper-Cam and the surface is unity, which is particularly true for the atmospheric window region (8-12 μm) observed with the Hyper-Cam. If we also assume that Kirchoff's law holds for the frequency (ν) and measurement angle (θ), then $\rho(\nu,\theta) = [1 - \varepsilon(\nu,\theta)]$, so that

$$\mathbf{R(\nu,\theta) = \varepsilon(\nu,\theta)B(\nu,T_{sfc}) + [1-\varepsilon(\nu,\theta)]\ Rsky(\nu,\theta)} \qquad \mathbf{(2)}$$

and

$$\mathbf{\varepsilon(\nu,\theta)= [R(\nu,\theta) - Rsky(\nu,\theta)] / [B(\nu,T_{sfc}) - Rsky(\nu,\theta)].} \qquad \mathbf{(3)}$$

The surface conditions observed were: wet, dry, and ice covered concrete and wet, dry, and ice covered non-skid surfaces. The wet covered concrete and non-skid concrete conditions were observed for different surface temperature and water temperature contrast conditions (i.e. warm water over cold concrete and non-skid concrete and cold water over warm concrete and non-skid concrete, as provided by the melting of the ice). The measurement sequence was (1) calibration BB views, (2) sky views, (3) surface views, (4) sky views, and (5) calibration blackbody views.

Diffuse Sky Radiance Estimation: The sky view obtained with the Hyper-Cam is for an elevation angle of about 9° and as a result the radiance observed does not represent the angularly integrated sky radiance being reflected by the surface. In order to account for this angular dependence, a diffuse gold plate was placed within the FOR of the Hyper-Cam measurements. Since gold is a nearly perfect reflector at infrared wavelengths (i.e. reflectance > 0.99), surface measurements for those pixels whose FOV are filled with the gold plate provide measurements of the diffuse sky radiance needed for the computation of emissivity from the radiance for pixels viewing the surrounding concrete and non-skid concrete surfaces. In order to estimate the diffuse sky radiance for those pixels not viewing the gold plate, a spectral diffusivity factor, **r(ν),** is defined from those pixels viewing the gold plate. This diffusivity factor is computed from equation (1):

$$\mathbf{r(\nu) = [R_g(\nu) - \varepsilon_g B(\nu,T_g)] / [(1 - \varepsilon_g)\ Rsky(\nu,\theta)]} \qquad \mathbf{(4)}$$

where $\mathbf{R_g(\nu)}$ is the radiance measured from the pixels viewing the gold plate with emissivity ε_g and temperature T_g, and **Rsky(ν,θ)** is the observed sky radiance. An average spectral diffusivity factor is calculated for all pixels viewing the gold plate, and is then multiplied by **Rsky(ν,θ)** to obtain the diffuse sky radiance, **Rdsky(ν,θ)**. This result is then used as an estimation of the diffuse sky radiance for all pixels in the Hyper-Cam array.

Surface Temperature and Emissivity Determination: The surface skin temperature is defined as that value that minimizes the local spectral variance in the emissivity calculated using equation (3). The emissivity calculated according to equation (3) will exhibit excessive local spectral variance for an incorrect surface skin temperature since atmospheric emission line features observed in the sky radiance (see figure 1 above) will propagate into the calculated surface emissivity spectrum [1]. Since the local spectral variance of the true surface emissivity is small compared to that produced by atmospheric emission line features, the correct surface skin temperature must be that temperature which produces minimal local spectral variance in the derived surface emissivity spectrum. The local variance of the surface emissivity spectrum is calculated as the standard deviation of the spectral derivatives of emissivity around every spectral point. The correct surface skin temperature, and associated surface emissivity spectrum, is assumed to be that which has the minimum local spectral variance of the calculated surface emissivity.

The surface temperature and associated spectral emissivity is derived by considering all temperatures within the range of 260 K to 360 K using a five step iterative process. In the first step, an increment of 10 K is used to define the temperature that minimizes the standard deviation of the local spectral derivative of the calculated surface spectral emissivity. Once this temperature is defined, then a 2 K increment is used within a 20 K interval centered on the first-defined surface temperature value. The iterative process is repeated a third, fourth, and final time, reducing the increment by a factor of 10 after each iteration, to provide a final surface temperature resolution of mK.

3. Results

Figure 2 shows images of the spectral emissivity derived for three wavelengths, 10 μm (1000 cm^{-1}), 9 μm (1100 cm^{-1}), and 8.3 μm (1200 cm^{-1}), along with the derived surface skin temperature. Significant differences are evident in the emissivity for the three wavelengths shown, depending on the surface condition, thereby providing a significant measure of the surface condition. As can be seen, ice and water have very little spectral variation, whereas dry concrete and non-skid surfaces provide large variations in spectral emissivity, dependent on their coverage with ice and/or water. Most interesting is the apparent accuracy of the surface skin temperature retrieved as that value which minimizes the local surface spectral emissivity variation. In-situ measurements, which were made with a hand-held thermistor probe, indicated the following surface temperatures: the dry concrete = 40 C (313 K), wet concrete = 34 C (307 K), dry non-skid pavement = 36 C (309.0 K), wet non-skid pavement = 18 C (291 K), ice = 0 C (273 K), and the ice water = 7 C (280K). The retrieved surface temperatures shown in figure 2 for these different surface conditions are in excellent agreement with these in-situ surface temperature measurements. Figure 3 shows example spectra of the derived surface emissivity for a few representative locations within the FOR of the Hyper-Cam instrument. It is clearly seen that the major spectral emissivity signal of different surface conditions is within the 1000 - 1250 cm^{-1} (8 -10 μm) spectral region. It is this spectral region that will be most useful for estimating runway surface condition and aircraft stopping distance from FLI measurements.

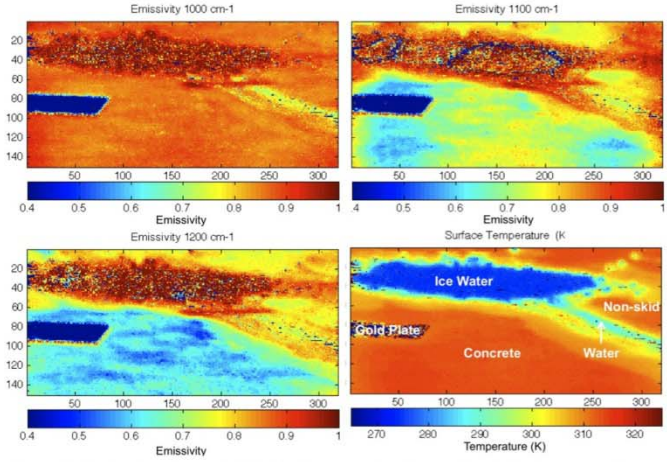

Figure 2. Derived surface emissivity for three wavelengths and the derived surface skin temperature (lower right hand panel). The dark spots are missing data due to excessive radiance noise in non-responsive detector elements.

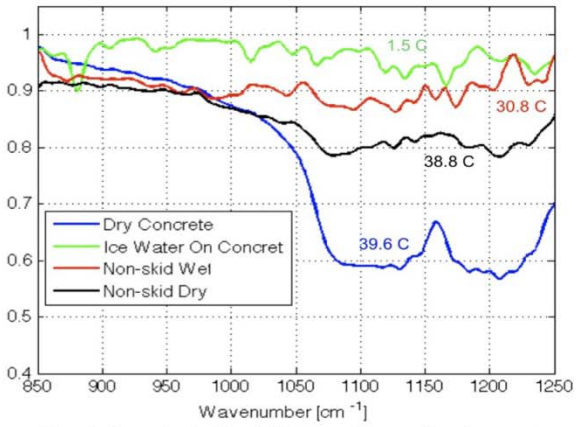

Figure 3. Spectral emissivity of different surface types (i.e., dry concrete, wet concrete, wet non-skid pavement, and dry non-skid pavement) retrieved from radiance spectra observed with the HyperCam instrument.

4. Summary and Conclusions

Measurements of surface and sky radiance were conducted with the Telops Hyper-Cam imaging interferometer. The scene, consisting of wet, dry, and ice covered concrete and wet, dry, and ice covered non-skid surfaces, possessed a large variability of emissivity conditions. By minimizing the variance of the local derivative of spectral emissivity, the physical temperature of the surface skin was determined simultaneously with the surface emissivity spectrum. This technique will be used to validate airborne and satellite emissivity spectra determinations.

5. References

[1] Huang, H-L, W. L. Smith, J. Li, P. Antonelli, X. Wu, R. O. Knuteson, B. Huang, B. J. Osborne, 2004: Minimum Local Emissivity Variance Retrieval of Cloud Altitude and Effective Spectral Emissivity—Simulation and Initial Verification. *J. Appl. Meteor.*, **43**, 795–809.

Acknowledgements:
The research described here was funded by the NASA Aeronautics Research Mission Directorate (ARMD) Aviation Safety (AvSafe) Program, under the Atmospheric Hazard Sensing & Mitigation (AHSM) area within the Atmospheric Environment Safety Technologies (AEST) project.

Appendix C: 2011 SPIE Paper

Detection of Aircraft Exhaust in Hyperspectral Image Data

IN SPIE PROCEEDINGS 8158
IMAGING SPECTROMETRY XVI
SAN DIEGO, CA
AUGUST 2011

Detection of Aircraft Exhaust in Hyperspectral Image Data

Sarah E. Lane[a], Leanne L. West[a], Gary G. Gimmestad[a],
William L. Smith, Sr.[b], Edward M. Burdette[a]
[a]Georgia Tech Research Institute, 925 Dalney Street, Atlanta, GA 30332
[b]Hampton University, 21 Tyler Street, Hampton, VA 23668

ABSTRACT

The use of a hyperspectral imaging system for the detection of gases has been investigated, and algorithms have been developed for various applications. Of particular interest here is the ability to use these algorithms in the detection of the wake disturbances trailing an aircraft. A dataset of long wave infrared (LWIR) hyperspectral data cubes taken with a Telops Hyper-Cam at Hartsfield-Jackson International Airport in Atlanta, Georgia is investigated. The methodology presented here assumes that the aircraft engine exhaust gases will become entrained in wake vortices that develop; therefore, if the exhaust can be detected upon exiting the engines, it can be followed through subsequent data cubes until the vortex disturbance is detected. Gases known to exist in aircraft exhaust are modeled, and the Adaptive Coherence/Cosine Estimator (ACE) is used to search for these gases. Although wake vortices have not been found in the data, an unknown disturbance following the passage of the aircraft has been discovered.

Keywords: hyperspectral image processing, standoff gas detection, remote sensing, aviation safety

1. INTRODUCTION

Aviation hazards, such as clear air turbulence, wake vortices, icing, and hazardous runway conditions, are often unforeseeable. Real-time detection of these hazards from an in-flight aircraft is not currently feasible; however, one possible method of detection is with the use of a Forward Looking Interferometer (FLI) sensor. Here, the focus is on the possible detection of wake disturbances that follow aircraft, which include vortices and turbulence. This paper investigates the measurement parameters and processing algorithms necessary for a FLI sensor to observe the phenomenology of these particular aviation hazards. If the phenomenology is detectable by a FLI sensor, it could potentially alert flight crews to hazardous conditions, allowing the pilot time to react. The detection of these particular hazards could also be helpful in determining runway spacing at airports from either a ground-based or an airborne FLI sensor. Hyperspectral image data cubes contain more information than a FLI sensor would need in this application. The data cubes contain both spatial and spectral information; therefore, they can be studied to determine the necessary parameters for a FLI system specific to the detection of aviation hazards.

2. MEASUREMENTS

2.1 Data collection at Hartsfield-Jackson Airport

A Telops LWIR Hyper-Cam[1] was used to record a series of hyperspectral data cubes at Hartsfield-Jackson International Airport (ATL) in Atlanta, GA in July of 2010. A construction site adjacent to the airport provided an ideal location for the test. The Hyper-Cam was oriented East toward oncoming aircraft as they approached for landing on ATL's Runway 26R; the setup is shown in Figure 1.

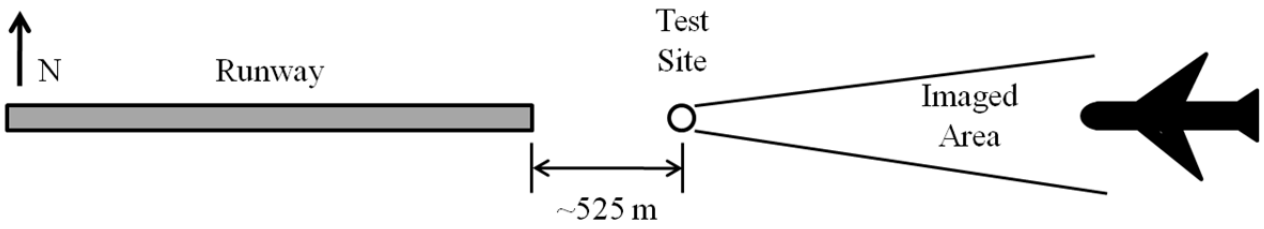

Fig. 1. The test setup just off runway 26R at Hartsfield-Jackson International Airport in Atlanta, GA.

Figure 2 shows the Hyper-Cam set up at the test site; the Hyper-Cam was inclined at a 10° elevation angle on its tripod in order to image the flights.

Fig. 2. The Hyper-Cam set up to image oncoming aircraft.

The clear view of the horizon allowed the data acquisition to begin before an aircraft entered the field of view of the Hyper-Cam. This arrangement allowed continuous collection of data cubes before, during, and after each flight in order to capture both the sky background before, and any trailing disturbances after, the passage of the aircraft.

2.2 Hyper-Cam settings

The Hyper-Cam has onboard blackbodies that allow for absolute calibration of radiance data. It has an IFOV of 0.35 mrad and a variable window size of up to 320 x 256 pixels. A reduced window size of 200 x 75 was used; therefore the FOV shown by the imaged area in Figure 1 is 4.0° x 1.5°. The resolution of the Hyper-Cam is variable, and sets of measurements were recorded at 1, 4, and 16 cm^{-1} resolutions. The focus here is on the 4 cm^{-1} resolution data cubes; these data cubes contain 165 spectral bands of information between 802.9 and 1349.4 cm^{-1}. At the 200 x 75 window size and 4 cm^{-1} resolution described, each data cube is collected in 873 ms, with a 137 ms delay between acquisitions.

The movement of the aircraft creates a highly dynamic scene. Indeed, the scene changes so drastically in the amount of time needed to acquire an entire data cube that artifacts are certain to be present. However, the interest is not in the aircraft itself, but the wake and/or vortices that follow the aircraft, which will not change as drastically in the time needed to collect one data cube. A methodology is presented that will be used in the attempt to detect these disturbances in the hyperspectral image data.

3. METHODOLOGY

3.1 Gas detection

As wake vortices form and fall, there is no way to tell where in the field of view they exist. They could form below the captured scene or be carried away by wind and not be captured at all. With no way to determine where in the imaged scene the vortices are located, a search methodology is developed. The methodology for the possible detection of wake vortices leverages the fact that vortices often entrain aircraft engine exhaust gases such as CO_2, CO, NO_x, and H_2O[2]. These gases, if they exist in the data cubes, are in mixed pixels that may show spectral influence from all scene elements, including the gas of interest, the background, and the intervening atmosphere. Because these gases are in the exhaust, if they can be detected immediately upon exiting the aircraft engine, it could be possible to follow the gases through the next data cubes in the sequence of measurements as they either become entrained in a vortex or disperse into the atmosphere.

Algorithms for gas detection in hyperspectral data have been developed and tested in various studies, which include testing of the algorithms on controlled gas releases[3] and modeled data[4]. Various approaches include Spectral Angle Mappers, Matched Filters, and the Adaptive Coherence/Cosine Estimator (ACE) [3,4,5]. This paper uses ACE as a possible means of gas detection in the hyperspectral image data cubes, although multiple algorithms have been investigated.

3.2 Target and background modeling

Gas detection algorithms commonly depend on *a priori* knowledge of the gas spectrum under search, e.g. the target gas spectrum. Under a controlled gas release, gas constituents, abundances, temperatures, and concentrations are known. However, in the data set under investigation, these characteristics must be estimated.

To model the target gas spectrum effectively, the background and the atmosphere must be considered. Therefore, a semi-empirical target gas spectrum is created from gas cell data from the online tool Spectral Calc[6], which accesses the HITRAN database to model multiple types of spectra, and the actual measured data.

The gas cell radiance spectrum is downloaded from Spectral Calc after having been smoothed with a Gaussian function, and the resulting spectrum is interpolated to match the spectral wavenumber values and resolution needed for each 4 cm^{-1} data cube collected. This resulting spectrum is combined with the measured data in the following manner. First, the data cube following the passage of the aircraft is divided into horizontal strips of sky and the radiance of each strip is averaged. These averages are computed for each piece of sky independently, because the radiance of the sky is expected to change with elevation angle. This method of averaging the radiance for horizontal strips of sky is similar to the Directional Mean Filter[7], with the exception that we are limiting the direction of our background average to the horizontal. The resulting radiances give a measure of the background atmospheric conditions as a function of elevation angle at the time of measurement. Next, the gas cell data is added to each resulting radiance average; the gas cell data is added because in this case, the hot engine exhaust is expected to act as an emitter against the cold sky. This method gives the semi-empirically modeled target gas spectrum for each elevation angle.

3.3 Search methodology

The ACE algorithm is run on the data cube after the aircraft has passed, using the target gas spectra estimates and the local averages as background. The result of the ACE algorithm gives a value, or score, for every pixel, which indicates how closely that pixel's spectrum matches that of the target gas. These results can be represented by a scaled image, which shows the spatial location in the data cube where the target gas might exist. This image of ACE scores can then be filtered with a median filter, similar to the procedure described by Vallières et. al.[3]. The effect of the median filter is to eliminate high scoring pixels that have no neighbors which score similarly high, which could be an indication of a false alarm.

The process of modeling the background and target gas spectra is then repeated, this time excluding portions of the image that show any possible detection after the first ACE run. This repetition is essential because we do not know the spatial location of the gas, if it exists in the data cube, and we do not want our background estimation to be influenced by its spectrum.

4. PRELIMINARY RESULTS

4.1 Data cube reduction

It was noted that some of the radiance data was quite noisy; these noisy values appeared at the extremes of the wavenumber scale. To determine where in the spectrum the data is least noisy, a row of pixels was selected from a data cube that was recorded prior to the aircraft entering the field of view, and the NESR from the radiance of these pixels was calculated. The assumptions here are that the sky is featureless (e.g. no gas or other contaminants are present) and that the pixels in this horizontal strip of sky are uniform. This NESR plot is shown in Figure 3.

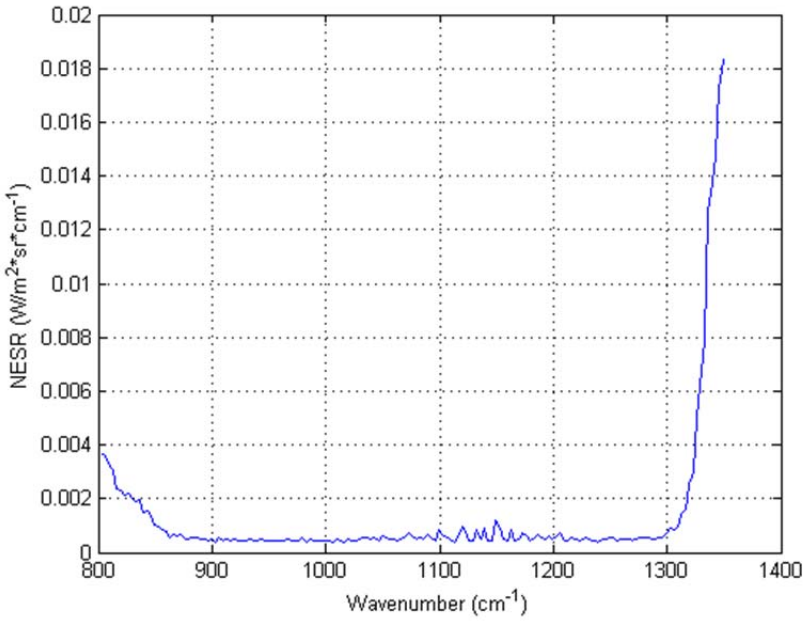

Fig. 3. The NESR calculated from the pixels from a horizontal strip of sky.

The NESR values were rounded to the nearest one thousandth, and the wavenumber values where the NESR was 0.001 or less were kept. These wavenumber values were from 845.9 to 1312.2 cm^{-1}, which corresponds to bands 15 through 151 of the original 165 wavebands. In all further analysis, the data cube under test has been reduced from the full 165 to the new 141 wavebands where noise is a minimum.

4.2 Radiance imagery

The radiance image from the data cube during the aircraft passage is shown in Figure 4. This average is calculated by averaging the spectral radiance values over the 141 remaining wavebands.

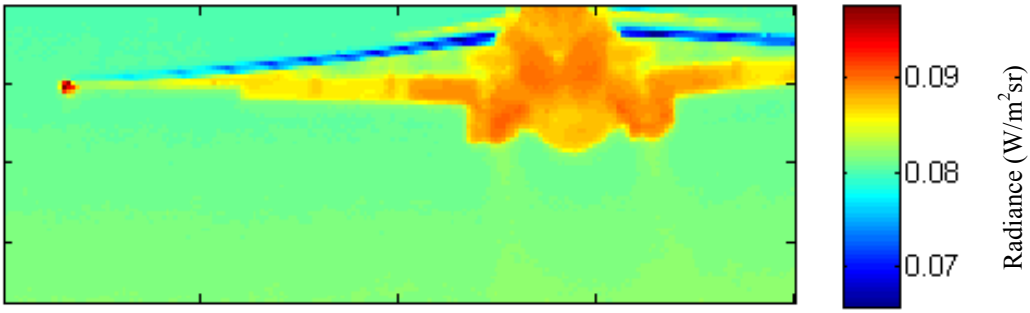

Fig. 4. The average radiance of the data cube with the aircraft passing through the FOV.

The data cube immediately following the passage of the aircraft (approximately one second later) is shown in Figure 5.

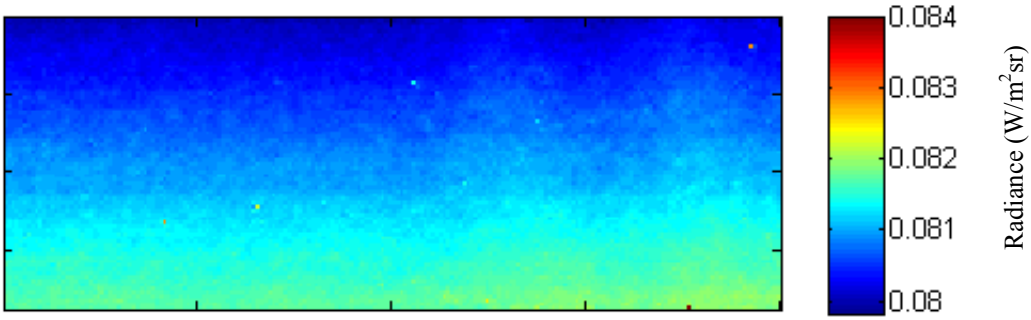

Fig. 5. The average radiance of the following data cube, approximately one second later.

The radiance images in Figures 4 and 5 show that no disturbances are immediately apparent in the radiance images alone. Therefore, the search methodology that exploits the spectral domain is implemented.

4.3 Search results

The ACE algorithm was run on the 4 cm^{-1} resolution data cube immediately following the passage of an aircraft. As the largest component of the exhaust, water vapor at 425 K was chosen as the target under search. This temperature was based on a derivation of a typical aircraft exhaust temperature following a method described by Mattingly[8].

As noted earlier, the detection algorithm is run twice, once to find any highly scoring pixels, and a second time with those pixels excluded from the background averages. The results of the first ACE run are shown in Figure 6.

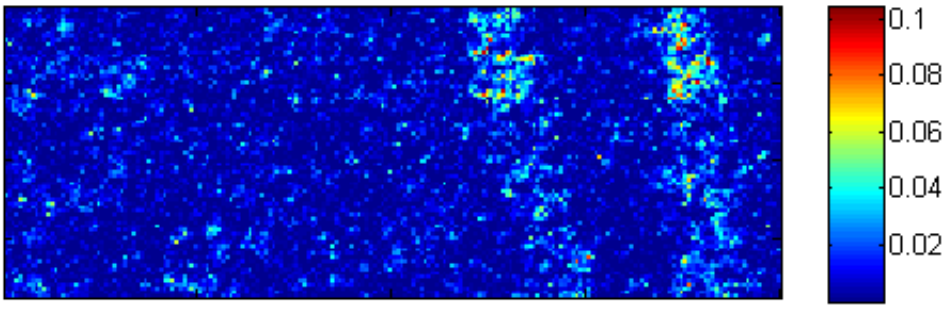

Fig. 6. The ACE results on the data cube following the passage of the aircraft, using every column in the background estimation.

The median filter was then applied to the image shown in Figure 6; this result is displayed in Figure 7.

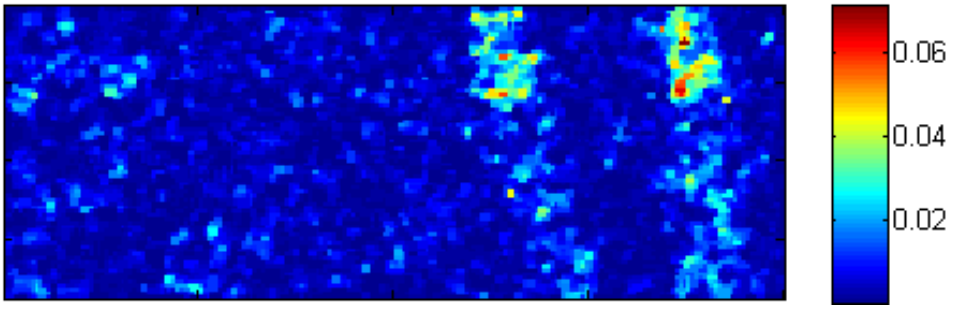

Fig. 7. The ACE results on the data cube following the passage of the aircraft, using every column in the background estimation, with a median filter applied.

The results of the first run of the ACE algorithm indicated that only the left 90 columns of pixels should be averaged for the second run of the algorithm, due to the streaks that appear in the right half of two scaled images (Figures 6 and 7 are 200 pixels wide). Limiting the pixels chosen as the background ensures that if these pixels do contain any target gas, they would not contaminate the background average and target gas spectra estimations.

The result of the second ACE run on the data cube following the passage of the aircraft which excludes these high scoring pixels is shown in Figure 8.

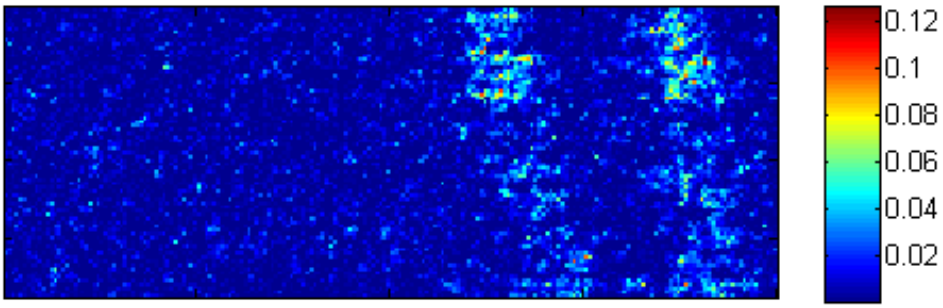

Fig. 8. The ACE results on the data cube following the passage of the aircraft, using columns 1-90 in the background estimation.

A median filter was then applied to the ACE result of Figure 8. The filtered result is shown in Figure 9.

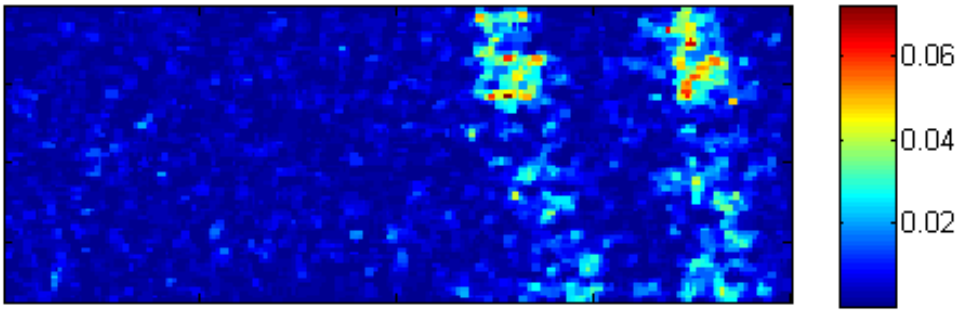

Fig. 9. The ACE results on the data cube following the passage of the aircraft, using columns 1-90 in the background estimation, with a median filter applied.

Two streaks appear in Figures 6 through 9 that are not apparent in the radiance image of Figure 5; by comparison with Figure 4, one sees the streaks are located right where the aircraft engines passed through the field of view. This location seems to indicate the detection of exhaust leaving the engine.

For comparison, the result of the ACE run on the same data cube following the passage of the aircraft when the usual method of applying the ACE is applied is shown in Figure 10. The data cube spectral dimension has not been reduced and the sky is not divided into horizontal strips.

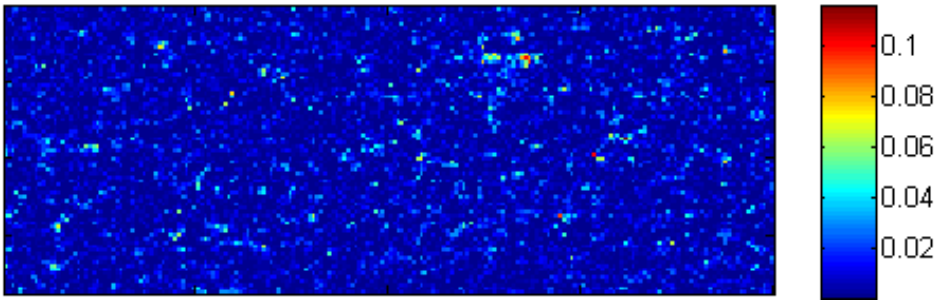

Fig. 10. The ACE results on the data cube following the passage of the aircraft when the data cube is not reduced and the background is not divided into horizontal strips for averaging.

The median filter was applied to Figure 10, and the result is shown in Figure 11.

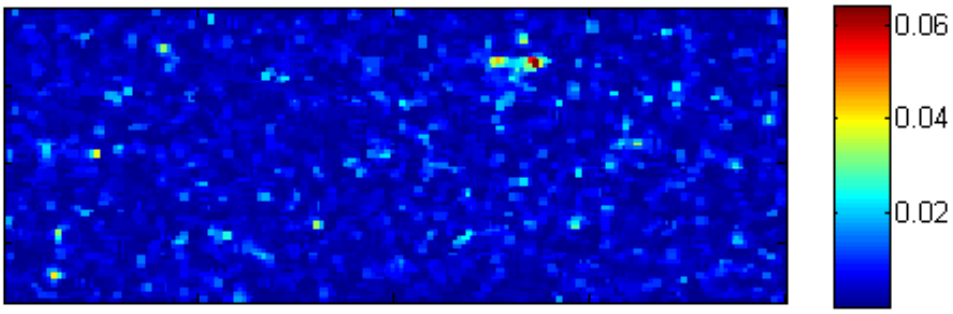

Fig. 11. The ACE results on the data cube following the passage of the aircraft when the data cube is not reduced and the background is not divided into horizontal strips for averaging, with a median filter applied.

Figures 10 and 11 do not contain the streaks seen in Figures 6 through 9, although there are some pixels that do score more highly than others in the general area where the streaks were seen in Figures 6 through 9.

4.3 Analysis of search results

The score of the pixel is equal to the cosine square of the angle between the spectrum of the pixel and the spectrum of the target gas. Therefore, a perfect scoring pixel would have a value of one, meaning that the angle between the target gas spectrum and the pixel is zero.

By comparing the actual pixel values in the images of Figures 6 through 9, the following deductions can be made. The first ACE run produces a maximum scoring pixel of 0.1048 in the unfiltered image of Figure 6 and a maximum scoring pixel of 0.0717 in the filtered image of Figure 7. Therefore, the smallest angles of separation between the target gas spectrum and pixel spectrum calculated from the first ACE run are 71.1136° and 74.4696° in the respective images. The second ACE run produces a maximum scoring pixel of 0.1270 in the unfiltered image of Figure 8 and a maximum scoring pixel of 0.0725 in the filtered image of Figure 9. Therefore, the smallest angles of separation between the target gas spectrum and pixel spectrum calculated from the second ACE run are 69.1187° and 74.3823° in the respective images. Figures 7 and 9 look nearly identical, and these results show that after the median filtering, there is only a small improvement in detection after the second ACE run.

Most pixels in the streaks have much lower scores and therefore even higher separation angles. The results at this point are still inconclusive as to what is causing the disturbances seen, because these scores do not strongly indicate the presence of water vapor. The two distinct streaks are still interesting and their source is still being investigated. If the result is not a detection of the gas but perhaps an artifact of turbulence, it is still relevant to our research

regarding aviation safety. When the sky background is not divided into horizontal strips of sky for the background averaging and target modeling, the streaks are not observed. Therefore, this methodology does uncover some type of disturbance, although it is still unknown.

The ACE algorithm was then run on following data cubes; however the distinct streaks dissipate and cannot be tracked through further data cubes.

5. CONCLUSIONS

A methodology for the detection of wake vortices in hyperspectral image data by detecting the exhaust gases that they entrain has been presented. However, from the results shown thus far, it is inconclusive as to whether the exhaust gases are actually being detected or some other disturbance is being seen. If the exhaust is indeed being detected, the results indicate that the detection is short lived because the same results cannot be repeated in successive data cubes. The method is therefore not applicable to the detection of vortices; however, *the method presented demonstrates a way to search for mixed pixel targets when the sky is the background*. Though no vortices were found, a disturbance was seen in the results that warrants further investigation. The low ACE scores indicate that gas is not being detected; however, if the disturbance is due instead to turbulence, it is still relevant in its applicability to aviation safety.

ACKNOWLEDGEMENTS

The research described here was funded by the NASA Aeronautics Research Mission Directorate (ARMD) Aviation Safety (AvSafe) Program, under the Atmospheric Hazard Sensing & Mitigation (AHSM) area within the Atmospheric Environment Safety Technologies (AEST) project.

Access to the test location just past the runway at Hartsfield-Jackson International Airport was provided courtesy of Jacoby Development.

REFERENCES

[1] Farley V., Vallières, A., Chamberland, M., Villemaire, A., and Legault, J-F. "Performance of the FIRST, a longwave infrared hyperspectral imaging sensor," Proc. SPIE 6398 (2006).

[2] West, L. L., et al., "Hazard detection analysis for a forward-looking interferometer," NASA Final Report NNX07AN17A, October 2008.

[3] Vallières, A., Villemaire, A., Chamberland, M., Belhumeur, L., Farley, V., Griouz, J., and Legault, J-F., "Algorithms for Chemical Detection, Identification, and Quantification for Thermal Hyperspectral Imagers," Proc. SPIE 5995 (2005).

[4] Larrieux, E. R., "Performance evaluation of chemical plume detection and quantification algorithms" Electrical and Computer Engineering Master's Theses, Dept of Electrical and Computer Engineering, Northeastern University. Paper 18. (2009) http://hdl.handle.net/2047/d10019297

[5] Manolakis, D. and Shaw, G., "Detection algorithms for hyperspectral imaging applications," *IEEE Signal Processing Magazine,* 19(1), 29-43 (2002).

[6] http://spectralcalc.com

[7] Caefer, C. E., Stefanou, M. S., Nielsen, E. D., Rizzuto, A. P., Raviv, O., and Rotman, S. R., "Analysis of false alarm distributions in the development and evaluation of hyperspectral point target detection algorithms," Optical Engineering, 46(7), (2007).

[8] Mattingly, J. D., *Elements of Gas Turbine Propulsion*, (McGraw-Hill, 1996).

Appendix D: 2012 SPIE Paper

Hyperspectral Image Turbulence Measurements of the Atmosphere

IN SPIE PROCEEDINGS 8355
INFRARED IMAGING SYSTEMS: DESIGN, ANALYSIS, MODELING, AND TESTING XXIII
BALTIMORE, MD
MAY 2012

Hyperspectral Image Turbulence Measurements of the Atmosphere

Sarah E. Lane[a], Leanne L. West[a], Gary G. Gimmestad[a],
Stanislav Kireev[b], William L. Smith, Sr.[b], Edward M. Burdette[a],
Taumi Daniels[c], and Larry Cornman[d]
[a]Georgia Tech Research Institute, Atlanta, GA 30332
[b]Hampton University, Hampton, VA 23668
[c]NASA Langley Research Center, Hampton, VA 23681
[d]University Corporation for Atmospheric Research, Boulder, CO 80307

ABSTRACT

A Forward Looking Interferometer (FLI) sensor has the potential to be used as a means of detecting aviation hazards in flight. One of these hazards is mountain wave turbulence. The results from a data acquisition activity at the University of Colorado's Mountain Research Station will be presented here. Hyperspectral data cubes from a Telops Hyper-Cam are being studied to determine if evidence of a turbulent event can be identified in the data. These data are then being compared with D&P TurboFT data, which are collected at a much higher time resolution and broader spectrum.

Keywords: hyperspectral image processing, remote sensing, aviation safety, atmospheric turbulence

1. INTRODUCTION

The real-time detection of atmospheric turbulence is of great interest due to the applicability to aviation safety. A FLI sensor has the potential to be used as a means of detecting aviation hazards in flight, giving the flight crew time to react. One of these hazards is mountain wave turbulence. Mountain waves are often associated with the presence of lenticular clouds, which pilots will avoid, and normally persist all day, so that pilot reports (PIREPS) can be used to avoid areas of moderate to severe turbulence. However, there have been reports[1] of unexpected encounters with mountain waves and turbulence that have resulted in damage to aircraft, injury, and loss of life that make the capability of real-time detection of these events desirable.

The results from a data acquisition activity at the Mountain Research Station near Boulder, Colorado during November of 2011 are presented here. This site experiences mountain waves and mountain wave turbulence in the fall and winter months, which affect flights into Denver International Airport. The two main objectives of this test were as follows:

- Observe slowly varying radiance patterns associated with standing waves.
- Observe short-term fluctuations associated with turbulence.

These objectives require that long data sets (approximately thirty minutes) at as high as possible temporal resolution be collected of the sky by interferometric means. This collection activity utilized both a long wave infrared Telops Hyper-Cam and a Designs and Prototypes (D&P) TurboFT spectrometer, both operating in continuous mode simultaneously for approximately thirty minutes for each data collection event. Each sensor provides unique information about the sky; the Hyper-Cam collects LWIR hyperspectral image data of the scene, while the TurboFT has the capability to collect approximately 100 spectra per second in the 2.5-16 micron region. Both sensors have on-board blackbodies, which allow for calibrated radiance in the field. The two sensors were co-located on a custom built mount which allowed boresighting of the sensors for the test so that they would be observing the same area of sky throughout each measurement period.

The Hyper-Cam data addressed the first objective in that the long data sets could capture slowly varying radiance, while the TurboFT data addressed the second objective in that the high temporal resolution and broader spectrum could capture short-term fluctuations. Both datasets are being investigated as a means of studying the feasibility of using a FLI sensor for the detection of turbulent events; this paper presents preliminary results from these data.

2. DATA COLLECTION ACTIVITY

2.1 Mountain Research Station Test Site

The Mountain Research Station (MRS) is located on the front range of the Rocky Mountains at an elevation of 2,900 m (9,500 ft), approximately 76 km (47 mi) WNW of Denver International Airport. This elevation and clear line of sight towards the airport makes the Mountain Research Station an ideal location for observing mountain waves that form over the Rockies.

Several sites at elevations higher than the main lab were selected for possible locations for the data collection; however, due to snow cover and an in-operational Sno-Cat, the data collection was confined to the dining hall and parking lot at the Mountain Research Station. However, this did not inhibit the data collection; even though the instruments were below the tree line, looking out of an open window from the second floor of the dining hall provided a clear view of the sky over the trees in the direction of Denver (shown in Figure 1).

Figure 1. Instrument set-up looking out the open window of the MRS dining hall (*left*), and instruments looking ESE toward Denver (*right*).

2.2 Hyper-Cam Settings

The Telops Hyper-Cam is a long-wave infrared hyperspectral imaging sensor[2] with variable resolution from 0.25 – 150 cm^{-1} and a variable image size of up to 320 x 256 pixels. The data it provides is referred to as a data cube; the three dimensions of data are (x, y, σ), where x and y are spatial information (i.e. the pixel in an image), and σ is the spectral information (i.e. radiance at wavenumber σ). Therefore, each data cube is composed of a radiance image at narrow wavebands within the LW portion of the spectrum.

The entire 320 x 256 window was used, and for the majority of the test, the Hyper-Cam was operated with a 0.25X magnification lens, which increased the field of view from 6.4° horizontal x 5.1° vertical FOV to 25.6° horizontal x 20.4° vertical FOV. However, for the runs discussed in this paper, the smaller field of view was used. In these tests the spectral resolution was set at 16 cm^{-1}. Sixteen wavenumber data cubes contain 41 frames in the spectral dimension between 810.06 and 1341.24 cm^{-1}; each is collected in approximately 1696 ms with a 65 ms delay between each cube.

This wavenumber resolution was chosen because previous models showed collection at 16 cm^{-1} resolution provides the highest temporal resolution while still capturing enough spectral information to distinguish a turbulent wave event[3]. The recording frequency of the Hyper-Cam instrument is not high enough to capture a turbulent event; however the spatial information it provides over 30 minutes could make it possible to visually detect the location of standing waves. This information can then be used to isolate certain time periods of TurboFT spectra for analysis.

2.3 TurboFT Settings

A Designs and Prototypes (D&P) TurboFT spectrometer was used simultaneously with the Hyper-Cam to provide spectral data at higher temporal resolution. The D&P TurboFT is a dual InSb/MCT detector instrument capable of providing up to 100 spectra per second from 2.5 to 16 μm. For this data collection activity, spectra were collected at 4 cm^{-1} resolution and set at four coadds, which corresponds to four interferograms being averaged to produce each spectrum. These settings resulted in a recording rate of 12 spectra per second. This higher temporal resolution than that of the Hyper-Cam allows for a better chance for observation of short-term fluctuations associated with turbulence.

The TurboFT sensor was equipped with a four inch telescope which provided a 1.2 degree FOV. It was determined early in test planning that the TurboFT 1.2 degree FOV must be aligned with the center of the Hyper-Cam FOV. A common mount that allowed for boresighting of the sensors, as well as protected the TurboFT from the elements, was developed and is explained in the next section.

2.4 Sensor Mount

The Hyper-Cam is capable of operation in the lower temperatures expected in Colorado in November, however, the safe operation of the TurboFT required that an enclosure be built for it that would provide a stable thermal environment. An insulated aluminum box was constructed to house the TurboFT, and a heater was placed inside. A mount for both the Hyper-Cam and the TurboFT enclosure was then constructed from unistrut that would allow both the Hyper-Cam and TurboFT enclosure to be mounted via dovetail slides. The mount was constructed such that both sensors could be rotated from 90 to zero zenith angle viewing geometry while maintaining boresight (it should be noted that the mount was never rotated to the zero zenith angle position with the D&P installed to avoid damage to the sensor). A SolidWorks representation of the mount with both Hyper-Cam and D&P installed is shown in Figure 2.

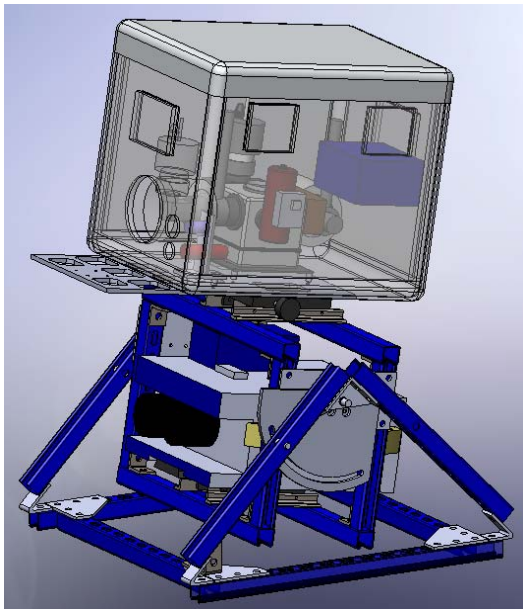

Figure 2. A SolidWorks representation of the boresight mount with TurboFT in aluminum enclosure (*top*) and Hyper-Cam (*bottom*).

Alignment of the center of the TurboFT FOV with the center pixel of the Hyper-Cam image was tested after a complete tear-down and reassembly of the sensor mount both before and during the field test.

2.5 Ancillary Data

During this test, the only ground truth data that exists to identify a turbulent event is from pilot reports (PIREPS) and Eddy Dissipation Rate (EDR) reports. During this test, PIREPS were continuously monitored by team members in the event that any severe turbulence was reported in the area of MRS; instruments could then be directed toward the location of the PIREP. During the time of the test, only moderate turbulence was reported. Full PIREP and EDR reports were compiled after the test. Meteorological data, including temperature, humidity, pressure, wind speed, and solar radiation data, was provided by MRS personnel for the dates of the test from a weather station at MRS's C1 site, located 0.78 km (0.49 mi) from the test site at 3,022 m (9,912 ft) elevation.

The Hyper-Cam comes equipped with a visible camera; however, a webcam was used instead to record visible imagery of the sky. While the webcam has a much wider field of view than either the Hyper-Cam or the TurboFT, it provided visible documentation of any obscurations to a clear field of view, such as clouds, aircraft, or aircraft contrails. The webcam was placed inside the TurboFT enclosure so that it too would be boresighted with all other instruments.

3. METHODOLOGY AND PRELIMINARY RESULTS

Each thirty minute data collection event produced approximately 1,000 Hyper-Cam data cubes and 20,000 TurboFT spectra. The Hyper-Cam data were investigated first in order to find visual cues to locations of possible waves or turbulence. Results from the fourth dataset from November 17, 2011 will be shown here. For this dataset, a large lenticular cloud was in the scene and the instruments were lined up to view the area right under the cloud, at 112° azimuth and 4° elevation viewing angle. Figure 3 shows the viewing geometry as recorded by the webcam.

Figure 3. A visible image of the viewing geometry for the fourth dataset collected on Nov. 17, 2011. The red box shows the approximate Hyper-Cam field of view.

3.1 Data cube Reduction

The series of data cubes produced a four dimensional dataset (x, y, σ, t). x, y, and σ comprise the dimensions of the original data cube; t is the time element. Variability in the time series of data cubes was investigated first, and was tested only at one spectral location in the data cube at a time. A reduced data cube was created with spatial and time dimensions only (x, y, t) for spectral locations of interest. The following criteria were considered when choosing spectral locations from the original Hyper-Cam data for processing in the reduced data cubes:

- Choose locations in the spectral domain where any variability can be considered true variability and not due to noise (i.e. not at the extremes of the spectral range of the Hyper-Cam, where the NESR is higher and noise is more prominent in the spectrum than signal).
- Choose locations which correspond to water vapor lines, because previous models[3] have demonstrated that temperature and moisture variations at these lines could be exploited for detection of waves and turbulence.

The reduced (x, y, t) data cubes were then corrected for bad pixels in order to avoid bad values creating unrealistically high variability. Bad pixel correction was performed by applying a spatial filter to each image, whereby each pixel was compared to the average of the neighboring eight pixels, and if the absolute value of the difference was greater than one standard deviation of the neighbors, the pixel was replaced with the average. Due to the small neighborhood of surrounding pixels, there were still some areas of each image that showed high spatial variability, and so a median filter was applied to smooth the images.

3.2 Data Cube Differencing by Subtraction of the Mean

After the filtering was applied to each image in the reduced data cube, the mean radiance value at each pixel index for all times was calculated, creating a mean image, which was then subtracted from each image in the reduced data cube to create a "difference cube". Each image from the difference cube was then strung together to create a movie file showing the time evolution of variability. See below for the video (linked in online version) for a run from November 17, 2011, showing the time evolution of variability in radiance at 956.13cm^{-1}. This wavenumber was chosen because models showed it exhibited the highest variability[3].

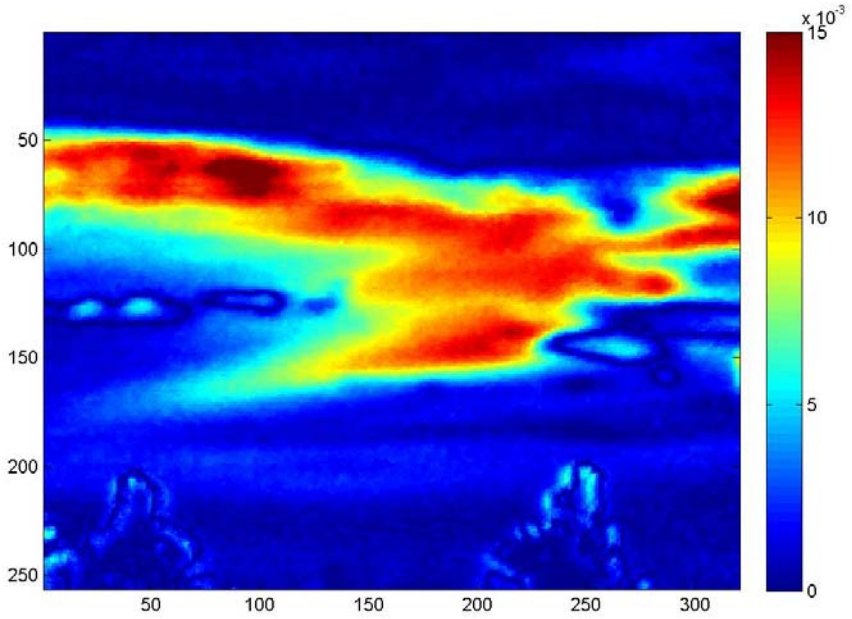

Video 1. "VariabilityMovie1.wmv", which shows the time evolution of radiance variability in the sky scene under the lenticular cloud. (available at spie.org)

3.3 Cloud Removal

The video file shows that there are areas of high variability in the area under the lenticular cloud; however, comparison with the visible imagery from the webcam indicated that this variability could be due to higher radiance of incoming clouds at the end of the time series. By exploiting the spectral nature of the Hyper-Cam data cubes, a simple test was developed to classify clear sky or clouds.

The sky is the coldest object in these scenes, more so than clouds, treetops, or any other obscuration. A comparison of sky radiance vs. cloud radiance is shown in Figure 4.

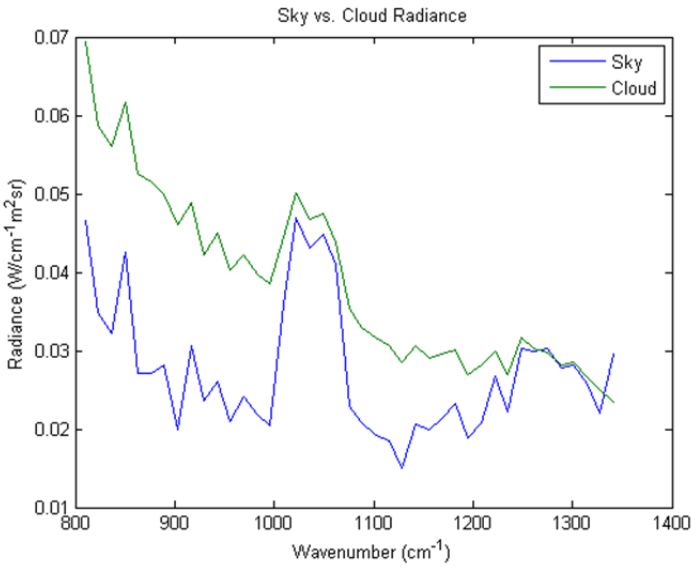

Figure 4. The radiance from a sky pixel compared to the radiance from a cloud pixel.

The spectra shown in Figure 4 are from the same row of pixels so that the elevation angle for both would be the same and not create a difference in magnitude. These spectra are at 16 cm^{-1} resolution, so the narrow spectral lines characteristic of a sky spectrum cannot be seen in the measured sky radiance; however, there is enough difference in the two spectra so that a determination of sky or "other" can be made for every pixel in the scene. The cloud spectrum exhibits much higher radiance than the sky spectrum; additionally it has fewer spectral features and follows more closely the trend of a blackbody.

In order to determine the areas of clear sky, the following procedure was followed. Frame 8 (903.02 cm^{-1}) from each data cube in time was chosen to be the frame that exhibited a substantial difference between sky and cloud spectra. Frame 35 (1261.67 cm^{-1}) from each data cube in time was chosen to be the frame that exhibited the most similarity between sky and cloud spectra. For every time in the series, frame 35 was subtracted from frame 8. A binary image was created for every time step, whereby if the result of the subtraction was positive, a one was assigned to the pixel, and if the result of the subtraction was negative, a zero was assigned to the pixel. By overlaying these binary images over the difference images described in the previous section, everything but clear sky should be masked, which aids in the determination of whether variability can be attributed to temporal changes in cloud position. Variability images from the beginning and end of the time series, both unmasked and masked, are shown in Figure 5.

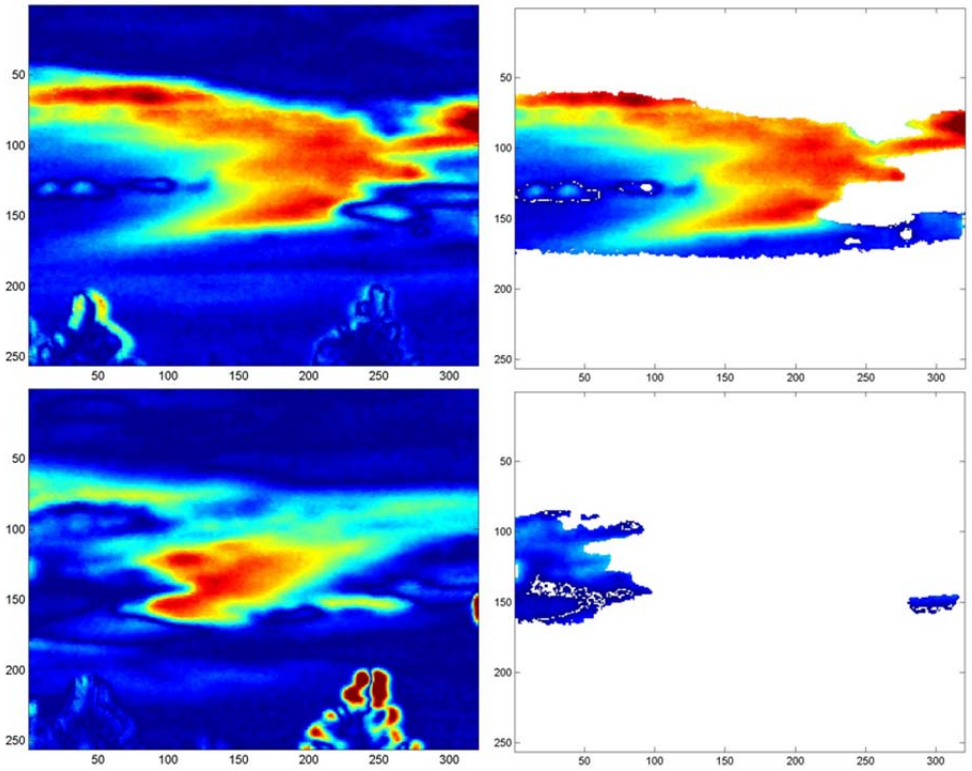

Figure 5. The variance in radiance at the beginning of the thirty minute run (*top two images*) vs. the variance in radiance at the end of the thirty minute run (*bottom two images*). The images on the right have been masked by the cloud removal test.

Figure 5 demonstrates that this simple algorithm to test for sky also masks clear sky at the horizon as the atmosphere here is more opaque and its radiance looks more like a blackbody. Therefore, a second test was developed that would compare the relative change in radiance between frame 8 (903.02 cm^{-1}) and frame 9 (916.30 cm^{-1}). As shown in Figure 6, both sky spectra, regardless of elevation angle, exhibit a much greater change between the two wavenumbers than the cloud spectrum.

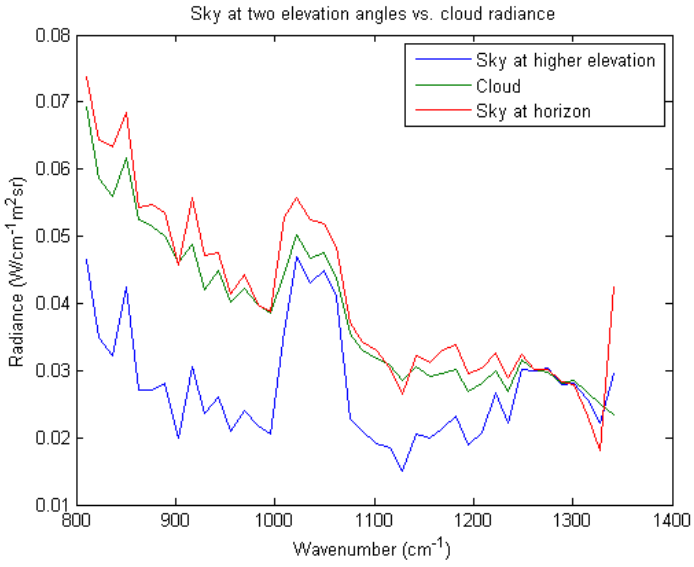

Figure 6. The radiance from sky pixels at two elevations compared to the radiance of a cloud pixel.

The relative difference of the local radiance between 903.02 cm^{-1} and 916.30 cm^{-1} of the three spectra in Figure 6is 8.133 x 10^{-4} W/m^2sr in the case of the sky at the high elevation, 2.410 x 10^{-4} W/m^2sr in the case of the cloud, and 7.681 x 10^{-4} W/m^2sr in the case of the sky at the horizon. Because the sky radiance changes approximately three times faster in the case of both sky spectra, this derivative is checked in addition to the radiance difference between 903.02 cm^{-1} and 1261.67 cm^{-1}. Variability images from the beginning and end of the time series, both unmasked and masked with the new constraint are shown in Figure 7. These images are from the same time as those shown in Figure 5.

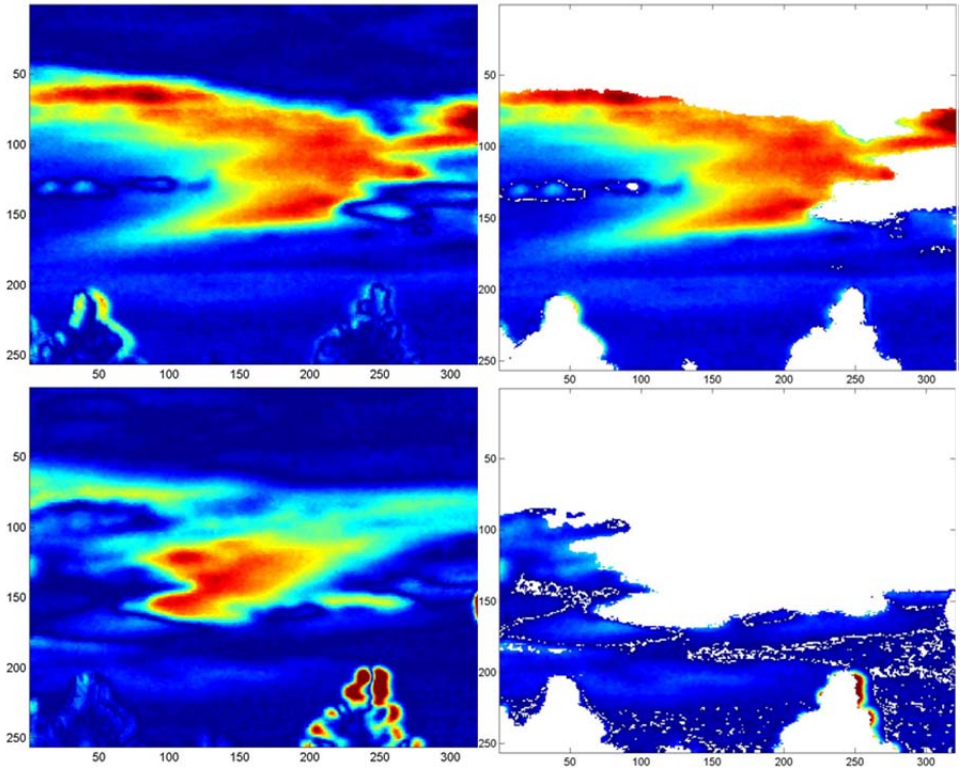

Figure 7. The variance in radiance at the beginning of the thirty minute run (*top two images*) vs. the variance in radiance at the end of the thirty minute run (*bottom two images*). The images on the right have been masked by the cloud removal test as in Figure 5, but with the additional constraint of checking the change in radiance between 903.02 cm^{-1} and 916.30 cm^{-1}.

3.4 Data Cube Differencing Using Rank Order Statistics

Applying the cloud mask showed that the appearance of clouds in the scene later in the time series was significantly contributing to the variability as the higher radiance of the clouds was affecting the mean. Therefore, instead of calculating the mean radiance of each pixel for the entire time series, the radiances of each pixel were ranked in ascending order prior to calculating a mean. Every pixel in the time series was sorted by ascending radiance; the higher radiances that can be attributed to clouds are therefore all located in the higher quantiles and can be excluded from analysis.

The upper and lower bounds for which to calculate an average radiance were chosen somewhat arbitrarily. The median values were found for every pixel and then these median values were subtracted from each image in the reduced data cube (x, y, t). Additionally, because the high radiance values are unwanted, an average was calculated from the ranked data between zero and 50%. This average was then subtracted from each image in the reduced data cube. These results were then compiled into a movie with the cloud mask applied, which can be seen in the following video.

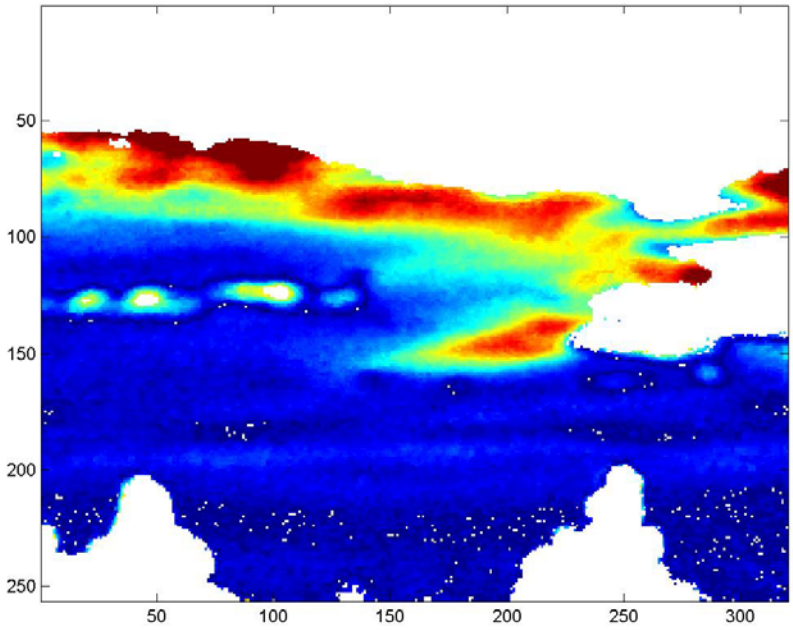

Video 2. "VariabilityMovie2.wmv", which shows the time evolution of radiance variability calculated from an average that includes only the first 50% of ranked radiance data. (available at spie.org)

The mean that is calculated to create the variability seen in Video 2 should not have as much cloud influence; however, the clouds affecting the mean still cannot be excluded. One should note the light blue band that appears in the clear portion of the sky between the trees. This variability change is most likely not due to clouds. The spectra of these pixels are currently under investigation to see if the source of variability can be identified.

4. FUTURE WORK

Analysis up to this point has only focused on visual examination of time evolution of variability in Hyper-Cam data. Because turbulence is associated with temperature and moisture variations, it could be possible to exploit the spectral domain of the data cubes by comparing measured radiance to water vapor spectra, modeled at different temperatures and concentrations, using standard gas detection algorithms. The authors have investigated these algorithms previously[4] as they apply to the detection of aircraft exhaust.

In addition to investigating gas detection algorithms for hyperspectral data, the authors plan to begin analysis of the TurboFT data. This high-temporal-resolution spectral data will be analyzed to see if short-term fluctuations in radiance can be identified in the time series. These short-term fluctuations could potentially indicate turbulent events. If fluctuations in the TurboFT data are identified, these times will then be compared to the Hyper-Cam hyperspectral imagery. Similarly, if standing waves are identified in the Hyper-Cam data, these times will then be compared to corresponding time sequences in D&P data.

5. CONCLUSIONS

This paper discussed preliminary results from a data collection at Mountain Research Station near Boulder, Colorado in November of 2011. As of this writing, only the Hyper-Cam data cubes have been investigated. The visual inspection of the time evolution of variability has been used as the main metric for determining where in the field of view standing waves or turbulence is most likely. Further analysis is needed for a conclusive determination on whether or not the turbulent events can be identified in these data; however, results thus far indicate that this identification could be possible.

ACKNOWLEDGEMENTS

The research described here was funded by the NASA Aeronautics Research Mission Directorate (ARMD) Aviation Safety (AvSafe) Program, under the Atmospheric Hazard Sensing & Mitigation (AHSM) area within the

Atmospheric Environment Safety Technologies (AEST) project.

The authors wish to thank Jack Wood of GTRI for designing and constructing the D&P enclosure and boresight mount, Kelly Matheson and Jennifer Morse of Mountain Research Station for providing access to and testing assistance at MRS, and Julie Prestopnik of UCAR for compiling EDR and PIREP reports.

REFERENCES

[1] West, L., Gimmestad, G., Smith, W., Kireev, S., Cornman, L. B., Schaffner, P. R., Tsoucalas, G., "Applications of a Forward-Looking Interferometer for the on-board detection of aviation weather hazards," NASA/TP-2008-215536; Added to NTRS: 2008-12-10; Document ID: 20080045836; Report Number: L-19522.

[2] Farley V., Vallières, A., Chamberland, M., Villemaire, A., and Legault, J-F. "Performance of FIRST, a longwave infrared hyperspectral imaging sensor," Proc. SPIE 6398 (2006).

[3] West, L., Gimmestad, G., Smith, W., Kireev, S., Daniels, T., Cornman, L., "Airborne Forward Looking Interferometer for the Detection of Terminal-Area Hazards," NASA Contract NNX09AR67A Annual Report, Year 2 (July 2011).

[4] Lane, S. E., West, L. L., Gimmestad, G. G., Smith, W. L., and Burdette, E. M., "Detection of aircraft exhaust in hyperspectral image data," Proc. SPIE 8158 (2011).

Appendix E: 2012 AIAA Paper

Experimental Validation of a Forward Looking Interferometer for Detection of Clear Air Turbulence due to Mountain Waves

IN THE 4TH AIAA ATMOSPHERIC AND SPACE ENVIRONMENTS CONFERENCE
NEW ORLEANS, LA
JUNE 2012

Experimental Validation of a Forward Looking Interferometer for Detection of Clear Air Turbulence due to Mountain Waves

Philip R. Schaffner[1] and Taumi S. Daniels[2]
NASA Langley Research Center, Hampton, Virginia 23681

Leanne L. West[3], Gary G. Gimmestad[4] Sarah E. Lane[5], and Edward M. Burdette[6]
Georgia Tech Research Institute, Atlanta, Georgia 30332

William L. Smith[7] and Stanislav Kireev[8]
Hampton University, Hampton, Virginia 23668

Larry Cornman [9] and Robert D. Sharman [10]
Science and Technology in Atmospheric Research [STAR] Institute, Boulder, Colorado 80301

The Forward-Looking Interferometer (FLI) is an airborne sensor concept for detection and estimation of potential atmospheric hazards to aircraft. To be commercially viable such a sensor should address multiple hazards to justify the costs of development, certification, installation, training, and maintenance. The FLI concept is based on high-resolution infrared Fourier Transform Spectrometry (FTS) technologies that have been developed for satellite remote sensing. These technologies have also been applied to the detection of aerosols and gases for other purposes. The FLI is being evaluated for its potential to address multiple hazards, during all phases of flight, including clear air turbulence (CAT), volcanic ash, wake vortices, low slant range visibility, dry wind shear, and icing. In addition, the FLI is being evaluated for its potential to detect hazardous runway conditions during landing, such as wet or icy asphalt or concrete. The validation of model-based instrument and hazard simulation results is accomplished by comparing predicted performance against empirical data. Models for FLI measurables for mountain wave turbulence were developed during the previous phases of the project. Prior to the field campaign, these models were used to predict what the sensors should have been able to detect, based on expected instrument performance. After the data collection activities, the empirical data was used to update and validate the existing models. This iterative process was employed during the course of the project as new empirical results became available. Previous research programs, focused on forward-looking airborne sensors such as Doppler radars and lidars to detect and forecast turbulence, have produced many tools for analysis, modeling, and simulation. Following on the methods used in the airborne radar turbulence detection problem, relationships between the statistics of an atmospheric disturbance (such as the temperature field) and those of the sensor measurements (the spectral radiance) will be developed. In the mountain lee wave

[1] Aerospace Technologist, Research Directorate Electromagnetics & Sensors Branch, 8 N Dryden Street, MS 473.
[2] Aerospace Technologist, Research Directorate Electromagnetics & Sensors Branch, 8 N Dryden Street, MS 473.
[3] Principal Research Scientist and Director, Landmarc Research Center, Electro-Optical Systems Laboratory, 925 Dalney St., MS 0834.
[4] Principal Research Scientist, Electro-Optical Systems Laboratory, 925 Dalney St., MS 0834, AIAA Member.
[5] Research Scientist I, Electro-Optical Systems Laboratory, 925 Dalney St., MS 0841.
[6] Research Scientist I, Electro-Optical Systems Laboratory, 925 Dalney St., MS 0841.
[7] Distinguished Professor, Dept. of Atmospheric and Planetary Sciences, 21 Tyler Street.
[8] Research Assistant Professor, Dept. of Atmospheric and Planetary Sciences, 21 Tyler Street.
[9] Project Scientist, Research Applications Laboratory, Aviation Applications Program, Senior Member AIAA .
[10] Project Scientist, Research Applications Laboratory.

data collected in the previous FLI project, the data showed a damped, periodic mountain wave structure. The wave data itself will be of use in forecast and nowcast turbulence products such as the Graphical Turbulence Guidance (GTG) and Graphical Turbulence Guidance Nowcast (GTG-N) products. Determining how turbulence hazard estimates can be derived from FLI measurements will require further investigation.

I. Introduction

THE Forward-Looking Interferometer (FLI) is an airborne sensor concept for detection and estimation of potential atmospheric hazards to aircraft. To be commercially viable such a sensor should address multiple hazards to justify the costs of development, certification, installation, training, and maintenance. The FLI concept is based on high-resolution infrared Fourier Transform Spectrometry (FTS) technologies that have been developed for satellite remote sensing. These technologies have also been applied to the detection of aerosols and gases for other purposes. The FLI is being evaluated for its potential to address multiple hazards, during all phases of flight, including clear air turbulence (CAT), volcanic ash, wake vortices, low slant range visibility, dry wind shear, and icing. In addition, the FLI is being evaluated for its potential to detect hazardous runway conditions during landing, such as wet or icy asphalt or concrete.

Prior research has addressed the physical basis for radiometric detection of these hazards.[1-3] The ability of the FLI to provide estimates of the range to in-flight hazards was also investigated, with the result that both detection and ranging are enabled by the high spectral resolution provided by the FTS. A sufficient infrared spectral signature appeared to be associated with the hazards to enable detection and/or mitigation of all of them, although detection of CAT at relevant ranges may also require that the FLI have high temperature resolution, dependent on a good signal-to-noise ratio. The combination of high spectral and temperature resolutions in an imaging instrument is expected to enable sophisticated algorithms with high detection rates and low false alarm rates. The FLI will also function as an infrared imager, providing a real-time video display with night vision capability and enhanced vision in obscured conditions. These capabilities will enable the FLI to detect runway obstructions during landing, including both vehicles and wild game or livestock.

The current project includes several ground-based field data collection events for hazards, including runway surface state and contamination, low visibility conditions, wake vortices, and mountain wave turbulence. The research is currently focused on mountain wave turbulence, and field data collection was conducted in November 2011 at the University of Colorado-Boulder's Mountain Research Station (MRS) near Boulder, CO. The Mountain Research Station (MRS) is located on the front range of the Rocky Mountains at an elevation of 2,900 meters (9,500 feet), approximately 76 kilometers (47 miles) west northwest of Denver International Airport (DEN). This elevation and clear line of sight to the atmosphere above the airport make MRS an ideal location for observing mountain waves that form over the Rocky Mountains. The instruments were located looking out of an open window from the second floor of the MRS dining hall, which provided a clear view of the sky over the trees in the direction of Denver, as shown in Figure 1.

Figure 1. MRS dining hall and instrumentation

The mountain wave research experiment has three major elements: 1) ground-based field measurements; 2) the validation of models and simulations by comparing predicted results to empirical data; and 3) the development of improved sensor models and hazard metrics. Simulations to determine test requirements Weather Research and Forecast (WRF) model data - temperature and H_2O profiles) were generated from an actual lee wave event on March 6, 2004. Although these fields do not develop identically for all cases, the model is perhaps representative of what one could expect of mountain waves in general. The vertical cross-section of the water vapor perturbations for this representative case is shown in Figure 2.

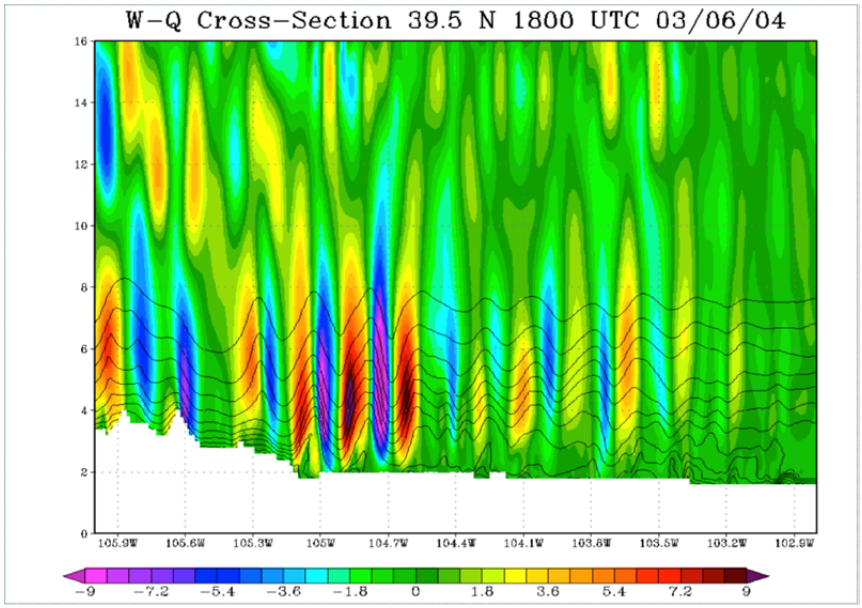

Figure 2. Vertical cross-section of water vapor for lee wave turbulent event, March 6, 2004.

In these simulations, the observer was placed at the Hyper-Cam location at MRS and directed east at 15, 30, 45, 60, and 90° elevation angles. The brightness temperature differences from the azimuthal mean from the simulation that most closely match the actual data collection configuration at MRS are shown in Figure 3; note that although the color scale was limited to +/- 0.5 K in order to accentuate signals beyond these limits, the results from the simulations in general did indicate that signals of 1 Kelvin or more should be observable. Distance to turbulence should be predictable from the spectrum due to differences in absorption along the sides of the spectral window, though this capability is only possible if the data is collected at 1cm^{-1} resolution. The data collected at MRS in November was collected at 1 cm^{-1}, 4 cm^{-1} and 16 cm^{-1} resolutions. The 1 cm^{-1} datasets have not yet been investigated.

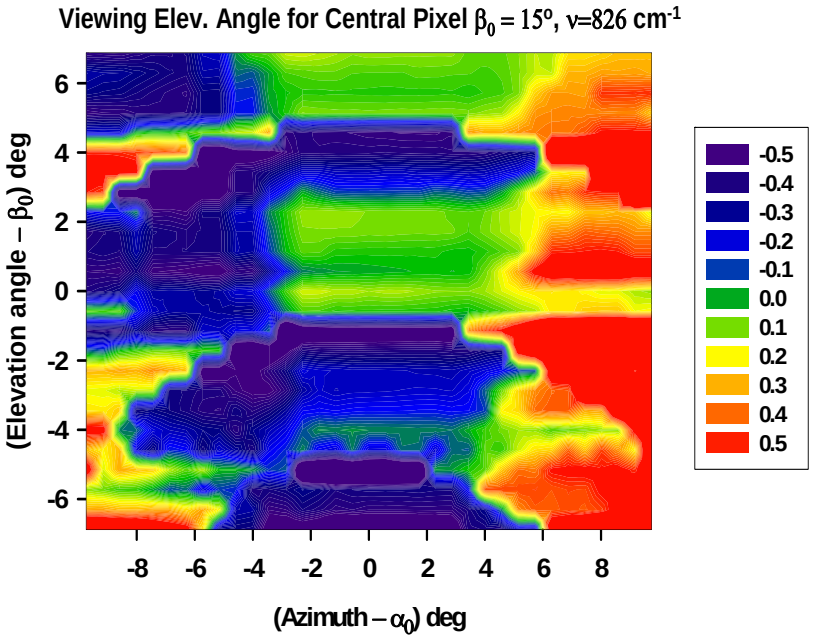

Figure 3. Brightness temperature difference (Kelvin) from the azimuthal mean.

II. Experimental Instrumentation

Instrumentation for these field tests included both a Telops Long Wave InfraRed (LWIR) Hyper-Cam interferometric imager and a Designs and Prototypes (D&P) TurboFT single pixel spectro-radiometer. Simulations have shown that mountain waves will cause a pattern of brightness temperature differences that should be observable with both the Hyper-Cam and the D&P. The Hyper-Cam combines imaging with high spectral resolution in the 870 – 1300 cm^{-1} infrared window region, but it requires times of seconds to minutes to acquire a single data cube, depending on the resolution and number of pixels used. These acquisition times are appropriate for mountain waves, which are almost stationary. These measurements were taken at the MRS, located at an altitude of 9,500 feet, so that measurements were gathered in a forward-looking manner, per the diagram in Figure 4 below.

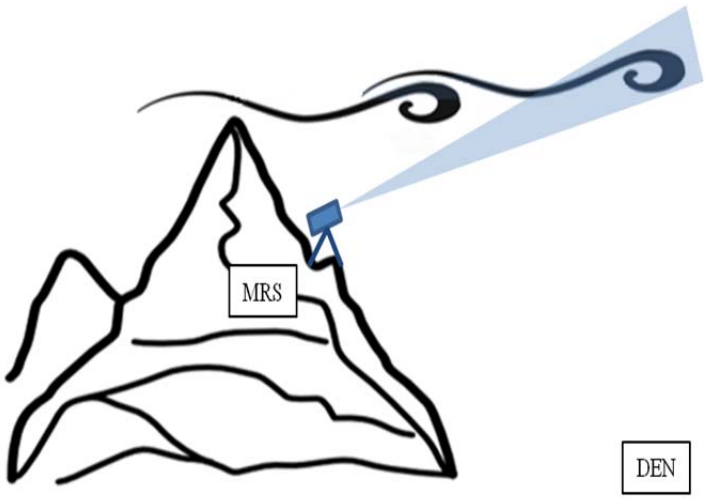

Figure 4. Mountain Wave Data Collection

The D&P spectrometer is complementary to the Telops instrument: it is very fast, with a set resolution of 4 cm^{-1} and a wide spectral range of 625 – 5000 cm^{-1}, with a single line of sight. In a previous phase of the program, data was collected at the NCAR Foothills Lab in Boulder, CO, in 2008. That data consists of sets of 5,000 spectra recorded at three per second, and statistical analyses of those time series have revealed fluctuations in the atmospheric spectral absorption window regions that are different on windy days and calm days. The D&P is expected to enable detection of fast fluctuations associated with turbulent air motion. In addition, its extended spectral range enables further analysis in the mid-wave infrared (MWIR) region of the spectrum.

III. Ancillary Data Collection

Other data collected includes weather and satellite data. Information such as winds, temperature, humidity, visibility, etc. will be valuable for later modeling and is important to understanding the sensor data collected. Atmospheric data was provided by the MRS on-site weather station and the Science and Technology in Atmospheric Research (STAR) Institute located about 45 minutes away in Boulder, CO. The location of the tests, on the front range of the Rocky Mountains, was advantageous for acquiring truth data due to the amount of air traffic in the area primarily comprising flights into, out of, and at cruise altitudes over the Denver International Airport (DEN). Air traffic provided a source for pilot reports (PIREPS) and automated reports from United Airlines (UAL) 757 and Delta Airlines (DAL) 737 aircraft as "ground truth" for the turbulence detection efforts.

The UAL and DAL aircraft run algorithms to estimate and automatically report eddy dissipation rates (EDR) to the one-third power. These reports consist of the peak and mean value of the EDR over the previous minute (in cruise). These reports cover "none" to "extreme" levels of turbulence. The truth data allow for the evaluation of both true detections and false alarms by the sensor and algorithms. Pilot reports (PIREPS) are subjective in nature. PIREPS are not always given for turbulence encounters (even severe ones); they are rarely given for null turbulence; the reported time and position can be in error; and the intensity level of the turbulence reported by the pilot is a subjective measure of the actual intensity level. Nevertheless, these data, when available, are valuable in the verification process. Figure 5 shows the flight tracks of the EDR-equipped UAL 757s over a 24-hour period. It can be seen that there are many flights in the Colorado area.

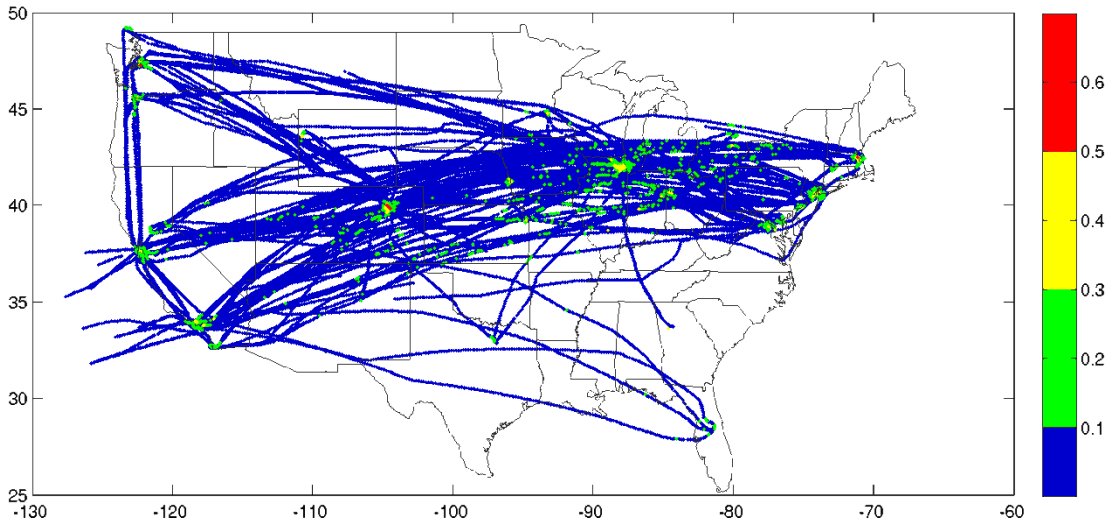

Figure 5. UAL 757 reports over a 24-hour period. Colors are assigned based on severity of turbulence. (0 = None/Smooth; 0.1 = Smooth to Light; 0.2 = Light; 0.3 = Light to Moderate; 0.4 = Moderate; 0.5 = Moderate to Severe; 0.6 = Severe; 0.7 = Severe to Extreme)

A useful tool for monitoring turbulence activity during the field test was the "EDR viewer." This viewer allows for the display of real-time and archival EDR data sets, which are displayed as color-coded square dots. Furthermore, the EDR viewer contains turbulence forecast information from the Graphical Turbulence Guidance (GTG) forecast product. The GTG data was used in real time during a data collection period and in archival mode for the verification effort. The viewer can also generate vertical cross-sections.

Additionally, MODIS satellite imagery was viewed during the test to identify days with mountain waves. A MODIS image from November 17, 2011 is shown in Figure 6. This figure clearly shows evidence of mountain waves along the Rocky Mountains.

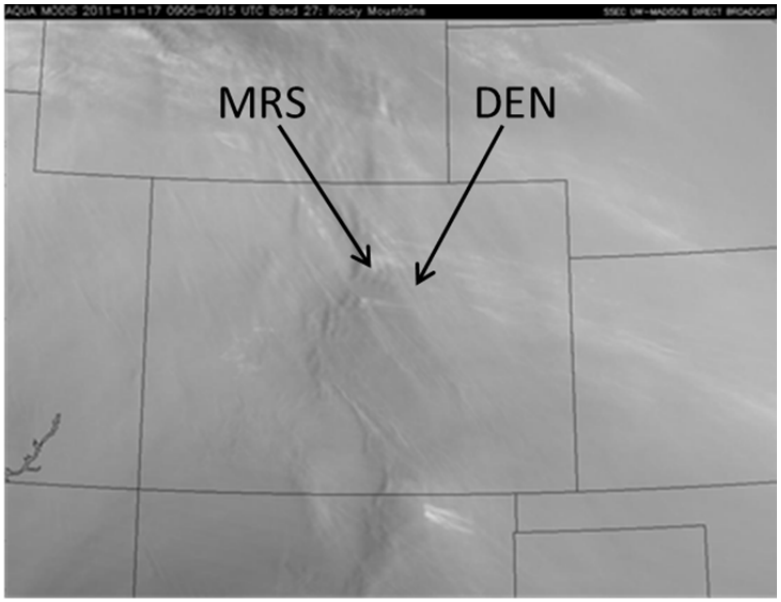

Figure 6. MODIS Imagery over Colorado Rockies, November 17, 2011. Band 27 (6.535 – 6.895 micron band)

IV. Data Analysis

Due to technical difficulties, some data sets collected at MRS in 2011 lacked not only webcam imagery to verify or exclude the existence of clouds, but also D&P data. However, several runs from November 17, 2011 had complete data sets and lenticular clouds were present. Lenticular clouds are formed in a standing wave pattern if there is sufficient moisture in the atmosphere and are an indication of mountain wave activity. During the 4th time series from November 17, clouds were crossing the instrument field of view (FOV), which resulted in significantly larger disturbances of the measured signal than was observed in other data analyzed. This difference in disturbance is clearly seen in Figure 7, which shows spectral dependence for temporal variability of the signal in radiance units for all 8 runs processed to date. Figure 8 shows the same quantity in brightness temperature units for Nov. 17, run 4 only. The difference in disturbance is estimated by a calculation of temporal variability. This variability is estimated by performing statistics over all data cubes for a given run after subtracting the row mean radiance for each cube/channel separately to eliminate the radiance dependence on the viewing elevation angle.

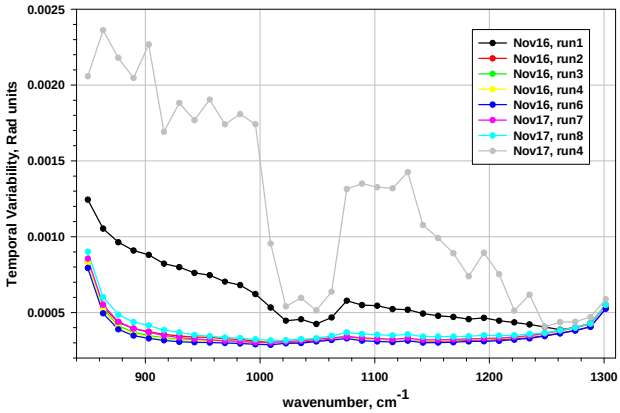

Figure 7. Spectral dependence of the temporal variability of the scene obtained by averaging over all image pixels for a given channel, 8 runs total, radiance units.

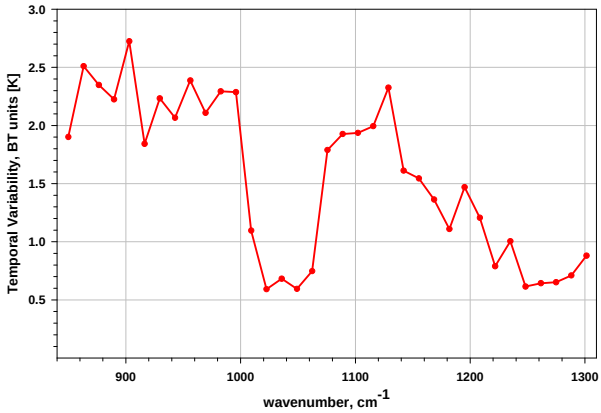

Figure 8. Spectral dependence of the temporal variability of the scene obtained by averaging over all image pixels for given channel, , brightness temperature units.

The computation of temporal variability produces one cube of data, which contains the estimated standard deviation for each pixel/channel separately. Averaging the standard deviation over all pixels, separately for each spectral channel, provides spectral dependence of the computed temporal variability. This result is presented in Figure 9 and Figure 10. Corresponding images of temporal variability for channels 4 and 23 are shown in Figure 9 and Figure 10. The most visible patterns in Figure 9 and Figure 10 are caused by cloud motion across the FOV during time series of measurements (see Figure 11).

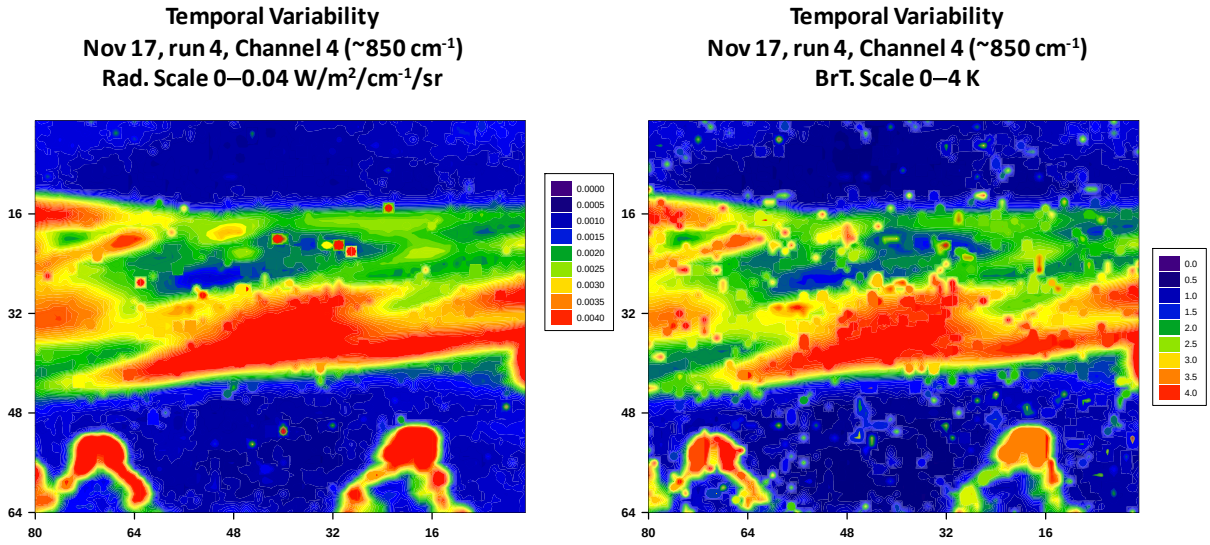

Figure 9. Image of temporal variability for channel 4, radiance units (left panel) and brightness temperature units (right panel): Nov 17, run 4.

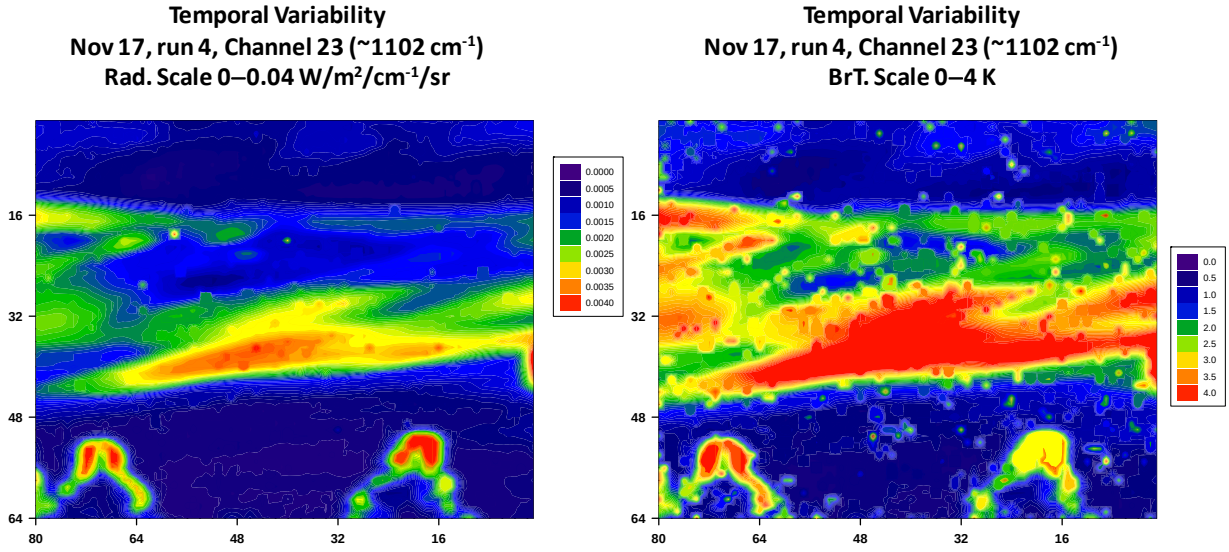

Figure 10. Image of temporal variability for channel 23, radiance units (left panel) and brightness temperature units (right panel): Nov 17, run4.

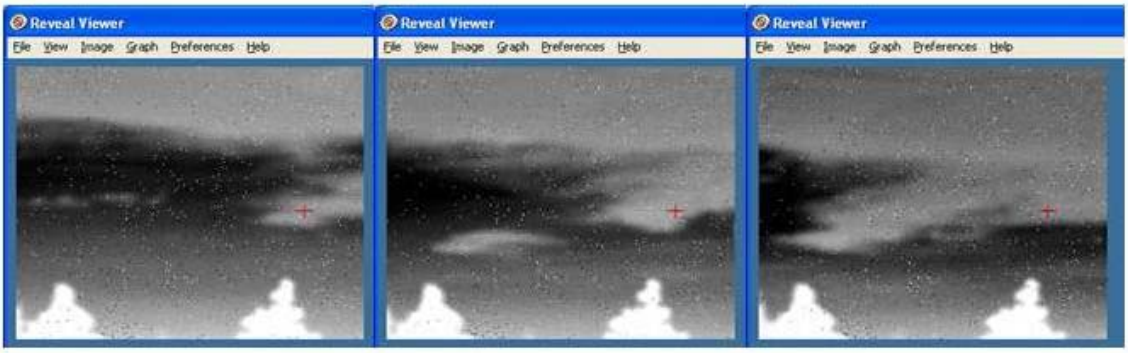

Figure 11. From left to right: channel #5 from the first, middle, and last cubes of data, Nov 17, run 4. One can see how clouds are moving during time of the observation.

In the above results, temporal variability had been computed over all good pixels, including cloudy ones. Now, we exclude them from the statistical averaging in order to reveal more clearly the temporal variability without cloud contamination. The cloud brightness temperature was estimated to be about 240 K. We have performed computations for cloud brightness temperatures (T_{CLD}) from 215 K to 250 K with 5 K increments to see how this threshold value affects the temporal variability pictures. A cloud mask was applied in such a way that all pixels with radiance (R) values higher than R (T_{CLD}=215, 250, 5 K) have been excluded from the consideration. This exclusion leads to a different number of pixels averaged over 1007 data cubes total: for example, as can be seen in Figure 11, the upper and bottom thirds of the whole frame are always excluded, while for the central 1/3 area, the number of averaged pixels is changing from 1007 (always clear) to 0 (always cloudy) from left to right. The number of averaged pixels depends also on the given value of threshold cloud temperature.

The temporal variability results, with cloud contributions over a threshold value (T_{CLD}=240 K) being eliminated, are presented in Figure 12. Eight channels with central wavenumbers from 863 cm^{-1} to 1115 cm^{-1} are shown in brightness temperature units, with the same scale of 0 - 4 K for each panel.

The temporal variability when T_{CLD} varies from 215 K to 250 K is presented in Figure 13 for the transparent channel at ~903 cm^{-1}. One can note that even as low as 215 K, there is cloud signal. For comparison, Figure 14 shows temporal variability for the opaque channel at ~1035 cm^{-1} (O_3 band). The panels shown are for threshold values of T_{CLD} = 260 K, 265 K, and 270 K. There is no signal for $T_{CLD} \leq$ 255 K in this channel. Note also that the color scale is a factor of 2 smaller (0 - 2 K) in Figure 15 than in Figure 12 and Figure 13.

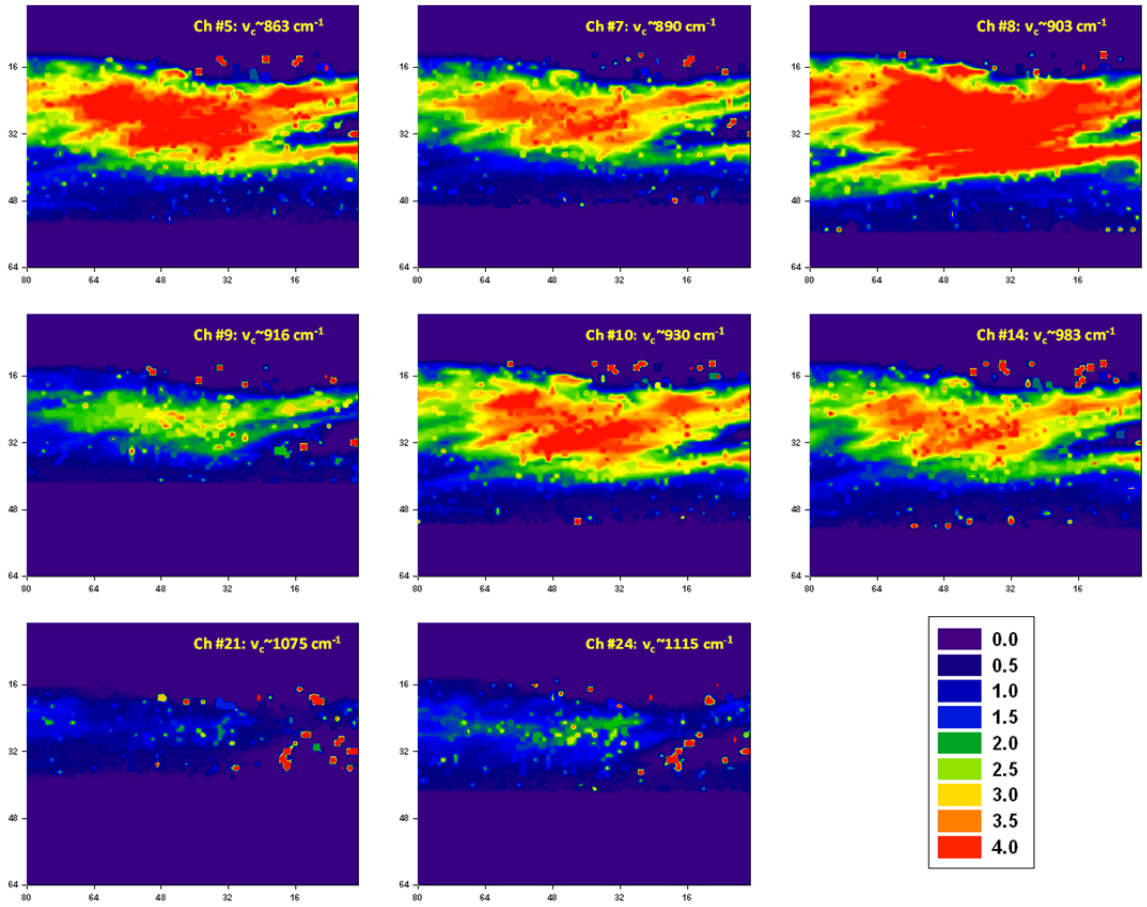

Figure 12. The temporal variability of the scene when cloudy pixels TB > 240 K are eliminated. Unit = brightness temperature, the same color scale 0-4 K is used for all panels; Nov 17, run 4.

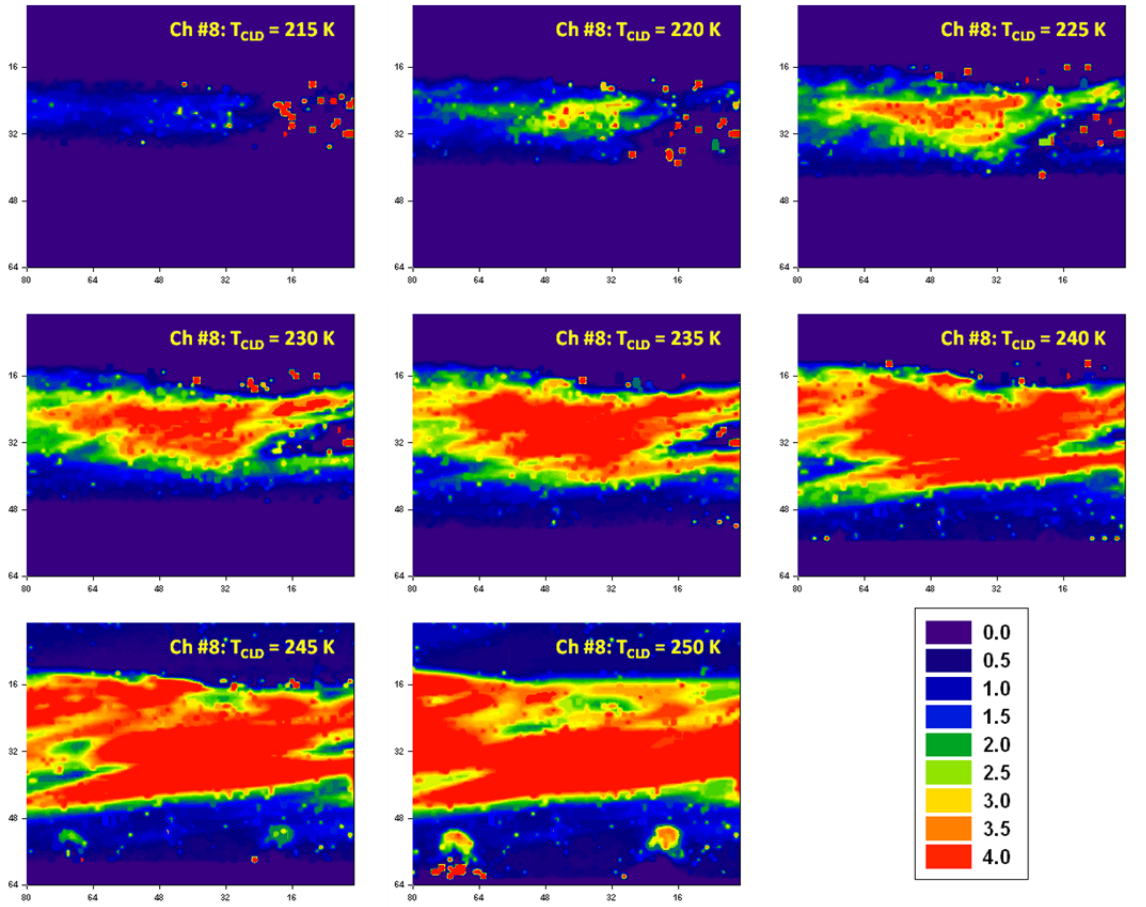

Figure 13. The temporal variability of the scene for the transparent channel #8 (~903 cm-1) when different cloud brightness temperature threshold values are applied (215 K to 250K, increment 5 K); Nov 17, run 4.

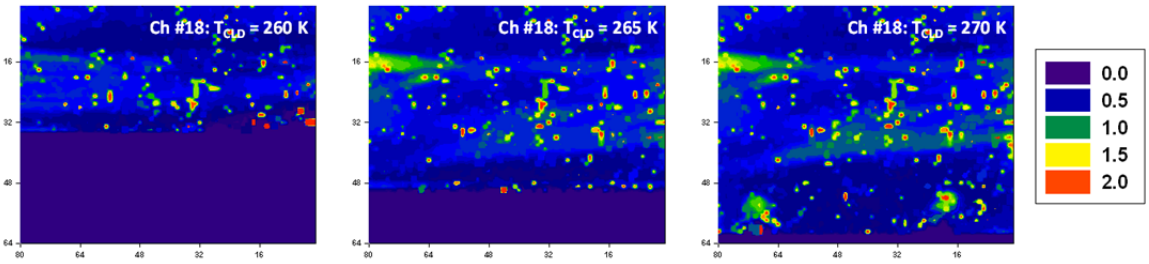

Figure 14. The temporal variability of the scene for the opaque channel #18 (~1035 cm-1) when different cloud brightness temperature threshold values are applied (260, 265,270 K); Nov 17, run 4. Note that color scale is a factor of two smaller (0-2 K) than the previous figures. There are no pixels for $T_{CLD} \leq 255$ K.

This study indicates that much of the variability seen is likely due to cloud variations, though more analysis is necessary. In a previous paper, we used different analysis techniques on the same data set.[4] In this analysis, the sky at the horizon was not excluded from analysis. The cloud mask applied by Lane in [4] was based on spectral features of cloud versus sky, as opposed to temperature. A figure from this paper, which shows the high sky radiance at lower elevation, is shown in Figure 15. Even though the sky radiance is higher, there are still spectral features which differentiate it from clouds.

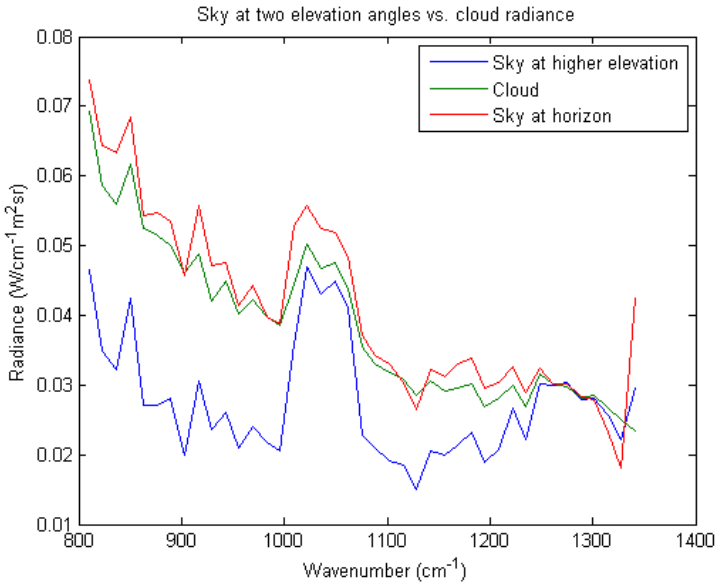

Figure 15. The radiance spectra from sky pixels at two elevations compared to the radiance of a cloud pixel.[4]

However, further analysis has shown that this portion of the sky is covered by a variable haze. Comparison of a truly clear day with the data from November 17th shows the difference in the horizon. Figure 16 shows two LWIR images from the data collection activity at MRS. The left image is from November 16th, a completely clear day, while the image on the right is from November 17th. Note that the FOV's of the two images are not the same. For comparison, the green box in the left image outlines the approximate FOV of the right image. There is still a haze evident at the horizon. This haze is natural and expected, even on the clearest of days; the radiance will be higher toward the horizon and will decrease with increasing elevation angle. On the 17th, however, we believe that there is a thicker haze than is expected when compared with numbers from the clear day. The brightness temperatures for the clear day, shown at 903 cm^{-1} (the same channel as displayed for a cloudy day in Figure 13), are shown in Figure 17. On this clear day, approximate brightness temperature in the haze seems to indicate that 215K could be a valid threshold for cloud masking. Further investigation and understanding is still warranted.

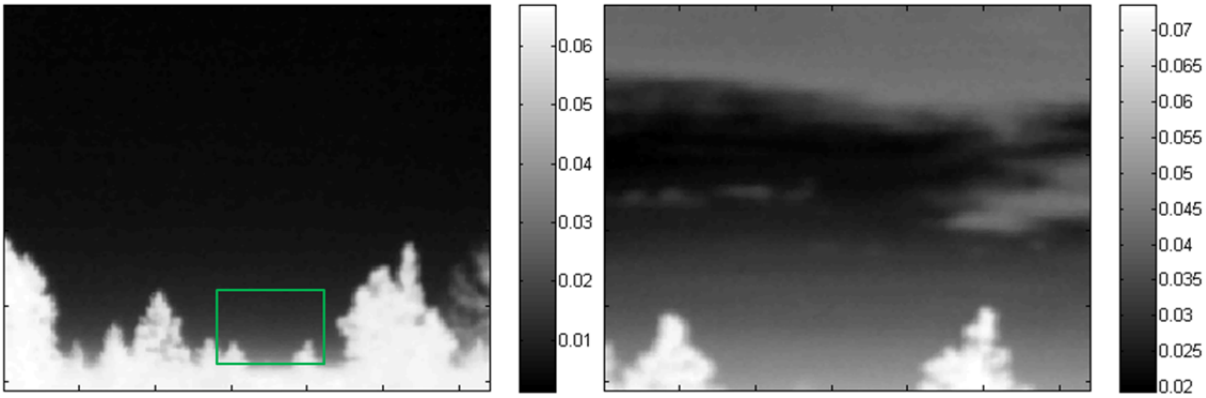

Figure 16. LWIR images from November 16, a clear day versus November 17, a cloudy day. Images shown are at 929.6 cm^{-1}. The radiance is scaled in W/m^2sr.

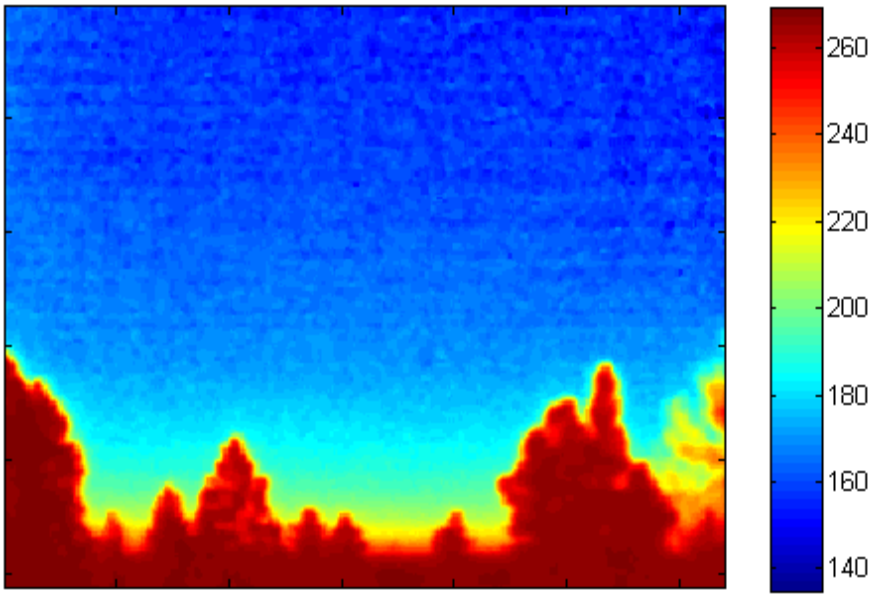

Figure 17. The brightness temperature of the sky on November 16, a clear day. Brightness temperature in Kelvin.

V. Conclusion

This paper presents a follow-on analysis to the SPIE paper[4] referenced regarding the atmospheric data collected over the Colorado Rockies, near Boulder, CO. Brightness temperature differences were used in the identification of clouds, as opposed to spectral features of clouds versus sky. When the clouds are removed using the cloud brightness temperature threshold values, the variability is almost eliminated. In addition, further spectral analysis from the SPIE paper of clear sky versus haze along and above the horizon, an area that was masked by the cloud brightness temperature threshold used here, showed that the variability is likely due to hazy clouds that are not apparent in the visible spectrum.

Although these studies have not shown the expected results as seen in simulations, some of the expected results could be masked by the noise threshold of the data collection instrumentation. It may still be possible to see mountain waves with the Hyper-Cam; there is much remaining data to be analyzed. However, we are in the process of identifying an instrument with at least an order of magnitude reduction in measurement noise, relative to the Hyper-Cam. The Hyper-Cam sensitive range is 870 to 1300 wavenumbers. Research has shown sensitive regions for detection of atmospheric temperature variations in the lower troposphere are specific narrow bands: 670-750, 1250-1450, 1580-1660, 1800-2100, and 2200-2350 wavenumbers.[5] This could lead to the design of new instruments optimized for detection of atmospheric turbulence. Lastly, even if the Telops Hyper-Cam is unable to detect the expected signal of a mountain wave, we expect that the turbulence associated with mountain waves may still be evident in the data from the D&P spectro-radiometer.

Acknowledgments

The NASA Aeronautics Research Mission Directorate (ARMD) Aviation Safety (AvSafe) Program, under the Atmospheric Hazard Sensing & Mitigation (AHSM) area within the Atmospheric Environment Safety Technologies (AEST) project, funded the research described here. In addition, the authors would like to thank personnel from the Mountain Research Station for their guidance and assistance with the data collection activity presented here.

References

[1]Gimmestad, G. G., Papanicolopoulos, C. D., Richards, M. A., Sherman, D. L., and West, L. L.; "Feasibility Study of Radiometry for Airborne Detection of Aviation Hazards." Funded by the NASA Aviation Safety Program Intelligent Integrated Flight Deck Project, (NASA/CR-2001-210855 under contract NAS1-99073), June 2001.

[2]West, L .L., Gimmestad, G.G., Smith, W .L., Kireev, S., Cornman, L. B., Schaffner, P. R.; Tsoucalas, G.: Applications of a Forward-Looking Interferometer (FLI) for the On-board Detection of Aviation Weather Hazards. NASA Technical Publication TP-2008-215536, Oct. 2008

[3]West, L. L., Gimmestad, G.G., Smith, W.L., Kireev, S., Daniels, T., Cornman, L., Sharman, R., Weekley, A., Perram, G., Gross, K., Smith, G., Feltz, W., Taylor, J., and Olson, E., "Hazard Detection Analysis for a Forward-Looking Interferometer." Final Report NASA/ NNX07AN17A, Oct 31, 2008.
[4]Lane, S. E., West, L. L., Gimmestad, G.G., Kireev, S., Smith, W.L., Burdette, E. M., Daniels T. S., and Cornman. L., "Hyperspectral Image Turbulence Measurements of the Atmosphere," *Proceedings of SPIE Infrared Imaging Systems: Design, Analysis, Modeling, and Testing XXIII*, Vol. 8355, Baltimore, MD, 2012.
[5]Daniels, T. S., Smith, W. L., and Kirev, S.: 2012, "Recent Developments on Airborne Forward Looking Interferometer for the Detection of Wake Vortices", AIAA-1302175, *4th AIAA Atmospheric and Space Environments Conference*, New Orleans, LA

REPORT DOCUMENTATION PAGE

Form Approved
OMB No. 0704-0188

1. REPORT DATE *(DD-MM-YYYY)*	2. REPORT TYPE	3. DATES COVERED *(From - To)*
01- 02 - 2014	Contractor Report	

4. TITLE AND SUBTITLE

Airborne Forward-Looking Interferometer for the Detection of Terminal-Area Hazards

5a. CONTRACT NUMBER

5b. GRANT NUMBER

NNX09AR67A

5c. PROGRAM ELEMENT NUMBER

6. AUTHOR(S)

West, Leanne; Gimmestad, Gary; Lane, Sarah; Smith, Bill L.; Kireev, Stanislav; Daniels, Taumi S.; Cornman, Larry; Sharman, Bob

5d. PROJECT NUMBER

5e. TASK NUMBER

5f. WORK UNIT NUMBER

648987.02.04.07.21

7. PERFORMING ORGANIZATION NAME(S) AND ADDRESS(ES)

NASA Langley Research Center
Hampton, Virginia 23681

8. PERFORMING ORGANIZATION REPORT NUMBER

9. SPONSORING/MONITORING AGENCY NAME(S) AND ADDRESS(ES)

National Aeronautics and Space Administration
Washington, DC 20546-0001

10. SPONSOR/MONITOR'S ACRONYM(S)

NASA

11. SPONSOR/MONITOR'S REPORT NUMBER(S)

NASA/CR-2014-218167

12. DISTRIBUTION/AVAILABILITY STATEMENT

Unclassified - Unlimited
Subject Category 03
Availability: NASA CASI (443) 757-5802

13. SUPPLEMENTARY NOTES

Final Report
Langley Technical Monitor: Philip R. Schaffner

14. ABSTRACT

The Forward Looking Interferometer (FLI) program was a multi-year cooperative research effort to investigate the use of imaging radiometers with high spectral resolution, using both modeling/simulation and field experiments, along with sophisticated data analysis techniques that were originally developed for analysis of data from space-based radiometers and hyperspectral imagers. This investigation has advanced the state of knowledge in this technical area, and the FLI program developed a greatly improved understanding of the radiometric signal strength of aviation hazards in a wide range of scenarios, in addition to a much better understanding of the real-world functionality requirements for hazard detection instruments. The project conducted field experiments on three hazards (turbulence, runway conditions, and wake vortices) and analytical studies on several others including volcanic ash, reduced visibility conditions, in flight icing conditions, and volcanic ash.

15. SUBJECT TERMS

Airborne; Aviation; Hazards; Imaging techniques; Interferometers; Radiometers; Safety; Spectrometers

16. SECURITY CLASSIFICATION OF:			17. LIMITATION OF ABSTRACT	18. NUMBER OF PAGES	19a. NAME OF RESPONSIBLE PERSON
a. REPORT	b. ABSTRACT	c. THIS PAGE			STI Help Desk (email: help@sti.nasa.gov)
					19b. TELEPHONE NUMBER *(Include area code)*
U	U	U	UU	349	(443) 757-5802